

Synthesis of Hexa-*peri*-hexabenzocoronenes

— *from Building Blocks to Functional Materials*

Dissertation

zur Erlangung des Grades

“Doktor der Naturwissenschaften”

am Fachbereich Chemie, Pharmazie und Geowissenschaften

der Johannes Gutenberg-Universität Mainz

vorgelegt von

Xi Dou

geboren in Shanxi, China, P. R.

Mainz 2008

Die vorliegende Arbeit wurde in der Zeit von Dezember 2004 bis Juni 2008 im Max-Planck-Institut für Polymerforschung in Mainz unter der Betreuung von Herrn Prof. Dr. K. Müllen ausgeführt.

Ich danke Herrn Prof. Dr. K. Müllen für seine wissenschaftliche und persönliche Unterstützung sowie für seine ständige Diskussionsbereitschaft.

Dedicate to my wife, Xie, Lei and parents

Table of Contents

1	INTRODUCTION	1
1.1	POLYCYCLIC AROMATIC HYDROCARBONS (PAHs)	3
1.2	CLAR’S SEXTET RULE AND “ALL-BENZENOID” PAHs	5
1.3	SYNTHESIS OF PAHs	7
1.3.1	INTRAMOLECULAR SCHOLL REACTION.....	10
1.3.2	SYNTHESIS OF OLIGOPHENYLENES VIA INTRAMOLECULAR DIELS-ALDER REACTION	11
1.3.3	SYNETHESIS OF OLIGOPHENYLENES VIA CYCLOTRIMERIZATION	13
1.3.4	SYNTHESIS OF OLIGOPHENYLENES VIA INTERMOLECULAR DIELS-ALDER REACTION	15
1.4	DISCOTIC LIQUID CRYSTALS	18
1.5	FROM VISUALIZATION OF SINGLE PAH MOLECULE AT THE INTERFACE TO SINGLE MOLECULAR DEVICES	22
1.6	AS SEMICONDUCTORS IN ELECTRONIC DEVICES	25
1.6.1	ORGANIC LIGHT EMITTING DIODES.....	25
1.6.2	PHOTOVOLTAIC CELLS.....	26
1.6.3	FIELD-EFFECT TRANSISTORS (FETs)	27
1.7	MOTIVATION AND OBJECTIVES	28
1.8	REFERENCES	33

2 NOVEL SYNTHESIS OF D_{2h} SYMMETRIC AND D_1 ASYMMETRIC DIHALIDE SUBSTITUTED HBC BUILDING BLOCKS	39
2.1 OLD SYNTHESIS PATHWAY TO D_{2h} SYMMETRIC DIBROMO HBC	40
2.2 NEW SYNTHESIS STRATEGY FOR D_{2h} SYMMETRIC HPBS.....	41
2.2.1 GENERAL METHOD AND REACTION MECHANISM	41
2.2.2 EXAMPLES OF SYNTHESIZED 1,4-DIODO-2,3,5,6-TETRA-ARYLBENZENES	43
2.2.3 CONDITION OPTIMIZATION OF STERICALLY HINDERED SUZUKI-MIYAJI CROSS-COUPLED REACTION	44
2.2.4 FROM 1,4-DIODO-2,3,5,6-TETRAARYLBENZENES 2-14 TO VERSATILE HPBS	47
2.2.5 LIMITATIONS IN THE PREPARATION FOR HBC DERIVATIVES	52
2.3 SYNTHESIS OF D_1 ASYMMETRIC DI-HALOSUBSTITUTED HBC BUILDING BLOCK VIA INTERMOLECULAR DIELS-ALDER REACTION	54
2.3.1 SYNTHESIS	55
2.3.2 STRUCTURE CHARACTERIZATION FOR THE PRODUCT AND SOME IMPORTANT INTERMEDIATES.....	57
2.4 SUMMARY	59
2.5 REFERENCES.....	61
3 MAGIC OF ELECTRON DONATING HETEROATOMS IN SCHOLL REACTIONS - UNEXPECTED PHENYL GROUP REARRANGEMENT	63
3.1 SYNTHESIS AND STRUCTURE VERIFICATION.....	64
3.2 PROPOSED MECHANISM FOR PHENYL GROUP REARRANGEMENT	72
3.3 PHASE BEHAVIOR OF LIQUID CRYSTALLINE 2-40	79
3.4 SUMMARY	84
3.5 REFERENCES.....	85

4	MOLECULAR DYNAMICS STUDIES OF DIPOLE FUNCTIONALIZED HBCS.....	87
4.1	SYNTHESIS	88
4.2	PHASE CHARACTERIZATION WITH DSC AND 2D WAXD	90
4.3	MOLECULAR DYNAMICS AND INTRAMOLECULAR STACKING STUDIES BY SOLID-STATE NMR.....	95
4.4	MOLECULAR DYNAMICS AND KINETICS STUDIES BY DIELECTRIC SPECTROSCOPY	100
4.4.1	BASIC BACKGROUND OF DIELECTRIC SPECTROSCOPY (DS).....	100
4.4.2	DYNAMICS INVESTIGATION WITH DIELECTRIC SPECTROSCOPY	103
4.5	SUMMARY	113
4.6	REFERENCES.....	114
5	SYNTHESIS OF DONOR-HBC-ACCEPTOR MOLECULES FROM <i>PARA</i>-IODO-BROMO-HBC BUILDING BLOCK AND THEIR SELF-ASSEMBLY BEHAVIORS STUDIES.....	117
5.1	SYNTHESIS	119
5.2	SELF-ASSEMBLY BEHAVIOR IN SOLUTION STUDIED BY ¹ H-NMR SPECTROSCOPY	121
5.2.1	TEMPERATURE DEPENDENT ¹ H-NMR SPECTROSCOPIC STUDIES.....	121
5.2.2	CONCENTRATION DEPENDENT ¹ H-NMR SPECTROSCOPIC STUDIES	124
5.2.3	TERMODYNAMIC STUDIES.....	126
5.3	SPECTROELECTRONIC SPECTROSCOPY	128
5.3.1	SELF-ASSEMBLY BEHAVIOR STUDIES	128
5.3.2	INTRAMOLECULAR CHARGE TRANSFER	133
5.3.2.1	Twisted intramolecular charge-transfer.....	133
5.3.2.2	Intramolecular charge transfer in 5-1 and 5-2	134
5.4	MOPHOLOGY OF MOLECULAR AGGREGATES OF 5-2 ON SURFACES	137
5.5	ENERGETIC LEVEL CHARACTERIZATION	140
5.6	BULK STATE CHARACTERIZATION.....	142

5.7	SUMMARY	144
5.8	REFERENCES.....	146
6	REINFORCED SELF-ASSEMBLY OF HBCS BY HYDROGEN BONDS	151
6.1	SYNTHESIS	153
6.2	SELF-ASSEMBLY BEHAVIOR IN SOLUTION	154
6.3	HYDROGEN BONDING INTERACTIONS AND SELF-ASSEMBLY BEHAVIOR IN THE BULK STATE.....	160
6.4	GELATION ABILITY TEST	167
6.5	SUMMARY	170
6.6	REFERENCES.....	172
7	SYNTHESIS AND SELF-ASSEMBLY OF MONO-FUNCTIONALIZED HBC DERIVATIVES ON SURFACES – APPROACHING MOLECULAR DEVICES.....	176
7.1	AZOBENZENE SUBSTITUTED HBCs.....	178
7.1.1	SYNTHESIS	178
7.1.2	TRANS / CIS PHOTOISOMERIZATION OF 7-1 AND 7-2 IN SOLUTION.....	180
7.1.3	STM STUDIES AT SOLID-LIQUID INTERFACES.....	186
7.2	MONO-SULFUR SUBSTITUTED HBCs AND THEIR SELF-ASSEMBLY ON AU (111) SURFACE	188
7.2.1	SYNTHESIS	188
7.2.2	STM STUDIES OF THE SELF-ASSEMBLED MONOLAYER ON AU (111) ELECTRODE.....	192
7.2.2.1	Monolayer formed by 7-3	192
7.2.2.2	Monolayer formed by 7-4	197
7.3	SUMMARY	201

7.4 REFERENCES.....	202
8 SUMMARY AND OUTLOOK	205
REFERENCES.....	211
9 EXPERIMENTAL DETAILS.....	212
APPENDIX I.....	262
SET-UP OF ATTENUATED MODEL (AK) FOR MOLECULAR AGGREGATION IN SOLUTION	262
PROGRAM USED FOR CURVE FITTING	265
ORIGINAL PROGRAM CODES.....	265
APPENDIX II.....	268
SINGLE CRYSTAL STRUCTURE DATA OF 5,11-BIS[4'-DODECYLPHENYL]-2,8- DIDODECYL-6,12-BIS[SPIRO(6'-OXO-CYCLOHEXA-1',4'-DIENE)-3']INDENO[1,2- B]FLUORENE (2-41):	268
ACKNOWLEDGEMENTS	295
CURRICULUM VITAE	297
LIST OF PUBLICATIONS	298

1 Introduction

Inorganic silicon and gallium arsenide semiconductors, silicon dioxide insulators, and metals such as aluminum and copper have been the backbone of the semiconductor industry for the past forty years.¹ However, there has been a growing research effort in “organic electronics” in the field of physics and chemistry for more than 50 years due to its expected low-costing, simpler processing and more physically robust properties in contrast to inorganic semiconductors. Up to only a short time ago, organic electronics and their optical phenomena have been the domain of fundamental research,^{2,3} somewhat far from practical application.^{4,5} The ability to modify chemical structures enables one to control the properties of the materials when deposited in thin films. Immense efforts have been devoted to improve the semiconducting, conducting, and light-emitting properties of organics (polymers, oligomers) and hybrids (organic-inorganic composites) through novel syntheses and fabrication techniques.^{6,7}

Among the organic semiconductors, the charge transporting properties of macromolecules, especially conjugated polymers, are the focus of many investigations. For totally disordered polymer films, the charge mobilities are small (in the range of 10^{-6} – 10^{-3} $\text{cm}^2/\text{V}\cdot\text{s}$).⁸ The mobilities significantly increase (up to about $0.6 \text{ cm}^2/\text{V}\cdot\text{s}$ in a recent report⁹) when the polymer chains self-assemble into ordered structures.^{10, 11} Some intensively studied polymers are listed in Figure 1-1.

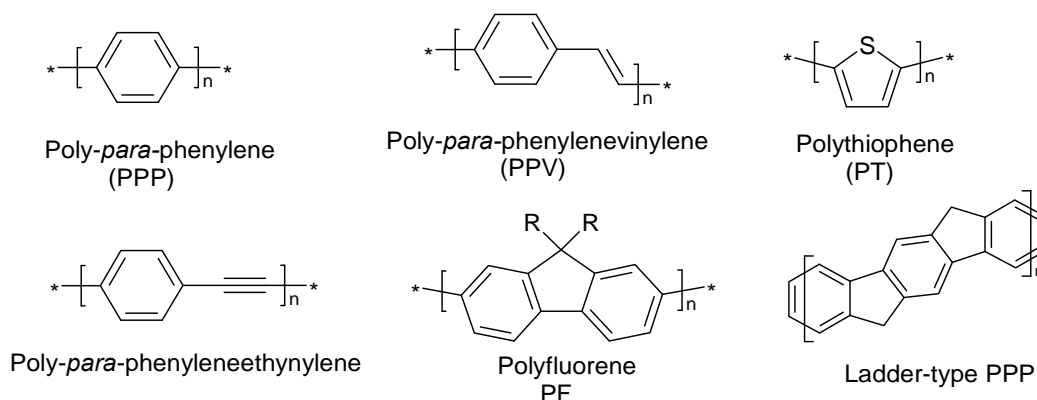


Figure 1-1. Some intensively studied organic polymeric semiconductors.

Another class of organic electronics materials is based on small molecules with defined molecular structure. Oligoacenes, especially pentacene, tetracene and derivatives exhibit excellent semiconductive properties.¹²⁻¹⁷ For example, triphenylamines have a long history as organic photoconductors in the Xerox industry⁸ and have been extensively used in organic light-emitting diodes (OLEDs) as hole transporting materials in the form of vacuum-deposited amorphous films.¹⁸ Tetrathiafulvalene (TTF) and derivatives were widely studied as donor entities in highly conducting charge-transfer salts^{19, 20} and their transport properties in thin films and crystals.²¹⁻²³ As one kind of liquid crystalline materials, discotic liquid crystals are composed of a two-dimensional, disc-like central conjugated cores substituted by saturated chains on the periphery. In their mesophase, the rigid aromatic cores separate from the attached flexible chains forming a quasi-one-dimensional columnar supramolecular structure via $\pi - \pi$ interactions, which originate from the overlapping of π orbitals between adjacent aromatic layers.^{24, 25} Such 1D columnar self-organization provide 1D pathways for electron and/or hole transport (the n- or p-type character can be tuned by the substituents). The representative systems are based on triphenylene, porphyrin, phthalocyanine, perylenediimide and hexabenzocoronene (HBC) cores (Figure 1-2). By enlarging the size of aromatic core, the intracolumnar charge carrier mobility increases from 0.26 cm²/V·s for triphenylenes,^{26, 27} over 0.67 cm²/V·s for phthalocyanines,²⁷ to 1.0 cm²/V·s for hexa-*peri*-hexabenzocoronenes,^{27, 28} which is comparable with amorphous silicon.²⁹

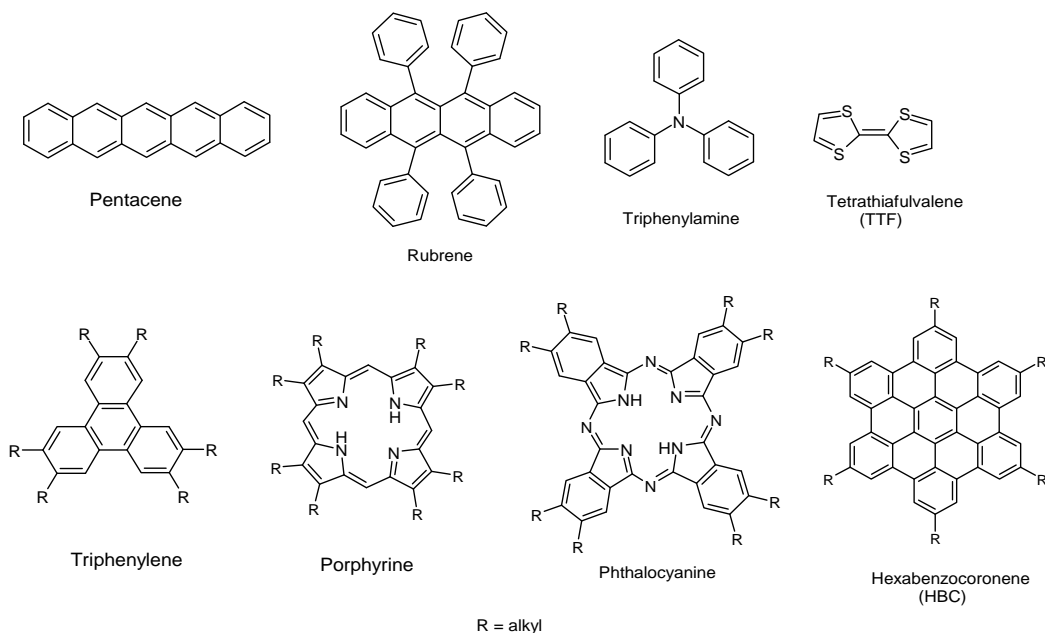


Figure 1-2. Selected organic molecular semiconductors.

1.1 Polycyclic Aromatic Hydrocarbons

When three of the four valence electrons in the carbon atom are equally shared covalently between another three carbon neighbors in a plane (forming σ -bonds) and the fourth is delocalized among all atoms (forming π -bonds), the resulting material is graphite. This sp^2 type of bonding builds a layered structure with strong in-plane bonds and weak out-of-plane bonding via van der Waals forces (Figure 1-3). The delocalization of π -electrons within these layers leads to a metallic conductivity, while the weak interlayer interaction results in graphite's lubricating properties. Although graphite is generally considered as an insulator along the direction perpendicular to those stacked layers, the inter sheet charge carrier mobility was found around $3 \text{ cm}^2/\text{V}\cdot\text{s}$,^{28, 30} which originates from optimized $\pi - \pi$ overlap of "aromatic sheets".

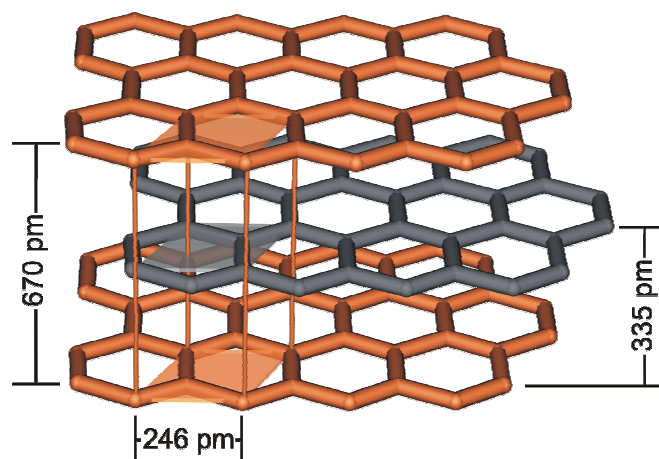


Figure 1-3. Schematic picture of graphite layered structure.

Polycyclic aromatic hydrocarbons (PAHs) can be regarded as subunits of 2D graphite sheet and they mostly serve as the central rigid aromatic cores in discotic liquid crystalline materials. PAHs were first discovered in coal tar in the middle of the 19th century,³¹ also found in the residues of domestic, incomplete combustion or pyrolysis of organic materials,^{32, 33} and even detected in comets.³⁴ This class of compounds has provoked intensive investigations both in organic synthetic chemistry and material science.³⁵⁻³⁸ Pioneers of the direct synthesis and characterization of polycyclic aromatics were R. Scholl³⁹⁻⁴² and E. Clar,⁴³⁻⁴⁷ who achieved the synthesis of numerous aromatic compounds under drastic conditions (at high temperatures in strong oxidant melts). Due to the limitation of analytic techniques of that time, only a limited number of relatively small-sized PAHs were isolated. As a result of enormous progress in analytical techniques, synthetic breakthroughs were achieved until recently, which allowed selective synthesis of various PAHs under mild conditions.⁴⁸

Depending upon the molecular structures, one class of PAHs exhibits much higher aromatic stability than their isomers containing the same number of rings. This kind of PAHs (all-benzenoid PAHs) represents only a small fraction of all the possible PAH isomers. For instance, there are only 17 kinds of all-benzenoid PAHs from the total of roughly 20600 possible alternating PAHs having between 4 and 10 fused benzene rings.⁴⁹ Although the all-benzenoid hydrocarbons are the minority in numerical terms, they are of special importance in both developing the theory of polycyclic aromatics^{38, 49, 50} and

forming stable columnar mesophases in discotic liquid crystalline materials. This kind of discotic liquid crystals are desirable in device processing due to their unique self-assembly and self-healing capability.⁵¹⁻⁵³

1.2 Clar's Sextet Rule and "All-Benzenoid" PAHs

In 1925 R. Robinson introduced a circle in a hexagon to describe the six identical π electrons in benzene.⁵⁴ It was claimed that the "*six electrons are able to form a group, which resists disruption*" and was called "*Aromatic Sextet*". However, the circle was not only used to depict benzene but also abused to represent all π electrons in other aromatics (i.e. every six-membered ring in the molecular structure was filled with such a circle) in the early time. For example, it stands simultaneously for six and four π electrons in naphthalene; six, two and six (or six, four and four) π electrons in anthracene; six, two and six π electrons in phenanthrene; and even zero π electrons in the central ring of perylene (Figure 1-4). E. Clar, later on, restricted the aromatic sextet symbolizing only six π electrons in a monocyclic system, which properly describes typical aromatic or benzenoid stability of PAHs.⁵⁵ According to Clar's sextet rule, the stability of aromatic isomers increases with the number of sextets.⁵⁵ This can be shown by comparing anthracene with phenanthrene. Anthracene has only one sextet, which is shared among all three rings, while two sextets exist in phenanthrene. Therefore, the aromatic energy of phenanthrene is 7 -12 kcal greater than that of anthracene.⁵⁶ However, this statement applies only to the whole molecule. While the rings marked with the sextet show benzenoid stability, the central ring has a double bond, which is different from the double bonds written in naphthalene and could be easily oxidized into phenanthrenequinone with chromium oxide in acetic acid.⁵⁷

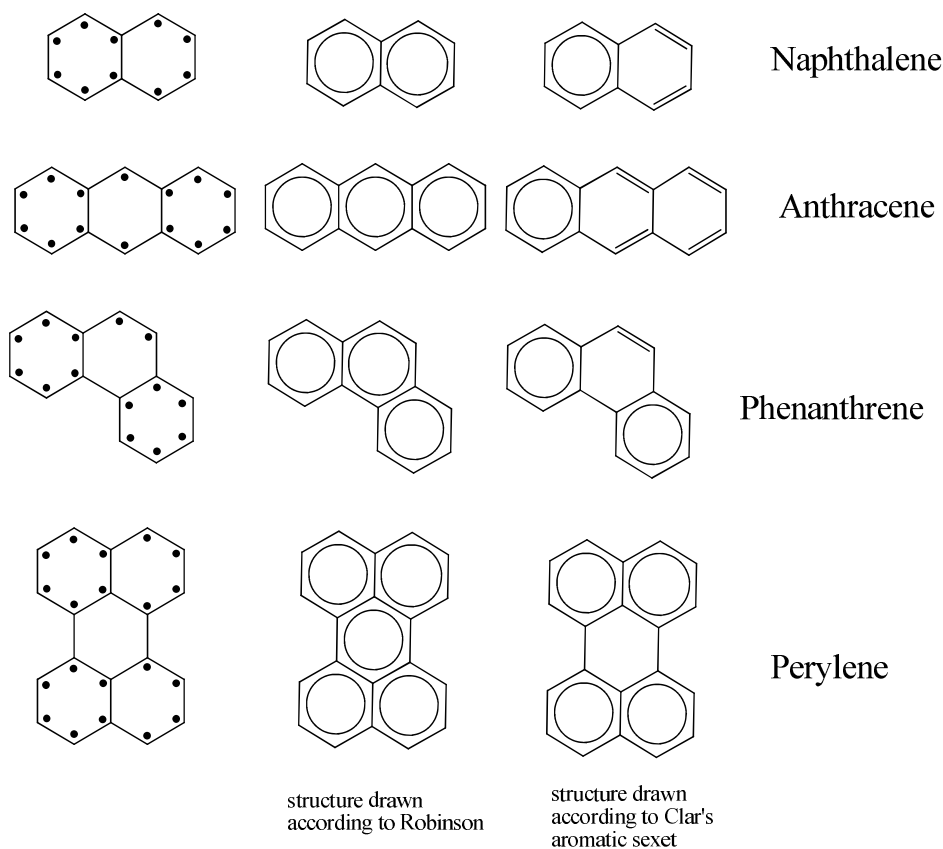


Figure 1-4. Aromatic sextet represents for some PAHs.

According to Clar's sextet rule, the hydrocarbons containing the maximum number of sextets show the highest stability among their isomers and are classified as all-benzenoid PAHs. Therefore, the number of π electrons in all-benzenoid PAHs must be the integer multiple of 6, which does not always follow Hückel's rule: $(2 + 4n)$ π electrons. The smallest all-benzenoid PAH, triphenylene (**1-1**), contains three sextets and one induced sextet (indicated by the arrows) in the central ring. Among the other *cata*-condensed isomers of triphenylene, one may draw at maximum two sextets in [4]-helicene (**1-2**), chrysene (**1-3**), benze[*a*]anthracene (**1-4**) and sole sextet in naphthacene (**1-5**) (Figure 1-5). Triphenylene (**1-1**) possesses a lower chemical reactivity and higher thermodynamic stability due to the largest resonance energy, the first ionization energy and the largest HOMO-LUMO gap within a molecular orbital description.^{52, 58} Triphenylene is colorless, while naphthacene is orange. Experimentally, triphenylene is not soluble in concentrated sulfuric acid and shows an intensive phosphorescence of long life time at low temperature in solution in contrast to its *cata*-condensed isomers.³⁵

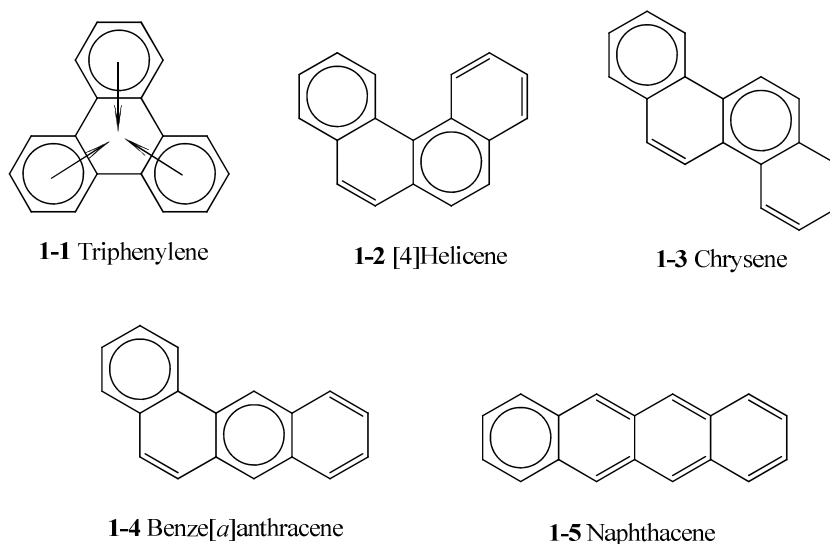


Figure 1-5. The smallest PAH, triphenylen and its *cata*-condensed isomers.

Although Clar's theory is concerning more chemical structural intuition than theoretical quantum principles, the qualitative concept was later confirmed by a wide variety of quantum mechanical studies.⁵⁹⁻⁶¹ Both experimental and theoretical studies suggested that Clar's aromatic sextet rule sketched a more realistic picture for all-benzenoid hydrocarbons.

1.3 Synthesis of PAHs

The synthesis of PAHs, however, is not easy, and becomes more difficult as increasing the ring numbers, in which the number of possible isomers grows at an even faster rate. There are two different methods to approach PAHs: i) one is the simultaneous production of a number of structures under drastic conditions in short unspecific synthesis, followed by the necessary isolation and structure determination, which has the advantage of yielding several different PAHs. This approach is more effective for small PAHs such as naphthalene, anthracene or phenanthrene, *etc.*, which can also be separated from coal tar^{62, 63} or side products of the catalytic hydrocracking of petroleum.⁶⁴ Figure 1-6 shows a more complex example, the four- and five-ring ketones (**1-6** and **1-7**) are reacted in the presence of zinc dust/zinc chloride/sodium chloride melt at 330 – 350 °C

resulting in a mixture of four ten-ring (**1-8** to **1-11**) and one eleven-ring (**1-12**) PAHs as major products.⁶⁵

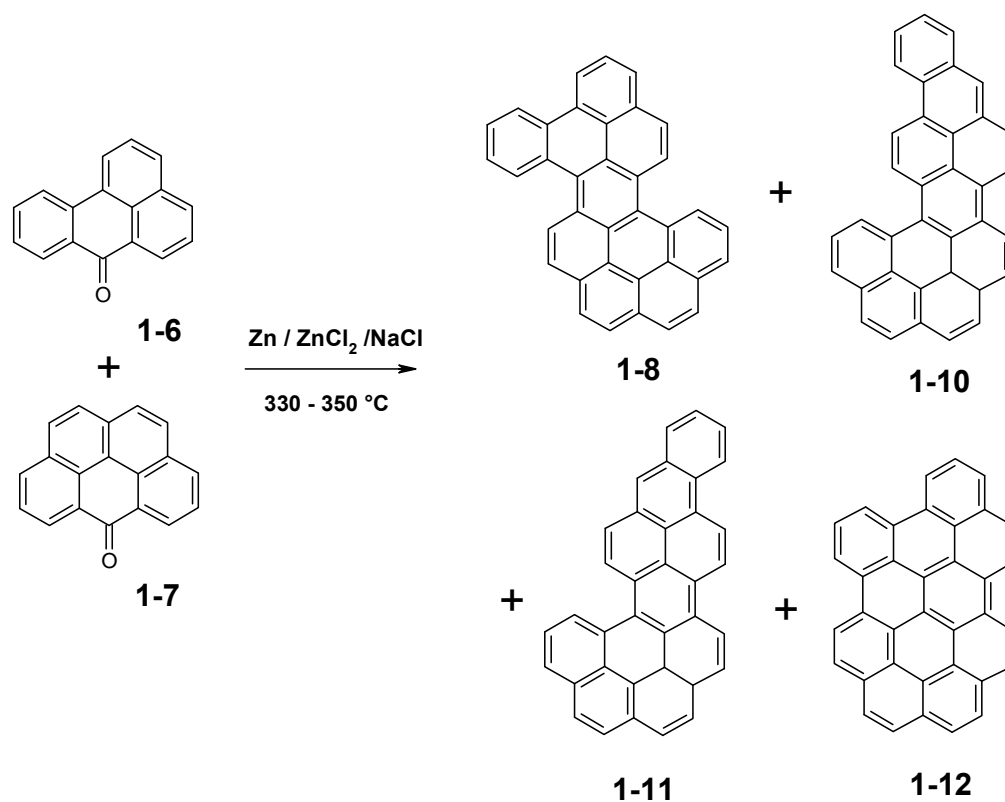


Figure 1-6. Mixed ketone condensation to produce new PAHs.

ii) The other method for the preparation of PAHs is more specific. It starts from simple compounds and employs series of discrete synthetic sequences, leading to the desired product. Due to the multiple synthetic steps, this method is not always “efficient”. Diedrich, F. et al. reported a full synthetic route for a thirteen-ring circumanthracene (**1-13**) in 1991 as exemplified in Figure 1-7.⁶⁶ The overall yield for such a ten-step synthesis is only 3.7 %. As with many multi-step synthesis, even high yields for each step can not prevent a low overall yield if the number of syntheses steps is large.

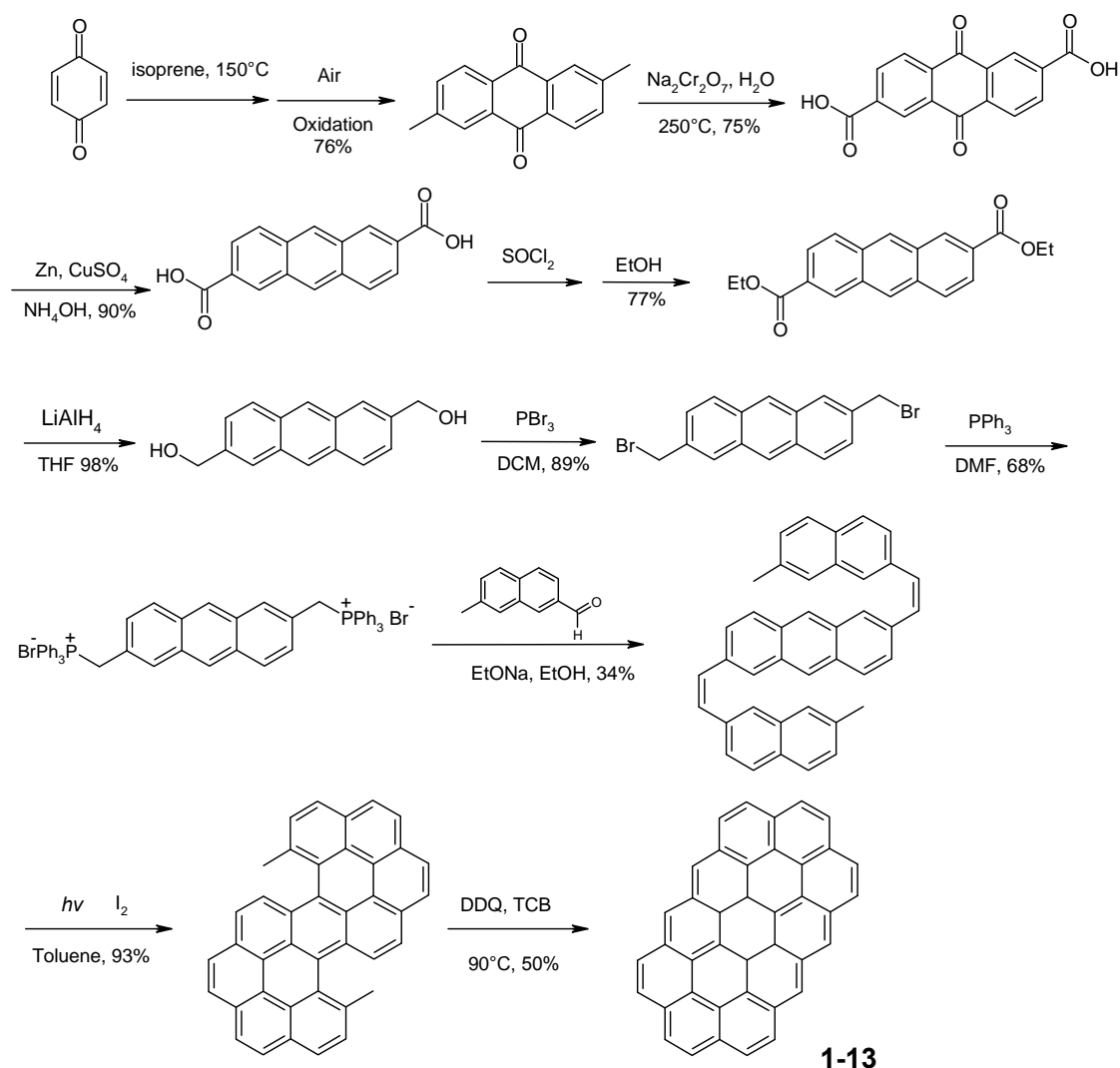


Figure 1-7. Synthetic route to circumanthracene (1-13).

Although the second strategy requires high synthetic efforts, it is preferred for the preparation of all-benzenoid PAHs. Since all-benzenoid PAHs possess $6n \pi$ electrons, oligophenylenes are suitable precursors for intramolecular cyclodehydrogenation reactions. On another aspect, the solubility of large PAHs decreases dramatically with increasing the size of the rigid aromatic cores, which hinders the purification, further chemical modifications, characterization, and processability. To circumvent such problems, a successful synthetic concept is to introduce flexible alkyl chains at the periphery of the rigid aromatic cores.^{67, 68} In so doing, large PAHs become accessible (which possess far better processability than their parent core structures). Also the

introduced soft alkyl substituents induce liquid crystalline behavior. Before further description of popular synthetic strategy for oligophenylenes, it is appropriate to give an overview of the final synthesis step to all-benzenoid PAHs, intramolecular cyclodehydrogenation reaction, which is also named after R. Scholl as Scholl reaction.

1.3.1 Intramolecular Scholl Reaction

In 1910, Scholl and Seer used aluminum(III)-chloride melts with atmospheric oxygen as oxidant to fuse biaryls, such as 1,1'-binaphthyl, to perylenes.³⁹⁻⁴² Subsequently, the intramolecular fusing of aromatic rings in the presence of Lewis acids was nominated as Scholl reaction. In 1960s, Kovacic used aluminum(III)-chloride and copper(II)-chloride as Lewis acid and oxidants to catalyze the formation of aryl-aryl bonds for the polymerization of benzene and its derivatives.⁶⁹⁻⁷¹ Later, he further optimized the reaction condition with iron(III)-chloride without other oxidants, which nowadays is the standard for a successful, highly selective, oxidative cyclodehydrogenation of oligophenylenes to PAHs.^{52, 72, 73} The modified conditions for intramolecular cyclodehydrogenation reaction avoided problems like dealkylation, migration of alkyl side chains, and dramatic chlorination of aromatic cores when stronger Lewis acids and oxidants were employed. Figure 1-8 gives an example for an intramolecular Scholl reaction, in which substituted hexaphenylbenzenes (**1-14**) were transformed to fully planarized HBC derivatives (**1-15**) with iron(III)-chloride in more than 90% yields. Although this reaction is powerful, the electron donating or withdrawing properties of substituents limit the varieties of functional groups in the later intramolecular cyclodehydrogenation step.⁷⁴⁻⁷⁶ For instance, nitrogen oxygen and sulfur direct attached HPBs do not always undergo the desired cyclodehydrogenation giving expected HBC derivatives. Trimethylsilyl group in **1-28** is easily cleaved under oxidative conditions. It, thus, has to be converted to halide (e.g. iodine, **1-30**) before being oxidized to hexa-iodo HBC (**1-31**), a practical HBC building block (Figure 1-10).

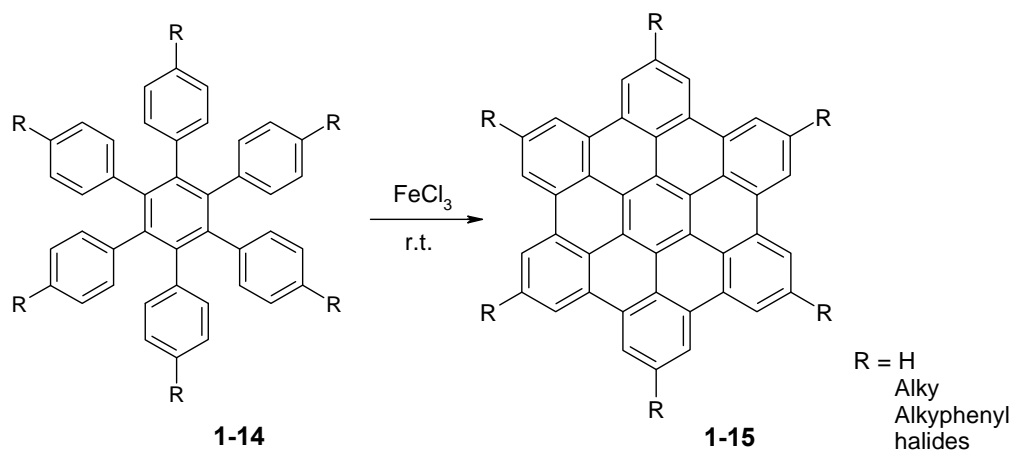


Figure 1-8. Intramolecular Scholl reaction in the presence of iron (III) chloride.

The preparation for suitable oligophenylene precursors in our group involves three different kinds of synthetic strategies: intramolecular Diels-Alder reaction with subsequent aromatization, cyclotrimerization and intermolecular Diels-Alder reaction with tetraphenylcyclopentadienone.⁷³

1.3.2 Synthesis of Oligophenylenes via Intramolecular Diels-Alder Reaction

Intramolecular [4+2] cycloaddition with suitable phenylenevinylene derivatives, followed by aromatization of the newly formed cyclohexene structures, offers a surprisingly simple route to oligophenylenes, further to extended aromatic hydrocarbons after an intramolecular cyclodehydrogenation step.^{77, 78} As illustrated in Figure 1-9, the phenylenevinylene precursors **1-16** and **1-17**, obtained via C-C coupling reactions, are heated in organic solvents, and the intramolecular Diels-Alder reaction yields quantitatively the corresponding cyclohexene derivatives (**1-18** and **1-19**). After a rearomatization with 2,3-dichloro-5,6-dicyano-1,4-benzoquinone (DDQ), the produced oligophenylenes (**1-20** and **1-21**) can further be oxidized into corresponding PAHs (**1-22** and **1-23**) via intramolecular cyclodehydrogenation reaction.

Nevertheless, the formation of oligophenylenes, particularly the alkyl-substituted derivatives, by intramolecular [4+2] cycloaddition requires suitable phenylenevinylene precursors, which are difficult to obtain. In addition, only certain topologies are accessible. Thus, it is rarely used in oligophenylene synthesis.⁷³

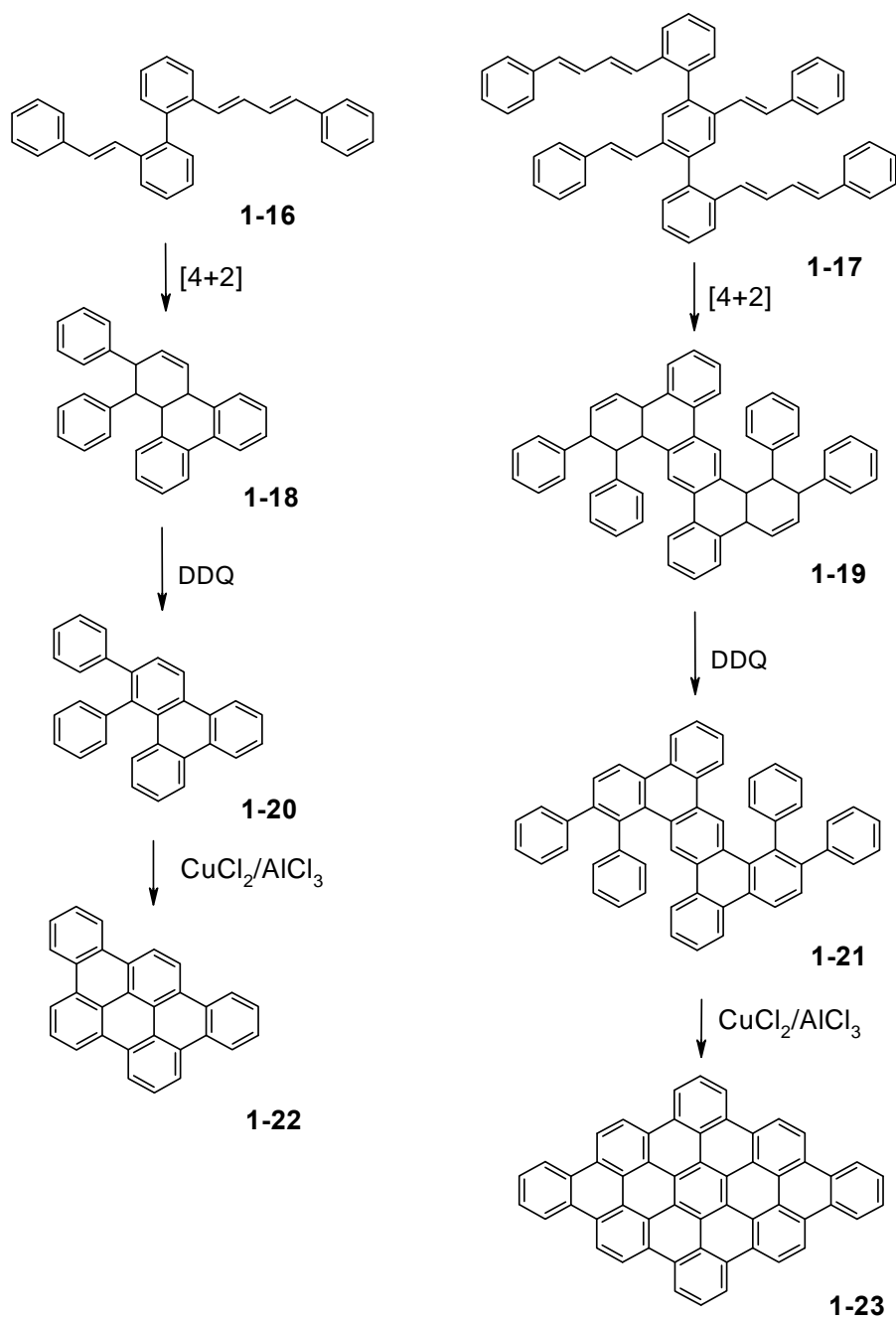


Figure 1-9. Formation of oligophenylenes via intramolecular Diels-Alder reaction with phenylenevinylens.

1.3.3 Synthesis of Oligophenylenes via Cyclotrimerization

Cobalt-catalyzed cyclotrimerization of symmetric diphenylacetylenes (**1-24**) is an efficient synthesis towards symmetrically six-fold substituted oligophenylenes. Alkyl chains, as well as certain functional groups, could be easily introduced to diphenylacetylene leading to hexaphenylbenzenes (**1-14**) and further to HBCs (**1-15**) (Figure 1-10). However, only symmetric diphenylacetylenes were widely used since asymmetric diphenylacetylenes (**1-25**) will result in 1,3,5- and 1,2,4-isomers (**1-26** and **1-27**), which are difficult to separate.

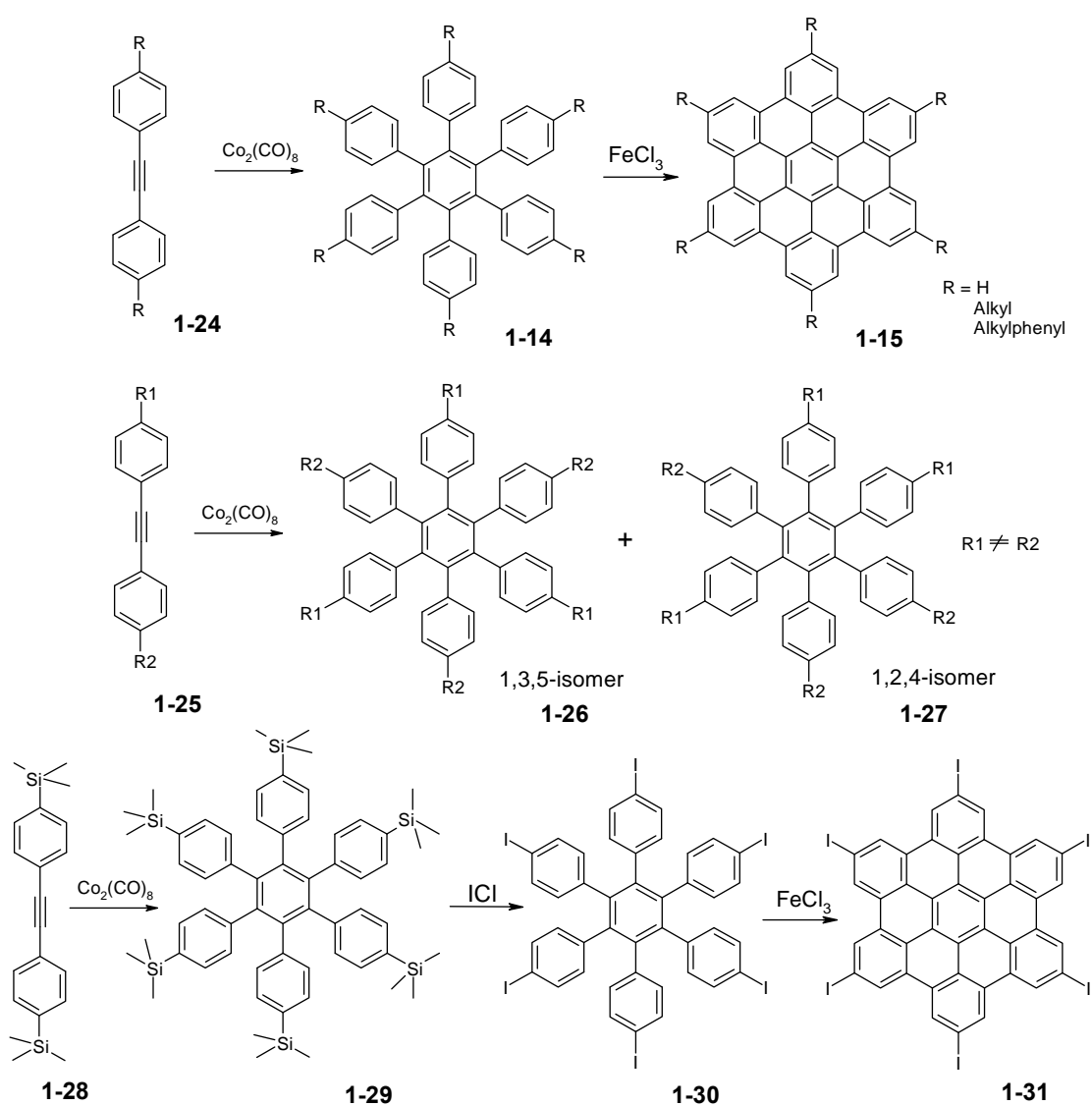


Figure 1-10. Route to hexaphenylbenzenes by cobalt-catalyzed cyclotrimerization.

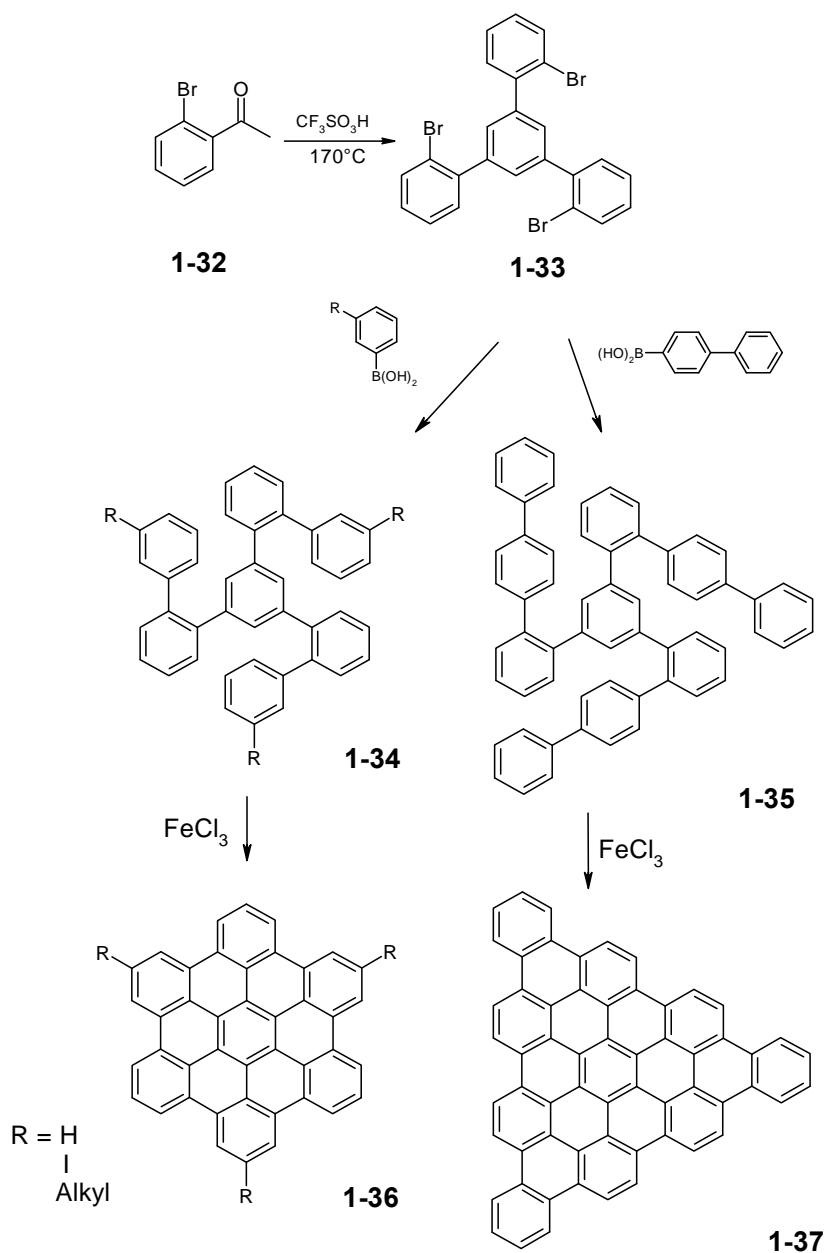


Figure 1-11. Lately developed synthesis route to D_{3h} -symmetric and triangle shaped oligophenylenes.

Recently, a new synthesis of D_{3h} -symmetric HBCs was developed, which is based on trifluoromethanesulfonic-acid-mediated trimerization of 2-bromoacetophenone (**1-32**) affording 1,3,5-tri(2'-bromophenyl) benzene (**1-33**). After applying palladium-catalyzed aryl-aryl coupling reactions and intramolecular cyclodehydrogenation, the topology of

PAHs could be changed from D_{3h} -symmetric HBCs (**1-36**) to triangle-shaped PAHs (**1-37**) containing 60 carbon atoms^{79,80} (Figure 1-11).

1.3.4 Synthesis of Oligophenylenes via Intermolecular Diels-Alder Reaction

For oligophenylenes of lower symmetry, the intermolecular Diels-Alder reaction is a more efficient and widely used method. When diphenylacetylene (**1-25**) and substituted tetraphenylcyclopentadienones (**1-38**) are mixed in high boiling temperature solvents, an intermediate Diels-Alder [4+2] adduct is formed, which extrudes *in situ* carbon monoxide at evaluated temperature (200 – 205 °C) to give the corresponding hexaphenylbenzene (**1-39**)⁷⁹⁻⁸¹ (Figure 1-12).

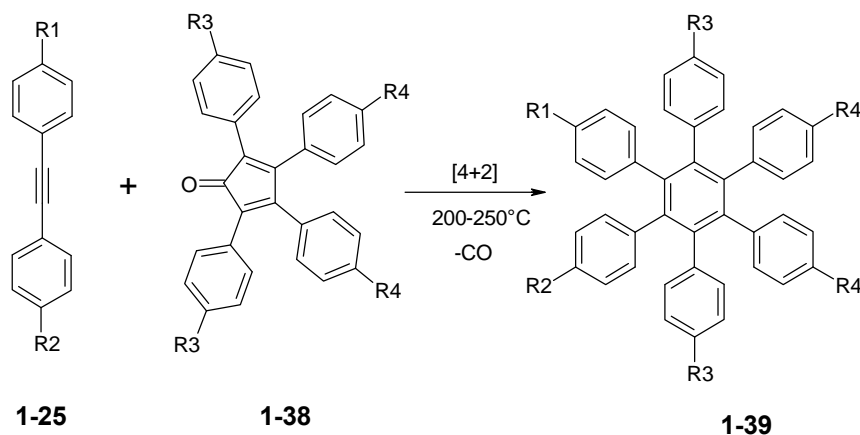


Figure 1-12. Intermolecular Diels-Alder reaction for the synthesis of hexaphenylbenzene.

Since R1, R2, R3 and R4 could respectively be introduced at an early synthetic stage, hexaphenylbenzenes with various symmetries become accessible, which increases the versatility of functionalized HBCs. In general, halides can be introduced at specific periphery positions on the HBC aromatic core as important functional groups for further modification via transition meta-catalyzed coupling reactions. In this way, a series of low symmetric functionalizable HBC building blocks can be prepared⁸² (Figure 1-13). Depending on the relative position of functional substituents, the nomenclature of “*ortho*”, “*meta*” and “*para*”, in analogy to benzene, is declared regarding HBC as “superbenzene”. The synthesis of HBC building blocks will be discussed in a greater detail in CHAPTER 2.

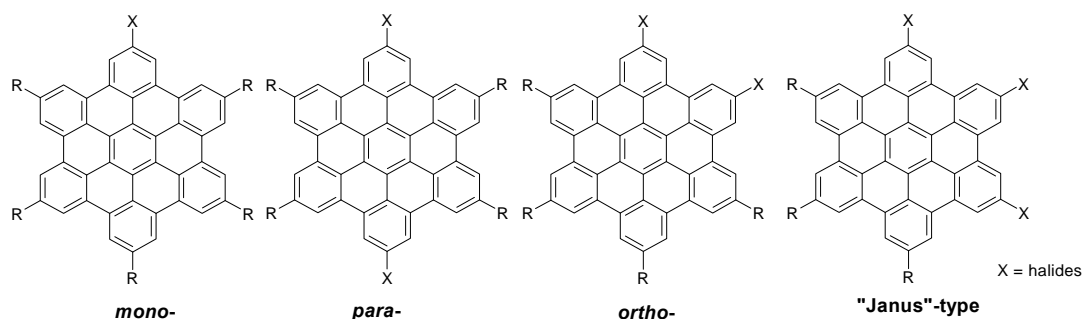


Figure 1-13. Versatile HBC building blocks.

By modifying the topology of cyclopentadienone and corresponding diphenylacetylenes, extended all-benzenoid PAHs with different topologies were prepared. For example, C₆₀ (**1-40**),⁸³ C₇₈ (**1-41**),⁸⁴ C₉₆ (**1-42**),⁸⁵ C₇₂ (**1-44**),⁸⁷ and C₁₃₂ (**1-43**)⁸⁶ PAHs were prepared in such synthetic strategy. By combining intermolecular Diels-Alder reaction and cyclotrimerization, the number of carbon atoms of the aromatic core were even extended up to 222 (**1-45**),⁷² which is the largest reported PAH prepared in a bottom up way (Figure 1-14).

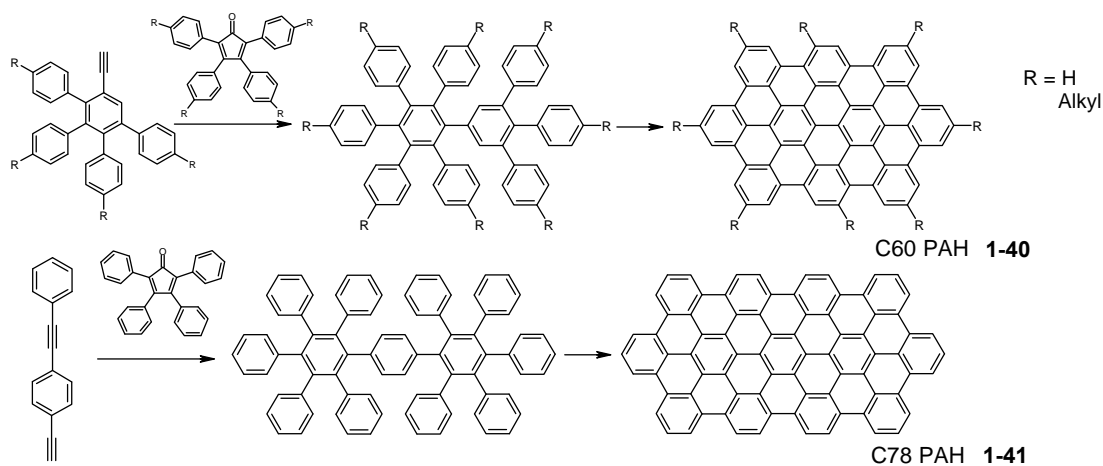


Figure 1-14. Synthesis of extended all-benzenoid PAHs via intermolecular Diels-Alder reaction.

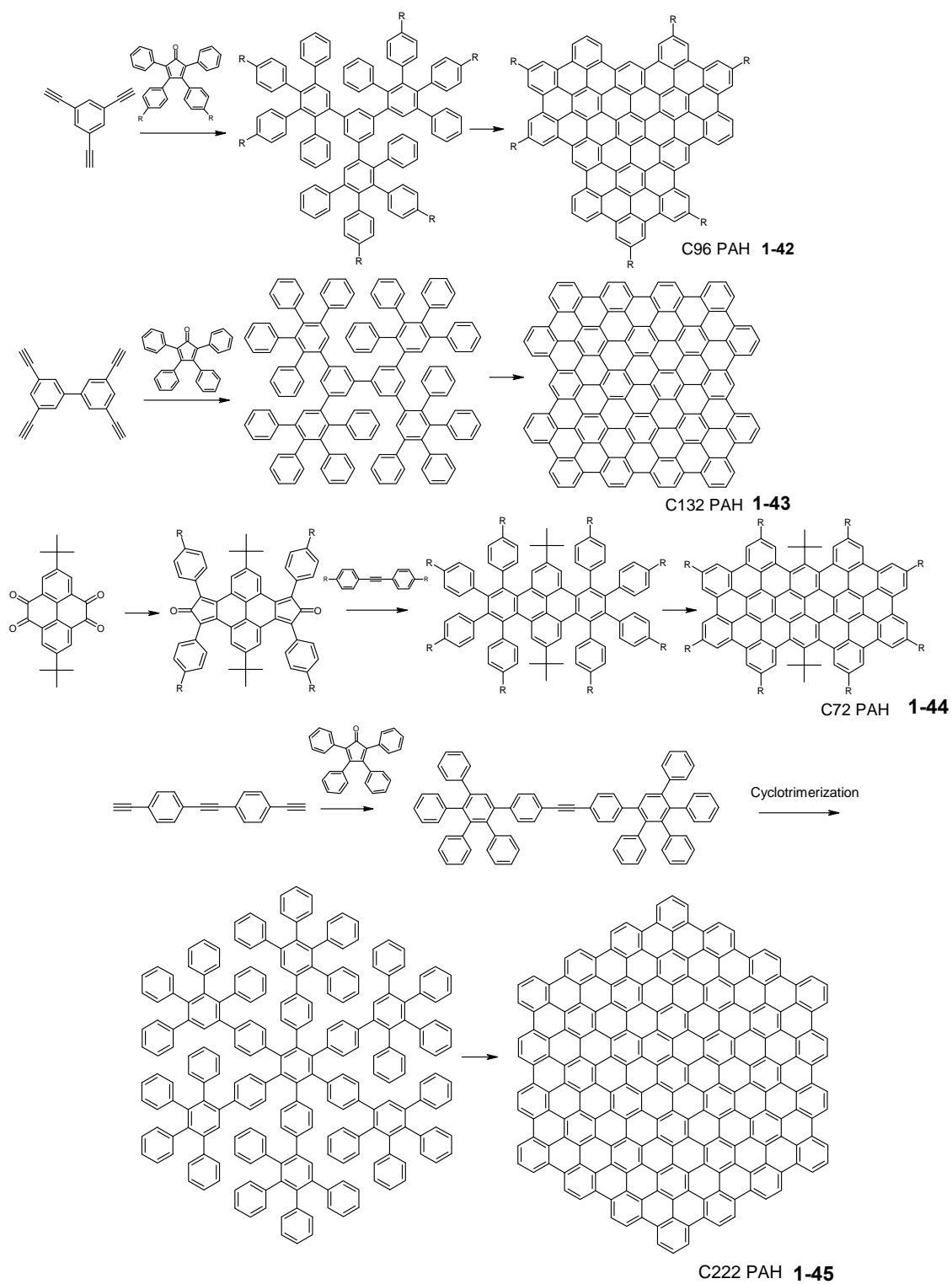


Figure 1-14. (continue)

1.4 Discotic Liquid Crystals

Liquid crystals (LCs) are materials which show both liquid and crystalline phase properties. In 1888 F. Reinitzer discovered the first liquid crystal phase behavior. He observed cholesteryl benzoate to show two distinct melting points⁸⁸. Upon heating, that kind of material melted first into a hazy liquid at 145.5 °C and further became clear at 178.5 °C. From then on, immense research efforts have been invested resulting in daily-used LC materials. S. Chandrasekhar was the first to use the term “mesophase” to describe the state between liquid and crystal of benzene-hexa-*n*-alkanates, the first discovered discotic LC molecule, in 1977.⁸⁹ In this phase, the material shows both liquid-like, “easily deformable (certain mobility)” characters and crystal-like, “(not-long-range) optical anisotropic” features. One distinguishes the thermotropic LCs, for which the formation of the mesophase is temperature dependent, and lyotropic LCs, the mesophase of which is formed from a multi-component mixture including solutes (providing crystalline features) and certain amount of solvents (filling the space around compounds to provide fluidity).

The molecules of thermotropic LCs generally consist of a rigid core (often aromatic) surrounded by flexible substituents. According to the shape of the rigid moiety of the molecule, it was subdivided to calamitic LCs (with a rod-like rigid core) and discotic LCs (with a disc-like rigid core).⁵¹ Depending on the nature of aromatic centers and flexible substituents, the discotic LCs show three types of mesophases with different degrees of order: discotic columnar (Col_h), discotic nematic (N_d) and discotic lamellar phases as illustrated in Figure 1-15.⁹⁰ The columnar phase consists of discs stacked one on top of the other to form pseudo one-dimensional columns, the different columns forming a two-dimensional lattice. Several variants of the columnar structure have been identified – upright columns, tilted columns (Figure 1-15d), hexagonal lattice (Figure 1-15a), rectangular lattice, *etc.* In some cases, the columns are liquid-like, i.e. their molecular centers are irregularly spaced within each single column as depicted in Figure 1-15e; while in others they are arranged in a regular, ordered fashion (Figure 1-15f). The discotic nematic phase (Figure 1-15b) has the lowest degree of order showing one-

dimensional order. The discotic lamellar phase (Figure 1-15c), however, has not been completely elucidated.

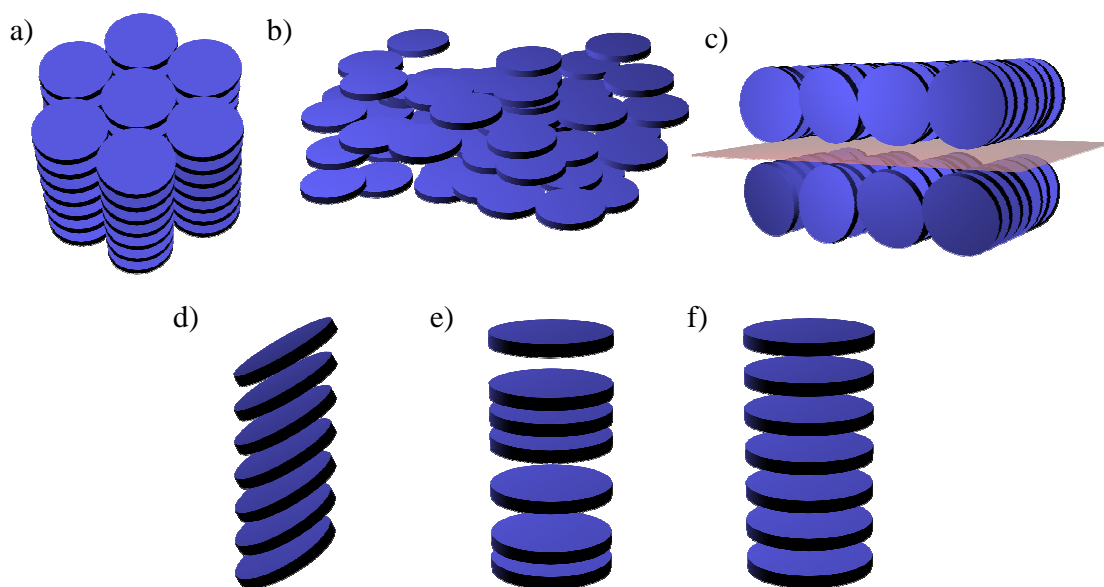


Figure 1-15. Schematic represents of mesophase of discotic LCs. a) hexagonal discotic columnar phase (Col_h); b) discotic nematic phase (N_d); c) discotic lamellar phase; d) tilted, e) disordered and f) ordered molecular disc packing within a single column.

The columnar arrangement of discotic LCs is a promising structure for anisotropic transport of charge carriers along columnar direction due to the considerable overlap of π orbitals between adjacent aromatic cores. They are recognized for their potential applications in photovoltaic devices, field effect transistors (FETs), light-emitting diodes (LEDs) and other molecular electronics.⁹¹ Figure 1-16 gives some examples of the most intensively investigated discotic LCs. As the size of the aromatic core increases, the enhanced $\pi - \pi$ overlap stabilizes the columnar supramolecular structure, which consequently leads to a broader and more stable mesophase. In the case of hexabenzocoronenes (HBCs, **1-52**), the high intrinsic charge carrier mobility is ascribed to the large discotic aromatic center, the diameter of which is about 1.4 nm, approximately three times the size of triphenylene. This relatively large size of molecular discs qualifies them as promising semi-conducting materials in organic devices.^{28,92} Both synthetic strategy and understanding of the structure-property relationships have been the

subjects of intensive investigation in Müllen's group since the first hexa-alkylated HBC was synthesized by Herwig in 1995.⁹³ (see also SECTION 1.3)

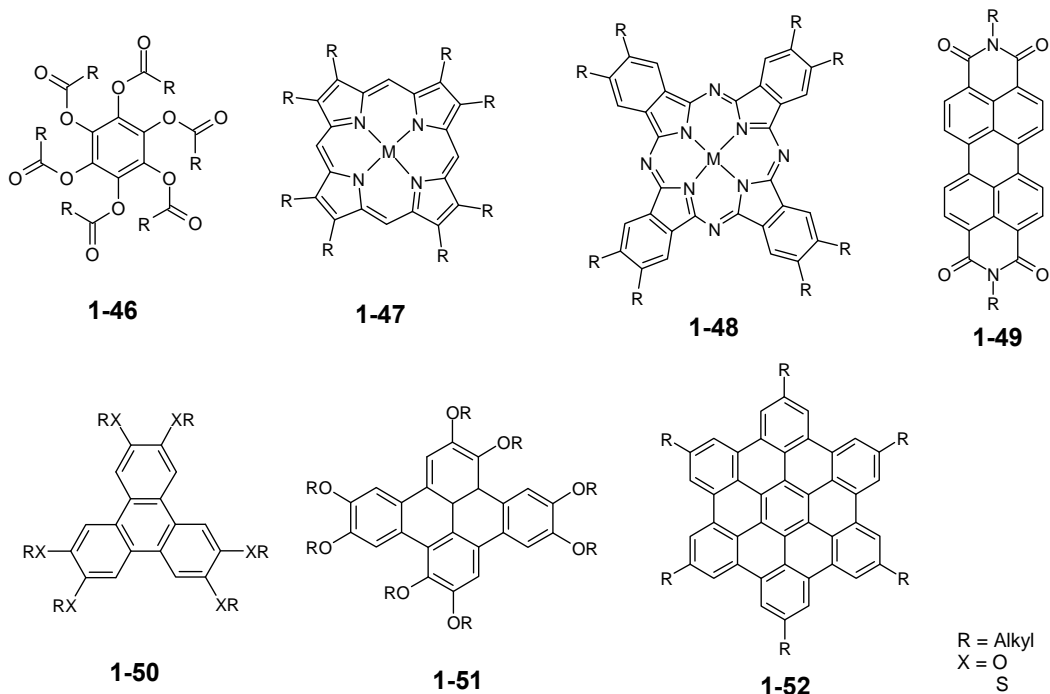


Figure 1-16. Some examples of discotic LC molecules.

Depending on the substituents, alkyl substituted HBCs change from “plastic crystalline” phase over columnar liquid crystalline phase to isotropic liquid upon increasing temperature. In the “plastic crystalline” phase, the degree of crystallinity of both flexible substituents and the rigid aromatic core reduces the mobility of molecules resulting in a tilted disc packing with respect to the column axis. The tilting of the discs disappears in the mesophase accompanied by a fast rotation around the columnar axis. The crystalline feature is completely overwhelmed when the material enters the isotropic phase, in which molecules behave like normal liquids. The phase transitions are depicted in Figure 1-17.

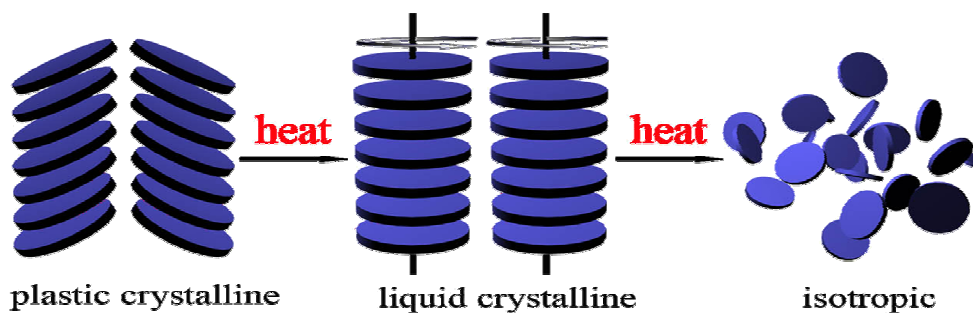


Figure 1-17. Schematic representation of different phases of HBCs.

The phase behavior of LCs is generally characterized by differential scanning calorimetry (DSC), polarized optical microscopy (POM), and X-ray diffractometry (XRD). DSC shows the transition temperatures and enthalpies between different phases. The type of mesophase could be assigned according to the appearance of a specific birefringence of the optical texture by using POM. The crystalline characters of the compounds in both crystalline phase and mesophase could be reflected by XRD method. Additionally, solid state NMR spectroscopy is a useful tool to understand the packing mode on a molecular level.^{94, 95}

Two-dimensional wide angle X-ray diffractometry (2D-WAXD) is a powerful method for the characterization of both columnar stacking and molecular packing within a single column. It is applied to a pre-organized fibrillar sample, which is extruded through a pinhole at high temperature (depending on the phase transition temperature of corresponding material), whereby the molecular discs adopt a columnar arrangement parallel to the extrusion direction resulting in macroscopically oriented supramolecular arrangement (Figure 1-18A). During the measurements, the incident X-ray beam passes the sample fiber perpendicularly giving a 2D diffractogram with information about molecular ordering (Figure 1-18A). The characteristic reflexes are summarized in Figure 1-18B. The peaks along equatorial direction in the inner part (Figure 1-18B, a) represent the 2D columnar arrangement in the plane perpendicular to the extrusion direction. The disordered flexible alkyl substituents give a “halo” ring with homogeneous reflection intensity (Figure 1-18B, b). The molecular packing within a single column is reflected by the peaks along the direction parallel to the filament. The intracolumnar periodic distance

is recorded by the reflexes along meridional axis (Figure 1-18B, c). If the disc is tilted with respect to the columnar direction, extra diffraction peaks appear in diagonal directions (Figure 1-18B, c'), which provide the cofacial distance between adjacent molecular discs within a single column. As indicated in Figure 1-18C, the tilting angle ϕ could also be estimated by the two distances, which is in good agreement with the value obtained from solid state NMR studies.⁹⁵

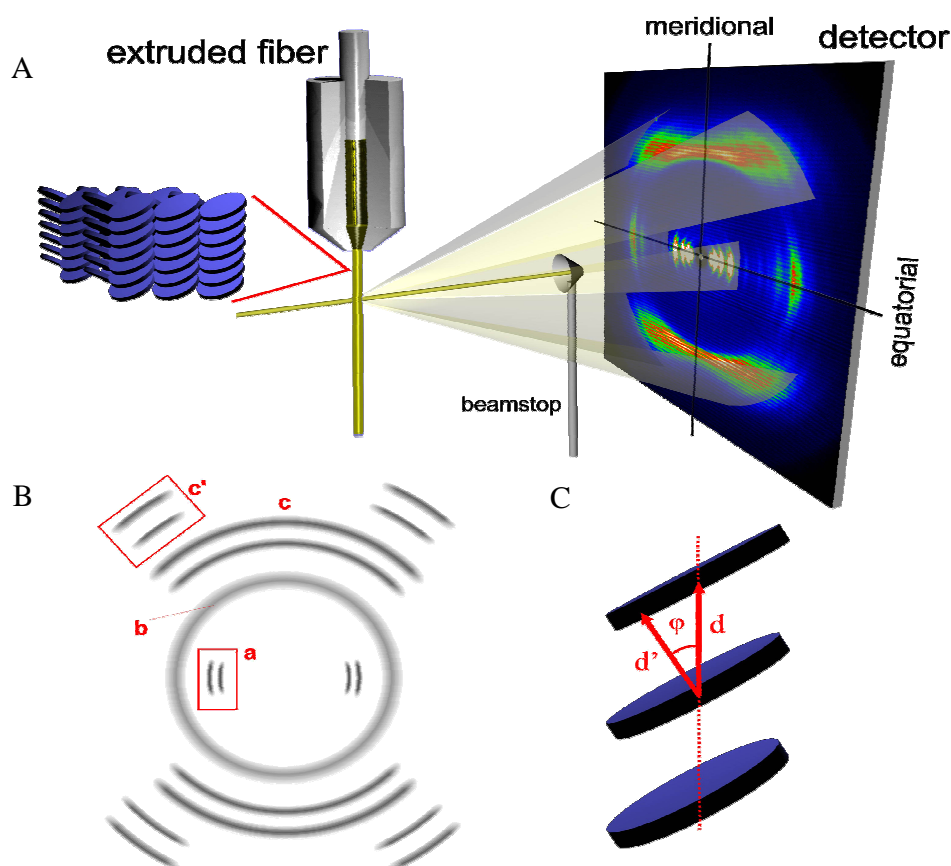


Figure 1-18. Schematic represent of A) experimental setup, B) 2D-WAXD pattern with typical reflexes (a, b, c, c') and C) intracolumnar arrangement with tilted discs.

1.5 From Visualization of Single PAH Molecule on Surface to Single Molecular Devices

In 1981G. Binnig and H. Rohrer developed scanning tunneling microscope (STM) based on the tunneling effect from quantum mechanics.⁹⁶ STM is nowadays a powerful

technique for visualization of surfaces at the atomic level. When a conducting tip is brought very close to a metallic or semiconducting surface, a bias between the two can allow electrons to tunnel through the gap in between. With low voltages, this tunneling current is a function of the local density of states (LDOS) at the Fermi level, E_f , of the sample.⁹⁷ Variations in current are translated into an image as the probe passes over the surface. For STM, good resolution is considered to be 0.1 nm laterally and 0.01 nm in depth.⁹⁸ The STM technique can be used in ultra high vacuum (UHV) as well as in air and various other liquids or gases. Temperatures ranging from near 0 K to a few hundred degrees Celsius can be applied.⁹⁷

STM provides a visual structure proof of single molecules. After UHV-sublimation of the thermally stable compound **1-23** onto a {001} face of a molybdenum sulfide single crystal, STM depicted the profile of single molecules, which has exactly the shape according to the molecular structure.⁷⁸ The image of single HBC molecules was recorded on a highly ordered pyrolytic graphite (HOPG) interface⁹⁹ (Figure 1-19).

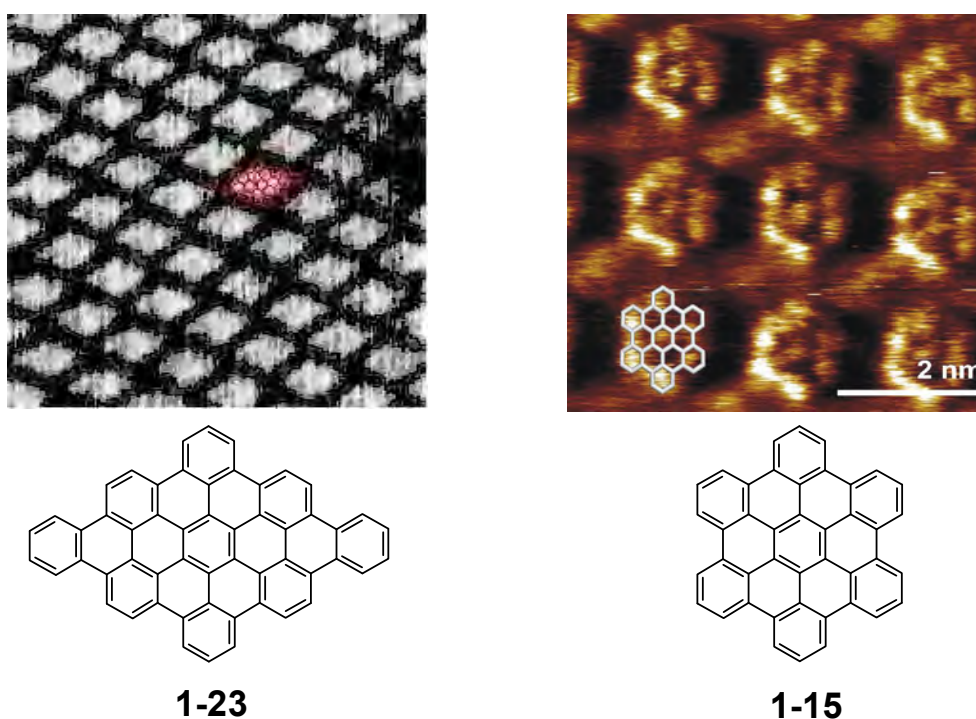


Figure 1-19. STM images of some PAHs.

Beyond the visualization of molecules on surfaces, STM can be used for the research towards single molecular devices. For example, Rabe *et. al.* proposed a prototypical single-molecule chemical-field-effect transistor (single-molecular CFET), in which the tip of the scanner serves as the source electrode and the semi-conductive substrate as the drain electrode. Through the introduction of a nanometer-sized charge transfer complex (gate electrode) which are covalently linked to the molecule in the STM junction, the tunneling current through a hybrid-molecular diode is modified¹⁰⁰ (Figure 1-20).

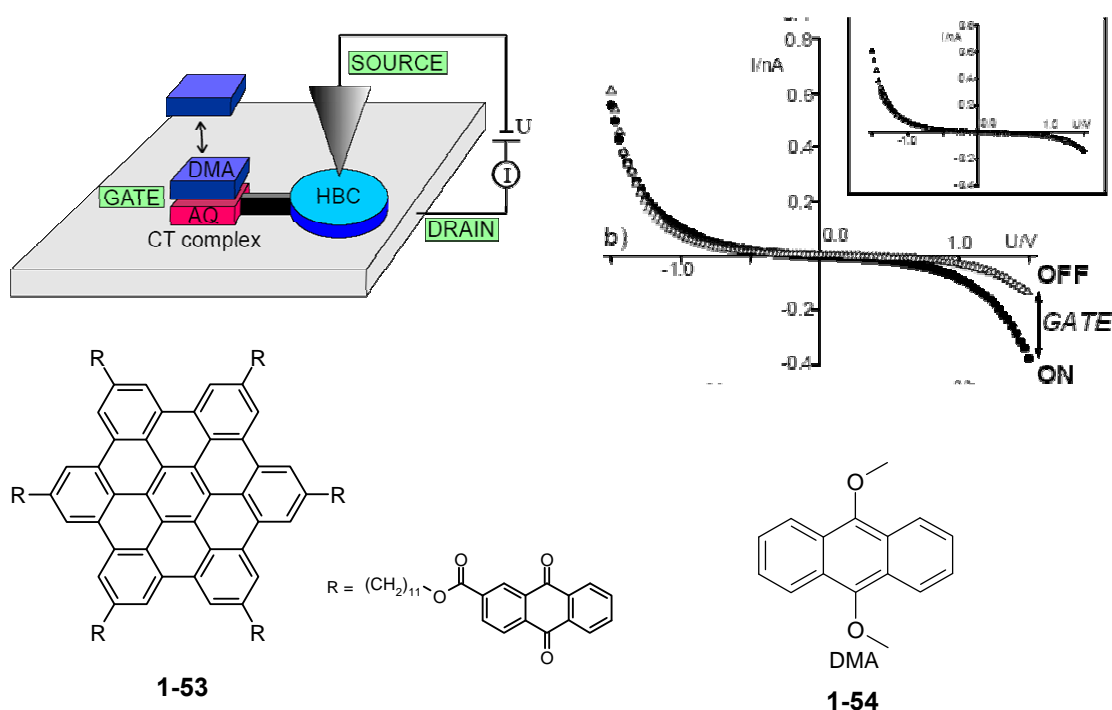


Figure 1-20. Schematic represents for single-molecule CFET and molecular structure of used molecules.

During the measurement, HBC derivative **1-53** with six electron acceptor substituents (anthraquinone) was deposited at a liquid-graphite interface and the tunneling current was recorded by scanning tunneling microscopy and spectroscopy (STS) measurements. As the donor molecule 9,10-dimethoxyanthraquinone (DMA) **1-54** got onto the interface, it formed charge transfer (CT) complexes with anthraquinone moiety (DMA-AQ-CT). The newly formed dipoles at the interface shifted the Fermi level of the

substrate and the adsorbate's molecular orbitals, which subsequently changed not only the tunneling current but also the unit cell of the molecular pattern at the interface.⁹⁹

In the devices based on a single molecule or a self-assembled monolayer (SAM), the HOMO-LUMO band gap of the bridge molecule plays a crucial role in the conductivity of the molecular bridged metal-molecule-metal junction on one hand.¹⁰¹ On the other hand, the formation of a uniform SAM on metal surfaces is also very important. HBCs have a small HOMO-LUMO band gap¹⁰² and excellent self-assembly ability, which makes them good candidates in the preparation of molecular devices. Rampi *et al* have successfully assembled Au-C₁₈//C₁₈-Hg (C₁₈ represents a SAM formed by octadecanethiol), Au-HBCS//C₁₈-Hg (HBCS represent a SAM formed by HBC with thiol functional group), and Au-HBCS//HBCS-Hg junction. The study concluded that HBC units are nearly transparent to electrons in comparison with the aliphatic chains and these molecules can act as active components in nanometer-scale transistors.¹⁰³

1.6 As Semiconductors in Electronic Devices

Discotic liquid crystalline materials have been intensively investigated as semiconductors in organic electronic devices. For their application in electronic devices, they were widely tested as active components in organic light-emitting diodes (OLEDs), photovoltaic cells and field-effect transistors (FETs).^{6, 91, 104} Compared with other mesogens, HBCs have larger aromatic rigid cores, which results in a larger overlap of π orbitals between adjacent aromatic rings and consequently to higher one-dimensional charge carrier mobility. Alkyl or alkyphenyl substituted HBCs showed the highest charge carrier mobility (up to 1.13 cm²/V·s) accompanied with high ordering and good solubility for device processing.²⁷

1.6.1 Organic Light Emitting Diodes

A simple OLED consists of a transparent anode and a metallic cathode with a thin organic film in between. Electrons and holes respectively are injected into the lowest unoccupied molecular orbital (LUMO) and the highest occupied molecular orbital

(HOMO) of the active organic material after applying a voltage between the electrodes. The electrons and holes drift in the organic layer under the external electric field until they combine with each other forming an exciton and emitting light at the same chromophore site. The good device performance requires high fluorescence quantum efficiency and charge carrier mobility for the active organic material.¹⁰⁵ The first light emitting device based on triphenylene was reported by Wendorff in 1997.¹⁰⁶ More recently, pyrene and perylene related discotic LCs were also used in constructing OLEDs.¹⁰⁷ The unique charge carrier mobility of HBCs consequently promises a potential application as p-type conducting materials in such devices.

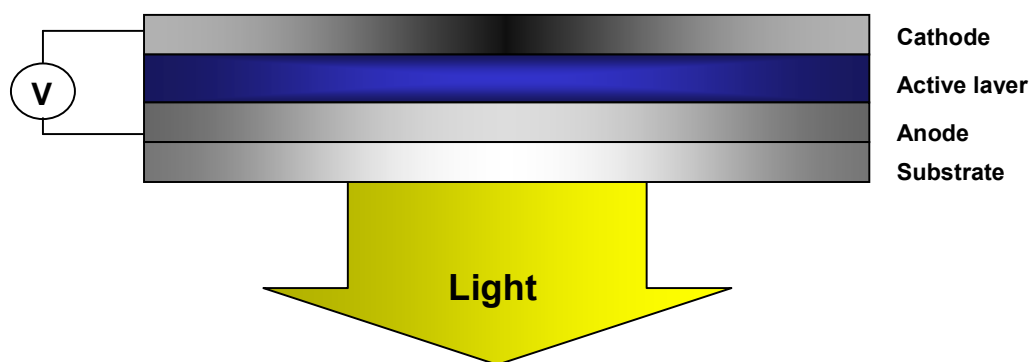


Figure 1-21. Schematic represent for organic light-emitting diode.

1.6.2 Photovoltaic Cells

The photovoltaic cell, or solar cell, is a device that converts light energy to electrical energy. The photovoltaic cell has a similar device setup as an LED. Instead of light-emitting material, the active semi-conductive layer in photovoltaic cells is made of either inorganic silicon or a blend of donor and acceptor components. After absorbing energy from the light source, the active layer produces excitons. The excitons separate to electrons and holes at the interface between donor and acceptor components and the charges are separately transported (in electron- or hole-transport layers) to the corresponding electrodes. PAHs show good performance in photovoltaic devices. For example, an HBC (donor component) and perylene diimide (acceptor component) based photovoltaic cell has exhibited excellent external quantum efficiencies up to 34% at a light wavelength of 490 nm.⁹²

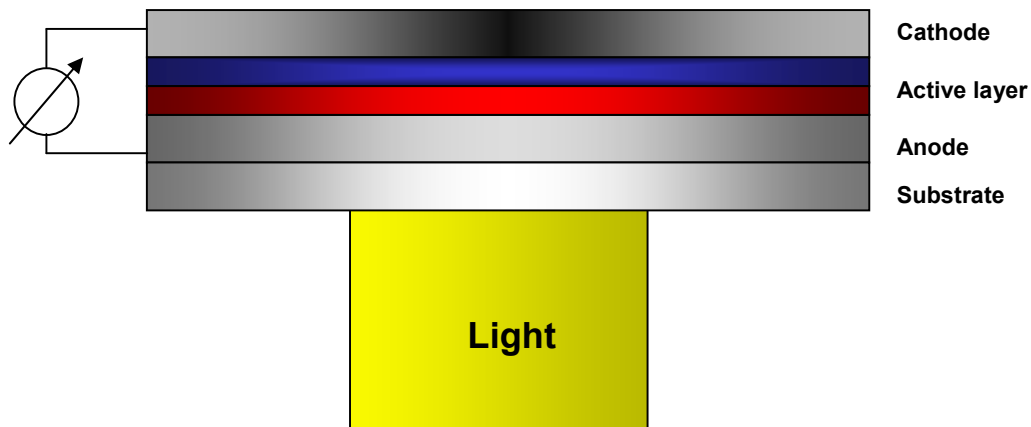


Figure 1-22. Device setup for photovoltaic cell.

1.6.3 Field-Effect Transistors (FETs)

The field-effect transistor relies on an electric field to control the conductivity of a semiconductor material. There are three electrodes called source, drain and gate in such a device. The gate voltage adjusts the current in the channel between source and drain. The performance of an FET is characterized by the on/off ratio and the charge carrier mobility of the semiconductors in the channel. HBC based discotic liquid crystalline materials have been deposited on an oriented polytetrafluoroethane (PTFE) film forming a highly ordered film, which was used in the fabrication of FET. Van de Craats *et al.* reported high FET mobility ($10^{-3} \text{ cm}^2/\text{V}\cdot\text{s}$) with high on/off ratio of 10^4 for such kind of material.¹⁰⁸

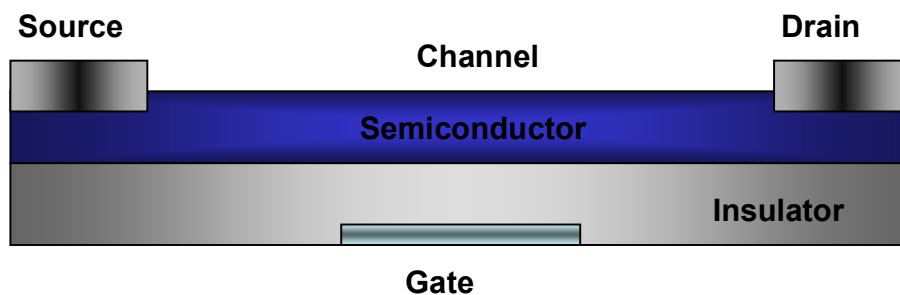


Figure 1-23. Device configuration of FET device.

1.7 Motivation and Objective

Discotic liquid crystalline materials show excellent electronic and optoelectronic properties. Therefore, they can potentially be used in organic electronic devices and conceptual molecular devices with good processibilities. Among the family of polycyclic aromatic hydrocarbons (PAHs), the large hexa-*peri*-hexabenzocoronenes (HBCs) have demonstrated superiority as organic semiconductors especially in photovoltaic cells and thin-film field effect transistors (FETs).^{109, 110} To simplify the synthetic strategy, further improve their performance in devices and explore novel properties as functional materials, the investigations of these compounds are still an attractive scientific field. Under the cooperation with lots of scientific colleagues in different fields, the work presented in this thesis covers the following topics:

- 1) As introduced above, the synthesis of PAHs with defined structure is not economic. The low efficiency stems from the complicated and tedious synthetic route. On the one hand, this leads to a low overall yield, and on the other hand, it needs lots of expensive transition-metal catalyzed reactions. For example, the current synthetic protocol for a D_{2h} symmetric dibromo HBC building block requires ten synthetic steps, four of which need transition-metal catalysts.⁸² Therefore, it is significant to find alternative low-cost and highly efficient ways to broaden their applications. A new synthetic concept, involving aryne intermediates, is developed to simplify the preparation of HBC derivatives. With such a synthetic protocol, the synthesis for D_{2h} -symmetric HBC building blocks is optimized to a large extent with only four synthetic steps and low costs. Moreover, this new synthetic strategy also shows advantages for the preparation of the *para*-asymmetric HPBs and provides a bottom-up pathway to 1D nanographenes.
- 2) Another synthetic challenge is to achieve versatile HBC building blocks that could be further modified with various functional groups. Currently, the methods for D_{6h} symmetric six-fold halide-substituted, D_{3h} symmetric three-fold halide substituted, D_{2h} symmetric two-fold halide substituted, and C_{2v} symmetric three-fold, two-fold and one-fold halide-substituted HBC building blocks have been well developed in the past decades (Figure 1-24). These building blocks have opened

versatile pathways to the preparation of functional HBCs. However, the direct introduction of different functionalities to a single HBC molecule, which requests different halides on the same HBC building block, is still a synthetic challenge.

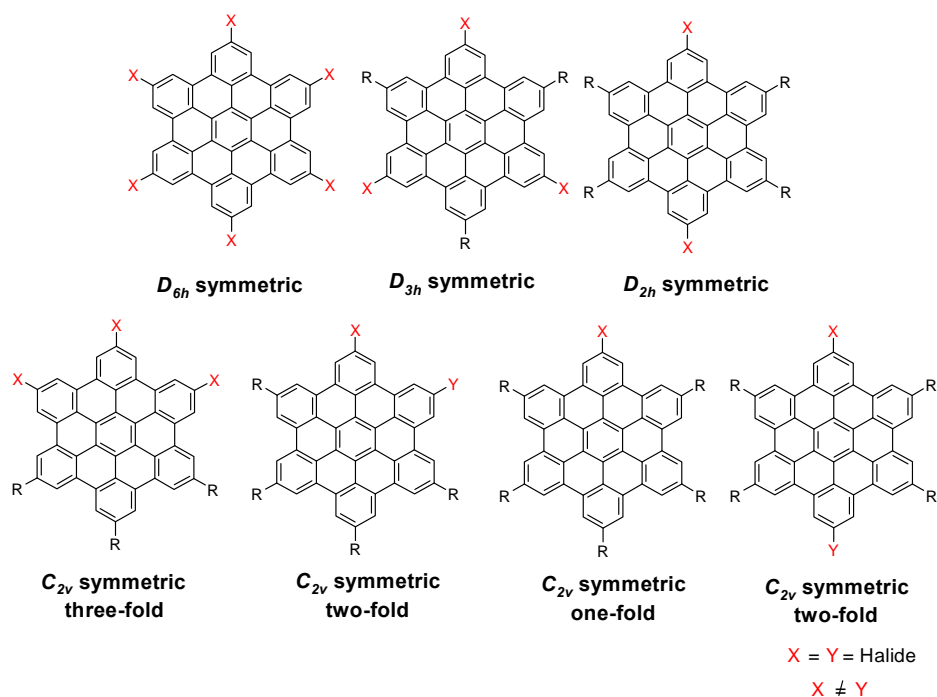


Figure 1-24. Synthesized HBC building blocks with different symmetry.

Although the lately developed synthetic method shows superiority in the preparation of *para*-asymmetric HPBs, the electron withdrawing and donating properties of the directly attached heteroatoms limit the last intramolecular Scholl reaction, which transforms the HPBs into HBC analogues. In order to improve the versatility of the functionalized HBCs, two different halides (one iodine, the other bromine) is introduced on the same HBC moiety in a *para* relationship through the traditional intermolecular Diels-Alder reaction route. Different functional groups could then be easily attached to the same HBC core by utilizing the different chemical reactivity between the iodo and bromo groups on the novel HBC building block.

- 3) To optimize the optoelectronic properties of PAHs, heteroatoms have been attached to the periphery of triphenylene, which dramatically enhanced its charge

carrier mobility.¹¹¹ In analogy, it was tried to introduce different heteroatoms directly onto HBC cores. Nevertheless, the electronic properties of different directly attached heteroatoms influence the last intramolecular cyclodehydrogenation step. For example, ether cleavage happens during the cyclodehydrogenation of alkoxy and alkylthio-substituted hexaphenylbenzenes.^{74, 112} The alkoxy groups can only be directly attached to HBC when all the periphery positions are occupied by either electron-donation methoxy groups or electron withdrawing fluorines on either side.^{113, 114} The mechanism how these heteroatoms influence the intramolecular Scholl reaction is still not well understood. Different mechanisms were proposed, but could not be confirmed due to the lack of experimental support.¹¹⁵⁻¹¹⁷ Conducting intramolecular Scholl reaction with hexaphenylbenzene containing heteroatoms and separation of intermediates or by-products will greatly help to accumulate data to support the mechanistic studies of this kind of reaction.

With the newly developed method, various HPB analogues containing different directly attached heteroatoms can be easily accessed. This provides an efficient synthetic route in the preparation of the precursors for the following intramolecular Scholl reaction mechanistic studies. For instance, by an intramolecular Scholl reaction with *para*-dimethoxy hexaphenylbenzene, a new phenomenon of phenyl group migration under oxidative Lewis acid condition is discovered. Based on the structure verification of obtained HBC molecule and a single crystal structure of a by-product, the influence of electron donating heteroatoms on cyclodehydrogenation reaction will be studied from a mechanistic point of view.

- 4) The intrinsic charge carrier mobility for the HBC mesogenes depends, to a large extent, upon the long range molecular order in the corresponding bulk phases. 2D WAXD and solid state NMR techniques have been applied to understand the macroscopic properties of HBC derivatives on a molecular level. Dielectric spectroscopy (DS) is another sensitive probe monitoring the molecular relaxation process under external frequency stimulation. This method provides supplemental

molecular dynamics information besides solid state NMR spectroscopy, however, requires a permanent molecular dipole moment.

To further understand the molecular self-assembly, dynamics and kinetics in different bulk phases, permanent dipole moments are introduced into HBC molecule by selecting different functional groups. Four different dipole functionalized HBCs are synthesized and studied with 2D WAXD, site-specific solid state NMR and dielectric spectroscopic techniques, which contributes the understanding of molecular dynamics and future molecular design for different material applications.

- 5) The most striking electronic property of HBC derivatives is their 1D charge transport along columnar direction. Highly ordered columnar supramolecular structures will, to a large extent, improve its performance in device applications. Non-covalent intermolecular interactions, *e.g.* hydrogen bonding, dipole-dipole interactions and Van der Waals forces as well as $\pi - \pi$ interactions are the dominant types of bonds in supramolecular chemistry.¹¹⁸ By appropriate molecular design, extra intermolecular interactions can be employed to stabilize the columnar stacks besides extending the rigidity of the aromatic cores. The introduced functional groups will also render HBC derivatives with new properties. For instance, a strong dipole moment brings HBCs non-linear optical properties and hydrogen bonds help HBC molecules to trap small organic solvent molecule forming organogels.

Based on the novel “*para*”-asymmetric HBC building block, a series HBC bridged donor acceptor molecules are synthesized. Upon the introduction of strong dipole moments, it is expected that these HBC molecules show distinct self-assembly behavior and non-linear optical properties (Figure 1-25 left).

Hydrogen bonds are also included along the columnar stacking direction through either amido or ureido functionalities to stabilize the columnar supramolecular organization. Depending on the strength and position at HBC periphery, the hydrogen bonds dominate the molecular self-assembly behavior both in liquid and bulk state (Figure 1-25 right).

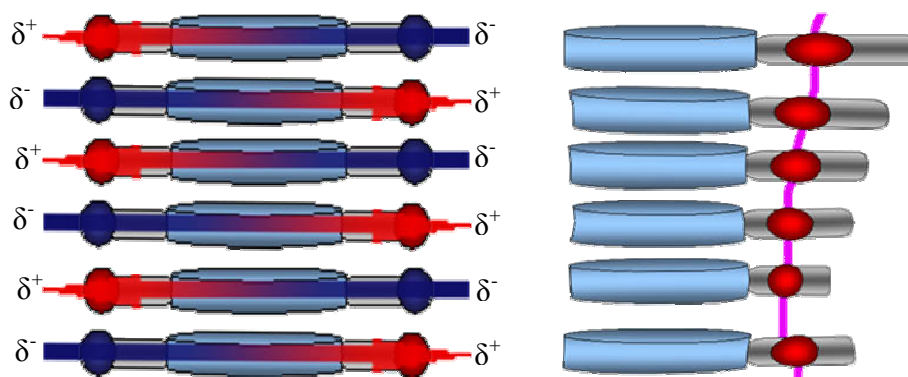


Figure 1-25. Schematic represents of the columnar stacking with extra non-covalent interactions; left: dipole-dipole interactions, right: hydrogen bonding interactions along single column.

- 6) The molecular devices are still currently at a theoretical stage. The single molecular CFET, based on anthraquinone and dimethylantracene complex, can not be switched reversibly yet. The SAM based devices require functional molecules with proper HOMO-LUMO band gap and excellent self-assembly tendency on different surfaces. Therefore, HBCs with different functional groups are regarded as promising candidates in this area.

For the application in the conceivable molecular devices, specific functional groups are connected with HBC moieties and their optoelectronic properties are investigated at a molecular level on surfaces. For example, a switchable azobenzene functional group is attached to the HBC aromatic core, which provides the reversibility in a single molecular CFET; the introduction of anchor groups assists HBC molecules to form long range well-ordered single molecular monolayers (SAMs) on specific surfaces, which qualifies such kind of materials as active components in metal-molecules-metal junctions.

1.8 References

1. Shaw, J. M., Seidler, P. F., *Ibm Journal of Research and Development* **2001**, *45*, 3-9.
2. Shirakawa, H., Louis, E. J., Macdiarmid, A. G., Chiang, C. K., Heeger, A. J., *Chem. Comm.* **1977**, 578-580.
3. Tang, C. W., VanSlyke, S. A., *Appl. Phys. Lett.* **1987**, *51*, 913-915.
4. Forrest, S. R., Thompson, M. E., *Chem. Rev.* **2007**, *107*, 923-925.
5. Forrest, S. R., *Chem. Rev.* **1997**, *97*, 1793-1896.
6. Dimitrakopoulos, C. D., Malenfant, P. R. L., *Adv. Mater.* **2002**, *14*, 99-117.
7. Mitzi, D. B., Feild, C. A., Schlesinger, Z., Laibowitz, R. B., *J. Sol. State Chem.* **1995**, *114*, 159-163.
8. Coropceanu, V., Cornil, J., daSilvaFilho, D. A., Olivier, Y., Silbey, R., Bredas, J. L., *Chem. Rev.* **2007**, *107*, 926-952.
9. McCulloch, I., Heeney, M., Bailey, C., Genevicius, K., MacDonald, I., Shkunov, M., Sparrowe, D., Tierney, S., Wagner, R., Zhang, W., Chabynyc, M. L., Kline, R. J., McGehee, M. D., Toney, M. F., *Nat Mater* **2006**, *5*, 328-333.
10. Sirringhaus, H., Brown, P. J., Friend, R. H., Nielsen, M. M., Bechgaard, K., Langeveld-Voss, B. M. W., Spiering, A. J. H., Janssen, R. A. J., Meijer, E. W., Herwig, P., de Leeuw, D. M., *Nature* **1999**, *401*, 685-688.
11. Sirringhaus, H., Tessler, N., Friend, R. H., *Science* **1998**, *280*, 1741.
12. Oana, D. J., Jacob, B., Thomas, T. M. P., *Appl. Phys. Lett.* **2004**, *84*, 3061-3063.
13. de Boer, R. W. I., Gershenson, M. E., Morpurgo, A. F., Podzorov, V., *Phys. Status Solidi A* **2004**, *201*, 1302-1331.
14. Mattheus, C. C., de Wijs, G. A., de Groot, R. A., Palstra, T. T. M., *J. Am. Chem. Soc.* **2003**, *125*, 6323-6330.
15. Zeis, R., Besnard, C., Siegrist, T., Schlockermann, C., Chi, X., Kloc, C., *Chem. Mater.* **2006**, *18*, 244-248.
16. Podzorov, V., Menard, E., Borissov, A., Kiryukhin, V., Rogers, J. A., Gershenson, M. E., *Phys. Rev. Lett.* **2004**, *93*, 086602.
17. Sundar, V. C., Zaumseil, J., Podzorov, V., Menard, E., Willett, R. L., Someya, T., Gershenson, M. E., Rogers, J. A., *Science* **2004**, *303*, 1644-1646.
18. Shirota, Y., *J. Mate. Chem.* **2005**, *15*, 75-93.
19. Ferraris, J., Cowan, D. O., Walatka, V., Perlstein, J. H., *J. Am. Chem. Soc.* **1973**, *95*, 948-949.
20. Otsubo, T., Takimiya, K., *Bull. Chem. Soc. Jpn* **2004**, *77*, 43-58.
21. Rovira, C., *Chem. Rev.* **2004**, *104*, 5289-5318.

22. Mas-Torrent, M., Durkut, M., Hadley, P., Ribas, X., Rovira, C., *J. Am. Chem. Soc.* **2004**, *126*, 984-985.
23. Mas-Torrent, M., Hadley, P., Bromley, S. T., Crivillers, N., Veciana, J., Rovira, C., *Appl. Phys. Lett.* **2005**, *86*, 012110.
24. Sinnokrot, M. O., Sherrill, C. D., *J. Am. Chem. Soc.* **2004**, *126*, 7690-7697.
25. Hunter, C. A., Sanders, J. K. M., *J. Am. Chem. Soc.* **1990**, *112*, 5525-5534.
26. van de Craats, A. M., Warman, J. M., de Haas, M. P., Adam, D., Simmerer, J., Haarer, D., Schuhmacher, P., *Adv. Mater.* **1996**, *8*, 823-826.
27. Warman, J. M., deHaas, M. P., Dicker, G., Grozema, F. C., Piris, J., Debije, M. G., *Chem. Mater.* **2004**, *16*, 4600-4609.
28. van de Craats, A. M., Warman, J. M., Fechtenkötter, A., Brand, J. D., Harbison, M. A., Müllen, K., *Adv. Mater.* **1999**, *11*, 1469-1472.
29. Kraft, A., *ChemPhysChem* **2001**, *2*, 163-165.
30. Dresselhaus, M. S., Dresselhaus, G., *Adv. Phys.* **1981**, *30*, 139-326.
31. Bäumlér, E., *Farben, Formeln, Forscher - Hoechst und die Geschichte der industriellen organischen Chemie in Deutschland*. Piper, S. R., München, Zürich, **1989**.
32. Mastral, A. M., Callen, M. S., Murillo, R., T., G., *Polycyclic Aromatic Compounds* **2000**, *18*, 1 - 11.
33. Cullum, B. M., Chi, Z., Vo-Dinh, T., *Polycyclic Aromatic Compounds* **2000**, *18*, 25 - 47.
34. Moreels, G., Clairemidi, J., Rousselot, P., Goidet, B., Vo-Dinh, T., *Polycyclic Aromatic Compounds* **1994**, *5*, 107 - 114.
35. Clar, E., *Polycyclic Hydrocarbons*. Academic Press: New York, **1964**; Vol. 1,2.
36. Harvey, R. G., *Polycyclic Aromatic Hydrocarbons*. Wiley-VCH: New York, **1997**.
37. Dias, J. R., *Polycyclic Aromatic Compounds* **2005**, *25*, 113 - 127.
38. Dias, J. R., *Handbook of Polycyclic Hydrocarbons, Part A: Benzenoid Hydrocarbons*. Elsevier: Amsterdam, **1987**.
39. Scholl, R., Seer, C., Weitzenböck, R., *Chem. Ber.* **1910**, *43*, 2202-2209.
40. Scholl, R., Neumann, H., *Chem. Ber.* **1922**, *55*, 118-126.
41. Scholl, R., Seer, C., *Chem. Ber.* **1922**, *55*, 330-341.
42. Scholl, R., Seer, C., *Liebigs Ann. der Chem.* **1912**, *394*, 111-177.
43. Clar, E., *Chem. Ber.* **1929**, *62*, 1574-1582.
44. Clar, E., John, F., Hawran, B., *Chem. Ber.* **1929**, *62*, 940-950.
45. Clar, E., Wallenstein, H., Avenarius, R., *Chem. Ber.* **1929**, *62*, 950-955.

46. Clar, E., *Chem. Ber.* **1929**, *62*, 350-359.
47. Clar, E., Stewart, D. G., *J. Am. Chem. Soc.* **1953**, *75*, 2667-2672.
48. Hagen, S., Hopf, H., *Top. Curr. Chem.: Carbon Rich Compounds I* **1998**, *196*, 45-89.
49. Gutman, I., Cyvin, C. J., *Introduction to the Theory of Benzenoid Hydrocarbons*. Springer, Berlin: Heidelberg, **1989**.
50. Zander, M., *Top. Curr. Chem. : Advances in the Theory of Benzenoid Hydrocarbons*. Spriger, Berlin: Heidelberg, **1990**; Vol. 153, p 101-122.
51. Sage, I. C., *Handbook of Liquid Crystals*. Demus, D., Goodby, J., Gray, G. W., Spiess, H. W., Vill, V., Wiley-VCH: Weinheim, **1998**; Vol. 1, p 731-762.
52. Watson, M. D., Fechtenkotter, A., Müllen, K., *Chem. Rev.* **2001**, *101*, 1267-1300.
53. Bushby, R. J., Lozman, O. R., *Current Opinion in Solid State and Materials Science* **2002**, *6*, 569-578.
54. Armit, J. W., Robinson, R., *J. Chem. Soc. Trans.* **1925**, *127*, 1604-1618.
55. Clar, E., *The Aromatic Sextet*. 1st ed.; John Wiley and Sons: London, **1972**.
56. Richardson, J. W., Parks, G. S., *J. Am. Chem. Soc.* **1939**, *61*, 3543-3546.
57. Wendland, R., LaLonde, J., *Organic Syntheses* **1954**, *34*, 76-78.
58. Zander, M., *Polycyclische Aromaten*. Teubner: Stuttgart, **1995**.
59. Schleyer, P. v. R., Maerker, C., Dransfeld, A., Jiao, H., Hommes, N. J. R. v. E., *J. Am. Chem. Soc.* **1996**, *118*, 6317-6318.
60. Moran, D., Stahl, F., Bettinger, H. F., Schaefer, H. F., Schleyer, P. R., *J. Am. Chem. Soc.* **2003**, *125*, 6746-6752.
61. Ormsby, J. L., King, B. T., *J. Org. Chem.* **2004**, *69*, 4287-4291.
62. Lang, K. F., Buffleb, H., Kalowy, J., *Chem. Ber.* **1962**, *95*, 1052-1053.
63. Lang, K. F., Buffleb, H., Kalowy, J., *Chem. Ber.* **1964**, *97*, 494-497.
64. Lang, K. F., Buffleb, H., Zander, M., *Angew. Chem.* **1963**, *75*, 170.
65. Fetzer, J. C., Biggs, W. R., *Polycyclic Aromatic Compounds* **1994**, *4*, 3 - 17.
66. Broene, R. D., Diederich, F., *Tetrahedron Lett.* **1991**, *32*, 5227-5230.
67. Rehahn, M., Schluter, A.-D., Wegner, G., Feast, W. J., *Polymer* **1989**, *30*, 1054-1059.
68. Koch, K.-H., Müllen, K., *Chem. Ber.* **1991**, *124*, 2091-2100.
69. Kovacic, P., Wu, C., *J. Polymer Sci.* **1960**, *47*, 45-54.
70. Kovacic, P., Kyriakis, A., *Tetrahedron Lett.* **1962**, *3*, 467-469.

71. Kovacic, P., Kyriakis, A., *J. Am. Chem. Soc.* **1963**, *85*, 454-458.
72. Iyer, V. S., Wehmeier, M., Diedrich, J., Menno, B., Keegstra, A., Müllen, K., *Angew. Chem. Int. Ed.* **1997**, *36*, 1604-1607.
73. Müller, M., Kübel, C., Müllen, K., *Chem. Eur. J.* **1998**, *4*, 2099-2109.
74. Weiss, K., Beernink, G., Dötz, F., Birkner, A., Müllen, K., Wöll, C. H., *Angew. Chem. Int. Ed.* **1999**, *38*, 3748-3752.
75. Lambert, C., Nöll, G., *Angew. Chem. Int. Ed.* **1998**, *37*, 2107-2110.
76. Lambert, C., Nöll, G., *Chem. Eur. J.* **2002**, *8*, 3467-3477.
77. Müller, M., Mauermann-Düll, H., Wagner, M., Enkelmann, V., Müllen, K., *Angew. Chem. Int. Ed.* **1995**, *34*, 1583-1586.
78. Müller, M., Petersen, J., Strohmaier, R., Günther, C., Karl, N., Müllen, K., *Angew. Chem. Int. Ed.* **1996**, *35*, 886-888.
79. Diltthey, W., Thewalt, I., Trösken, O., *Chem. Ber.* **1934**, *67*, 1959-1964.
80. Diltthey, W., Hurtig, G., *Chem. Ber.* **1934**, *67*, 2004-2007.
81. Diltthey, W., Hurtig, G., *Chem. Ber.* **1934**, *67*, 495-496.
82. Ito, S., Wehmeier, M., Brand, J. D., Kübel, C., Epsch, R., Rabe, J. P., Müllen, K., *Chem. Eur. J.* **2000**, *6*, 4327-4342.
83. Iyer, V. S., Yoshimura, K., Enkelmann, V., Epsch, R., Rabe, J. P., Müllen, K., *Angew. Chem. Int. Ed.* **1998**, *37*, 2696-2699.
84. Müller, M., Iyer, V. S., Kübel, C., Enkelmann, V., Müllen, K., *Angew. Chem. Int. Ed.* **1997**, *36*, 1607-1610.
85. Zeljko, T., Watson, M. D., Müllen, K., *Angew. Chem. Int. Ed.* **2004**, *43*, 755-758.
86. Morgenroth, F., Reuther, E., Müllen, K., *Angew. Chem. Int. Ed.* **1997**, *36*, 631-634.
87. Wasserfallen, D., Kastler, M., Pisula, W., Hofer, W. A., Fogel, Y., Wang, Z., Müllen, K., *J. Am. Chem. Soc.* **2006**, *128*, 1334-1339.
88. Reinitzer, F., *Monatsh. Chem.* **1888**, *9*, 421-441.
89. Chandrasekhar, S., B. K. Sadashiva, Suresh, K. A., *Pramana* **1977**, *9*, 471-480.
90. Chandrasekhar, S., Prasad, S. K., *Contemp. Phys.* **1999**, *40*, 237 - 245.
91. O'Neill, M., Kelly, S. M., *Adv. Mater* **2003**, *15*, 1135-1146.
92. Schmidt-Mende, L., Fechtenkotter, A., Müllen, K., Moons, E., Friend, R. H., MacKenzie, J. D., *Science* **2001**, *293*, 1119-1122.
93. Stabel, A., Herwig, P., Müllen, K., Rabe, J. P., *Angew. Chem. Int. Ed.* **1995**, *34*, 1609-1611.

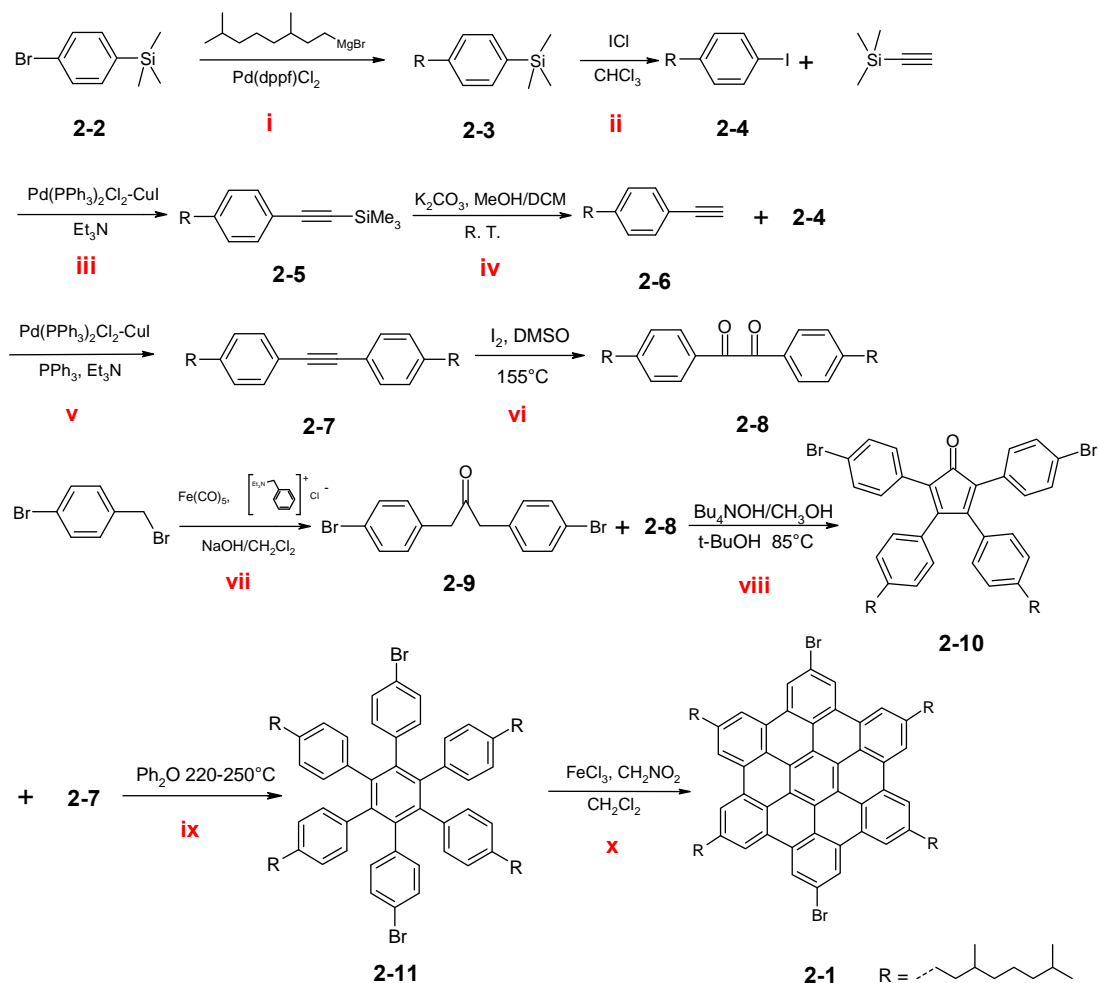
94. Brown, S. P., Schnell, I., Brand, J. D., Müllen, K., Spiess, H. W., *J. Am. Chem. Soc.* **1999**, *121*, 6712-6718.
95. Fischbach, I., Pakula, T., Minkin, P., Fechtenkotter, A., Müllen, K., Spiess, H. W., Saalwachter, K., *J. Phys. Chem. B* **2002**, *106*, 6408-6418.
96. Binnig, G., Rohrer, H., *Ibm Journal of Research and Development* **1986**, *30*, 279.
97. Chen, C. J., *Introduction to Scanning Tunneling Microscopy*. Oxford University Press: New York, **1993**.
98. Bai, C., *Scanning Tunneling Microscopy and its Applications*. 2ed ed.; Springer Verlag: New York, **1999**.
99. Samori, P., Severin, N., Simpson, C. D., Müllen, K., Rabe, J. P., *J. Am. Chem. Soc.* **2002**, *124*, 9454-9457.
100. Jäckel, F., Watson, M. D., Müllen, K., Rabe, J. P., *Phys. Rev. Lett.* **2004**, *92*, 188303.
101. Newton, M. D., *Chem. Rev.* **1991**, *91*, 767-792.
102. Duati, M., Grave, C., Tcbeborateva, N., Wu, J., Müllen, K., Shaporenko, A., Zharnikov, M., Kriebel, J. K., Whitesides, G. M., Rampi, M. A., *Adv. Mater.* **2006**, *18*, 329-333.
103. Tran, E., Duati, M., Ferri, V., Müllen, K., Zharnikov, M., Whitesides, G. M., Rampi, M. A., *Adv. Mater.* **2006**, *18*, 1323-1328.
104. Gilles, H., *Adv. Mater.* **1998**, *10*, 365-377.
105. Seguy, I., Jolinat, P., Destruel, P., Farenc, J., Mamy, R., Bock, H., Ip, J., Nguyen, T. P., *J. App. Phy.* **2001**, *89*, 5442-5448.
106. Wendorff, J. H., Christ, T., Glösen, B., Greiner, A., Kettner, A., Sander, R., Stümpflen, V., Tsukruk, V. V., *Adv. Mater.* **1997**, *9*, 48-52.
107. van de Craats, A. M., Warman, J. M., Schlichting, P., Rohr, U., Geerts, Y., Müllen, K., *Synth. Met.* **1999**, *102*, 1550-1551.
108. van de Craats, A. M., Stutzmann, N., Bunk, O., Nielsen, M. M., Watson, M., Müllen, K., Chanzy, H. D., Siringhaus, H., Friend, R. H., *Adv. Mater.* **2003**, *15*, 495-499.
109. Schmidt-Mende, L., Fechtenkotter, A., Müllen, K., Friend, R. H., MacKenzie, J. D., *Physica E: Low-dimensional Systems and Nanostructures* **2002**, *14*, 263-267.
110. Pisula, W., Menon, A., Stepputat, M., Lieberwirth, I., Kolb, U., Tracz, A., Siringhaus, H., Pakula, T., Müllen, K., *Adv. Mater.* **2005**, *17*, 684-689.
111. Adam, D., Schuhmacher, P., Simmerer, J., Haussling, L., Siemensmeyer, K., Etzbachi, K. H., Ringsdorf, H., Haarer, D., *Nature* **1994**, *371*, 141-143.
112. Fechtenkötter, A. PhD Thesis. Johannes Gutenberg Universität Mainz, 2001.
113. Wang, Z., Dötz, F., Enkelmann, V., Müllen, K., *Angew. Chem. Int. Ed.* **2005**, *44*, 1247-1250.

114. Zhang, Q., Prins, P., Jones, S. C., Barlow, S., Kondo, T., An, Z., Siebbeles, L. D. A., Marder, S. R., *Org. Lett.* **2005**, *7*, 5019-5022.
115. Rempala, P., Jiri Kroulik, King, B. T., *J. Am. Chem. Soc.* **2004**, *126*, 15002-15003.
116. Rempala, P., Kroulik, J., King, B. T., *J. Org. Chem.* **2006**, *71*, 5067-5081.
117. Stefano, M. D., Negri, F., Carbone, P., Müllen, K., *Chem. Phys.* **2005**, *314*, 85-99.
118. Schalley, C., *Analytical Methods in Supramolecular Chemistry*. 1st ed.; Wiley-VCH: Weinheim, **2006**.

2 Novel Synthesis of D_{2h} and C_{2v} Symmetric Dihalide HBC Building Blocks

The importance of discotic liquid crystals has been illustrated in CHAPTER 1. HBC building blocks with different symmetries have opened up pathways to achieve versatile HBC-based liquid crystalline materials with specific functionalities.¹⁻³ It was also pointed out that the preparation for polycyclic aromatic hydrocarbon (PAH)-based discotic liquid crystalline materials requires lengthy and tedious multiple-step synthesis and tremendous synthetic efforts. The lower the symmetry of the HBC derivatives, the more complicated is the synthetic work, which leads to low efficiency and high costs.^{2,4} The synthesis for C_{2v} -symmetric mono-bromo HBC, which is used for one fold functionalization, involves 13 synthetic steps, while there are still 10 steps to go for D_{2h} symmetric dibromo HBC **2-1** (Figure 2-1). To synthesize the all-benzoid PAHs, the preparation of suitable precursors, hexaphenylbenzenes (HPBs),⁵⁻⁷ is of particular importance for the last step intramolecular cyclodehydrogenation, the so-called Scholl reaction. Herein, a more effective synthetic approach to D_{2h} symmetrically dihalide substituted HPBs via one-pot Hart and Suzuki-Miyaura cross-coupling reactions on sterically hindered substrate will be described.

On the other hand, the diversity of the properties of functionalized HBCs increases the demands for various HBC building blocks. The synthesis of a HBC building block containing two different halide groups, which could respectively be modified, preserves challenge. It will be demonstrated that, although the newly developed synthetic concept shows not only superiority in the preparation of D_{2h} -symmetric HBC building blocks, but also in the achievement of C_{2v} -symmetric HPBs, the strict selectivity of the precursors for the last-step intramolecular Scholl reaction⁸⁻¹⁰ limits its application. Following the classic route based on intermolecular [4+2] Diels-Alder reaction, this object is realized via an asymmetric carbonylative coupling of benzyl halides.¹¹

2.1 Old synthetic pathway to D_{2h} symmetric dibromo HBCFigure 2-1. Ten-step synthesis for *para*-dibromo HBC 2-1.

The old synthetic route starts with 4-bromo-trimethylsilyl benzene **2-2**. After a palladium catalyzed Kumada cross coupling reaction, a flexible alkyl chain is attached to the *para*-position of the phenyl ring (**2-3**). In the following step, the trimethylsilyl group is transformed into iodo group for further functionalization. A trimethylsilyl ethynyl group is, then, connected to the phenyl ring via a Hagihara-Sonogashira coupling reaction affording **2-5**. The trimethylsilyl group is removed under basic condition resulting in compound **2-6**, which is submitted to another Hagihara-Sonogashira reaction with **2-4**. Part of the resulting alkylated tolane **2-7** is oxidized to the corresponding benzil **2-8**, while the rest is used in later [4+2] Diels-Alder reaction for the formation of HPB **2-11**.

Besides **2-8**, another reactant, diphenyl acetone **2-9**, is synthesized from 4-bromobenzyl bromide and pentacarbonyl iron. Applying a Knoevenagel condensation with **2-8** and **2-9** leads to an important intermediate, tetraphenyl substituted cyclopentadienone **2-10**, for the aforementioned Diels-Alder reaction. Dibromo HBC **2-1** is then obtained after an intramolecular Scholl reaction with the HPB **2-11**.²

Although this synthetic route was simplified later by a one-pot alkylation of dibromo tolane for **2-7** instead of starting with **2-2**, this synthetic protocol is still necessary for the preparation of the mono-bromo HBC, which requires a mono bromine substituted tolane as intermediate. Additionally, the synthesis is very expensive not only due to the multiple synthetic steps but also because four out of ten reactions rely on the expensive transition-metal catalysts. In order to improve the efficiency and reduce the costs, Dr. Xiaoyin Yang and I developed a new synthetic strategy involving six steps, only two of which need transition-metal catalysts.

2.2 New synthetic strategy for D_{2h} symmetric HPBs

2.2.1 General method and reaction mechanism

In 1930 Durand reported that hexabromobenzene reacts with phenyl-magnesium bromide to give hexaphenylbenzene,¹² Dilthey later found that the product was in fact the 1,2,4,5-tetraphenylbenzene.¹³ Geissman confirmed these results and showed that the actual reaction product was the tetraphenyl 1,4-di-Grignard compound.¹⁴ Hart et al. improved Durand's and Geissman's reaction to give synthetically useful yields of tetraarylbenzenes.¹⁵ The new synthetic strategy follows the pioneering work employing hexahalobenzene and aryl-Grignard reagents as starting material.

The synthesis starts with *para*-dichlorobenzene, which is first brominated in oleum with bromine and iron as catalyst (yield, 80%).¹⁶ The resulting 1,2,4,5-tetrabromo-3,6-dichlorobenzene **2-12** is then treated with 9.5 equivalents of arylmagnesium bromide in THF at r.t. for 12 h. Iodine is then used to quench the product, 1,4-di-Grignard intermediate **2-13**, for further functionalization. The product 1,4-diiodo-2,3,5,6-

tetraarylbenezene **2-14** is then treated with different arylboronic acids via a sterically hindered Suzuki-Miyaura cross coupling reaction under optimized conditions affording D_{2h} symmetric HPBs **2-15**. Depending upon the directly attached heteroatom, some HPB derivatives can be oxidized to the corresponding HBCs **2-16** via the intramolecular Scholl reaction (Figure 2-2).

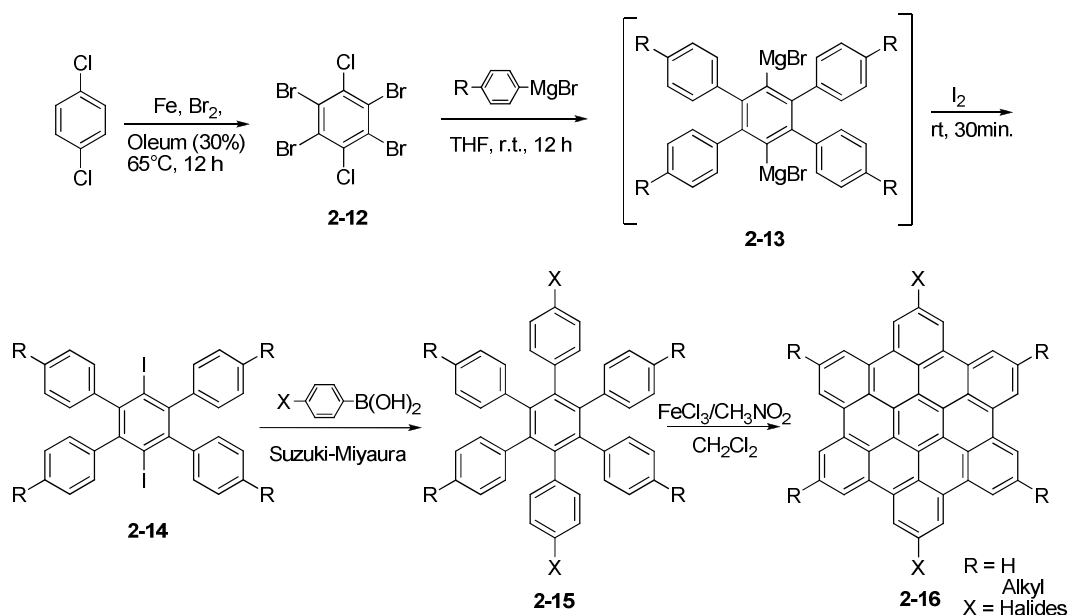


Figure 2-2. Novel synthetic concept for D_{2h} symmetric HPBs and HBCs.

The reaction mechanism involves the 1,4-di-Grignard reagent **2-18** as key intermediates and various organometallic arynes as outlined in Figure 2-3. A bromine atom firstly exchanged with one molecule of Grignard reagent forming mono- and di-halogenated phenylmagnesium bromide **2-17** and **2-18**, which was discovered by Smith et al. and proved by Hart et al.¹⁷⁻²⁰ Since the charges on the same molecule prefer being as far apart as possible, the two carbon anions should always locate at the *para*-position, which is experimentally confirmed by the isolation of the only 1,4-di-Grignard intermediates.¹⁸ Once **2-18** forms, a metallic aryne intermediate **2-19** appears after the elimination of one molecule of MgBr_2 . Another molecule of arylmagnesium bromide nucleophilically adds to the aryne intermediate **2-19** leading to another 1,4-di-Grignard compound **2-20** containing one aryl substitute. After a series of eliminations of MgBr_2

and regioselective additions of arylmagnesium bromides to aryne intermediates (**2-21**, **2-23** and **2-25**), the 1,4-di-Grignard product **2-26** is produced with four aryl substituents. The subsequent quenching with iodine consequently yields the product **2-14**.

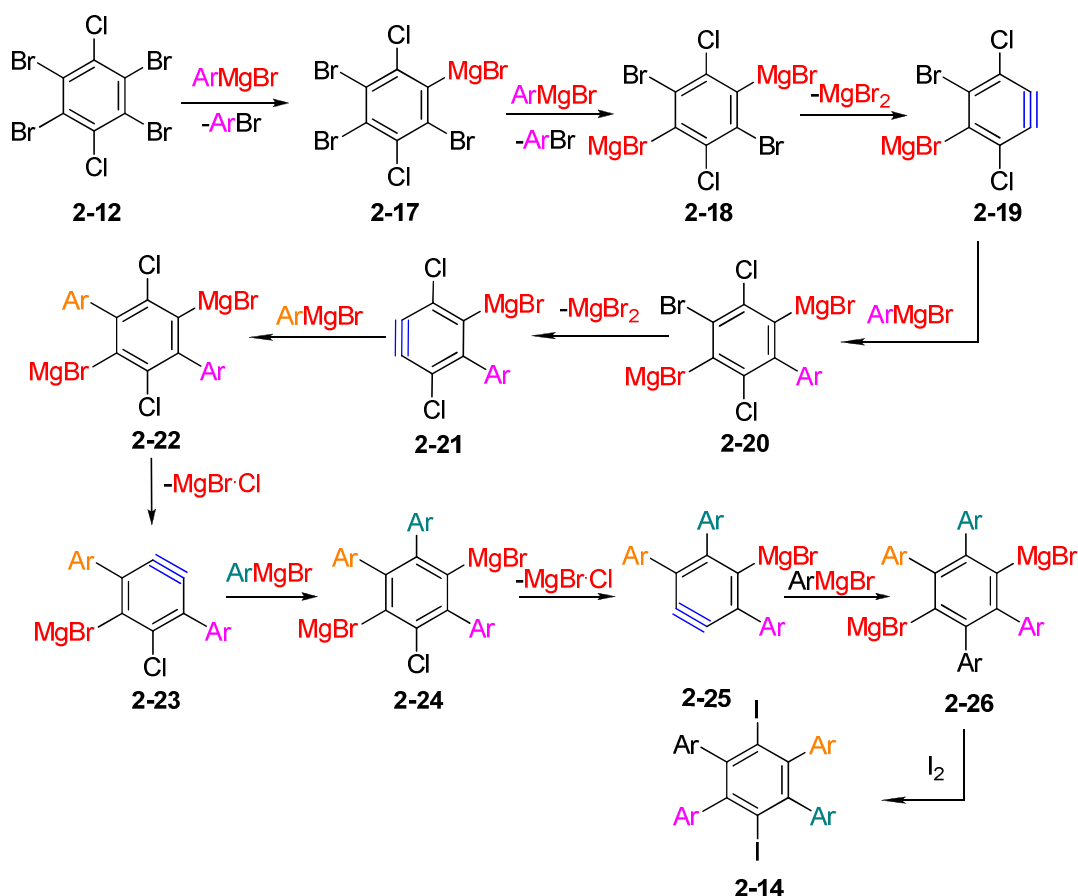


Figure 2-3. Reaction mechanism for the formation of **2-14**.

2.2.2 Examples of synthesized 1,4-diiodo-2,3,5,6-tetra-arylbenzenes

Three kinds of 1,4-diiodo-2,3,5,6-tetraaryl benzene **2-14** were synthesized based on easily accessible Grignard reagents (Figure 2-4). Compounds **2-14a** and **2-14b** were prepared with commercially available Grignard reagents according to the procedure described in the SECTION 2.2 in a yield of 40% and 60% respectively.

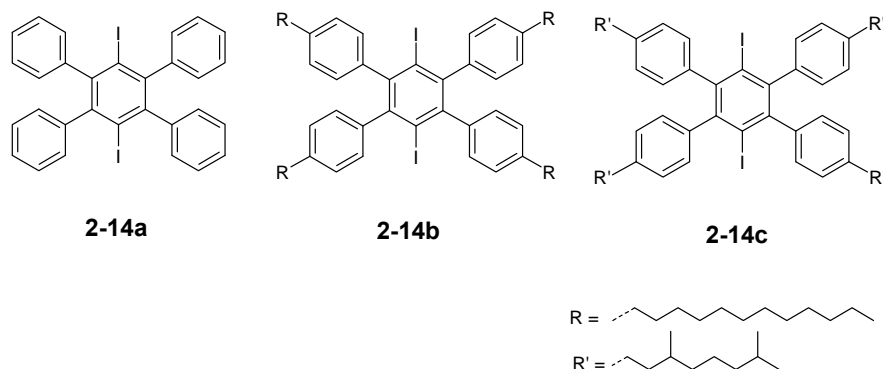


Figure 2-4. Synthesized 1,4-diiodo-2,3,5,6-tetraarylbenzene 2-14.

In order to increase the solubility for simpler processing in later HBC chemistry, the 3,7-dimethyloctyl substituents were introduced by a freshly prepared Grignard reagent, which later leads to **2-14c**. The 1-trimethylsilyl-4-(3,7-dimethyloctanyl) benzene **2-3**, was first brominated with bromine in the presence of anhydrous sodium acetate²¹ affording 1-bromo-4-(3,7-dimethyloctanyl) benzene **2-27** in a 82% yield. **2-27** was then transformed to the corresponding arylmagnesium bromide and subjected to the reaction with 1,2,4,5-tetrabromo-3,6-dichlorobenzene **2-12** resulting in **2-14c** in 40% yield.

2.2.3 Condition optimization of sterically hindered Suzuki-Miyaura cross-coupling reaction

The Suzuki-Miyaura cross-coupling reaction is one of the most powerful biaryl C-C bond-forming transformations nowadays. This kind of reaction enjoys a broad scope and wide functional group tolerance.²²⁻²⁵ However, in the case of sterically hindered aryl or alkenyl halides, special ligands and harsh conditions have to be applied.²⁶⁻²⁹ The work of Buchwald et al. provides a general protocol for the Suzuki-Miyaura cross-coupling reactions on sterically hindered substrates, in which a novel and readily available phosphine, S-phos (2-dicyclohexylphosphino-2',6'-dimethoxybiphenyl), was used as a ligand in conjunction with Pd₂(dba)₃.³⁰⁻³³ Considering the sterically hindered nature of the 1,4-diiodo-2,3,5,6-tetraarylbenzenes **2-14**, Buchwald's catalyst system was employed in the initial test, which leads to a yield of 65%. In order to improve the yield,^{30, 32} the reaction conditions were optimized using the easily obtained compound **2-14a** and commercially available phenylboronic acid as substrates.

The results are summarized in Table 2-1. The best palladium source was found to be $\text{Pd}(\text{PPh}_3)_4$. The effect of the base was also examined, from which K_2CO_3 was found out to be the most effective one (entries 5-8). Furthermore, the use of solid K_2CO_3 (entry 6, 94%) was more effective than the use of aqueous 2M K_2CO_3 solution (entry 9, 70%). Increasing the reaction temperature from 100°C to 120°C had a detrimental effect on the reaction and several by-products, such as mono-coupled and de-iodinated compounds, were observed (entry 10). Interestingly, the introduction of the phase transfer catalyst Aliquat[®] 336 (2 mol%) was found to accelerate the reaction rate and the desired product was obtained in an excellent yield of 95% after a reaction period of 12 h (entry 11). The structure of Aliquat[®] 336 is illustrated in Figure 2-5. While other phase transfer catalysts, such as Bu_4NBr , do not seem to promote this reaction (entry 12).

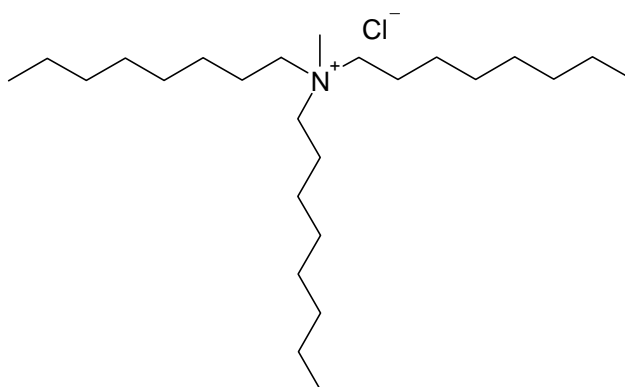
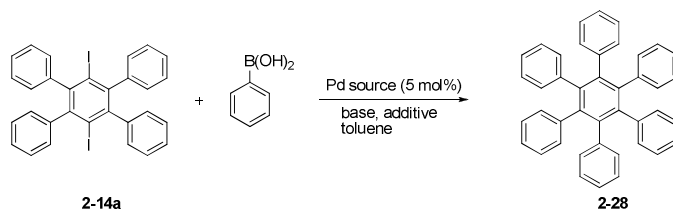


Figure 2-5. Molecular structure of Aliquat[®] 336.

Table 2- 1. Optimization of reaction conditions for the sterically hindered Suzuki-Miyaura coupling reaction.



Entry	Catalyst system	Temp. (°C)	Time(h)	Base	Yield ^a
1	Pd ₂ (dba) ₃ + S-phos	100	24	K ₃ PO ₄	65%
2	PdCl ₂ (PPh ₃) ₂	100	24	K ₃ PO ₄	30%
3	PdCl ₂ (dppf)	100	24	K ₃ PO ₄	56%
4	Pd(OAc) ₂ + PPh ₃	100	24	K ₃ PO ₄	- ^b
5	Pd(PPh ₃) ₄	100	24	K ₃ PO ₄	86%
6	Pd(PPh ₃) ₄	100	24	K ₂ CO ₃	94%
7	Pd(PPh ₃) ₄	100	24	Cs ₂ CO ₃	85%
8	Pd(PPh ₃) ₄	100	24	Ba(OH) ₂ ·8H ₂ O	- ^b
9	Pd(PPh ₃) ₄	100	24	K ₂ CO ₃	70% ^c
10	Pd(PPh ₃) ₄	120	12	K ₂ CO ₃	56%
11	Pd(PPh ₃) ₄ + Aliquat [®] 336	100	12	K ₂ CO ₃	95%
12	Pd(PPh ₃) ₄ + Bu ₄ NBr	100	12	K ₂ CO ₃	45%

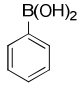
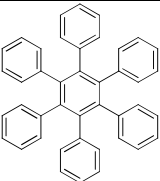
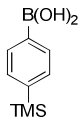
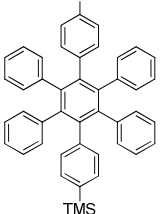
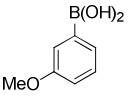
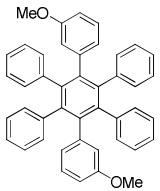
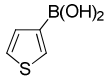
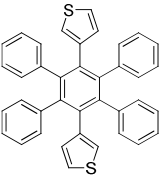
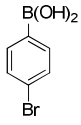
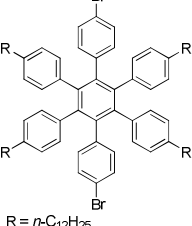
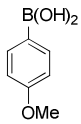
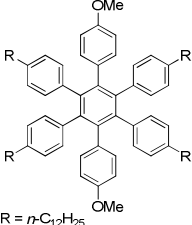
^a Isolated yield of analytically pure compound; ^b No desired product was detected; ^c K₂CO₃ was used as a 2 M aqueous solution.

2.2.4 From 1,4-diiodo-2,3,5,6-tetraarylbenzenes 2-14 to versatile HPBs

With this novel efficient method, different HPB derivatives can be easily prepared with **2-14** and the corresponding arylboronic acids in high yield. Table 2-2 lists some examples of the Suzuki-Miyaura coupling reaction of the tetra-aryl-diiodo benzene **2-14** with various arylboronic acids (For more examples see reference 34).³⁴ The electronic nature of the substituted phenylboronic acids have little effect on the yield of the coupling, and thus HPBs with electron-donating groups were synthesized in good yields (Table 2-2, entries 2 – 3, 5 - 6). For the coupling with 4-bromophenylboronic acid, a lower temperature (80 °C) and longer time (18 h) are required to achieve chemoselectivity between the hindered aryl iodides and the non-hindered aryl bromide on 4-bromophenylboronic acid. Under these conditions, the dibromo HPB **2-32** was prepared in 91% yield on a gram scale. Additionally, the variation of the position of the substituent on the phenylboronic acids does not significantly reduce the yield of such a reaction (Table 2-2, entry 3, 6). Additionally, not only phenylboronic acids but heteroaromatic boronic acids also react well, which was demonstrated by the efficient formation of compounds **2-31** (Table 2-2, entry 4).

This Suzuki-Miyaura cross-coupling reaction not only affords an expedient approach for D_{2h} symmetric HPBs like compounds **2-28** to **2-33**, but can also be used to prepare the C_{2v} -symmetric HPBs with a 1-Ar₁-2,3,5,6-Ar₂-4-Ar₃ pattern by stepwise Suzuki-Miyaura cross-coupling reactions. In the first step, 1.05 equivalent of arylboronic acid reacts with one of the iodo groups in tetraaryl diiodobenzene **2-14** at relatively low temperature. Subsequently, the remaining iodine is coupled with 4-bromo phenyl boronic acid affording the C_{2v} -symmetric HPB. (For further examples, see reference 34)³⁴ It should be noticed that a relatively polar functional group is required in the first Suzuki-Miyaura cross-coupling step for the purification.

Table 2-2. Preparation of symmetrically substituted HPBs by sterically hindered Suzuki-Miyaura coupling reaction.

entry	2-14	ArB(OH) ₂	product	yield (%)
1	2-14a		 2-28	95
2	2-14a		 2-29	93
3	2-14a		 2-30	94
4	2-14a		 2-31	88
5	2-14b		 2-32 R = <i>n</i> -C ₁₂ H ₂₅	91
6	2-14b		 2-33 R = <i>n</i> -C ₁₂ H ₂₅	91

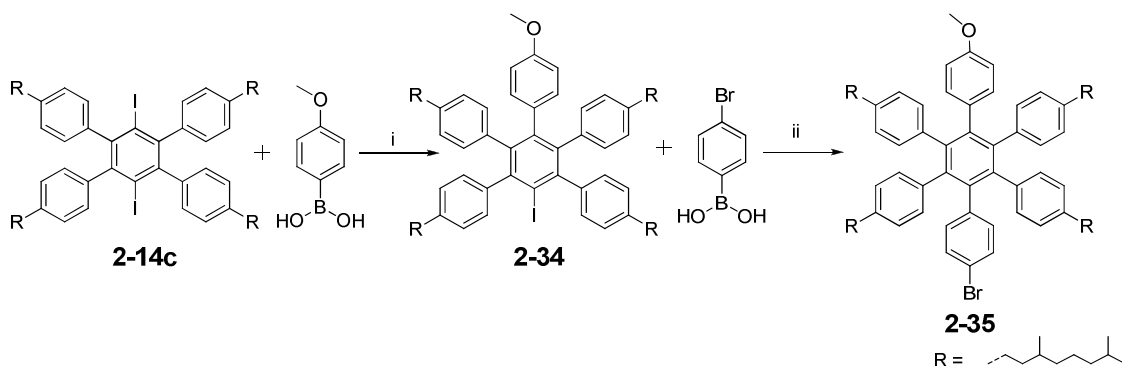


Figure 2-6. An example of synthesis of C_{2v} symmetric HPB derivative; i) $\text{Pd}(\text{PPh}_3)_4$, K_2CO_3 , Aliquat[®] 336, toluene, 80 °C, 12 h, 35%; ii) $\text{Pd}(\text{PPh}_3)_4$, K_2CO_3 , Aliquat[®] 336, toluene, 80 °C, 12 h, 69%.

Figure 2-6 depicts one example of the stepwise Suzuki-Miyaura cross-coupling reaction. The treatment of **2-14c** with 1.05 equivalent of 4-methoxyphenylboronic acid at 80 °C for 12 h resulted in the mono-coupled product **2-34** in 35% yield. Since the selectivity of this step is controlled only by the stoichiometric amount of the arylboronic acid and a relatively low reaction temperature, small quantities of bis-coupled by-products are unavoidable. Therefore, the polarity of the firstly introduced arylboronic acids is essential for the subsequent purification. The remaining iodine is transformed to 4-bromophenyl group in the second step Suzuki-Miyaura cross-coupling reaction in 69% yield. By comparison of the ¹H-NMR spectra of these compounds, the pronounced chemical shift variations of the specific hydrogen atoms clearly illustrate the changing of molecular symmetries (Figure 2-7).

In the spectra, compound **2-14c** has a higher symmetry than the other two. Its aromatic protons (**Ha** and **Hb**, **2-14c**) split into two sets of doublets at 7.00 and 6.92 ppm, respectively, with an over-three-bond coupling constant of 7.8 Hz for each. The α -protons (**Hc**, **2-14c**) give a broad signal at around 2.52 ppm.

The introduction of the 4-methoxyphenyl group significantly reduces the molecular symmetry (**2-34**). The six kinds of aromatic protons exert three sets of resonances. The methoxy group shifts the signals of the adjacent two aromatic protons (**Hf**, **2-34**) to higher field showing a doublet at 6.37 ppm (${}^3J = 8.5$ Hz). Although the chemical environment of the inner aromatic proton **Ha** is different from that of **Hc** (**2-34**), a sharp signal appears at

the lowest field with an integration number four times larger than that of **Hf**. Due to the compensation of aromatic π electron shielding and electron-withdrawing effect from the methoxy group, the signal of the two inner aromatic protons on the methoxyphenyl ring (**He**, **2-34**) overlaps with those from the eight outer aromatic protons (**Hb** and **Hd**, **2-34**) showing a broad peak at 6.69 ppm. More evidently, these signals from the different α -protons (**Hh** and **Hi**, **2-34**) are separated into two sets of multiple peaks, among which those near the 4-methoxyphenyl group (**Hh**, **2-34**) appear at upper field than **Hi** (assigned by comparing the spectrum with the one of **2-14c**).

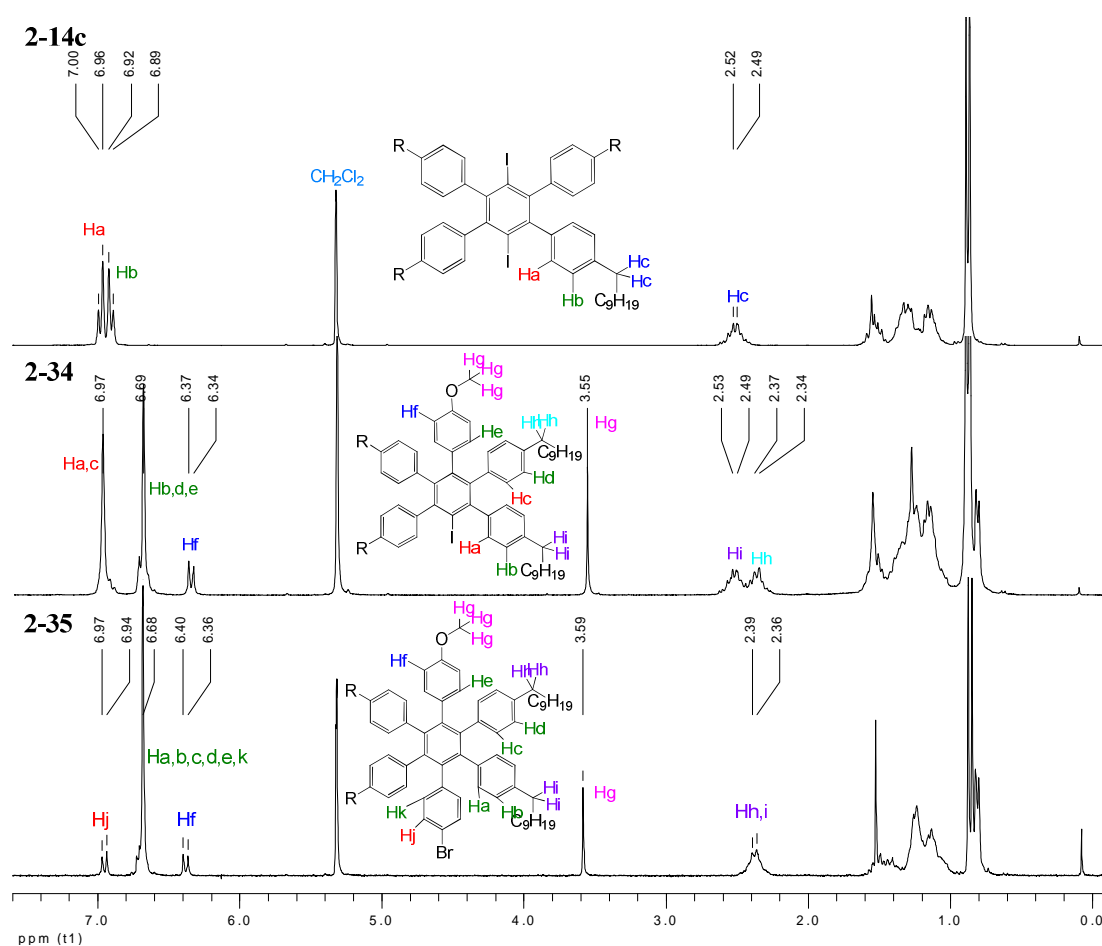


Figure 2-7. ¹H-NMR spectra of **2-14c**, **2-34** and **2-35**, (250 MHz, CD₂Cl₂ at r.t.)

In the case of compound **2-35**, the chemical environment of all the aromatic protons differs from each other. However, its ¹H-NMR spectrum does not reflect the molecular asymmetry as that of compound **3-34**. Because of the similar chemical environments, the

signals of the twenty aromatic protons (Ha, Hb, Hc, Hd, He and Hk) in **2-35** overlap with each other giving rise to an intensive signal at 6.68 ppm. The electron-withdrawing property of the methoxy group and the induced electron-donating nature of the bromine atom shift the resonance signals of their respective neighboring aromatic protons (Hf next to -OCH₃ and Hj next to bromine, **2-35**) apart from each other, and merges the resonances of the two kinds of α -protons (Hh and Hi, **2-35**) into broad multiple peaks in the range of 2.39 – 2.36 ppm in contrast to those in **2-34** (Figure 2-7).

With this powerful method in hand, different oligophenylenes become easily accessible, which effectively expands the diversity of subsequently made PAHs. One example is the preparation of the longest graphene nanoribbons (up to 12 nm) by bottom-up synthetic approach (Figure 2-8, for detailed experiments see the work cooperated with Dr. X. Yang).³⁵

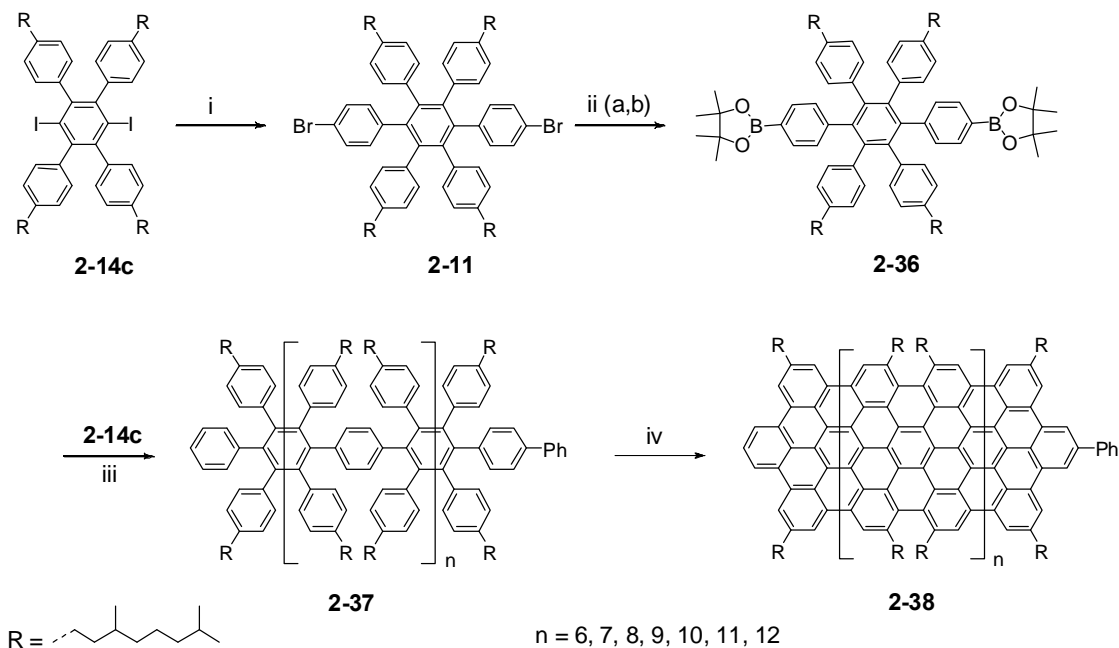


Figure 2-8. Synthesis of graphene nanoribbons; (i) 4-bromophenylboronic acid, Pd(PPh₃)₄, Aliquat[®] 336, K₂CO₃, toluene, 80°C, 24 h, 93%; (ii) ii-a) *n*-BuLi, THF, -78 °C, 1 h; ii-b) 2-isopropoxy-4,4,5,5-tetramethyl-[1,3,2]dioxaborolane, r.t., 2 h, 82%; (iii) Pd(PPh₃)₄, Aliquat[®] 336, K₂CO₃, toluene/H₂O, reflux, 72 h, 75%; (iv) FeCl₃/CH₃NO₂, CH₂Cl₂, r.t., 48 h, 65%.

2.2.5 Limitations in the preparation for HBC derivatives

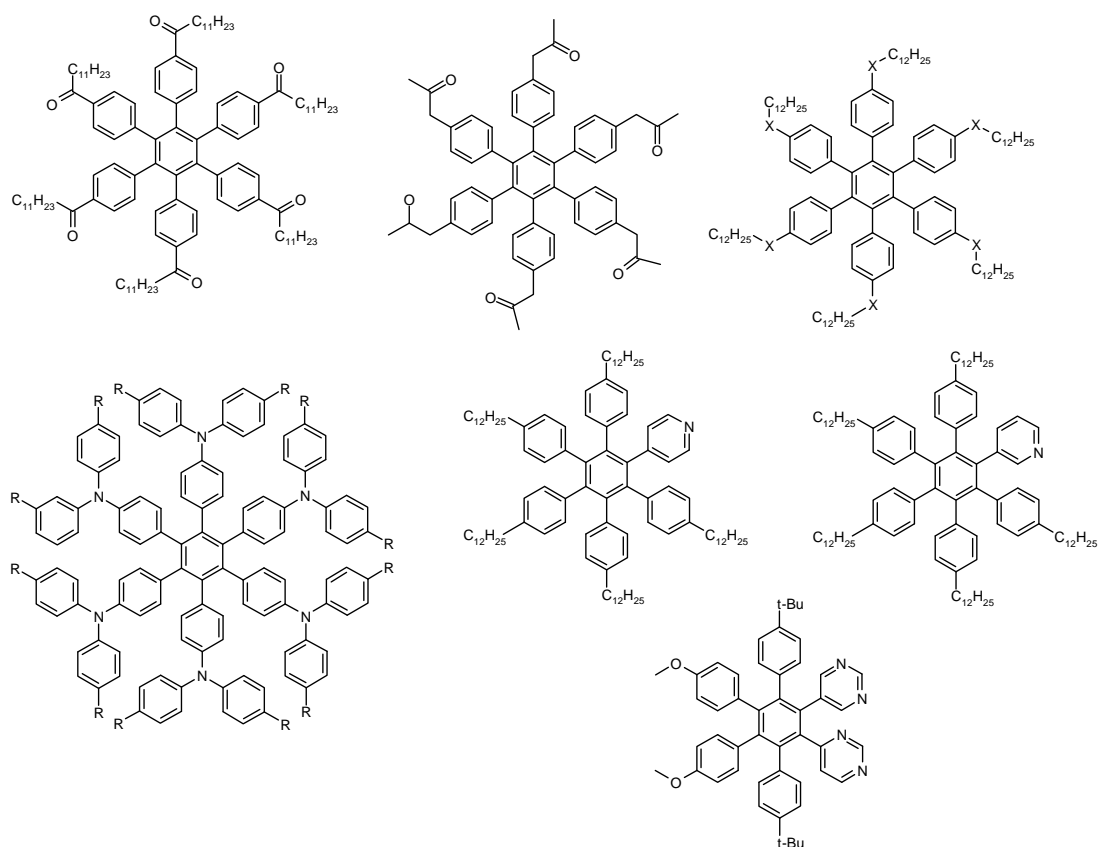


Figure 2-9. Some HPB analogues which failed in the formation of HBC derivatives; X = O, S.

As mentioned before, the electron donating and withdrawing property of the directly attached heteroatoms limits the intramolecular Scholl reaction.^{8, 36-38} Figure 2-9 lists some HPB analogues which do not form the corresponding HBC derivatives in the intramolecular cyclodehydrogenation step.^{1, 10}

Although the new synthetic protocol shows superiority over the traditional intermolecular Diels-Alder reaction route in the preparation for HPB analogues, many heteroatoms (except halides) attached on the phenylboronic acids are limited by their compatibility with the last oxidation step. For example, compound **2-33**, which contains two methoxy groups at *para*-position, was subjected to the intramolecular Scholl reaction. Instead of obtaining a *para*-dimethoxy HBC **2-39**, an unexpected methoxyphenyl group migration was observed resulting in a *meta*-dimethoxy HBC **2-40** and a bis-spirocyclic

dienone **2-41** (Figure 2-10). The detailed structural verification and possible mechanism postulation are presented in CHAPTER 3.

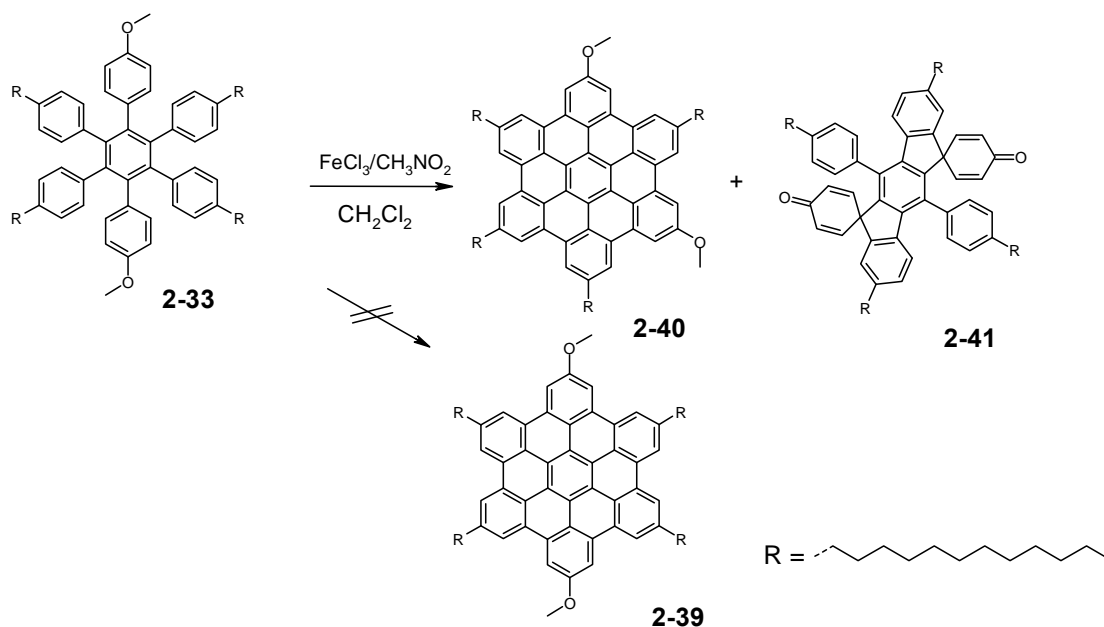


Figure 2-10. An intramolecular Scholl reaction with “*para*”-dimethoxy HBC leads to unexpected methoxyphenyl group migration and bis-spirocyclic dienone.

In order to get a functionalizable C_{2v} symmetric dihalide HBC derivative, the HPB **2-35**, which is asymmetrically modified with one methoxy group and one bromine atom, was also attempted for the intramolecular cyclodehydrogenation (Figure 2-10). During the reaction, **2-35** was dissolved in dichloromethane with a concentration of 8.4×10^{-4} M, and then 1.9 M FeCl_3 (20.4 equivalent) nitromethane solution was added dropwise. Depending on the reaction time, the HPB compound **2-35** was converted to the HBC product **2-42**, however accompanied with one- and two-fold chlorination. After iterative purification with column chromatography, a small amount of **2-42** was collected in a yield of 7%. Its MALDI-TOF spectrum shows a strong peak corresponding to the target molecular weight and small amount of chlorinated by-products. However, lots of impurities are recorded in the aromatic region of its ^1H spectrum (Figure 2-12).

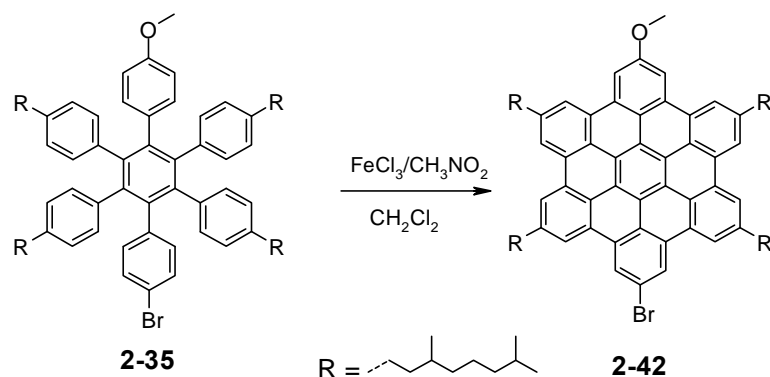


Figure 2-11. Synthetic attempt for *para*-asymmetric HBC 2-42.

The low yield and difficult purification strongly prevent the utilization of this route to build up di-functionalized HBCs with C_{2v} -symmetry. A different HBC building block has to be made to reach this goal.

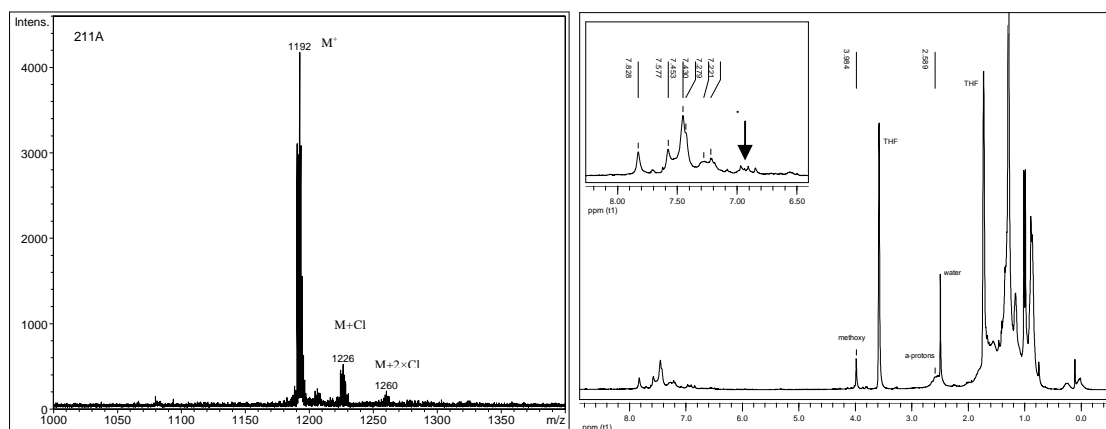


Figure 2-12. MALDI-TOF (measured in TCNQ matrix) and $^1\text{H-NMR}$ (250 MHz, THF, r.t.) spectra of purified 2-42

2.3 Synthesis of C_{2v} -symmetric dihalide HBC building block via intermolecular Diels-Alder reaction

Despite the fact that two different 4-halophenyl groups could be introduced to HPB by the stepwise Suzuki-Miyaura cross-coupling reactions, the similarity of the polarities between the reactant and product cause purification difficulties. The approach to new HBC building blocks containing one iodine and one bromine atoms at *para* position (2-47)

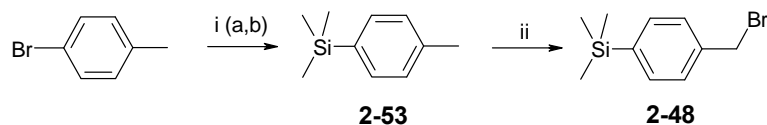


Figure 2-14. Synthesis of 2-48; (i) i-a) *n*-BuLi, THF, -78°C , 15 min. i-b) $(\text{CH}_3)_3\text{SiCl}$, r.t. 16 h, 84%; ii) benzoyl peroxide, NBS, CCl_4 , reflux, 3 h, 72%.

In the following step, *p*-bromobenzyl bromide firstly forms an organometallic complex **2-54**^{11, 40, 41} with 1.02 equivalents of freshly prepared Collman's reagent (Figure 2-15).⁴² The formed complex **2-54** then slowly undergoes oxidative addition to the *p*-trimethylsilylbenzyl bromide, followed by a rearrangement to an acetyl intermediate. After a reductive elimination, the asymmetric ketone **2-49** is obtained in 66% yield.^{11, 40, 41} An alkylated benzil **2-8** further reacts with the asymmetric diphenylketone **2-49** in a Knoevenagel condensation affording tetraarylcyclopentadienone **2-50** in a 50% yield. The next intermolecular [4+2] Diels-Alder reaction between the tolane **2-7** and **2-50** affords the C_{2v} -symmetrically dihalide functionalized hexaphenylbenzene **2-51** in 49% yield. It is worth to notice that the reaction temperature is not as high as that in other similar reactions since the Si-C bond is weak and can not stand harsh conditions. In the next step the trimethylsilyl group is quantitatively transformed to iodine by ICl leading to *para*-iodobromo HPB **2-52** in 95% yield. Since most halides show a certain stability in the cyclodehydrogenation condition, this HPB derivative is then transformed into C_{2v} -symmetric *para*-iodobromo HBC **2-47** (93% yield).

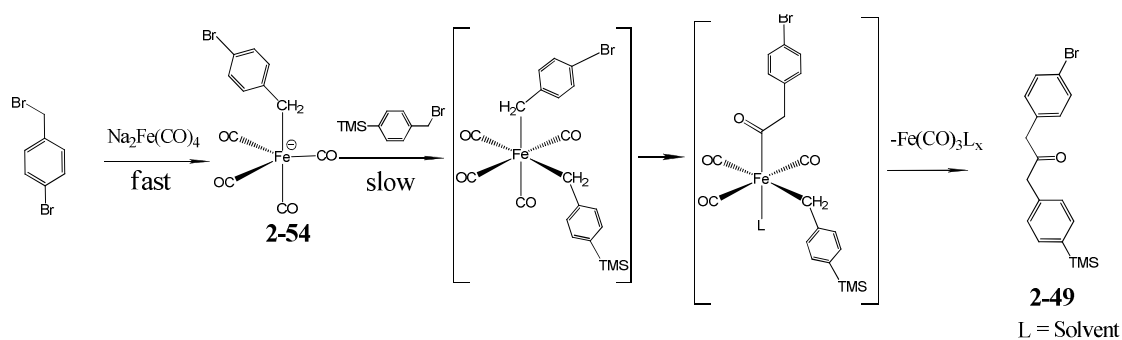


Figure 2-15. Presumed mechanism of carbonylative coupling of benzyl bromides.⁴⁰

2.3.2 Structure characterization for the product and some important intermediates

The molecular asymmetry of **2-49** and **2-50** containing a polar ketone groups is clearly reflected by the chemical shifts of specific protons in the $^1\text{H-NMR}$ spectra (Figure 2-16). Due to the trimethylsilyl group, the nearby aromatic protons (**Hd** in **2-49**, **Hf** in **2-50**) are up-field shifted in contrast to those near bromine (**Ha** in **2-49**, **He** in **2-50**). Especially, the two kinds of α -protons in **2-49** (**He** and **Hf**), which are further away from the aryl substituents, also manifest the chemical-environmental difference with 0.03 ppm difference in chemical shifts.

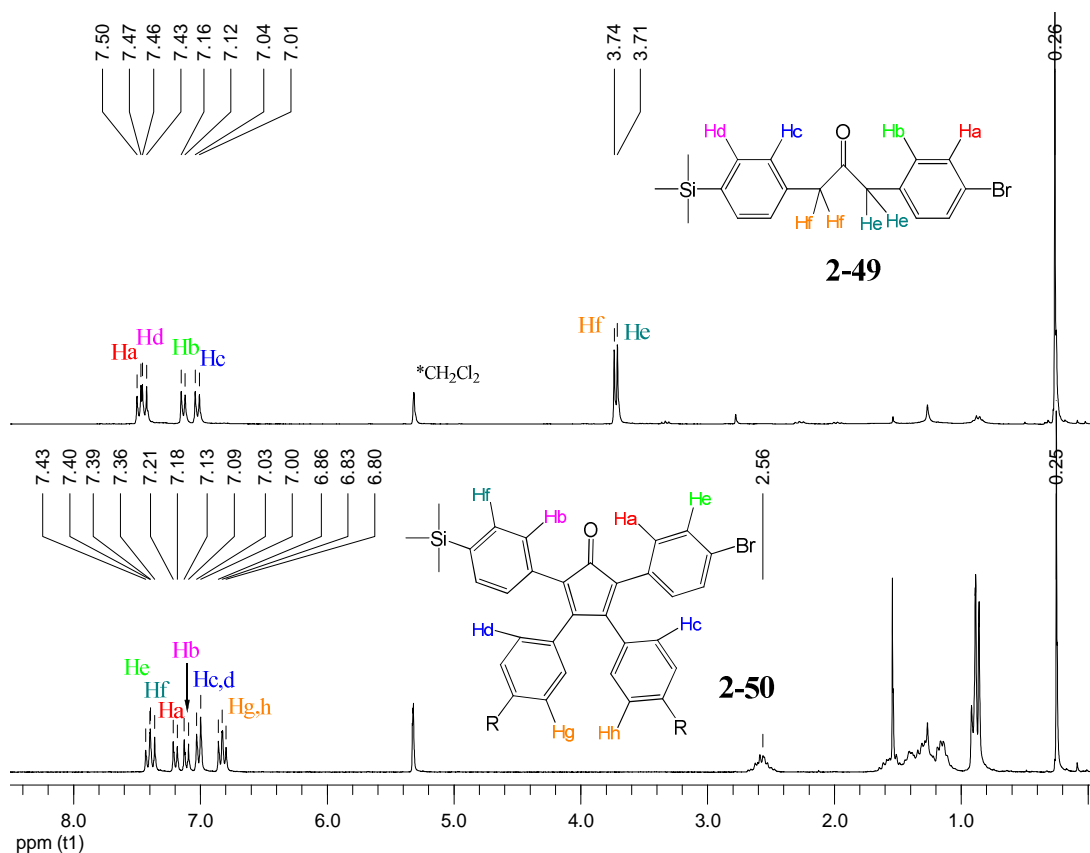


Figure 2-16. ^1H NMR spectra of **2-49** and **2-50**; (250 MHz, CD_2Cl_2 , r.t.)

After the Diels-Alder cycloaddition the disappearance of the polar ketone group reduces the discrepancy of these aromatic protons showing overlapped resonances (Figure 2-17, **2-51**). When the iodine atom is introduced into the system, the chemical

shifts of its neighboring aromatic protons (**Ha**, **Hb**, **2-52**) are low-field shifted due to the enhanced shielding effect.

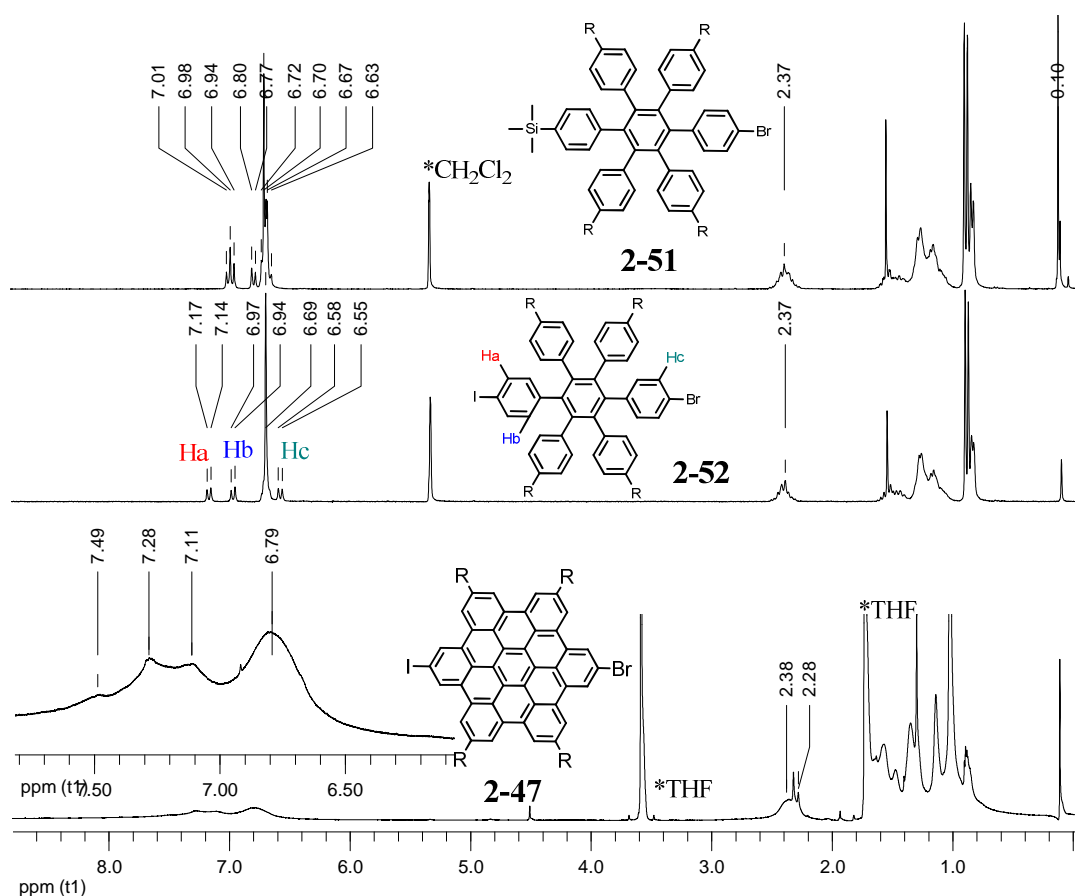


Figure 2-17. $^1\text{H-NMR}$ spectra of HPB **2-51**, **2-52** (250 MHz, CD_2Cl_2 , r.t.) and HBC**2-47** (250 MHz, THF, r.t.); inset: enlarged aromatic area of **2-47**.

Unlike that of its precursors, the $^1\text{H-NMR}$ spectrum of the HBC building block **2-47** is not well-resolved since the planarized structure aggregates much stronger. The six different aromatic protons only show broad peaks, from which four kinds of aromatic protons are recognizable (Figure 2-17, inset). The MALDI-TOF mass spectrum and high temperature $^1\text{H-NMR}$ spectrum confirm the molecular structure by a peak representing exact molecular mass with exact isotope distribute pattern (Figure 2-18).

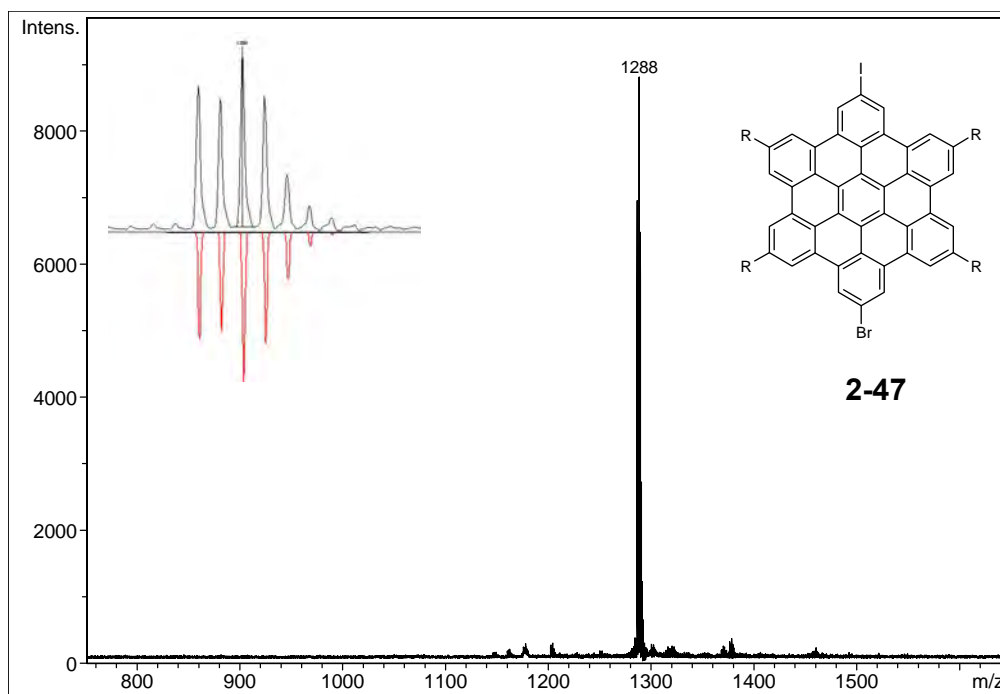


Figure 2-18. MALDI-TOF mass spectrum of 2-47 (measured with TCNQ as matrix) with isotope distribution pattern; red: calculated value.

2.4 Summary

In this chapter, a recently developed simple synthetic approach to HBC derivatives has been demonstrated. The new method involves the one-pot Hart-reaction and sterically hindered Suzuki-Miyaura cross-couplings. Instead of the basic aqueous solution, the condition of Suzuki-Miyaura cross-couplings is optimized by using tri-octyl-methyl ammonium chloride (Aliquat 336[®]) as a phase transfer catalyst. In the traditional reaction condition, such a reaction employs basic aqueous solution and proceeds at the aqueous and organic interface. Under the optimized reaction conditions, the inorganic K_2CO_3 base is effectively dispersed into the organic phase by the phase transfer catalyst leading to nearly quantitative yields. This synthetic strategy has shown superiority in the preparation of D_{2h} -symmetric HBC derivatives over the traditional Diels-Alder route with fewer synthetic steps, high yields and low costs. Based on this method, not only were many HPBs with either D_{2h} - or C_{2v} - symmetries prepared, but novel one-dimensional graphene nanoribbons, with a length up to 12 nm, were also obtained.

Although this method opens an effective pathway to various hexaphenylbenzene derivatives containing directly attached heteroatoms, it is limited by the last intramolecular Scholl reaction in the preparation of corresponding HBC derivatives. In order to obtain versatile HBC functional materials, a new C_{2v} -symmetric HBC building block **2-47** containing two different halogen atoms (one bromine and one iodine) at *para*-position was synthesized via the classical intermolecular Diels-Alder reaction route. Based on the chemical reactivity difference between the bromo and iodo groups, it becomes possible to directly attach two different functionalities on the same HBC core. In so doing, it will render HBC derivatives with novel optoelectronic properties and expand their applications as different functional materials. The asymmetric functionalization of HBCs based on this building block will be further discussed in CHAPTER 5.

2.5 References

1. Wu, J. PhD Thesis. Johannes Gutenberg Universität Mainz, **2004**.
2. Ito, S., Wehmeier, M., Brand, J. D., Kübel, C., Epsch, R., Rabe, J. P., Müllen, K., *Chem. Eur.J.* **2000**, *6*, 4327-4342.
3. Wu, J., Pisula, W., Müllen, K., *Chem. Rev.* **2007**, *107*, 718-747.
4. Fechtenkötter, A., Tchegotareva, N., Watson, M., Müllen, K., *Tetrahedron* **2001**, *57*, 3769-3783.
5. Knochel, P., *Handbook of Functionalized Organometallics*. Wiley-VCH: Weinheim, **2005**.
6. Snieckus, V., *Metal-Catalyzed Cross-Coupling Reactions*. de Meijere, A., Diederich, F., Wiley-VCH: Weinheim, **2004**.
7. Draper, S. M., Gregg, D. J., Madathil, R., *J. Am. Chem. Soc.* **2002**, *124*, 3486-3487.
8. Weiss, K., Beernink, G., Dötz, F., Birkner, A., Müllen, K., Wöll, C. H., *Angew. Chem. Int. Ed.* **1999**, *38*, 3748-3752.
9. Fechtenkötter, A. PhD Thesis. Johannes Gutenberg Universität Mainz, 2001.
10. Gregg, D. J., Ollagnier, C. M. A., Fitchett, C. M., Draper, S. M., *Chem. Eur.J.* **2006**, *12*, 3043-3052.
11. Potter, R. G., Hughes, T. S., *Org. Lett.* **2007**, *9*, 1187-1190.
12. Durand, J. F., Hsun, L. W. C. R., *Hebd. Seances Acad. Sci* **1930**, *191*, 1460.
13. Dilthey, W., Hurtig, G., *Chem. Ber.* **1934**, *67*, 2004-2007.
14. Geissman, T. A., Mallatt, R. C., *J. Am. Chem. Soc.* **1939**, *61*, 1788-1790.
15. Harada, K., Hart, H., Frank Du, C. J., *J. Org. Chem.* **1985**, *50*, 5524-5528.
16. Hennion, G. F., Anderson, J. G., *J. Am. Chem. Soc.* **1946**, *68*, 424-426.
17. Smith, C. F., Moore, G. J., Tamborski, C., *J. Organomet. Chem.* **1971**, *33*, C21-C24.
18. Hart, H., Harada, K., Du, C. J. F., *J. Org. Chem.* **1985**, *50*, 3104-3110.
19. Hart, H., Harada, K., *Tetrahedron Letters* **1985**, *26*, 29-32.
20. Crowther, G. P., Sundberg, R. J., Sarpeshkar, A. M., *J. Org. Chem.* **1984**, *49*, 4657-4663.
21. Jacob, J., Sax, S., Piok, T., List, E. J. W., Grimdsdale, A. C., Müllen, K., *J. Am. Chem. Soc.* **2004**, *126*, 6987-6995.
22. Miyaura, N., Suzuki, A., *Chem. Rev.* **1995**, *95*, 2457-2483.
23. Suzuki, A., *Metal-Catalyzed Cross-coupling Reactions*. Meijere, A. d., Stang, P. J., Wiley-VCH: Weinheim, **1998**.

24. Suzuki, A., *Modern Arene Chemistry*. Astruc, D., Wiley-VCH: Weinheim, **2002**.
25. Miyaura, N., *Metal-Catalyzed Cross-coupling Reactions*. Meijere, A. d., Diederich, F., Wiley-VCH: Weinheim, **2004**.
26. Altenhoff, G., Goddard, R., Lehmann, C. W., Glorius, F., *J. Am. Chem. Soc.* **2004**, *126*, 15195-15201.
27. Dai, C., Fu, G. C., *J. Am. Chem. Soc.* **2001**, *123*, 2719-2724.
28. Littke, A. F., Dai, C., Fu, G. C., *J. Am. Chem. Soc.* **2000**, *122*, 4020-4028.
29. Altenhoff, G., Goddard, R., Lehmann, C. W., Glorius, F., *Angew. Chem. Int. Ed.* **2003**, *42*, 3690-3693.
30. Walker, S. D., Barder, T. E., Martinelli, J. R., Buchwald, S. L., *Angew. Chem. Int. Ed.* **2004**, *43*, 1871-1876.
31. Anderson, K. W., Buchwald, S. L., *Angew. Chem. Int. Ed.* **2005**, *44*, 6173-6177.
32. Barder, T. E., Walker, S. D., Martinelli, J. R., Buchwald, S. L., *J. Am. Chem. Soc.* **2005**, *127*, 4685-4696.
33. Yin, J., Rainka, M. P., Zhang, X. X., Buchwald, S. L., *J. Am. Chem. Soc.* **2002**, *124*, 1162-1163.
34. Xiaoyin Yang, Dou, X., Müllen, K., "Efficient Synthesis of symmetrically and Unsymmetrically Substituted Hexaphenylbenzene (HPB) Analogues via Sterically Hindered Suzuki-Miyaura Coupling Reactions." *Chem. Asian. J.* **2008**; accepted.
35. Yang, X., Dou, X., Rouhanipour, A., Zhi, L., Räder, H.-J., Müllen, K., "Two-dimensional Graphene Nanoribbons." *J. Am. Chem. Soc.* **2008**; accepted.
36. Fechtenkötter, A. PhD Thesis. Johannes Gutenberg Universität Mainz, 2001.
37. Lambert, C., Nöll, G., *Chem. Eur. J.* **2002**, *8*, 3467-3477.
38. Lambert, C., Nöll, G., *Angew. Chem. Int. Ed.* **1998**, *37*, 2107-2110.
39. Nishide, K., Ohsugi, S.-i., Miyamoto, T., Kumar, K., Node, M., *Monatsh. Chem. / Chem. Month.* **2004**, *135*, 189-200.
40. Collman, J. P., Winter, S. R., Clark, D. R., *J. Am. Chem. Soc.* **1972**, *94*, 1788-1789.
41. Collman, J. P., *Acc. Chem. Res.* **1975**, *8*, 342-347.
42. Finke, R. G., Sorrell, T. N., *Organic Syntheses* **1979**, *59*, 102.

3 Magic of Electron Donating Heteroatoms in Scholl Reactions - Unexpected Phenyl Group Rearrangement

In CHAPTER 1, it has been mentioned that the special electronic and optoelectronic properties of polycyclic aromatic hydrocarbons (PAHs) meet with increasing scientific interests.¹⁻³ Hexa-*peri*-hexabenzocoronene (HBC), a disc-like, all-benzenoid PAH, and many of its derivatives have been successfully synthesized via the intramolecular Scholl reaction⁴ under mild reaction conditions.^{5, 6} The incorporation of heteroatoms to the periphery is desirable as the example of triphenylene shows a dramatic increase in charge carrier mobility. However, the direct attachment of heteroatom substituents to the periphery of the HBC skeleton, which influences the electronic properties,⁷ remains a synthetic challenge^{8, 9} despite lots of efforts invested in this area. In the literature one finds the synthesis of an arylamine-substituted HBC as a “coaxial” hole-transport material,⁷ a permethoxylated HBC as a host molecule for co-crystallization with C₆₀,¹⁰ and an “unwrapped” HBC with three neighbouring dodecyloxy chains on one side that exhibits good solution processability.¹¹ On the other hand, the attempted cyclodehydrogenation of hexakis-dodecyloxy-substituted hexaphenylbenzene only resulted in the formation of a quinoidal compound in 96% yield.⁹ This problem was recently circumvented by the introduction of electron-withdrawing fluorine atoms on either side of every alkoxy group.⁸ In this chapter it will be demonstrated that the cyclodehydrogenation reaction of compound **2-33**, the *para*-dimethoxy hexaphenylbenzene, gives two unexpected products, namely *meta*-dimethoxy HBC **2-40** and the bis-spirocyclic dienone **2-41** as well as the phase behavior of the only resulting HBC compound (**2-40**).

3.1 Synthesis and structure verification

Compound **2-33** was synthesized via a Suzuki-Miyaura cross-coupling reaction¹² between the sterically crowded 1,4-diiodo-2,3,5,6-tetraphenylbenzene **2-29** and 4-methoxyphenylboronic acid (91% yield) (Figure 3-1). Instead of the expected *para*-dimethoxy HBC **2-39**, the cyclodehydrogenation reaction of **2-33** with 20.4 equivalents of iron(III) chloride in dichloromethane surprisingly delivered 2,8-dimethoxy-5,11,14,17-tetradodecyl-hexa-*peri*-hexabenzocoronene **2-40** in a yield of 20% as the only HBC product. Its structure was determined using mass spectrometry, ¹H-NMR, ¹³C-NMR, ¹H,¹H NOESY and ¹H,¹H COSY experiments. The major product of the reaction is the bis-spirocyclic dienone **2-41** (in 70% yield), which was successfully purified by recrystallization from a dichloromethane / acetone (1:1) mixture. Its structure was unambiguously determined by the single crystal X-ray diffraction.¹³ The formation of the spirocyclic dienone substructure was reported recently in a related cyclodehydrogenation reaction,¹⁴ but the formation of two of these units in the same molecule is unprecedented.

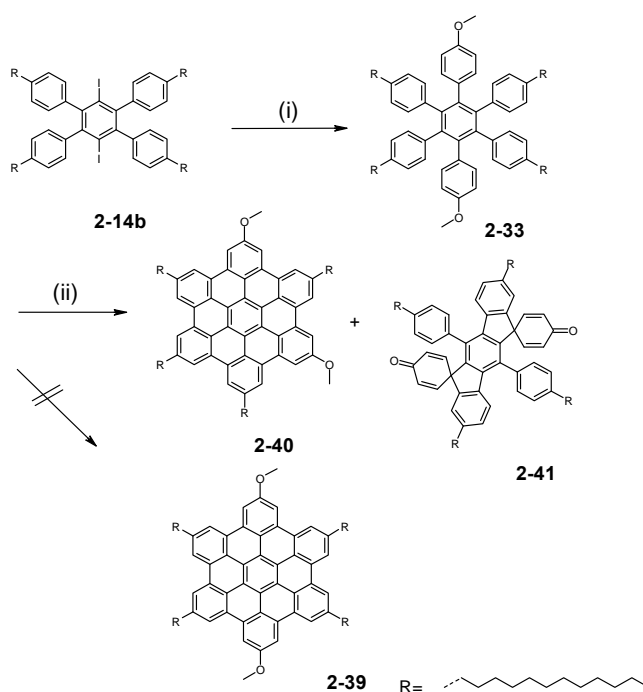


Figure 3-1. Synthesis of compounds **2-40** and **2-41**; (i) 4-methoxyphenylboronic acid, Pd(PPh₃)₄, K₂CO₃, toluene, 100 °C, 91%; (ii) FeCl₃ (20.4 equiv.)/CH₃NO₂, CH₂Cl₂, 20 min, 20% for **2-40**, 70% for **2-41**.

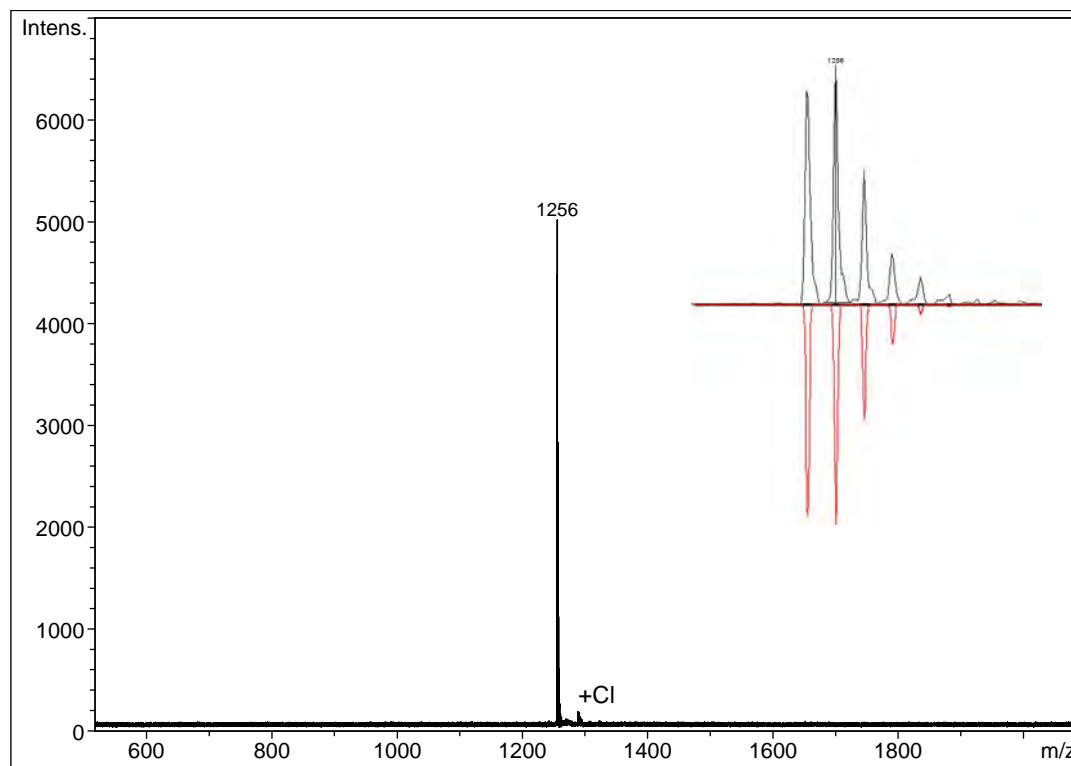


Figure 3-2. MALDI-ToF spectrum of **2-40**; inset: isotope distribution pattern (red, calculated value)

The formation of HBC-type structure (**2-40**) was firstly proven by MALDI-TOF spectrometry, which displayed an intensive m/z peak at the calculated mass of **2-40** with the exact isotope distribution and trace amount of one fold chlorinated product (Figure 3-2). The structure assignment was achieved with the help of NMR spectroscopies. Figure 3-3 shows the ^1H - and ^{13}C -NMR spectra of **2-40** in CDCl_3 . The three alkyl α -proton signals (from 2.79 to 2.35 ppm) and six well resolved aromatic proton signals (six singlets from 7.91 to 7.21 ppm) only fit to the *meta*'-dimethoxy HBC and not to the *para*-isomer, which should show signals for only one alkyl α -proton and three aromatic protons, or the *ortho*- system, which would give two alkyl α -proton and six aromatic proton signals. This assignment was further confirmed by ^{13}C -NMR spectroscopy, whereby 24 well resolved aromatic peaks are recorded in the range of 148 to 96 ppm. These correspond exactly to the *meta*-dimethoxy HBC **2-40**. By comparison, 12 and 21 different aromatic carbon signals are expected for the *para*- and *ortho*- HBC isomers, respectively.

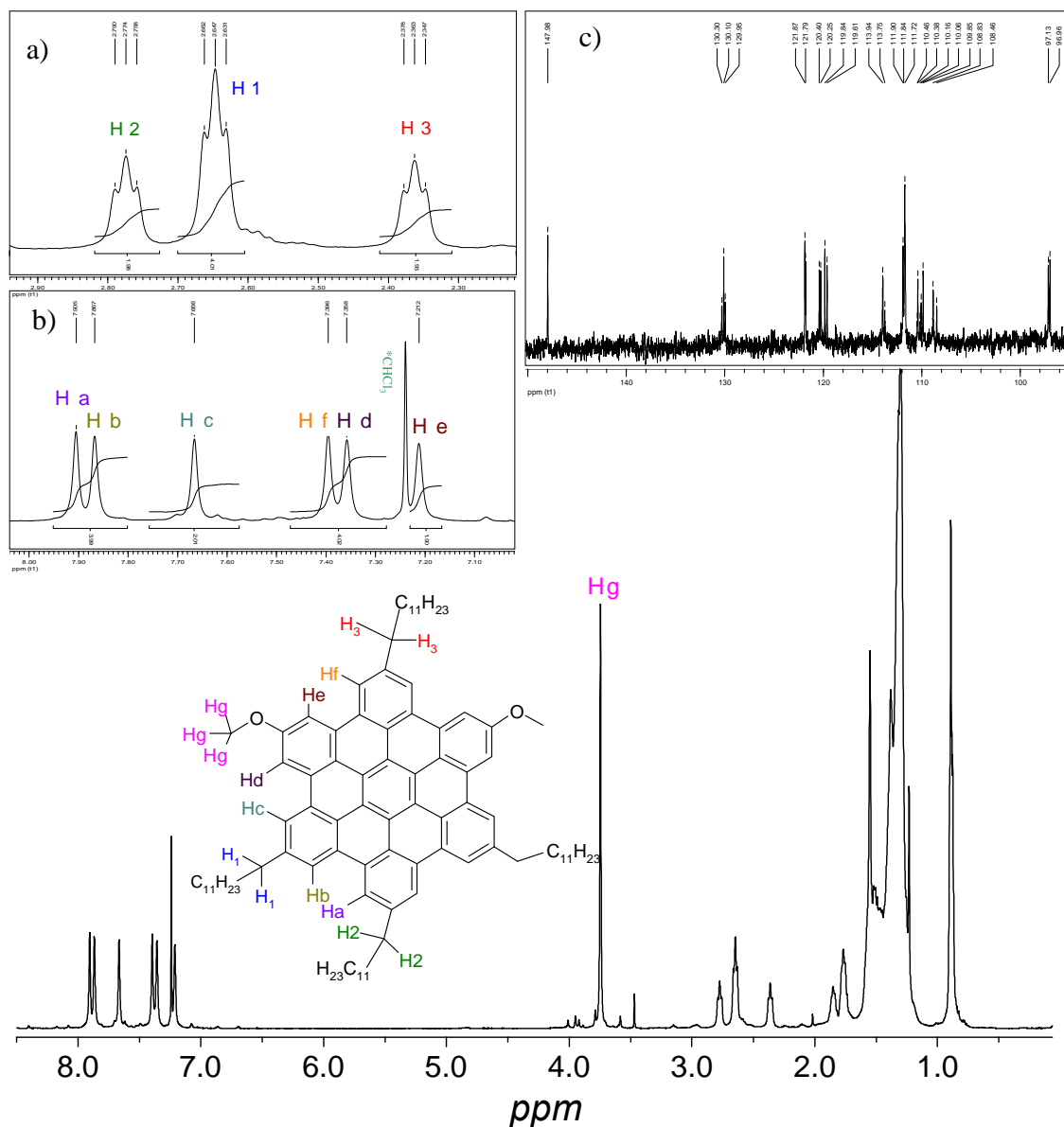


Figure 3-3. ^1H and ^{13}C NMR spectra of compound 2-40 (CDCl_3 , r.t., 500 MHz); inset: enlarged a) alkyl α -proton, b) aromatic proton, c) enlarged ^{13}C spectrum of aromatic region and structural indication.

The structure of compound 2-40 is further verified with the help of ^1H , ^1H NOESY and ^1H , ^1H COSY experiments. On the one dimensional ^1H -NMR spectrum (Figure 3-3), the three triplets with a coupling constant $^3J = 7.5$ Hz in the region from 2.79 to 2.35 ppm are assigned to the three different alkyl α -protons next to the aromatic core. According to their selective integrity, the triplet at around 2.65 ppm, with an selective integrity two times bigger than the values of the other two triplets peaks (at 2.78 and 2.36 ppm) are

attributed to H₁, which couples with four aromatic protons, Ha, Hb, Hc and Hd in the ¹H,¹H NOESY spectrum (Figure 3-4 for the correlations, Figure 3-5A for spectra). The alkyl α-proton signal at 2.78 ppm, which only show correlation peaks with two aromatic protons (Ha and Hb, which also coupled with H₁) in the ¹H,¹H NOESY spectrum, is evaluated as H₂. The remaining one at 2.36 ppm is finally assigned as H₃, showing two coupling signals with the two aromatic protons He and Hf in the ¹H,¹H NOESY spectrum. The singlet peak at 3.75 ppm represents six protons on two methoxy groups, Hg, with same chemical environment. This assignment is also confirmed by its correlation with four nearby aromatic protons, Hc, Hd, He and Hf in the ¹H,¹H NOESY spectrum (Figure 3-5B).

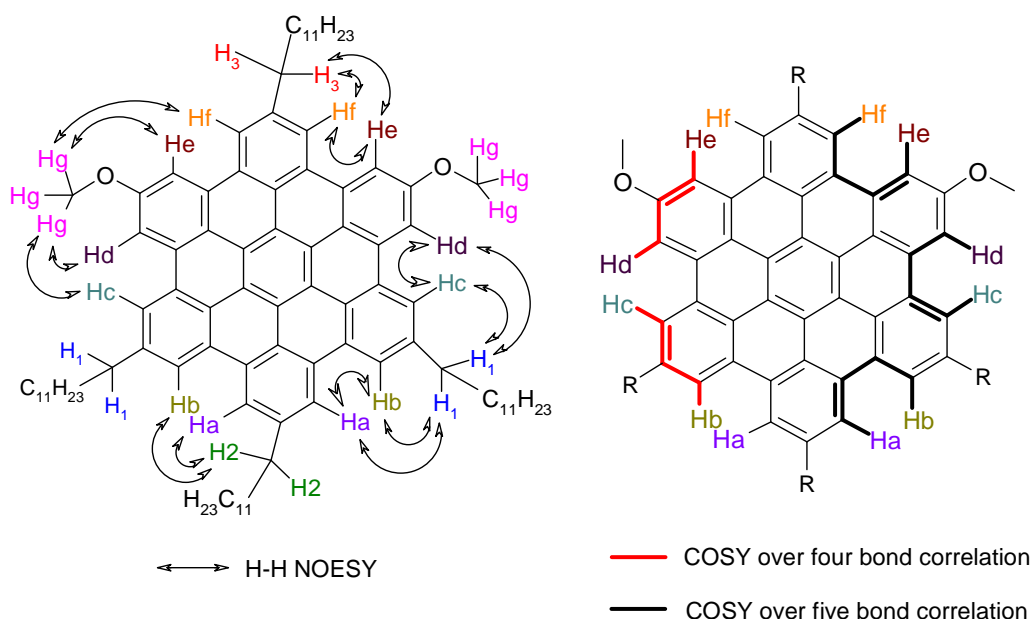
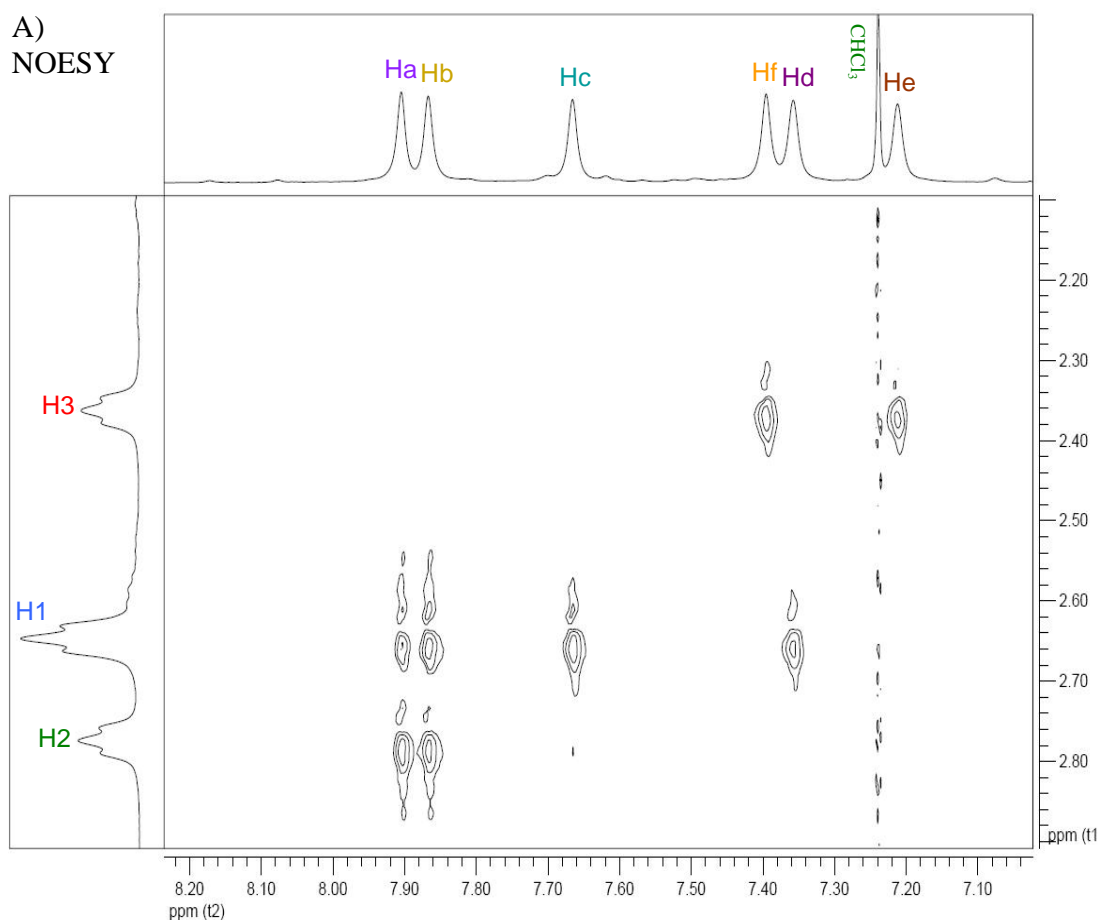
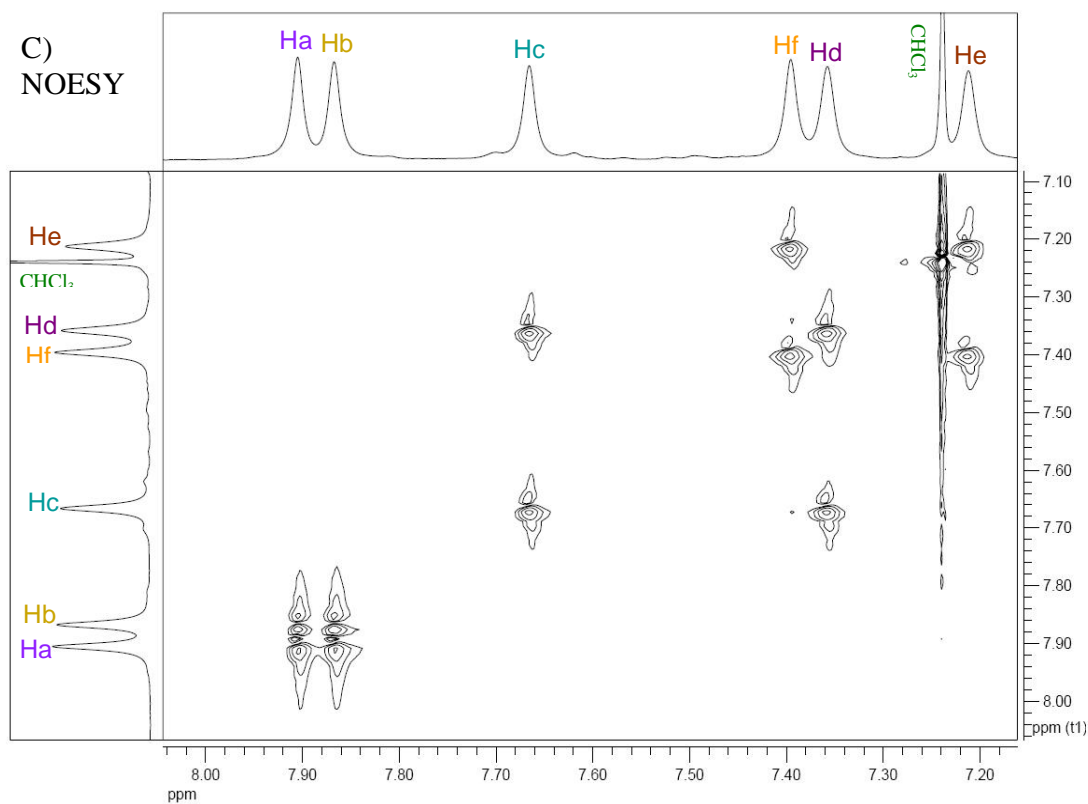
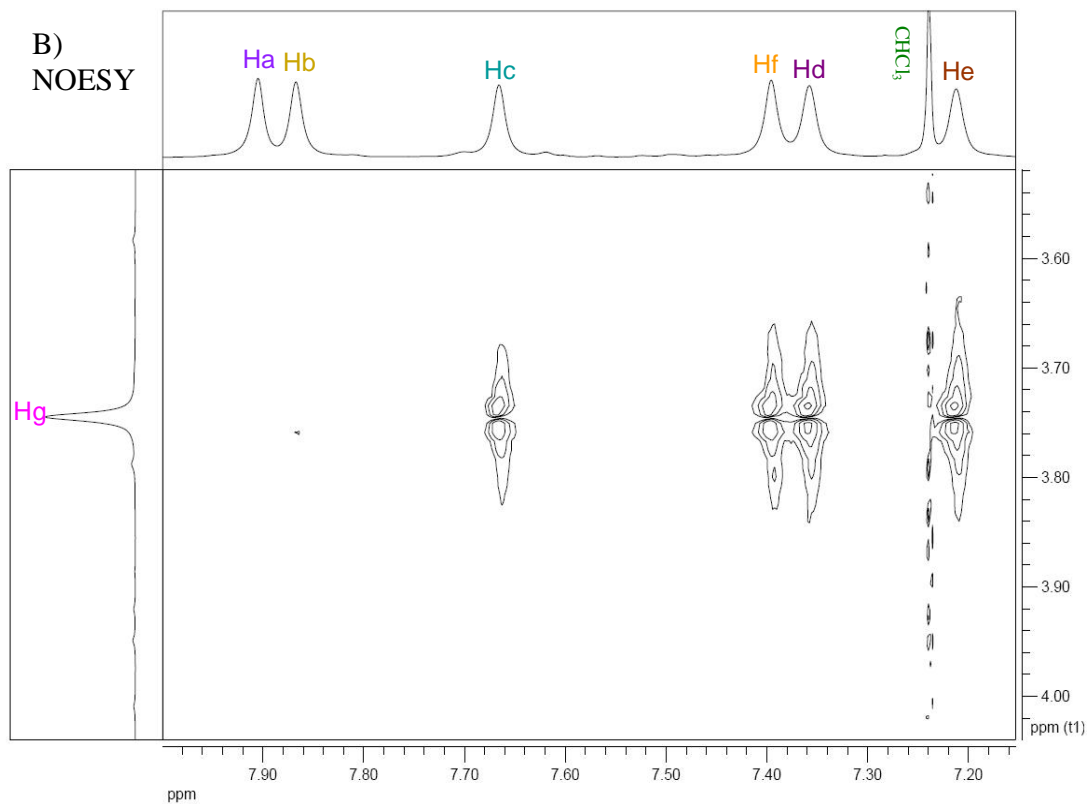


Figure 3-4. ¹H,¹H NOESY and ¹H,¹H COSY correlation of compound 2-40.

The differentiation between the aromatic protons Ha and Hb; Hc and Hd; He and Hf is further achieved by the ¹H,¹H COSY spectrum (Figure 3-5D) and supported by the data from the ¹H,¹H NOESY spectrum (Figure 3-5C). On the ¹H,¹H COSY spectrum, the two protons at 7.91 and 7.40 ppm each show only one over-five-bond coupling signal with the protons at 7.87 and 7.21 ppm, respectively. The one at 7.91 ppm is substantiated as Ha because it does not correlate with the protons on methoxy group, Hg, according to the ¹H,¹H NOESY spectrum. The signal at 7.40 ppm is therefore proven to belong to Hf

coupling with Hg, as described before. Consequently, Hb and He are, respectively, verified at 7.87 and 7.21 ppm as the solely coupled protons of Ha and Hf in the $^1\text{H}, ^1\text{H}$ COSY spectrum. Theoretically, Hb should not only be correlated with Ha over five aromatic bonds but also with Hc over four bonds. Thus, the signal at 7.67 ppm, the other coupling signal of Hb, is allocated to Hc. Hd is assigned to the signal at 7.36 ppm due to its correlation with both He and Hc in a similar way. All the assignments are further proven by aromatic proton couplings in the $^1\text{H}, ^1\text{H}$ NOESY spectrum, which shows correlations between Ha and Hb, Hc and Hd, He and Hf.





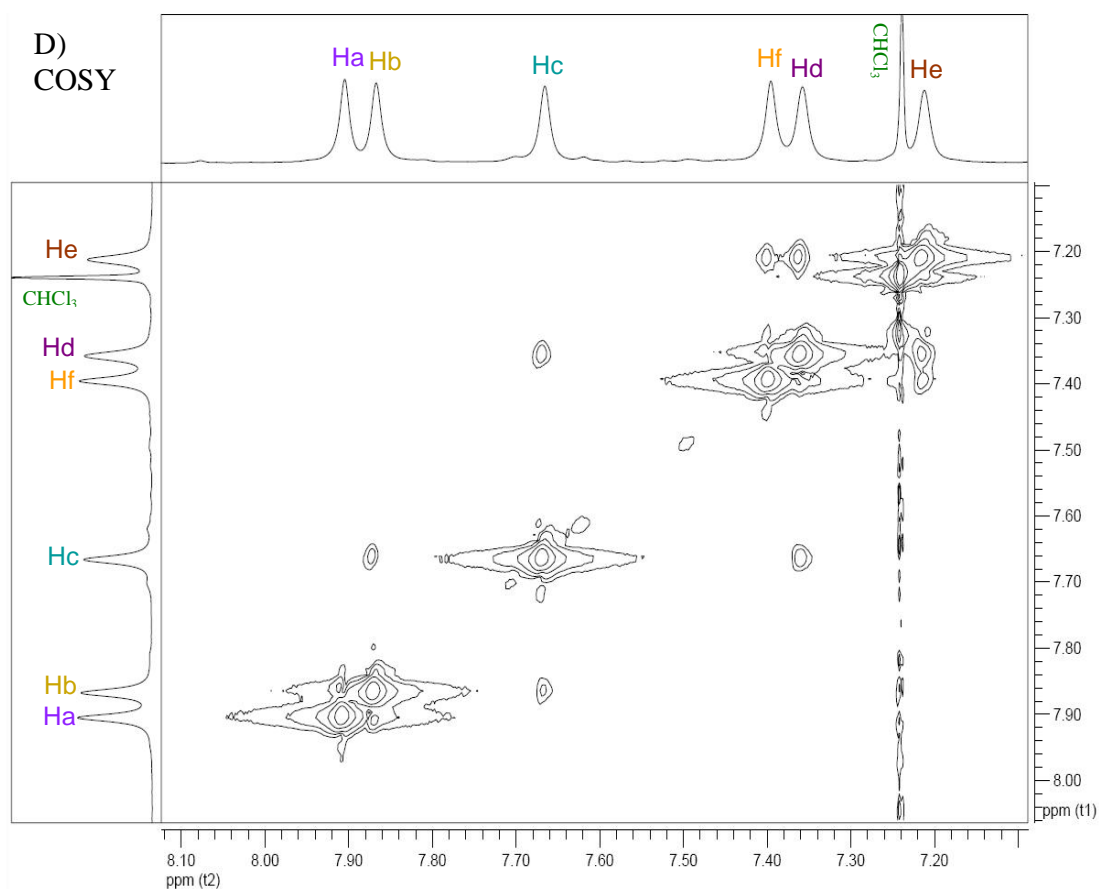


Figure 3-5. $^1\text{H},^1\text{H}$ NOESY and COSY spectra of compound **2-40** (CDCl_3 , r.t., 500 MHz); coupling between A) alkyl α -protons and aromatic, B) methoxy protons and aromatic, aromatic, C) aromatic protons in $^1\text{H},^1\text{H}$ NOESY spectrum and D) aromatic protons in $^1\text{H},^1\text{H}$ COSY spectrum

The single crystal structure of **2-41** shows a face-centered monoclinic unit cell with parameters of $a = 23.05 \text{ \AA}$, $b = 6.81 \text{ \AA}$, $c = 23.90 \text{ \AA}$, $\alpha = \gamma = 90^\circ$ and $\beta = 97.8^\circ$. Every unit cell contains three molecules, two of which are located in the center with a cofacial distance of 5.12 \AA and the remaining one is centered on the faces between b and c vectors with a dihedral angle of 75.14° between the planes of indenofluorene backbones and that of inner molecules (Figure 3-6).

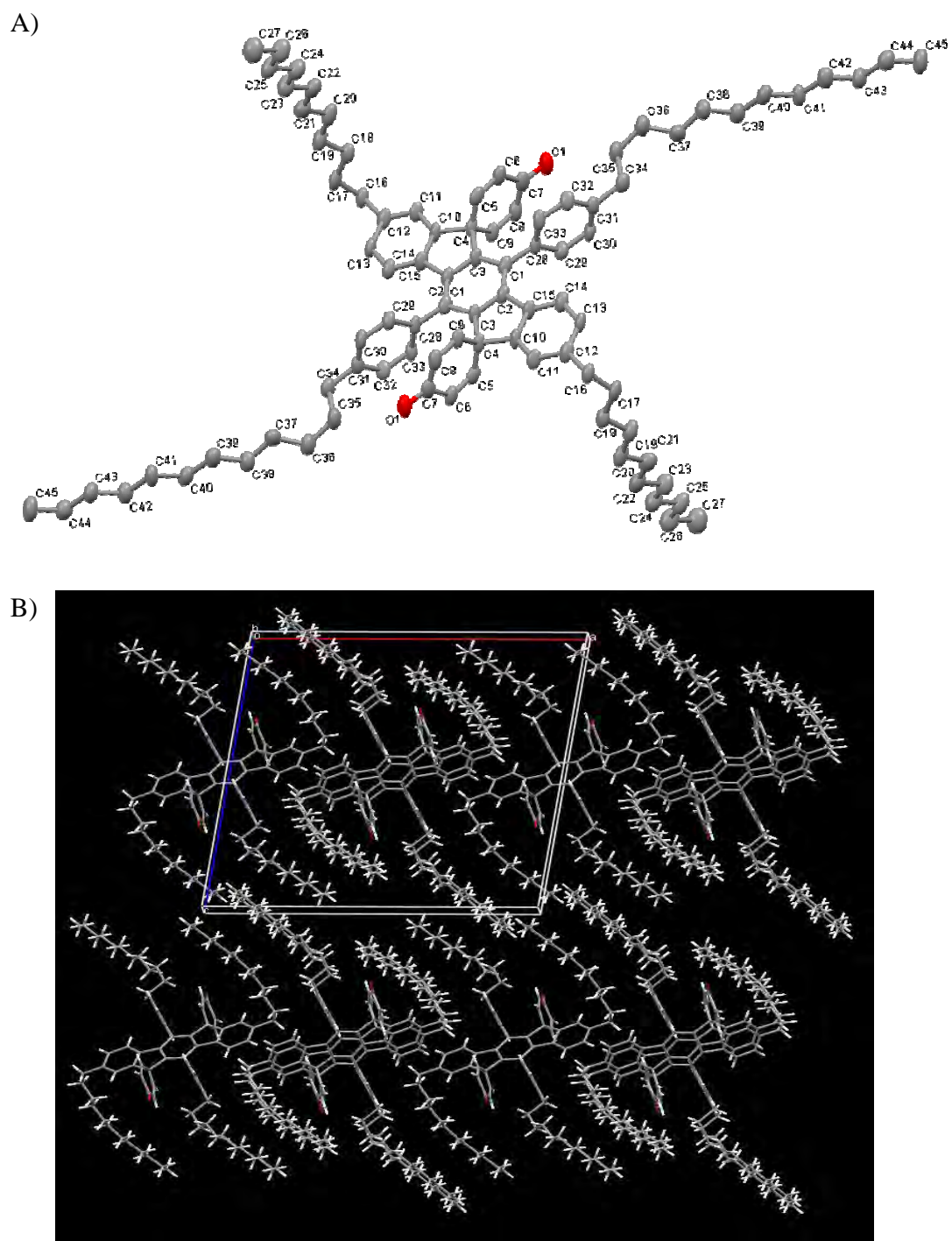


Figure 3-6. A) X-ray crystallographic structure of 2-41; B) molecular packing in crystal structure.

3.2 Proposed mechanism for phenyl group rearrangement

The migration of alkyl groups under Friedel-Crafts conditions^{15, 16} and skeletal rearrangements leading to planar PAHs from “non-planarizable” oligophenylenes¹⁷ have been observed previously, as the degenerate rearrangement of biphenyl¹⁸ under Lewis acid catalysis. This is the first time that a position-exchange of substituents has been observed during the cyclodehydrogenation process. PM3-calculated^{19, 20} heats of formation for compounds **2-40** and **2-39** indicate that they are nearly isoenergetic (**2-40** is 0.03 kcal/mol lower in energy than **2-39**). Thus the driving force for the rearrangement must be exerted at some intermediate stage. Mechanisms for the Scholl reaction^{21, 22} involving either radical cations or arenium cations have been put forward. Several mechanisms, including either type of intermediate, can be drawn to account for the formation of **2-40** and **2-41**, which is summarized in the reaction “landscape” shown in Figure 3-7. This involves initial interconversion of *para*-HPB **2-33** to *meta*-HPB **3-1** and subsequent reaction of these two isomers by different pathways. Whatever mechanisms are considered, a number of interesting mechanistic questions present themselves.

The first key question to be answered is how HPB **3-1** is formed. This can be explained by invoking Scott’s biphenyl rearrangement mechanism to convert **2-33** to **3-1**¹⁸ (Figure 3-8). Protonation of **2-33** on the central ring *ipso* to a 4-methoxyphenyl group affords a cation **3-7** that can undergo ring closure to give phenonium ion.^{23, 13} Opening of **3-8** leads to cation **3-9**, which bears two aryl groups on the same carbon atom. Migration of the more nucleophilic 4-methoxyphenyl group leads back towards **2-33**, whereas migration of the 4-dodecylphenyl group affords a new phenonium ion **3-10**, which can open to afford the cation **3-11** and then **3-1** after deprotonation. Since the formation of **2-40** and **2-41** is favored under Curtin-Hammett control,²⁴ the positions of the equilibrium between **2-33** and **3-1** are probably of little consequence. However, it is worth noting that the positive charge in protonated **3-1** (i.e. **3-11**) can be stabilized by both methoxy groups, while the positive charge in protonated **2-33** (i.e. **3-7**) can only be stabilized by one methoxy group. Once HPB **3-1** has been generated, HBC **2-40** can form in a Scholl reaction.

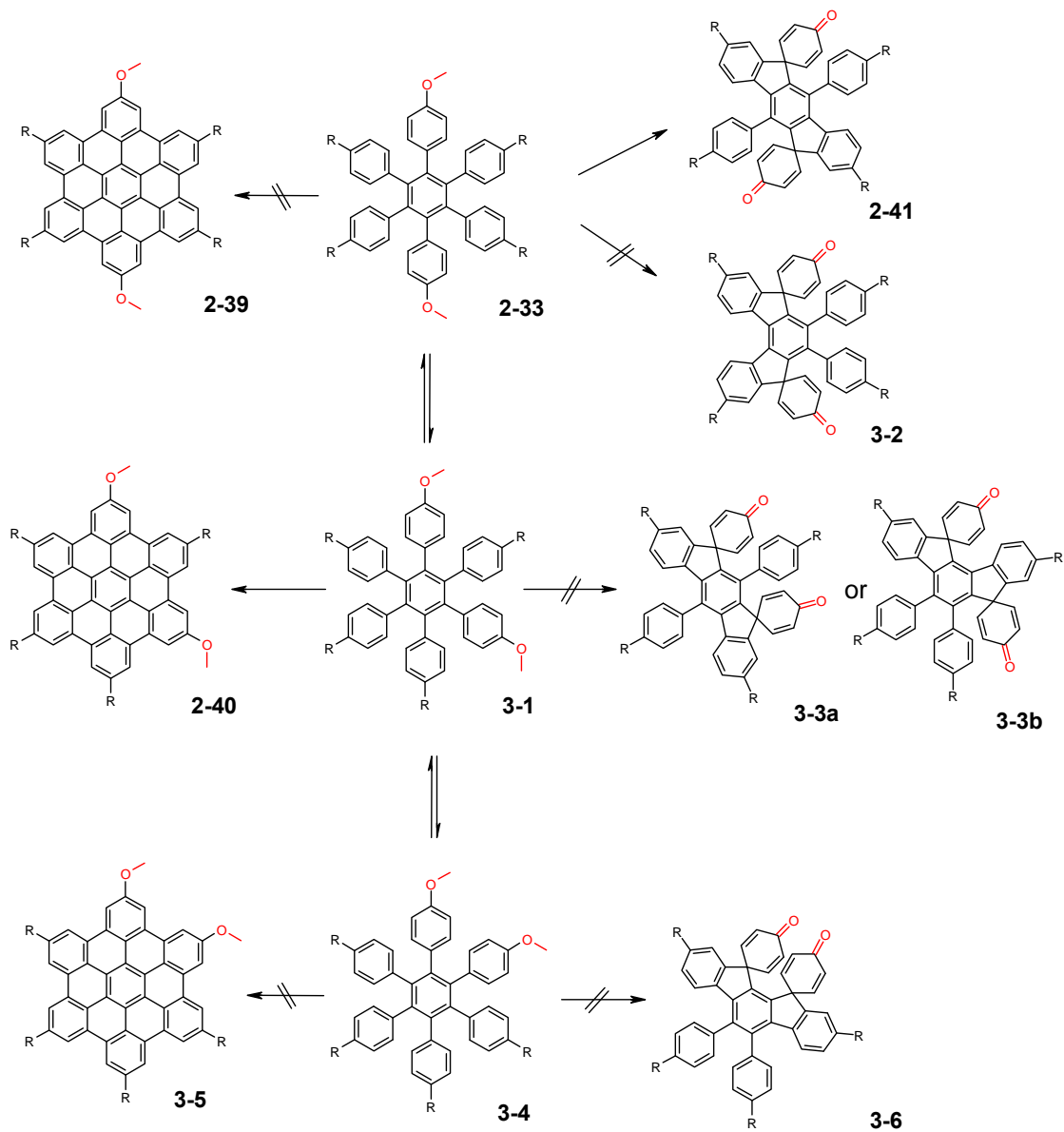


Figure 3-7. Proposed Reaction “Landscape”.

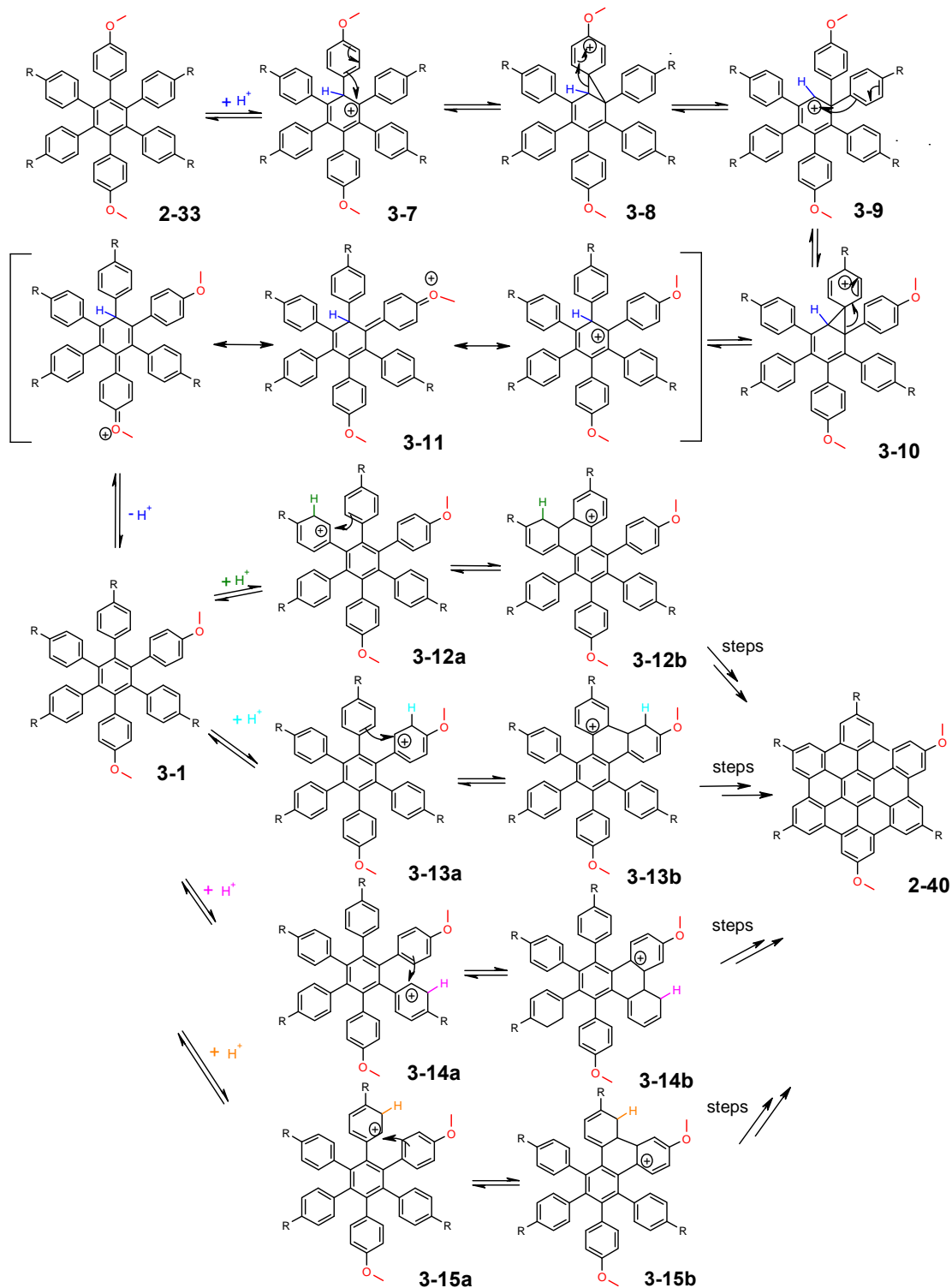


Figure 3-8. Proposed mechanism for the methoxyphenyl migration and the formation of compound 2-40.

Why does HPB **3-1** undergo Scholl reaction, but HPB **2-33** does not? Following an arenium cation mechanism, in which the six protonations occur on the 4-methoxyphenyl groups and the 4-dodecylphenyl group meta to both 4-methoxyphenyl groups (i.e. **3-1** to **3-12a** and **3-1** to **3-13a**), it is evident that the cations resulting from six-membered ring closure (e.g. **3-12b** and **3-13b**) are all stabilized by direct conjugation with both methoxy groups. By comparison, the pathway from **3-1** to **2-40** via cations **3-14a** and **3-15a**, proceeds through ring-closed cations akin to **3-14b** and **3-15b**, which are stabilized by neither methoxy group. More importantly, arenium cation mechanisms leading from **2-33** to the corresponding *para*-HBC **2-39** (which did not form) all go through ring-closed cations (**3-16b** and **3-17b**) that are only stabilized by a single methoxy group (Figure 3-9). If the stabilization of positive charge by the methoxy groups in these systems manifests itself to a significant extent in the transition state of the rate-limiting step, then the rate of reaction leading to **2-40** should be considerably faster than that leading to **2-39**.

Why does HPB **2-33** react to afford bis-spirocyclic dienone **2-41** instead of participating in a Scholl reaction to give **2-39**? Again following an arenium cation mechanism, **2-33** can be protonated either on a 4-methoxyphenyl group to give cation **3-16a** or on a 4-dodecylphenyl group to give cation **3-17a** (Figure 3-9). Both of these cations can conceivably continue towards HBC **2-39** by undergoing six-membered ring formation to give cations **3-16b** and **3-17b**, respectively. However, cation **3-17a** can react to form a five-membered ring through the attack of the relatively nucleophilic carbon atom situated *para* to the methoxy group. Presumably, this process (or the first irreversible step following it) is faster than the alternative six-membered ring forming process. The question of why the C_{2h} symmetric product **2-41** is produced and its C_2 symmetric isomer **3-2** is not formed may have its origin in strain rather than electronic effects. In examining analogous mechanisms leading to **3-2** and **2-41**, no significant electronic differences could be identified. However, PM3 calculations predict **3-2** to be 3.18 kcal/mol higher in energy than **2-41**. The difference in energy is most likely due to the additional strain associated with the helical conformation adopted by the indeno[2,1-b]fluorene skeleton of **3-2** compared to the perfectly planar indeno[1,2-b]fluorene skeleton of **2-41** (Figure 3-10).

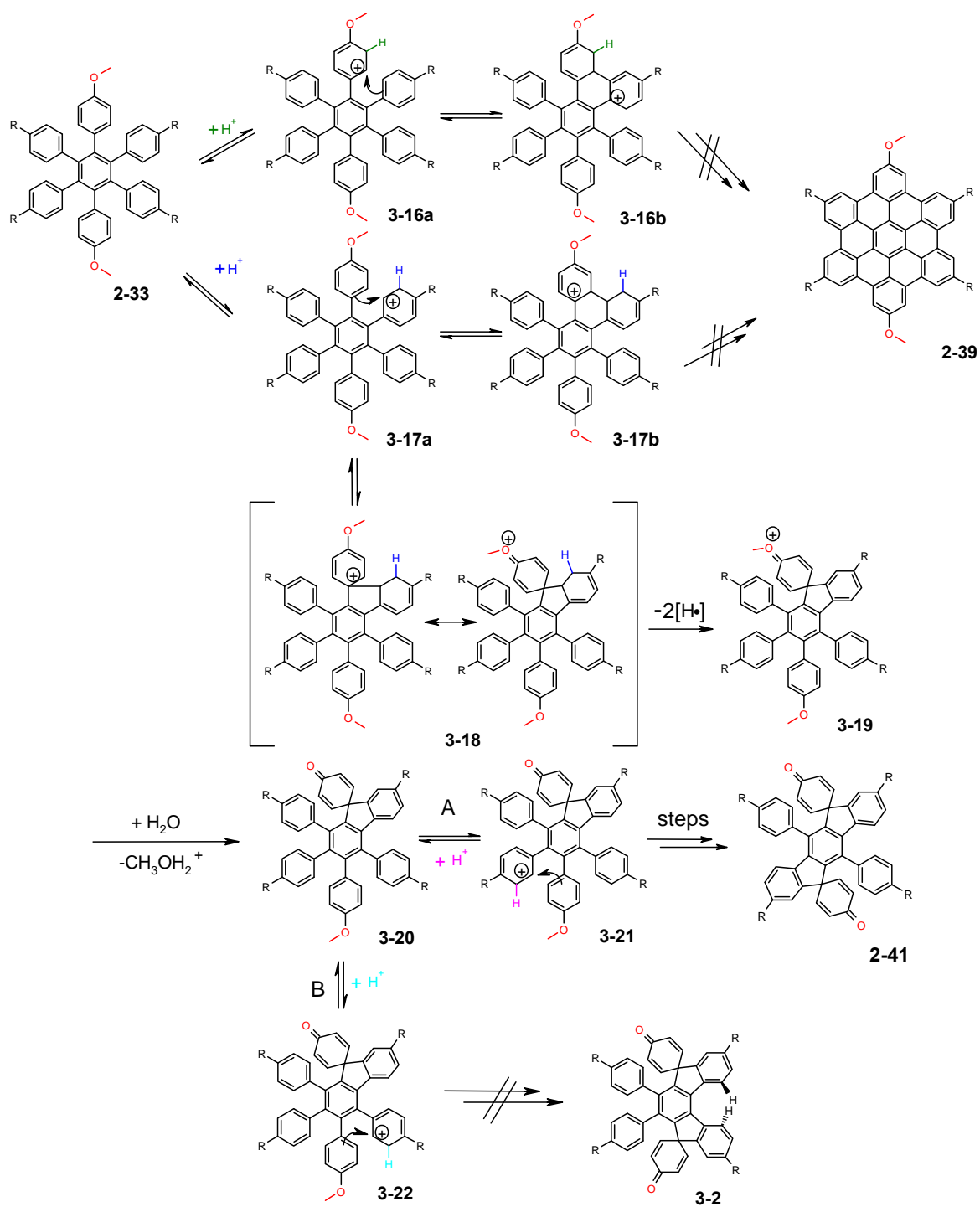


Figure 3-9. Proposed mechanism for the formation of *para*-dimethoxy HBC 2-39, C_{2h} - and C_2 -symmetric bis-spirocyclic dienone (2-41 and 3-2) from *para*-dimethoxy HPB 2-33.

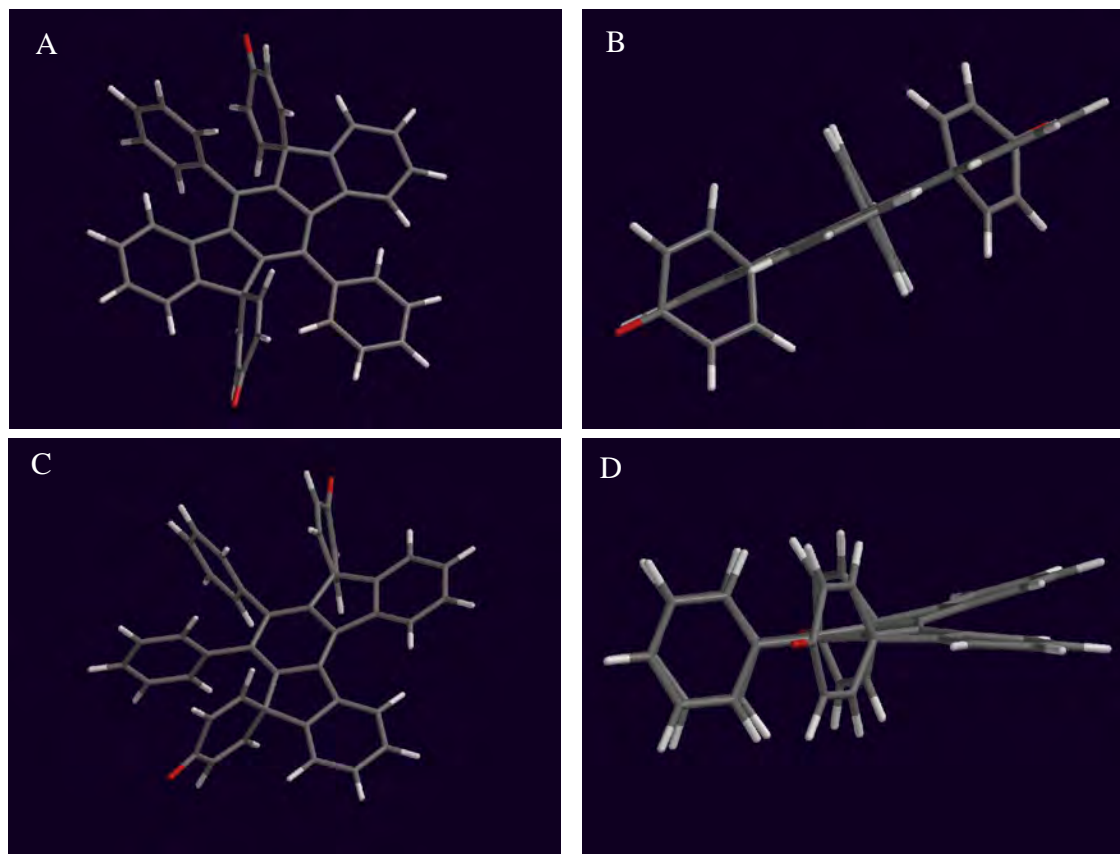


Figure 3-10. PM3-calculated molecular geometry of compound **2-41** (A, top view; B, side view) and **3-2** (C, top view; D, side view). All alkyl chains are neglected to simplify the calculation.

If HPB **2-33** affords bis-spirocyclic dienone **2-41**, why does HPB **3-1** not give analogous products (**3-3a/3-3b**)? Examination of the arenium cation mechanisms leading to such products and those leading to **2-41** does not reveal any differences that would foster the expectation of significantly different rates (Figure 3-11). It is worth noting that cations **3-14a** and **3-15a**, which are on unproductive pathways to **3-1** and **2-40**, are also the first cation species *en route* to **3-3a/3-3b**. Consequently, the wholesale difference in reactivity between **2-33** and **3-1** is consistent with the following scenario: the rates of conversion of **2-33** \rightarrow **2-40** and those of **3-1** to analogous products (**3-3a/3-3b**) are roughly equivalent and they are intermediate between the rate of conversion of HPB **3-1** \rightarrow HBC **2-40** (fast due to cooperative stabilization of (developing) charge) and that of HPB **2-33** \rightarrow HBC **2-39** (slow).

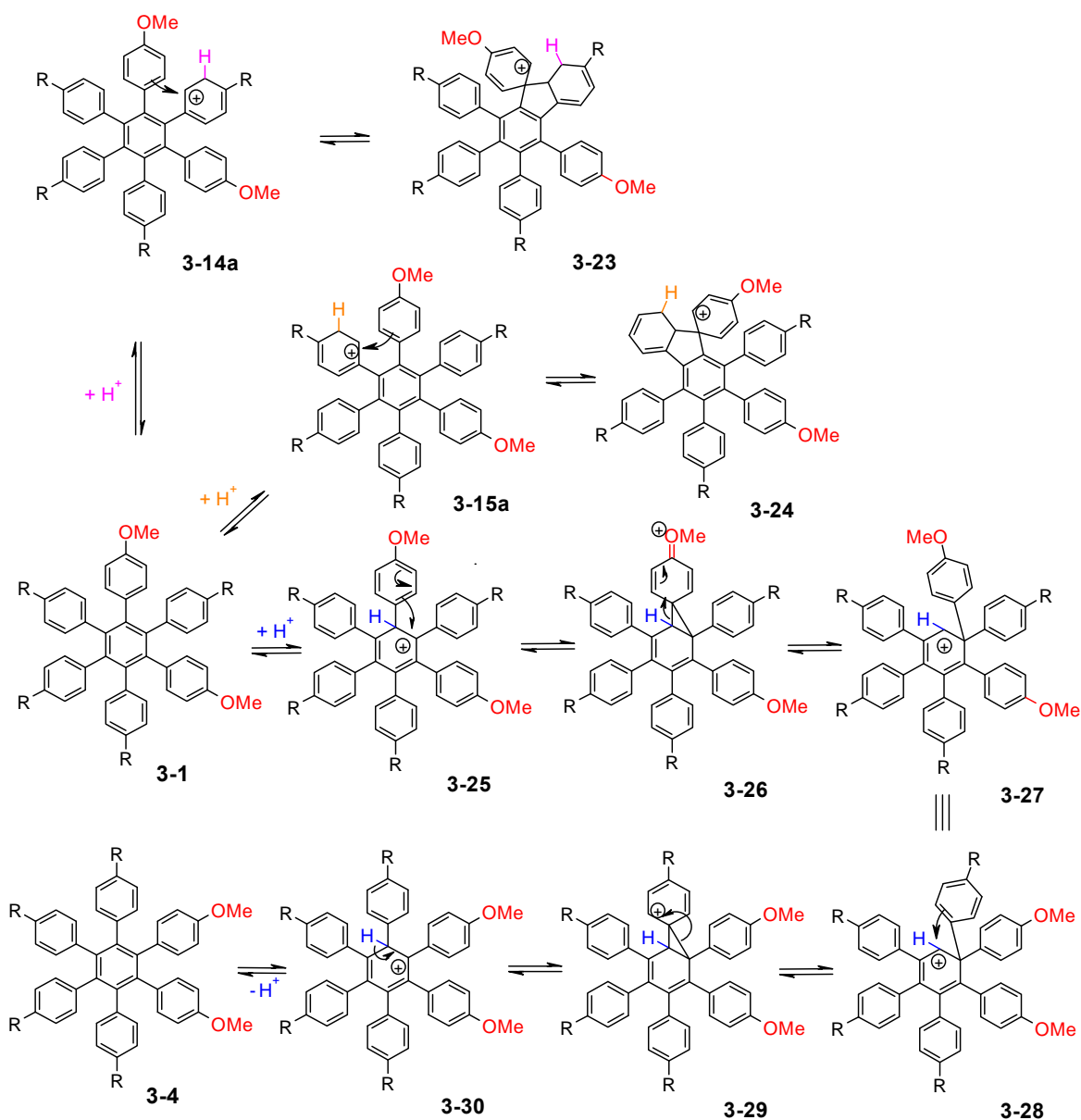


Figure 3-11. Proposed mechanism for the five-membered-ring closure of *meta*-dimethoxy HPB **3-1** and the formation of a possible intermediate *ortho*-dimethoxy HPB **3-4**.

Under such a scenario, which includes the equilibration of **2-33** and **3-1**, the question of whether **3-1** can further isomerize to **3-4** arises. Considering the mechanism of the conversion of **2-33** to **3-1**, there is nothing to suggest that further isomerization to **3-4** would not occur (Figure 3-11). If **3-4** is indeed accessible, the absence of products derived from it could be due either to its formation being unproductive (HBC formation would be expected to be relatively slow for the same reasons as HBC formation from **2-**

33) or the rate of conversion of 3-1 to 2-40 being fast enough to rule out its formation altogether.

3.3 Phase behavior of liquid crystalline 2-40

The bulk thermotropic liquid crystalline property of 2-40 was studied by differential scanning calorimetry (DSC), polarized optical microscopy (POM) and 2D wide angle X-ray diffraction (2D WAXD). The DSC traces were recorded at 10 K/min and shown in figure 3-12, which revealed a first order transition from crystalline (C_r) to liquid crystalline (LC) phase (proved by 2D WAXD) with an enthalpy of 65.41 kJ/mol for heating (68.16 kJ/mol for cooling).

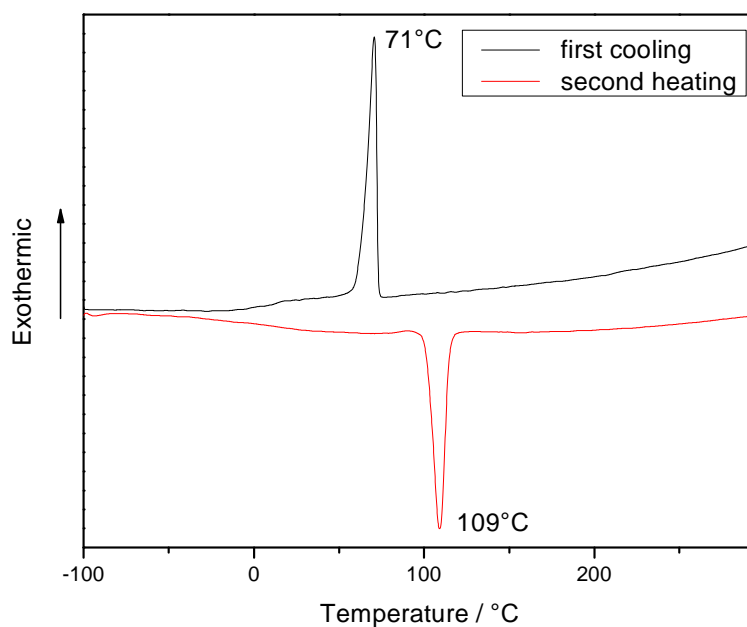


Figure 3-12. DSC traces of 2-40 recorded at 10 K/min.

Its thermotropic mesophase behavior was further investigated by temperature dependent 2D WAXD with an oriented sample, which was extruded through a pinhole with an approximate diameter of 0.7 mm at 120 °C.²⁵ 2D WAXD patterns in transmission were recorded with vertical orientation of the filament axis and the beam perpendicular to

the sample fiber. Figure 3-13 illustrates the diffraction pattern recorded at 30 °C and 150 °C.

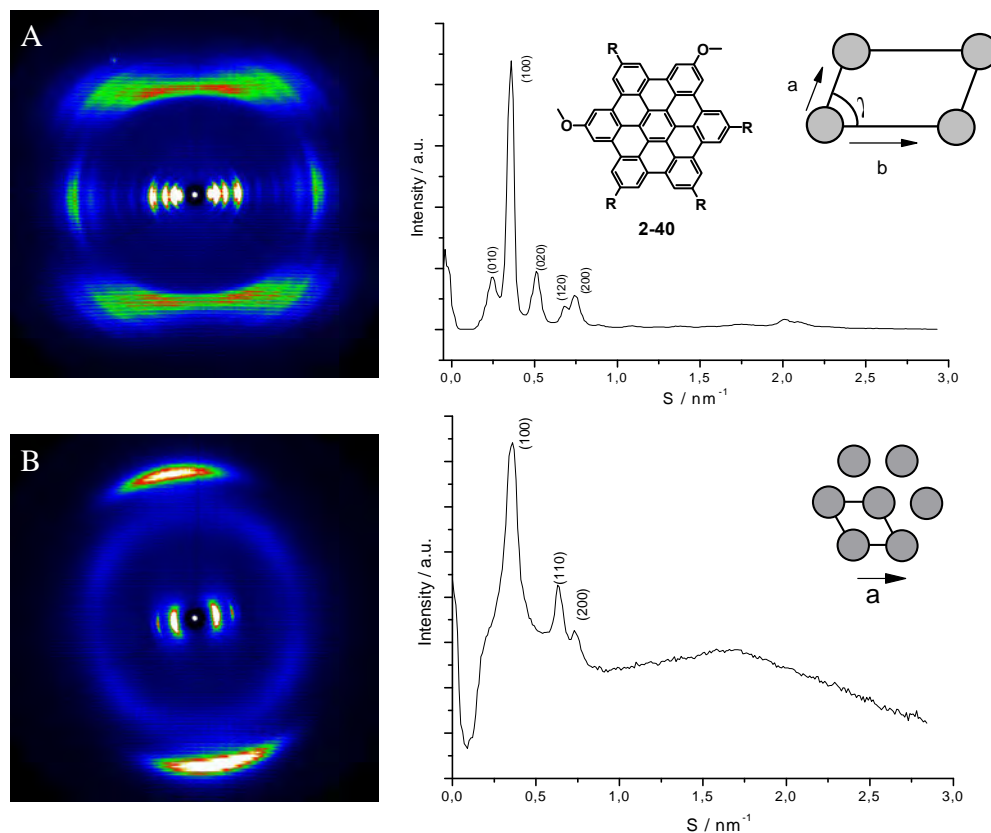


Figure 3-13. 2D WAXD pattern of 2-40 recorded at A) 30 °C and B) 150 °C and equatorial intensity distributions; unit cell parameters: $a = 2.34$ nm, $b = 3.33$ nm, $\gamma = 96^\circ$, $d = 0.44$ nm at 30 °C; $a_{\text{hex}} = 2.90$ nm, $d = 0.36$ nm at 150 °C.

The large number of sharp reflections in the pattern recorded at 30 °C indicated pronounced supramolecular order in the crystalline phase at lower temperatures (Figure 3-13A). HBC columns pack into a monoclinic 2D unit cell with parameters of $a = 2.34$ nm, $b = 3.33$ nm and $\gamma = 96^\circ$. The reflexes along the meridional direction reveal a periodicity of 0.44 nm along the columnar axis. The off-meridional reflections indicate a tilt of the discotic cores with respect to the columnar by an angle of c.a. 36° corresponding to the known “herringbone” structure.²⁷ When entering the liquid crystalline phase, the tilting of molecular disc disappears and the monoclinic lattice of columnar packing changes to hexagonal with a unit cell parameter of $a_{\text{hex}} = 2.90$ nm according to the presence of the equatorial reflections with relative ratios of 1: $\sqrt{3}$:2. The

two intense symmetric meridional arcs indicate a cofacial stacking distance of 0.36 nm, which is a typical value for π - π stacking as observed for other alkylated disc-type PAHs.²⁶

As measured by DSC, the hexagonal liquid crystalline (Col_h) to crystalline (C_r) phase transition revealed a hysteresis (Figure 3-12). This is also supported by temperature dependent 2D WAXD experiments, which tracks the supramolecular order changing upon cooling the sample from the Col_h to C_r phase. The 2D WAXD images display mixed reflections around the phase transition temperature and the Col_h supramolecular organization was preserved shortly after the sample was cooled back (Figure 3-14).

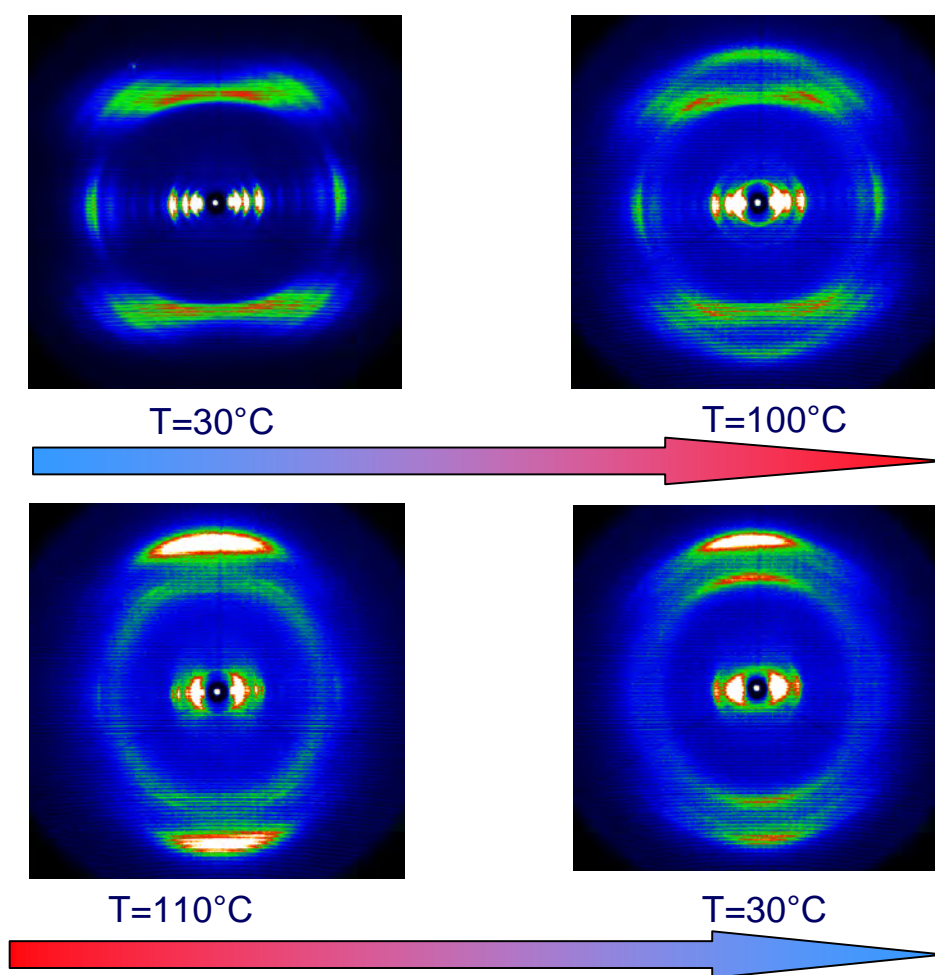


Figure 3-14. 2D WAXD reflection images of 2-40 recorded on heating and subsequent cooling; the last image was taken at 30 °C after the sample was cooled from 110 °C one hour.

The supramolecular ordering gradually turned back at 30 °C (as the one in C_r phase before heating, Figure 3-15A obtained after keeping the sample at 30 °C for 5 h). The slow phase transformation is also evident in the POM image of **2-40**, which was taken at 30 °C upon cooling from 227 °C. (Figure 3-15B) The image shows several circular textures with columnar growth around the multiple nucleation centers (Col_h) and some spherulitic textures with a radial columnar orientation (C_r). It is also worth to note that the nucleation density of the former features exceeds the latter as well as the absence of any correlation between nucleation sites of the Col_h and C_r phases.

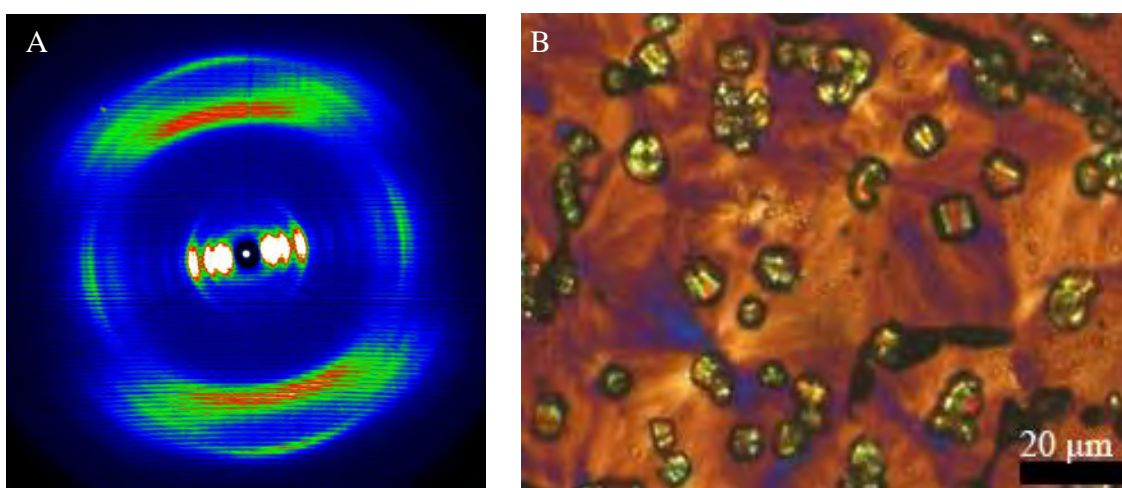


Figure 3-15. A) WAXD pattern of **2-40** recorded at 30 °C after being cooled down from 110 °C for 5h; B) POM image of **2-40** taken at 30 °C after being cooled from 227 °C.

To exploit the influence of the directly attached heteroatoms on the self-assembly behavior of the HBC molecules in bulk state, it is appropriate to compare **2-40** with its analogues HBC- C_{12} **3-31**²⁸ and 2,8,11-trimethoxy HBC **3-32**²⁹ (Figure 3-16). The *meta*-dimethoxy HBC **2-40** shows a similar C_r to Col_h phase transition temperature (109 °C upon heating and 71 °C upon cooling) with that of HBC- C_{12} **3-31**, the transition temperature of which is located at 107 °C upon heating and 82 °C upon cooling as determined by DSC. Upon the introduction of the third methoxy group (**3-32**), the C_r phase is expanded with the C_r to Col_h phase transition temperature being elevated to a higher temperature (145 °C upon heating and 102 °C upon cooling). The difference between the transition temperatures recorded for the heating and cooling curves reflects a hysteresis effect due to slow phase transition kinetics. By comparing the hysteresis effect

of these three compounds (Table 3-1), it can be expected that the introduced electron donating methoxy groups increase the intermolecular interactions resulting in a slower phase transformation process (as shown by the phase coexistence of **2-40** in Figure 3-14 and 3-15). The enhanced intermolecular interactions also manifest themselves as decreased enthalpic energy differences between C_r and Col_h phases (ΔH values, Table 3-1). The above mentioned results are in good consistence with similar studies on dipole functionalized triphenylene derivatives, whereby this phenomenon is attributed to enhanced intermolecular interactions due to strong dipole moments.³⁰

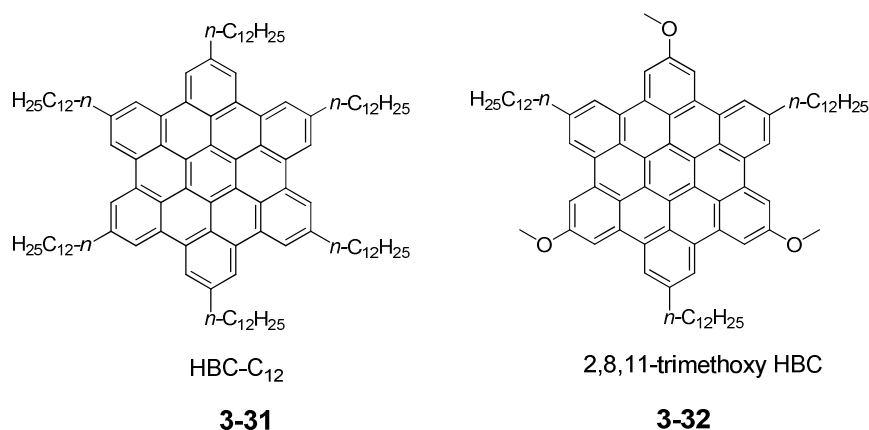


Figure 3-16. Molecular structure of HBC-C₁₂ (**3-31**) and 2,8,11-trimethoxy HBC (**3-32**).

Table 3-1. Phase transition data of HBC-C₁₂ (**3-31**), *meta*-dimethoxy HBC (**2-40**) and 2,8,11-trimethoxy HBC (**3-32**).

	Transition temperature / °C	Hysteresis ΔT / °C	ΔH / KJ·mol ⁻¹
HBC-C ₁₂ (3-31)	107 (heating)	25	91.96
	82 (cooling)		
<i>meta</i> -dimethoxy HBC (2-40)	109 (heating)	38	68.16
	71 (cooling)		
2,8,11-trimethoxy HBC (3-32)	145 (heating)	43	14.56
	102 (cooling)		

The three compounds demonstrate similar hexagonal columnar supramolecular organization in LC phase ($a_{\text{hex}} = 2.86$ nm for **3-31**, $a_{\text{hex}} = 2.90$ nm for **2-40** and $a_{\text{hex}} = 2.51$ nm for **3-32**). In the crystalline phase, the weak molecular dipole (due to the attached methoxy groups, see CHAPTER 4) gives rise to interesting molecular packing behavior.

Unlike HBC-C₁₂ **3-31**, which forms a rectangular 2D lattice showing lots of relatively weak reflection peaks,²⁸ the 2D WAXD reflections of *meta*-dimethoxy HBC **2-40** are more pronounced and better ordered demonstrating a monoclinic 2D unit cell. When the molecular dipole is slightly weakened by the introduction of the third methoxy group (due to molecular symmetry, 2,8,11-trimethoxy HBC **3-32**), the molecules organized into a complex helical hexagonal superstructure like monoethynyl HBC **4-3** (see CHAPTER 4) under the guidance of intermolecular $\pi - \pi$ and dipole – dipole interactions.²⁹

3.4 Summary

It has been demonstrated in this chapter that the intramolecular Scholl reaction of **2-33** resulted in the formation of two unexpected products, **2-40** and **2-41**, which may mean that the course of the intramolecular Scholl reaction might be subject to some degree of control through the judicious use of substituents.¹⁴ These results provide experimental facts for the mechanistic investigation of the Scholl reaction as well. Following the pioneers' work in this aspect, a reasonable mechanism was proposed involving common intermediates for the formation of both of these very unusual compounds. Moreover, two methoxy groups without any extra peripheral decoration have successfully been attached directly to the HBC core, albeit with a *meta* instead of the expected *para* relationship. This compound showed typical liquid crystalline phase behavior as six-fold alkylated HBC analogues. In addition, temperature dependent 2D WAXD and POM results implied very slow transformation kinetics with the coexistence of Col_h and C_r phase during cooling the compound from Col_h to C_r phase, due to the introduced weak permanent dipole moment (see CHAPTER 4) on HBC moiety. By comparing its phase behavior in the bulk state with that of related compounds (**3-31** and **3-32**), it can be concluded that the enhanced intermolecular interactions apparently increase the supramolecular ordering and the stability of the liquid crystalline phase.

The influence of the dipole moment on the HBC molecular dynamics, kinetics and phase behavior will be further explored with the techniques of site-specific solid state NMR and dielectric spectroscopy in the following chapter.

3.5 References

1. S. M. Kelly, M. O'Neill, *Adv. Mater.*, **2003**, *15*, 1135-1146.
2. C. D. Simpson, J. Wu, M. D. Watson, K. Müllen, *J. Mater. Chem.*, **2004**, *14*, 494-504.
3. A. C. Grimsdale, K. Müllen, *Angew. Chem. Int. Ed.*, **2005**, *44*, 5592-5629.
4. R. Scholl, J. Mansfeld, *Ber. Dtsch. Chem. Ges.*, **1910**, *43*, 1734-1746.
5. A. Stabel, P. Herwig, K. Müllen, J. P. Rabe, *Angew. Chem. Int. Ed.*, **1995**, *34*, 1609-1611.
6. M. Müller, H. Mauermann-Düll, M. Wagner, V. Enkelmann, K. Müllen, *Angew. Chem. Int. Ed.*, **1995**, *34*, 1583-1586.
7. J. Wu, M. Baumgarten, M. G. Debije, J. M. Warman, K. Müllen, *Angew. Chem. Int. Ed.*, **2004**, *43*, 5331-5335.
8. Q. Zhang, P. Prins, S. C. Jones, S. Barlow, T. Kondo, Z. An, L. D. A. Siebbeles, S. R. Marder, *Org. Lett.*, **2005**, *7*, 5019-5022.
9. K. Weiss, G. Beernink, F. Dötz, A. Birkner, K. Müllen, C. H. Wöll, *Angew. Chem. Int. Ed.*, **1999**, *38*, 3748-3752.
10. Z. Wang, F. Dötz, V. Enkelmann, K. Müllen, *Angew. Chem. Int. Ed.*, **2005**, *44*, 1247-1250.
11. Z. Wang, M. D. Watson, J. Wu, K. Müllen, *Chem. Commun.*, **2004**, 336-337.
12. X. Yang, X. Dou, K. Müllen, "Efficient Synthesis of symmetrically and Unsymmetrically Substituted Hexaphenylbenzene (HPB) Analogues via Sterically Hindered Suzuki-Miyaura Coupling Reactions." *Chem. Asian. J.* **2008**, accepted.
13. Crystals suitable for X-ray structure analysis were obtained by slow evaporation of a CH₂Cl₂/acetone (1:1) solution of compound 4 at room temperature. Crystal structure determination was carried out on a KCCD diffractometer with graphite-monochromated Mo K α irradiation. The structure was solved by direct methods.
14. D. J. Gregg, C. M. A. Ollagnier, C. M. Fitchett, S. M. Draper, *Chem. Eur. J.*, **2006**, *12*, 3043-3052.
15. A. T. Balaban, C. D. Nenitzescu, *Friedel-Crafts and Related Reaction*, G. A. Olah, ed. Vol. 2, Wiley & Sons, New York, **1964**, 979-1047.
16. V. S. Iyer, K. Yoshimura, V. Enkelmann, R. Epsch, J. P. Rabe, K. Müllen, *Angew. Chem. Int. Ed.*, **1998**, *37*, 2696-2699.
17. M. Müller, V. S. Iyer, C. Kübel, V. Enkelmann, K. Müllen, *Angew. Chem. Int. Ed.*, **1997**, *36*, 1607-1610.
18. A. Necula, A. Racoveanuschiketanz, M. D. Gheorghiu, L. T. Scott, *J. Org. Chem.*, **1995**, *60*, 3448-3451.
19. J. J. P. Stewart, *J. Comput. Chem.*, **1989**, *10*, 209-220.
20. J. J. P. Stewart, *J. Comput. Chem.*, **1989**, *10*, 221-264.

21. M. Di Stefano, F. Negri, P. Carbone, K. Müllen, *Chem. Phys.*, **2005**, *314*, 85-99.
22. P. Rempala, J. Kroulík, B. T. King, *J. Org. Chem.*, **2006**, *71*, 5067-5081.
23. E. del Rio, M. I. Menendez, R. Lopez, T. L. Sordo, *J. Am. Chem. Soc.*, **2001**, *123*, 5064-5068.
24. D. Y. Curtin, *Record Chem. Progr. (Kresge-Hooker Sci. Lib.)* **1954**, *15*, 111-128.
25. I. Fischbach, T. Pakula, P. Minkin, A. fechtenkötter, K. Müllen, jH. W. Spiess, *J. Phys. Chem. B* **2002**, *106*, 6408-6418.
26. S. Chandrasekhar, B. K. Sadashiva, K. A. Suresh, *Pramana* **1977**, *9*, 471-480.
27. W. Pisula, M. Kastler, D. Wasserfallen, J. W. F. Robertson, F. Nolde, C. Kohl, K. Müllen, *Angew. Chem. Int. Ed.* **2006**, *45*, 819-823.
28. I. Fischbach, T. Pakula, P. Minkin, A. Fechtenkötter, K. Müllen, H. W. Spiess, *J. Phys. Chem. B* **2002**, *106*, 6408-6418.
29. X. Feng, W. Pisula, M. Takase, X. Dou, V. Enkelmann, M. Wagner, N. Ding, K. Müllen, *Chem. Mater.* **2008**, *20*, 2872-2874.
30. E. J. Foster, R. B. Jones, C. Lavigneur, V. E. Williams, *J. Am. Chem. Soc.* **2006**, *128*, 8569-8574.

4 Molecular Dynamics Studies of Dipole Functionalized HBCs

As introduced in CHAPTER 1, nano-graphene sheets have the capacity to serve as active electronic components in electronic devices.¹ Alkylated HBCs, in particular, were found to be promising as active semi-conductive components in organic field-effect transistors and photovoltaic devices.² A key factor in the design of HBCs for electronic applications is the high one-dimensional charge carrier mobility (above $1 \text{ cm}^2/\text{Vs}$) that is approaching the value for the intersheet mobility in graphite ($3 \text{ cm}^2/\text{Vs}$).^{3,4} The origin of this favorable charge carrier mobility is the optimized $\pi - \pi$ overlap of the aromatic cores. The purpose of the alkyl chains is to introduce solubility, processability and thermotropic behavior. During the process of self-organization, the disc-shaped molecules organize into columns that assemble into two-dimensional arrays, whereas the alkyl chains fill the intercolumnar space.⁵ The balance of enthalpic and entropic interactions is shifted in HBCs towards the former that stabilize two main columnar structures: a hexagonal liquid crystalline phase (Col_h) and a crystalline phase (C_r), at higher and lower temperatures, respectively. Nevertheless, to understand the stability of these phases requires the investigation of the dynamics and kinetics of these materials at a molecular level. In view of the high charge carrier mobility of the crystalline phase, the stability of this phase towards temperature and pressure variations needs to be explored in detail. Since the electronic charge carrier mobility arises from the stacked HBC cores, the knowledge of the intrinsic molecular dynamics of the discs is important for the design and application of HBC derivatives. Earlier efforts through NMR,⁶⁻¹¹ dielectric spectroscopy,⁹⁻¹⁷ neutron scattering¹⁸ and computer simulations have shed some light on the dynamics of discotic liquid crystals. The NMR studies have identified i) the axial rotation of the discs around the columnar axis, which corresponds to a so-called α -process (in the later dielectric spectroscopic studies, see in SECTION 4.4.1) and ii) different packing densities in certain regions along the columns,^{6,9} which were predicted in a model proposed by Gennes and were described as a periodic sequence of regions of core packing.¹⁹ Hexabenzocoronenes

possess lower order within the columnar mesophase than conventional triphenylenes.⁷ In this respect, a study of the molecular dynamics in HBCs would be more informative.

With respect to the molecular self-assembly, the dynamics, the thermodynamic phase state and the pathways of structure formation with possible meta-stable states, a systematic investigation of discotic liquid crystals requires a combination of model systems bearing dipoles (a result of non-uniform distributions of positive and negative charges on the various atoms due to attached electron donating or withdrawing atoms / groups) over the central aromatic core and different microscopic techniques that are sensitive probes of the time-scale and the geometry of motion. A series of dipole functionalized HBCs were synthesized and the effect of the dipole substitution on the stability of the mesophase were studied for the first time. In addition, the core dynamics within a single column were investigated by combining dielectric spectroscopy with site-specific NMR spectroscopy. These probes provide unambiguously the rate and geometry of molecular motions. Upon variation of the pressure, the stability of both the crystalline and liquid crystalline phase was studied resulting in the thermodynamic phase diagrams for certain HBCs. This study delineates the pressure and temperature stability limits of the crystalline phase associated with the highest charge carrier mobility.

These studies were conducted in the cooperation with Dr. M. Mondeshki from the polymer spectroscopy group of Prof. Dr. Spiess' group, MPIP and Dr. M. M. Elmahdy from the group of Prof. Dr. G. Floudas in the department of physics, University of Ioannina, Greece.

4.1 Synthesis

Four HBC derivatives were synthesized (Figure 4-1). One bears a cyano group (**4-1**), one a bromine atom (**4-2**), one an ethynyl group (**4-3**) and one bears two methoxy groups (**2-40**). The synthesis of mono-bromo HBC (**4-2**) has been reported earlier²⁰ and the preparation for dimethoxy HBC (**2-40**) was described in CHAPTER 3.

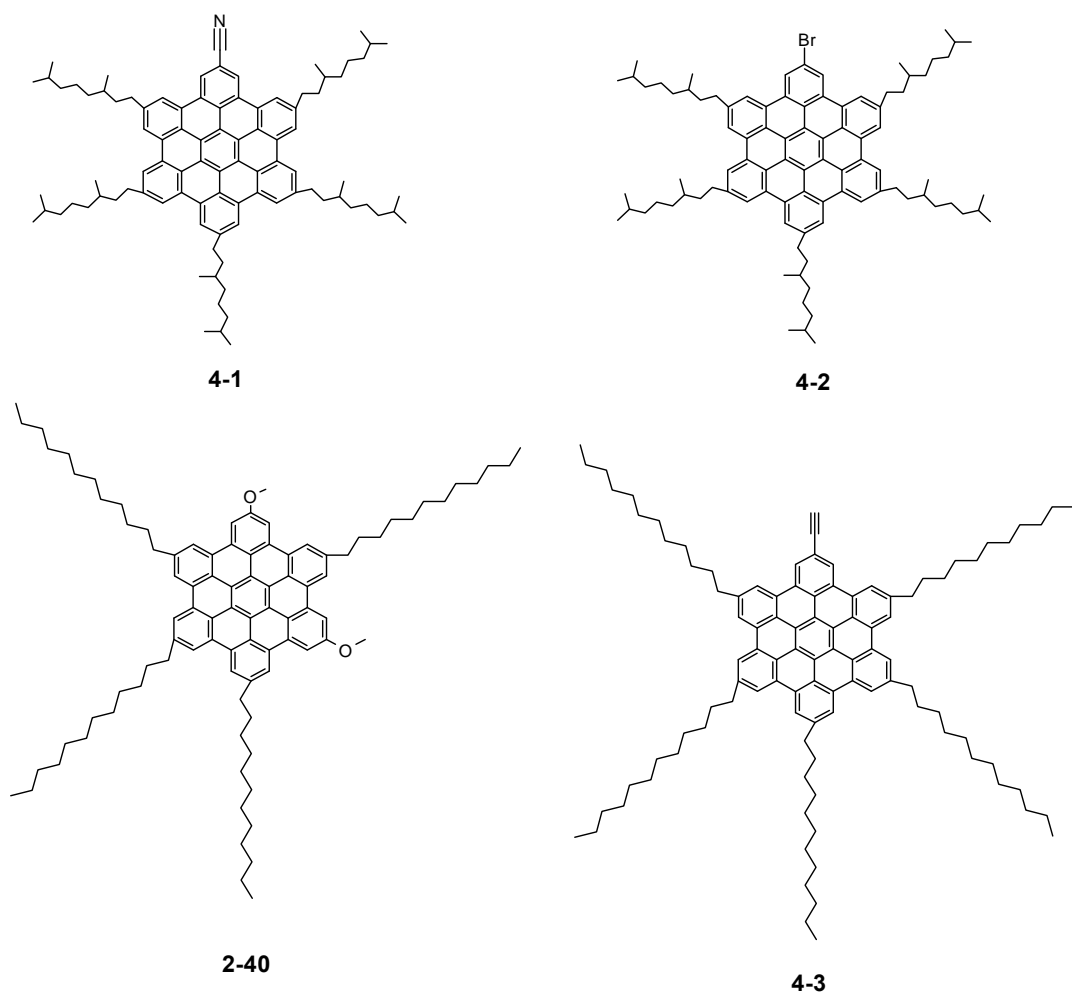


Figure 4-1. Schematic structures of the mono-cyano HBC (4-1), mono-bromo HBC (4-2), dimethoxy HBC (2-40) and mono-ethynyl HBC (4-3).

The mono-cyano HBC (4-1) was isolated in a yield of 80% after treating mono-bromo HBC (4-2) with cuprous cyanide and a catalytic amount of Pd(PPh₃)₄ in NMP in a microwave reactor for 6 h at 170 °C. The mono-ethynyl HBC (4-3) was synthesized via a Hagihara-Sonogashira coupling reaction between a mono-brominated HBC (4-4)²⁰ and triisopropylsilyl acetylene followed by treatment with tetra-*n*-butyl ammonium fluoride in THF to remove the silyl protection group²¹ (Figure 4-2). All compounds were characterized by MALDI-TOF mass spectrometry, ¹H- and ¹³C-NMR spectroscopy.

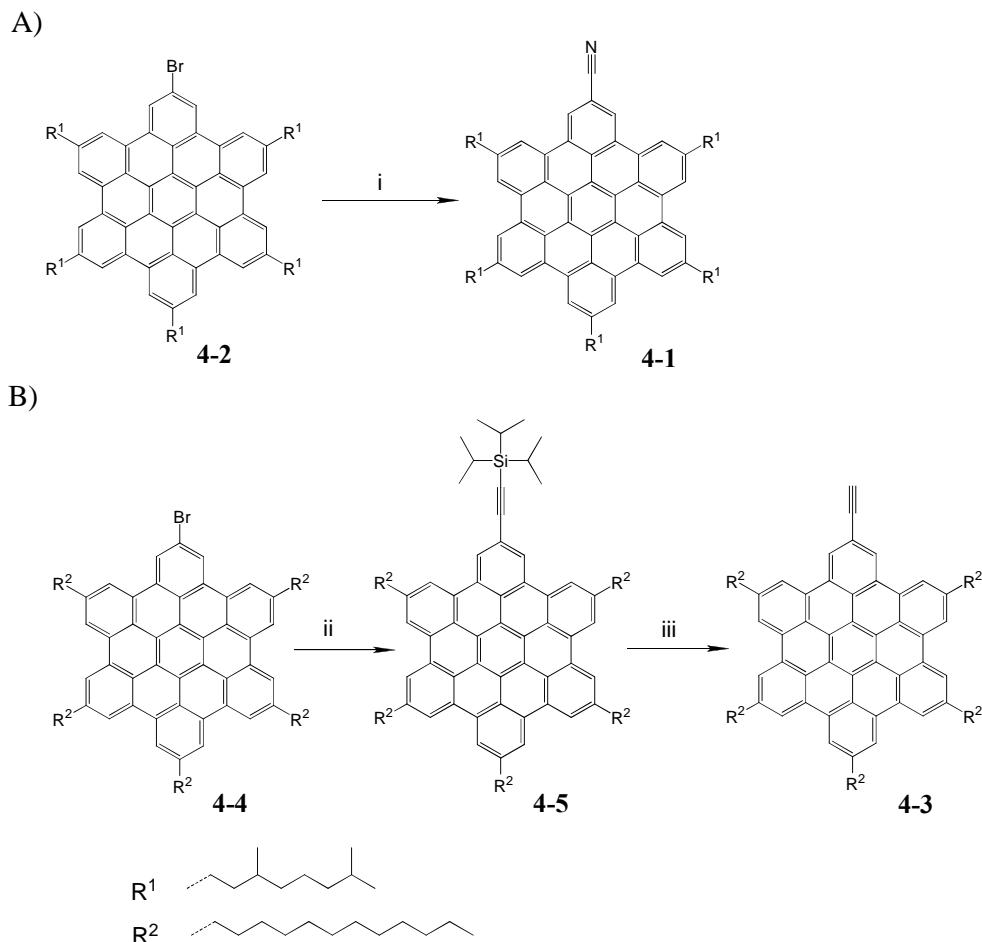


Figure 4-2. Synthesis of A) mono-cyano HBC (**4-1**) and B) mono-ethynyl HBC (**4-3**); i) CuCN, Pd(PPh₃)₄, NMP, microwave reactor (300W), 170 °C, 6 h, yield 80 %; ii) triisopropylsilyl acetylene, CuI, Pd(PPh₃)₄, THF/Et₃N (1/1), 50 °C, 20 h, yield 56 %; iii) tetra *n*-butyl ammonium fluoride, THF, r.t., 20 min., yield 95 %.

4.2 Phase characterization with DSC and 2D WAXD

The thermal behavior of these compounds was determined by DSC on cooling and subsequent heating with a rate of 10 K/min revealing the absence of phase transitions for mono-cyano HBC (**4-1**) and mono-bromo HBC (**4-2**) within the temperature range from -100 to 250 °C. However, a glass transition was identified at -39 °C for **4-1** with a dipole moment (a vector quantity which characterizes the dipole and has a magnitude equal to the strength of each charge times the separation between the charges) of $\mu = 4.55$ D (calculated with B3LYP functional and 6-311G-d,p basis set) and -35 °C for **4-2** ($\mu =$

1.62 D), respectively. For compounds **2-40** and **4-3**, which have relatively weak dipole moments ($\mu = 0.64$ D for **2-40**, $\mu = 0.25$ for **4-3**), a first order transitions from crystalline phase to liquid crystalline phase are detected at 109 °C on heating (71 °C on cooling) for **2-40** and 32 °C on heating (6.6 °C on cooling) for **4-3**, respectively. The phases and transition temperatures determined by DSC and dielectric spectroscopy (DS) for all compounds are summarized in table 4-1 and the DSC traces are shown in Figure 4-3.

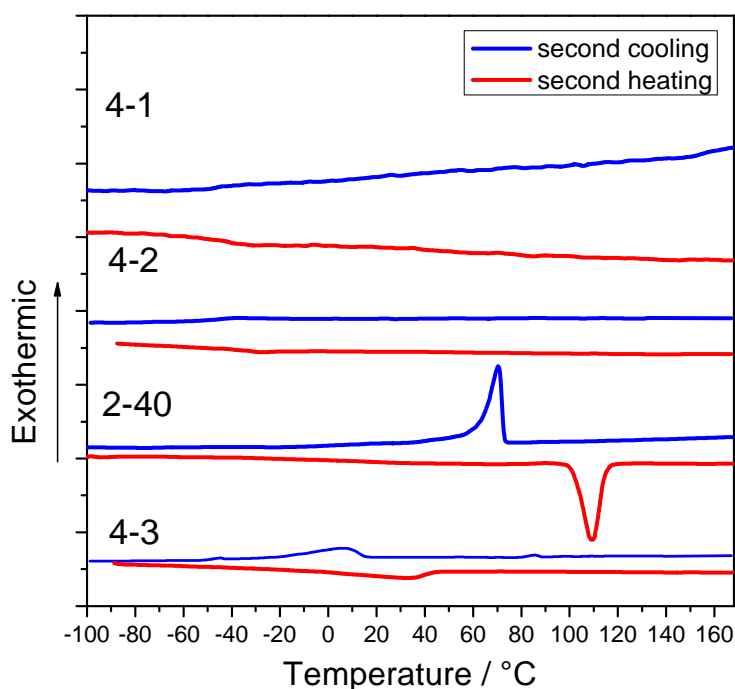


Figure 4-3. DSC curves for dipole functionalized HBCs at 10 K/min.

Table 4- 1 Thermal properties and transition temperatures.

Sample	Transition temperature (°C)	Enthalpy (kJ/mol)	Phase/Phase transition
4-1	-39 ^a (-45) ^b -36 ^c	-	Col _h /Glass transition Col _h /Glass transition
4-2	-35 ^a (-47) ^b -36 ^c	-	Col _h /Glass transition
2-40	109 ^a (71) ^b 30 ^c	65.4 ^a (68.2) ^b	C _r -Col _h / Glass transition
4-3	32 ^a (6.6) ^b -37 ^c	33.3 ^a (25.0) ^b	C _r -Col _h / Glass transition

^a heating (DSC), ^b cooling (DSC), ^c cooling (DS), C_r: crystalline phase; Col_h: columnar hexagonal liquid crystalline phase.

Temperature dependent 2D WAXD experiments were performed for all compounds with macroscopically oriented cylindrical filaments, which were extruded through a pinhole with a diameter of 0.7 mm at specific temperatures²² (30 °C for **4-1** and **4-2**, 120 °C for **2-40**, 40 °C for **4-3**). The phase behavior of **2-40** has been described in details in CHAPTER 3 and the one of **4-2** was discussed elsewhere.²³

The main effect of a dipole moment in HBC derivatives is the stabilization of the columnar hexagonal liquid crystalline phase (Col_h).²⁴ According to the studies of a series dipole functionalized discotic triphenylene²⁵ and dibenzo[a,c]phenazine derivatives,²⁶ Rego, J. *et al* and Williams, V. *et al* concluded that the intermolecular dipole - dipole interactions limit the molecular intracolumnar rotational freedom leading to a higher degree of positional order in the mesophase. The 2D WAXD patterns of **4-1** is essentially unchanged within the investigated temperature range from -20 to 150 °C as shown in Figure 4-4.

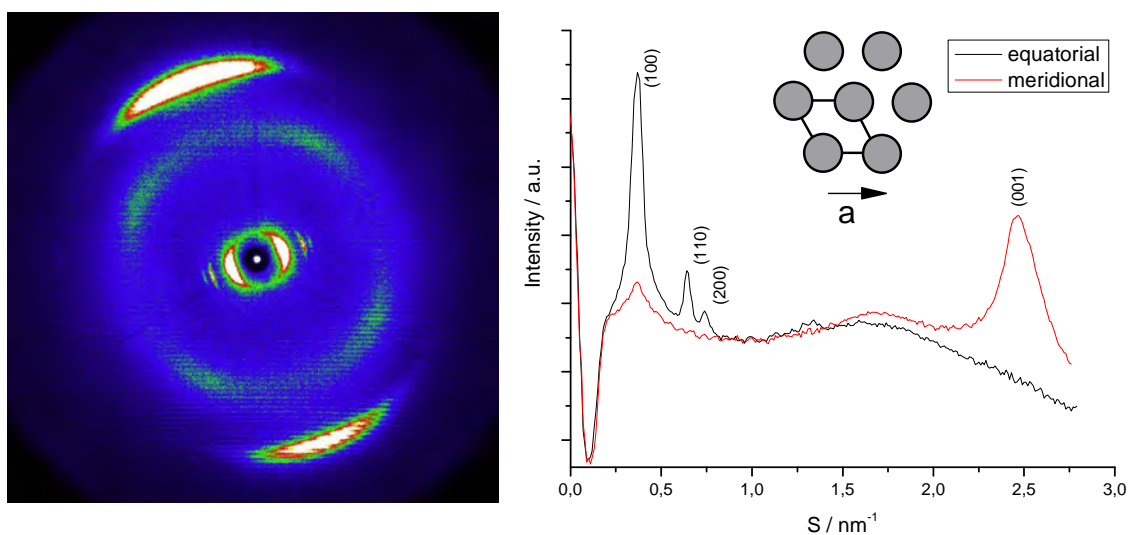


Figure 4-4. 2D WAXD pattern of **4-1** recorded at 150 °C (left) and intensity distributions (right, black: equatorial direction; red: meridional direction, unit cell parameters: $a_{\text{hex}} = 2.68$ nm).

The strong meridional reflections indicate a periodicity of 0.35 nm along columnar direction. Thereby, the molecular discs are arranged perpendicularly to the columnar axis. The set of equatorial reflexes with the relative ratios of $1: \sqrt{3}: 2$ reveal the typical hexagonal columnar packing with a parameter of $a_{\text{hex}} = 2.68$ nm. Additionally, the weak

reflections at intermediate distances imply dipole-dipole correlations with an angle of 90° as disclosed by azimuthal intensity distribution.¹⁷

In the case of compound **4-3**, a similar supramolecular ordering was recorded in the mesophase, in which non-tilted molecular discs are oriented into a typical 2D hexagonal arrangement of columnar structures with a packing parameter of $a_{\text{hex}} = 2.91$ nm (Figure 4-5A).

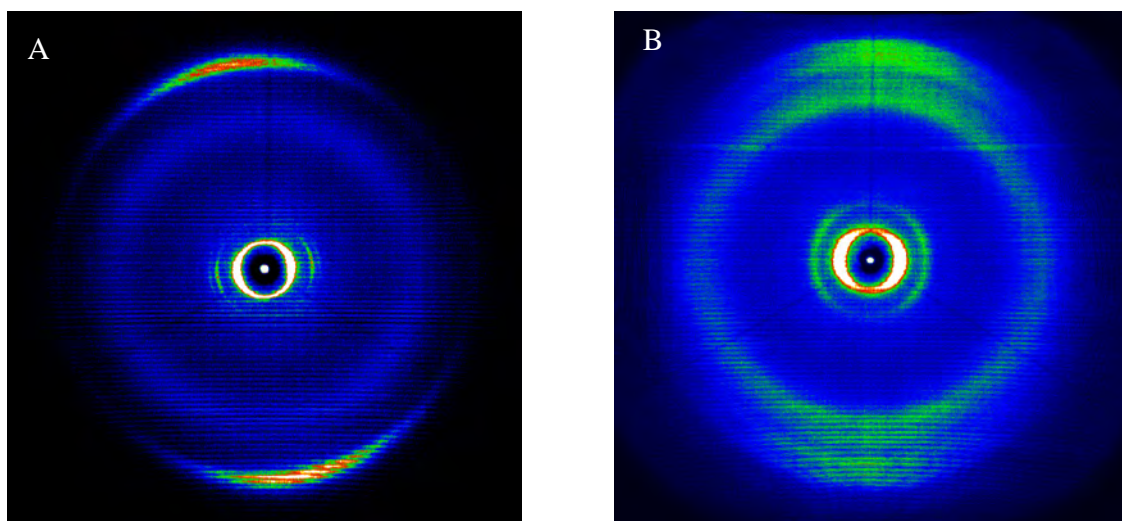


Figure 4-5. 2D WAXD pattern of **4-3** in A) mesophase, measured at 120 °C with unit cell parameter of $a_{\text{hex}} = 2.91$ nm; B) crystalline phase, measured at -30 °C.

In contrast to **2-40**, compound **4-3** exhibits a more complicated ordering in the crystalline phase. The large number of reflexes along the meridional direction and complex reflections along equatorial direction reveal a similar supramolecular packing mode as hexa-hydroxypentyl HBC (**4-6**) and 2,8,11-trimethoxy HBC (**3-32**) in the crystalline phase.²⁷ Thereby, the molecular discs remain non-tilted with an interval π - π interaction distance of 0.35 nm as in mesophase, but with a significantly larger intercolumnar distance. The reciprocal spacing of the first layer line formed by the off-meridional reflections in the small angle indicates significantly larger repeating periodicity along the stacking direction,²⁸ which could be attributed to intermolecular correlations of discs possessing an identical lateral position within a single column.²⁹ This implies that the molecules are slightly laterally rotated by a certain angle with respect to each other resulting in a helical packing.^{30, 31} However, further accurate assignment of

such a crystalline supramolecular arrangement for **4-3** is impossible since the relatively high molecular dynamics make these reflections not as clear as the ones in the case of **4-6** and **4-7**. Such an unusual helical ordering is probably a result of the relatively weak local dipole moment. Both π -stacking and dipole-dipole interaction are known to play an important role for the self-assembly leading to complex supramolecular organization.³²⁻³⁴

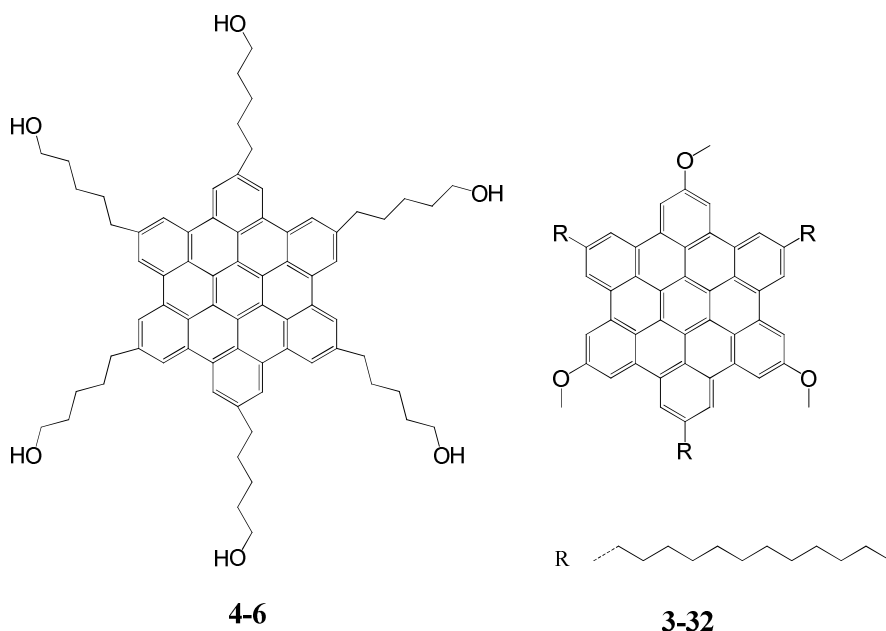


Figure 4-6. Chemical structure of **4-6** and **3-32**.

The introduction of dipole moments leads to an antiferroelectric molecular ordering within the columns; in other words, the adjacent mesogens will be approximately antiparallel with respect to one another.²⁶ The stronger dipole moment in the case of **4-1** ($\mu = 4.55$ D) will favor the antiparallel orientation of neighboring HBC molecules, which gives rise to a more stable mesophase over a large temperature range ruling out the crystalline (C_r) phase. With a relatively weaker dipole moment, **2-40** ($\mu = 0.64$ D) forms stable C_r phase with high molecular ordering (sharper ordered reflections on 2D WAXD pattern in contrast to those of HBC- C_{12} **3-31**). When the dipole moment further reduces, the effect of the dipole – dipole interaction decreases and results in a complex supramolecular organization in corporation with intermolecular $\pi - \pi$ interactions (as shown in the case of **4-3** and **3-32**).

4.3 Molecular dynamics and intramolecular stacking studies by solid-state NMR

The measurements presented in this section were recorded and analyzed by Dr. M. Mondeshki. ^1H magic-angle spinning (MAS) and ^1H - ^1H double-quantum (DQ) MAS NMR experiments were conducted to probe the type of columnar packing of the HBC derivatives (**2-40** and **4-3**) in the crystalline states. The ^1H - ^1H DQ MAS spectra revealed typical NMR signal patterns (Figure 4-7A) for **2-40**, arising from a tilted arrangement of the HBC discs, which is also referred to a “herringbone”-type packing. One- and two-dimensional ^1H - ^1H DQ spectra exhibited three distinct resonances of the aromatic protons situated in the “bays” of the HBC cores, which are known to arise from the tilted packing effects resulting in different degrees to which the aromatic protons experience the ring current from adjacent aromatic layers³⁵⁻³⁷ (Figure 4-7B). When heating the samples to the transition temperature into the mesophase, the HBC molecules undergo a reorientation from the tilted to a planar arrangement and start a rapid rotation around the columnar axis. In the ^1H MAS spectra, this transition manifests itself in the narrowing of the resonance lines. Moreover, the three distinct aromatic peaks observed in the solid state merge into a single aromatic ^1H resonance. In the case of **4-3**, only one kind of aromatic proton signal is recorded both in crystalline and mesophases indicating a non-tilted packing of HBC molecules, which is consistent with the results obtained from 2D WAXD experiments.

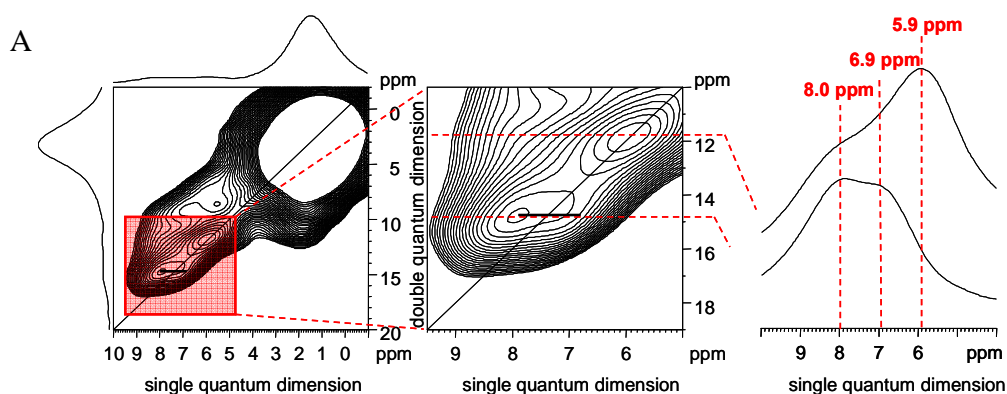


Figure 4-7 A (Left) Two-dimensional solid-state ^1H - ^1H DQ MAS NMR spectrum of the dimethoxy HBC (**2-40**) recorded at 37 °C (effective sample temperature), 40 μs used to excite and reconvert the DQ coherences and 25 kHz MAS, (middle) the magnified aromatic region and (right) two one-dimensional slices at 11.8 and 14.9 ppm with the aromatic proton chemical shifts assigned; **B**) schematic represents of (left) columnar “herring-bone” packing and (right) three kinds of aromatic protons with different chemical environment due to such kind of molecular packing.

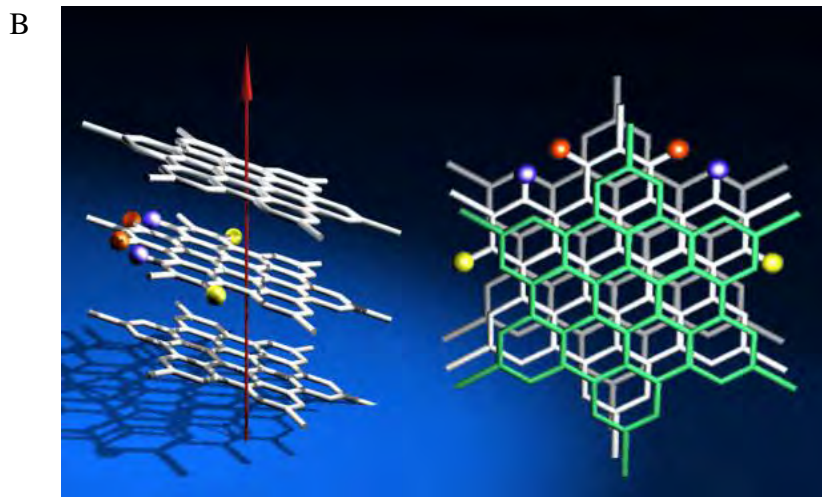


Figure 4-7. (contiuue)

The molecular dynamics of the HBC derivatives were investigated by means of sideband patterns observed in ^1H - ^{13}C rotor-encoded rotational echo double resonance (REREDOR) NMR experiments performed under fast MAS conditions.³⁸ This is facilitated by the effective ^1H - ^{13}C dipole-dipole coupling constants D_{CH} , with the related local dynamic order parameters, S , representing the residual motional anisotropy of a given molecular segment,⁸ which is obtained experimentally as the ratio of the measured effective dipole-dipole coupling constant to that of a static pair:

$$S_{CH} = \left\langle \frac{1}{2} (3 \cos^2 \theta_{CH}(t) - 1) \right\rangle_t = \frac{\langle D_{CH}(t) \rangle_t}{D_{CH,static}}, \quad (1)$$

while the static ^1H - ^{13}C dipole-dipole coupling constant, $D_{CH,static}$ is calculated according to

$$D_{CH,static} = \frac{\mu_0}{4\pi} \cdot \frac{\hbar \cdot \gamma_C \cdot \gamma_H}{r^3} \approx 21\text{kHz}.^{39} \quad (2)$$

As can be derived from the formula (1), a rigid system ($\langle D_{CH}(t) \rangle = D_{CH,static}$) gives a maximum $S = 1$. Whereby, S value approaches to 0 when the molecule is highly mobile.

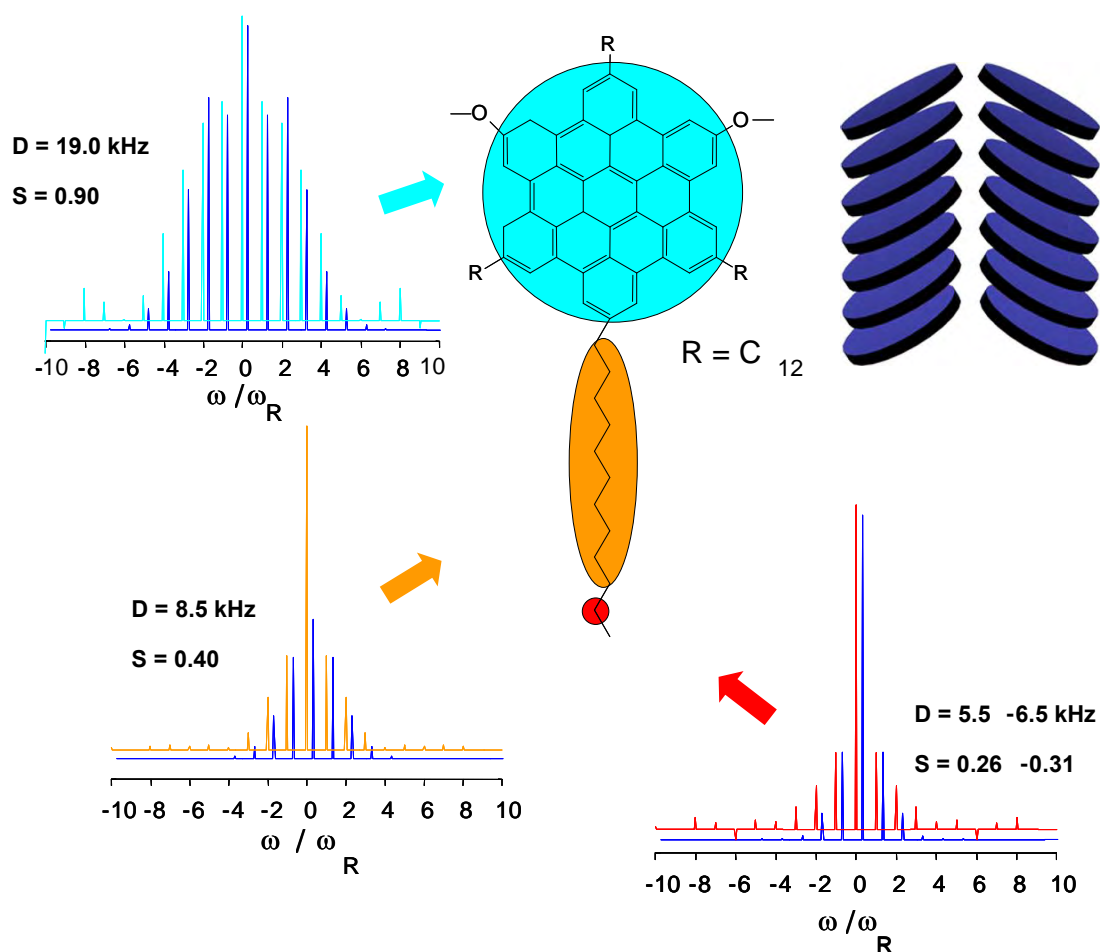


Figure 4-8. ^{13}C - ^1H REREDOR spinning sideband patterns for the dimethoxy HBC (2-40) recorded at 25 kHz MAS, 80 μs recoupling time at 37 $^\circ\text{C}$ in the crystalline phase (C_r), with the calculated patterns (in blue) superimposed. The derived ^1H - ^{13}C dipole-dipole coupling constants for the respective CH_2 moieties are presented together with the related local dynamics order parameters, for the HBC core $S = 0.90$ (top, left), the alkyl chains $S = 0.40$ (bottom, left), the most mobile chain ends (CH_3) $S = 0.28$ (bottom right), and typical herring-bone supramolecular packing (top, right).

For dimethoxy HBC (2-40), these experiments were performed both in the crystalline phase and in the mesophase at 37 $^\circ\text{C}$ and 127 $^\circ\text{C}$. In the crystalline phase, the measured ^1H - ^{13}C dipole-dipole coupling constant for aromatic CH pairs is c.a. 19 kHz ($S = 0.90$) showing that the aromatic core is essentially rigid. The slight reduction of the ^1H - ^{13}C dipole-dipole coupling constant from the “ideal” rigid state ($S = 1$) can be attributed to the slight in-plane fluctuations as well as the out-of-plane disc excursions. On the contrary, the alkyl chains retain significant mobility within the crystalline state. The effective dipole-dipole coupling constants measured for the CH_2 groups in the alkyl chain

($D_{CH} = 8.5$ kHz, $S = 0.4$) and the chain ends ($D_{CH} \sim 5.9$ kHz, $S \sim 0.28$) clearly show that, on average, the alkyl chains remain flexible and amorphous. Therefore, HBC discs are not completely fixed in the lattice but are able to undergo small-angle rotations whereas the alkyl chains retain significant mobility (Figure 4-8).

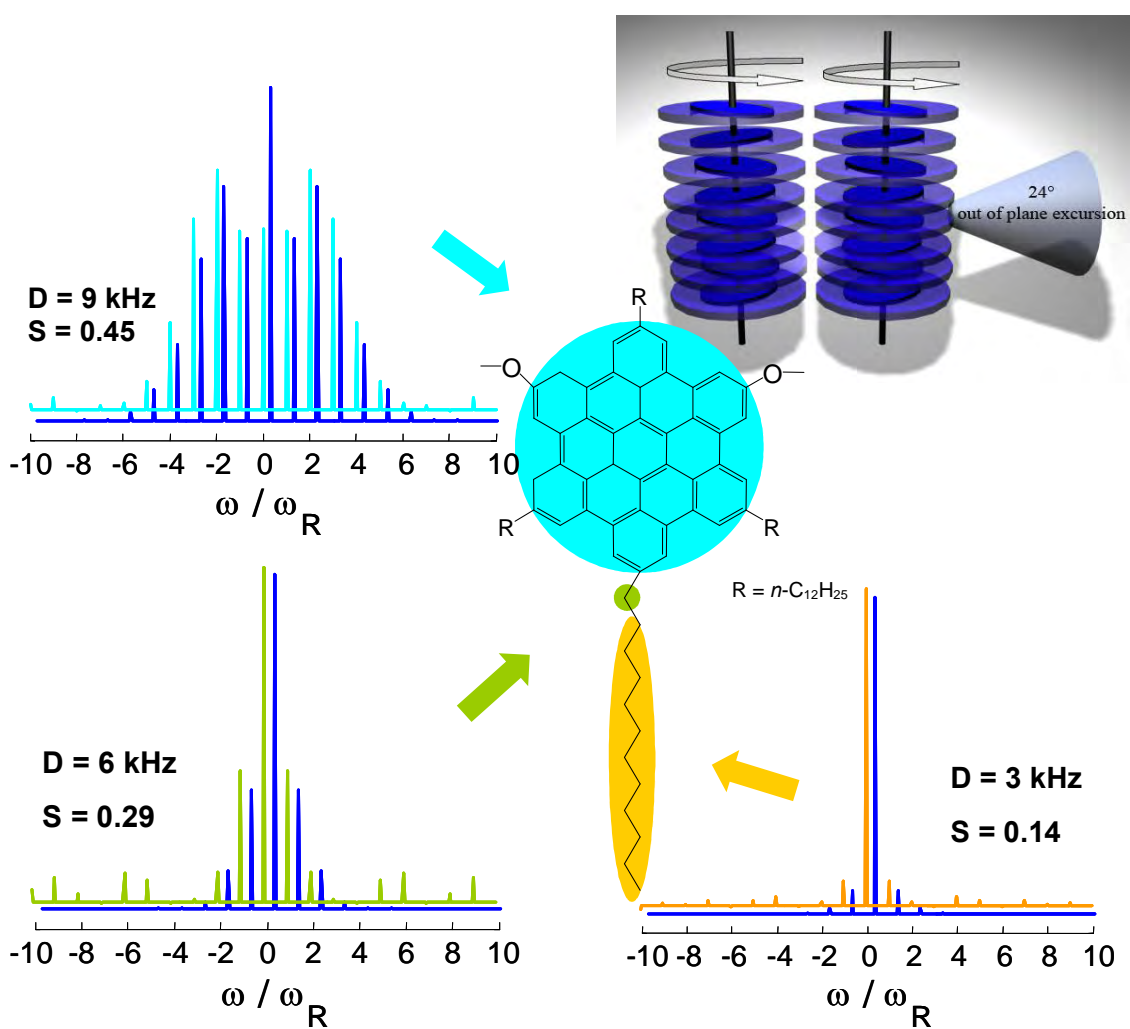


Figure 4-9. ^{13}C - ^1H REREDOR spinning sideband patterns for the dimethoxy HBC (2-40) recorded at 25 kHz MAS, 160 μs recoupling time at 127 $^\circ\text{C}$ in liquid crystalline phase (Col_h), with the calculated patterns (in blue) superimposed. The derived ^1H - ^{13}C dipole-dipole coupling constants for the respective CH_n ($n = 2, 3$) moieties are presented together with the related local dynamics order parameters S ; for the aromatic core, $S = 0.45$ suggesting both in-plane rotation and out-of-plane excursions, while the higher degree of motional freedom for the alkyl chains results in S values in the range of 0.29 to 0.14; the columnar supramolecular organization is shown at top right.

In the mesophase, the fast disc rotation decreases the ^1H - ^{13}C dipole-dipole couplings for the aromatic CH pairs by a factor of two as long as the rotation axis

parallels the columnar axis and both are perpendicular to the HBC core plane.³⁹ In contrast to the crystalline phase, the dynamic order parameter of the aromatic core CH segments is reduced to an out-of-plane disc excursion of 24° , which is determined by assuming that the local dynamics order parameter, S , results from a Gaussian orientation distribution of displacement angles.⁴⁰ The alkyl chain dynamics is further increased in the mesophase exhibiting a mobility gradient from the spatially most restrained $\alpha-CH_2$ groups ($D_{CH} = 6.0$ kHz, $S = 0.29$) to the distant alkyl groups ($D_{CH} = 3.0$ kHz, $S = 0.14$) (Figure 4-9).

Although mono-cyano (**4-1**) and mono-bromo (**4-2**) HBCs do not show phase transitions within the investigated temperature range of the DSC measurement, similar solid state behavior was observed in a glassy phase at the temperature below -33 °C (the glass transition temperature recorded by DSC), where the aromatic core is practically immobilized ($D_{CH} = 21.5$ kHz, $S \rightarrow 1$). In the case of compound **4-1**, the 1H - ^{13}C dipole-dipole coupling constants of the CH_2 groups in alkyl chains are reduced to an average value of $D_{CH} = 14.5$ kHz, $S = 0.69$.

In the mesophase of **4-1**, the 1H - ^{13}C dipole-dipole couplings for aromatic CH moieties are substantially reduced due to the fast in-plane rotation and out-of-plane excursions leading to further reduction of the dynamic order parameter to $S = 0.42$ at 87 °C. The mean angle (38°) of this kind of motion is determined. At intermediate temperatures, the disc dynamics interferes with the frequencies in the kHz range pertinent to the NMR experiments. At the glass transition temperature of organic compounds, the time scale of the molecular dynamics often exhibits a heterogeneous distribution of the correlation times.^{41, 42} Indeed, such behavior is found here by recording 1H - ^{13}C REREDOR spinning sideband patterns with different recoupling time at an intermediate temperature of -6 °C. For a short recoupling time of 40 μs , the sideband patterns of the fixed discs with $S \rightarrow 1$ are recorded, whereas the sideband pattern recorded using a recoupling time of 160 μs gives $S = 0.42$, due to the fraction of mobile discs performing in- and out-of-plane motion (Figure 4-10). For the recoupling time of 80 μs , the spinning sideband pattern shows both features.

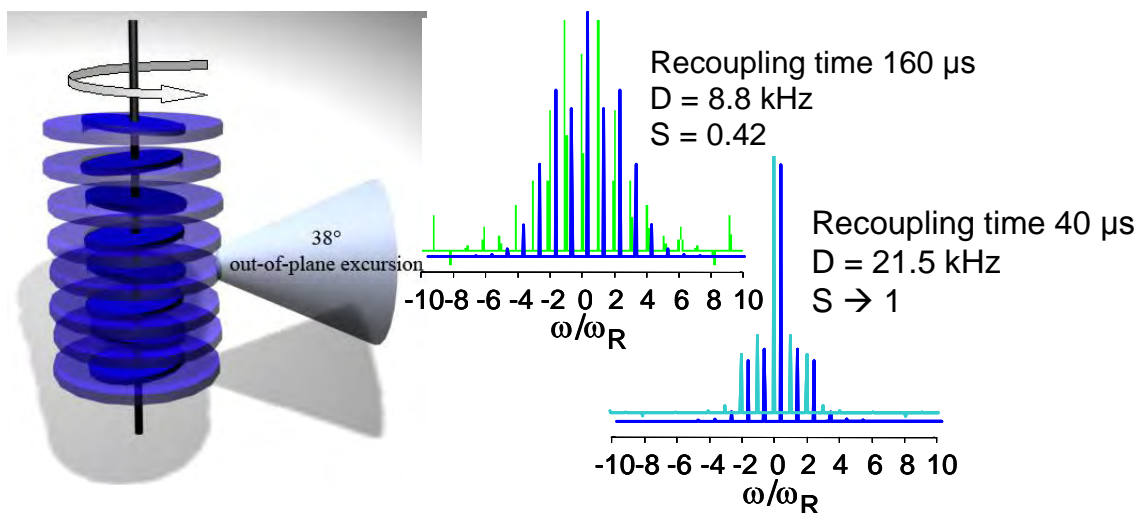


Figure 4-10. ^1H - ^{13}C REREDOR spinning sideband patterns of 4-1 recorded at 25 kHz MAS and 160 μs recoupling time (middle) and 40 μs recoupling time (right) at -6°C with the simulated patterns (in blue) superimposed; and schematic represent of molecular in- and out-of-plane motion (left).

4.4 Molecular dynamics and kinetics studies by dielectric spectroscopy

4.4.1 Basic background of dielectric spectroscopy (DS)

The results presented herein are investigated and analyzed by Dr. M. M. Elmahdy from University of Ioannina, Greece. Dielectric spectroscopy is based on the universal property of a substance to respond to an external electrodynamic stimulation, which measures the dielectric properties of a medium as a function of frequency.^{43,44} The value and the temporal delay of a response as functions of the external stimulation are expressed in terms of measurable quantities, i.e. dispersion and absorption, which are determined only by the microscopic properties of a substance in a linear approximation. Depending on the frequencies of the responding processes, the dielectric mechanisms can be divided into relaxation (lower frequency) and resonance (higher energy) processes (Figure 4-11). The resonance processes constitute of electronic and atomic polarizations corresponding to different inducing frequencies. The electronic polarization resonance process occurs in a neutral atom when the electric field influences the electron density relative to the nucleus it surrounds. The deformation of the electronic cloud under the

force of the applied field results in a formation of the negative and positive charge, i.e. atomic polarization. The relaxation process (dielectric relaxation) is the result of the movement of dipoles (dipole relaxation) and electric charges (ionic relaxation) due to an applied alternating field, and usually observed in the frequency range 10^2 - 10^{10} Hz. Relaxation mechanisms are relatively slow in contrast to resonant electronic transitions or molecular vibrations, which usually have frequencies above 10^{12} Hz.⁴⁴

In the case of dipole relaxation, broadband dielectric spectroscopy is a powerful tool to analyze the details of the scaling of relaxation processes. Typically four dielectric loss processes are observed: the dynamic glass transition (α -relaxation), a slow secondary relaxation (β_{slow}), a fast secondary relaxation (β_{fast}) and the boson peak at 10^{12} Hz. Below 10^{10} Hz, the dynamic glass transition and the β_{slow} relaxation are primarily present.

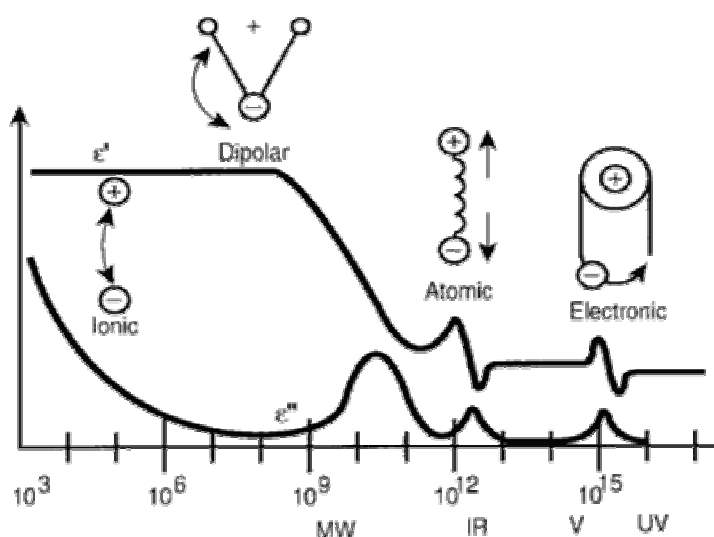


Figure 4-11. A dielectric permittivity spectrum over a wide range of frequencies. The real (ϵ') and imaginary (ϵ'') parts of permittivity are shown, and various processes are depicted: ionic and dipolar relaxations, and atomic and electronic resonances at higher energies.

The dipole relaxation is often described in terms of dielectric permittivity, $\hat{\epsilon}$, as a function of frequency, which is expressed as a pair of quantities, namely the real (ϵ') and imaginary parts (ϵ'') as $\hat{\epsilon} = \epsilon' - i\epsilon''$ and can, for ideal systems, be described by the Debye equation⁴³:

$$\hat{\varepsilon}(\omega) = \varepsilon_{\infty} + \frac{\Delta\varepsilon}{1 + i\omega\tau},$$

where $\varepsilon_{\infty} = \lim_{\omega\tau \gg 1} \varepsilon'(\omega)$ is the permittivity at the high frequency limit, $\Delta\varepsilon = \varepsilon_s - \varepsilon_{\infty}$ where $\varepsilon_s = \lim_{\omega\tau \ll 1} \varepsilon'(\omega)$ is the static, low frequency permittivity, and τ is the characteristic relaxation time of the medium. The Debye relaxation model could be empirically modified to Havriliak-Negami form (HN equation) accounting for the asymmetry and broadness of the dielectric dispersion curve. The model was first used to describe the dielectric relaxation of some polymers by adding two exponential parameters,⁴⁵ in which m , and n are called fractional shape parameters describing symmetrical and asymmetrical broadening of the dispersion, whereas $m > 0$, $mn \leq 1$ holds.^{43, 46, 45}

$$\hat{\varepsilon}_{HN}(\omega) = \varepsilon_{\infty} + \frac{\Delta\varepsilon}{\left(1 + (i\omega\tau_{HN})^m\right)^n}$$

The parameters m and n are related to the limiting behavior of the complex dielectric function at low and high frequencies:

$$\begin{aligned} \varepsilon_s - \varepsilon'(\omega) &\sim \omega^m; \varepsilon'' \sim \omega^m \text{ for } \omega \ll 1/\tau_{HN} \\ \varepsilon'(\omega) - \varepsilon_{\infty} &\sim \omega^{-n}; \varepsilon'' \sim \omega^{-n} \text{ for } \omega \gg 1/\tau_{HN} \text{ with } n = mn. \end{aligned}$$

For a glassy material (non-crystalline solid including the so-called plastic crystals and orientational glasses except amorphous polymers and glass ceramics), a molecule fluctuates in the cage of its neighbors. Its “rattling” motion is assigned to a fast secondary β -relaxation, which takes place on a time scale of 10^{-10} s to 10^{-12} s following an Arrhenius-type temperature dependence

$$\tau = \tau_0 e^{\left(\frac{E}{k_B T}\right)}$$

where E is the activation energy, k_B , the Boltzmann constant and τ_0 , the relaxation time at the high temperature limit. The reorientations of the molecules forming the “cage” corresponds to the dynamic glass transition (or α -relaxation) obeying the empirical Vogel-Fulcher-Tammann (VFT) temperature dependence

$$\tau(T) = \tau_0 e^{\left(\frac{B}{T-T_0}\right)}$$

where B is a constant and T_0 denotes the Vogel temperature (ideal glass transition temperature).⁴³ In some cases, the α -relaxation is attributed to transverse dipole moments rotating around the mesogen's long axis.⁴⁷ Additionally, many systems show a slow secondary β -relaxation (with an Arrhenius-type temperature dependence). This process observed for relaxation rates $\sim < 10^8$ Hz can often be assigned to intramolecular fluctuations. The slow β -relaxation separates from the α -process in the frequency range from 10^7 to 10^8 Hz.⁴³ In the DS experiment, these relaxation processes are tracked and the changes give information about the molecular dynamics and phase transitions.

4.4.2 Dynamics investigation with dielectric spectroscopy

Dimethoxy HBC (**2-40**) undergoes a transformation from the crystalline to the columnar hexagonal liquid crystalline phase. Figure 4-12 depicts a series of dielectric loss curves measured at different temperatures, both below and above the transition, reflecting the in-plane disc rotation (α -process). The curves show increasing broadening and a reduction in the dielectric strength when going from the high temperature Col_h phase to the C_r phase. The crystallization temperature (71 °C) determined by DSC is substantially higher than the one assigned by DS (30 °C / 303 K; based on the broadening of the loss curves; Table 4-1) reflecting a strong rate dependence of the critical temperature T_c . The figure also depicts some faster process known as β -process.

The relaxation times of the different processes in **2-40** are shown in Figure 4-13 with Arrhenius representation. The low-temperature β -process has an Arrhenius temperature dependence ($\tau(T)$) with a single activation energy $E = 50 \pm 4$ kJ/mol and $\tau_0 = 4 \times 10^{-14}$ s, which are characteristic values of a local process associated with small amplitude vibrations due to the high mobility of alkyl substituents within the C_r phase. A broad distribution of relaxation times is evident by the values of the HN shape parameters ($m = mn = 0.3$). The mere presence of this process is in consistence with the NMR results ($S = 1$, within C_r phase), in which averaging of ¹H-¹³C dipole-dipole couplings requires motions on a time scale faster than 10^{-5} s.

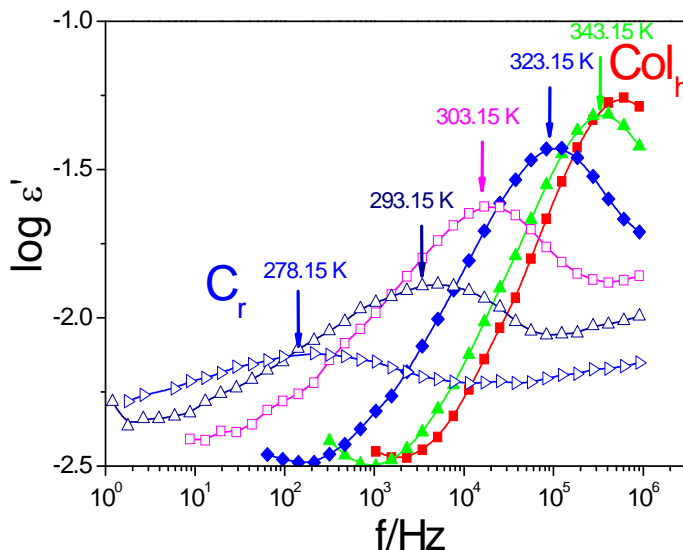


Figure 4-12. Dielectric loss for the dimethoxy HBC (2-40) obtained on cooling at 0.1 MPa, shown at different temperatures: (filled squares): 353.15 K, (filled up triangles): 343.15 K, (filled rhombus): 323.15 K, (open squares): 303.15 K, (open up triangles): 293.15 K and (open right triangles): 278.15 K. Notice the loss in dielectric strength and the broadening of the relaxation spectrum on entering the C_r phase. The spectrum at 343.15 K corresponds to the DSC exotherm and the one at 303.15 K is the critical temperature suggested by DS.

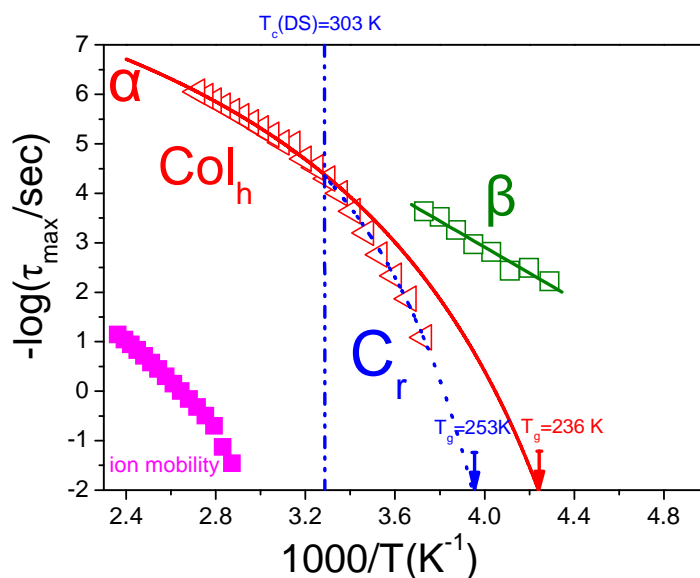


Figure 4-13. Temperature dependence of the relaxation times (obtained on cooling) for all dielectrically active processes and of the ionic mobility in the dimethoxy HBC (2-40) (filled squares): ionic mobility, (open squares): β -process, (left triangles): α -process. Notice the change in the α -process dynamics in going from the high temperature Col_h to the C_r phase (vertical dashed-dotted line). Full and dotted lines extrapolate to the glass temperature (defined at $\tau \sim 10^2$ s) of the Col_h (hypothetical) and C_r phases, respectively.

NMR techniques reveal the geometry of motions on longer time-scales.^{6, 40} Based on the combined information from NMR (geometry of motion) and DS (rate of motion), the α -process reflects collective axial disc motions around the columnar axis. The α -process displays unique characteristics in going from C_r to the Col_h phase. Within the Col_h phase, its relaxation time ($\tau(T)$) follows the VFT-temperature dependence as described in SECTION 4.4.1. The B , T_0 and T_g parameters assume the following values: 1345 ± 50 K, 185 ± 7 K, 236 ± 7 K, respectively. On entering the C_r phase, the α -process displays a stronger T-dependence with B , T_0 and T_g parameters assuming values of 1013 ± 2 K, 214 ± 4 K, 253 ± 4 K, respectively. The ionic relaxation process is also extracted from the dielectric modulus representation. This process is about 7 orders of magnitude slower than the α -process dynamics but shows a similar VFT temperature dependence. This suggests that the dynamics of ionic impurities, presumably introduced during intramolecular cyclodehydrogenation step, are affected by the disc rotational dynamics.

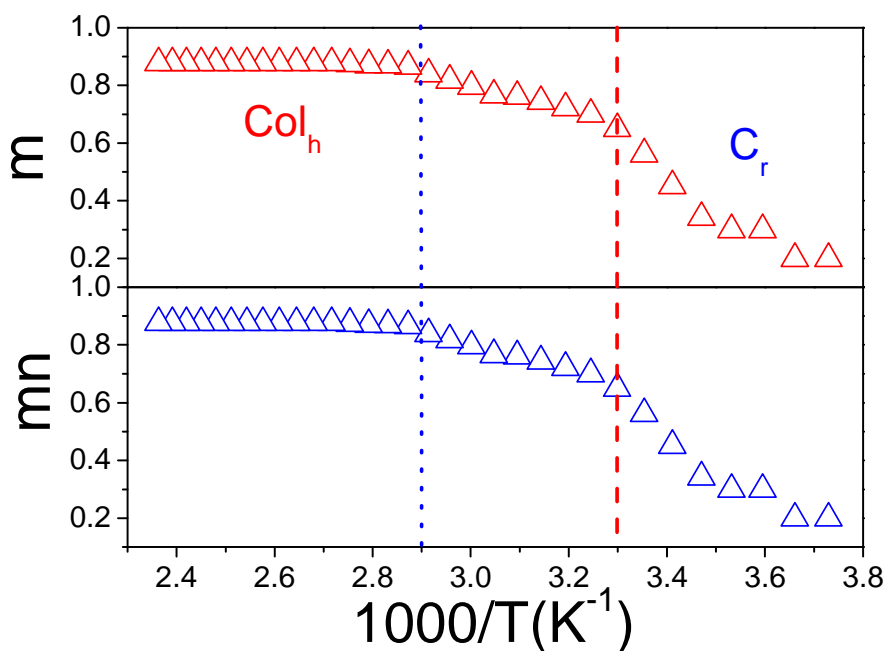


Figure 4-14. Temperature dependence of the low- (m) and high- (mn) frequency slopes characterizing the distribution of relaxation time spectrum of the α -process. Dotted and dashed lines give the critical temperatures of the Col_h to C_r transformation as seen from DSC and DS, respectively.

The HN shape parameters for the α -process are also sensitive indicators for the phase transformation. Figure 4-14 depicts the low- (m) and high- (n) frequency slope of

the α -process as a function of temperature. The plot shows a narrow, non-Debye process ($m = mn = 0.9$) within the Col_h phase, and a much broader distribution within the C_r state. Therefore, the axial disc motion within the crystalline phase is a collective process characterized by a heterogeneous environment, which gives rise to the broad distribution of relaxation times. The onset of such a broadening coincides with the DSC transition (cooling), however the transition, as seen from DS (assigned to the temperature where the width of the α -process doubles its high T value), appears at even lower temperatures ($T_c^{DS} \sim 30$ °C), implying kinetic effects.

In the case of mono-cyano HBC (**4-1**), three dielectrically active processes are detected associated with the cyano dipole relaxation and one process associated with the ionic mobility. The relaxation times of the different processes are shown in Figure 4-15A in the usual Arrhenius representation. The low-temperature β -process has an Arrhenius temperature dependence like **2-40** with a single activation energy $E = 55 \pm 5$ kJ/mol and $\tau_0 = 4 \times 10^{-16}$ s, which is characteristic for a local process. Thus, the β -process is assigned to small angular vibrational motions of the cyano group induced by the more mobile alkyl chains. At higher temperatures, two processes exist, called α and α' , with a stronger temperature dependence that can be described by the VFT equation. The B , T_0 and T_g parameters assume the following values: 900 ± 23 K, 161 ± 2 K and 237 ± 3 K for α -process and 1730 ± 115 K, 128 ± 6 K and 255 ± 6 K for α' -process. The characteristic relaxation times of the ionic mobility also display the common VFT dependence. Interestingly, the T_g recorded by DSC corresponds to the freezing of the DS α -process (at $\tau \sim 10^2$ s). This process is less restricted and less volume demanding (see below with respect to the pressure dependence) and thus freezes at a lower temperature. Both processes are non-Debye with low- (m) and high- (mn) frequency HN slopes of $m = mn = 0.7$ and $m = mn = 0.4$ for the α - and α' -processes, respectively. Clearly, the fast axial motion, as seen in NMR, leaves an uncompensated residual dipole moment as the dipole breaks the symmetry of the HBC disc and results in unevenly populated sites for the axial motion. This residual dipole moment then relaxes in the slower α' -process with considerably lower relaxation strength. Consistent with the results of NMR and X-ray diffraction, the α -process reflects collective axial motions of the discs, which leaves a residual dipole with a defined average orientation with the column. The orientation correlation of the

dipoles within the columns (*i.e.* small blocks, in which several molecular discs are correlated with each other through intermolecular dipole – dipole interactions within a single column), however, has a limited lifetime and relaxes through highly collective intra- and perhaps inter-columnar rotational dynamics (α' -process) (Figure 4-15B). In other words, these dipole – dipole interaction “define” molecular blocks relaxing in a much slower process (α' -process) in comparison with the single molecule relaxation (α -relaxation).

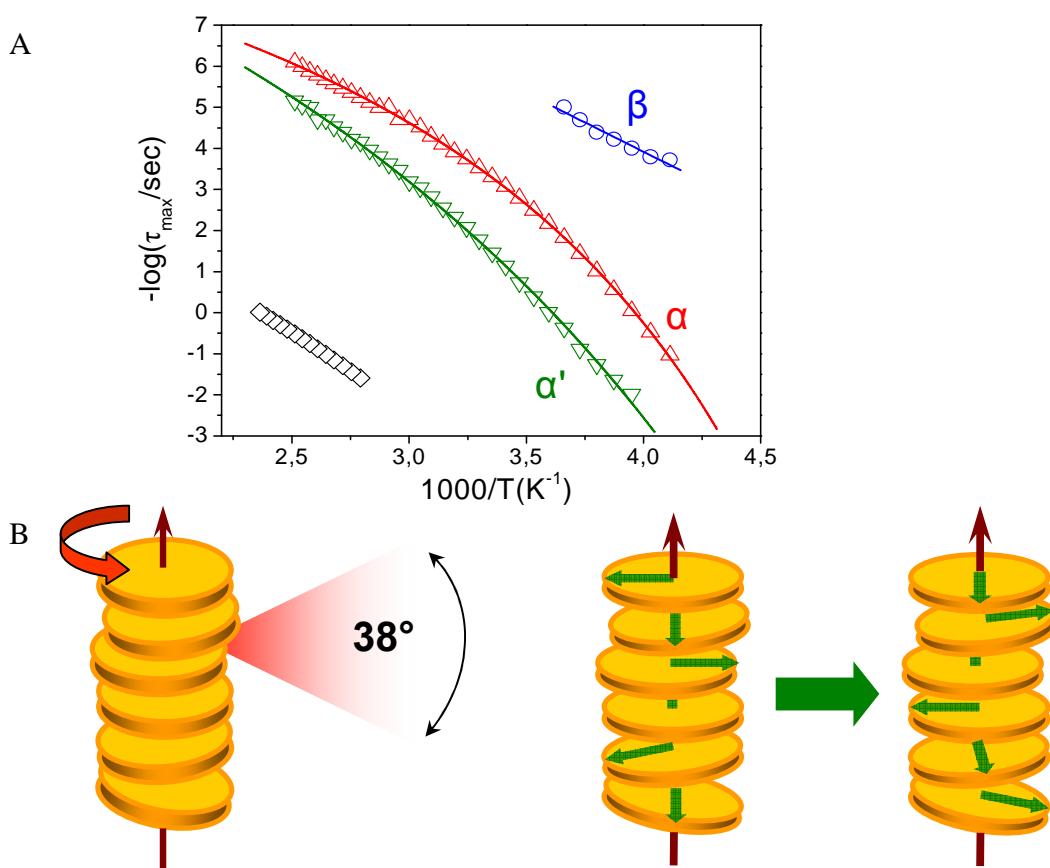


Figure 4-15. A) Arrhenius relaxation map for all dielectrically active processes and ionic relaxation., whereas the β -process (circles) with an Arrhenius T-dependence; the α (up triangles) and α' (down triangles) processes with VFT dependence; and the “slow” process (rhombus) that is coupled to the ionic conductivity. B) Schematic represent of α -process – both in- and out-of-plane molecular motion (left); and α' -process – a relaxation of orientation correlation of dipoles within the columns (right).

The axial disc dynamics (including both in- and out-of-plane motions) are compared among the four HBC molecules (2-40, 4-1, 4-2 and 4-3) in Figure 4-16. Within the Col_h phase, the $\tau(T)$ dependencies are nearly identical. Additionally, there is no

remarkable change in the distribution of relaxation times, reflecting that the phase state (Col_h) largely controls both the $\tau(T)$ and distribution of relaxation times. From the VFT dependence of the α -process, the glass transition temperature assumes similar values for the three HBCs (**4-1**, **4-2**, and **4-3**), in the range 235-237 K. The nearly indistinguishable $\tau(T)$ dependencies for the three samples within the same phase (Col_h) suggest that the time-scale of the collective axial disc motion depends on T , P and only weakly on alkyl chain branching. On the other hand, for dimethoxy- (**2-40**) and mono-ethynyl (**4-3**) HBCs undergoing a phase transition, the temperature dependence $\tau(T)$ becomes much stronger on entering the C_r phase, which again indicates that the dynamics are controlled – to a large extent – by the thermodynamic state.

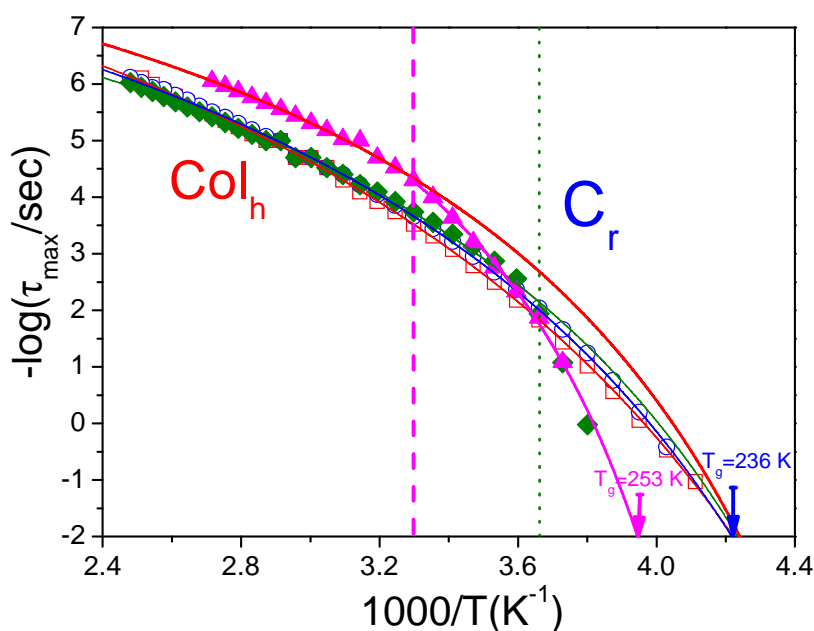


Figure 4-16. Comparison of the α -process relaxation times for the different dipole functionalized discotics: mono-cyano HBC (**4-1**, open squares), mono-bromo HBC (**4-2**, open circles), mono-ethynyl HBC (**4-3**, filled rhombus), and dimethoxy HBC (**2-40**, filled up triangles). Notice: the similarity in the $\tau(T)$ dependence within the Col_h phase and the steeper $\tau(T)$ within the C_r phase for the dimethoxy- (**2-40**, thick vertical dash line) and mono-ethynyl HBC (**4-3**, dotted vertical line).

Applications of HBCs as advanced electronic materials require knowledge of the thermodynamic temperature and pressure boundaries and stability of the different phases. Introducing pressure as an additional thermodynamic parameter helps the construction of the complete phase diagram (P - T). In these experiments, pressure is applied isothermally at temperatures corresponding to Col_h phase where the α -process for dimethoxy HBC (**2-**

40) or α - and α' -process for mono-cyano HBC (4-1) are probed within the experimental window.

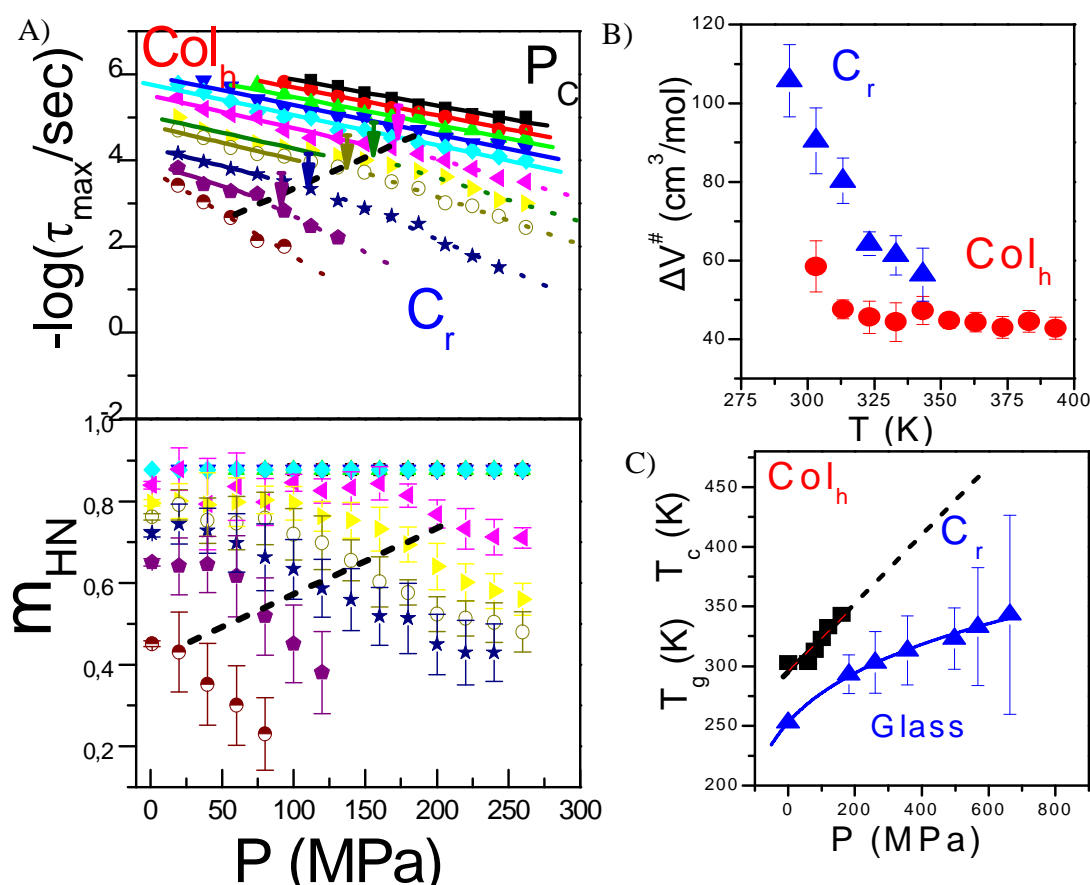


Figure 4-17. A) (top) α -process relaxation times as a function of pressure for the following “isotherms”: (filled squares): 393.15 K, (filled circles): 383.15 K, (filled up triangles): 373.15 K, (filled down triangles): 363.15 K, (filled rhombus): 353.15 K, (filled left triangles): 343.15 K, (filled right triangles): 333.15 K, (open circles) 323.15 K, (stars): 313.15 K, (filled polygons): 303.15 K and (half-filled circles): 293.15 K. Lines represent linear fits to the respective regimes. The dashed black line gives the critical pressure (P_c) for the $\text{Col}_h - \text{C}_r$ transformation. (Bottom): HN low frequency parameter of the α -process as a function of pressure for the different isotherms (as above). The black dashed line gives again the critical pressure P_c ; B) Temperature dependence of the apparent activation volume corresponding to the crystalline (C_r) and liquid crystalline (Col_h) phases of the dimethoxy HBC (2-40); C) phase diagram for the dimethoxy HBC (2-40) depicting the pressure dependence of the $\text{Col}_h - \text{C}_r$ transition temperature (squares) and of the glass temperature (up triangles) the latter defined as the temperature where the α -relaxation times are at ~ 1 s.

Figure 4-17A shows a pressure dependent α -process relaxation of 2-40. Increasing the pressure slows down the α -process initially, and subsequently induces the transformation to the C_r phase. The transformation is evident by the stronger $\tau(P)$ dependence within C_r state, and manifests itself as the increased broadening of the α -

process. The included low-frequency HN parameter depicts a dramatic pressure induced broadening under isothermal conditions. Thus the critical pressure, P_c , required for the transformation, can be obtained either from the change in the $\tau(P)$ dependence or from the $m(P)$ dependence as indicated by the thick line.

The linear dependence of $\log \tau$ vs. P can be used to extract the apparent activation volume, ΔV^\ddagger , as

$$\Delta V^\ddagger = 2.303RT \left(\frac{\partial \log \tau}{\partial P} \right)_T,$$

where ΔV^\ddagger represents the difference between the molar volumes of the initial and final (activated) states.⁴⁷ ΔV^\ddagger is plotted in Figure 4-17B within the Col_h and C_r phases, as a function of temperature and reveals a higher activation volume for the α -process within the C_r state, which is also the case in crystallizing polymers and suggests a more cooperative disc rotation within the C_r phase.⁴⁸

Based on the T- and P-investigations, the phase diagram for **2-40** can be constructed and is depicted in Figure 4-17C. The figure contains the pressure dependence of the glass temperature corresponding to the freezing of the disc axial motion within the crystalline phase and the pressure dependence of the critical temperature, T_c , for the Col_h to C_r transformation obtained from the data of Figure 4-17A. The former can be described by the empirical equation:⁴⁹

$$T_g(P) = T_g(0) \left(1 + \frac{b}{c} \right)^{1/b}$$

where $T_g(0) = 253$ K, b and c are fitting parameters ($b = 6 \pm 1$, $c = 810 \pm 90$ MPa and $(\partial T / \partial P)_{p \rightarrow 0} = 0.3$ K/MPa). These dependences separate the T-P phase space in three regimes depicted as “glass”, “ C_r ” and Col_h ”. As a result of the stronger pressure dependence of the first order phase transition (from C_r to Col_h), the increase of pressure effectively stabilizes the C_r phase. For example, the crystalline phase can be stabilized to 450 K at 600 MPa, i.e. about 150 K above its atmospheric pressure limit. This

stabilization of the crystalline phase at higher temperatures can have consequences in applications in view of the higher charge carrier mobility found in the C_r phase.

Similar experiments were performed with mono-cyano HBC (**4-1**), where both α - and α' -processes are probed within the experimental window. Both processes are slowed down by increasing the pressure, but are more effective for α' -process with a stronger P -dependence (Figure 4-18). The apparent activation volume, ΔV^\ddagger , is plotted in the inset as a function of the temperature difference from the respective T_g . The apparent activation volume for the two processes decreases with increasing temperature and $\Delta V_{\alpha'}^\ddagger > \Delta V_{\alpha}^\ddagger$, which indicates that the pressure slows down the highly collective slower process (α' -process) more than the less volume demanding axial motion of the discs (α -process). The phase diagram for the **4-1** is constructed in a similar way as for **2-40** and shown in Figure 4-19. The two $T_g(P)$ dependences corresponding to the freezing of the fast axial (α -process) and of the slower collective re-orientation (α' -process) are described by the empirical equation used for **2-40**, with $b = 3.9$, $c = 540$ MPa and $(\partial T / \partial P)_{p \rightarrow 0} = 0.44$ K/MPa for the α -process and $b = 4.8$, $c = 370$ MPa and $(\partial T / \partial P)_{p \rightarrow 0} = 0.69$ K/MPa for the α' -process. These dependencies separate the T-P phase space into three regimes depicted as “glass I”, “glass II” and Col_h . As a result of the stronger pressure dependence for the slow collective re-orientation, increasing the pressure effectively stabilizes the “glass II” phase, whereby no dipole-correlated molecular block relaxation happens.

Comparing the dynamics of these dipole functionalized HBCs, it is noticed that α - and α' -processes are clearly separated only for the HBCs bearing the stronger dipoles (**4-1** and **4-2**). In the mono-ethynyl HBC (**4-3**), the peak shape of the DS spectrum is still asymmetric. However, the deconvolution of the two processes (α -relaxation and α' -relaxation processes) is difficult. This is consistent with the assignment of the α' -relaxation process as the orientation correlation of the discs within the columns due to strong molecular dipole – dipole coupling, whereas, this kind of interaction is expected to be much less effective for the molecules bearing weak dipole moments (**4-3** and **2-40**).

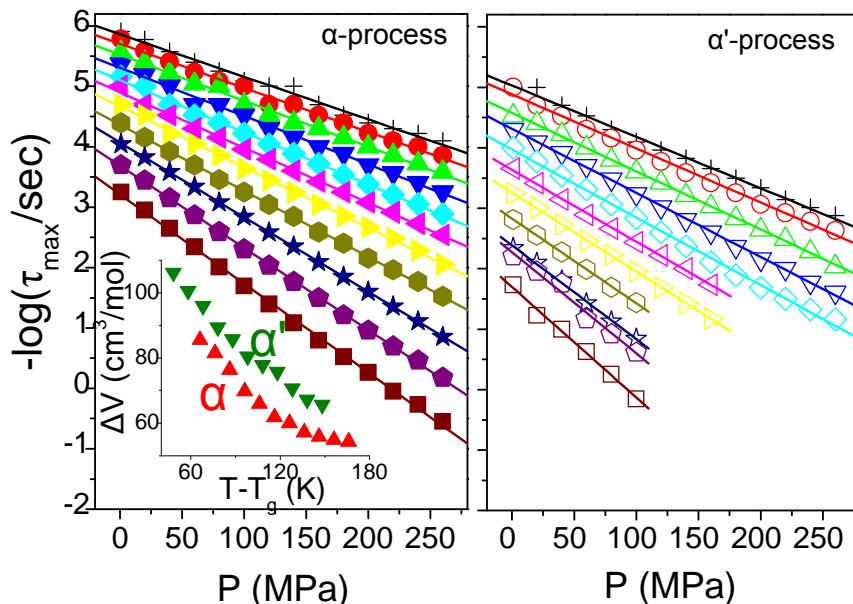


Figure 4-18. Pressure dependence of the relaxation times at maximum loss corresponding to the α - (left) and α' - (right) processes of mono-cyano HBC (4-1). The symbols indicate temperatures in the range from 303 (squares) to 403 K (crosses) in steps of 10 K. The lines are the result of the fit giving rise to the apparent activation volume. (Inset) Temperature dependence of the apparent activation volumes (ΔV^\ddagger) plotted as a function of the temperature difference from the respective T_g

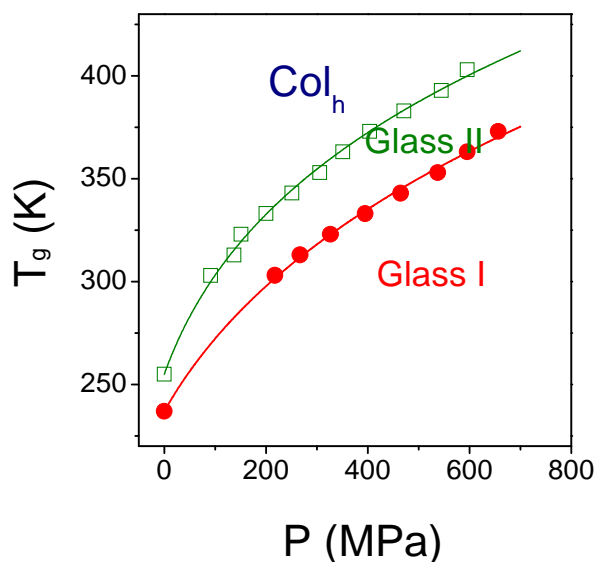


Figure 4-19. Phase diagram for the monocyano-HBC (4-1) showing two “glass” phases and the columnar hexagonal liquid crystalline phase (Col_h) at higher temperatures.

4.5 Summary

A series of dipole functionalized HBCs, their self-assembly and disc dynamics within the columnar phases were studied with DSC, 2D WAXD, site-specific NMR techniques and dielectric spectroscopy (DS). DSC and 2D WAXD experiments demonstrated that there exist both C_r and Col_h phases in the HBC molecules bearing a relatively weaker dipole (in the case of dimethoxy HBC **2-40** and mono-ethynyl HBC **4-3**); and the mesophase of strong-dipole-functionalized HBCs (mono-cyano HBC **4-1** and mono-bromo HBC **4-2**) are stabilized over a large temperature range excluding the C_r phase. Site-specific NMR experiments revealed a fast rotation dynamics of the HBC discs along the column axis within the Col_h phase, which is recognized as α -relaxation process in DS studies, and this kind of rotation is frozen in the C_r phase causing an abrupt broadening of the α -relaxation curve in the DS spectrum. Additionally, the molecular orientation correlation of the dipoles within the columns was detected in DS as a relatively slower relaxation, which also fits the VFT equation and is called α' -relaxation process. It has also shown that the glass transition temperature, associated with the freezing of the axial disc rotation, is around $-37\text{ }^\circ\text{C}$ for these discotics within the liquid crystalline phase and at $30\text{ }^\circ\text{C}$ for the dimethoxy HBC (**2-40**) in the crystalline state. Therefore, it is concluded that the phase state controls the dynamic response. The relaxation times and wideness of the α -relaxation curves have different temperature and pressure dependencies on entering the crystalline state.

These studies help us to recognize the phase behavior of HBC molecules from a molecular dynamics point of view and understand the property differences in various phases, for instance, the sudden drop of the intramolecular charge-carrier mobility of HBC derivatives from C_r to Col_h phases.⁵⁰ Through creating the phase diagram (T - P), the C_r phase of dimethoxy HBC **2-40** is stabilized up to $177\text{ }^\circ\text{C}$ under 600 MPa with possible consequent preservation of high charge carrier mobilities. This opens an alternative pathway to achieve the distinct low-temperature material properties at elevated temperatures.

Although the introduced strong dipole moment fails in the formation of more ordered C_r phase, the enhanced intermolecular interactions have been observed through

α^{\prime} -relaxation process, which is crucial for the uniform alignment of these columnar superstructures on surfaces, and consequently improves the self-healing abilities of these molecular columns leading to a good long-time performance of a device.⁸

4.6 References

1. Novoselov, K. S., Geim, A. K., Morozov, S. V., Jiang, D., Katsnelson, M. I., Grigorieva, I. V., Dubonos, S. V., Firsov, A. A., *Nature* **2005**, *438*, 197-200.
2. Wu, J., Pisula, W., Müllen, K., *Chem. Rev.* **2007**, *107*, 718-747.
3. Pisula, W., Menon, A., Stepputat, M., Lieberwirth, I., Kolb, U., Tracz, A., Siringhaus, H., Pakula, T., Müllen, K., *Adv. Mater.* **2005**, *17*, 684-689.
4. Craats, A. M. v. d., Warman, J. M., Fechtenkötter, A., Brand, J. D., Harbison, M. A., Müllen, K., *Adv. Mater.* **1999**, *11*, 1469-1472.
5. Demus, D., Goodby, J., Gray, G. W., Spiess, H. W., *Handbook of Liquid Crystals*. Vill, V., Wiley-VCH: Weinheim, **1998**.
6. Leisen, J., Werth, M., Boeffel, C., Spiess, H. W., *J. Chem. Phys.* **1992**, *97*, 3749-3759.
7. Herwig, P., Kayser, C. W., Müllen, K., Spiess, H. W., *Adv. Mater.* **1996**, *8*, 510-513.
8. Fischbach, I., Pakula, T., Minkin, P., Fechtenkötter, A., Müllen, K., Spiess, H. W., Saalwachter, K., *J. Phys. Chem. B* **2002**, *106*, 6408-6418.
9. Vallerien, S. U., Werth, M., Kremer, F., Spiess, H. W., *Liquid Crystals* **1990**, *8*, 889 - 893.
10. Werth, M., Vallerien, S. U., Spiess, H. W., *Liquid Crystals* **1991**, *10*, 759 - 770.
11. Möller, M., Wendorff, J. H., Wert, M., Spiess, H. W., Bengs, H., Karthaus, O., Ringsdorf, H., *Liquid Crystals* **1994**, *17*, 381 - 395.
12. Möller, M., Wendorff, J. H., Werth, M., Spiess, H. W., *Non-Cryst. Solids* **1994**, *170*, 295-299.
13. Ngai, K. L., *Non-Cryst. Solids* **1996**, *197*, 1-7.
14. Glösen, B., Kettner, A., Kopitzke, J., Wendorff, J. H., *Non-Cryst. Solids* **1998**, *241*, 113-120.
15. Yildirim, Z., Wubbenhorst, M., Mendes, E., Picken, S. J., Paraschiv, I., Marcelis, A. T. M., Zuilhof, H., Sudholter, E. J. R., *Non-Cryst. Solids* **2005**, *351*, 2622-2628.
16. Kruglova, O., Mendes, E., Yildirim, Z., Wubbenhorst, M., Mulder, F. M., Stride, J. A., Picken, S. J., Kearley, G. J., *ChemPhysChem* **2007**, *8*, 1338-1344.
17. Elmahdy, M. M., Floudas, G., Mondeshki, M., Spiess, H. W., Dou, X., Müllen, K., *Phys. Rev. Lett.* **2008**, *100*, 107801.

18. Mulder, F. M., Stride, J., Picken, S. J., Kouwer, P. H. J., de Haas, M. P., Siebbeles, L. D. A., Kearley, G. J., *J. Am. Chem. Soc.* **2003**, *125*, 3860-3866.
19. Gennes, P. G. d., *J. Physique Lett.* **1983**, *44*, 657-664.
20. Fechtenkotter, A., Tchegotareva, N., Watson, M., Müllen, K., *Tetrahedron* **2001**, *57*, 3769-3783.
21. Wu, J., Qu, J., Tchegotareva, N., Müllen, K., *Tetrahedron Letters* **2005**, *46*, 1565-1568.
22. Pisula, W., Tomovic, Z., Simpson, C., Kastler, M., Pakula, T., Müllen, K., *Chem. Mater.* **2005**, *17*, 4296-4303.
23. Tchegotareva, N. PhD Thesis. Johannes Gutenberg Universität 2003.
24. Ito, S., Wehmeier, M., Brand, J. D., Kübel, C., Epsch, R., Rabe, J. P., Müllen, K., *Chem. Eur.J.* **2000**, *6*, 4327-4342.
25. Rego, J. A., Kumar, S., Ringsdorf, H., *Chem. Mater.* **1996**, *8*, 1402-1409.
26. Foster, E. J., Jones, R. B., Lavigueur, C., Williams, V. E., *J. Am. Chem. Soc.* **2006**, *128*, 8569-8574.
27. Feng, X., Pisula, W., Takase, M., Dou, X., Enkelmann, V., Wagner, M., Müllen, K., "Synthesis, Helical Organization, and Long-range Fibrous Assembly of C₃ Symmetric Methoxy-substituted Hexa-*peri*-hexabenzocoronene." *Chem. Mater.* **2008**; submitted.
28. Kakudo, M., Kasi, N., *X-ray Diffraction by Polymers*. Kodansha Ltd.: Tokyo, **1972**.
29. Holst, H. C., Pakula, T., Meier, H., *Tetrahedron* **2004**, *60*, 6765-6775.
30. Pisula, W., Tomovic, Z., Watson, M. D., Müllen, K., Kussmann, J., Ochsenfeld, C., Metzroth, T., Gauss, J., *J. Phys. Chem. B* **2007**, *111*, 7481-7487.
31. Feng, X., Pisula, W., Müllen, K., *J. Am. Chem. Soc.* **2007**, *129*, 14116-14117.
32. Lim, G. S., Jung, B. M., Lee, S. J., Song, H. H., Kim, C., Chang, J. Y., *Chem. Mater.* **2007**, *19*, 460-467.
33. Datta, A., Pati, S. K., *Chem. Soc. Rev.* **2006**, *35*, 1305-1323.
34. Haino, T., Tanaka, M., Fukazawa, Y., *Chem. Commun.* **2008**, 468-470.
35. Brown, S. P., Schnell, I., Brand, J. D., Müllen, K., Spiess, H. W., *J. Am. Chem. Soc.* **1999**, *121*, 6712-6718.
36. Ochsenfeld, C., Brown, S. P., Schnell, I., Gauss, J., Spiess, H. W., *J. Am. Chem. Soc.* **2001**, *123*, 2597-2606.
37. Brown, S. P., Schnell, I., Brand, J. D., Müllen, K., Spiess, H. W., *J. Mol. Struct.* **2000**, *521*, 179-195.
38. Saalwachter, K., Schnell, I., *Solid State Nucl. Magn. Res.* **2002**, *22*, 154-187.
39. Schnell, I., *Prog. Nucl. Magn. Reson. Spectrosc.* **2004**, *45*, 145-207.

40. Schmidt-Rohr, K., Spiess, H. W., *Multidimensional solid State NMR and Polymers*. Academic Press: New York, **1994**.
41. Schmidt-Rohr, K., Spiess, H. W., *Phys. Rev. Lett.* **1991**, *66*, 3020.
42. Tracht, U., Wilhelm, M., Heuer, A., Feng, H., Schmidt-Rohr, K., Spiess, H. W., *Phys. Rev. Lett.* **1998**, *81*, 2727.
43. Kremer, F., Schonhals, A., Luck, W., *Broadband Dielectric Spectroscopy*. Springer: Berlin, **2003**.
44. Molkov, Y. I., Mukhin, D. N., Suvorov, E. V., Feigin, A. M., *Radiophysics and Quantum Electronics* **2003**, *46*, 675-685.
45. Havriliak, S., Negami, S., *Polymer* **1967**, *8*, 161-210.
46. Sokol, R., Nedbal, J., Fährnich, J., Ilavský, M., Kolařík, J., *Polymer Bulletin* **2000**, *44*, 555-562.
47. Floudas, G., *Prog. Polym. Sci.* **2004**, *29*, 1143-1171.
48. Mierzwa, M., Floudas, G., Ā tepĀjnek, P., Wegner, G., *Phys. Rev. B* **2000**, *62*, 14012.
49. Drozd-Rzoska, A., Rzoska, S. J., Imre, A. R., *J. Non-Crys. Solids* **2007**, *353*, 3915-3923.
50. van de Craats, A. M., Warman, J. M., Fechtenkötter, A., Brand, J. D., Harbison, M. A., Müllen, K., *Adv. Mater.* **1999**, *11*, 1469-1472.

5 Synthesis of Donor-HBC-Acceptor Molecules from *para*-Iodo-bromo-HBC Building Block and their Self-assembly Behaviors Studies

The discovery of conducting and semiconducting organic polymers in 1970s has led to applications in the field of organic electronics.¹⁻³ Following the pioneers, organic chemists have pursued various π -conjugated systems as active components for the electronic and optoelectronic devices, such as light-emitting diodes, field-effect transistors (FET) and solar cells.^{4,5} Conjugated polymers and oligomers are a class of organic semiconductors that are by far the most intensively investigated. However, the one-dimensional nature of these chain structures possesses several limitations since it results in low-dimensional conductors in the solid state.⁶⁻⁸ Disc-like PAHs are considered as two-dimensional charge transporting materials with high purity and have attracted intensive scientific interest.⁹⁻¹¹ Typical examples of these materials are triphenylenes and hexa-*peri*-hexabenzocoronene (HBC) derivatives. As introduced in CHAPTER 1, the device performance depends upon the order of these discotic molecules in thin films.¹²⁻¹⁴ Tremendous efforts have, therefore, been invested to achieve monodomain ordered structures. Extra intermolecular interactions, such as hydrogen bonds,¹⁵⁻¹⁸ amphiphilic interactions,¹⁹⁻²³ and even covalent bonding interaction²⁴⁻²⁷ were added to stabilize their columnar supramolecular organization.

As it will be demonstrated in CHAPTER 6, the introduced rigid hydrogen bonds (along the columnar direction) either assist the HBC molecules to form stable columnar structures or compete against $\pi - \pi$ interactions resulting in short-range ordered supramolecular arrangement. Unlike hydrogen bonds, the strength of which is in the range of 10 - 65 kJ mol⁻¹, dipole-dipole interactions are relatively weak having a comparable strength value of 5 - 50 kJ mol⁻¹ with $\pi - \pi$ interactions (0 - 50 kJ mol⁻¹).²⁸ In order to achieve highly ordered stable columnar supramolecular organization, strong

dipole moments are, thus, introduced by the asymmetric functionalization of HBC cores with one electron donating and one electron accepting group. In addition, it has also been shown that hexa(4-dodecylphenyl)hexa-*peri*-hexabenzocoronene (HBC-PhC₁₂) is able to form highly oriented films under the influence of a magnetic field leading to a significantly enhanced charge carrier mobility with respect to the unaligned material.²⁹ The strong molecular dipoles will further provide extra interactions between single molecules and an external electromagnetic field, probably, resulting in optimal films for future device applications.

On the other hand, electron-transfer (ET) reactions between separate molecules (intermolecular) or between distinct regions within a single molecule (intramolecular), are some of the most frequently encountered photochemical processes.³⁰ The ET reaction product in such an inter- or intramolecular processes is usually called charge-transfer (CT), or an intramolecular CT state (ICT). The photoinitiated ET processes and the resulting CT states play a fundamental role in photosynthesis, and in numerous existing or conceived applications (e.g. the molecular devices of future technologies, see examples in CHAPTER 7).³⁰ These phenomena were mainly found in the compounds containing electron donating (D) and accepting (A) moieties, i.e. D-bridge-A (DBA) systems.³¹⁻³⁶ When the bridge group is a π system (the so-called D- π -A molecule), the CT phenomenon renders this kind of materials nonlinear optical properties.³⁷ The precedent π -electron linker covers conjugated oligomers,³⁷ hexaphenylbenzenes,³⁸ porphyrins,³⁹⁻⁴¹ perylene diimides,⁴² naphthyridine,⁴³ tetra-phenylethynyl benzenes,⁴⁴ and boron-fluorine complexes,⁴⁵ etc. The spontaneous introduction of one donor and one acceptor group to an HBC core constitutes a novel D- π -A system, which contains the largest π -bridge group so far. In so doing, the application of HBC derivatives will be further expanded to nonlinear optics.

Following the aforementioned concepts, two D-HBC-A molecules with different dipoles (**5-1**, $\mu = 8.25$ D and **5-2**, $\mu = 8.64$ D)⁴⁶ were synthesized (Figure 5-1). Additionally, another HBC derivative (**5-3**), which has no dipole moment but similar symmetry, was prepared to compare the effect of the introduced strong dipole moments. The self-assembly behaviors of these compounds in solution were systematically studied

by means of ^1H NMR and spectroelectronic spectroscopies. The UV/Vis absorption and photoluminescence spectroscopy is also used to characterize the CT effects of these D-HBC-A molecules. The morphology and inner structure of the molecular aggregates are visualized by Scanning Electron and Transmission Electron microscopes (SEM and TEM). The liquid crystalline characters are investigated by Differential Scanning Calorimetry (DSC) and two-dimensional Wide Angle X-ray Diffraction (2DWAXD) techniques.

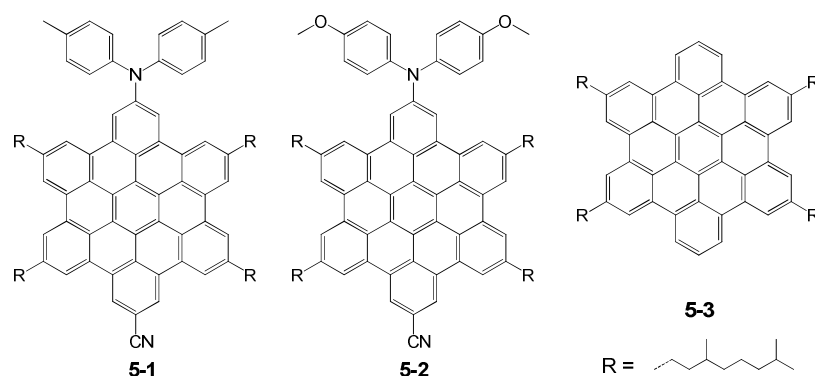


Figure 5-1. Molecular structures of D-HBC-A systems (5-1, 5-2) and HBC without dipole moment (5-3).

5.1 Synthesis

Compound **5-1** and **5-2** were synthesized from the novel *para*-iodo bromo-HBC building block **2-47** (Figure 5-2). Like *para*-iodo bromo-benzene, the iodine in **2-47** shows higher reactivity than bromine at the *para* position and can easily be converted to a cyano group by treatment with copper(I)-cyanide and $\text{Pd}(\text{PPh}_3)_4$ in THF at $65\text{ }^\circ\text{C}$, which leads to **5-4** in 81% yield. The remaining bromo group was then reacted with the corresponding diphenyl amines via Buchwald cross couplings affording **5-1** in 79% yield, and **5-2** in 74% yield. Lithiation of dibromo HBC **2-1**, followed by quenching with methanol, gives **5-3** in 90% yield, which contains only protons at the *para* position. The structures of these compounds are characterized by MALDI-TOF spectrometry, ^1H - and ^{13}C -NMR spectroscopy. Figure 5-3 illustrates the MALDI-TOF spectra of these compounds with calculated isotope distribution patterns.

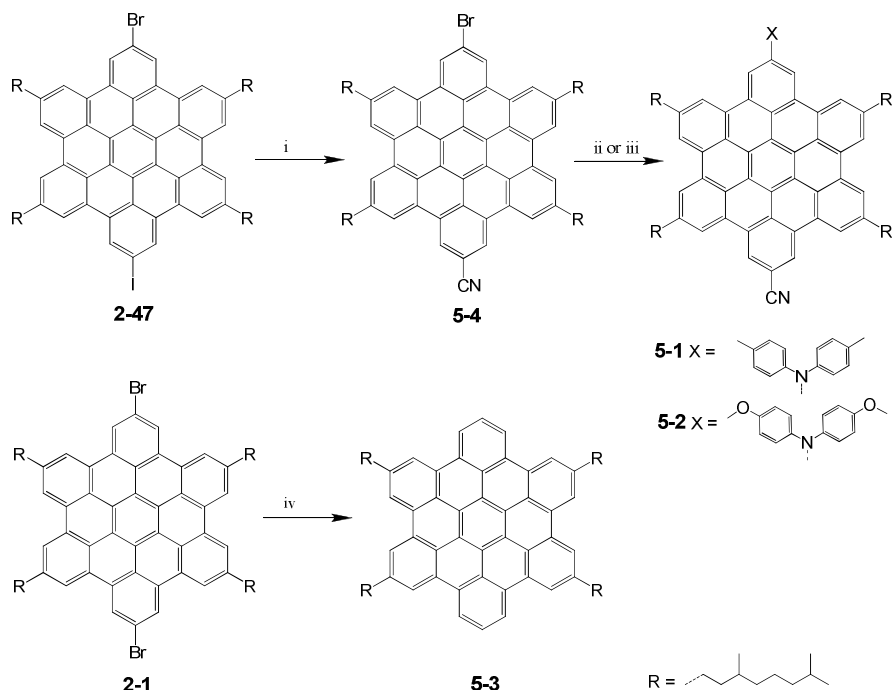


Figure 5-2. Synthesis of 5-1, 5-2 and 5-3; i) CuCN, THF, Pd(PPh₃)₄, reflux, 15 h, 81%; ii) di-tolyl amine, Pd₂(dba)₃, *t*-Bu₃P, sodium butoxide, toluene, 80°C, 16 h, 79%; iii) di-4-methoxyphenyl amine, Pd₂(dba)₃, *t*-Bu₃P, sodium butoxide, toluene, 80°C, 16 h, 74%; iv) *n*-butyl lithium, -78 °C, 30 min., MeOH, 90%.

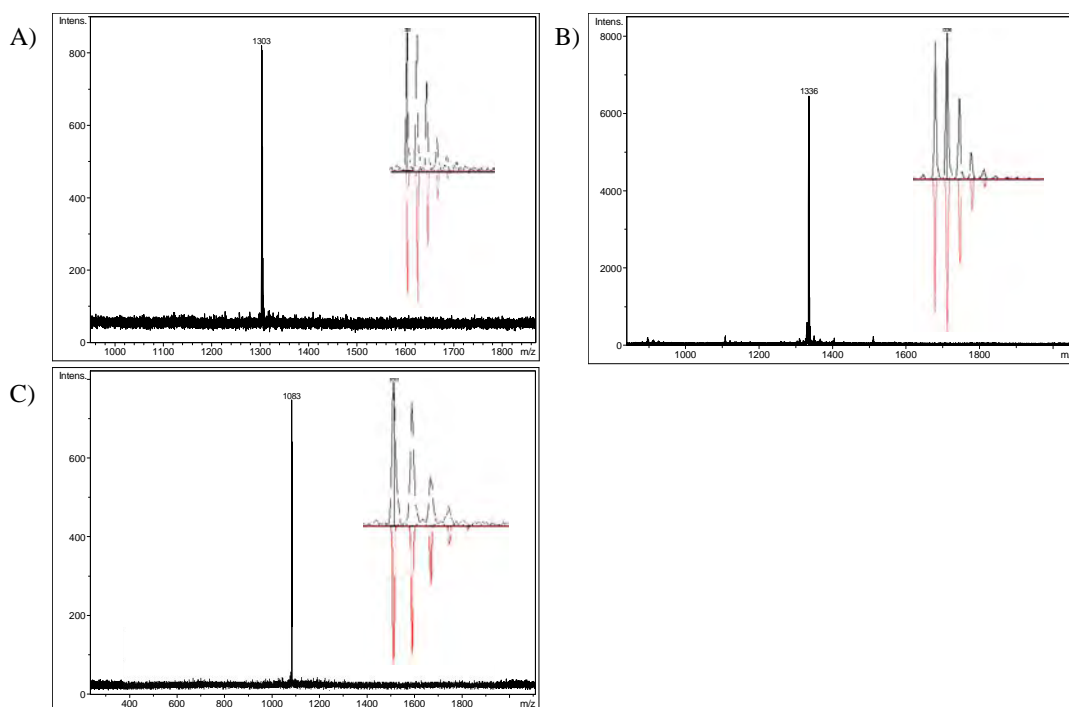


Figure 5-3. MALDI-TOF spectra of A) 5-1, B) 5-2 and C) 5-3 (measured with TCNQ as matrix); insets: corresponding isotope distribution patterns (black: measured, red: calculated value).

5.2 Self-assembly behavior in solution studied by $^1\text{H-NMR}$ spectroscopy

The aggregation of aromatic cores influences the local electron density and / or the aromatic ring current.⁴⁷ As a result, the $^1\text{H-NMR}$ spectra of the molecular aggregates differ from those of monomers. The temperature / concentration dependency can be used as a probe of molecular self-association propensity.⁴⁸⁻⁵⁰ Thereby, the aggregates typically give rise to significant line broadening and shielding effect (characterized by up-field shifts of proton signals) on the $^1\text{H-NMR}$ spectra.⁵¹ The temperature and concentration dependent $^1\text{H-NMR}$ spectroscopy has, therefore, been used frequently to estimate the molecular aggregation tendency.⁴⁸ Both change of aromatic proton and $\alpha\text{-CH}_2$ resonances in temperature and concentration-dependent $^1\text{H-NMR}$ spectra proves that the molecular self-association propensity increases dramatically with the increase of molecular dipole moments.

5.2.1 Temperature dependent $^1\text{H-NMR}$ spectroscopic studies

The temperature dependent $^1\text{H-NMR}$ spectra of **5-1**, **5-2** and **5-3** were recorded over a temperature range of 30 - 140 °C with d_2 -1,1,2,2-tetrachloroethane solutions (2.05×10^{-2} M) as shown in Figure 5-4. Similar to the hexadecyl-HBC (HBC- C_{12} **3-31**), the aromatic signal of which is shifted to lower field by 0.26 ppm (from 8.11 to 8.37 ppm) when the temperature is increased from 60 °C to 120 °C,⁵² the two sets of aromatic signals of **5-3** show a 0.38 ppm down-field shift with the increase of temperature from 30 °C to 140 °C (Figure 5-4A). Additionally, the signal of the two aromatic protons (**Ha**) at the bay positions can only be resolved as a triplet signal (7.83 ppm) at elevated temperatures and show a 0.30 ppm down-field shift (from 7.54 to 7.83 ppm) when the sample is heated from 30 °C to 140 °C. For the $\alpha\text{-CH}_2$ groups the 3,7-dimethyloctyl substituents, a less pronounced down-field shift (0.25 ppm, from 30°C to 140 °C) is observed. Interestingly, the molecular aggregation enhances the difference between the two kinds of α -protons (**Hb** and **Hc**, on the same carbon atom) due to the nearby chiral carbon atom on the alkyl chains (*). This results in two separated multiple signals with an interval of 0.09 ppm at 30 °C. The discrepancy of the two kinds of α -protons diminishes and shows one broad multiple signals at 3.14 ppm at elevated temperature indicating a

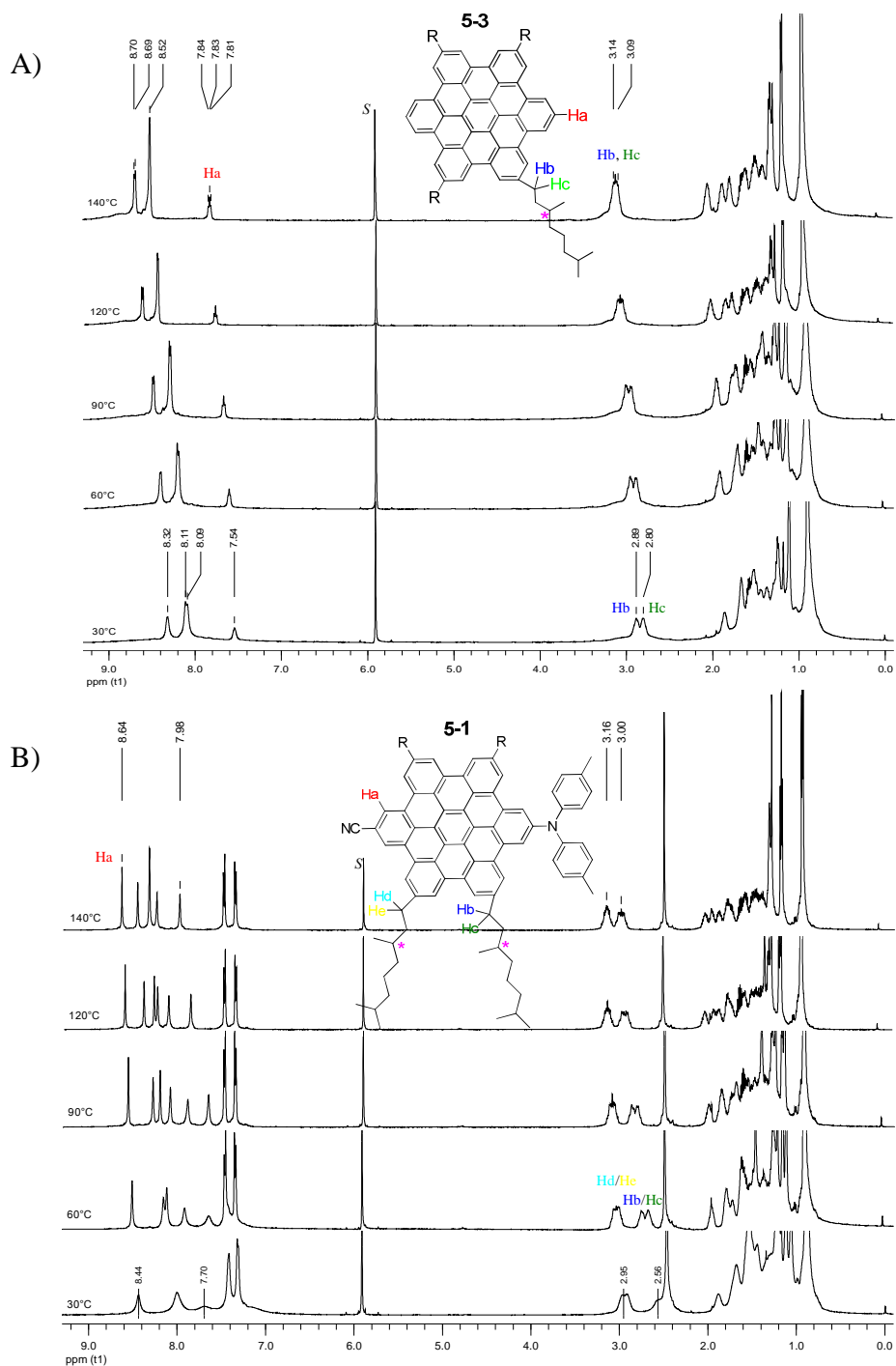


Figure 5-4. Temperature dependent $^1\text{H-NMR}$ spectra of A) **5-3** (500 MHz, $\text{CDCl}_2\text{CDCl}_2$), B) **5-1** (500 MHz, $\text{CDCl}_2\text{CDCl}_2$), and C) **5-2** (700 MHz, $\text{CDCl}_2\text{CDCl}_2$); measured with 2.05×10^{-2} M solution; S: solvent signal, * one of the chiral centers.

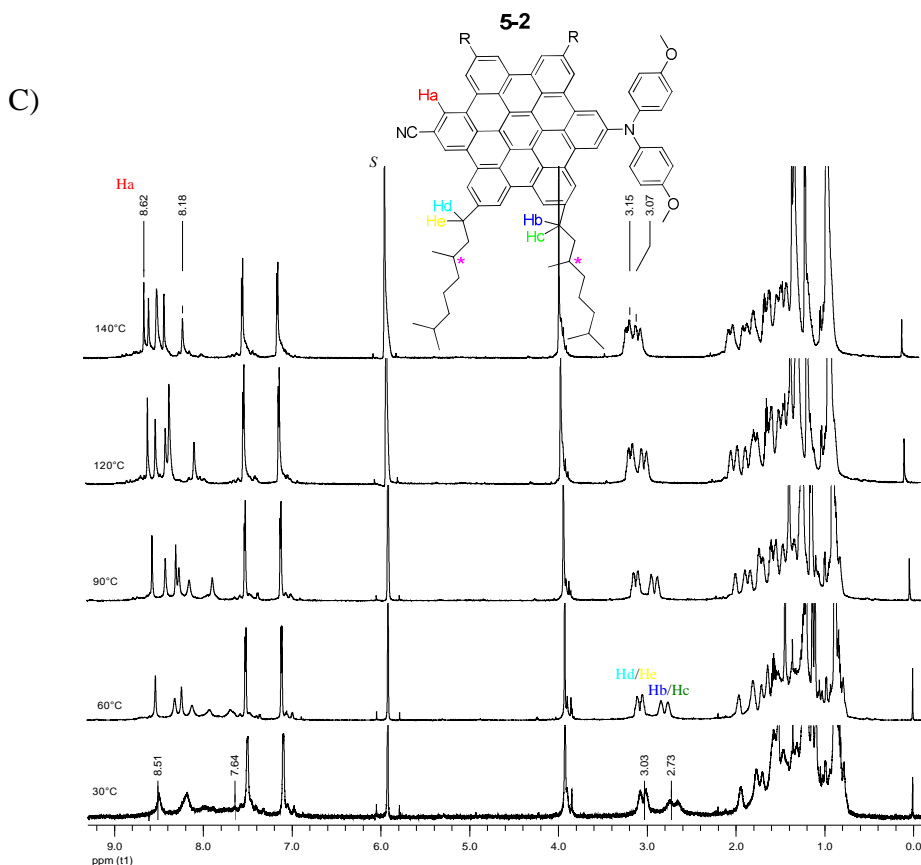


Figure 5-4. (Continue).

weakened aggregation effect and the existence of larger aggregates at lower temperatures, which is in congruence with the often observed phenomena in other disc-like aromatic systems.^{27, 49, 53-60}

The temperature dependent ¹H-NMR spectra of **5-1** and **5-2** (Figure 5-4B,C) display similar trends as that of **5-3**. In contrast to **5-3**, the three sets of aromatic signals of which are clearly resolved at 30 °C (Figure 5-4A), the line shape of the spectra of **5-1** and **5-2** (Figure 5-4B,C) at lower temperatures is much broader and the six different aromatic proton signals can only be well recognized at above 90 °C. In the case of **5-3**, the aromatic signal (**Ha**, Figure 5-4A) is down-field shifted by 0.38 ppm with the increase of temperature from 30 to 140 °C. The signals of the aromatic protons (**Ha**) next to the cyano group in **5-1** and **5-2** (the one shows lowest chemical shift) are down-field shifted by only 0.20 and 0.11 ppm, respectively (Figure 5-4B,C), which indicates a weaker

temperature effect on the molecular aggregates than that in the case of **5-3**. This is also supported by the later temperature dependent UV/Vis absorption spectroscopic studies (see SECTION 5.3.1).

The four kinds of α -CH₂ protons of **5-1** give rise to two sets of broad multiple signals in the region of 2.46 to 3.12 ppm (Figure 5-4B). The difference between the two α -protons on the same carbon atom for each set (Hb/Hc and Hd/He, Figure 5-4B) is recorded as 0.05 ppm and 0.08 ppm at 60 °C, respectively. At temperatures above 120 °C, this difference disappears leaving two sets of broad multiple peaks corresponding to the two chemically environmentally different alkyl substituents. In the case of **5-2** (Figure 5-4C), the two pairs of α -protons (Hb/Hc and Hd/He, Figure 5-4C) respectively show a difference of 0.07 ppm and 0.09 ppm at 60 °C, and the four different α -protons are still clearly recognized even at 140 °C, which stands in strong contrast to **5-1**. These phenomena imply that the strong-dipole-functionalized compounds **5-1** and **5-2** have a stronger aggregation tendency than the non-polar **5-3**. The change of the resonance signals of aromatic and α -protons further indicates that **5-2**, which has a stronger dipole moment ($\mu = 8.64$ D), has the stronger self-association propensity than that of **5-1**.

5.2.2 Concentration dependent ¹H-NMR spectroscopic studies

Concentration dependent ¹H-NMR spectra also provide a sensitive probe for the detection of molecular aggregates in solution.^{50, 57} Figure 5-5 shows the concentration dependent ¹H-NMR spectra of **5-1** and **5-2** in *d*₂-1,1,2,2-tetrachloroethane. The aromatic protons next to the cyano group resonance in **5-1** (Ha, Figure 5-5A) is up-field shifted by 0.38 ppm (from 8.89 to 8.51 ppm) as the concentration increases from 1.00×10^{-5} M to 2.05×10^{-2} M; a comparable up-field shift (0.39 ppm, from 8.93 to 8.54 ppm) of such a proton (Ha, Figure 5-5B) is observed in **5-2** within an even narrower concentration range (from 3.00×10^{-5} M to 1.20×10^{-2} M). At lower concentrations, the four kinds of α -protons give rise to one set of multiple peaks and they are split into two sets of signals as the increase of concentration for both compounds. In the case of **5-1** (Figure 5-5A), the four different α -protons are not completely recognized and show three multiple peaks at a concentration of 2.05×10^{-2} M. For **5-2** (Figure 5-5B), they are well resolved as four individual peaks even at a relatively lower concentration (1.20×10^{-2} M).

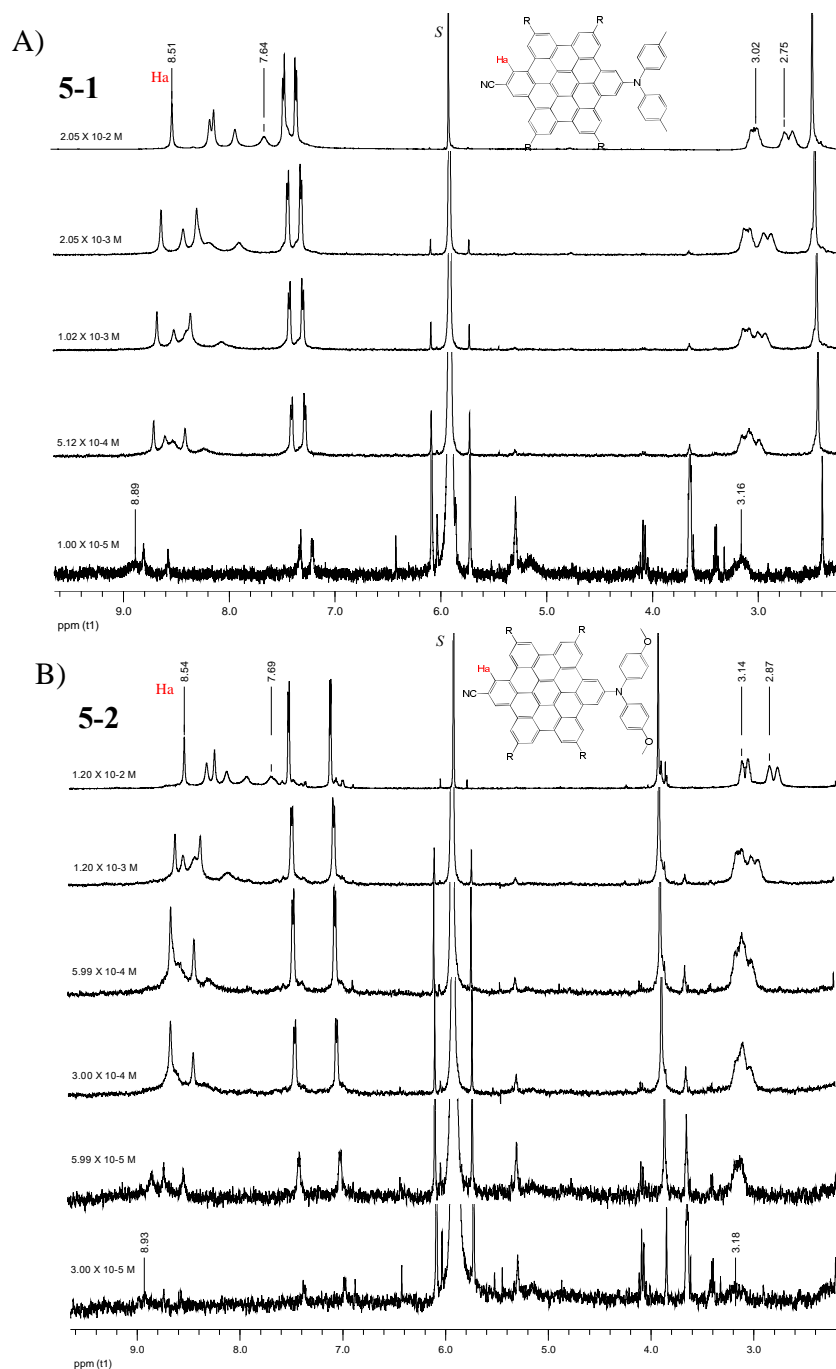


Figure 5-5. Concentration dependent $^1\text{H-NMR}$ spectra of A) 5-1 and B) 5-2 (500 MHz, 60 °C, $\text{CDCl}_2\text{CDCl}_2$, 9.6 - 2.2 ppm region); S: solvent signal.

These observed changes are consistent with the results obtained from the temperature dependent $^1\text{H-NMR}$ spectroscopic investigations. In contrast to 5-1, the larger chemical shift change within a narrower concentration range in the case of 5-2

further supports the expectation that a stronger molecular dipole moment ($\mu = 8.64$ D for **5-2**, $\mu = 8.25$ D for **5-1**) leads to a stronger molecular aggregation tendency. This is in good agreement with the results obtained in CHAPTER 4, whereby the introduced strong dipole moment effectively stabilizes the columnar mesophase of HBC derivatives due to the intermolecular dipole – dipole interactions in the bulk state.

5.2.3 Thermodynamic studies

In order to quantize the strength of intermolecular interactions, the molecular self-association process has been described in different mathematic models in terms of molecular thermodynamics. As reviewed by Martin, R. B.,⁴⁸ two models, called Equal K (EK) and Attenuated K (AK) model, are widely used concerning the equilibrium constant (K_E) in the EK model and self-association constant (K_A) in the AK model. The EK model simplified the mathematic calculation by assuming an identical free energy and equilibrium constant (K_E) during the addition of each monomer to an existing aggregate. Although the enthalpy of adding a monomer to a growing stack may be constant, successive additions should be increasingly less probable and hence less favored entropically, and successive equilibrium constants (K) should taper off in value. The AK model goes beyond the EK model with an ensemble term (K_A) by considering the entropic changes during the successive addition of monomer to an aggregate. Both models have been applied to osmometry, sedimentation equilibria and NMR experiments, wherein the NMR technique gives direct concentration information without concern for nonideality.⁴⁸

In our group, the AK model has been used to fit the concentration dependent ¹H-NMR data for hexa-alkylated HBCs deriving association constants, which demonstrated the distinct self-assembly abilities of HBC derivatives.^{49, 50} Hereby, similar studies were applied to characterize the dipole functionalized HBC **5-1** and 2,8,11-trimethoxy HBC **3-32**. The ¹H-NMR data of **5-1** were collected with *d*²-1,1,2,2-tetrachloroethane solutions over a concentration range from 5.00×10^{-7} to 2.05×10^{-2} M on 500MHz NMR spectrometer at 60°C. The ¹H-NMR data of **3-32** (measured *d*²-1,1,2,2-tetrachloroethane solutions with the concentration ranging from 2.38×10^{-5} to 1.19×10^{-2} M on 500MHz NMR spectrometer at 60 °C) were provided by Dr. Xinliang Feng. The mathematical

curve fitting was performed with a program based on the non-linear least squares method by Lei Xie from Prof. R. Nordmann's group at TU-Darmstadt. Detailed AK-model setup and the original mathematical curve fitting program code are described in appendix.

Table 5-1. Experimental data of **5-1**, **3-32** and parameters calculated for the AK models; K_A : association constant; τ : factor by which dimer formation differs from other polymer formation in AK models ($K_2 = \tau K_A / 2$); f : factor relating shift of end molecule to that of the monomer and the interior molecule ($P_\lambda = (1-f)P_\alpha + fP_\xi$); P_α : NMR shift of monomer; P_ξ : NMR shift of the interior molecule.

Experimental data of 5-1										
concentration / M	2.05×10^{-2}	2.05×10^{-3}	1.02×10^{-3}	5.12×10^{-4}	6.00×10^{-5}	3.00×10^{-5}	1.00×10^{-5}	5.00×10^{-6}	1.00×10^{-6}	5.00×10^{-7}
chemical shift / ppm	8.51	8.63	8.67	8.71	8.76	8.82	8.89	8.98	9.04	9.06
Experimental data of 3-32										
concentration / M	1.19×10^{-2}	7.16×10^{-3}	2.38×10^{-3}	1.19×10^{-3}	7.16×10^{-4}	2.38×10^{-4}	1.19×10^{-4}	7.16×10^{-5}	2.38×10^{-5}	
chemical shift / ppm	8.36	8.44	8.62	8.65	8.79	8.88	8.90	8.93	8.95	
AK model calculation										
5-1	$K_A = 1405.93(4)$ L/mol	$\tau = 25.915(7)$	$f = 0.117(3)$	$P_\alpha = 8.985(7)$ ppm	$P_\xi = 6.520(2)$ ppm					
3-32	$K_A = 658.05(4)$ L/mol	$\tau = 3.653(4)$	$f = 0.597(5)$	$P_\alpha = 8.88(4)$ ppm	$P_\xi = 7.459(2)$ ppm					
HBC-C₁₂ (3-31)	$K_A = 457.32$ L/mol	$\tau = 3.834$	$f = 0.3773$	$P_\alpha = 8.978$ ppm	$P_\xi = 7.239$ ppm					

Table 5-1 lists the ^1H -NMR data and calculated parameters in AK model for **5-1**, 2,8,11-trimethoxy HBC **3-32** and HBC-C₁₂ **3-31**. The association constant K_A of **5-1** is about three times larger than that of non-polar HBC-C₁₂ **3-31** and more than two times that of 2,8,11-trimethoxy HBC **3-32**, a compound shows enhanced intermolecular interactions leading to helical supramolecular organization.⁶¹ The calculated chemical shifts for the monomers (P_α) of all three compounds do not show obvious difference.

Whereas, the simulated chemical shift of the molecule within a stack (P_z) of **5-1** is more than 1 ppm smaller than those of **3-31** and **3-32**. These reflect a much stronger self-association propensity in compound **5-1** comparing with the other two.

The parameter τ describes the ability of forming a dimer in contrast to that in formation of bigger aggregates (see Appendix I).⁴⁸ The dipole – dipole interaction enhanced intermolecular association is unambiguously proved by the dramatically increased τ value (in comparison with those of the other two compounds) during the formation of molecular dimers.

In congruence with the quantitative studies in SECTION 5.2.1 and 5.2.2, these results demonstrate that the introduced strong molecular dipole moment effectively increases the intermolecular interactions in solution from the thermodynamic point of view. However, to derive these parameters for compound **5-2** is limited by the unreachable monomeric chemical shift due to the reduced sensitivity of experimental NMR technique to the very dilute solutions. It will be demonstrated in the following section that the strong intermolecular dipole – dipole interactions not only result in larger molecular aggregates in solution, but also give rise to a series of interesting spectroelectronic changes.

5.3 Spectroelectronic spectroscopy

The spectroelectronic spectroscopy gives the information of both the molecular electronic states and the molecular aggregates in solution.^{62,63} In this part, it will first be used to probe the molecular self-assembly behavior and then to investigate the charge transfer states of **5-1** and **5-2**.

5.3.1 Self-assembly behavior studies

Figure 5-6 shows the concentration dependent UV/Vis absorption and photoluminescence spectra of **5-1**, **5-2** and **5-3** in chloroform and DMF/THF (1/1) solutions.

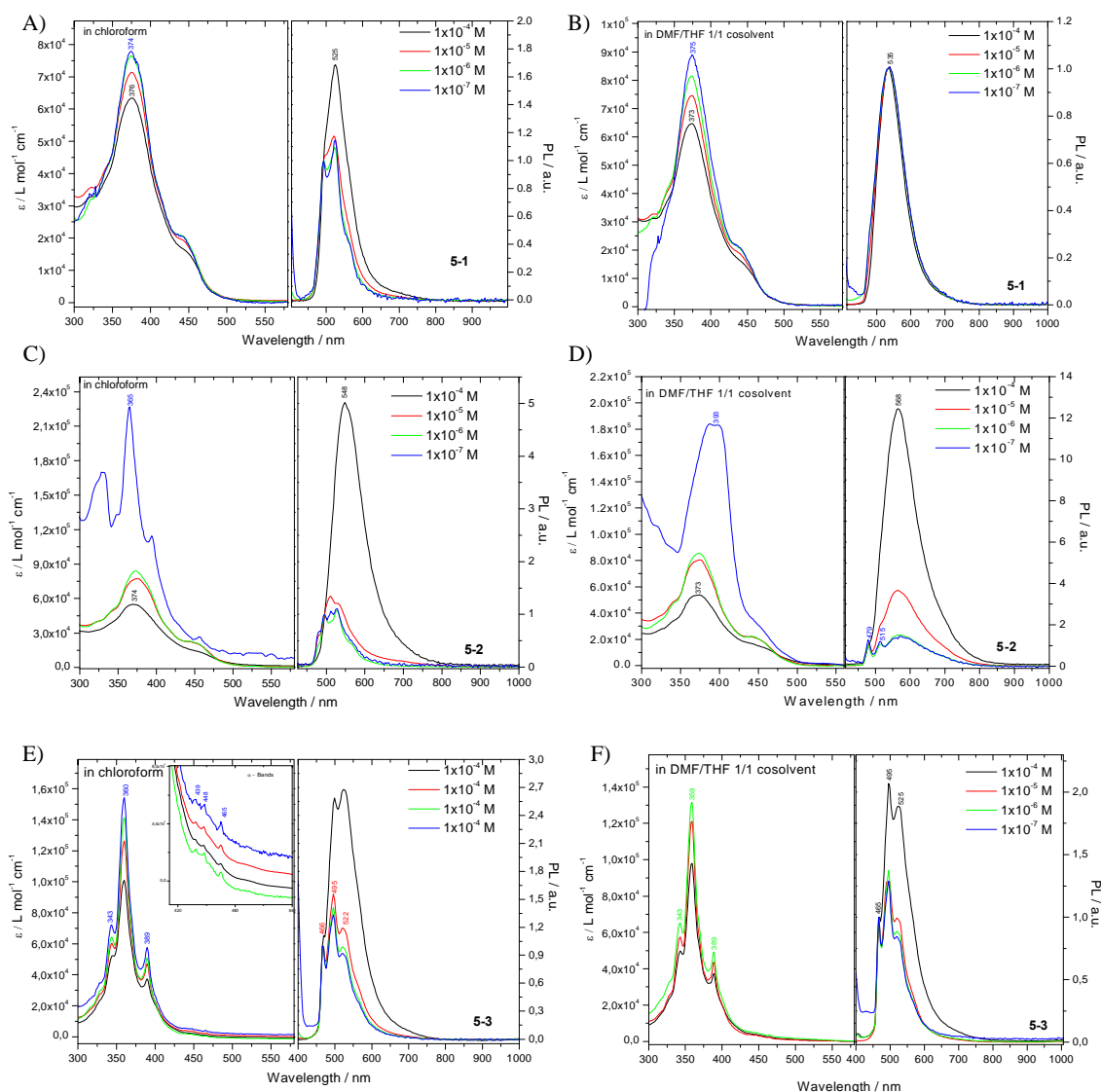


Figure 5-6. Concentration dependent UV/Vis absorption and fluorescence spectra (excited at 377 nm) of A,B) 5-1, C,D) 5-2 and E,F) 5-3; measured at r.t. in chloroform (A,C and E) and DMF/THF 1/1 cosolvent (B,D and F); the intensity of fluorescence spectra were respectively normalized at 492 (A), 531 (B), 495 (C), 479 (D), 465 nm (E, F); inset: the α -bands of 5-3 recorded in chloroform.

Non-Lambert-Beer behavior is observed for all three compounds in the concentration dependent UV/Vis absorption spectra.⁵⁰ The extinction coefficients of these compounds, especially in the case of **5-2**, dramatically decrease as the concentration increases. In the case of **5-3**, which bears neither donor nor acceptor moieties, the typical absorption bands for polycyclic aromatic hydrocarbons, the p , β , β' bands (according to Clar's nomenclature),⁶⁴ are well recognized as three intensive sharp peaks at 389, 360 and

Clar's nomenclature),⁶⁴ are well recognized as three intensive sharp peaks at 389, 360 and 343 nm. Additionally, the α -bands are clearly recorded as well in the region of 439 – 465 nm. This series of bands are normally weak and correspond to not strictly forbidden transitions from the ground state, S_0 , to the first excited state, S_1 , due to the molecular geometry.^{64, 65} As indicated by the $^1\text{H-NMR}$ spectroscopic studies, **5-1** and **5-2** have stronger self-association propensities than the non-polar **5-3**. The line shapes of their UV/Vis absorption spectra are much broader and the absorption bands are red-shifted in contrast to those of **5-3**. Interestingly, when increasing the concentration from 1×10^{-7} M to 1×10^{-4} M, the absorption bands of **5-2** are either red-shifted by 9 nm (from 365 to 374 nm, Figure 5-6C) with loosing vibrational transition details (transition bands become broader) in chloroform or blue-shifted by 20 nm (from 393 to 373 nm, Figure 5-6D) in DMF/THF 1/1 solutions.

The temperature-dependent UV/Vis absorption spectra demonstrate similar spectroscopic changes (Figure 5-7). Unlike the concentration dependent UV/Vis spectra, 2 nm red-shifts and 3 nm blue-shifts are respectively recorded with a decrease of temperature from 60 °C to 10 °C (limited by the boiling temperature of solvents) in chloroform and DMF/THF solutions.

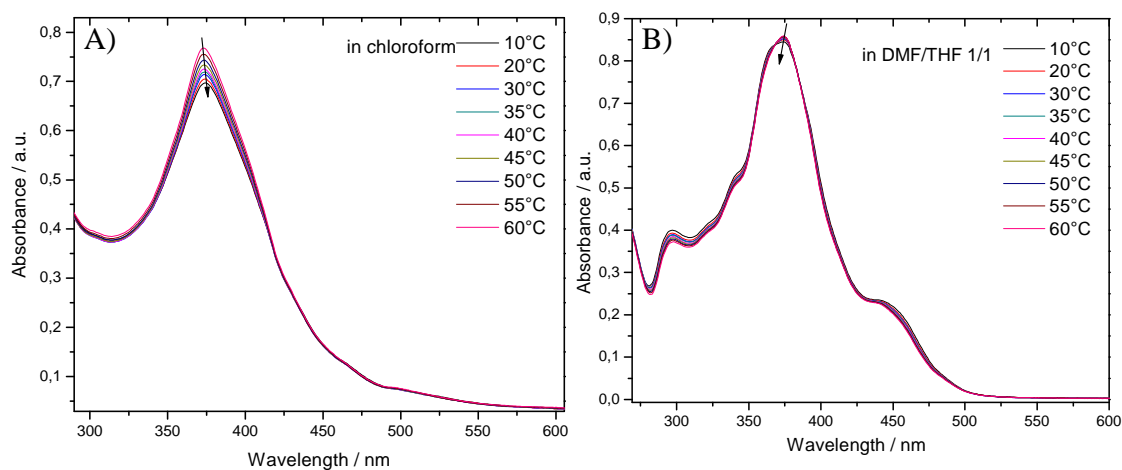


Figure 5-7. Temperature-dependent UV/Vis absorption spectra of **5-2**; measured in A) chloroform and B) DMF/THF 1/1 solution at a concentration of 1×10^{-5} M; arrows indicate the direction of change with decreasing temperature.

The red- and blue-shift of absorption bands are related to the one-dimensional alignment of molecules in aggregates and called J-aggregation and H-aggregation, respectively.⁶⁶⁻⁷¹ They are widely observed in porphyrins^{55, 72-74} but seldom reported in HBC derivatives.^{17, 75} The J-aggregation is formed with the monomeric molecules arranged in one dimension so that the transition moment of the monomers are parallel and the angle between the transition moment and the line joining the molecular centers is zero (idea case).⁷⁶ The strong coupling of several identical monomers results in a coherent excitation at red-shifted wavelengths relative to the monomer. In addition, the signal gets narrower and the vibrational coupling to the molecular modes will be largely absent.⁷² H-aggregation is also a one-dimensional arrangement of strongly coupled monomers, but the transition moments of the monomers are perpendicular (idea case) to the line of centers.⁷⁶ In contrast to the side-by-side arrangement of molecules in J-aggregates, the molecular arrangement in H-aggregates is face-to-face. Theory predicts that the dipolar coupling between monomers leads to a blue shift of the absorption band.^{77, 78} Additionally, the H-aggregates are not known to have sharp spectra like the J-aggregates. Both J-aggregation and H-aggregation are commonly observed for donor, acceptor modified dyes.^{79, 80} For a polar compound, there exist much stronger interactions between solute molecules and solvent molecules in polar solvents than in apolar solvents. The intermolecular interactions between solute and solvent can only be maximized in J-aggregates in contrast to in H-aggregates (as interpreted in Figure 5-8C,D). This consequently explains the formation of J-aggregates in a polar solvent (chloroform), and nearly invisible spectral shifts in non-polar solvent systems. Hereby the spectrum of **5-2** recorded with dilute chloroform solution (1×10^{-7} M) shows sharp well-resolved absorption bands in contrast to those measured with concentrated solutions, which serves as the criterion for J-type aggregation.^{72, 78} Although DMF/THF 1/1 co-solvent is also a kind of polar solvent, the molecules stack in a H-aggregation mode (bathochromic blue-shifts at high concentrations) presumably due to the much lower solubility reflecting the cofacial molecular stacks of the aromatic π -systems, which is consistent with former studies.⁴⁹ The temperature-dependent UV/Vis absorption spectroscopic changes confirm the formation of J- and H-type aggregations in chloroform and DMF/THF 1/1 solutions, whereby the much less pronounced red- / blue-shifts coincide with the results obtained

from temperature dependent $^1\text{H-NMR}$ spectroscopic studies: the intermolecular dipole – dipole interactions are not effectively influenced by a temperature factor. The formation of H-/J-aggregates in solution unambiguously demonstrates the enhanced self-aggregation tendency by the introduction of strong dipoles.

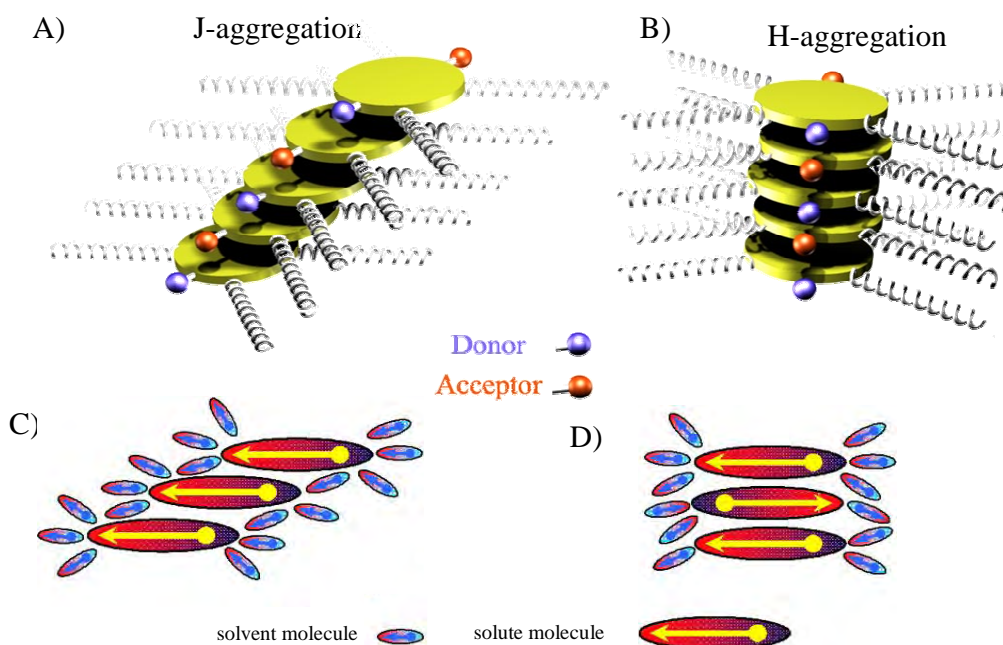


Figure 5-8. Proposed A) J- and B) H-aggregates formed by **5-2**; and schematic represents of intermolecular interactions between solute and solvent molecules in C) J-aggregates and D) H-aggregates.

Figure 5-8 shows cartoons of the proposed molecular stacks in solution. Similar changes are recorded for **5-1**, which bears a weaker electron donating group comparing with **5-2**, though, in a much less pronounced fashion.

The photoluminescence spectroscopy is more sensitive to the existence of molecular aggregates.⁵⁰ The photoluminescence spectra of these compounds were recorded with different solutions in the same concentration range and normalized at the first intensive fluorescence band (Figure 5-6). The spectra of **5-3** show three sharp fluorescence bands (465, 495 and 525 nm) from the HBC moiety. As increasing the concentration, the shape of the bands becomes broader and the intensity of the bands in the long-wavelength region (above 500 nm) is dramatically pronounced. This is a typical character for the formation of molecular aggregates in conjugated π -systems caused by the excimer

formation or migration of photogenerated species to low-energy domains.⁸¹⁻⁸⁴ In the case of **5-1** and **5-2**, the fluorescence peaks from the HBC moiety can only be partially recognized in diluted chloroform solution. Additionally, the spectra measured in polar solvents (DMF/THF 1/1) show particular features in contrast to **5-3**. Only one broad peak at 536 nm is observed in the spectra of **5-1** for all different concentrations. While for **5-2**, the sole broad peak recorded at high concentration is split into two sharp peaks at 479 and 515 nm and a new broad peak at 568 nm with decrease of concentration. The two sharp peaks are assigned to the HBC moiety by the comparison with the spectra of **5-3**; and the new broad peak is attributed to the intramolecular charge transfer (see SECTION 5.3.2), which is a typical feature of charge separation in Donor-Acceptor molecules. The changes of photoluminescence spectra of **5-1** and **5-2** are rather complicated due to the existence of intramolecular charge transfer bands. However, the less-resolved broad fluorescence bands recorded at higher concentrations, in contrast to those obtained with dilute solutions, ambiguously point out the existence of molecular aggregates.

5.3.2 Intramolecular charge transfer

5.3.2.1 Twisted intramolecular charge-transfer

The small analogous molecules, 4-(*N,N*-dimethylamino)-benzointrile (DMABN) and its derivatives, have been discovered as “amazing” molecules that emit two fluorescence bands. The two bands strongly depend on solvent polarity.^{85,86} In nonpolar solvents, only the fluorescence band at short-wavelength appears, which originates from the 1L_b state and is called as *B fluorescence* (F_B) or *locally excited fluorescence* (LE). In polar solvents, a further long-wavelength fluorescence band (from 1L_a state) grows, while the intensity of the first band decreases with increasing polarity of the medium. Lippert et al⁸⁶ initially explained the origin of the second fluorescence band as follows. With the polar solvent reorientation, an inversion of states turns 1L_a into the lowest excited state, within the life time of the excited state (Figure 5-9). The two emissions are usually called fluorescence B (or F_B) and A (F_A).⁸⁵ The long wavelength-emitting state (A^*) is characterized by its very large dipole moment.³⁰ The Lippert hypothesis lasted over a decade until new experimental evidence compelled several authors to seek new interpretations. Starting from 1970s, numerous hypotheses were proposed covering the formation of excimer,

protonated species, exciplex with solvent, intramolecular structural change (TICT), pseudo-Jahn-Teller (PJT) distortion, rehybridization of the amino group or cyano group and planarization of the molecule in the CT state, etc.³⁰ The vivid discussions and controversial views have lasted for 30 years and seem to reach final conclusions now, which concerns intramolecular twisted charge transfer (TICT).³⁰ This hypothesis assigns the F_B band to an approximately coplanar structure and F_A to a CT excited-state conformation with a highly twisted NMe₂ group, possibly perpendicular to the aromatic ring (A*, Figure 5-9B).

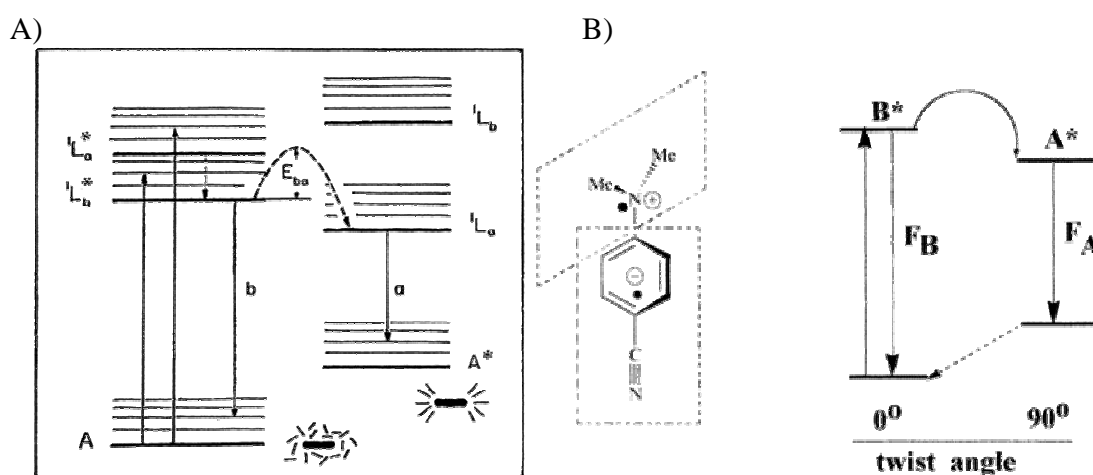


Figure 5-9. A) Lippert's scheme of the inversion of states of different polarity; in polar solvent, the orientational relaxation of the solvents shell leads to an avoided level crossing (potential barrier E_{ba}); after relaxation, the more polar state, 1L_a , becomes the lowest excited singlet (fluorescent) state;⁸⁵ B) TCIT model of DMABN; A*: the pair of mutually orthogonal radical ions, linked by a single bond; in the scheme of terms, the 90° twist corresponds to the top of a potential barrier to internal rotation.⁸⁷

5.3.2.2 Intramolecular charge transfer in 5-1 and 5-2

Typical CT emissions undergo strong red-shifts with an increase of the polarity of solvents. Both compounds (**5-1** and **5-2**) show strong solvatochromic effects. The fluorescence color of the solutions of **5-1** and **5-2** changes from green to light yellow and green to orange, respectively (Figure 5-10A,C). The fluorescence spectra in different solvent systems provide more detailed information (Figure 5-10B,D). A 20 nm red-shift (from 518 to 538 nm) of maximum fluorescence peak is observed for **5-1** as increasing solvent polarity. **5-2** exerts a more pronounced effect showing a 73 nm red-shift within the same solvent systems as in the case of **5-1**. More remarkably, the band shape of **5-2** in

polar solvents (DMSO/THF 1/1 and DMF/THF 1/1 co-solvents) is well resolved with an appearance of a broad CT band at long-wavelength region. At higher concentrations, this CT band merges with the bands from HBC moiety to one broad peak (Figure 5-6C,D).

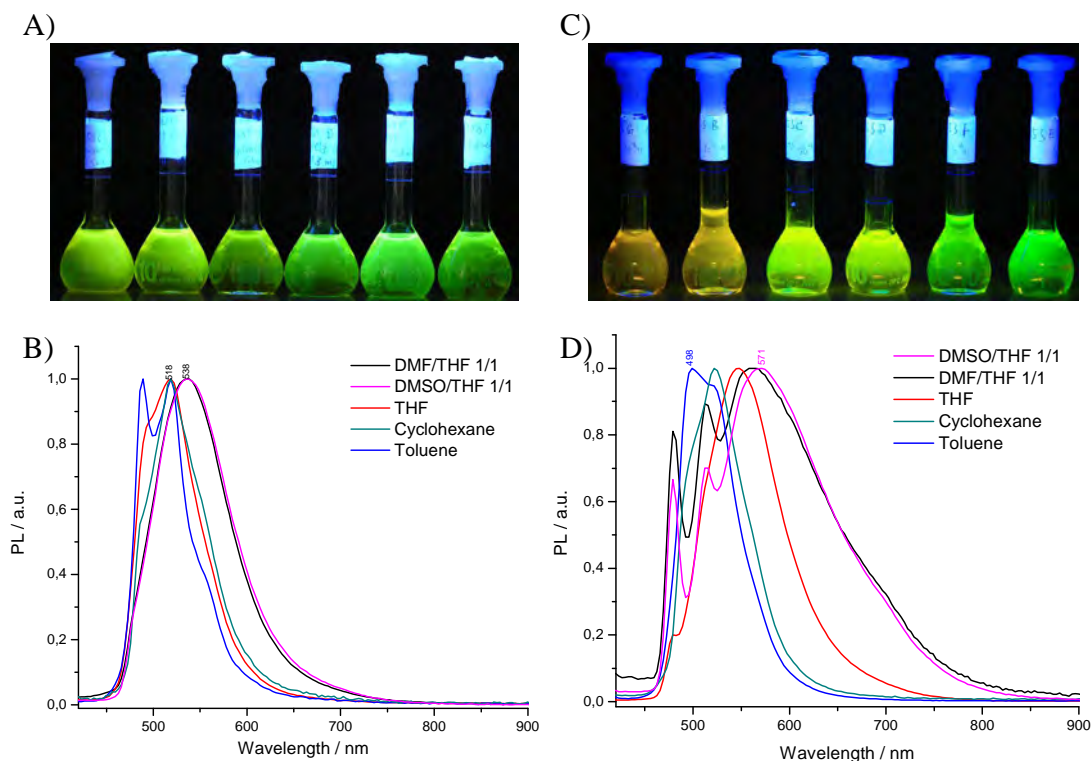


Figure 5-10. Images of fluorescent solutions and fluorescence spectra of **5-1** (A,B) and **5-2** (C,D) in different solvent (excited at 377 nm, measured with 1×10^{-6} M solutions at r.t., normalized at maximum fluorescence bands); solvents in images (from left to right): DMSO/THF 1/1, DMF/THF 1/1, THF, chloroform, cyclohexane, toluene; pictures were taken under irradiation of UV light at 366 nm.

Since the electron donating ability of the donor substituent in **5-1** (*N,N*-ditolylamino group) is weaker than the one in **5-2** (*N,N*-di-4-methoxyphenylamino group) and the 1L_a state is much more red-shifted than 1L_b with increasing donor and acceptor strength,³⁰ **5-1** shows less pronounced solvatochromic dependency than **5-2**. Although, The CT band of **5-1** is not as clearly resolved as that of **5-2**, it can still be recognized. Figure 5-11 depicts the normalized photoluminescence spectra of all three compounds measured in the same solvent system (DMF/THF 1/1). No CT band is expected in the spectrum of **5-3** and the typical p , β and β' bands of HBC derivatives are well recognized. In contrast, the β and β' bands are red-shifted to 495 and 479 nm in the spectrum of **5-2**, which also shows an

intensive broad CT band at 568 nm. Because the donor group in **5-1** is weaker and the molecule demonstrates lower aggregation tendency in comparison with **5-2**, the β band of **5-1** must be located at a position between 495 and 512 nm (the β bands of **5-2** and **5-3**). Additionally, the CT band in **5-2** exerts a higher intensity than that of the β band in all well-resolved spectra (in both DMF/THF 1/1 and DMSO/THF 1/1 solutions with concentrations below 1×10^{-4} M). Therefore, the fluorescence maximum at 538 nm in **5-1**, which is at the right side of 495 – 512 nm region, must be due to a CT band rather than a β band from HBC moiety. The merging of CT and LE band is also often observed in other relatively weaker donor- π -acceptor systems.⁸⁸

The low resolution of the fluorescence spectra of **5-2** at higher concentrations (Figure 5-6C,D) can be attributed to the strong molecular aggregation. As introduced in SECTION 5.3.2.1, the F_A fluorescence band originates from a twisted intramolecular CT state, which requires a perpendicular arrangement of the *N,N*-dimethoxyphenylamino group with respect to the HBC disc plane. The large molecular aggregates at higher concentration, on the one hand, hinder the rotation of the *N,N*-dimethoxyphenylamino group reducing the probability of the formation of TICT state, and, on the other hand, change the molecular electronic states leading to new broad fluorescence bands in longer wavelength region.⁵⁸

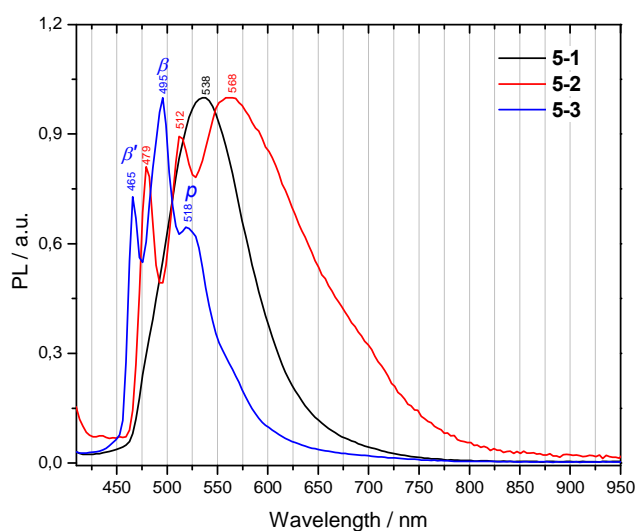


Figure 5-11. Normalized fluorescence spectra of **5-1**, **5-2** and **5-3**; measured with 1×10^{-6} M DMF/THF 1/1 solutions at r.t.(excited at 377 nm, normalized at maximum peaks).

5.4 Morphology of molecular aggregates of 5-2 on surfaces

For the solution processing of organic semiconductors in electronic devices, the control of the morphology formation on surfaces is an essential procedure which determines in many cases the performance. Much effort has thus invested to achieve homogeneous, highly ordered thin films.⁸⁹ Zone-casting and Langmuir-Blodgett (LB) techniques, exipial growth on preoriented and friction-deposited poly(tetrafluoroethylene) (PTFE) surfaces layers, strong gradient magnetic field and homeotropic alignment by cooling the sample from isotropic phase have been used with HBC derivatives.⁸⁹ Before the application of these complicated techniques, it is logical to first study the morphologies of these molecular aggregates on surfaces.

Depending on the solvents, the molecules of compound **5-2** self-associate into either J- or H-type aggregates. Different **5-2** solutions (in different solvents) with a concentration of 1×10^{-4} M were respectively dropped on silicon wafers and studied by scanning electronic microscope (SEM). Interestingly, lots of flat slice-like structures (abbreviated as “slices”) of different sizes were observed for the sample prepared from a DMSO/THF 1/1 solution, in which HBC molecules formed H-aggregates (Figure 5-12). The largest slice extends up to 13 μm in length and 3 μm in width. The spherical particles on their surface indicate that these slices are formed in solution rather than during the solvent evaporation process on silicon wafer. High-resolution transmission electron microscopy (HR-TEM) provides more detailed structural information about these slices (Figure 5-13). The highly oriented columnar domains are visualized in the image with an enlarged scale. As indicated by these lines, HBC columns align parallel to the long side of a slice. The sharp reflexes in the electron diffraction pattern (inset of Figure 5-13) correspond to a $\pi - \pi$ stacking distance of 0.35 nm indicating the well-oriented columnar structures. An intra-columnar distance of 2.6 nm is evaluated, which is in good agreement with the value determined in the bulk state (2D WAXD, see SECTION 5.6).

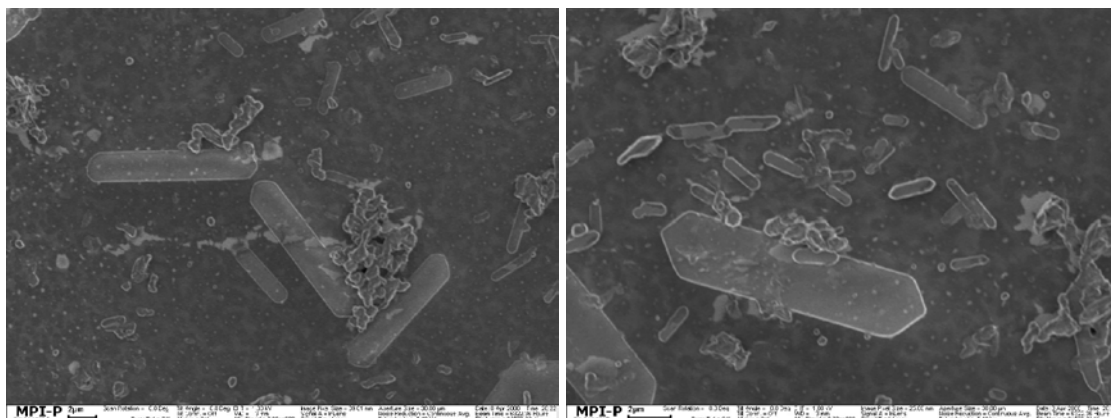


Figure 5- 12. SEM images of 5-2 prepared from 1×10^{-4} M DMSO/THF 1/1 solution.

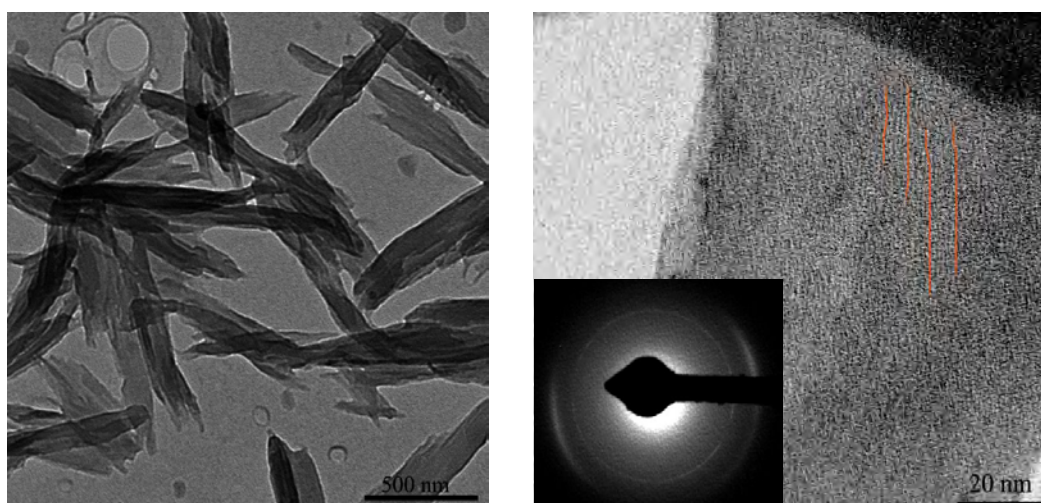


Figure 5-13. HR-TEM images of slices obtained from 1×10^{-4} M DMSO/THF 1/1 solution of 5-2; lines indicating columnar alignments; insets: small-area selected electron diffraction pattern.

The morphology of the compound on silicon surfaces is highly solvent dependent. Like from DMSO/THF 1/1 solution, the sample prepared with DMF/THF 1/1 forms similar slices, which, however, stack densely together (Figure 5-14A). With chloroform solution, from which molecules self-assemble into J-aggregates, an amorphous film was obtained (Figure 5-14B). Not only were these slices and film observed, but also the typical fibrillar structures were visualized. Depending on the solubility, these molecules form either long soft fibers in toluene or bundles of rigid needle-like assemblies in cyclohexane solutions like other HBC derivatives (Figure 5-14C,D).^{17, 49, 50, 61}

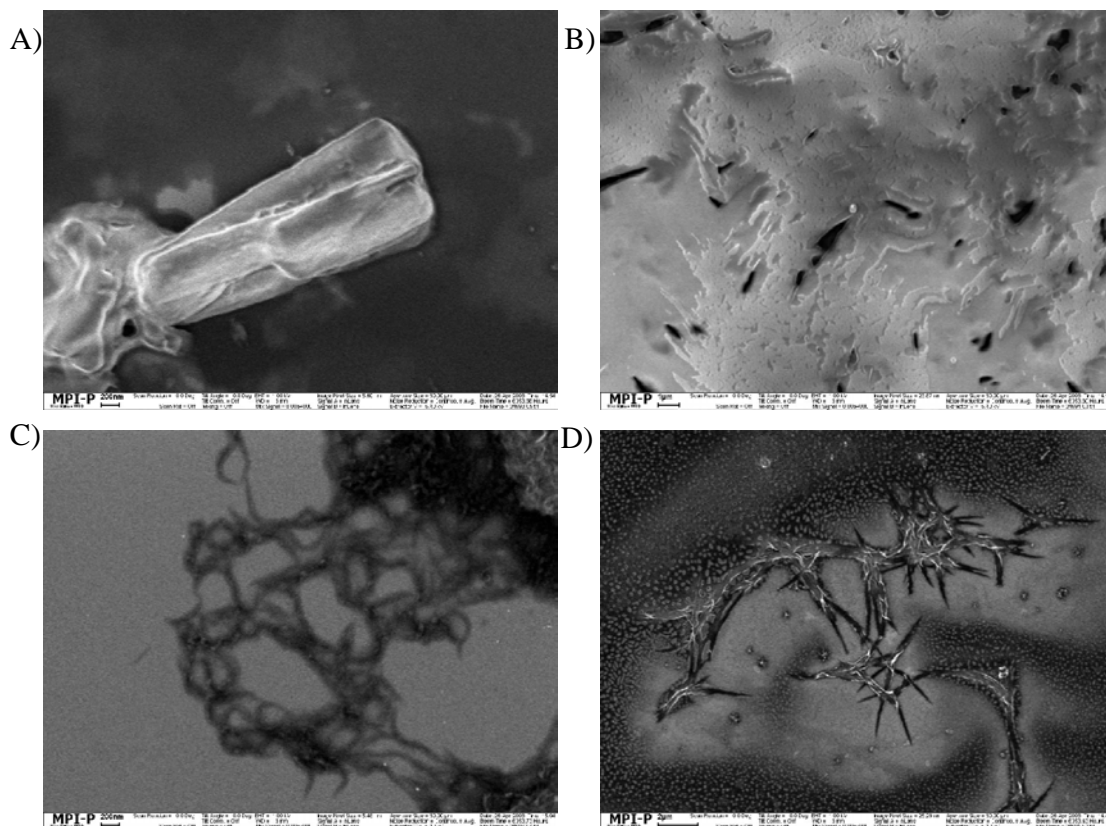


Figure 5- 14 SEM images of 5-2 nano-aggregates obtained from A) DMF/THF 1/1, B) chloroform, C) toluene, D) cyclohexane solutions.

The mechanism of the formation of these nano-sized molecular aggregates might be complicated. However, there is no wonder that, under the influence of solvent polarity, the strong dipole moment along the molecular axis dominates the self-association process. One mechanism for the formation of those unique morphologies is proposed as follows. For a dipole-functionalized discotic molecule, antiparallel molecular arrangement is expected in the bulk state (see CHAPTER 4).⁹⁰ In DMSO/THF 1/1 and DMF/THF 1/1 solvent mixtures, HBC molecules self-assemble into H-type aggregates under the guidance of $\pi - \pi$ and dipole – dipole interactions. Different from $\pi - \pi$ interactions, which take effect along the HBC columnar axis, the dipole – dipole interactions also exist between adjacent HBC columns (Figure 5-15A). As demonstrated in the TEM image (Figure 5-13), this kind of intercolumnar dipole – dipole interactions assembles individual HBC columns into large-sized slices. In the side-by-side J-type aggregates (in chloroform solution), it can be imagine that the HBC columnar structures are not as

uniform as those in H-aggregates and the overlapping area of molecules between neighboring columns are much bigger than that in H-aggregates (Figure 5-15 B), which results in homogeneous films. Additionally, it is also worth to be aware that the rate of solvent evaporation should also play a role since the volatilization ability of these solutions decides the morphology of the precipitates during solvent evaporation.

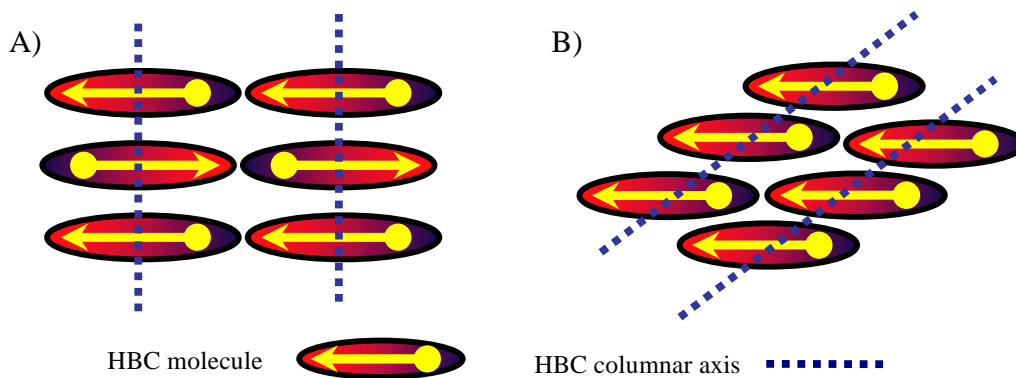


Figure 5-15. Schematic represents of intercolumnar aggregation in A) H-type aggregates and B) J-type aggregates.

5.5 Energetic level characterization

The future application in electronic devices requires the knowledge of the molecular energy levels. Computer simulation and cyclic voltammetry (CV) experiments were performed for **5-1** and **5-2** to obtain an overview of the electronic levels.

The highest occupied molecular orbital (HOMO) and lowest unoccupied molecular orbital (LUMO) were calculated by using ZINDO semi-empirical method with B3LYP functional and 6-311G(d,p) basis set-optimized molecular geometries⁹¹ (Figure 5-16). To determine the electron affinity and thus the absolute LUMO values, CV measurements were carried out under inert atmosphere in a DCM solution of Bu_4NPF_6 (0.1 M) in a three-electrode cell using a Pt wire as working/counter electrodes and a Ag quasi-reference electrode (calibrated with the Fc/Fc^+ redox couple $E^\circ = -4.8$ eV). One reversible redox wave related to the oxidation of the amine group was recorded in the positive scans of both **5-1** and **5-2** (Figure 5-17) suggesting effective charge delocalization through the adjacent π system in the oxidized radical mono-cation species.⁹² From the onsets of these

redox peaks in CV curves and the p bands in UV/Vis absorption spectra, the energy levels of the HOMO and LUMO are calculated as -5.2 eV and -2.6 eV for **5-1**, -5.2 eV and -2.7 eV for **5-2**, respectively, which is in good agreement with the calculated values (-5.2 eV and -2.2 eV for **5-1**; -5.1 eV and -2.1 eV for **5-2**)⁴⁶. When comparing with 2,5,8,11,14,17-hexa-(2'-ethyl-hexyl)-hexa-*peri*-hexabenzocoronene (HBC-C_{6,2})⁹³ the HOMO / LUMO band gap drops from 2.9 eV (HBC-C_{6,2}) over 2.6 eV (**5-1**) to 2.5 eV (**5-2**) with the increase of the dipole moment. The lowered HOMO-LUMO band gap optimizes the optoelectronic properties of these materials and will improve their performance as n-type organic field effect transistors.⁹⁴

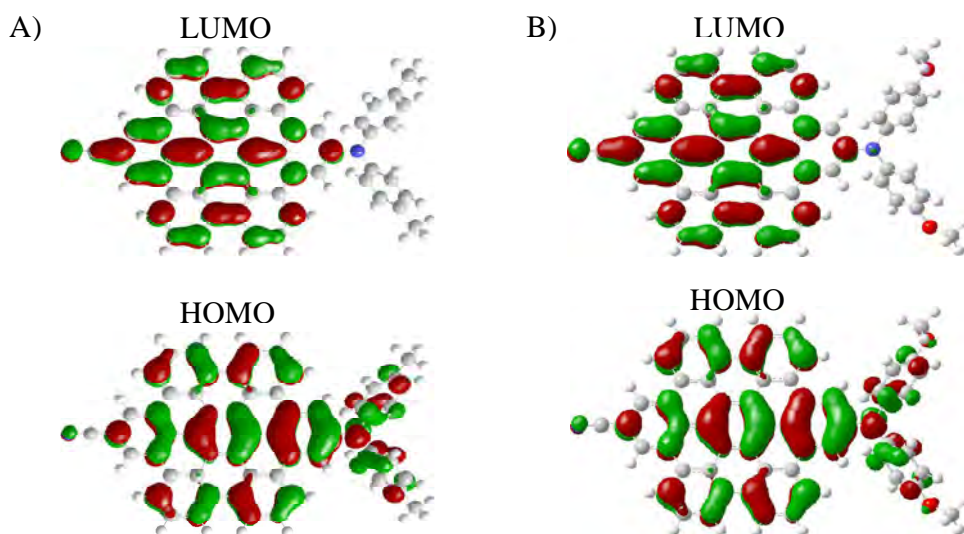


Figure 5-16. Pictorial represents of the HOMO / LUMO orbitals of A) **5-1** and B) **5-2**; calculated at the B3LYP/6-31g* level in vacuum.

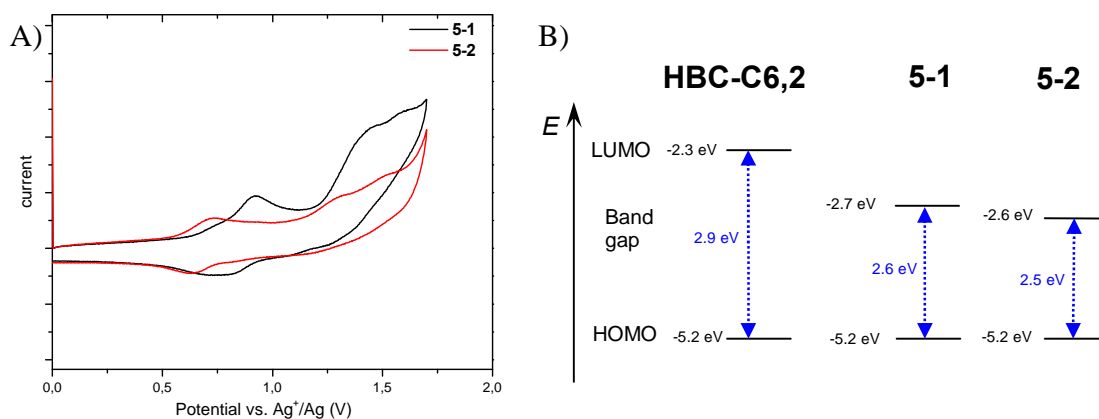


Figure 5-17. A) Cyclic voltammograms of **5-1** and **5-2**; measured with a scan rate of 50 mV/s at r.t. under argon; B) HOMO/LUMO energetic level scheme of HBC-C_{6,2}, **5-1** and **5-2**.

5.6 Bulk state characterization

The bulk thermotropic properties of **5-1** and **5-2** were characterized with differential scanning calorimetry (DSC) and two-dimensional wide angle X-ray diffraction (2D WAXD) techniques. As expected, no phase transition is observed in a temperature range of -100 °C to 250 °C in DSC traces for both compounds (Figure 5-18) which coincides with the conclusions obtained in CHAPTER 4 that a strong molecular dipole moment effectively enlarges the mesophase.

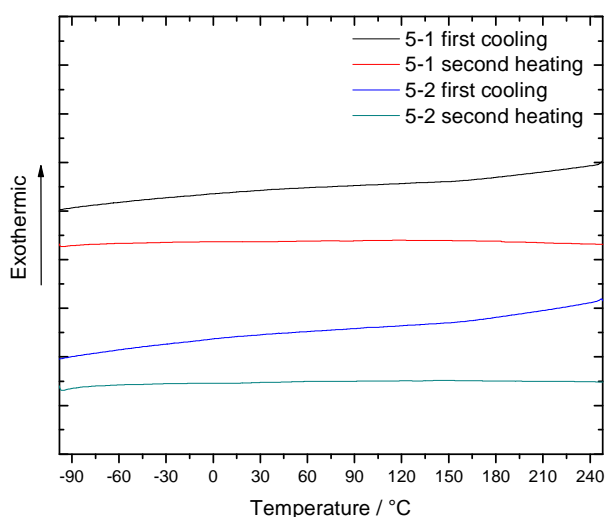


Figure 5-18. DSC traces of **5-1** and **5-2** recorded at 10 K/min.

The 2D WAXD experiments of both compounds are performed at different temperatures (Figure 5-19). Both compounds display the exactly same supramolecular organization in the mesophase. The reflection patterns further reveal that these two compounds form a stable hexagonal liquid crystalline phase showing a set of equatorial reflexes with the relative ratios of $1:\sqrt{3}:2$ (Figure 5-20). Due to the increase of the molecular thermodynamic energy, the hexagonal 2D unit cell parameter expands from $a_{\text{hex}} = 2.52$ nm over $a_{\text{hex}} = 2.59$ nm to $a_{\text{hex}} = 2.65$ nm and the cofacial disc distance increases from 0.34 to 0.36 nm as the temperature changes from -80 °C over 30 °C to 170 °C. Additionally, the correlations between dipole moments manifest themselves through the four reflexes at the intermediate distance, which overlaps with the “halo ring” aroused by alkyl substituents.⁹⁵

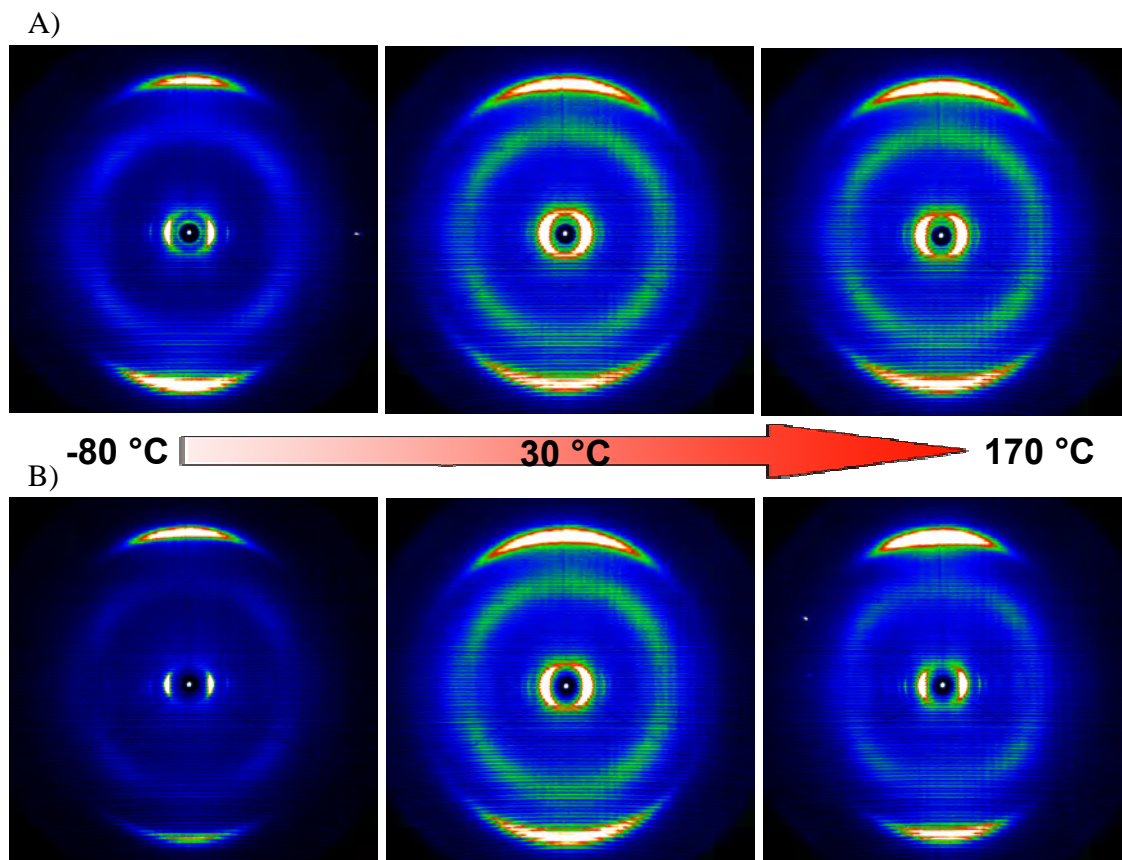


Figure 5-19. Temperature dependent 2D WAXD patterns of A) 5-1 and B) 5-2; from left to right: temperature changes from -80 °C over 30 °C to 170 °C.

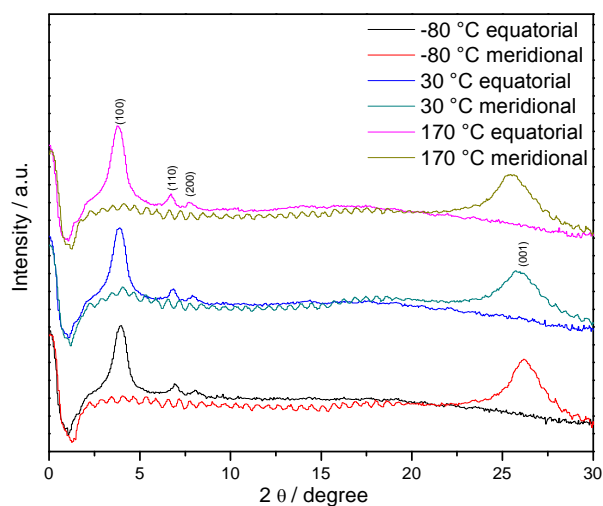


Figure 5-20. Equatorial and meridional intensity distributions of 2D WAXD diffragrams of 5-2; (unit cell parameters: $a_{\text{hex}} = 2.52$ nm, $d = 0.34$ nm at -80 °C, $a_{\text{hex}} = 2.59$ nm, $d = 0.34$ nm at 30 °C, $a_{\text{hex}} = 2.65$ nm, $d = 0.36$ nm at 170 °C).

2D WAXD experiments were performed under an external electronic field with an intensity of 2.5×10^5 V/m within a temperature range of -80 °C to 150 °C. However, no apparent change on the diffraction pattern was recorded. This can be understood from two aspects. On the one hand, since the molecular mobility is high within liquid crystalline phase and HBC molecules undergo a fast rotation along columnar axis (see CHAPTER 4), it might be difficult for the molecules to overcome an entropic energy barrier and align towards a uniform direction even under external forces. On the other hand, 2D WAXD collects an ensemble average over a relatively large time scale, during which a slow motion of molecules might compensate a short-time directional alignment. Additionally, the strength of external forces should also be considered. Therefore, the study of the influence of external forces on the molecular superstructure requires a guidance of computer simulation, which is currently undergoing in corporation with Dr. Denis Andrienko from Prof. Kremer's group.

5.7 Summary

With the novel asymmetric *para*-iodo bromo HBC (**2-47**), two HBC molecules bearing strong dipole moment ($\mu = 8.25$ D for **5-1** and $\mu = 8.64$ D for **5-2**) have been synthesized. Additionally, a compound bearing no dipole moment but similar symmetry (**5-3**) was prepared as well from *para*-dibromo HBC (**2-1**) for comparison. By temperature and concentration dependent $^1\text{H-NMR}$ and spectroelectronic spectroscopic studies, it has been demonstrated that the introduced strong dipole moment effectively enhanced the molecular self-association propensity in solution. Interestingly, the concentration and temperature dependent UV/Vis absorption spectroscopic studies demonstrate that the strong intermolecular dipole – dipole interactions control these HBC molecules to self-assemble into either H- or J-type aggregates in different polar solvents, which leads to unique morphologies on surfaces (as being visualized by electronic microscopes). The long range well-ordered supramolecular organization highlights the performance optimization in electronic devices.⁸⁹

Like many other donor-acceptor systems, the intramolecular charge transfer (ICT) phenomenon was observed by both solvatochromic effect and the appearance of charge transfer emission band at long wavelength in photoluminescence spectra. The ICT phenomenon brings this kind of HBC materials non-linear optical properties and further expands the application of these materials in non-linear optics.³⁰ The computer simulation and cyclic voltammetry experiments revealed that the HOMO-LUMO band gap of these molecules was reduced with increasing the strength of the molecular dipole moments in contrast to other HBC derivatives. The simultaneous introduction of different donor and acceptor groups provides a new synthetic approach to optimize the HBC molecular HOMO-LUMO band gap for their application in electronic devices.

In the bulk state, the conclusions withdrawn from CHAPTER 4 are verified. On one hand, the strong molecular dipole moment stabilizes the mesophase showing no phase transition over a large temperature range. On the other hand, the molecular dynamics in liquid crystalline phase is high resulting in little influence of external electronic field (up to 2.5×10^5 V/m electronic field intensity) on the supramolecular organization.

5.8 References

1. Shirakawa, H., *Angew. Chem. Int. Ed.* **2001**, *40*, 2574-2580.
2. MacDiarmid, A. G., *Angew. Chem. Int. Ed.* **2001**, *40*, 2581-2590.
3. Heeger, A. J., *Angew. Chem. Int. Ed.* **2001**, *40*, 2591-2611.
4. Skotheim, T. A., Elsenbaumer, R. L., Reynolds, J. R., *Handbook of Conducting Polymers*. 2nd ed.; Marcel Dekker: New York, **1998**.
5. Hadziioannou, G., van Hutten, P. F., *Semiconducting Polymers: Chemistry, Physics, and Engineering*. Wiley-VCH: Weinheim, **2000**.
6. Müllen, K., Wegner, G., *Electronic Materials: The Oligomer Approach* Wiley-VCH: Weinheim, **1998**.
7. Sirringhaus, H., *Adv. Mater.* **2005**, *17*, 2411-2425.
8. Rainer E. Martin, Diederich, F., *Angew. Chem. Int. Ed.* **1999**, *38*, 1350-1377.
9. Sage, I. C., *Handbook of Liquid Crystals*. Demus, D., Goodby, J., Gray, G. W., Spiess, H. W., Vill, V., Wiley-VCH: Weiheim, **1998**; Vol. 1.
10. Watson, M. D., Fechtenkotter, A., Müllen, K., *Chem. Rev.* **2001**, *101*, 1267-1300.
11. Simpson, C. D., Wu, J., Watson, M. D., Müllen, K., *J. Mater. Chem.* **2004**, *14*, 494-504.
12. Pisula, W., Menon, A., Stepputat, M., Lieberwirth, I., Kolb, U., Tracz, A., Sirringhaus, H., Pakula, T., Müllen, K., *Adv. Mater.* **2005**, *17*, 684-689.
13. Kubowicz, S., Pietsch, U., Watson, M. D., Tchegotareva, N., Müllen, K., Thunemann, A. F., *Langmuir* **2003**, *19*, 5036-5041.
14. Breiby, D. W., Bunk, O., Pisula, W., Solling, T. I., Tracz, A., Pakula, T., Müllen, K., Nielsen, M. M., *J. Am. Chem. Soc.* **2005**, *127*, 11288-11293.
15. Beeson, J. C., Fitzgerald, L. J., Gallucci, J. C., Gerkin, R. E., Rademacher, J. T., Czarnik, A. W., *J. Am. Chem. Soc.* **1994**, *116*, 4621-4622.
16. R.I. Gearba, Lehmann, M., Levin, J., Ivanov, D. A., Koch, M. H. J., Barberá, J., Debije, M. G., Piris, J., Geerts, Y. H., *Adv. Mater.* **2003**, *15*, 1614-1618.
17. Xi Dou, Pisula, W., Wu, J., Bodwell, Graham J., Müllen, K., *Chem. Eur. J.* **2008**, *14*, 240-249.
18. Liu, C.-y., Bard, A. J., *Nature* **2002**, *418*, 162-164.
19. Leclère, P., Surin, M., Jonkheijm, P., Henze, O., Schenning, A. P. H. J., Biscarini, F., Grimsdale, A. C., Feast, W. J., Meijer, E. W., Müllen, K., Brédas, J. L., Lazzaroni, R., *Eur. Polym. J.* **2004**, *40*, 885-892.
20. Schenning, A. P. H. J., Kilbinger, A. F. M., Biscarini, F., Cavallini, M., Cooper, H. J., Derrick, P. J., Feast, W. J., Lazzaroni, R., Leclere, P., McDonnell, L. A., Meijer, E. W., Meskers, S. C. J., *J. Am. Chem. Soc.* **2002**, *124*, 1269-1275.

21. Hill, J. P., Jin, W., Kosaka, A., Fukushima, T., Ichihara, H., Shimomura, T., Ito, K., Hashizume, T., Ishii, N., Aida, T., *Science* **2004**, *304*, 1481-1483.
22. Jin, W., Fukushima, T., Niki, M., Kosaka, A., Ishii, N., Aida, T., *Proc. Nat. Acad. Sci.* **2005**, *102*, 10801-10806.
23. Motoyanagi, J., Fukushima, T., Ishii, N., Aida, T., *J. Am. Chem. Soc.* **2006**, *128*, 4220-4221.
24. Watson, M. D., Jackel, F., Severin, N., Rabe, J. P., Müllen, K., *J. Am. Chem. Soc.* **2004**, *126*, 1402-1407.
25. Heng, K. L., Chua, S. J., Wu, P., *Chem. Mater.* **2000**, *12*, 1648-1653.
26. Spraul, B. K., Suresh, S., Glaser, S., Perahia, D., Ballato, J., Smith, D. W., *J. Am. Chem. Soc.* **2004**, *126*, 12772-12773.
27. Kastler, M., Pisula, W., Davies, Richard J., Gorelik, T., Kolb, U., Müllen, K., *Small* **2007**, *3*, 1438-1444.
28. Steed, J. W., Atwood, J. L., *Supramolecular Chemistry*. Wiley & Sons: Chichester, **2000**.
29. Shklyarevskiy, I. O., Jonkheijm, P., Stutzmann, N., Wasserberg, D., Wondergem, H. J., Christianen, P. C. M., Schenning, A. P. H. J., deLeeuw, D. M., Tomovic, Z., Wu, J., Müllen, K., Maan, J. C., *J. Am. Chem. Soc.* **2005**, *127*, 16233-16237.
30. Grabowski, Z. R., Rotkiewicz, K., Rettig, W., *Chem. Rev.* **2003**, *103*, 3899-4032.
31. Dreyer, J., Kummrow, A., *J. Am. Chem. Soc.* **2000**, *122*, 2577-2585.
32. Rappoport, D., Furche, F., *J. Am. Chem. Soc.* **2004**, *126*, 1277-1284.
33. Gomez, I., Reguero, M., Boggio-Pasqua, M., Robb, M. A., *J. Am. Chem. Soc.* **2005**, *127*, 7119-7129.
34. Cogan, S., Zilberg, S., Haas, Y., *J. Am. Chem. Soc.* **2006**, *128*, 3335-3345.
35. Goldsmith, R. H., Wasielewski, M. R., Ratner, M. A., *J. Am. Chem. Soc.* **2007**, *129*, 13066-13071.
36. Mattias P. Eng, Albinsson, B., *Angew. Chem. Int. Ed.* **2006**, *45*, 5626-5629.
37. Meier, H., *Angew. Chem. Int. Ed.* **2005**, *44*, 2482-2506.
38. Boris Traber, Wolff, J. J., Rominger, F., Oeser, T., Gleiter, R., Goebel, M., Wortmann, R., *Chem. Eur. J.* **2004**, *10*, 1227-1238.
39. van der Boom, T., Hayes, R. T., Zhao, Y., Bushard, P. J., Weiss, E. A., Wasielewski, M. R., *J. Am. Chem. Soc.* **2002**, *124*, 9582-9590.
40. Kelley, R. F., Lee, S. J., Wilson, T. M., Nakamura, Y., Tiede, D. M., Osuka, A., Hupp, J. T., Wasielewski, M. R., *J. Am. Chem. Soc.* **2008**, *130*, 4277-4284.
41. M. O. Senge, Fazekas, M., Notaras, E. G. A., Blau, W. J., Zawadzka, M., Locos, O. B., Ni Mhuircheartaigh, E. M., *Adv. Mater.* **2007**, *19*, 2737-2774.

42. Beckers, E. H. A., Meskers, S. C. J., Schenning, A. P. H. J., Chen, Z., Wurthner, F., Marsal, P., Beljonne, D., Cornil, J., Janssen, R. A. J., *J. Am. Chem. Soc.* **2006**, *128*, 649-657.
43. Huang, J. H., Wen, W. H., Sun, Y. Y., Chou, P. T., Fang, J. M., *J. Org. Chem.* **2005**, *70*, 5827-5832.
44. Samori, S., Tojo, S., Fujitsuka, M., Spitler, E. L., Haley, M. M., Majima, T., *J. Org. Chem.* **2007**, *72*, 2785-2793.
45. Zhou, Y., Xiao, Y., Chi, S., Qian, X., *Org. Lett.* **2008**, *10*, 633-636.
46. *The dipole moments were calculated with the B3LYP functional and 6-311G(d,p) basis set by Dr. Denis Andrienko.*
47. Hunter, C. A., Sanders, J. K. M., *J. Am. Chem. Soc.* **1990**, *112*, 5525-5534.
48. Martin, R. B., *Chem. Rev.* **1996**, *96*, 3043-3064.
49. Wu, J., Fechtenkotter, A., Gauss, J., Watson, M. D., Kastler, M., Fechtenkotter, C., Wagner, M., Müllen, K., *J. Am. Chem. Soc.* **2004**, *126*, 11311-11321.
50. Kastler, M., Pisula, W., Wasserfallen, D., Pakula, T., Müllen, K., *J. Am. Chem. Soc.* **2005**, *127*, 4286-4296.
51. Wu, J. PhD Thesis. Johannes Gutenberg-Universität Mainz, 2004.
52. Fechtenkötter, A. PhD Thesis. Johannes Gutenberg-Universität, Mainz, 2001.
53. Schutte, W. J., Sluyters-Rehbach, M., Sluyters, J. H., *J. Phys. Chem.* **1993**, *97*, 6069-6073.
54. Kadish, K. M., Sazou, D., Liu, Y. M., Saoiabi, A., Ferhat, M., Guillard, R., *Inorg. Chem.* **1988**, *27*, 686-690.
55. Kano, K., Fukuda, K., Wakami, H., Nishiyabu, R., Pasternack, R. F., *J. Am. Chem. Soc.* **2000**, *122*, 7494-7502.
56. Zhang, J., Moore, J. S., *J. Am. Chem. Soc.* **1992**, *114*, 9701-9702.
57. Shetty, A. S., Zhang, J., Moore, J. S., *J. Am. Chem. Soc.* **1996**, *118*, 1019-1027.
58. Lahiri, S., Thompson, J. L., Moore, J. S., *J. Am. Chem. Soc.* **2000**, *122*, 11315-11319.
59. Hoger, S., Bonrad, K., Mourran, A., Beginn, U., Moller, M., *J. Am. Chem. Soc.* **2001**, *123*, 5651-5659.
60. Tobe, Y., Utsumi, N., Kawabata, K., Nagano, A., Adachi, K., Araki, S., Sonoda, M., Hirose, K., Naemura, K., *J. Am. Chem. Soc.* **2002**, *124*, 5350-5364.
61. Feng, X., Pisula, W., Takase, M., Dou, X., Enkelmann, V., Wagner, M., Ding, N., Müllen, K., *Chem. Mater.* **2008**, *20*, 2872-2874.
62. Hoeben, F. J. M., Jonkheijm, P., Meijer, E. W., Schenning, A. P. H. J., *Chem. Rev.* **2005**, *105*, 1491-1546.
63. Prince, R. B., Saven, J. G., Wolynes, P. G., Moore, J. S., *J. Am. Chem. Soc.* **1999**, *121*, 3114-3121.

64. Clar, E., *Polycyclic Hydrocarbons*. Academic: New York, **1964**.
65. Fetzer, J. C., *large ($C \geq 24$) Polycyclic Aromatic Hydrocarbons*. John Wiley & Sons: New York, **2000**.
66. Kasha, M., *Rad. Res.* **1963**, *20*, 55-70.
67. Mooney, W. F., Brown, P. E., Russell, J. C., Pedersen, L. G., Whitten, D. G., *J. Am. Chem. Soc.* **1984**, *106*, 5659-5667.
68. Dou, X. Master Thesis. Johannes Gutenberg-Universität, Mainz, 2004.
69. Coril, J., Santos, D. A. D., Beljonne, D., Shuai, Z., Bredas, J. L., *Semiconducting Polymers*. Hadziioannou, G., Huttern, P. F. v., Wiley-VCH: Weinheim, **2000**.
70. Lewis, F. D., Wu, T., Burch, E. L., Bassani, D. M., Yang, J.-S., Schneider, S., Jaeger, W., Letsinger, R. L., *J. Am. Chem. Soc.* **1995**, *117*, 8785-8792.
71. Liang, K., Farahat, M. S., Perlstein, J., Law, K. Y., Whitten, D. G., *J. Am. Chem. Soc.* **1997**, *119*, 830-831.
72. Maiti, N. C., Mazumdar, S., Periasamy, N., *J. Phys. Chem. B* **1998**, *102*, 1528-1538.
73. Lou, J., Hashimoto, M., Berova, N., Nakanishi, K., *Org. Lett.* **1999**, *1*, 51-54.
74. Shirakawa, M., Kawano, S. i., Fujita, N., Sada, K., Shinkai, S., *J. Org. Chem.* **2003**, *68*, 5037-5044.
75. Wu, J., Watson, M. D., Tchegotareva, N., Wang, Z., Müllen, K., *J. Org. Chem.* **2004**, *69*, 8194-8204.
76. Bohn, P. W., *Annu. Rev. Phys. Chem.* **1993**, *44*, 37-60.
77. Czikkely, V., Forsterling, H. D., Kuhn, H., *Chem. Phys. Lett.* **1970**, *6*, 207-210.
78. Nüesch, F., Grätzel, M., *Chem. Phys.* **1995**, *193*, 1-17.
79. Würthner, F., Chen, Z., Hoeben, F. J. M., Osswald, P., You, C. C., Jonkheijm, P., Herrikhuyzen, J. v., Schenning, A. P. H. J., vander Schoot, P. P. A. M., Meijer, E. W., Beckers, E. H. A., Meskers, S. C. J., Janssen, R. A. J., *J. Am. Chem. Soc.* **2004**, *126*, 10611-10618.
80. Würthner, F., Thalacker, C., Diele, S., Tschierske, C., *Chem. Eur. J.* **2001**, *7*, 2245-2253.
81. Lemmer, U., Heun, S., Mahrt, R. F., Scherf, U., Hopmeier, M., Siegner, U., Göbel, E. O., Müllen, K., Bäessler, H., *Chem. Phys. Lett.* **1995**, *240*, 373-378.
82. Cornil, J., Beljonne, D., Heller, C. M., Campbell, I. H., Laurich, B. K., Smith, D. L., Bradley, D. D. C., Müllen, K., Brédas, J. L., *Chem. Phys. Lett.* **1997**, *278*, 139-145.
83. Su, W. P., Schrieffer, J. R., Heeger, A. J., *Phys. Rev. Lett.* **1979**, *42*, 1698.
84. Gomes da Costa, P., Conwell, E. M., *Phys. Rev. B* **1993**, *48*, 1993.
85. Lippert, E., Lüder, W., Boos, H., *Advances in molecular Spectroscopy*. Mangini, A., Pergamon Press: Oxford, **1962**.

86. Lippert, E., Lüder, W., Moll, F., Nägele, W., Boos, H., Prigge, H., Margot Becke-Goehring, Latscha, H. P., *Angew. Chem.* **1962**, *74*, 695.
87. *images are cited from reference 83.*
88. Il'ichev, Y. V., Kuhnle, W., Zachariasse, K. A., *J. Phys. Chem. A* **1998**, *102*, 5670-5680.
89. Wu, J., Pisula, W., Müllen, K., *Chem. Rev.* **2007**, *107*, 718-747.
90. Foster, E. J., Jones, R. B., Lavigueur, C., Williams, V. E., *J. Am. Chem. Soc.* **2006**, *128*, 8569-8574.
91. *All calculations were conducted using the Gaussian 03 package.*
92. Wu, J., Baumgarten, M., Debije, M. G., Warman, J. M., Müllen, K., *Angew. Chem. Int. Ed.* **2004**, *43*, 5331-5335.
93. Li, J. L., Kastler, M., Pisula, W., Robertson, J. W. F., Wasserfallen, D., Grimsdale, A. C., Wu, J. S., Müllen, K., *Adv. Funct. Mater.* **2007**, *17*, 2528-2533.
94. Yoon, M. H., Facchetti, A., Stern, C. E., Marks, T. J., *J. Am. Chem. Soc.* **2006**, *128*, 5792-5801.
95. Elmahdy, M. M., Floudas, G., Mondeshki, M., Spiess, H. W., Dou, X., Müllen, K., *Phys. Rev. Lett.* **2008**, *100*, 107801.

6 Reinforced Self-assembly of HBCs by Hydrogen Bonds

As introduced in the first chapter, π -interactions have aroused both theoretical¹ and experimental² interest during the past several decades. They are the origin of the semi-conductive properties of PAHs and the driving force for the supramolecular self-assembly. Like hydrogen bonds, the strength of which ranges from 4 to 120 kJ mol⁻¹,³ π -interactions (0 to 50 kJ mol⁻¹) are important secondary interactions for the construction of supramolecular architectures.³ Hydrogen bonding has been described as the “master key interaction in supramolecular chemistry” because of its relatively strong and highly directional nature,³ In particular, hydrogen bonds are responsible for the overall shape of many proteins, the recognition of substrates by numerous enzymes and the double helix structure of DNA.³ On the other hand, the comparatively weak π -interactions are responsible for the slippery feel of graphite and its useful lubricant properties.³ By combining hydrogen bonding and π -interactions, it has been possible to obtain, for example, nanotubes,⁴ organogels⁵ and a diversity of helical filaments^{6,7} via self-assembly.

In the case of hexa-*peri*-hexabenzocoronenes (HBCs), π -interactions induce a columnar self-assembly and provide the basis for the distinct intrinsic charge-carrier mobility.⁸ Considerable effort has therefore been invested into the successful implementation of these materials in electronic devices such as field-effect transistors (FETs),⁹ light-emitting diodes (LEDs)¹⁰ and photovoltaic cells.¹¹ Hereby, the device performance depends, to a large extent, upon the degree of intra-columnar order of these discotic molecules in thin films, which is an important factor to reach high charge-carrier mobilities.¹² The processing of such materials is a key issue in the production of well-ordered films, which can be obtained either by a thermal¹³ or solution-based treatment.^{12,}

14

It has already been shown for HBCs bearing carboxylic-acid-terminated alkyl chains that intercolumnar hydrogen-bonds can strongly influence the π -mediated

columnar self-assembly in the bulk state.¹⁵ To enhance the degree of order of discotic molecules within a single column, relatively strong and directional hydrogen bonds were brought into play by attaching ureido or amido groups to HBC, either directly or linked through rigid spacers. In so doing, it was expected that intracolumnar hydrogen bonds would form instead of the aforementioned intercolumnar hydrogen-bond networks.¹⁵ In this chapter, some novel HBC derivatives containing either amido or ureido units were synthesized (Figure 6-1). These functional groups are commonly used in hydrogen-bond-assisted supramolecular chemistry.^{3, 16} Generally, ureido groups supply stronger and more rigid hydrogen bonding interactions than amido groups.¹⁷ A second ureido group was added to further enhance the interactions between these discotic molecules. The intermolecular interactions between compounds bearing the same kind of hydrogen bond providers were further adapted by adjusting the size of substituents. The self-assembly properties of these compounds in solution were investigated by electronic spectroscopy, whereas bulk behavior was examined by differential scanning calorimetry (DSC) and two-dimensional wide-angle X-ray scattering (2D WAXS) experiments.

Finally, some of the compounds form organogels as expected. The gelation ability of these compounds was tested in different solvent systems. Thus, a novel potential application of HBC derivatives as low molecular-mass organic gelators (LMOGs)⁵ will be demonstrated.

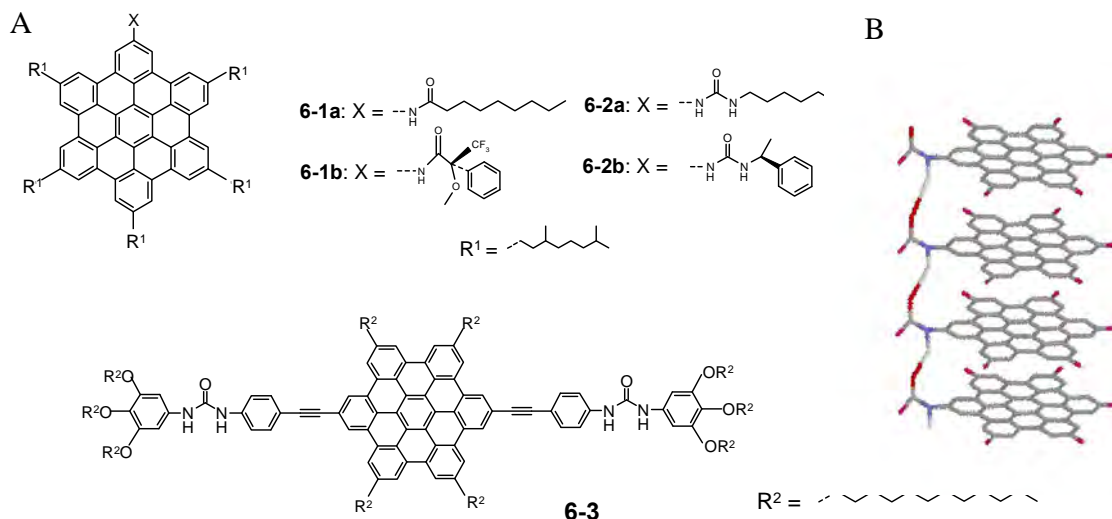


Figure 6-1. A) Synthesized HBC derivatives bearing amido (**6-1a** and **6-1b**) and ureido groups (**6-2a**, **6-2b** and **6-3**); B) schematic representation of assumed intracolumnar hydrogen bonding interactions and π -stacking of mono-substituted HBC moieties.

6.1 Synthesis

Mono-functionalized compounds **6-1a**, **6-1b**, **6-2a**, and **6-2b** were synthesized from 2-bromo-5,8,11,14,17-penta(3,7-dimethyloctanyl)-hexa-*peri*-hexabenzocoronene¹⁸ (**4-2**) as shown in Figure 6-2. Compound **4-2** was reacted with benzophenonimine via a Buchwald-Hartwig cross-coupling to yield 2-benzophenonimino-5,8,11,14,17-penta(3,7-dimethyloctanyl)-hexa-*peri*-hexabenzocoronene (**6-4**) in 95% yield. The hydrolysis of **6-4** in 2.5 M aqueous hydrochloric acid quantitatively afforded the amino-substituted HBC (**6-5**), 2-amino-5,8,11,14,17-penta(3,7-dimethyloctanyl)-hexa-*peri*-hexabenzocoronene as its hydrochloride salt. Compound **6-5** was then reacted with the corresponding acetyl chlorides or isocyanates to give **6-1a**, **6-1b**, **6-2a**, and **6-2b**. Compound **6-3** was generated via a Hagihara-Sonogashira cross-coupling reaction between 2,11-diiodo-5,8,14,17-tetra(dodecyl)-hexa-*peri*-hexabenzocoronene (**6-6**) and N-(4-ethynylphenyl)-N'-(3,4,5-tridecyloxyphenyl)urea¹⁹ (**6-7**) in 13% yield. The low yield originated from the difficult workup, which was presumably a consequence of strong intermolecular hydrogen bonds.

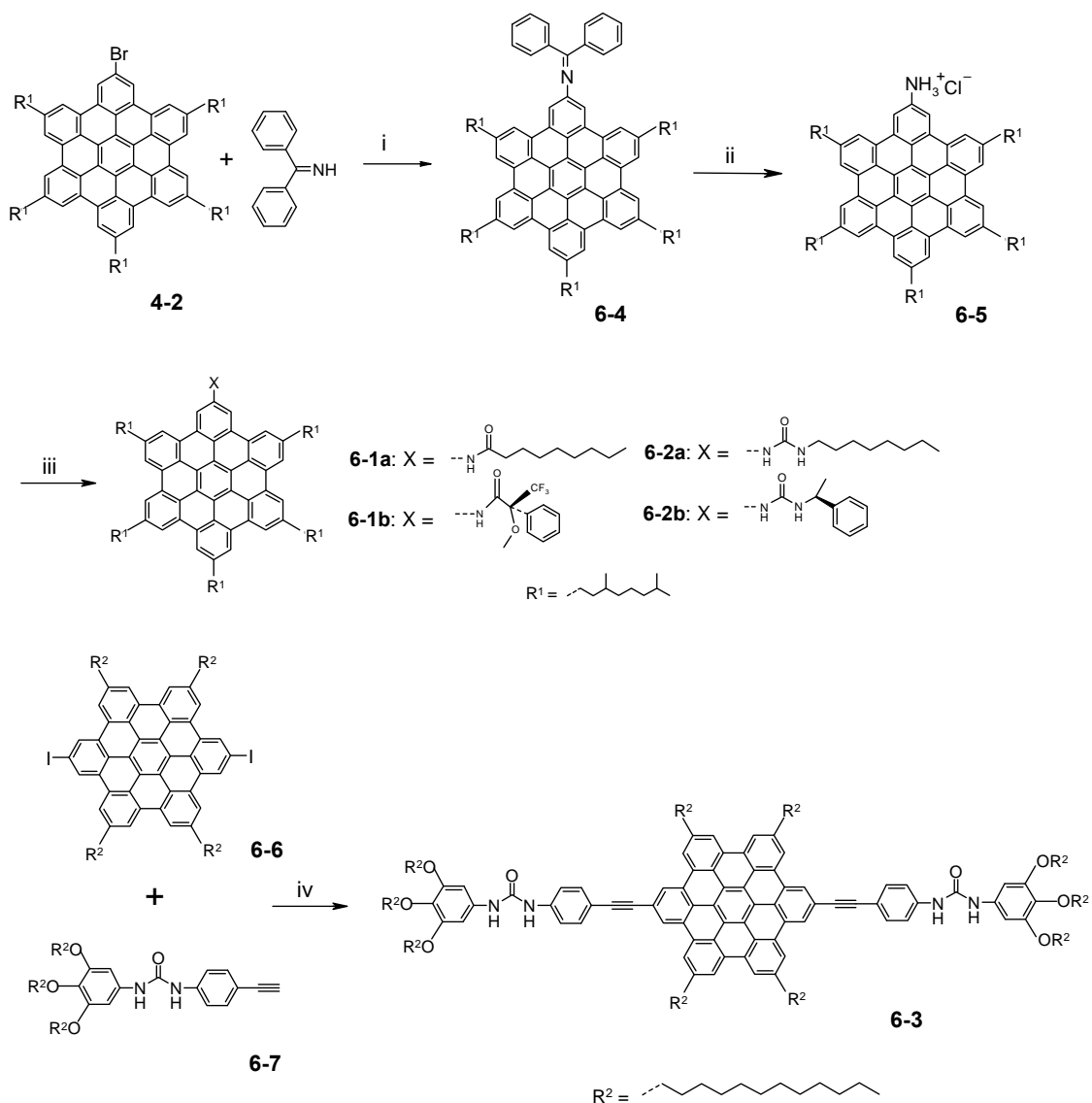


Figure 6-2. Synthesis of compounds 6-1a, 6-1b, 6-2a, 6-2b, 6-3: i) $\text{Pd}_2(\text{dba})_3$, BINAP, $\text{NaOC}(\text{CH}_3)_3$, toluene, 80 °C, 16 h, 95%; ii) 2.5 M HCl/THF, 5 h, 87%; iii) corresponding acetyl chlorides or isocyanates, Et_3N , THF/toluene (1:1), 80 °C, overnight, 6-1a, 88%; 6-1b, 81%; 6-2a, 60%; 6-2b, 54%; iv) $\text{Pd}(\text{PPh}_3)_4$, CuI, $\text{Et}_3\text{N}/\text{THF}$ (2/1), 50 °C, 4 d, 13%.

6.2 Self-assembly behavior in solution

The way in which HBCs self-associate in solution serves as a valuable indication for the subsequent processing of these materials into aligned films.²⁰ The electronic spectra of π -conjugated chromophores in solution are highly sensitive to aggregational

effects. For example, a variation of concentration and / or temperature can result in significant changes of the intensities, shapes, positions and / or number of the bands.^{21,22} Therefore such investigations were conducted for all the compounds described here.

In contrast to the other compounds, only **6-2b** (Figure 6-3D) and **6-3** (Figure 6-4) showed distinct changes in their respective concentration dependent UV-Vis absorption spectra. With decreasing concentration, not only do the extinction coefficients of compounds **6-2b** and **6-3** increase substantially, but the resolution of some bands (297, 349 and 397 nm) also improves. Additionally, a slight blue-shift of 4 nm was recorded at higher concentrations for some absorption bands (301, 373 nm) in the case of **6-3**.

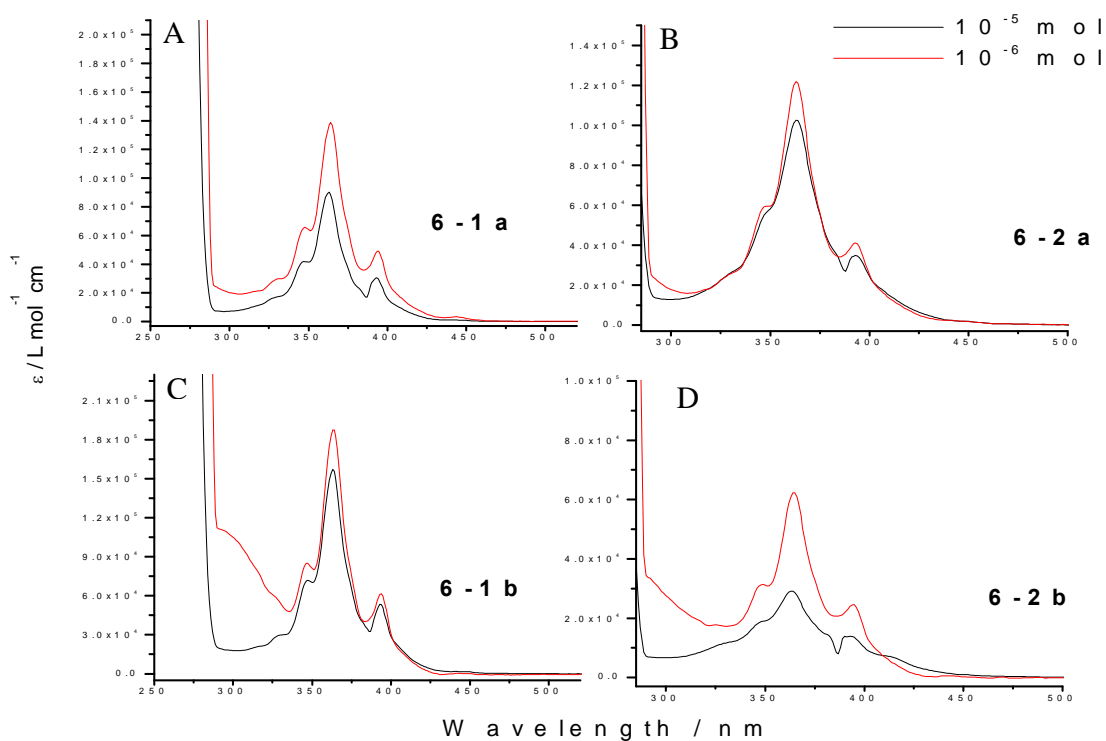


Figure 6-3. Concentration dependent UV/Vis spectra of A) 6-1a, B) 6-1b, C) 6-2a and D) 6-2b measured in toluene; black, 1.0×10^{-5} M; red, 1.0×10^{-6} M.

The fluorescence spectra of **6-2a**, **6-2b** and **6-3** vary with increasing concentration (Figure 6-5). In particular, the bands at longer wavelengths became more intense and broader.

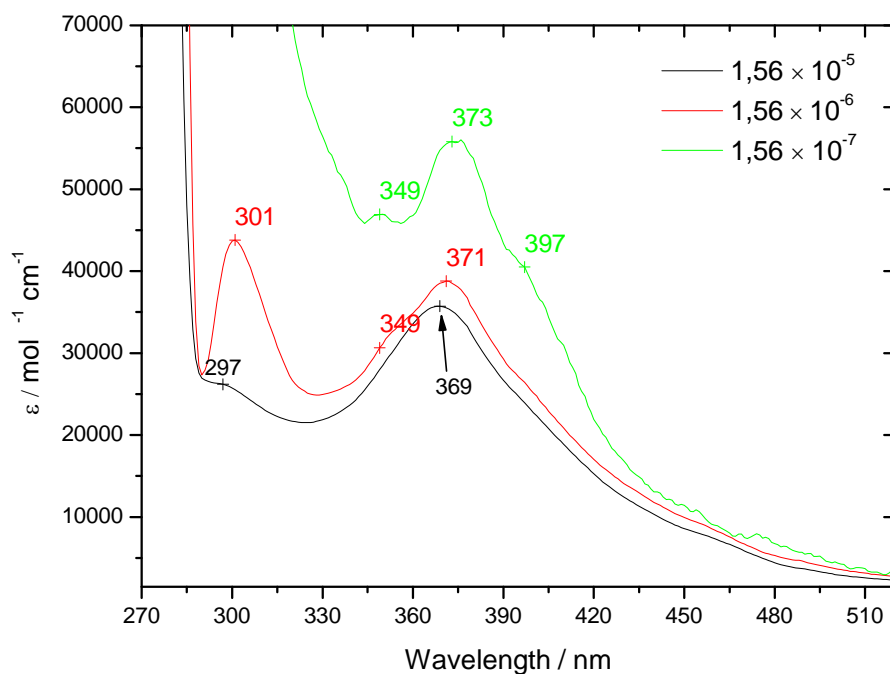


Figure 6-4. Concentration dependent UV-Vis absorption spectra of **6-3** in toluene solution: black line 1.56×10^{-5} M; red line 1.56×10^{-6} M; green line 1.56×10^{-7} M.

The observed non-Lambert-Beer law behavior and the concentration dependence of the absorption spectra (sharp, well resolved band shape with larger extinction coefficient at lower concentration) indicate the existence of larger aggregates at higher concentrations.^{13c} The slight blue shift of one of the absorption bands (from 373 to 369 nm) in the spectrum of **6-3** is also consistent with cofacial stacking of the aromatic π -systems in the aggregates.^{13a,23b} This phenomenon has been studied both theoretically and experimentally.^{23b} The existence of increasing aggregation with increasing concentration for **6-2a**, **6-2b** and **6-3** is further supported by concentration dependent fluorescence experiments, which exhibit broad, less resolved and concentration-dependent bands above 500 nm. The relatively weaker photophysical changes in the cases of **6-1a** and **6-1b** point to lower self-association propensities, which are likely due to the weaker hydrogen bonding interactions between amido functionalities than these between ureido groups.¹⁷

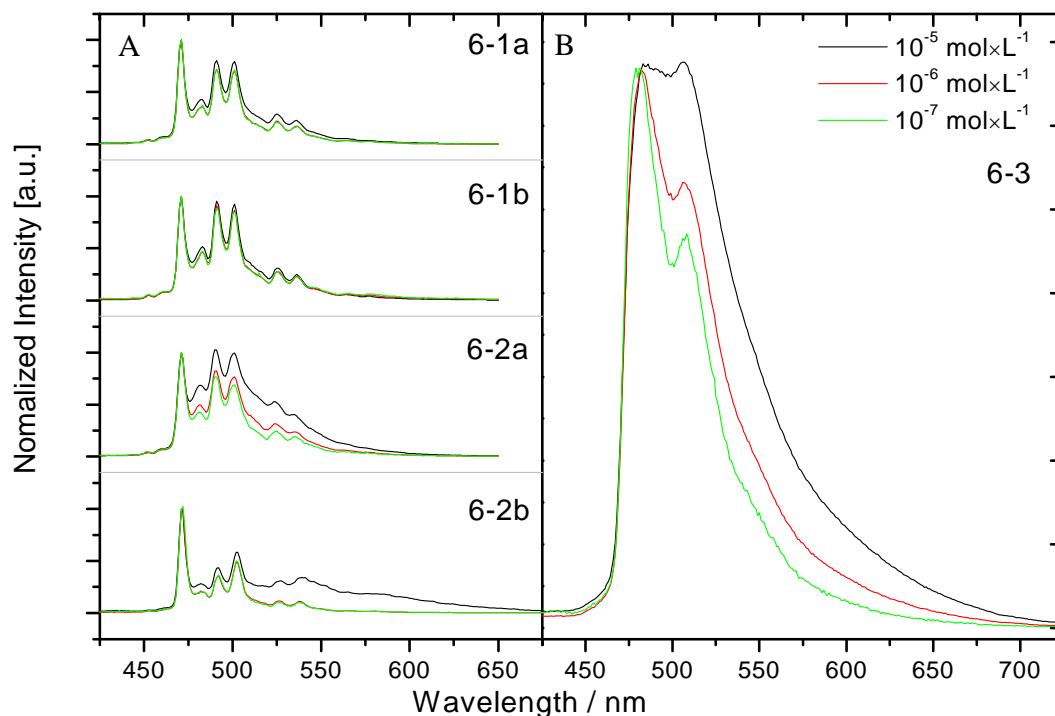


Figure 6-5. Concentration dependent fluorescence spectra of **6-1a**, **6-1b**, **6-2a**, **6-2b** (A) and **6-3** (B) in toluene: black 10^{-5} M, red 10^{-6} M, green 10^{-7} M; for **6-1a**, **6-1b**, **6-2a**, **6-2b**, excited at 360 nm and normalized at 471 nm; for **6-3**, excited at 369 nm and normalized at 482 nm.

In the temperature dependent absorption spectra of the mono-functionalized HBCs, compound **6-2b** exhibits the most pronounced effects. Compounds **6-1a** (Figure 6-6A) and **6-2a** (Figure 6-6C) show similar, but gentler effects, whereas **6-1b** does not display any recognizable change (Figure 6-6B). Upon increasing the temperature of the solutions of **6-1a** and **6-2b** (Figure 6-6A,D), the absorption bands at shorter wavelength gain resolution and some broad bands at longer wavelengths (approximate 410 – 420 nm) become less intense with the appearance of an isosbestic point at around 400 nm. Moreover, the α bands (named according to Clar's nomenclature²⁴), which are generally very weak for HBC derivatives,²⁵ are also much better resolved at higher temperature.

Significant changes are also observed in the temperature dependent UV-Vis absorption spectrum of **6-3** (Figure 6-7), where two isosbestic points are apparent (at 349 nm and 389 nm). For the bands at around 300 nm and those at longer wavelengths, the

intensity decreases with increasing temperature, while the one between the isosbestic points changes in the opposite sense.

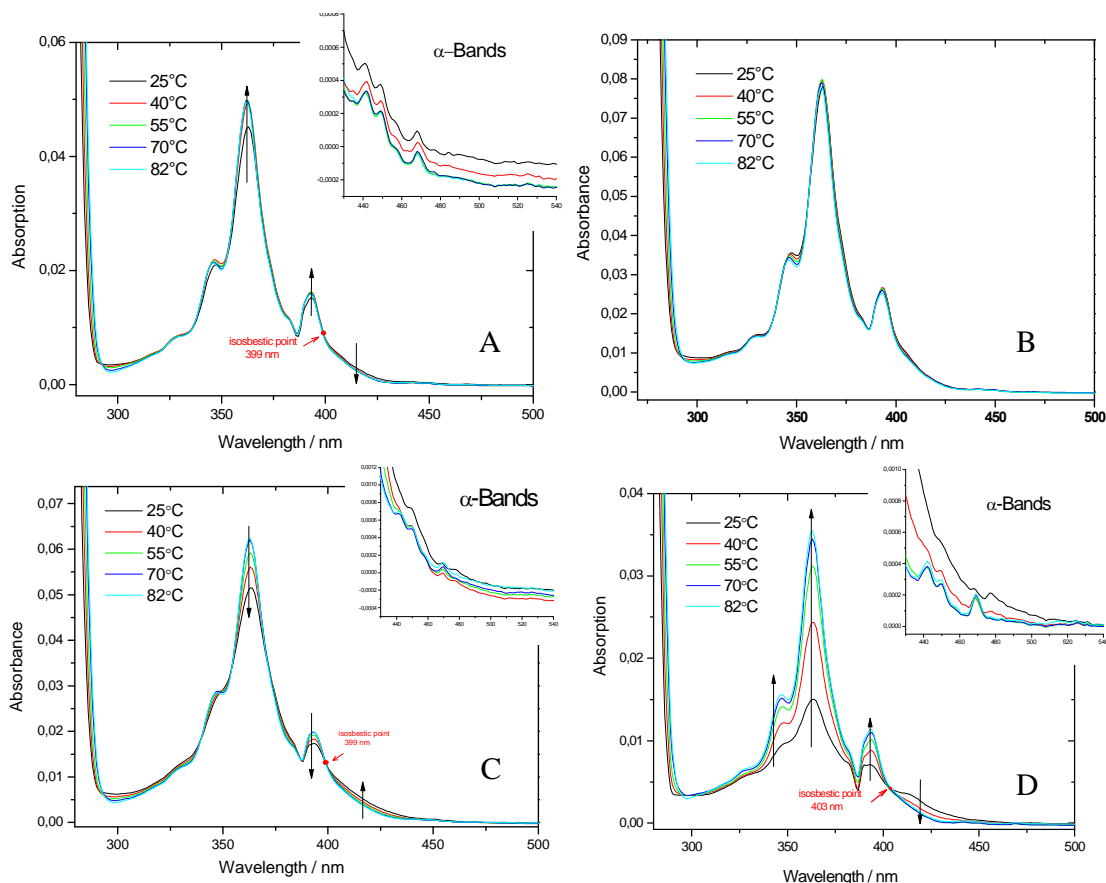


Figure 6-6. Temperature dependent UV-Vis absorption spectra of A) 6-1a, B) 6-1b, C) 6-2a and D) 6-2b; measured with 1.0×10^{-5} M toluene solutions; arrows indicate the direction of change with increasing temperature

As the aromatic moieties of the compounds **6-1a**, **6-1b**, **6-2a** and **6-2b** consist of the same basic structure, only little difference in the strength of the π -interactions is expected. Therefore, the different self-assembly abilities can be attributed to the differences in the degree of hydrogen bonding,^{16, 17a} which is strongly influenced by the temperature,²⁶ the steric demands of the side chains attached to the hydrogen bonding groups and the number of hydrogen bonding functionalities. Concerning the influence of the temperature, the effects are effectively suppressed upon moderate heating as indicated by the close similarity of the absorption spectra at 82 °C and their marked differences at 25 °C regardless of the nature of the hydrogen bonding group (Figure 6-6). Superimposed upon

the temperature effect is a steric effect. Specifically, the spectrum of **6-1b**, which carries the most voluminous side chain (2-(*R*)-(-)- α -methoxy- α -(trifluoromethyl)phenylethylamido group), shows very little changes with respect to temperature variation (Figure 6-6B). In contrast, the spectrum of **6-1a**, which bears a less bulky substituent, displays more pronounced changes (Figure 6-6A). The dominant effect is the nature of the hydrogen bonding group. The spectra of the ureido-containing HBCs, **6-2a** and **6-2b** (Figure 6-6C, D) exhibit much greater temperature-dependence than those of the amido-containing HBCs (**6-1a** and **6-1b**). The number of hydrogen bonding groups present also plays a significant role, as demonstrated by the strong temperature dependence observed in the spectrum of **6-3** (two ureido groups). In this case, the spectrum is still changing at the upper temperature limit (85 °C), which indicates that hydrogen bonding interactions are not yet suppressed.

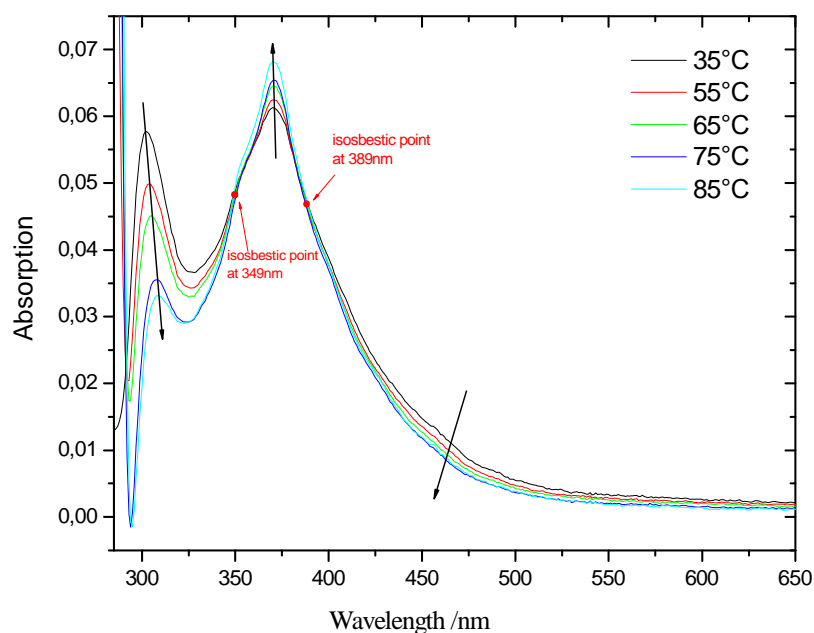


Figure 6-7. Temperature dependent UV-Vis absorption spectra of **6-3**, measured with 1.56×10^{-6} M toluene solution; arrows indicate the direction of change with increasing temperature.

Compound **1b** and **2b** each carry one chiral center in the functional substituent. Circular dichroism (CD) spectroscopy reveals weak Cotton effects for **6-1b**, but not **6-2b**, presumably due to the size of the molecule in relation to the number of chiral centers (Figure 6-8). Nevertheless, the observed pattern is congruent with a clockwise helical

aggregation of the molecular dipole moments in solution.²⁷ The SEM images of xerogel prepared from **6-2b** (which show no CD signal) appear to show discernable left-handed helical structure in the gel fibers of **2b** (Figure 6-15B-D).

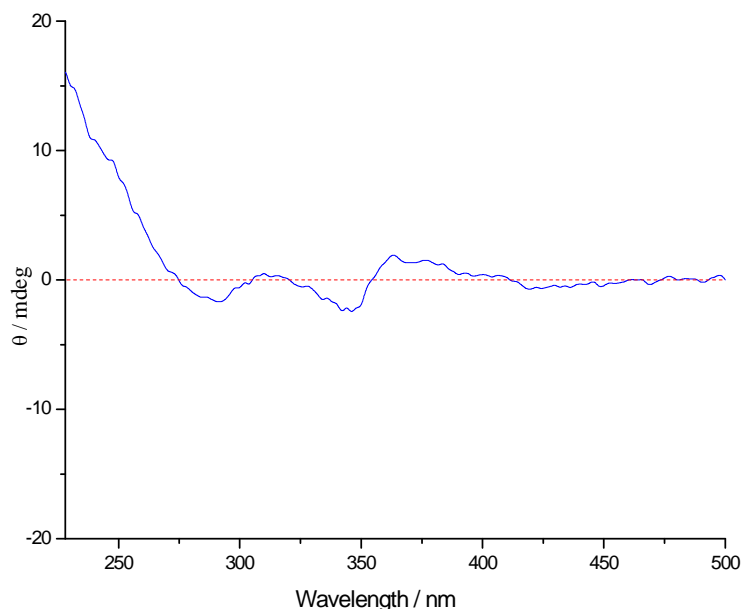


Figure 6-8. CD spectrum of compound 6-1b in 1.02×10^{-4} M *n*-heptane solution measured at 20 °C.

6.3 Hydrogen bonding interactions and self-assembly behavior in the bulk state

Infrared spectroscopy of the bulk samples supports the establishment of hydrogen bonds in these compounds according to the characteristic changes of the vibrational frequency of the N-H groups and carbonyl groups.²⁸

The characteristic stretching vibrations of the N-H bond and the carbonyl group are listed in Table 6-1 (see reference 29 for full spectra). For amide and urea compounds, which involve hydrogen bonds, the characteristic N-H stretching vibrations usually give rise to multiple bands in the range of $3400 - 3060 \text{ cm}^{-1}$ and the carbonyl stretching vibrations, so-called amide I bands, appear at lower frequencies ($1700 - 1640 \text{ cm}^{-1}$) in contrast to a saturated aliphatic ketone (1715 cm^{-1}) due to the resonance effect.^{28a} For compounds **6-1b**, carrying a sterically hindered amido functionality, and **6-3**, bearing two

ureido groups, only one kind of N-H and carbonyl stretching bands were recorded. Specifically, both the N-H and carbonyl stretching bands for **6-1b** are located at higher wavenumbers than those for **6-3**. The other compounds all show two kinds of N-H stretching bands and **6-2a** even shows two carbonyl stretching signals.

Table 6-1. Stretching frequencies [cm^{-1}] of N-H and carbonyl groups of compounds **6-1a, **6-1b**, **6-2a**, **6-2b** and **6-3** in KBr pellet.**

compound	N-H stretch vibrations	Carbonyl stretch vibrations
6-1a	3430 (medium, broad) 3310 (shoulder)	1660 (medium)
6-1b	3400 (medium, broad)	1700 (medium)
6-2a	3430 (medium, broad) 3310 (shoulder)	1710 (medium) 1650 (weak)
6-2b	3390 (medium, broad) 3310 (medium, broad)	1640 (medium)
6-3	3310 (medium, broad)	1650 (medium)

The differences in the degree of hydrogen bonding interactions in the bulk state are also obvious. The observation of multiple N-H stretching vibrations for **6-1a**, **6-2a** and **6-2b** in their FT-IR spectra (Table 6-1) suggests the amido / ureido groups might bind to produce dimers with an *s*-cis conformation or polymers with an *s*-trans conformation.^{28a} In comparing the two amido-containing compounds (**6-1a** and **6-1b**), the carbonyl stretching of **6-1a** is observed at 40 cm^{-1} lower wavenumber than the one of **6-1b**, suggesting the existence of stronger hydrogen bonds in **6-1a**. Among the ureido-containing compounds, **6-2b** and **6-3** give only one carbonyl stretching signal (1640 cm^{-1} for **6-2b**, 1650 cm^{-1} for **6-3**), whereas two carbonyl stretching bands are observed for **6-2a** (1710 cm^{-1} and 1650 cm^{-1}). This may reflect different hydrogen bonding interactions

in these three compounds.³⁰ These observations are in congruence with the results obtained from solution studies: **6-1b**, with a bulky amido substituent, forms the weakest hydrogen bonds and that hydrogen bonding is significantly strengthened by both reducing the size of substituent and using a more effective hydrogen bonding ureido group.

DSC is a commonly used method for the investigation of thermotropic phase behavior.³¹ For **6-1a**, **6-1b** and **6-3**, there was no visible phase transition peak recorded in the temperature range from -100 °C to 250 °C. In the case of **6-2b**, the DSC trace showed only an irreversible endothermic transition at 220 °C during both the first and second heating cycles (Figure 6-9).

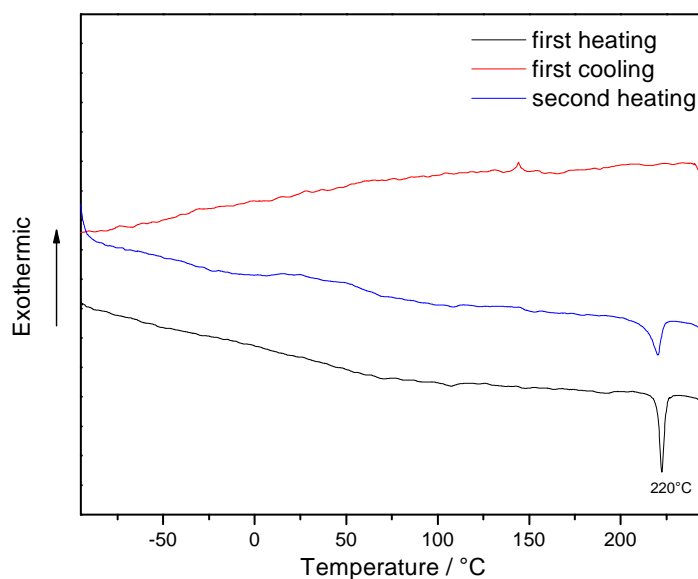


Figure 6-9. DSC traces of **6-2b** recorded at 10 K/min.

2D WAXS experiments,³² which provide information about supramolecular arrangement in the solid state, were conducted for all compounds at both ambient and elevated temperatures. Compounds **6-1a**, **6-2a** and **6-2b** show similar phase behavior. Figure 6-10 presents the temperature-dependent 2D WAXS patterns of **6-1a** and **6-2b** (for **6-2a** see reference 29). At 30 °C, the characteristic distribution of the reflections indicates an identical monoclinic columnar stacking for both compounds.³² From the meridional and off-meridional scattering intensities, it is determined that the discotic molecules are

tilted by approximately 40° , the columnar axis has a periodic distance of 0.47 nm and the co-facial π -stacking distance is 0.37 nm.^{32a}

Upon heating to 170°C , the 2D patterns of both compounds (Figure 6-10) display a typical liquid crystalline (LC) arrangement of the molecules,³² where the discs self-arrange perpendicularly to the columnar axis with a stacking distance of 0.37 nm in a hexagonal columnar lattice. Interestingly, upon cooling the samples to room temperature after about one hour at 170°C , the highly ordered LC organization does not return to the previously recorded crystalline phase (as observed for other alkylated disc-type PAHs),³³ but rather keep the non-tilted, hexagonal 2D packing observed in the mesophase.

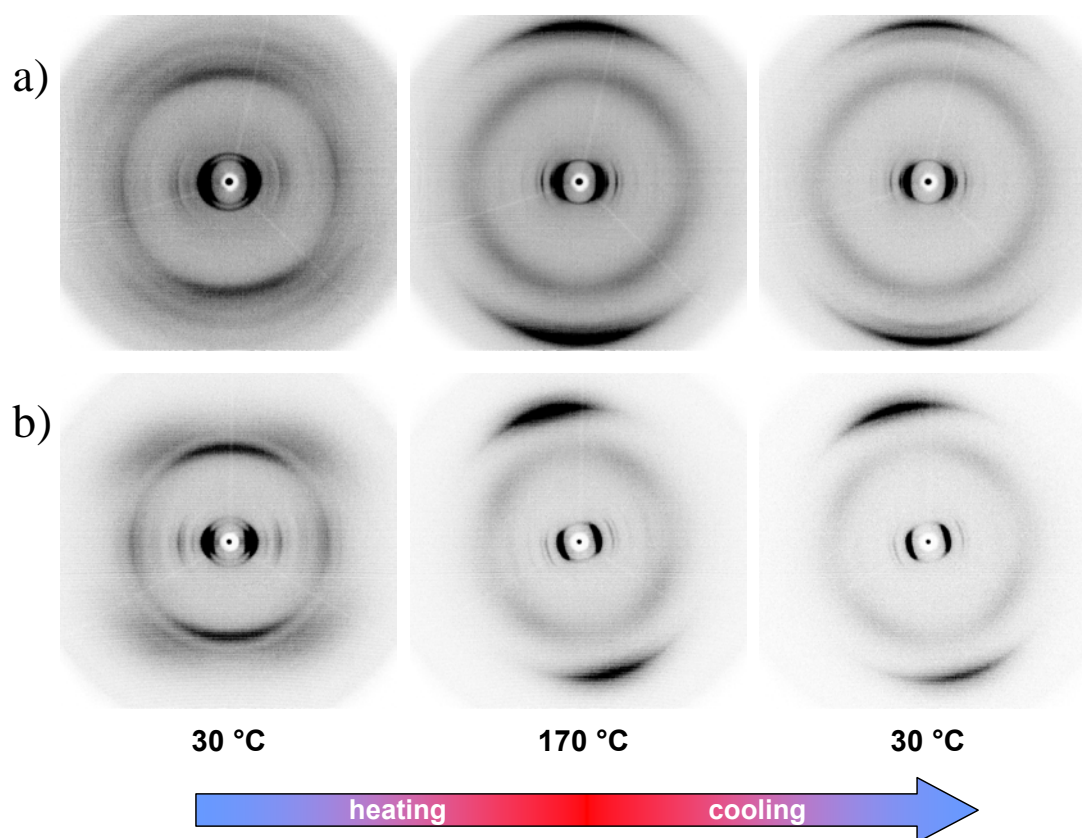


Figure 6-10. Temperature-dependent 2D-WAXS experiments of a) 6-1a and b) 6-2b; 2D monoclinic unit cell parameters (at 30°C): $a = 2.46\text{ nm}$, $b = 1.93\text{ nm}$, $\gamma = 115^\circ$ for 6-1a and $a = 2.50\text{ nm}$, $b = 1.86\text{ nm}$, $\gamma = 95^\circ$ for 6-2b; hexagonal unit cell parameters (at 170°C and after annealing): $a_{\text{hex}} = 2.77\text{ nm}$ for 6-1a and $a_{\text{hex}} = 2.80\text{ nm}$ for 6-2b

Compound **6-3** shows significantly less order over the entire temperature range, which renders the assignment of the unit cell impossible. At room temperature, no π -

stacking signal is recorded. At 120 °C, meridional reflections are apparent, which correspond to a co-facial stacking distance of 0.38 nm. The π - π distance decreases to a typical aromatic stacking value of 0.36 nm at 180 °C. In contrast to the behavior observed for **6-1a**, **6-2a** and **6-2b**, the LC organization at higher temperature is not retained after annealing (Figure 6-11). Unlike the above mentioned derivatives, **6-1b** shows a non-tilted, hexagonal columnar stacking ($a_{\text{hex}} = 2.58$ nm) with a cofacial distance of 0.36 nm over the whole investigated temperature range (Figure 6-12).

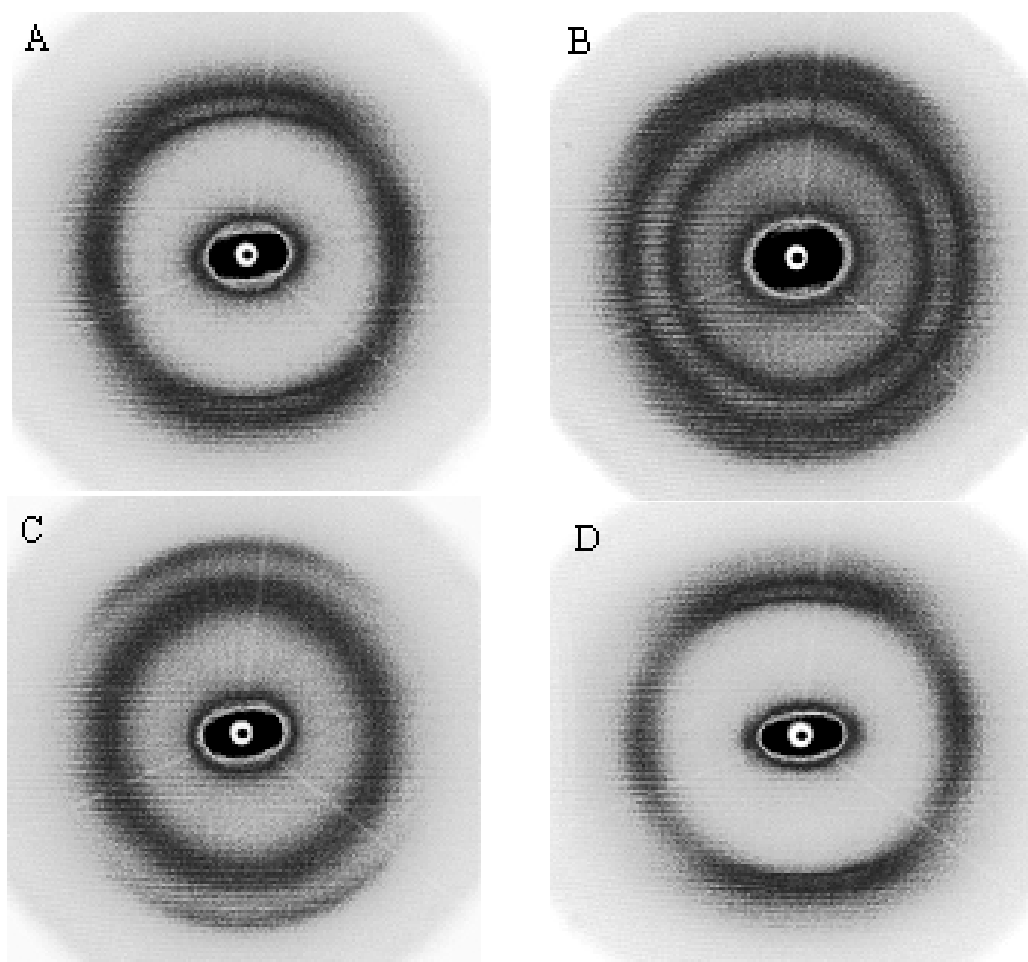


Figure 6-11. Temperature dependent 2D WAXD diagrams of extruded fibers of **6-3** at A) room temperature, B) 120 °C, C) 180 °C and D) cooled to room temperature.

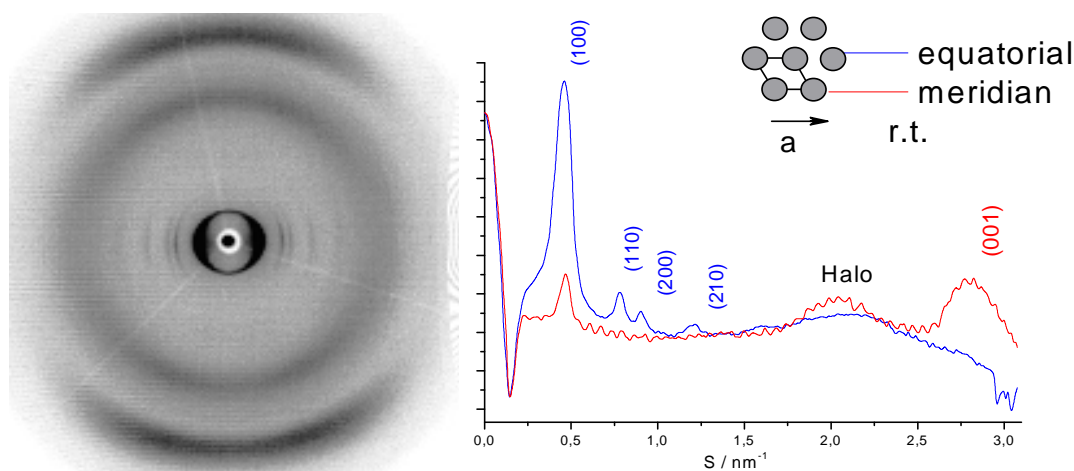


Figure 6-12. . Diffractogram and equatorial (blue line) and meridian (red line) intensity distribution graphs of **6-1b** at room temperature; hexagonal unit cell parameters: $a_{\text{hex}} = 2.58$ nm, and a π - π stacking distance, 0.36 nm

The supramolecular columnar arrangements of these compounds at different temperatures investigated by 2D WAXS indicate that the hydrogen bonding interactions strongly influence the stacking and especially the thermal properties of these materials. The most interesting observation is the irreversibility of the mesophase formation for the compounds **6-1a**, **6-2a** and **6-2b** after annealing, which is a quite unique property for HBC derivatives. The columnar stacking at room temperature before annealing resembles that of most other HBC molecules in the crystalline phase.^{32a} The periodic distance along columns is determined to be 0.47 – 0.46 nm (0.47 nm for **6-1a/6-2b**, and 0.46 nm for **6-2a**), which is in good agreement with the length of hydrogen bonding units between ureido and amido groups (0.44 – 0.48 nm).^{16, 17a, 34} This provides the opportunity for a near optimum arrangement of hydrogen bonding functional groups. As the temperature is increased to 170 °C, the effect of the hydrogen bonds is weakened and π -interactions become the dominant influence on the supramolecular arrangement. This leads to a typical LC organization with non-tilted molecular discs, a typical intermolecular π -stacking distance (0.36 nm) and a hexagonal 2D columnar packing. Thereby stacked arenes separated by 0.36 nm and hydrogen bonds of 0.47/6 nm can be simultaneously accommodated in the structure shown in Figure 6-13, which has a helical arrangement. The unexpected preservation of the LC supramolecular organization after prolonged annealing is in line with the observation of only an irreversible endothermic transition during the heating cycle on the DSC diagram (**6-2b**). This behavior can be explained in

terms of the relative importance of various weak interactions at different temperatures. At low temperature, the hydrogen bonding and the crystallinity of the alkyl substituents dictate the supramolecular arrangement to give a monoclinic columnar packing with tilted molecular discs. At high temperature, the relative importance of hydrogen bonding drops off²⁶ and π -interactions become dominant. As such, a hexagonal columnar arrangement forms. Upon cooling, the order imposed by the π -stacking remains in place and intermolecular hydrogen bonding between side chains stabilizes the structure. Thus, the cooperative effects of the weak interactions (π -stacking, hydrogen bonding and side chain crystallinity) are responsible for the preservation of the LC phase. Again, it is noteworthy that the functional groups are attached directly to the aromatic cores and the intracolumnar hydrogen bonds are thus established between discs within the same supramolecular column. This stands in strong contrast to the previously reported HBC derivatives, which had hydrogen-bonding functionalities that were separated from HBC cores by long alkyl spacers and resulted in the formation of intercolumnar hydrogen bonds.¹⁵

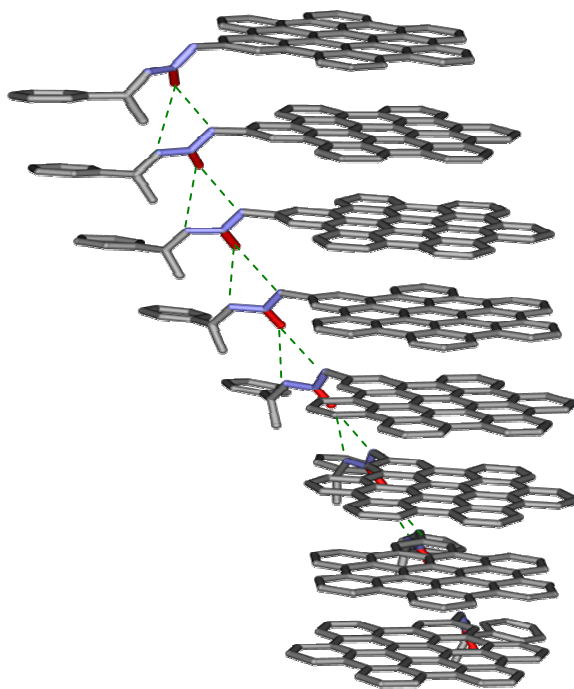


Figure 6-13. Schematic representation of the coincidence of hydrogen bonding interactions and π - π interactions after annealing for 6-2b.

The observation that **6-1b** maintains the same columnar arrangement over the whole temperature range suggests a less pronounced influence of hydrogen bonds on the supramolecular arrangement at low temperature.

Upon inclusion of a second ureido group (i.e. **6-3**), the 2D WAXS pattern reveals an increased disorder at low temperature, implying an even stronger influence of the hydrogen bonds. The decrease of the co-facial stacking distance (from 0.38 to 0.36 nm) upon increasing the temperature (from 120 °C to 180 °C) shows that the supramolecular arrangement induced by the π -interactions can only be obtained after the hydrogen bonds are significantly weakened at higher temperatures. The loss of long range order upon cooling not only indicates that hydrogen bonding is more important than π -interactions at room temperature, but also that the two effects do not operate cooperatively in this system.

All the results discussed above clearly demonstrate that, for a successful cooperative implementation of two secondary forces to improve the self-assembly propensity, the spatial demands and geometrical requirements need to coincide. By selecting a stronger hydrogen bond provider, i.e. the ureido unit, and reducing the size of the side chain attached to the functional group, e.g. as in **6-2b**, the HBC derivative exhibits excellent self-assembly ability both in solution and in the solid state. The introduction of a second strong hydrogen bond provider at the “*para*-” position (in the case of **6-3**) is, however, counterproductive. A voluminous side chain and a relatively feeble hydrogen bonding group, in the case of **6-1b**, results in a nearly undetectable influence on the self-assembly behavior of the HBCs.

6.4 Gelation ability test

For initial gelation testing, attempts to dissolve each of the compounds in a small amount of an apolar solvent (e.g. hexane, heptane or toluene) at refluxing temperature were made. THF was then progressively added as a polar solvent if a particular compound did not dissolve under the initial conditions. The solution was then slowly

cooled down (by placing it in a 60 °C oil bath and allowing the oil bath to cool to ambient temperature) and the substance was judged to be a gel if the vessel could be inverted without apparent movement of the content.¹⁷ The minimum gelation concentration, which describes the gelation ability of the compounds, was determined by continuously diluting a gel (with the same solvent mixture as the one used to form the gel) with heating and cooling cycles until the gel did not regenerate. Another important parameter of gels, the so-called sol-to-gel phase transition temperature (T_g), which describes their thermodynamic stability, was measured using the “falling drop” method.³⁵

The efficient combination of hydrogen bonding and π -interactions leads to distinct gelation properties of two of the compounds (**6-2b** and **6-3**). Only these two examples developed stable fluorescent organogels (Figure 6-15A) in the tested solvents. The minimum gelation concentrations are shown with the corresponding T_g values in Table 6-2. Laser scanning confocal microscopy (LSCM) indicated that the fluorescence comes from the fibrillar structure itself and not from amorphous material (Figure 6-14).

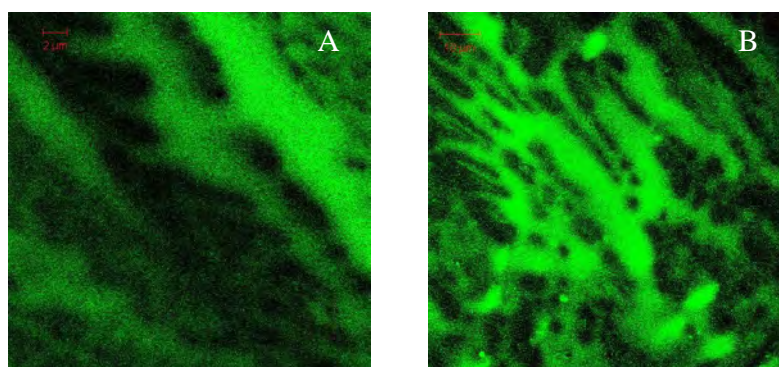


Figure 6-14. LSCM images for A) **6-2b** and B) **6-3** drop-cast on cover glass; two photon excitation mode $\lambda_{ex} = 780$ nm.

Table 6-2. Gelation test of **6-2b** and **6-3** in n-hexane/THF, n-heptane/THF and toluene/THF.

	Hexane	THF	Min.G.C. ^[a]	Phase/ T_g	Heptane	THF	Min.G.C.	Phase/ T_g	Toluene	THF	Min.G.C.	Phase/ T_g
	/ mL	/ mL	/ w.t.%	/ °C	/ mL	/ mL	/ w.t.%	/ °C	/ mL	/ mL	/ w.t.%	/ °C
6-2b (1 mg/vol)	0.55	1.30	0.068	G ^[b] /43	0.60	1.10	0.081	G/31	0.50	0.35	0.15	G/A ^[c]
6-3 (0.6 mg/vol)									1.90	0	0.035	G/42

[a] Min. G.C. = minimum gelation concentration; [b] G = gel at room temperature; [c] A = being destroyed by mechanical agitation.

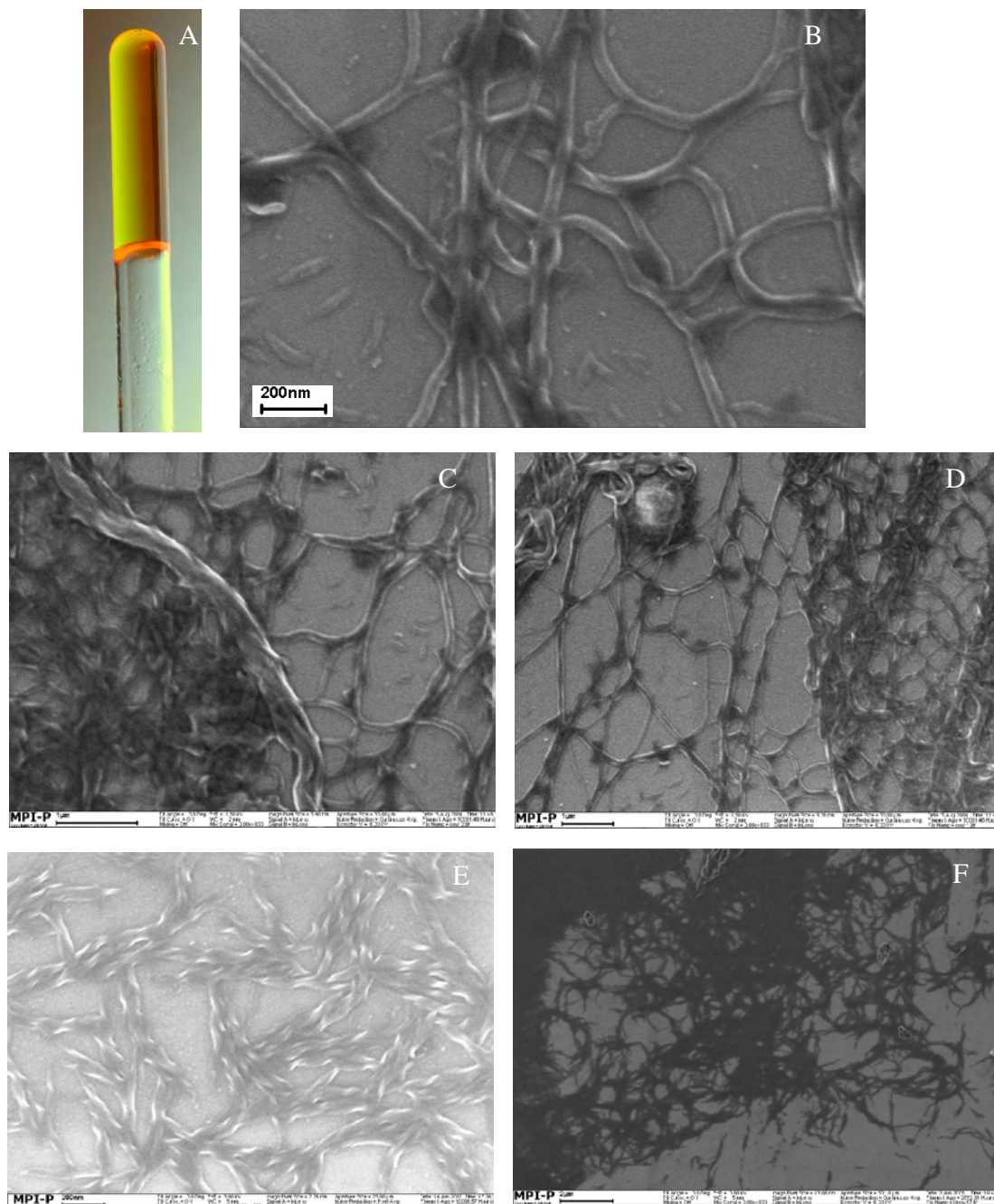


Figure 6-15. A) Photograph of fluorescent gel from **6-3** in toluene; SEM images of xerogel prepared from B-D) **6-2b** in hexane/THF; E,F) **3** in toluene

To visualize how the nanoscale hydrogen-bonding interactions manifest themselves in the macroscopic superstructures, an SEM image of a xerogel of **6-2b** was recorded (Figure 6-14B, C, D).³⁶ The molecules aggregate into long fibrillar structures (up to several microns in length) with a diameter of approximate 100 nm. These fibers further

interwind with each other, establishing three-dimensional networks, which are the only known examples for HBC derivatives. Due to the stronger hydrogen bonds existing in **6-3** and solvent effect, shorter and more rigid aggregates are observed for the xerogel formed from **6-3** in toluene. (Figure 6-15E, F).

It has been previously observed that amphiphilic HBCs are capable of gelling some organic solvents under certain conditions.³⁷ In the case of compounds **6-2b** and **6-3**, the combination of stronger and more rigid hydrogen bonds and their intrinsic π -interactions cause the behavior of these HBCs as LMOGs. Both materials show excellent gelation abilities with very low minimum gelation concentrations compared to perylene-³⁸ and porphyrin-based^{17c,d,34g} LMOGs, which also combine π -interactions with hydrogen bonds. The gelling process could be assumed to be as follows. The hydrogen bonds are initially significantly weakened in the refluxing solution and the π -interactions dominate the molecular aggregation. As in the bulk state, the hydrogen bonding interactions stabilize these aggregates upon cooling and further accumulate these microscopic aggregates into fibrillar supramolecular structures. An SEM image of the xerogel (Figure 6-15) shows that the resulting three-dimensional network traps small solvent molecules and stabilizes the substance in a “meta-state” between liquid and solid leading to fluorescent organogels.

6.5 Summary

By the introduction of hydrogen bonds along the HBC columnar axis, the self-association propensities of HBC derivatives have been considerably improved, which are strongly influenced by varying both the size of the substituents and the nature of the hydrogen bonding groups at the same time. The self-assembly abilities of these compounds increase substantially as the hydrogen bonding interactions become stronger and the steric demand of the side chains diminishes. Accordingly, the compound having the weaker hydrogen bonding group and the bulkier substituent (**6-1b**) show the lowest aggregation tendency. By the same token, either reducing the steric hindrance of substituent (**6-1a**) or incorporating a stronger hydrogen bonding unit (**6-2a**, **6-2b**) endows the HBCs with stronger self-assembly ability. When a second hydrogen-bond exerting

group is connected to the aromatic core at the “*para*-” position (**6-3**), the molecule displays the strongest aggregation tendency in solution.

Nevertheless, in the bulk state, depending upon the strength of the intermolecular interactions and the geometry of functional groups, hydrogen bonds either cooperate with π -interactions to stabilize the HBC columnar superstructures, which even result in the preservation of a highly ordered LC phase after annealing (**6-1a**, **6-2a** and **6-2b**), or compete against the π -interactions leading to a short-range ordered supramolecular arrangement (**6-3**).

Finally, the relatively stronger hydrogen bonds of **6-2b** and **6-3** render these HBC derivatives as LMOGs, which has previously not been characterized for this kind of compounds. HBC molecules **6-2b** and **6-3** assemble into stable, three-dimensional networks under the collaboration of hydrogen bonding and π -interactions, which trap small solvent molecules to form fluorescent organogels. Although the hydrogen bonds incorporating HBC systems fail to decrease the intermolecular distance within molecular columns like the hydrogen bonds decorated triphenylene derivatives,^{30b} the cofacial molecular distance of which was reduced to 3.18 Å, the hydrogen bonds significantly enhance the self-assembly abilities of the HBCs resulting in distinct self-healing abilities^{32a} and thus endow them with excellent gelation abilities. In so doing, the optoelectronic properties of HBCs have been made available for the exploitation in the area of functional organogels.¹⁷ Owing to the intrinsic semiconducting properties of the stacked HBCs, such gels are also promising candidates for the application in the areas such as energy transfer along one-dimensional aligned chromophores,^{17d, 39a} and enhanced charge transport based on organic semi-conducting layers^{39b} with a long time performance.^{32a}

6.6 References

1. a) M. O. Sinnokrot, C. D. Sherrill, *J. Am. Chem. Soc.* **2004**, *126*, 7690-7697; b) C. A. Hunter, J. K. M. Sanders, *J. Am. Chem. Soc.* **1990**, *112*, 5525-5534.
2. a) J. M. Tour, *Chem. Rev.* **1996**, *96*, 537-554; b) M. Müller, C. Kübel, K. Müllen, *Chem. Eur. J.* **1998**, *4*, 2099-2109.
3. J. W. Steed, J. L. Atwood, *Supramolecular Chemistry* Wiley & Sons: Chichester, **2000**, p. 22-28.
4. M. A. B. Block, C. Kaiser, A. Khan, S. Hecht, *Topics in Current Chemistry: Functional Molecular Nanostructures* Springer, **2005**.
5. a) P. Terech, R. G. Weiss, *Chem. Rev.* **1997**, *97*, 3133-3160; b) D. J. Abdallah, R. G. Weiss, *Adv. Mater.* **2000**, *12*, 1237-1247. c) F. Camerel, R. Ziessel, B. Donnio, C. Bourgogne, D. Guillon, M. Schmutz, C. Iacovita, J-P. Bucher, *Angew. Chem. Int. Ed.* **2007**, *46*, 2659-2662; *Angew. Chem.* **2007**, *119*, 2713-2716.
6. H. Engelkamp, S. Middelbeek, R. J. M. Nolte, *Science* **1999**, *284*, 785-788.
7. S. Shinkai, K. Murata, *J. Mater. Chem.* **1998**, *8*, 485-495.
8. A. M. van de Craats, J. M. Warman, K. Müllen, Y. Geerts, J. D. Brand, *Adv. Mater.* **1998**, *10*, 36-38.
9. C. D. Dimitrakopoulos, P. R. L. Malenfant, *Adv. Mater.* **2002**, *14*, 99-117.
10. a) J. H. Burroughes, D. D. C. Bradley, A. R. Brown, R. N. Marks, K. Mackay, R. H. Friend, P. L. Burns, A. B. Holmes, *Nature* **1990**, *347*, 539-541; b) R. H. Friend, R. W. Gymer, A. B. Holmes, J. H. Burroughes, R. N. Marks, C. Taliani, D. D. C. Bradley, D. A. Dos Santos, J. L. Brédas, M. Lögdlund, W. R. Salaneck, *Nature* **1999**, *397*, 121-128.
11. L. Schmidt-Mende, A. Fechtenkötter, K. Müllen, E. Moons, R. H. Friend, J. D. MacKenzie, *Science* **2001**, *293*, 1119-1122.
12. a) W. Pisula, A. Menon, M. Stepputat, I. Lieberwirth, U. Kolb, A. Tracz, H. Siringhaus, T. Pakula, K. Müllen, *Adv. Mater.* **2005**, *17*, 684-689. b) S. Kubowicz, U. Pietsch, M. D. Watson, N. Tchebotareva, K. Müllen, A. F. Thünemann, *Langmuir* **2003**, *19*, 5036-5041. c) D. W. Breiby, O. Bunk, W. Pisula, T. I. Sølling, A. Tracz, T. Pakula, K. Müllen, M. M. Nielsen, *J. Am. Chem. Soc.* **2005**, *127*, 11288-11293.

13. a) J. Wu, A. Fechtenkötter, J. Gauss, M. D. Watson, M. Kastler, C. Fechtenkötter, M. Wagner, K. Müllen, *J. Am. Chem. Soc.* **2004**, *126*, 11311-11321; b) J. Wu, M. D. Watson, N. Tchebotareva, Z. Wang, K. Müllen, *J. Org. Chem.* **2004**, *69*, 8194-8204; c) M. Kastler, W. Pisula, D. Wasserfallen, T. Pakula, K. Müllen, *J. Am. Chem. Soc.* **2005**, *127*, 4286-4296.
14. a) C. D. Simpson, J. Wu, M. D. Watson, K. Müllen, *J. Mater. Chem.* **2004**, *14*, 494-504; b) J. Wu, M. Baumgarten, M. G. Debije, J. M. Warman, K. Müllen, *Angew. Chem. Int. Ed.* **2004**, *43*, 5331-5335; *Angew. Chem.* **2004**, *116*, 5445-5449; c) A. M. Van de Craats, N. Stutzmann, O. Bunk, M. M. Nielsen, M. D. Watson, K. Müllen, H. D. Chanzy, H. Siringhaus, R. H. Friend, *Adv. Mater.* **2003**, *15*, 495-499.
15. D. Wasserfallen, I. Fischbach, N. Chebotareva, M. Kastler, W. Pisula, F. Jäckel, M. D. Watson, I. Schnell, J. P. Rabe, H. W. Spiess, K. Müllen, *Adv. Funct. Mater.* **2005**, *15*, 1585-1594.
16. a) L. J. Prins, D. N. Reinhoudt, P. Timmerman, *Angew. Chem. Int. Ed.* **2001**, *40*, 2382-2426; *Angew. Chem.* **2001**, *113*, 2446-2492; b) K. J. C. van Bommel, A. Friggeri, S. Shinkai, *Angew. Chem. Int. Ed.* **2003**, *42*, 980-999; *Angew. Chem.* **2003**, *115*, 1010-1030.
17. a) M. Shirakawa, S. Kawano, N. Fujita, K. Sada, S. Shinkai, *J. Org. Chem.* **2003**, *68*, 5037-5044; b) J. J. Van Gorp, J. A. J. M. Vekemans, E. W. Meijer, *J. Am. Chem. Soc.* **2002**, *124*, 14759-14769; c) S. -i. Tamaru, M. Nakamura, M. Takeuchi, S. Shinkai, *Org. Lett.* **2001**, *3*, 3631-3634; d) K. Sugiyasu, N. Fujita, S. Shinkai, *Angew. Chem. Int. Ed.* **2004**, *43*, 1229-1233; *Angew. Chem.* **2004**, *116*, 1249-1253.
18. a) S. Ito, M. Wehmeier, J. D. Brand, C. Kübel, R. Epsch, J. P. Rabe, K. Müllen, *Chem. Eur. J.* **2000**, *6*, 4327-4342. b) A. Fechtenkötter, N. Tchebotareva, M. D. Watson, K. Müllen, *Tetrahedron* **2001**, *57*, 3769-3783.
19. J. Zhang, G. Podoprygorina, V. Brusko, V. Böhmer, A. Janshoff, *Chem. Mater.* **2005**, *17*, 2290-2297.
20. a) W. J. Schutte, M. Sluyters-Rehbach, J. H. Sluyters, *J. Phys. Chem.* **1993**, *97*, 6069-6073; b) K. Kano, K. Fukuda, H. Wakami, R. Nishiyabu, R. F. Pasternack, *J. Am. Chem. Soc.* **2000**, *122*, 7494-7502; c) A. Tracz, J. K. Jeszka, M. D. Watson, W. Pisula, K. Müllen, T. Pakula, *J. Am. Chem. Soc.* **2003**, *125*, 1682-1683.
21. F. J. M. Hoeben, P. Jonkheijm, E. W. Meijer, A. P. H. J. Schenning, *Chem. Rev.* **2005**, *105*, 1491-1546.
22. R. B. Prince, J. G. Saven, P. G. Wolynes, J. S. Moore, *J. Am. Chem. Soc.* **1999**, *121*, 3114-3121.

23. a) J. Coril, D. A. dos Santos, D. Beljonne, Z. Shuai, J. L. Brédas, *Semiconducting Polymers G*. Hadziioannou, P. F. van Huttern, Eds. Wiley,-VCH: Weinheim, **2000**, p 88; b) F. D. Lewis, T. Wu, E. L. Burch, D. M. Bassani, J-S. Yang, S. Schneider, W. Jäger, R. L. Letsinger, *J. Am. Chem. Soc.* **1995**, *117*, 8785-8792; c) K. Liang, M. S. Farahat, J. Perlstein, K. -Y. Law, D. G. Whitten, *J. Am. Chem. Soc.* **1997**, *119*, 830-831.
24. E. Clar, *Polycyclic Hydrocarbons* Academic: New York, **1964**.
25. a) F. Dörr, *DMS UV ATLAS of Organic Compounds*, Vol. III, Verlag Chemie, Weinheim; Butterworths, London, **1966**, p. E1; b) J. Beier, Ph.D. Thesis University of Bayreuth, Germany, **2000**, p. 50-62.
26. a) G.A. Jeffrey, in *An Introduction to Hydrogen Bonding* Oxford University Press: Oxford, **1997**;
b) S. H. Gellman, G. P. Dado, G. B. Liang, B. R. Adams, *J. Am. Chem. Soc.* **1991**, *113*, 1164-1173;
and the references cited there.
27. a) S. Kawano, S. Tamaru, N. Fujita, S. Shinkai, *Chem. Eur. J.* **2004**, *10*, 343-351; b) H. J. Tian, K. Inoue, K. Yoza, T. Ishi-i, S. Shinkai, *Chem. Lett.* **1998**, 871-872; c) L. Lu, M. Cocker, R. E. Bachman, R. G. Weiss, *Langmuir*, **2000**, *16*, 20-34.
28. a) R. M. Silverstein, G. C. Bassler, T. C. Morrill, *Spectrometric Identification of Organic Compounds 5th Ed*, John Wiley & Sons, Inc. **1991**, p. 122; b) N.B. Colthup, L. H. Daly, S. E. Wiberley, *Introduction to Infrared and Raman Spectroscopy 3rd Ed*, Academic Press, Inc., **1990**, p. 320.
29. a) X. Dou, W. Pisula, J. Wu, G. J. Bodwell, K. Müllen, *Chem. Eur. J.* **2008**, *14*, 240-249; b) X. Dou, Master Thesis University of Mainz, **2004**.
30. a) K. Hanabusa, C. Koto, M. Kimura, H. Shirai, A. Kakehi, *Chem. Lett.* **1997**, 429-430; b) R. I. Gearba, M. Lehmann, J. Levin, D. A. Ivanov, M. H. J. Koch, J. Barberá, M. G. Debije, J. Piris, Y. H. Geerts, *Adv. Mater.* **2003**, *15*, 1614-1618.
31. DSC experiments were performed from -100 to 250 °C with a heating/cooling rate of 10 °C/min.
32. 2D WAXS experiments were performed with the fibers that were mechanically extruded at 150 °C; for details: a) I. Fischbach, T. Pakula, P. Minkin, A. Fechtenkötter, K. Müllen, H. W. Spiess, *J. Phys. Chem. B* **2002**, *106*, 6408-6418; b) W. Pisula, Z. Tomovic, C. Simpson, M. Kastler, T. Pakula, K. Müllen, *Chem. Mater.* **2005**, *17*, 4296-4303.
33. S. Chandrasekhar, B. K. Sadashiva, K. A. Suresh, *Pramana* **1977**, *9*, 471-480.

34. a) X. Zhao, Y. L. Chang, F. W. Fowler, J. W. Lauher, *J. Am. Chem. Soc.* **1990**, *112*, 6627-6634; b) M. C. Etter, Z. Urbanczyk-Lipkowska, M. Zia-Ebrahimi, T. W. Panunto, *J. Am. Chem. Soc.* **1990**, *112*, 8415-8426; c) J. van Esch, S. De Feyter, R. M. Kellogg, F. De Schryver, B. L. Feringa, *Chem. Eur. J.* **1997**, *3*, 1238-1243; d) L. E. Orgel, *Reviews of Modern Physics* **1959**, *31*, 100-102; e) M. L. Bushey, A. Hwang, P. W. Stephens, C. Nuckolls, *Angew. Chem. Int. Ed.* **2002**, *41*, 2828-2831; *Angew. Chem.* **2002**, *114*, 2952-2955; f) M. P. Lightfoot, F. S. Mair, R. G. Pritchard, J. E. Warren, *Chem. Commun.* **1999**, 1945-1946; g) S. Tamaru, S. Uchino, M. Takeuchi, M. Ikeda, T. Hatano, S. Shinkai, *Tetrahedron Letters* **2002**, *43*, 3751-3755.
35. The inverted gel was slowly heated in a water bath from 25 °C with a speed of 0.5 °C/min. The temperature, at which the gel started to flow, was recorded as T_g .
36. The xerogels were prepared by dropping the formed gel onto a pre-cleaned silicon wafer under the corresponding solvent atmosphere and the solvent was slowly evaporated.
37. a) J. P. Hill, W. Jin, A. Kosaka, T. Fukushima, H. Ichihara, T. Shimomura, K. Ito, T. Hashizume, N. Ishii, T. Aida, *Science* **2004**, *304*, 1481-1483; b) W. Jin, T. Fukushima, M. Niki, A. Kosaka, N. Ishii, T. Aida, *PNAS* **2005**, *102*, 10801-10806.
38. F. Würthner, B. Hanke, M. Lysetska, G. Lambright, G. S. Harms, *Org. Lett.* **2005**, *7*, 967-970.
39. a) V. K. Praveen, S. J. George, R. Varghese, C. Vijayakumar, A. Ajayaghosh, *J. Am. Chem. Soc.* **2006**, *128*, 7542-7550; b) F. S. Schoonbeek, J. H. van Esch, B. Wegewijs, D. B. A. Rep, M. P. de Hass, T. M. Klapwijk, R. M. Kellogg, B. L. Feringa, *Angew. Chem. Int. Ed.* **1999**, *38*, 1393-1397; *Angew. Chem.* **1999**, *111*, 1486-1490.

7 Synthesis and Self-assembly of Mono-Functionalized HBC Derivatives on Surfaces – Approaching Molecular Devices

One of the major issues in electronics is the construction, measurement, and understanding of the current-voltage response of an electronic circuit. Traditional metal-molecule-metal junctions comprises thin molecular films between macroscopic metal electrodes.¹⁻⁵ As the semiconductor technology nowadays leads us making devices of ever smaller size, the transistors approach the size of molecules. Thereby the single-molecule transport junctions are currently the subject of substantial experimental, theoretical, and technological interests.⁶⁻¹⁰ These nanoscale molecular interconnects act as novel chemical environments, such as switches, gates or transport elements, providing new molecular functions, and may help to minimize the computer circuit dimensions and enhance their performance. Molecular conductors can be subdivided into single-molecule junctions and molecular monolayer junctions.¹⁰ The molecules in the junctions can be divided into rigid, linear structures such as carbon nanotubes and silicon nanowires^{11, 12} and soft, molecular organic materials like 1,4-benzene dithiol,^{1, 13} copper phthalocyanine,¹⁴ or 4,4'-biphenyl dithiol.^{12, 15} In the latter case, small (nano-ampere) currents are recorded between two electrodes, one of which, the measuring tip, is not bonded to the molecular component, and the other one is connected with the molecules through either strong interactions, e.g. $\pi - \pi$ interactions between highly oriented pyrolytic graphite (HOPG) and PAH molecules,¹⁶ or anchor group, e.g. sulfur with Au electrode in most scanning probe measurements.¹⁰ As an important member of organic semiconductor materials, hexa-*peri*-hexabenzocoronenes (HBCs) show distinct self-assembly propensity and outstanding charge carrier mobility. Thus, they, are selected as active component for such kind of measurements. Rabe, *et. al.* reported a prototype single-molecular chemical-field-effect transistor (single-molecular CFET) based on HBC

molecules, whereas the current-voltage characteristics through HBC moiety is tuned via the formation of charge-transfer complex between guest molecules and the substituents of HBC molecules at a solid-liquid interface.⁸ Rampi *et. al.* studied the electron transport across the self-assembled monolayers (SAMs) formed by HBC molecules bearing thiol anchor group between a metal-molecules-metal junction.^{6,7}

Although HBC molecules have displayed excellent properties, there is still space to improve their performance in these devices by designing new derivatives carrying special functionalities. In the case of single-molecular CFET, the irreversible complex formation and the consequent switching are due to the diffusion of an electron donor in the solution towards the acceptor at the interface, which is a random and slow process. By the incorporation of a functional group which changes the dipole moment when being exposed to irradiation, transistor switching processes will be accelerated and better controlled. A suitable candidate is azobenzene, which can be switched optically from a *trans*- to *cis*-conformation^{17, 18} with a dipole moment change from 0 D (in *trans*-conformation) to 3 D (in *cis*-form).¹⁹⁻²⁶ Two azobenzene substituted HBC derivatives were synthesized and their light induced *trans* / *cis* transformation was studied in solution by UV/Vis absorption and NMR spectroscopic techniques. The molecular monolayers were characterized by scanning tunneling microscopy (STM) at a liquid-solid interface.

In the aforementioned investigations of current metal-molecules-metal junctions, which are based on the SAMs formed by HBCs,^{6,7} the tether between anchor group and the rigid aromatic core is undecyl 1,2-dithiolane-3-pentanoate. The linker group contains 17 carbon atoms. The long, soft, insulating spacer hinders the conductivity of the monolayers. For a desired metal-molecules-metal junction, an upright orientation of the molecular plane with respect to the metal electrode surface is required.⁷ Following this concept, two HBC molecules containing sulfur anchor groups were designed. The anchor groups are connected to the HBC moiety by either a short stiff ethynylbenzyl tether or a short flexible propyl spacer. Both compounds were deposited on the Au (111) electrodes and the formed SAMs were investigated by STM and Reflection Absorption Infrared Spectroscopy (RAIR).

7.1 Azobenzene substituted HBCs

7.1.1 Synthesis

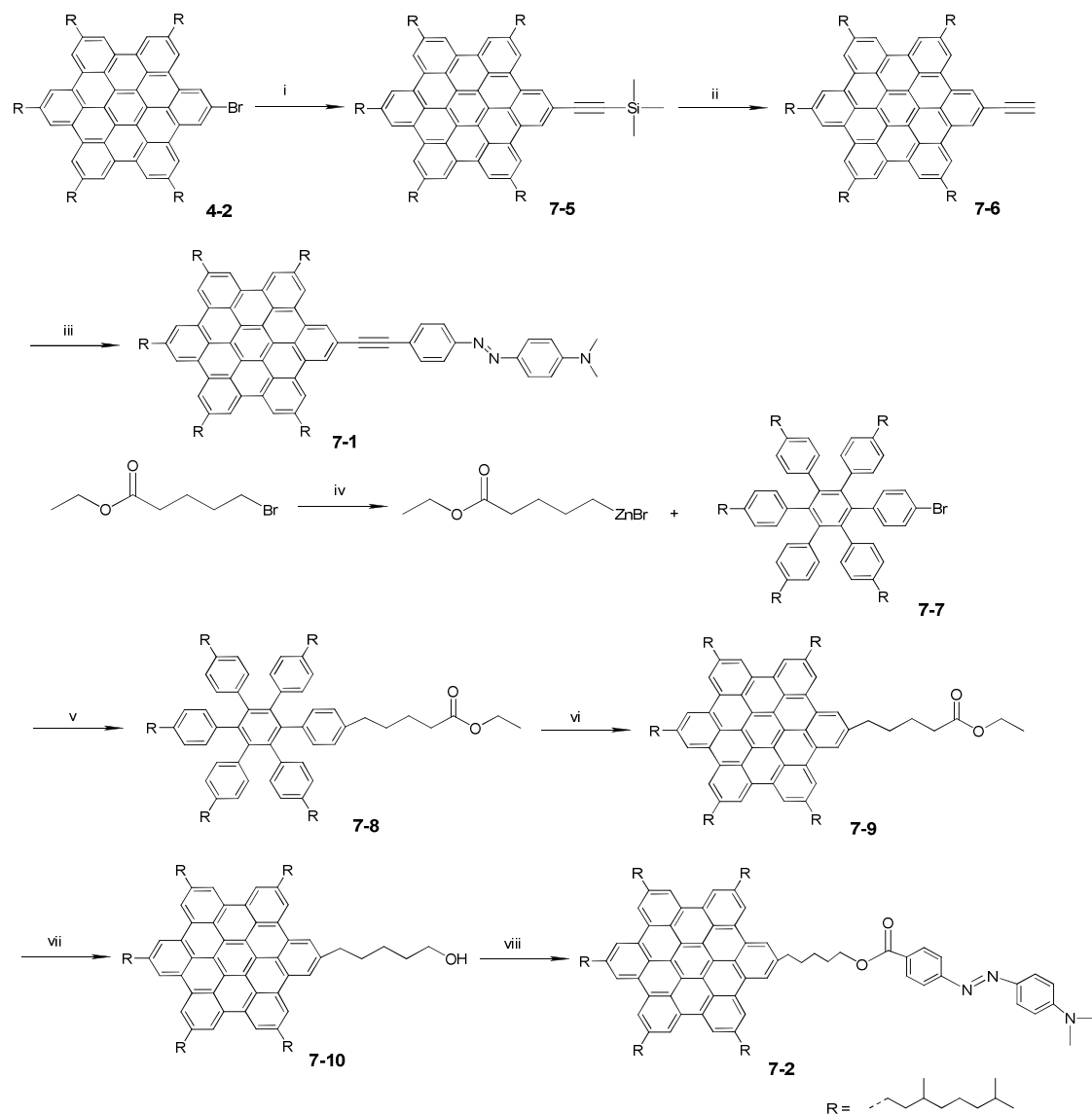


Figure 7-1. Synthesis of compound 7-1 and 7-2; i) trimethylsilyl acetylene, Pd(PPh₃)₄, CuI, Et₃N / THF (1/1), 80 °C, 15 h, 76%; ii) Bu₄NF, THF, r.t., 20 min, 97%; iii) 4'-iodo-4-dimethylamino azobenzene, Pd(PPh₃)₄, CuI, Et₃N / THF (1/1), 50 °C, 16 h, 46%; iv) Zn, DMA, 80 °C, 16 h; v) Pd(dppf)Cl₂, THF, 50 °C, 18 h, 91%; vi) FeCl₃, CH₃NO₂, DCM, r.t., 20 min, 88%; vii) LiAlH₄, THF, r.t., 12 h, 92%; viii) 4-dimethylaminoazobenzene-4'-carboxylic acid, EDC, DMAP, Et₃N, THF, r.t., 3 d, 41%.

The 4-*N,N*-dimethylamino azobenzene group was connected to the HBC core by either a rigid ethynyl bridge (**7-1**) or a soft alkyl ester linker (**7-2**). The synthetic route is depicted in Figure 7-1. Compound **7-6** was synthesized via a palladium catalyzed Hagihara-Sonogashira coupling between the mono-bromo HBC (**4-2**) and trimethylsilyl acetylene (in 76% yield) followed by the treatment with tetra-*n*-butyl ammonium fluoride in THF to remove the silyl protection group (in 97% yield).²⁷ Compound **7-6** was then reacted with 4-iodo-4'-dimethylamino azobenzene via Hagihara-Sonogashira coupling reaction affording compound **7-1** in 46% yield. To prepare compound **7-2**, a methyl valerate was first attached to the mono-bromo HPB (**7-7**)²⁸ via a Negishi coupling reaction²⁹ giving **7-8** in 91% yield. After an intramolecular Scholl reaction, the methyl valerate substituted HBC (**7-9**) was obtained as yellow powder in a yield of 88%. The ester group in **7-9** was then quantitatively reduced to a hydroxyl group with LiAlH₄ in THF. An EDC ester coupling reaction between the 5-hydroxyl pentyl HBC (**7-10**) and 4'-dimethylamino azobenzene-4'-carboxylic acid led to the final compound **7-2** in 41% yield. All these compounds were characterized with mass spectrometry, ¹H- and ¹³C-NMR spectroscopy. The MALDI-TOF spectra of the two destination compounds (**7-1** and **7-2**) show exact molecular mass peak and perfect coincident isotope distribution pattern with calculated one (Figure 7-2).

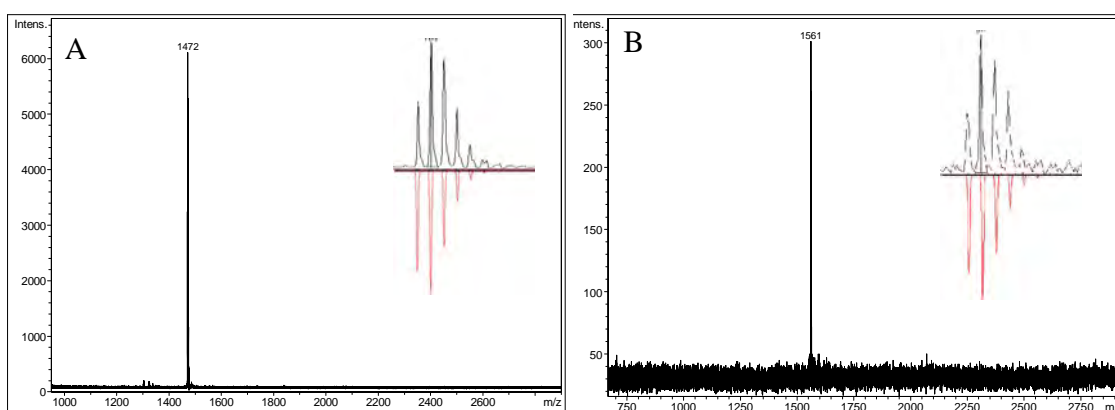


Figure 7-2. MALDI-TOF mass spectra of A) **7-1** and B) **7-2**, measured with TCNQ as matrix and isotope distribution patterns (insets); red: calculated value.

7.1.2 *trans*- / *cis*- Photoisomerization of 7-1 and 7-2 in solution

Generally, the isomerization of azobenzene derivatives can be induced by light in both directions or by heat from *cis* to *trans* conformation. In the UV/Vis absorption spectrum of the *trans*-isomer, a weak, low-energy band is identified, which is well separated from the intense, higher-energy bands.¹⁸ The less intensive low energy band is attributed to the transition from a non-bonding orbital to the anti-bonding orbital ($n \rightarrow \pi^*$), which is forbidden under the C_{2h} symmetry of *trans*-form azobenzene.³⁰⁻³² In the spectrum of *cis*-azobenzene, the $n \rightarrow \pi^*$ transition is allowed under a symmetry of C_{2v} . The intensity of the $n \rightarrow \pi^*$ band is consequently much higher than that of *trans*-azobenzene. And the variation of this band is widely used to track the *trans* / *cis* isomerization. The $\pi \rightarrow \pi^*$ band in *trans*-azobenzene shows an intense absorption peak and is situated in the higher energy region.³¹ Therefore, the *trans* to *cis* isomerization normally manifests itself as diminishing the $\pi \rightarrow \pi^*$ band in the shorter wavelength region and increasing the $n \rightarrow \pi^*$ band intensity in the longer wavelength region. Figure 7-3 shows the photoisomerization of 7-1 and 7-2, which differs from each other by the rigidity of the linker group leading to different molecular packing on surfaces (see STM studies). The isomerization test between *trans*- to *cis*-conformation in solution was performed by the irradiating the corresponding solution with UV light and tracked by UV/Vis absorption spectroscopy.

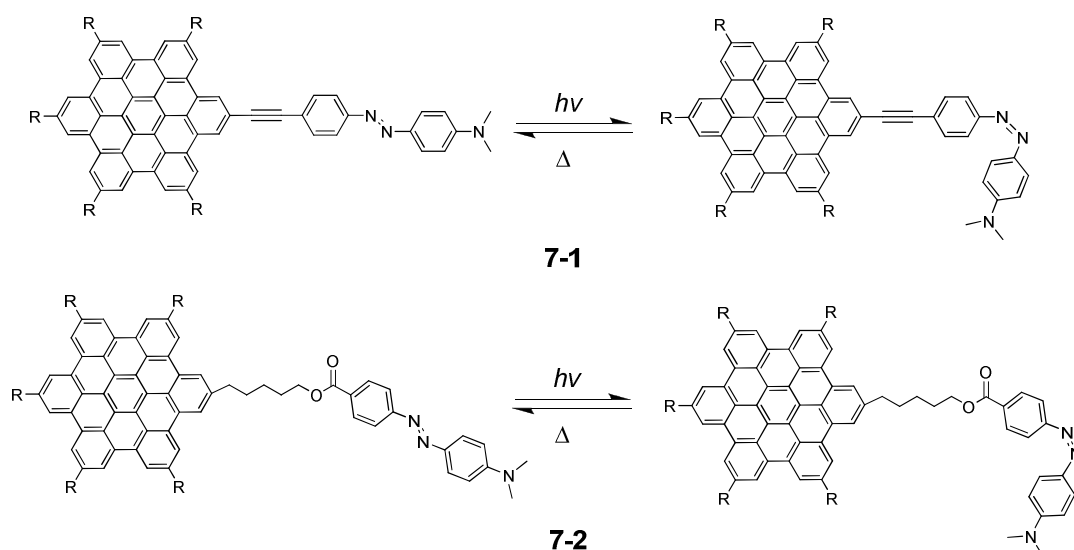


Figure 7-3. Photo-induced *trans* / *cis* isomerization of 1 and 2.

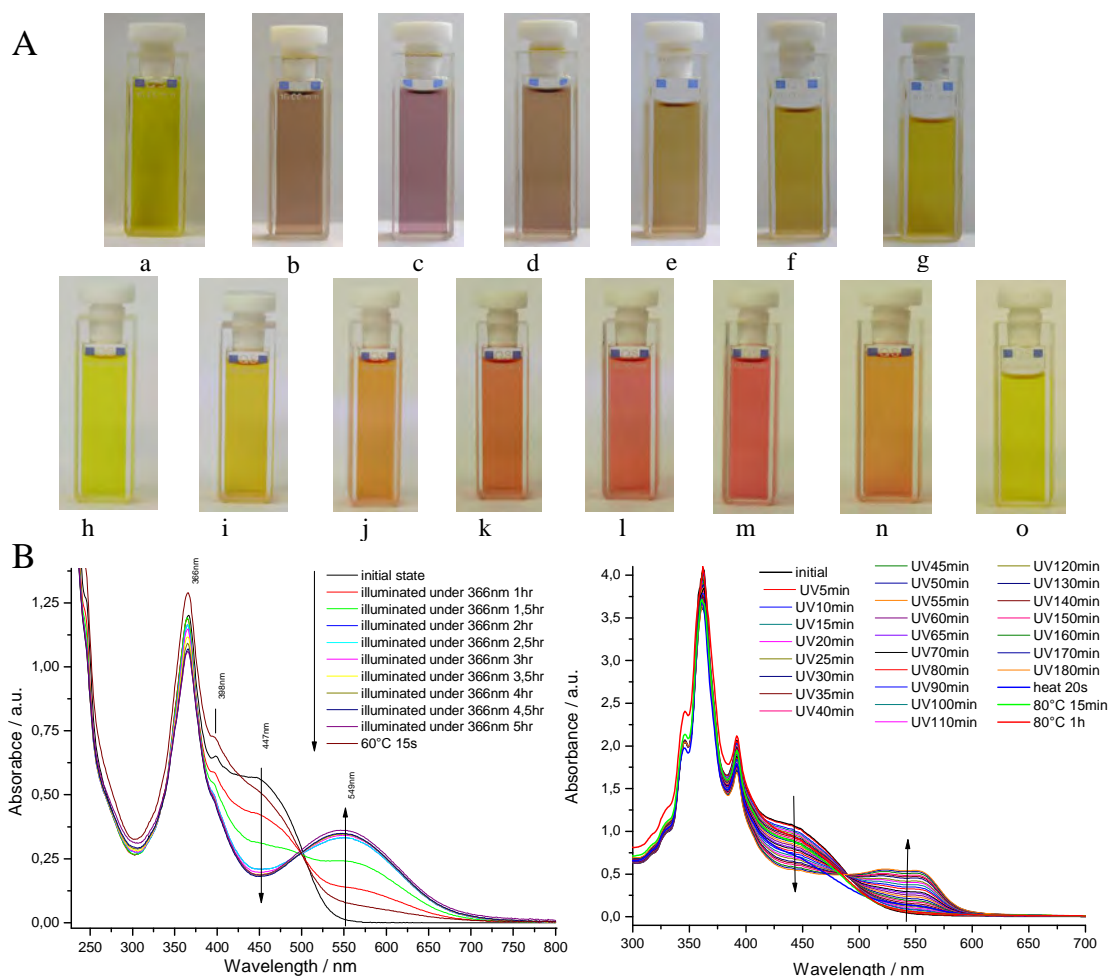


Figure 7-4. A) Pictures of 7-1 and 7-2 solutions; a – g, 7-1 in DCM solution (initial state (a), irradiated for 90 min (b), 180 min (c), heated at 40 °C for 20 s (d), 10 min (e); reflux at 60 °C for 10 s (f), 30 s (g)); h – o, 7-2 in chloroform solution (initial state (h), irradiated for 30 min (i), 70 min (j), 120 min (k), 150 min (l) 180 min (m) reflux at 80 °C for 20 s (n), 15 min (o)); B) UV light (366 nm) irradiation time dependent UV/Vis absorption spectra of 7-1 (left, measured in 1.02×10^{-5} M DCM solution) and 7-2 (right, measured in 3.20×10^{-5} M chloroform solution), arrow directs the increasement of irradiation time.

When illuminating the solutions with UV light (366 nm), the *trans*-isomers of 7-1 and 7-2 gradually convert to the *cis*-isomers accompanied by a color change from yellow to purple. The *trans*-isomers can be fully recovered by simply heating afterwards (Figure 7-4A). Prolonging the UV irradiation time, the UV/Vis absorption spectra of both 7-1 and 7-2 show nearly unchanged absorption bands from the HBC moieties around 366 nm and a gradual decrease of the $\pi \rightarrow \pi^*$ transition band (around 450 nm, from *trans*-isomer) with an increase of the $n \rightarrow \pi^*$ transition band (around 550 nm, from *cis*-isomer, Figure 7-4B). Thermal isomerization from the photogenerated *cis*- to *trans*-conformer was

realized by heating within seconds.¹⁷ The isosbestic points (slightly below 500 nm) indicate a clean switching between these two states under these conditions.

Similar studies were also carried out in 1,2,4-trichlorobenzene solutions for these two compounds. Instead of using 366 nm UV light, these solutions were illuminated by a light with a 450 nm wavelength, which corresponds to the $\pi - \pi^*$ transition of the *trans*-isomer. The same experimental results were obtained, where the *trans*-band diminishes with an increase of the *cis*-band around 552 nm with irradiation time and the *trans*-isomer can be recovered by heating (Figure 7-5). The light-induced isomerization at different incident light (366 nm and 450 nm) indicates a strong electronic coupling between the HBC and azobenzene moieties since the excitation of the former, which fluoresces above 450 nm,³³ switches the latter.

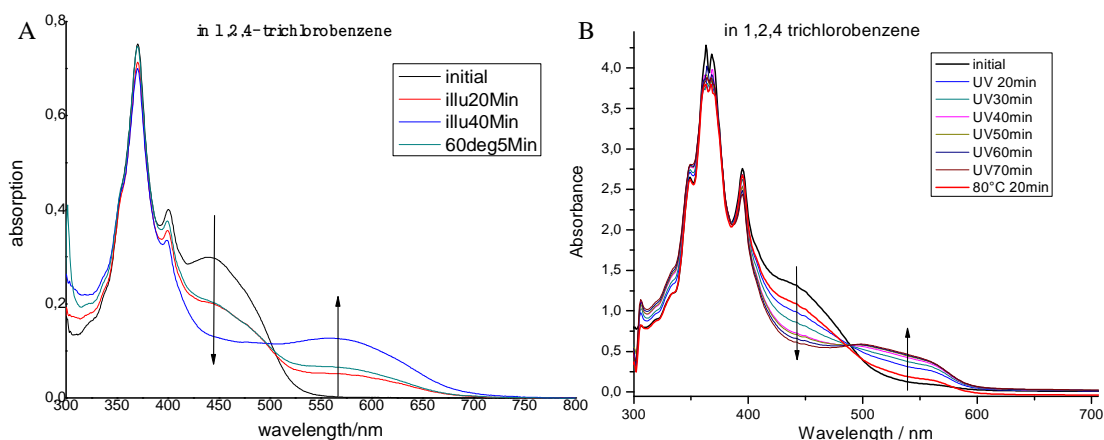


Figure 7-5. Optical absorption spectra of A) 7-1 in 1.0×10^{-5} M 1,2,4-trichlorobenzene solution and B) 7-2 in 3.2×10^{-5} M 1,2,4-trichlorobenzene solution; irradiated at 450 nm.

$^1\text{H-NMR}$ spectroscopy reveals the chemically different environment of protons. The change of molecular conformation, which causes a chemical environmental difference for a specific hydrogen atom, and consequently manifests itself as a variation of chemical shift. The conformation change of these compounds was studied with $^1\text{H-NMR}$ techniques. Figure 7-6 shows the change of the $^1\text{H-NMR}$ spectra of compound 7-1 in $\text{THF-}d_8$ solution upon the irradiation with the 366 nm UV light. It is obvious that the intensity of the doublet peak at 6.88 ppm decreases accompanied by the appearance of four new doublets with increasing intensity at 8.61, 7.86, 7.09 and 6.69 ppm (Figure 7-

7B). Additionally, another new peak at 3.03 ppm appears, which originates from a splitting of the dimethyl amino group (Figure 7-6).

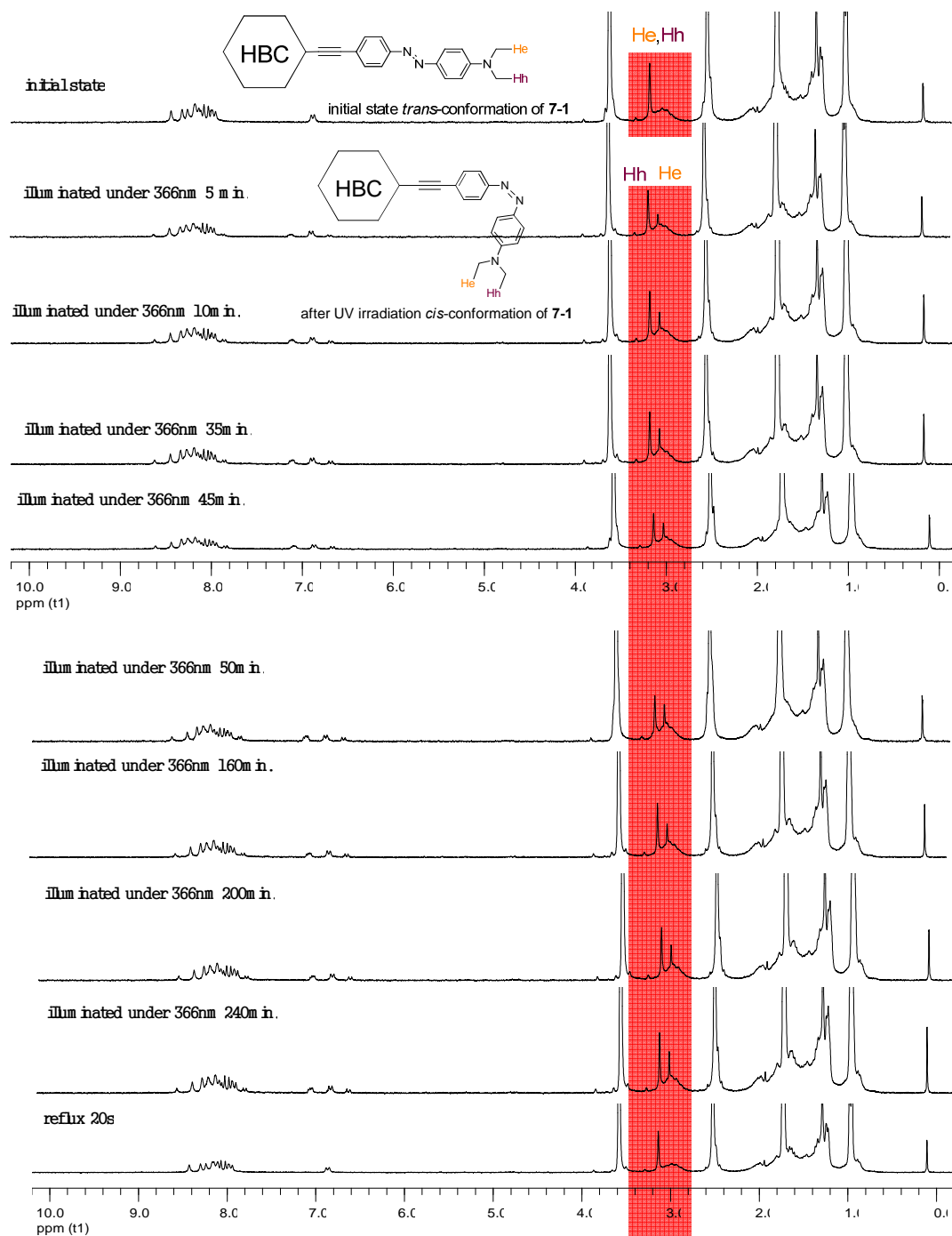


Figure 7-6. $^1\text{H-NMR}$ spectra of 7-1 (measured in $\text{THF-}d_8$ at r.t., 250 MHz) with an irradiation of UV light (366 nm) up to 4 h and subsequent heating (reflux 20s).

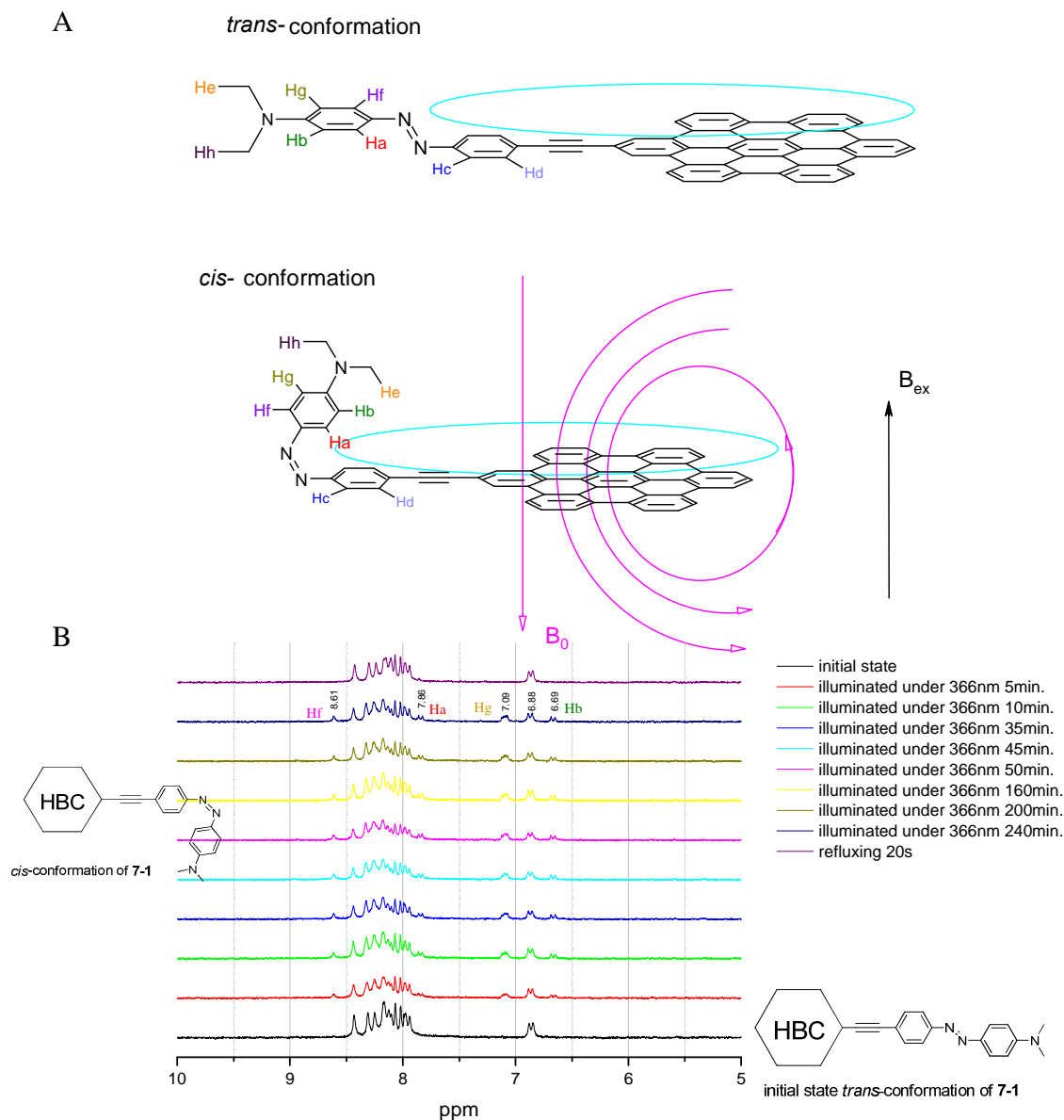


Figure 7-7. A) schematic represents of the shielding and de-shielding effect from aromatic π electron ring in *cis*-conformation of 7-1; B) Enlarged aromatic region (5 to 10 ppm) of the ^1H -NMR spectra of 7-1.

The appearance of new peaks at 8.61, 7.86, 7.09 and 6.69 ppm (Figure 7-7B) indicates a non-planar molecular geometry and can be elucidated by the influence of the adjacent anisotropy magnetic cone created by the HBC π electrons on these specific protons (Figure 7-7A). When the molecule is in a *trans*-conformation, the chemical environment of Hb and Hg is identical giving rise to a doublet signal at 6.88 ppm. Upon illumination with UV light, the molecule changes from the *trans*-conformation to the *cis*-

one, in which the outer benzene ring bends out of the molecular plane and the chemical environment of **Hb** differs from the one of **Hg** due to the rigid ethynyl linker between HBC and azobenzene moieties. In this conformation, **Hb** is on top of the π electron ring of the aromatic core and **Hg** extends out of the π electron ring. In the external magnetic field B_{ex} , the π electron ring generates a weak local magnetic field B_0 , the direction of which is opposite to the external one (B_{ex}) inside the π electron ring and parallel to that of B_{ex} outside the π electron ring. **Hb** is thus situated in a weaker magnetic field ($B_{ex}-B_0$) and **Hg** is in a stronger magnetic field ($B_{ex}+B_0$). Consequently, the signal of **Hb** is up-shifted to 6.69 ppm while **Hg** is down-shifted to 7.09 ppm (Figure 7-7B). In a similar scenario, the chemically environmentally identical **Ha** and **Hf** (in *trans*-conformation) differentiate from each other in the *cis*-conformer giving rise to two new signals at 7.86 and 8.61 ppm. Similarly, the resonance signal of **He** and **Hh** at 3.14 ppm (in *trans*-conformation) are also split into two signals at 3.03 and 3.14 ppm in *cis*-conformation (Figure 7-6). (Notice, the broad peak, which overlaps the signal of **He**, originates from the α -protons of the alkyl substituents.)

The same experiments were also carried out for the compound **7-2**, the azobenzene moiety of which is linked to HBC core via a relatively long soft alkyl chain. Unlike **7-1**, no obvious change was observed in the $^1\text{H-NMR}$ spectra of **7-2**, which implies that the chemical environments of these protons on the azobenzene group in **7-2** are not apparently affected by the molecular conformation change. This can be elucidated by the different freedom of azobenzene moieties in these two kinds of compounds. In the case of **7-1**, the bridge between azobenzene and HBC core is rigid and short. The chemical environments of these protons attached to the azobenzene group are, to a large extent, influenced by the π -electron rings on the HBC aromatic core, which results in the obvious degenerations of the protons on the azobenzene part during the molecular *trans* / *cis* isomerization. Since the linker in **7-2** is relatively long and flexible, the azobenzene group has a much higher freedom and the chemical environment change of the protons is not as apparent as these in **7-1** showing nearly identical $^1\text{H-NMR}$ spectra for both *trans*- and *cis*-isomers.

These results imply that the **7-1** possesses a rigid non-planar molecular geometry in the *cis*-conformation and the azobenzene group in **7-2** suspends around the HBC aromatic core like other alkyl substituents. It turns out that the non-planarity in the *cis*-isomer of **7-1** obstructs the surface adsorption process in the later STM investigation and hinders its future application in the single-molecular CFET devices.

7.1.3 STM studies at solid-liquid interfaces

The STM experiments were performed by Min Ai and Nikolai Severin from Prof. Dr. Rabe's group at Humboldt University, Berlin. The packing behaviors of both **7-1** and **7-2** were studied by STM at the interface between an organic solution and the basal plane of HOPG under ambient conditions.^{34, 35} Both compounds align flatly on the HOPG surface in a so-called "face-on" mode.

Figure 7-8 displays the *in situ* STM images of the *trans*-isomers of **7-1** (measured between a solution of 1,2,4-trichlorobenzene and the basal plane of HOPG) showing a double row pattern with grain boundaries, which reflects the three-fold symmetry of the substrate (Figure 7-8A). The high resolution image reveals a nanophase corresponding to the azobenzene moieties with their rigid linker between the flat lying HBC cores (Figure 7-8B). However, no *cis*-isomer was visualized at the interface after irradiating the solution with 450 nm light for more than hour (the formation of *cis*-isomer in this condition has been proved by UV/Vis absorption spectroscopic studies, SECTION 7.1.2).

The dimerized structure has been observed for small azobenzene derivatives both on Cu (110)³⁶ and Au (111)^{37, 38} surfaces by STM under ultra-high vacuum (UHV). The formation of such a dimer supramolecular organization in **7-1** can be attributed to the intermolecular Ph-H...N hydrogen bonds, which is the same as the situation of other azobenzene derivatives.³⁶⁻³⁹ Due to the non-planarity of the *cis*-isomer, the *cis*-azobenzene derivatives are seldom detected by STM. Thereby, they were only observed on Au (111)^{37, 39} but not on Cu (110)³⁶ surfaces. In the UHV-STM images of *cis*-isomers, few *cis*-isomeric azobenzene molecules are surrounded by a large amount *trans*-isomers in a well-ordered array showing bright protrusions, which represents the upward pointing phenyl ring.³⁷ As concluded from ¹H-NMR studies, the *cis*-isomer of **7-1** also has a non-

planar molecular geometry, which subsequently explains the failure of observing *cis*-isomer of **7-1** at solid-liquid interfaces.

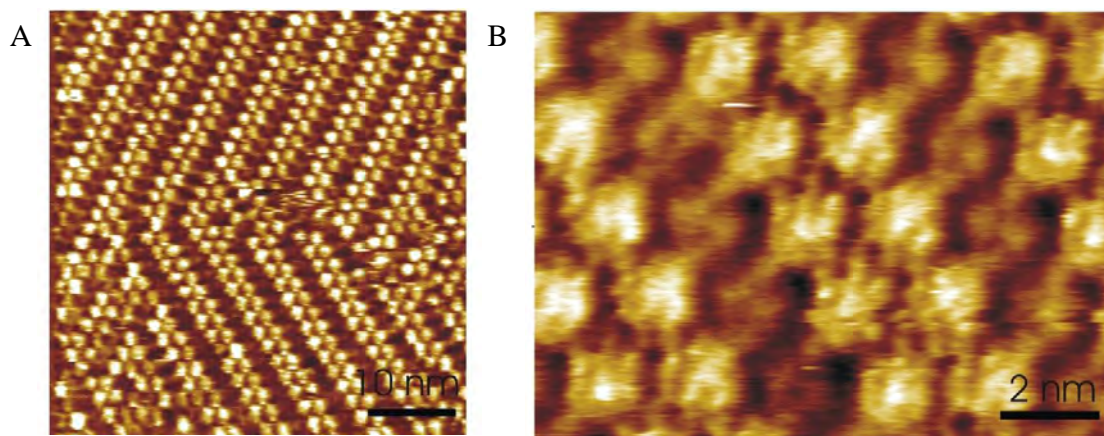


Figure 7-8. STM images of monolayer formed by **7-1** at the interface between an organic solution in 1,2,4-trichlorobenzene and the basal plane of HOPG; A) characteristic double row pattern with grain boundaries; B) in larger scale.

The *in situ* STM images of the monolayer formed by **7-2** are shown in Figure 7-9 (measured between a solution of octylbenzene and the basal plane of HOPG). In contrast to compound **7-1**, which forms a dimer superstructure, the molecule of **7-2** self-assembles into a less ordered pattern. Since the azobenzene moiety is connected with HBC core via a soft alkyl spacer, it possesses much higher mobility in contrast to the one in **7-1**. Therefore, the HBC cores are able to pack together in a denser fashion, like other hexa-alkylated HBC,^{40, 41} with the azobenzene moieties being dissolved in the liquid phase and suspending around in the liquid phase as presumed in SECTION 7.1.2. The compact ordered molecular islands in the middle area prove that the azobenzene substituents are bent up into the supernatant solution (Figure 7-9B).

It is expected that the azobenzene group can freely undergo *trans/cis* isomerization in the liquid phase without disturbance of the packing of HBC moieties at the interface. The change of the dipole moment in azobenzene part induced by the *trans/cis* isomerization might consequently adjust the scanning tunnelling current in STS investigation and guarantees **7-2** as a good candidate in the single-molecular CFET application. The further investigation in this field is currently undergoing.

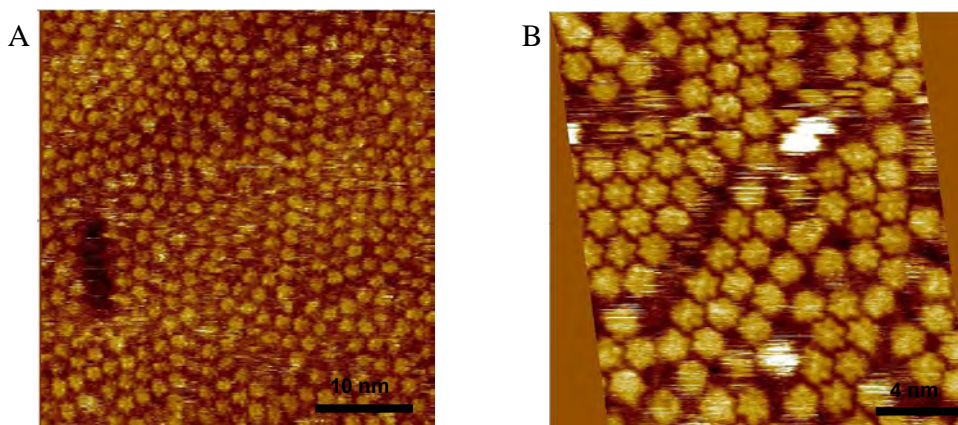


Figure 7-9. STM images of a monolayer formed by 7-2 at the interface between an octylbenzene solution and the basal plane of HOPG; A) in big length scale; B) enlarged area.

7.2 Mono-sulfur substituted HBCs and their self-assembly on Au (111) surface

7.2.1 Synthesis

Mono-sulfur substituted HBC derivatives were made by linking a thiol acetyl group to the HBC core by either a short rigid ethynyl-benzyl bridge (7-3) or a short flexible propyl chain (7-4). The synthetic route is depicted in Figure 7-10. 7-3 was prepared via a Hagihara-Sonogashira coupling reaction between the mono-ethynyl HBC (7-6) and 4-iodo-benzyl thiolacetate (7-11)⁴² in a yield of 41%. To synthesize 7-4, HBC substituted by a mono-ethyl propionate (7-12) was first prepared via a palladium-catalyzed Negishi coupling reaction between the mono-bromo HBC (4-2) and a freshly prepared Zink reagent²⁹ in 42% yield. The ester group was subsequently reduced to a hydroxyl group by LiAlH₄ in THF affording a mono-hydroxyl HBC (7-13, 97% yield). The hydroxyl group in the resulting 7-13 was then converted into a mesylate group with methanesulfonyl chloride followed by a nucleophilic substitution with potassium thioacetate leading to 7-4 in 56% yield. The structure of these compounds was fully characterized by mass spectrometry, ¹H- and ¹³C-NMR spectroscopy.

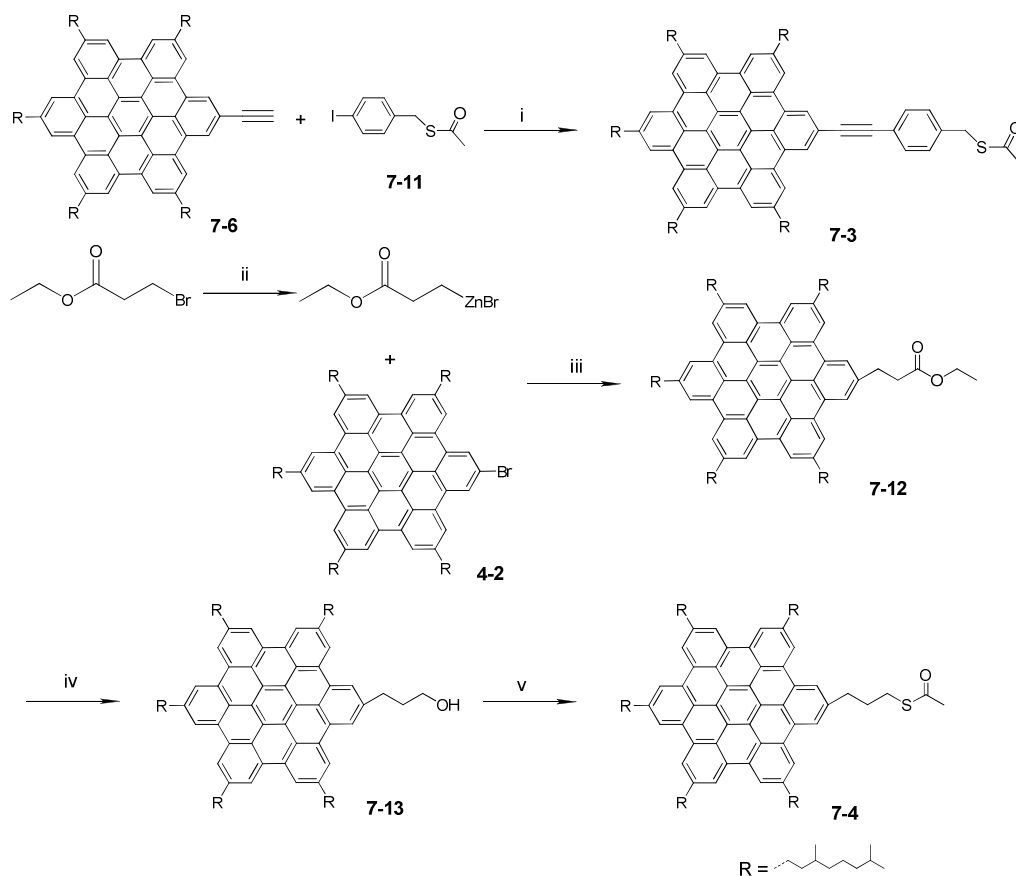


Figure 7-10. Synthesis of compound 7-3 and 7-4; i) Pd(PPh₃)₄, CuI, Et₃N / THF (1/1), 80 °C, 15 h, 41%; ii) Zn, DMA, 80 °C, 16 h; iii) Pd(dppf)Cl₂, THF, 50 °C, 2 d, 42%; iv) LiAlH₄, THF, r.t., 12 h, 98%; v) methanesulfonyl chloride, potassium thioacetate, DMF / THF (1:1), 45 °C, 6 d, 56%.

Since the sulfur-carbon bond is weak, the molecule is easily fragmented by the intensive laser beam during the desorption process of the mass spectrometric measurements. Figure 7-11 demonstrates the change of the MALDI-TOF mass spectra upon different incident laser beam power. With higher laser beam power, lots of molecular fragments were detected. The relative intensity of these peaks decreases with the incident laser beam power, which implies that these peaks arise rather from fragmentation than impurities. Additionally, these peaks can be assigned to specific fragments based on the rupture of the S-C bond. For instance, the *m/z* peak at 1369 g/mol represents the cleavage of acetyl group; the peak at 1352 g/mol might be a result of the cleavage of thioacetate group followed by an addition of one methyl group; a fragment,

which has lost a thiolacetate, gives rise to a peak at 1337 g/mol; the one located at 1323 g/mol may be due to the cleavage of the phenyl-methylene bond.

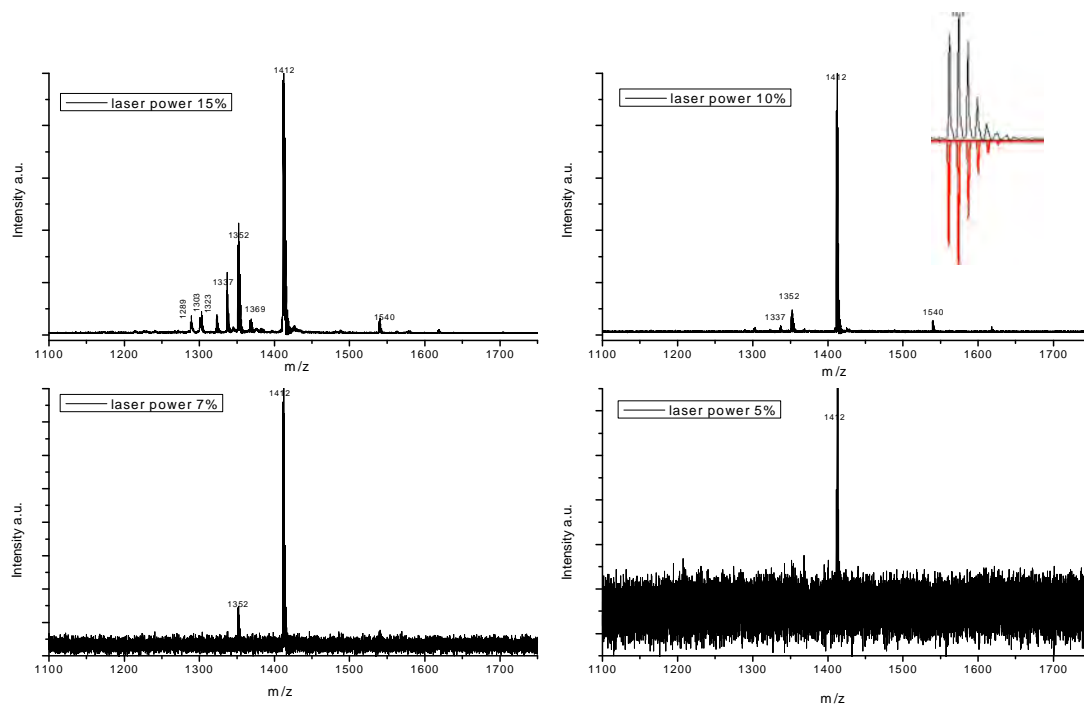


Figure 7-11. MALDI-TOF Mass spectra of 7-3 under different incident laser beam power; inset: isotope distribution (black: measured and red: calculated).

The structure of 7-3 and 7-4 was unambiguously proven by the $^1\text{H-NMR}$ spectroscopy. In the spectrum of 7-3 (Figure 7-12A), six signals of aromatic protons on the HBC core are well resolved in the range from 8.64 to 8.35 ppm. The signal of the proton next to the ethynyl group (He) is downfield-shifted to 8.64 ppm in contrast to the rest due to the enhanced shielding effect of the ethynyl neighbor. The two phenyl protons on the benzyl group (Hc and Hd) give rise to two doublets at 7.56 and 7.85 ppm, respectively. The singlet at 4.31 ppm is assigned to the methylene proton (Hb). The three acetyl group signals are downfield-shifted to 2.44 ppm in comparison to the remaining methyl protons in the alkyl substituents. The ten α -protons of the alkyl chains lead to a broad peak at 3.06 ppm. In the case of 7-4 (Figure 7-12B), the 12 aromatic proton signals merge to three singlets around 8.20 ppm and the signals of the two alkyl α -protons (Hd) in the propyl thiolacetate chain are separated from the those in the alkyl substituents (Hf)

giving a triplet at 3.14 ppm. The methyl proton signal of the acetyl group in **7-4** (**He**) appears as a single peak at 2.44 ppm at the same position as these in **7-3**.

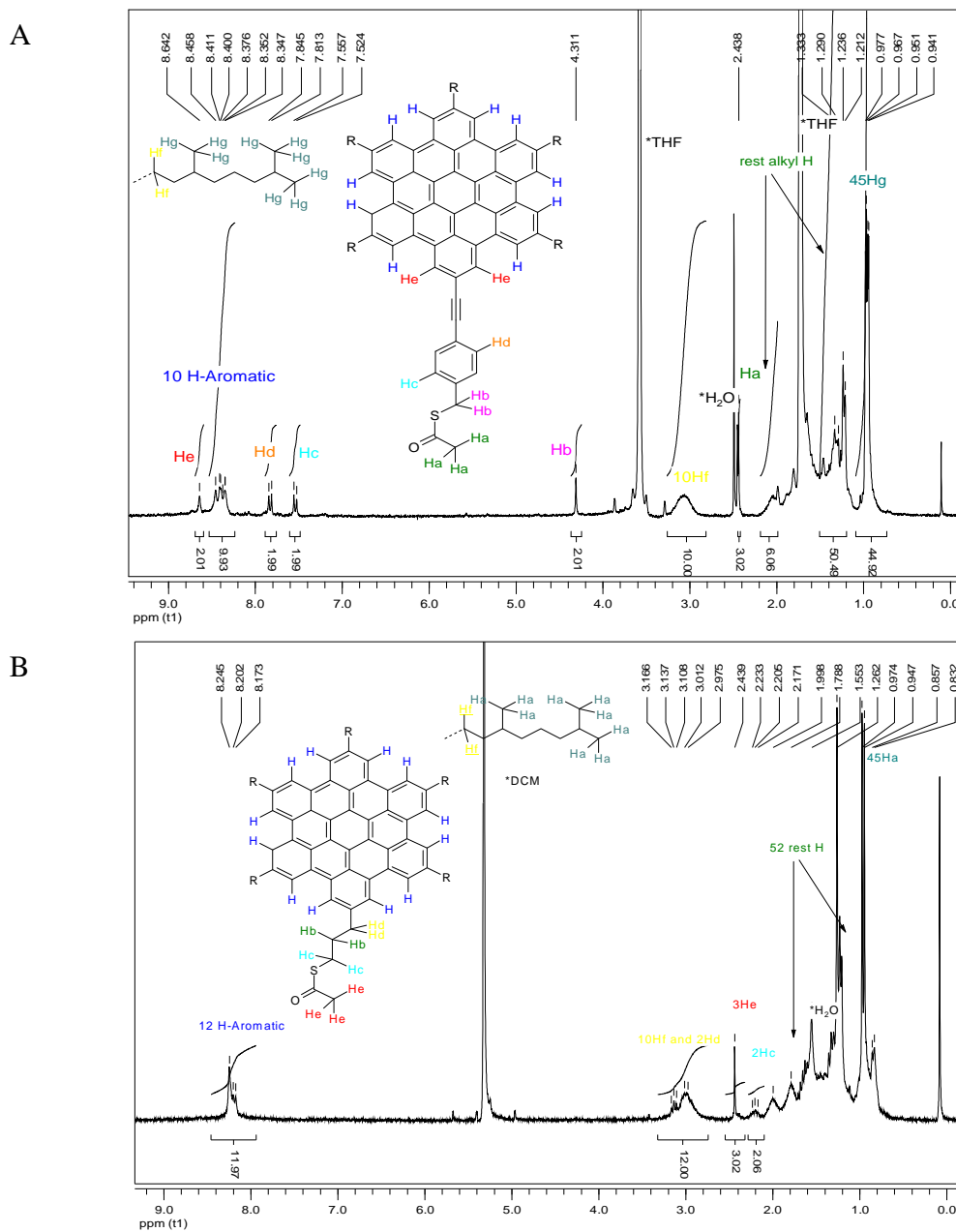


Figure 7-12. $^1\text{H-NMR}$ spectra of A) **7-3** (250 MHz, $\text{THF-}d_8$, r.t.) and B) **7-4** (250 MHz, CD_2Cl_2 , r.t.).

7.2.2 STM studies of the self-assembled monolayer on Au (111) electrode

The studies of the self-assembled monolayers (SAMs) on Au (111) electrodes formed by **7-3** and **7-4** were performed by Asif Bashir from Prof. Dr. Wöll's group at Rhur-Universität, Bochum. The SAMs of **7-3** and **7-4** on Au (111) surfaces were prepared by immersing the Au (111) substrates into an ethanol solution (0.1 μM) of either **7-3** or **7-4** for 18 – 24 h followed by rinsing with acetone, ethanol and drying under N_2 stream. The STM measurements were conducted either in ambient condition or in vacuum.

7.2.2.1 Monolayer formed by 7-3

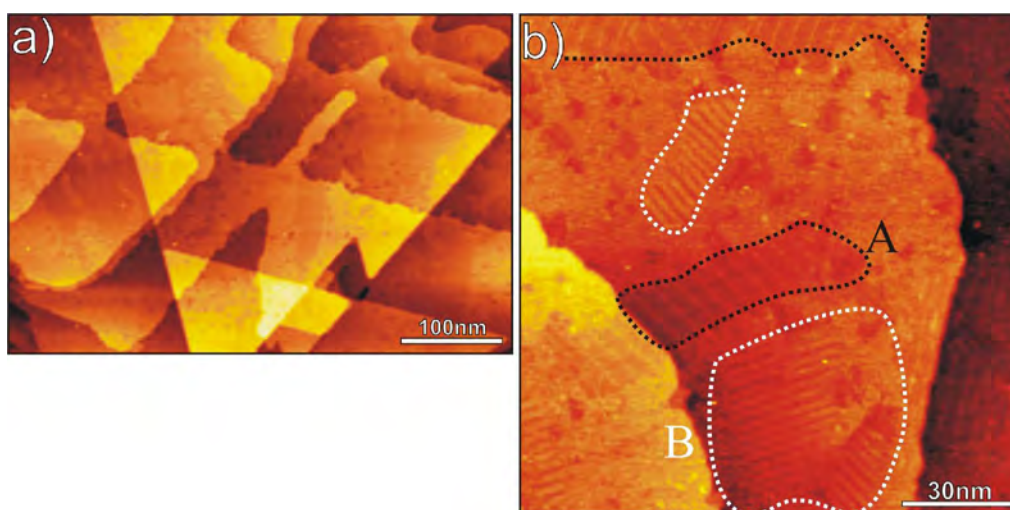


Figure 7-13. Constant-current STM images of the SAMs on Au(111) formed by **7-3** (SAMs prepared at 273 K, measured in ambient); a) large scale image showing the presence of characteristic close step edges of the substrate; b) small scale image with the coexistent phases labeled as A and B; tunneling parameters: $U_t=500$ mV, $I_t=100$ pA.

Figure 7-13 shows the STM images of a large area of a SAM on Au (111) surface formed by **7-3**. Interestingly, the depressions or etch pits, which have been reported in the studies of the SAMs on Au (111) surfaces formed by alkynethiol or aromatic thiols (biphenyl, terphenyl) compounds,⁴³⁻⁴⁶ were not found. This is probably due to the lower surface strain on the gold surface after the adsorption of the bulky discotic molecules. In analogy to the bulk state, **7-3** forms long range well-ordered columnar structures with equidistance. Two kinds of relatively small domains with lateral dimensions of 50 – 100 nm are observed, which are respectively marked as phase A and B in Figure 7-13b. The

adlayer is stable for a repeated scanning (on the same sample area) over 1 – 2 hours without any morphological changes. Phase A reveals a similar packing as in the one of 7-4 (see SECTION 7.2.2.2). In phase B, the molecules are self-assembled into a denser pattern with a unit cell size half of the one in phase A (see below).

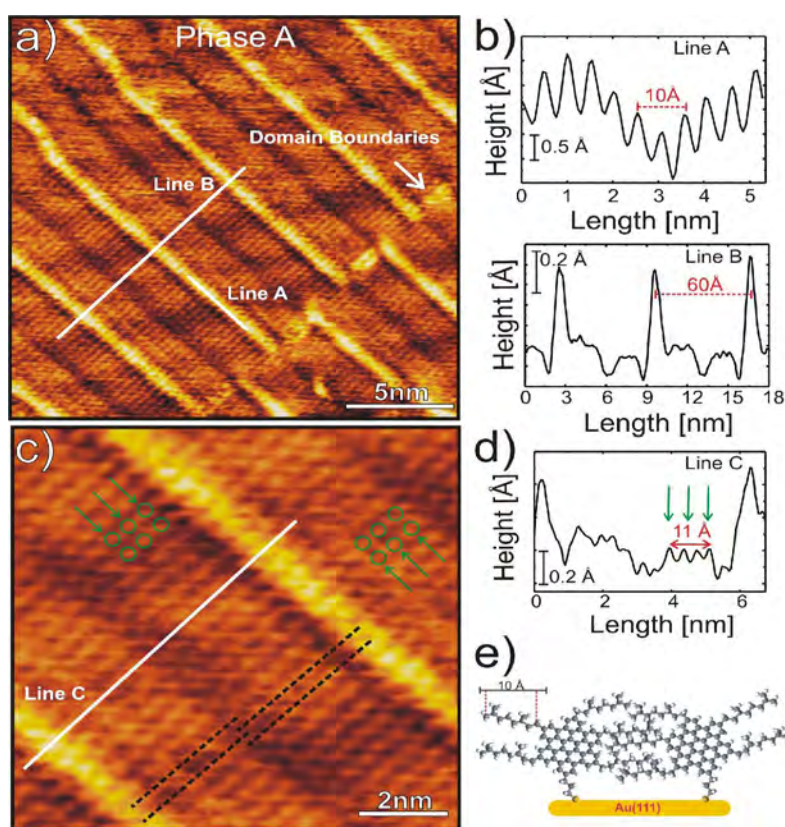


Figure 7-14. Constant-current STM data of the SAMs on Au (111) (phase A) formed by 7-3 (SAMs prepared at 273 K, measured in ambient); a) single domain of phase A with domain boundary being indicated by a white arrow; b) cross-sectional height profiles along lines A and B (labeled in (a)), revealing corrugation periodicity; c) high-resolution STM micrograph with a substructure labeled by green arrows and circles; d) cross-sectional height profiles along line C (marked in (c)); e) schematic sketch of the substructure found in the lamella shown in (d); tunneling parameters: $U_t=500$ mV, $I_t=100$ pA.

The STM micrograph presented in Figure 7-14a demonstrates the equidistant columnar structure in phase A. The boundary of the domain is indicated with a white arrow. Figure 7-14b shows the cross-sectional height profiles along the intra- and inter-columnar direction (labeled as lines A and line B in Figure 7-14a). Line A and B define the rectangular unit cell with a length of 5.0 ± 0.5 Å and 59.5 ± 0.5 Å respectively. By scanning between the two adjacent columns (along line C, labeled in Figure 7-14c), it is

determined that the molecules are oriented parallel to the $\langle 11\bar{2} \rangle$ azimuth and perpendicular to the close packed $\langle 1\bar{1}0 \rangle$ direction of the underlying gold substrate. A close inspection of the STM data further reveals the presence of well defined substructures (marked with green circles and arrows in Figure 7-14c) between the regularly spaced rows. The distance of these substructures is calculated to be 11 Å from the corresponding height profile graph (Figure 7-14d), which is correlated to the alkyl substituent in good agreement with a theoretical value for a 3,7-dimethyloctyl substituent (9.6 Å, Figure 7-14e).⁴⁷

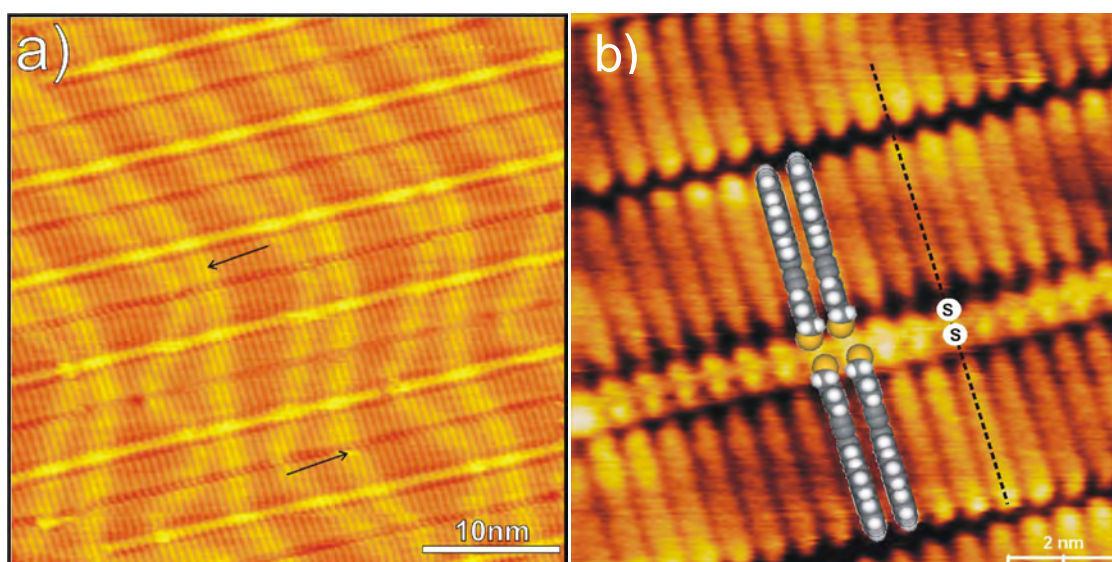


Figure 7-15. Constant-current STM images obtained from the SAMs on Au (111) (phase A) formed by 7-3 (SAMs prepared at 273 K, measured in UHV); a) in large scale, black arrows indicate the characteristic herringbone reconstruction direction; b) in small scale with schematic molecular structure; tunneling parameters: $U_t=500$ mV, $I_t=100$ pA.

In order to achieve the detailed structure information about the SAMs, another SAMs of 7-3 were scanned in ultra-high vacuum (UHV). The large scale constant-current STM image (Figure 7-15a) displays the formation of well-ordered long range columnar alignment on the Au (111) substrate driven by $\pi - \pi$ interactions. The stiff discotic HBC molecules and even the sulfur groups are individually recognized in the high-resolution STM image (as indicated with schematic structure in 7-15b). It is clear that two HBC columns pair together with sulfur groups next to each other in a so-called “edge-on” fashion. As indicated by the black arrow in Figure 7-15a, the long distance columnar

pattern reflects the well-known herringbone arrangement of the gold substrate. The periodicities along inter- and intra-columnar directions amount $5.0 \pm 0.5 \text{ \AA}$ and $59.5 \pm 0.5 \text{ \AA}$ in congruence with the values measured in ambient condition. It is also worth to notice that the intermolecular distance along a single column ($5.0 \pm 0.5 \text{ \AA}$) is slightly larger than a typical cofacial $\pi-\pi$ stacking value (3.6 \AA),⁴⁸ which implies a tilted packing mode with respect to the normal direction of the gold substrate (see SECTION 7.2.2.2). A two-dimensional rectangular unit cell ($a = 60 \text{ \AA}$, $b = 1 \text{ \AA}$) is subsequently derived with respect to the unit cell of Au (111) substrate containing two HBC molecules per unit cell (Figure 7-16).

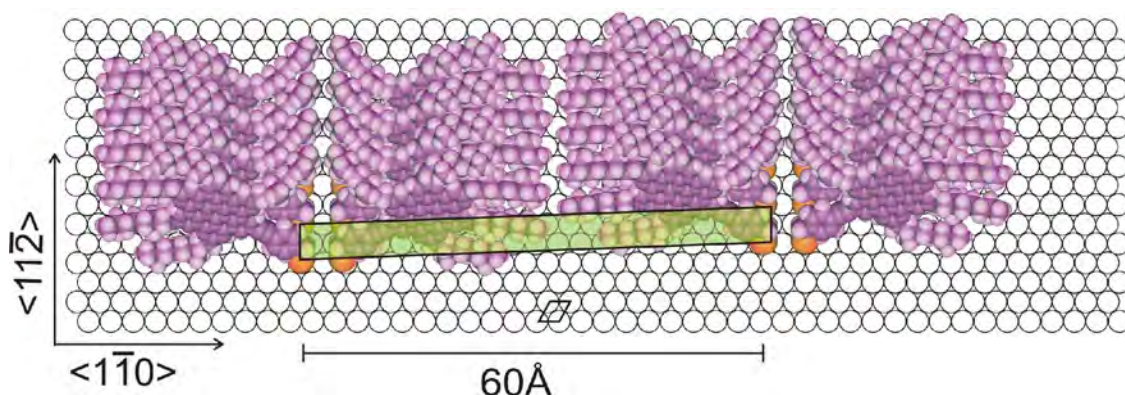


Figure 7-16. Top view of the structural model for phase A in the SAMs on Au (111) formed by 7-3; the unit cell is marked by a large rectangle; the unit cell of Au (111) is marked by a small oblique.

The SAMs formed by 7-3 in phase B are packed in a similar fashion as the one in phase A showing an equidistant columnar structure (Figure 7-17a). However, the distance between these paired columnar structures ($28.0 \pm 0.2 \text{ \AA}$) was found to be almost half of the one in phase A implying denser packing. This indicates stronger overlapping between the adjacent HBC molecules and a more upright oriented molecular configuration (Figure 7-17b). Interestingly, the cross-sectional height profile (Figure 7-17c) along line A (labeled in Figure 7-17b) reveals a substructure with an interval of $5.0 \pm 0.2 \text{ \AA}$, which further proves the existence of overlap between the adjacent molecules.

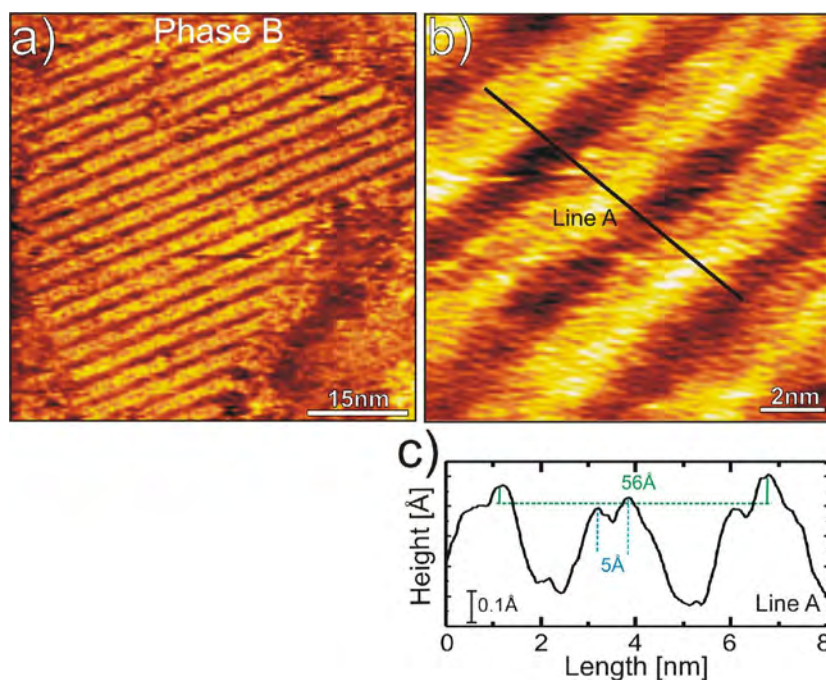


Figure 7-17. Constant-current STM images of the SAMs on Au (111) (phase B) formed by 7-3 (SAMs prepared at 273 K, measured in ambient; a) a single domain of phase B; b) the densely packed equidistant columnar structure; c) the cross-sectional height profiles along line A (labeled in (b)) revealing a corrugation periodicity of $28 \pm 0.2 \text{ \AA}$; tunneling parameters: $U_t=500 \text{ mV}$, $I_t=100 \text{ pA}$.

The periodicities along the inter-columnar direction and intra-columnar direction in phase B account $28.0 \pm 0.2 \text{ \AA}$ and $5.0 \pm 0.2 \text{ \AA}$, which spans a rectangular unit cell as $a = 28 \text{ \AA}$, $b = 1 \text{ \AA}$ containing two HBC molecules per unit cell (Figure 7-18). (Discussion see the end of Section 7.2.2.2)

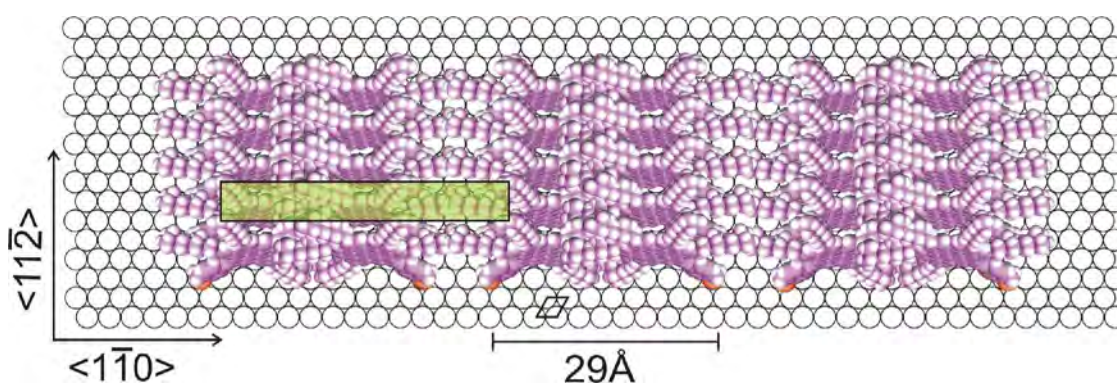


Figure 7-18. Top view of the structural model for phase B in the SAMs on Au (111) formed by 7-3; the unit cell is marked by a large rectangle; the unit cell of Au (111) is marked by a small oblique.

7.2.2.2 Monolayer formed by 7-4

Different from the SAMs formed by 7-3, the adlayer formed by 7-4 shows a homogeneous long range columnar orientation with a height of 2.4 Å (Figure 7-19). Remarkably, the size of the domain, which corresponds to a lateral dimension of 150 – 200 nm shown in Figure 7-19a, extends over the whole gold terrace without being affected by the step edges on the substrate (Figure 7-19a). The homogeneity of the SAMs over the whole substrate probably benefits from the soft propyl tether, which gives the molecule higher flexibility to construct such a large monolayer. A close inspection of these STM data further discloses that the domains of 7-4 SAMs are rotated by 120° relative to each other reflecting the symmetry of the underneath gold substrate. The adlayer formed by 7-4 is also as robust as the one formed by 7-3 with no apparent morphological changes during a 1 – 2 hours repeated scanning on the same sample area. The high-resolution STM image clearly depicts that the HBC columnar structure is oriented parallel to the $\langle 11\bar{2} \rangle$ azimuth and perpendicular to the $\langle 1\bar{1}0 \rangle$ direction of the gold substrate like the SAMs formed by 7-3 (Figure 7-19b). The periodicity within a single column was determined to be 5.0 ± 0.5 Å and the distance between two adjacent columns amounts 59.5 ± 0.5 Å (line I,II,III and line A marked in Figure 7-19b). The height profiles along single columns (line I,II,III) also reveal a slight mismatch between two consecutive columnar rows (Figure 7-19d), which consequently constitute a substructure in the height profiles of the “inter-columnar” scanning (along line A, Figure 7-19c). This indicates that there exist not only the intra-columnar molecular interactions but also inter-columnar correlations between the molecules in neighboring columns. Based on the STM data, a rectangular unit cell of the SAMs, containing two HBC molecules per unit cell, was deduced with respect to the unit cell of Au (111) substrate: $a = 60$ Å, $b = 1$ Å. A proposed structural model is schematized with a unit cell of 59.5 Å \times 5.0 Å in Figure 7-19e.

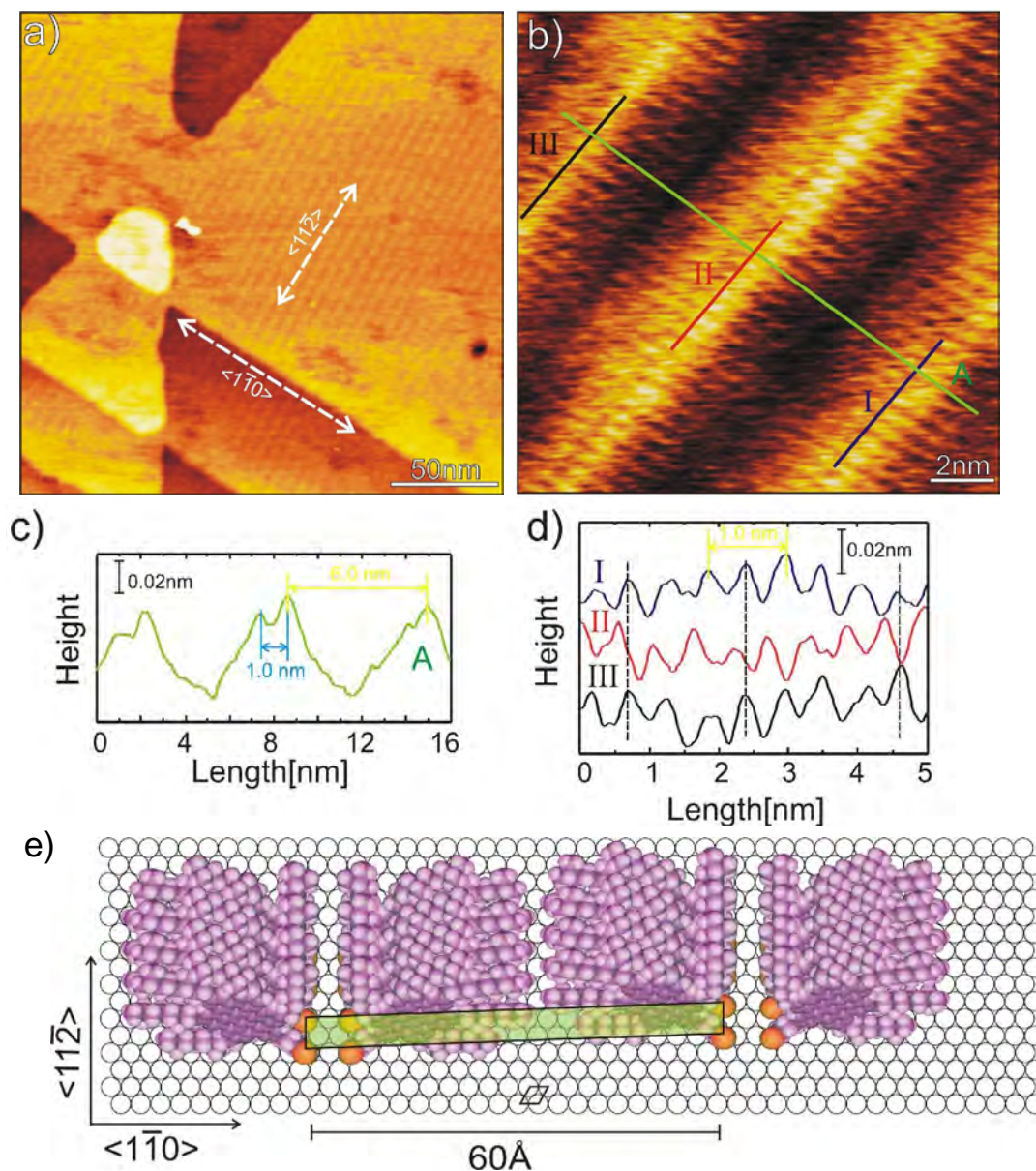


Figure 7-19. STM data and structural model of the SAMs on Au(111) formed by 7-4, measured in ambient; a) large scale STM micrograph, inset: structural formula of 7-4; b) high resolution STM image with line scans (black, red, blue showing the periodicity along a single column and green showing the periodicity perpendicular to column direction); c,d) height profiles of line scans; e) schematic represent of structural model, the unit cell of SAMs is marked by the large rectangle and the unit cell of the substrate is marked by an oblique; tunneling parameters: $U_t=500$ mV, $I_t=100$ pA.

As mentioned above, the periodicity along a single column (5.0 ± 0.5 Å) in both SAMs formed by 7-3 and 7-4 is c.a. 1.4 Å larger than a typical cofacial $\pi - \pi$ stacking distance. Reflection absorption infrared spectroscopy (RAIR) is used to characterize the SAMs and the molecular orientation can be evaluated according to a so-called surface

selection rule.⁴⁹ This method compares the difference between the out-of-plane vibrational bands (having the transition dipole moment perpendicular to molecular axis) and the in-plane vibrational bands (having the transition dipole moment parallel to molecular axis). To measure the RAIR spectrum, a SAM of **7-4** was prepared on a polycrystalline gold substrate. The low and high frequency regions of the RAIR spectra of the SAM are shown in Figure 7-20A with a spectrum obtained in the bulk state (measured with KBr pellet). The lower frequency region shows complicated vibrational absorptions, which are related to the complex vibration modes of the aromatic core. Moreover, a new band at 734 cm^{-1} appears in the RAIR spectra representing an out-of-plane vibration of the aromatic hydrocarbons.⁴⁹ This can be used to derive the qualitative information about the aromatic molecular orientation. For a perpendicularly oriented HBC molecule (with respect to the surface normal), the intensity of the out-of-plane vibration absorption is zero since the corresponding transition dipole moment is oriented parallel to the surface.⁴⁹ The presence of such a band at 734 cm^{-1} in Figure 7-20, therefore, indicates a tilted molecular orientation from the surface normal, which has been predicted with the results obtained from STM studies. The quantitative analysis of the molecular orientation by this method is difficult due to the complicated aromatic vibrations.

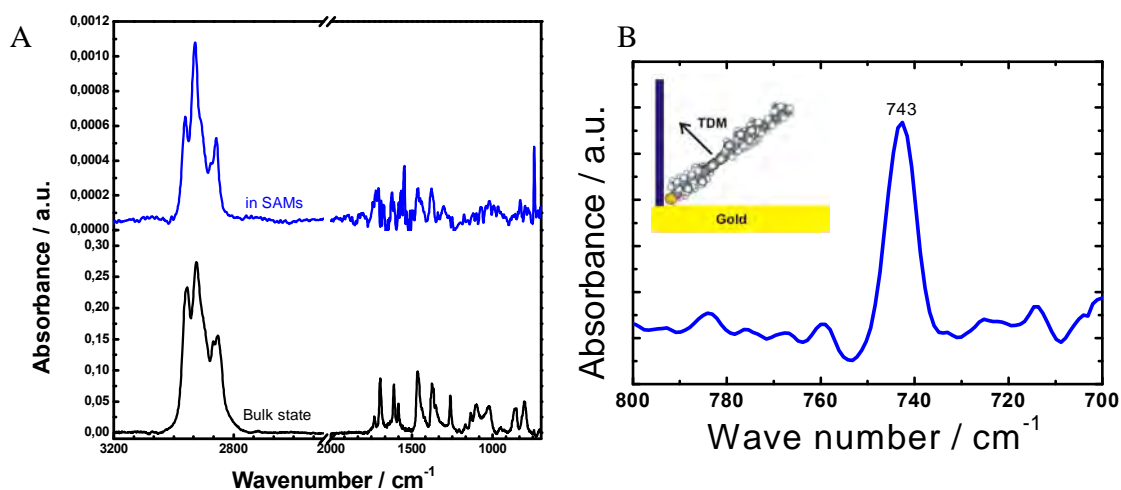


Figure 7-20. A) RAIR spectra of **7-4** in bulk (KBr) and in SAMs on Au (111) surfaces; B) enlarged area around 743 cm^{-1} ; inset: schematic represent of molecular orientation (TDM: transition dipole moment).

The strong $\pi - \pi$ interactions between HBC moieties assist the self-assembly of both compounds into robust monolayers with long range columnar supramolecular structures.

The HBC molecular plane packs in an upright fashion in both cases, which fulfills the required molecular orientation for the SAMs-based electronic devices. The tilting of the molecule discs, with respect to the normal plane of the Au (111) surface, clearly manifests the strong $\pi - \pi$ interactions between adjacent HBC molecules.⁴⁸

In the previous studies on the charge transport across a single molecule, it has been demonstrated that the charge transport ability depends on the details of the interaction between the molecule and the metallic electrodes, such as the anchoring groups^{50, 51} and the molecular orientation⁵²⁻⁵⁴. Silva, R. *et al* pointed out that the simple benzene-1,4 dithiol (BDT) molecule has the lowest adsorption energy, which gives rise to the most relevant charge transport, with either a perpendicular or close to a perpendicular configuration relative to the Au surface.²⁴ However, the obtained experimental conductance for BDT molecules coincidences with the calculated value^{52, 55} for these molecules having their phenyl rings closer to being parallel to the surface.²⁴ The achievement of desired molecular upright orientation relies on a sufficiently high surface coverage. By the comparison of the SAMs formed by **7-3** and **7-4** with these of their analogous compound **7-14**,⁵⁶ which contains a much longer soft alkyl tether between thiol anchor group and HBC core (Figure 7-21), the SAMs formed by **7-3** and **7-4** possess much more homogeneous and highly condensed features. This will ambiguously improve the molecular conductance of HBC derivatives in electronic devices.

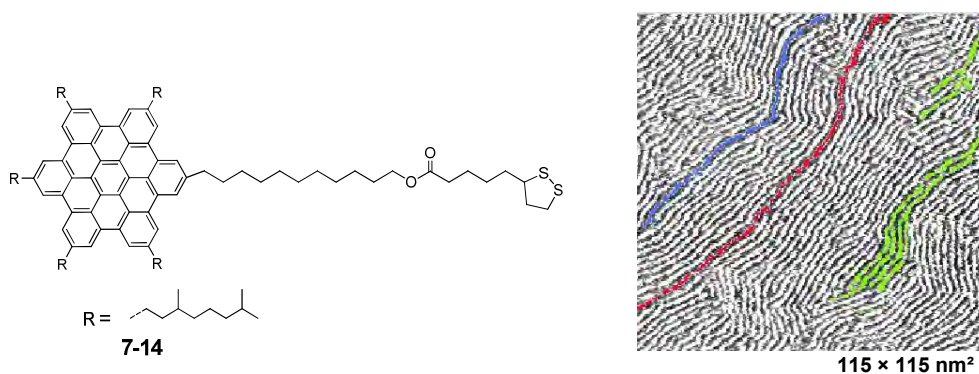


Figure 7-21. Molecular structure of 7-14 (left) and the STM image of its SAMs (right).

7.3 Summary

In order to extend the application of discotic HBC derivatives in electronic devices at a molecular level, different functional groups were introduced to the HBC core. It has been demonstrated that the molecular orientation on a surface can easily be controlled in a “face-on” or “edge-on” mode by incorporating different functional groups. The influence of the tether groups on the supramolecular organization was investigated at a molecular level by STM techniques.

In the case of azobenzene substituted HBCs, a short rigid linker group results in a well-ordered dimer-like supramolecular structure. In contrast, the rigidity of the molecule, which is caused by a stiff bridge, limits the non-planar *cis*-azobenzene isomer to adsorb onto the HOPG surfaces. Through a soft alkyl tether, the azobenzene moiety is liberated from the adlayer and the HBC cores pack densely at the liquid-solid interface in a “face-on” fashion. It is expected that the free azobenzene moiety can undergo *trans* / *cis* isomerization in the liquid phase, and the change of the dipole moment (caused by the azobenzene *trans* / *cis* conversion) can subsequently adjust the tunneling current in the future scanning tunneling spectroscopic (STS) experiments. As a consequence, the reversible azobenzene *trans/cis* isomerization overcomes the irreversible drawback of anthraquinone-based single molecular CFET⁸ and further improves the performance of HBC derivatives in monomolecular electronics.

The incorporation of specific anchor groups leads to the formation of HBC SAMs in an “edge-on” mode with an increased molecular-surface interaction. Both compounds containing sulfur anchors form stable monolayers on Au (111) surfaces in a large area. The molecular packing density is tuned by the rigidity of the bridge groups. The SAMs of the molecule with short soft alkyl linker homogeneously grow over the whole substrate, though, in a relatively loose molecular packing mode. The short rigid linker promotes the formation of a more condensed monolayer, however, with losing homogeneity. More importantly, both kinds of HBC molecules orient in an upright conformation showing condensed molecular superstructure in contrast to the one bearing long flexible alkyl tether 7-14.²⁴ This guarantees them having higher mechanical stability and better electrical conductivity in a metal-SAMs-metal junction.^{6,7}

7.4 References

1. Reed, M. A., Zhou, C., Müller, C. J., Burgin, T. P., Tour, J. M., *Science* **1997**, *278*, 252-254.
2. Chen, J., Reed, M. A., Rawlett, A. M., Tour, J. M., *Science* **1999**, *286*, 1550-1552.
3. Holmlin, R. E., Haag, R., Chabynyc, M. L., Ismagilov, R. F., Cohen, A. E., Terfort, A., Rampi, M. A., Whitesides, G. M., *J. Am. Chem. Soc.* **2001**, *123*, 5075-5085.
4. Salomon, A., Cahen, D., Lindsay, S., Tomfohr, J., Engelkes, V. B., Frisbie, C. D., *Adv. Mater.* **2003**, *15*, 19-32.
5. R. E. Holmlin, Ismagilov, R. F., Haag, R., Mujica, V., Ratner, M. A., Rampi, M. A., Whitesides, G. M., *Angew. Chem. Int. Ed* **2001**, *40*, 2316-2320.
6. Tran, E., Duati, M., Ferri, V., Müllen, K., Zharnikov, M., Whitesides, G. M., Rampi, M. A., *Adv. Mater.* **2006**, *18*, 1323-1328.
7. Duati, M., Grave, C., Tcbeborateva, N., Wu, J., Müllen, K., Shaporenko, A., Zharnikov, M., Kriebel, J. K., Whitesides, G. M., Rampi, M. A., *Adv. Mater.* **2006**, *18*, 329-333.
8. Jäckel, F., Watson, M. D., Müllen, K., Rabe, J. P., *Phys. Rev. Lett.* **2004**, *92*, 188303.
9. Huber, R., Gonzalez, M. T., Wu, S., Langer, M., Grunder, S., Horhoiu, V., Mayor, M., Bryce, M. R., Wang, C., Jitchati, R., Schonenberger, C., Calame, M., *J. Am. Chem. Soc.* **2008**, *130*, 1080-1084.
10. Nitzan, A., Ratner, M. A., *Science* **2003**, *300*, 1384-1389.
11. Dekker, C., *Phys. Today* **1999**, *52*, 22.
12. Tans, S. J., Devoret, M. H., Dai, H., Thess, A., Smalley, R. E., Geerligs, L. J., Dekker, C., *Nature* **1997**, *386*, 474-477.
13. Kushmerick, J. G., Holt, D. B., Yang, J. C., Naciri, J., Moore, M. H., Shashidhar, R., *Phys. Rev. Lett.* **2002**, *89*, 086802.
14. Hersam, M. C., Guisinger, N. P., Lyding, J. W., *Nanotechnology* **2000**, *11*, 70-76.
15. Hong, S., Reifenberger, R., Tian, W., Datta, S., Henderson, J. I., Kubiak, C. P., *Superlat. Microstr.* **2000**, *28*, 289-303.
16. Müllen, K., Rabe, J. P., *Acc. Chem. Res.* **2008**, in press.
17. Kumar, G. S., Neckers, D. C., *Chem. Rev.* **1989**, *89*, 1915-1925.
18. Rau, H., *Photoreactive Organic Thin Films*. Sekkat, Z., Knoll, W., Academic Press: San Diego, California, **2002**.
19. DeLang, J. J., Robertson, J. M., Woodward, I., *Proc. R. Soc. London, Sect. A* **1939**, *171*, 398.
20. Hartley, G. S., *J. Chem. Soc.* **1938**, 633-634.
21. Wyman, G. M., Brode, W. R., *This Journal* **1951**, *73*, 1487.

22. Brode, W. R., Wyman, G. M., *J. Research Natl. Bur. Standards* **1951**, *47*, 170.
23. Zhang, Y., Chen, P., Liu, M., *Langmuir* **2006**, *22*, 10246-10250.
24. Pontes, R. B., Novaes, F. D., Fazzio, A., daSilva, A. J. R., *J. Am. Chem. Soc.* **2006**, *128*, 8996-8997.
25. Sinan, M., Panda, M., Ghosh, A., Dhara, K., Fanwick, P. E., Chattopadhyay, D. J., Goswami, S., *J. Am. Chem. Soc.* **2008**.
26. Conti, I., Garavelli, M., Orlandi, G., *J. Am. Chem. Soc.* **2008**.
27. Wu, J., Qu, J., Tchebotareva, N., Müllen, K., *Tetrahedron Letters* **2005**, *46*, 1565-1568.
28. Fechtenkotter, A., Tchebotareva, N., Watson, M., Müllen, K., *Tetrahedron* **2001**, *57*, 3769-3783.
29. Huo, S., *Org. Lett.* **2003**, *5*, 423-425.
30. Bock, H., Rudolph, G., Baltin, E., Kroner, J., *Angew. Chem. Int. Ed* **1965**, *4*, 457-471.
31. Hermann, R., *Angew. Chem. Int. Ed* **1973**, *12*, 224-235.
32. Rau, H., *Ber. Bunsenges. Physik. Chem.* **1968**, *72*, 408-414.
33. Kastler, M., Pisula, W., Wasserfallen, D., Pakula, T., Müllen, K., *J. Am. Chem. Soc.* **2005**, *127*, 4286-4296.
34. Müllen, K., Rabe, J. P., *Acc. Chem. Res.* **2008**, in press.
35. Rabe, J. P., Buchholz, S., *Science* **1991**, *253*, 424-427.
36. Miwa, J. A., Weigelt, S., Gersen, H., Besenbacher, F., Rosei, F., Linderoth, T. R., *J. Am. Chem. Soc.* **2006**, *128*, 3164-3165.
37. Alemani, M., Peters, M. V., Hecht, S., Rieder, K. H., Moresco, F., Grill, L., *J. Am. Chem. Soc.* **2006**, *128*, 14446-14447.
38. Wang, Y., Ge, X., Schull, G., Berndt, R., Bomholdt, C., Koehler, F., Herges, R., *J. Am. Chem. Soc.* **2008**, *130*, 4218-4219.
39. Henzl, J., Mehlhorn, M., Gawronski, H., Rieder, K.-H., Morgenstern, K., *Angew. Chem. Int. Ed* **2006**, *45*, 603-606.
40. Bäuerle, P., Fischer, T., Bidlingmeier, B., Rabe, J. P., Stabel, A., *Angew. Chem. Int. Ed* **1995**, *34*, 303-307.
41. Piot, L., Marchenko, A., Wu, J., Müllen, K., Fichou, D., *J. Am. Chem. Soc.* **2005**, *127*, 16245-16250.
42. Aoyama, T., Takido, T., Kodomari, M., *Synthetic Communications* **2003**, *33*, 3817 - 3824.
43. Edinger, K., Goelzhaeuser, A., Demota, K., Woell, C., Grunze, M., *Langmuir* **1993**, *9*, 4-8.
44. Azzam, W., Bashir, A., Terfort, A., Strunskus, T., Woll, C., *Langmuir* **2006**, *22*, 3647-3655.

45. Azzam, W., Cyganik, P., Witte, G., Buck, M., Woll, C., *Langmuir* **2003**, *19*, 8262-8270.
46. Poirier, G. E., Pylant, E. D., *Science* **1996**, *272*, 1145-1148.
47. The length of 3,7-dimethyloctyl substituent is simulated with PM3 method by the Spaton '02 semi-empirical program
48. Fischbach, I., Pakula, T., Minkin, P., Fechtenkotter, A., Müllen, K., Spiess, H. W., Saalwachter, K., *J. Phys. Chem. B* **2002**, *106*, 6408-6418.
49. Arnold, R., Terfort, A., Woll, C., *Langmuir* **2001**, *17*, 4980-4989.
50. Ke, S. H., Baranger, H. U., Yang, W., *J. Am. Chem. Soc.* **2004**, *126*, 15897-15904.
51. Xue, Y., Ratner, M. A., *Phy. Rev. B* **2004**, *69*, 085403.
52. Di Ventra, M., Pantelides, S. T., Lang, N. D., *Phy. Rev. Lett.* **2000**, *84*, 979.
53. Emberly, E. G., Kirzenow, G., *Phy. Rev. Lett.* **2003**, *91*, 188301.
54. Basch, H., Cohen, R., Ratner, M. A., *Nano Lett.* **2005**, *5*, 1668-1675.
55. Stokbro, K., Taylor, J., Brandbyge, M., Mozos, J. L., Ordejón, P., *Comput. Mater. Sci.* **2003**, *27*, 151-160.
56. *This molecule was synthesized by Dr. Wu, J. and the STM image was measured by Dr. Piot, L. from the group of Prof. Fischou at LRC Nanostructures et Semiconducteurs Organiques, France.*

8 Summary and Outlook

Discotic hexa-*peri*-hexabenzocoronene (HBC) derivatives have attracted intensive scientific interest due to their unique optoelectronic properties,¹ which depends, to a large extent, upon the attached functional groups. The presented work covers the synthesis of novel HBC building blocks and new HBC derivatives as functional materials.

I. Synthesis of HBC building blocks:

The preparation of HBC derivatives requires elaborate synthetic techniques and tremendous effort. Especially, more than 10 synthetic steps are usually necessary to approach HBCs with lower symmetries. In order to simplify the synthetic work and reduce the high costs, a novel synthetic strategy involving only four steps was developed based on 2,3,5,6-tetraphenyl-1,4-diiodobenzene **2-14** intermediates and palladium catalyzed Suzuki cross coupling reactions (Figure 8-1). This method has shown superiority in the preparation of hexaphenyl benzenes (HPBs) **2-16**, the precursors of HBCs, with different symmetries. Additionally, the so-far longest graphene nanoribbons (with a length up to 12 nm) were prepared by using a similar synthetic strategy in corporation with Dr. X. Yang.²

On another aspect, the synthesis of versatile HBC building blocks with different symmetries, e.g. D_{6h} -, D_{3h} - and D_{2h} -symmetries, has been well developed in the past decades. However, the only known HBC building blocks with C_{2v} -symmetry are mono-halide substituted HBCs (monobromo and monoiodo HBCs) before. In order to introduce various functionalities and expand the diversity of multi-functionalizations, a novel C_{2v} -symmetric dihalo HBC building block **2-47**, which contains one iodine and one bromine in *para* positions, was prepared following the traditional intermolecular [4+2] Diels-Alder reaction route (Figure 8-1). The outstanding chemical selectivity between iodo and bromo groups in this compound consequently leads to lots of HBC derivatives bearing different functionalities.

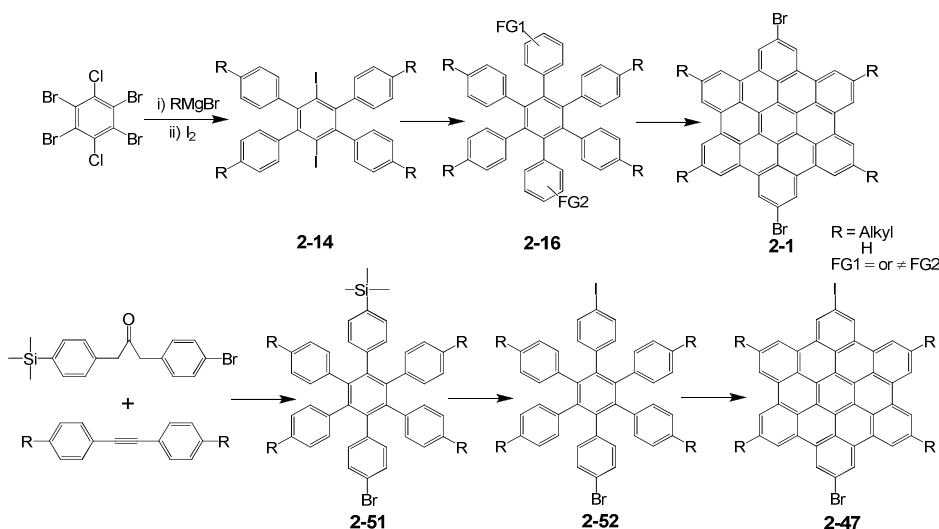


Figure 8-1. Lately developed synthetic strategy towards versatile HPBs, *para*-dibromo and *D*₁ asymmetric *para*-iodo bromo HBC building blocks.

II. From the introduction of different functionalities to novel functional materials:

In all-benzoid PAH chemistry, the last cyclodehydrogenation step (intramolecular Scholl reaction) from oligophenylene to PAH results in planarized structures. However, the intramolecular Scholl reaction is limited by the electronic properties of the appended heteroatoms, which would improve the material properties. In the past, different mechanisms of this reaction have been postulated, however, without sufficient experimental support. With the aforementioned powerful method, different heteroatoms can easily be attached to the HPB periphery, which provide experimental support of the later mechanistic studies. For example, a phenyl group rearrangement was observed when *para*-dimethoxy HPB **2-33** was subjected to an intramolecular cyclodehydrogenation affording a *meta*-dimethoxy HBC **2-40** (Figure 8-2). Thereby, several interesting mechanistic details were discussed involving arenium cation intermediates.

For the better utilization of a material, it is important to understand the molecular dynamics in different phases. The two oxygen groups introduced directly to the aromatic core, albeit with a “*meta*” instead of the expected “*para*” relationship, bring this HBC molecule a weak dipole moment and a phase transition from crystalline to liquid crystalline phase. The weak dipole moment could consequently serve as a probe in dielectric spectroscopy measurements, which traces the molecular relaxation process

under inducing electronic pulses revealing molecular dynamics. With another three more dipole-functionalized HBCs **4-1**, **4-2** and **4-3**, the self-assembly behavior and dynamics in different phases were systematically investigated using DSC, 2D WAXD, site-specific NMR and dielectric spectroscopic (DS) techniques. It was concluded that the dipole moment can effectively stabilize the mesophase and the correlation between molecular dipoles manifests itself as a new α -type relaxation process, called α' -relaxation, in DS spectra.

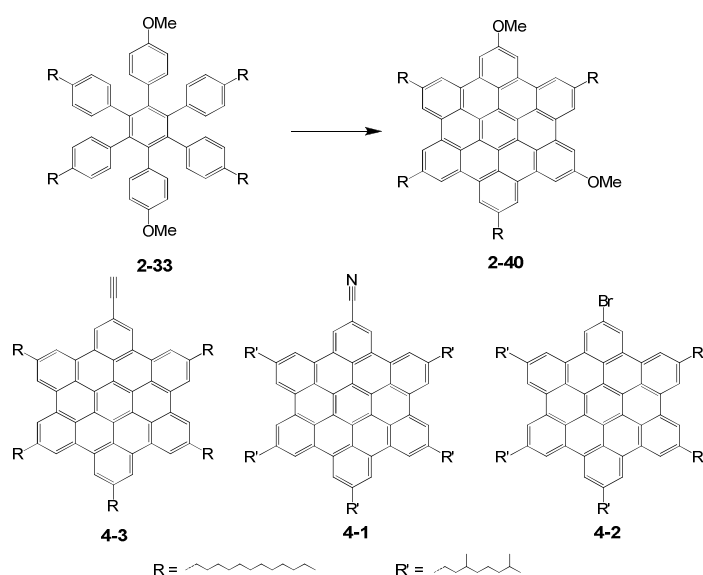


Figure 8- 2. An unexpected phenyl group migration during intramolecular Scholl reaction and dipole-functionalized HBCs.

High charge carrier mobility is an important parameter for a semiconductive material and depends on the degree of intramolecular order of the discotic molecules in thin films for HBC derivatives. A large amount of effort has, thus, been devoted to obtain well-ordered films by thermal or solution-based processes. From the molecular interaction point of view, different non-covalent interactions were considered to strengthen the intracolumnar order. Dipole-dipole interactions and hydrogen bonds were, therefore, utilized to stabilize the columnar supramolecular organization. Starting from the *para*-iodo bromo HBC **2-47**, one cyano and one amino group were consequently connected to the HBC aromatic core resulting in compounds (**5-1** and **5-2**) with large dipole moments (up to 8.64 D) (Figure 8-3). Besides a stabilized mesophase in a wide

temperature-range, the strong dipole moment prompts HBC molecules to self-assemble into either H- or J-aggregates (depending on the solvents) in solutions and gives rise to different morphologies on surfaces. Additionally it shows obvious intramolecular charge transfer phenomena, which broadens the application of such materials in non-linear optics.

Directly attached hydrogen bonds were also brought into play to improve the intramolecular order (Figure 8-3). These HBC derivatives (**6-1**, **6-2** and **6-3**) are functionalized with either amido or ureido groups. They form stable aggregates in solution and reveal a unique phase behavior in the bulk state. Whereas, depending upon the strength of the intermolecular interactions and the geometry of functional groups, the hydrogen bonds either cooperate with $\pi - \pi$ interactions to stabilize the HBC columnar superstructures or compete against the $\pi - \pi$ interactions resulting in a short-range ordered supramolecular arrangement. In addition, strong hydrogen bonding interactions also render these molecules new properties as low molecular-mass organic gelators (LMOGs).

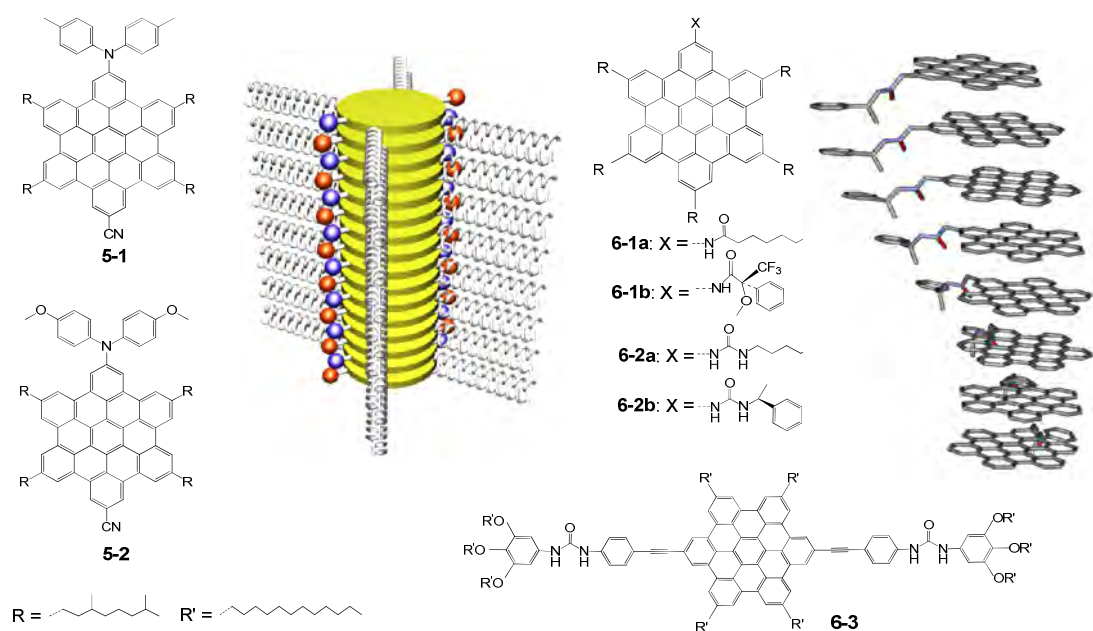


Figure 8-3. Molecular structures of dipole and hydrogen bonds functionalized HBC derivatives and cartoon represents of presumed molecular stacks.

In the field of conceivable electronic devices at a molecular level, HBCs hold high promise. They have been employed in single-molecular chemical field effect transistors

(single-molecular CFET)³ and their self-assembled monolayers (SAMs) have been used between two metal junctions at a molecular level.⁴ In order to improve their performance, azobenzene functionalities and thiol acetate anchor groups were connected to HBC cores through either a rigid ethynyl bridge or a soft short alkyl tether (Figure 8-4). In the case of azobenzene substituted HBCs (**7-1** and **7-2**), the *trans*- / *cis*-isomerization was realized by irradiation with UV lights and thermal treatment. The accompanied dipole moment change in the azobenzene moiety is expected to induce scanning tunneling current switching in single-molecular CFET devices. Depending on the length and rigidity of the linking group, the thiol functionalized HBCs (**7-3** and **7-4**) self-assembled into well-ordered monolayers on Au (111) with different densities. The outstanding properties shown in both kinds of materials promise their exciting potential applications in molecular devices.

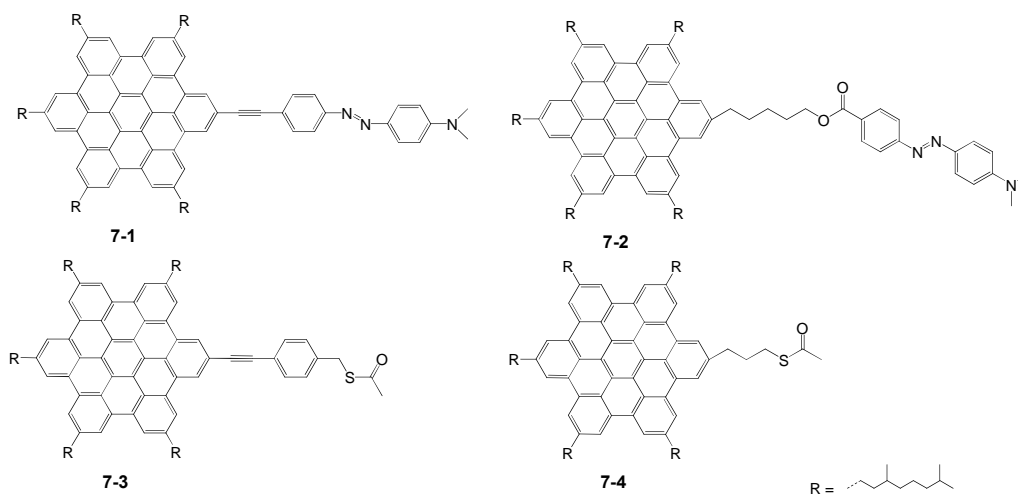


Figure 8-4. Molecular structure of synthesized azobenzene and thiol acetate attached HBCs.

The novel efficient synthetic strategy facilitates a bottom up approach of graphene nanoribbons. However, the length and size-dispersity of these ribbons are limited by the solubility of corresponding precursors, oligophenylenes. In the future, the dove-shaped 2-decyl tetradecyl alkyl substituents, which have dramatically improved the processibility of HBC derivatives,⁵ can be incorporated. In so doing, longer ribbon lengths and lower polydispersities can be expected.

Concerning the superiority of this method in the preparation of asymmetric HPBs, HBC **8-1** is designed, which can be synthesized via two steps Negishi cross coupling reactions (Figure 8-5). After hydrolysis, an A-B HBC building block **8-2** can be obtained. The subsequent polycondensation polymerization will afford a new polymer doped with HBC units, which will improve the mechanical property through the HBC cofacial $\pi - \pi$ interactions.

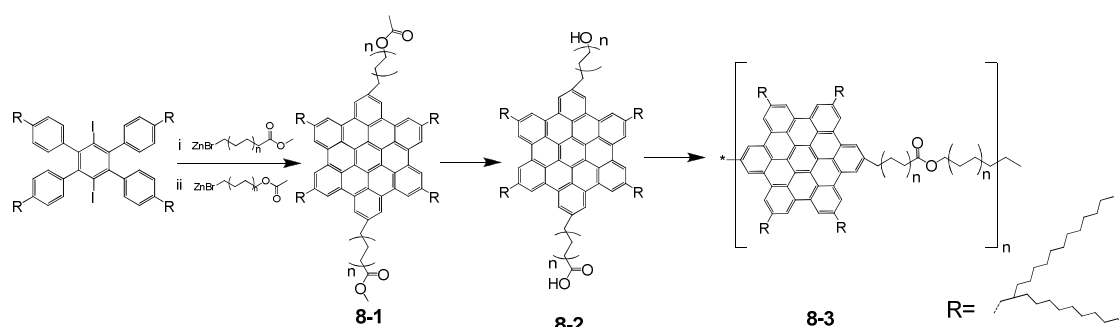


Figure 8-5. Synthesis of HBC doped polymer.

The donor-HBC-acceptor molecules have shown interesting self-assembly behavior and intramolecular charge transfer phenomena. The more than ten-micrometer aggregates have reached the length requirement for FET devices. By the adjustment of solvents and concentrations, these aggregates can be utilized as active components in FETs. The intramolecular charge separation also broadens the application of HBC derivatives as new functional materials in non-linear optics. With *para*-iodo bromo HBC **2-47**, series of donor-HBC-acceptor molecules can be designed bearing different electron donating and accepting groups to improve their device performances.

The dipole-dipole interactions and hydrogen bonds have effectively influenced the molecular stacking. One can consider to bring both non-covalent interactions together to achieve supramolecular organization. For instance, through the attachment of an alkyl chain containing hydrogen bonding groups to the HBC core at specific distance on one side and a strong electron acceptor on the other, these two kinds of non-covalent interactions are brought together and should be able to cooperatively stabilize the columnar superstructure, which can be regarded as a HBC “double-chain” column (Figure 8-6). It is important to be aware that the length of the alkyl linker between

hydrogen bonding groups and the HBC core must satisfy the distance of both corresponding hydrogen bonds and $\pi - \pi$ stacking. In addition, helical columnar supramolecular structure can be obtained by selecting enantiomerically pure alkyl substituents. This would produce a series of interesting self-assembly phenomena and find new applications of HBC derivatives in supramolecular chemistry.

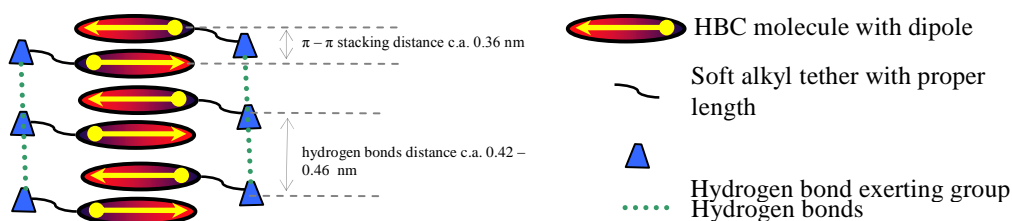


Figure 8- 6. Schematic represents of HBC “double-chain” columns.

Overall, the versatile HBC building blocks with different symmetries make it possible to realize lots of functionalities on the liquid crystalline HBC molecules expanding the application of HBC derivatives as functional materials.

References

1. Wu, J., Pisula, W., Müllen, K., *Chem. Rev.* **2007**, *107*, 718-747.
2. Yang, X., Dou, X., Rouhanipour, A., Zhi, L., Rader, H. J., Müllen, K., *J. Am. Chem. Soc.* **2008**, *130*, 4216-4217.
3. Jäckel, F., Watson, M. D., Müllen, K., Rabe, J. P., *Phys. Rev. Lett.* **2004**, *92*, 188303.
4. M. Duati, Grave, C., Tcbeborateva, N., Müllen, J. W. K., Shaporenko, A., Zharnikov, M., Kriebel, J. K., Whitesides, G. M., Rampi, M. A., *Adv. Mater.* **2006**, *18*, 329-333.
5. Pisula, W., Kastler, M., Wasserfallen, D., Pakula, T., Müllen, K., *J. Am. Chem. Soc.* **2004**, *126*, 8074-8075.

9 Experimental Details

Materials: Chemicals were obtained from Fluka, Aldrich, and ABCR and used as received. Column chromatography and TLC was performed with Merck silica gel 60 (70-230 mesh) and Merck silica gel 60 F₂₅₄, respectively. THF was freshly distilled over Na metal. Hexane was distilled with CaH₂.

Microwave assisted reactions: Some reactions were performed in a microwave oven (CEM GmbH, Kamp-Lintfort, Germany, model: Discover) using the maximum power to heat the system. The temperature was adjusted by changing the flow rate for a jet of air around the glass reaction vessel. The reaction vessels were sealed and could hold a pressure of 10 bars.

Field Desorption (FD) Mass spectrometry (MS): FD mass spectra were obtained on a VG Instruments ZAB 2-SEFPD.

MALDI- TOF Mass Spectrometry: MALDI-TOF mass spectra were measured using a Bruker Reflex II-TOF spectrometer using a 337 nm nitrogen laser and 7,7,8,8-tetracyanoquinodimethane (TCNQ) as matrix.

Electron Spray Ionization High Resolution Mass Spectrometry (ESI-HRMS):

Solution NMR Spectroscopy: ¹H-NMR, ¹³C-NMR, ¹H,¹H COSY, ¹H,¹H COSY and NOESY experiments were carried out with

Bruker DRX-700

Bruker DRX-500

Bruker AMX-300

Elementaranalyse (EA): the Elemental Analysis was measured in Institut für Organische Chemie der Johannes Gutenberg Universität in Mainz for: C, H, N: Foss Heraeus vario EL.

Solid state NMR Spectroscopy: The two-dimensional rotor-synchronized double quantum (DQ) magic-angle spinning (MAS) spectra were recorded on a Bruker Avance 700 spectrometer using a standard double-resonance probe supporting rotor of 2.5 mm outer diameter. The ^1H - ^1H back-to-back (BABA) recoupling technique for the excitation and reconversion of double-quantum coherences (DQCs) was applied for one cycle at 25 kHz MAS. The molecular dynamics investigations were performed by recording ^{13}C - ^1H REREDOR spinning sideband patterns, at 80 μs recoupling time and 25 kHz magic angle spinning (MAS) on a Bruker Avance 500 spectrometer using a Bruker double-resonance probe supporting rotors of 2.5 mm outer diameter. All experimental temperatures were corrected for the frictional heating effects arising from the fast rotor spinning.

Infrared-Spectroscopy (IR): Infrared spectroscopy was measured with Nicolet FT-IR 320 spectrometer.

UV-Vis Absorption Spectroscopy: The optical absorption measurements were performed at ambient temperature using a UV/vis/NIR Perkin-Elmer Lambda 900 spectrometer.

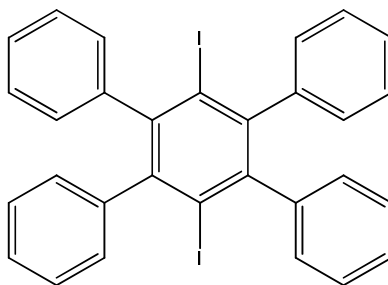
Photoluminescence Spectroscopy: The photoluminescence in solution was recorded on a SPEX Fluorolog 2 type 212 steady-state fluorometer.

Dielectric Spectroscopy: Dielectric measurements were made under “isobaric” conditions as a function of temperature and under “isothermal” conditions as a function of pressure. The “isobaric” measurements were performed at different temperatures in the range 123.15-423.15 K, at atmospheric pressure, and for frequencies in the range from 10^{-2} to 10^6 Hz. The “isothermal” measurements were made for temperatures in the range from 303.15 to 403.15 K and for pressure up to 300 MPa.

Differentialcalorimetry (DSC): DSC was measured by Mettler DSC 30 with heating rate 10 K/min in the range from -150 °C to 250 °C.

Polarized Optical Microscopy: Zeiss Axiophot optical microscope with a nitrogen flushed Linkam THM 600 hot stage.

X-ray diffraction: 2D WAXS measurements of oriented filaments were conducted using a rotating anode (Rigaku 18 kW) X-ray beam ($\text{CuK}\alpha$, pinhole collimation, double graphite monochromator) and CCD camera. The patterns were recorded with vertical orientation of the filament axis and with the beam perpendicular to the filament. Data collections for the single crystal structure analyses were performed on a Nonius KCCD diffractometer with graphite monochromated $\text{Mo K}\alpha$ radiation at a temperature of 120 K.

1,4-Diiodo-2,3,5,6-tetraphenyl benzene (2-14a):

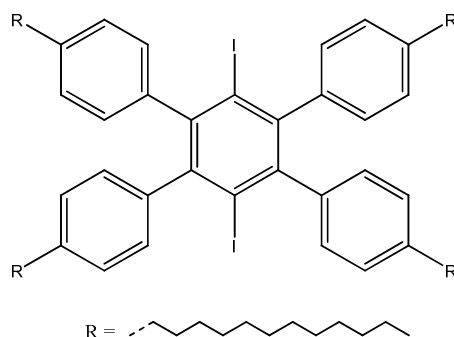
A suspension of 1,4-dichloro-2,3,5,6-tetrabromobenzene (1.85 g, 4.0 mmol) in dry THF (20 mL) was added to a solution of phenylmagnesium bromide (32 mmol) in dry THF (32 mL) under argon atmosphere and the resulting mixture was stirred at r.t. for 12 h. I₂ (6.35 g, 25 mmol) was added directly to the reaction mixture at 0 °C and the mixture was further stirred at r.t. for 2 h. The reaction was quenched with water and the resulting mixture was extracted with CHCl₃ (100 mL × 3). The combined organic layers were washed with 2M aqueous NaHSO₃ solution (200 mL × 2), brine (50 mL) and water (50 mL), and dried with MgSO₄. After filtration off the MgSO₄, the solvent was removed in vacuo and the resulting mixture was filtered. The solid was washed with a little bit benzene and hexane to give 0.7 g of **2-14a**. The filtrate was purified with chromatography with an eluent (*n*-Hexane/Benzene = 30/1) to give 0.3 g of **2-14a** as white solid. The total yield is 40%.

FD-MS (8 kV): $m/z = 634.7$ (100%, M⁺), (calcd. for C₃₀ H₂₀ I₂ = 634.3 g mol⁻¹).

¹H-NMR (250 MHz, CD₂Cl₂): $\delta = 7.05$ (m, 20 aryl-H) ppm.

¹³C-NMR (75 MHz, CD₂Cl₂): $\delta = 146.8, 143.6, 141.9, 130.1, 127.6, 108.9$ ppm.

HRMS (ESI): calcd. for C₃₀ H₂₀ I₂ [M⁺] = 633.9654, found: 633.9629.

1,4-Diiodo-2,3,5,6-tetrakis(4'-dodecylphenyl) benzene (2-14b):

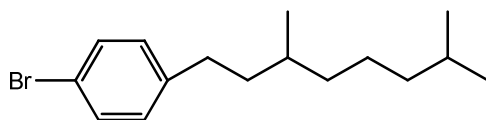
A suspension of 1,4-dichloro-2,3,5,6-tetrabromobenzene (4.16 g, 9.0 mmol) in dry THF (45 mL) was added to a solution of 4-dodecylphenyl magnesium bromide (72.0 mmol) in dry THF (72 mL) under argon atmosphere and the resulting mixture was stirred at r.t. for 12 h. I₂ (12.7 g, 50.0 mmol) was added directly to the reaction mixture at 0 °C and the mixture was further stirred at r.t. for 2 h. The reaction was quenched with water and the resulting mixture was extracted with CH₂Cl₂ (200 mL × 3). The combined organic layers were washed with 2M aqueous NaHSO₃ solution (200 mL × 2), brine (250 mL) and water (250 mL), and dried over MgSO₄. After filtering off the MgSO₄, the solvent was removed in vacuo and the resulting mixture was purified with chromatography with an eluent (*n*-Hexane/Benzene = 30/1) to give 7.1 g of **2-14b** as white solid in a yield of 60%.

FD-MS (8 kV): $m/z = 1307.4$ (100%, M⁺), (calcd for C₇₈H₁₁₆I₂ = 1307.6 g mol⁻¹).

¹H-NMR (250 MHz, CD₂Cl₂): δ = 6.81 (d, J = 7.7 Hz, 8H, aryl-*H*), 6.75 (d, J = 7.6 Hz, 8H, aryl-*H*), 2.43 (t, J = 7.2 Hz, 8H, α-*CH*₂), 1.24 (m, 80H, alkyl-*H*), 0.72 (t, J = 6.6 Hz, 12H, -*CH*₃) ppm.

¹³C-NMR (75 MHz, CD₂Cl₂): δ = 146.9, 143.7, 142.0, 130.2, 127.7, 109.0, 35.9, 32.4, 31.7, 30.2, 30.1, 29.9, 29.8, 29.6, 23.1, 14.3 ppm.

HRMS (ESI): calcd. for C₇₈H₁₁₆I₂ [M⁺]: 1306.7166, found: 1306.7169.

4-(3',7'-Dimethyloctyl)phenyl bromide (2-27):

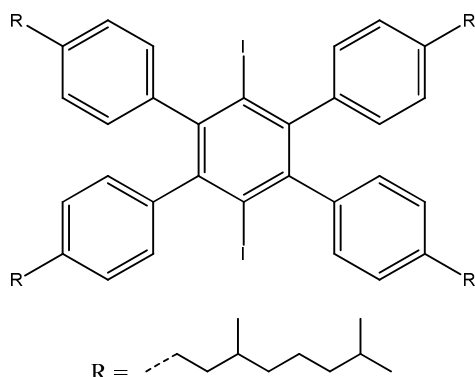
1-Trimethylsilyl-4-(3,7-dimethyloctyl) benzene (23.6g, 81.4mmol) and sodium acetate (13.4g, 163.3mmol) were dissolved in THF (400 mL) at 0 °C. Then, bromine (26.7g, 171.1mmol) was added dropwise via a dropping funnel. The mixture was stirred for 20 min. The reaction was quenched with saturated sodium sulfite aqueous solution (300 mL). The organic layer was then extracted with CH₂Cl₂ (500 mL × 3) and dried over MgSO₄. After being filtered out, the solvent was removed in vacuo and the crude product was purified by column chromatography (eluent petroleum ether) affording 19.7g **2-27** as transparent oil in a yield of 82%.

FD-MS (8 kV): $m/z = 296.1$ (100%, M⁺), (calcd. for C₁₆H₂₅Br = 297.3 g mol⁻¹).

¹H-NMR (250 MHz, CD₂Cl₂): $\delta = 7.38$ (d, J = 8.5 Hz, 2H, aryl-*H*), 7.10 (d, J = 8.5 Hz, 2H, aryl-*H*), 2.59 (m, 2H, α -CH₂), 1.59-1.15 (m, 10H, alkyl-*H*), 0.94-0.87 (m, 9H, -CH₃) ppm.

¹³C-NMR (62.5 MHz, CD₂Cl₂): $\delta = 142.83, 131.58, 130.60, 119.40, 39.70, 39.18, 37.48, 33.23, 32.84, 28.39, 25.08, 22.86, 22.77, 19.72$ ppm.

Elemental Analysis: C 65.04%, H 8.59% (calcd. for C₁₆H₂₅Br, C 64.65%, H 8.48%, Br 26.88%).

1,4-Diiodo-2,3,5,6-tetrakis[4'-(3'',7'')-dimethyloctyl]phenyl] benzene(2-14c):

2-27 (19.7 g, 66.4 mmol) was dissolved in dry THF (100 mL) and the solution was added dropwise to magnesium (2.4 g, 100 mmol), which was first activated with 1,2-dibromoethane (0.5 mL), in a pre-dried 250 mL three-necked flask at 0 °C. The mixture was stirred for 12 h at ambient temperature. The obtained Grignard reagent was transferred to another 500 mL three-necked flask under argon atmosphere. 1,4-diiodo-2,3,5,6-tetrachlorobenzene (3.2 g, 7.0 mmol), which was suspended in dry THF (50 mL), was added dropwise. The mixture was stirred for another 12 h at r.t. followed by adding iodine (16.9 g, 66.4 mmol). Three hours later, the reaction was quenched with large amount of saturated sodium sulfite aqueous solution (200 mL). The organic phase was then extracted with CH₂Cl₂ (300 mL × 3) and washed with brine (300 mL). The obtained organic phase was dried with MgSO₄. The solvent was removed in vacuo. The residue was purified by column chromatography with an eluent of petroleum ether (PE), followed by twice recrystallization from CH₂Cl₂/acetone (1/1) mixture (50 mL). 3.4 g **2-14c** was obtained as white solid in a yield of 40%.

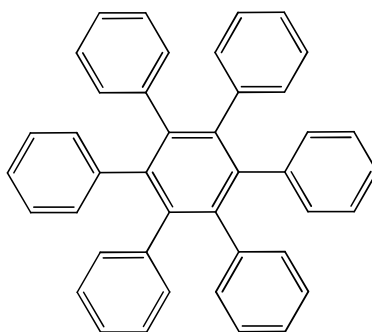
FD-MS (8 kV): $m/z = 1194.7$ (100%, M⁺), (calcd. for C₇₀H₁₀₀I₂ = 1195.4 g mol⁻¹).

¹H-NMR (250 MHz, CD₂Cl₂): $\delta = 6.97$ (d, J = 7.75 Hz, 8H, aryl-*H*), 6.89 (d, J = 7.75 Hz, 8H, aryl-*H*), 2.52 (m, 8H, α -CH₂), 1.55-1.13 (m, 40H, alkyl-*H*), 0.88-0.86 (m, 36H, -CH₃) ppm.

¹³C-NMR (62.5 MHz, CD₂Cl₂): $\delta = 146.70, 143.56, 142.19, 130.09, 127.62, 109.03, 39.69, 39.03, 37.45, 33.41, 32.78, 28.36, 25.07, 22.83, 22.75, 19.77$ ppm.

Elemental Analysis: C 70.27%, H 8.47% (calcd. for $C_{70}H_{100}I_2$, C 70.34%, H 8.43%, I 21.23%).

Hexaphenylbenzene (2-28)



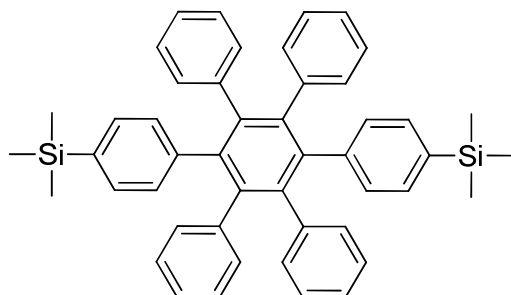
A pre-dried 100 mL Schlenk tube equipped with a magnetic stirring bar and a septum was charged with a suspension of **2-14a** (100 mg, 0.16 mmol, 1.0 equiv), phenylboronic acid (58 mg, 0.47 mmol, 3.0 equiv), K_2CO_3 (441 mg, 3.2 mmol, 20 equiv) and aliquat[®] 336 (1.0 mg, 3.3 μ mol, 0.020 equiv) in toluene (15 mL). The mixture was degassed by three “freeze-pump-thaw” cycles and then $Pd(PPh_3)_4$ (9.1 mg, 7.9 μ mol, 0.05 equiv) was added. The resulting mixture was degassed again by “freeze-pump-thaw” cycle. The mixture was heated to 100 °C and stirred for 12 h under argon. The reaction mixture was quenched with methanol and extracted with CH_2Cl_2 . The organic layer was washed with brine (150 mL \times 3), dried over $MgSO_4$ and concentrated in vacuo. Flash chromatographic purification on silica gel (eluent petroleum ether (PE) / CH_2Cl_2 (7/1)) furnished 80 mg **2-28** as white solid in a yield of 95%.

FD-MS (8 kV): $m/z = 534.9$ (100%, M^+), (calcd for $C_{42}H_{30} = 534.7$ g mol^{-1}).

1H -NMR (250 MHz, CD_2Cl_2): $\delta = 7.05$ (m, 30H, aryl-*H*) ppm.

^{13}C -NMR (75 MHz, CD_2Cl_2): $\delta = 140.6, 142.0, 131.4, 126.6, 125.2$ ppm.

Elemental Analysis: C 94.31%, H 5.69% (calcd. for $C_{42}H_{30}$, C 94.34%, H 5.66%).

1,4-Bis(4'-trimethylsilylphenyl)-2,3,5,6-tetraphenyl benzene (2-29):

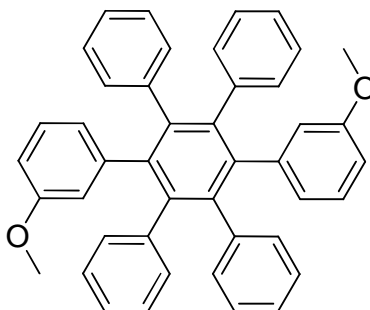
The synthetic procedure follows that in the preparation of **2-28** with **2-14a** (200 mg, 0.32 mmol, 1.0 equiv), 4-trimethylsilylphenylboronic acid (183 mg, 0.95 mmol, 3.0 equiv), K_2CO_3 (871 mg, 6.31 mmol, 20 equiv), aliquat[®] 336 (2.5 mg, 6.3 μ mol, 0.020 equiv), $Pd(PPh_3)_4$ (18.2 mg, 0.0158 mmol, 0.05 equiv) and toluene (20 mL). Flash chromatographic purification on silica gel (eluent petroleum ether (PE) / CH_2Cl_2 (8/1)) afforded 199 mg **2-29** as white solid in a yield of 93%.

FD-MS (8 kV): $m/z = 678.8$ (100%, M^+), (calcd for $C_{48}H_{46}Si_2 = 679.0$ g mol⁻¹).

¹H-NMR (250 MHz, $CDCl_3$): $\delta = 6.89$ (d, $J = 7.8$ Hz, 4H, aryl-*H*), 6.73 (m, 20H, aryl-*H*), 6.69 (d, $J = 8.0$ Hz, 4H, aryl-*H*), 0.00 (s, 18H, - CH_3) ppm.

¹³C-NMR (75 MHz, $CDCl_3$): $\delta = 142.2, 141.8, 141.6, 141.5, 137.7, 132.7, 132.6, 131.9, 127.7, 125.3, 0.00$ ppm.

Elemental Analysis: C 84.27%, H 5.68% (calcd. for $C_{48}H_{46}Si_2$, C 84.90%, H 6.83%, Si 8.27%).

1,4-Bis(3'-methoxyphenyl)-2,3,5,6-tetraphenyl benzene (2-30):

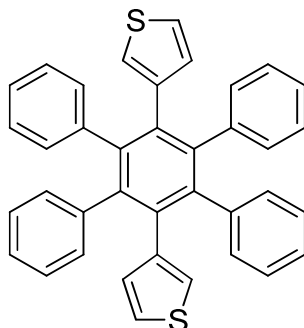
The synthetic procedure follows that in the preparation of **2-28** with **2-14a** (200 mg, 0.32 mmol, 1.0 equiv), 3-methoxyphenylboronic acid (144 mg, 0.95 mmol, 3.0 equiv), K_2CO_3 (871 mg, 6.31 mmol, 20 equiv), aliquat[®] 336 (2.5 mg, 6.3 μmol , 0.020 equiv), $\text{Pd}(\text{PPh}_3)_4$ (18.2 mg, 0.0158 mmol, 0.050 equiv) and toluene (20 mL). The resulting mixture was degassed again by “freeze-pump-thaw” cycle. The mixture was heated to 100 °C and stirred for 12 h under argon. The reaction mixture was quenched with methanol, extracted with CH_2Cl_2 . The organic layer was washed with brine (150 mL \times 3), dried over MgSO_4 and concentrated in vacuo. Flash chromatographic purification on silica gel (eluent *n*-hexane/ethyl acetate 8/1) resulted in 182 mg **2-30** as white solid in a yield of 94%.

FD-MS (8 kV): $m/z = 593.6$ (100%, M^+) (calc. for $\text{C}_{44}\text{H}_{34}\text{O}_2 = 594.76 \text{ g mol}^{-1}$).

$^1\text{H-NMR}$ (250 MHz, CD_2Cl_2): $\delta = 6.91\text{-}6.8764$ (m, 20H, aryl-*H*), 6.77 (t, $^3J = 7.75 \text{ Hz}$, 2H, aryl-*H*), 6.47-6.38 (m, 6H, aryl-*H*), 3.48 (s, 6H, $-\text{OCH}_3$) ppm.

$^{13}\text{C-NMR}$ (62.5 MHz, CD_2Cl_2): $\delta = 158.56, 142.29, 141.15, 141.11, 140.73, 140.61, 140.47, 131.74, 131.68, 131.63, 131.54, 127.77, 126.89, 125.70, 125.63, 125.57, 124.57, 124.53, 117.19, 111.86, 55.30$ ppm.

HRMS (ESI): calcd for $\text{C}_{44}\text{H}_{34}\text{O}_2\text{Na}$ [$\text{M}+\text{Na}^+$]: 617.2457, found 617.2449.

1,4-Bis(3'-thiophene)-2,3,5,6-tetraphenyl benzene (2-31):

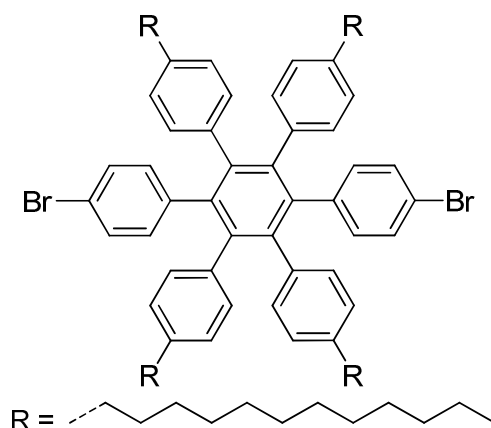
The synthetic procedure follows that in the preparation of **2-28** with **2-14a** (200 mg, 0.32 mmol, 1.0 equiv), 3-thiopheneboronic acid (122 mg, 0.95 mmol, 3.0 equiv), K_2CO_3 (871 mg, 6.31 mmol, 20 equiv), aliquat[®] 336 (2.5 mg, 6.3 μ mol, 0.020 equiv), $Pd(PPh_3)_4$ (18.2 mg, 0.0158 mmol, 0.05 equiv) and toluene (20 mL). Flash chromatographic purification on silica gel (eluent *n*-hexane/ethyl acetate 8/1) gave 152 mg **2-31** as white solid in a yield of 88%.

FD-MS (8 kV): $m/z = 546.0$ (100%, M^+) (calc. for $C_{30}H_{26}S_2 = 546.76$ g mol⁻¹).

¹H-NMR (250 MHz, CD₂Cl₂): $\delta = 6.97$ -6.87 (m, 20H, aryl-*H*), 6.81-6.78 (m, 2H, aryl-*H*), 6.53-6.48 (m, 4H, aryl-*H*) ppm.

¹³C-NMR (62.5 MHz, CD₂Cl₂): $\delta = 141.58, 141.38, 141.32, 141.17, 140.95, 140.81, 140.73, 135.90, 131.69, 131.36, 131.05, 130.87, 127.16, 127.03, 126.93, 125.88, 125.75, 125.64, 125.03, 123.03$ ppm.

HRMS (ESI): calcd for $C_{38}H_{26}S_2Na$ [$M+Na^+$]: 569.1374, found 569.1395.

1,4-Bis(4'-bromophenyl)-2,3,5,6-tetrakis(4'-dodecylphenyl) benzene (2-32):

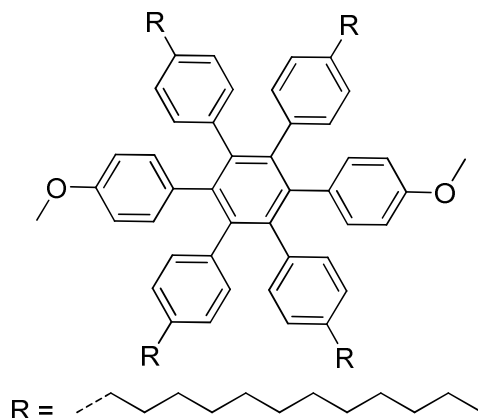
The synthetic procedure follows that in the preparation of **2-28** with **2-14b** (196 mg, 0.15 mmol, 1.0 equiv), 4-bromophenylboronic acid (90 mg, 0.45 mmol, 3.0 equiv), K_2CO_3 (414 mg, 3.0 mmol, 20 equiv), aliquat[®] 336 (1.0 mg, 3.0 μ mol, 0.020 equiv), $Pd(PPh_3)_4$ (9.0 mg, 7.5 μ mol, 0.05 equiv) and toluene (20 mL) at 80 °C for 18 h under argon. Flash chromatographic purification on silica gel (eluent petroleum ether (PE) / CH_2Cl_2 (15/1)) gave 186 mg **2-32** as transparent oil in a yield of 91%.

FD-MS (8 kV): $m/z = 1365.6$ (100%, M^+) (calc. for $C_{90}H_{124}Br_2 = 1365.7$ g mol⁻¹).

¹H-NMR (250 MHz, $CDCl_3$): $\delta = 6.88$ (d, $J = 8.4$ Hz, 4H, aryl-*H*), 6.62 (d, $J = 8.4$ Hz, 4H, aryl-*H*), 6.60 (s, 16H, aryl-*H*), 2.29 (t, $J = 7.5$ Hz, 8H, α - CH_2), 1.18 (m, 80H, alkyl-*H*), 0.80 (t, $J = 6.9$ Hz, 12H, $-CH_3$) ppm.

¹³C-NMR (75 MHz, $CDCl_3$): $\delta = 140.7, 140.6, 140.3, 139.7, 138.0, 133.5, 131.5, 129.9, 127.1, 119.5, 35.6, 32.3, 31.6, 30.2, 30.1, 30.0, 29.9, 29.8, 29.2, 23.1, 14.3$ ppm.

Elemental Analysis: C 80.93%, H 9.38% (calcd. for $C_{90}H_{124}Br_2$, C 79.15 %, H 9.15%, Br 11.70%).

1,4-Bis(4'-methoxyphenyl)-2,3,5,6-tetrakis(4'-dodecylphenyl) benzene (2-33):

The synthetic procedure follows that in the preparation of **2-28** with **2-14b** (1.3 g, 1.0 mmol, 1 equiv), 4-methoxyphenylboronic acid (0.76 g, 5.0 mmol, 5 equiv), Pd(PPh₃)₄ (60 mg, 0.050 mmol, 0.05 equiv), K₂CO₃ (2.7 g, 19.6 mmol, 20 equiv), Aliquat[®] 336 (7 mg, 0.02 mmol, 0.02 equiv) and toluene (30 mL) at 100 °C for 48 h. The residue was purified by column chromatography using petroleum ether (PE) / CH₂Cl₂ (8/1) as eluent (*R_f* = 0.2). Compound **2-33** (1.15 g, 91%) was isolated as a colorless oil.

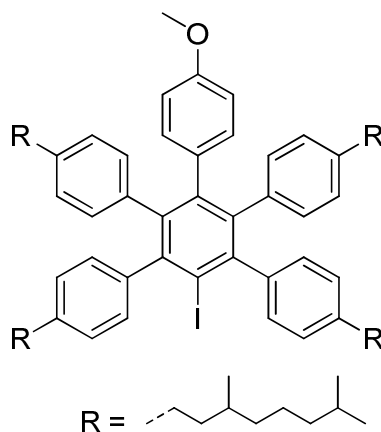
FD-MS (8 kV): *m/z* = 1267.6 (100%, M⁺) (calcd. for C₉₂H₁₃₀O₂ = 1268.06 g mol⁻¹).

¹H-NMR (250 MHz, CD₂Cl₂): δ = 6.73-6.64 (m, 20H, aryl-*H*), 6.40 (d, ³*J* = 8.8 Hz, 4H, aryl-*H*), 3.59 (s, 6H, -OCH₃), 2.37 (t, ³*J* = 6.8 Hz, 8H, α-CH₂), 1.43-1.13 (m, 80H, alkyl-*H*), 0.88 (m, 12H, -CH₃) ppm.

¹³C-NMR (62.5 MHz, CD₂Cl₂): δ = 157.3, 140.9, 140.2, 139.8, 138.7, 133.9, 132.8, 131.6, 126.9, 112.2, 55.2, 35.6, 32.3, 31.6, 30.09, 30.06, 30.0, 29.9, 29.82, 29.76, 29.3, 23.1, 14.3 ppm.

Elemental Analysis: C 87.03%, H 10.01%, (calcd. for C₉₂H₁₃₀O₂, C 87.14%, H 10.33%).

1-Iodo-4-(4'-methoxyphenyl)-2,3,5,6-tetrakis[4'-(3'',7''-dimethyloctyl)phenyl]benzene (2-34):



The synthetic procedure follows that in the preparation of **2-28** with **2-14c** (597 mg, 0.5mmol, 1 equiv), 4-bromophenyl boronic acid (83.6 mg, 0.55 mmol, 1.1 equiv), Pd(PPh₃)₄ (30 mg, 0.03 mmol, 0.06 equiv), K₂CO₃ (1.38 g, 10 mmol, 20 equiv) and toluene (20 mL) at 80 °C for 12 h. The product was purified by a column chromatography with Petroleum ether (PE) / CH₂Cl₂ (20/1) as eluent affording 201mg **2-34** as white solid (yield, 35%).

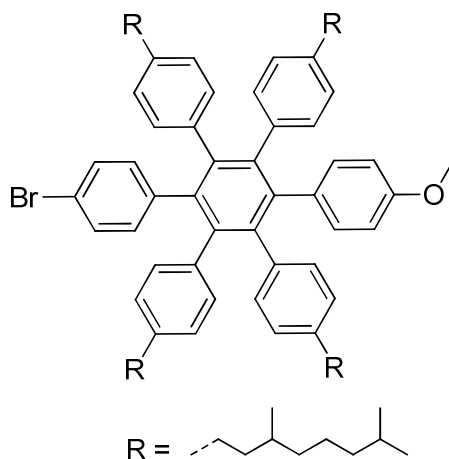
FD-MS (8 kV): $m/z = 1176.1$ (100%, M⁺), (calcd. for C₇₇H₁₀₇IO = 1175.6).

¹H-NMR (250 MHz, CD₂Cl₂): $\delta = 6.97$ (m, 8H, aryl-*H*), 6.72 (m, 10H, aryl-*H*), 6.37 (d, ³J = 8.5Hz, 2H aryl-*H*), 3.55 (s, 3H, -OCH₃), 2.54-2.34 (m, 8H, α -CH₂), 1.33-1.13 (m, 40H, alkyl-*H*), 0.88-0.79 (m, 36H, -CH₃) ppm.

¹³C-NMR (62.5 MHz, CD₂Cl₂): $\delta = 157.53, 146.30, 143.70, 141.94, 141.85, 141.58, 140.56, 138.56, 132.95, 132.54, 131.21, 130.69, 127.56, 126.90, 112.27, 107.67, 39.79, 39.17, 38.96, 37.55, 37.49, 33.52, 33.23, 32.88, 32.60, 30.14, 28.44, 25.16, 25.11, 22.91, 22.84, 19.85, 19.80$ ppm.

Elemental Analysis: C 78.40%, H 9.34%, (calcd. for C₇₇H₁₀₇IO, C 78.67%, H 9.17%, I 10.79%, O 1.36%).

1-(4'-Bromophenyl)-4-(4'-methoxyphenyl)-2,3,5,6-tetrakis[4'-(3'',7''-dimethyloctyl)phenyl] benzene (2-35):



The synthetic procedure follows that in the preparation of **2-28** with **2-34** (572 mg, 0.49 mmol, 1.0 equiv), 4-bromophenyl boronic acid (489 mg, 2.44 mmol, 5.0 equiv), Pd(PPh₃)₄ (28.1 mg, 0.02 mmol, 0.04 equiv), K₂CO₃ (1.3 g, 9.74 mmol, 20 equiv) and toluene (100 mL) at 80 °C for 12 h. The product was purified by a column chromatography with Petroleum ether (PE) / CH₂Cl₂ (8/1) as eluent affording 407 mg **2-35** as colorless oil in a yield of 69%.

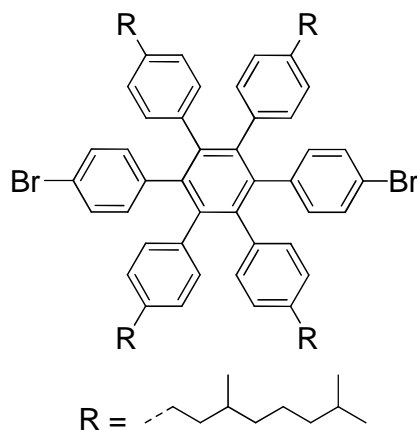
MALDI-TOF MS (TCNQ): $m/z = 1205$ (100%, M⁺), (calcd. for C₈₃H₁₁₁BrO = 1204.7).

¹H-NMR (250MHz, CD₂Cl₂): $\delta = 6.97$ (d, ³J = 8.4Hz, 2H, aryl-*H*), 6.68 (s, 20H, aryl-*H*), 6.40 (d, ³J = 8.7Hz, 2H aryl-*H*), 3.59(s, 3H, -OCH₃), 2.40-2.36 (m, 8H, α -CH₂), 1.26-1.13 (m, 40H, alkyl-*H*), 0.88-0.80 (m, 36H, -CH₃) ppm.

¹³C-NMR (62.5MHz, CD₂Cl₂): $\delta = 157.39, 141.01, 140.73, 140.69, 140.58, 140.43, 140.21, 139.30, 138.43, 138.37, 138.21, 133.65, 133.58, 132.75, 131.58, 129.83, 127.01, 126.87, 119.32, 112.21, 55.17, 39.72, 38.97, 37.44, 33.19, 33.16, 32.52, 32.39, 28.35, 25.04, 22.83, 22.76, 22.75, 19.72$ ppm.

Elemental Analysis: C 82.61%, H 9.41%, (calcd. for C₈₃H₁₁₁BrO, C 82.75%, H 9.29%, Br 6.63%, O 1.33%).

1,4-Bis(4'-bromophenyl)-2,3,5,6-tetrakis[4'-(3'',7'')-dimethyloctyl]phenyl] benzene (2-11):



The synthetic procedure follows that in the preparation of **2-28** with **2-14c** (1.2 g, 1.0 mmol), 4-bromophenylboronic acid (800 mg, 4.0 mmol), K_2CO_3 (2.76 g, 20 mmol), Aliquat® 336 (8 mg, 0.02 mmol), $Pd(PPh_3)_4$ (58 mg, 0.05 mmol) and toluene (30 mL) at 80 °C for 18 h. The residue was purified by column chromatography (petroleum ether (PE) / CH_2Cl_2 (15/1)) to give **2-11** as a yellow solid (1.17 g, yield, 93%).

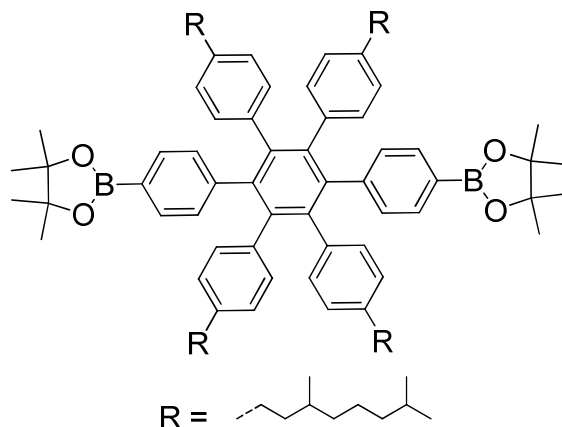
FD-MS (8 kV): $m/z = 1253.7$, (calcd. for $C_{82}H_{108}Br_2 = 1253.6 \text{ g mol}^{-1}$).

1H -NMR (250 MHz, CD_2Cl_2): $\delta = 6.87$ (d, $^3J = 8.26 \text{ Hz}$, 4H, aryl-*H*), 6.60 (m, 20H, aryl-*H*), 2.30 (m, 8H, α - CH_2), 1.50-0.90 (m, 40 H, alkyl-*H*), 0.78-0.73 (m, 36H, - CH_3) ppm.

^{13}C -NMR (62.5 MHz, CD_2Cl_2): $\delta = 141.1, 141.0, 140.9, 140.2, 138.4, 133.9, 131.9, 130.3, 127.5, 119.8, 40.1, 39.3, 37.8, 33.6, 32.8, 28.8, 25.5, 23.2, 23.2, 20.1$ ppm.

Elemental Analysis: C 78.51%, H 8.72% (calcd. for $C_{82}H_{108}Br_2$, C 78.57%, H 8.68%, Br 12.75%).

1,4-Bis[4'-(4'',4'',5'',5''-tetramethyl-1'',3''-dioxaborolan-2''-yl)phenyl]-2,3,5,6-tetrakis[4'-(3'',7''-dimethyloctyl)phenyl] benzene (2-36):



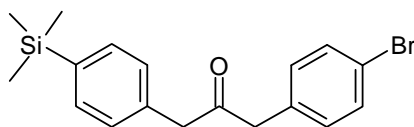
To a solution of **2-11** (600 mg, 0.48 mmol) in dry THF (8 mL) under argon at $-78\text{ }^{\circ}\text{C}$, *n*-BuLi (1.6 M/*n*-Hexane, 0.78 mL, 1.24 mmol) was added and the resulting solution was stirred at $-78\text{ }^{\circ}\text{C}$ for 1 h. Then 2-isopropoxy-4,4,5,5-tetramethyl-[1,3,2]dioxaborolane (267 mg, 1.44 mmol) was added at $-78\text{ }^{\circ}\text{C}$ and the reaction was allowed to be stirred at r.t. for 3 h. The reaction was quenched with water (5 ml) and the resulting mixture was extracted with CH_2Cl_2 (15 mL \times 3). The combined organic layers were washed with brine (10 mL), dried with MgSO_4 and concentrated in vacuum. The residue was purified by column chromatography (eluent, *n*-hexane/ CH_2Cl_2 = 4/1) to give 530 mg **2-36** as oily liquid in a yield of 82%.

FD-MS (8 kV): m/z = 1347.0 (100%, M^+), (calcd. For $\text{C}_{94}\text{H}_{132}\text{B}_2\text{O}_4$ = 1347.7 g mol^{-1}).

$^1\text{H-NMR}$ (250 MHz, CD_2Cl_2): δ = 7.14 (d, ^3J = 7.91 Hz, 4H, aryl-*H*), 6.78 (d, ^3J = 7.88 Hz, 4H, aryl-*H*), 6.61 (d, ^3J = 8.44 Hz, 8H, aryl-*H*), 6.57 (d, ^3J = 8.54 Hz, 8H, aryl-*H*), 2.83 (m, 8H, $\alpha\text{-CH}_2$), 1.55-0.93 (m, 40 H, alkyl-*H*) 0.78-0.71 (m, 36H, -CH_3) ppm.

$^{13}\text{C-NMR}$ (62.5 MHz, CD_2Cl_2): δ = 145.0, 141.0, 140.9, 140.7, 138.6, 133.6, 132.0, 131.6, 127.2, 84.3, 40.1, 39.3, 37.8, 33.6, 32.9, 28.7, 25.5, 25.4, 23.2, 23.2, 20.2 ppm.

Elemental Analysis: C 83.56%, H 9.93% (calcd. for $\text{C}_{94}\text{H}_{132}\text{B}_2\text{O}_4$, C 83.77%, H 9.87%, B 1.60%, O 4.75%).

1-(4'-Trimethylsilylphenyl)-3-(4'-bromophenyl)-propan-2-one (2-49):

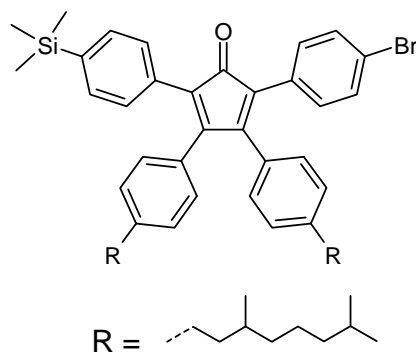
Freshly prepared Collman's reagent (450 mg, 1.2 mmol) was charged in a flame-dried 50 mL Schlenk tube. 4-Trimethylsilybenzyl bromide (**2-48**) (243 mg, 1 mmol) in 7 mL dry NMP was carefully degassed with three "freeze-pump-thaw" cycles method three times in another 25 mL Schlenk tube. The solution of **2-48** was then transferred to the Schlenck tube containing Collman's reagent dropwise at 0 °C. The mixture was stirred at 0 °C for 30 min followed by warming to r.t. 1 h later, the mixture was cooled to 0 °C again and 4-bromobenzyl bromide (500 mg, 2 mmol), which was dissolved in 10 mL dry NMP and carefully degassed with "freeze-pump-thaw" method, was added dropwise. The reaction mixture was allowed to be heated to 45 °C and stirred for 14 h. large amount of saturated NH₄Cl aqueous solution (10 mL) was used to quench the excess Collman's reagent after cooling down. The crude product was extracted with CH₂Cl₂ (150 mL × 3) and washed with brine. After being dried over MgSO₄, the organic phase was filtered out and the solvent was removed under reduced pressure. The residue was purified by column chromatography (eluent, hexane/ethyl acetate 20/1). 210 mg **2-49** was collected as white solid in a yield of 58%.

FD-MS (8 kV): $m/z = 362.5$ (100%, M⁺), (calcd. for C₁₈H₂₁BrOSi = 361.4 g mol⁻¹).

¹H-NMR (250 MHz, CD₂Cl₂): $\delta = 7.50$ (d, ³J = 7.9Hz, 2H, aryl-*H*), 7.46 (d, ³J = 8.4Hz, 2H, aryl-*H*), 7.16 (d, ³J = 7.8Hz, 2H, aryl-*H*), 7.04 (d, ³J = 8.3Hz, 2H aryl-*H*), 3.74 (s, 2H, -CH₂-CO-), 3.71 (s, 2H, -CH₂-CO-), 0.26 (s, 9H, -CH₃) ppm.

¹³C-NMR (62.5 MHz, CD₂Cl₂): $\delta = 205.03, 139.47, 134.89, 134.04, 133.72, 131.93, 131.74, 129.27, 121.17, 49.65, 48.65, -1.11$ ppm.

2-(4'-Trimethylsilylphenyl)-5-(4'-bromophenyl)-3,4-bis[4'-(3'',7'')-dimethyloctyl]phenyl]cyclopentadien-1-one (2-50):



Compound **2-49** (210 mg, 0.6 mmol) and compound **2-8** (299 mg, 0.6 mmol) were dissolved in 3 mL *t*-butanol in a 25 mL Schlenk tube under argon. The mixture was heated to 85 °C. Subsequently, Bu₄NOH (0.75 mL, 1 M solution in methanol) was added dropwise. 10 min later, the mixture was cooled in an ice bath and diluted with CH₂Cl₂ (10 mL). After being washed with brine (30 mL) and extracted with CH₂Cl₂ (30 mL × 3), the organic layer was dried over MgSO₄. The solvent was removed in vacuo and the residue was purified by column chromatography with an eluent of petroleum ether (PE) /CH₂Cl₂ (6/1). 297 mg **2-50** was collected as dark reddish solid in a yield of 51%.

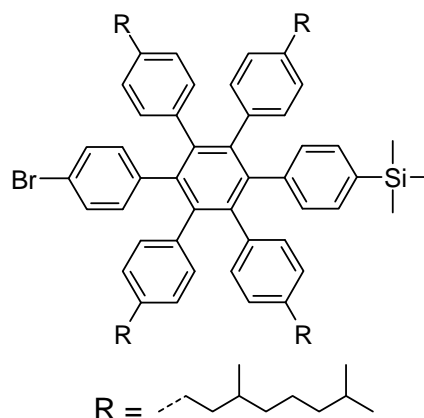
FD-MS (8 kV): $m/z = 816.7$ (100%, M⁺), (calcd. for C₅₂H₆₇BrOSi = 816.1 g mol⁻¹).

¹H-NMR (250 MHz, CD₂Cl₂): δ = 7.43 (d, ³J = 8.2Hz, 2H, aryl-*H*), 7.39 (d, ³J = 8.6Hz, 2H, aryl-*H*), 7.21 (d, ³J = 8.1Hz, 2H, aryl-*H*), 7.13 (d, ³J = 8.6Hz, 2H, aryl-*H*), 7.03 (d, ³J = 8.1Hz, 2H aryl-*H*), 6.86 (d, ³J = 7.1Hz, 2H, aryl-*H*), 6.83 (d, ³J = 6.9Hz, 2H, aryl-*H*), 2.62-2.53 (m, 4H, α-CH₂), 1.40-1.14 (m, 20H, alkyl-*H*), 0.89-0.86 (m, 36H, -CH₃), 0.25 (s, 9H, -CH₃) ppm.

¹³C-NMR (62.5 MHz, CD₂Cl₂): δ = 200.36, 156.11, 155.27, 144.66, 144.43, 140.12, 133.27, 132.09, 131.81, 131.46, 130.69, 130.64, 130.44, 129.59, 129.54, 128.36, 128.27, 125.59, 124.25, 121.77, 39.68, 38.91, 38.88, 37.49, 33.64, 32.83, 28.34, 25.09, 22.82, 22.75, 19.73, -1.15 ppm.

Elemental Analysis: C 76.90%, H 8.65% (calcd. for C₅₂H₆₇BrOSi, C 76.53%, H 8.28%, Br 9.79%, O 1.96%, Si 3.44%).

1-(4'-Trimethylsilylphenyl)-4-(4'-bromophenyl)-2,3,5,6-tetrakis[4'-(3'',7'')-dimethyloctyl]phenyl] benzene (2-51):



Compound **2-50** (4.2 g, 5.15 mmol) and compound **2-7** (2.36 g, 5.15 mmol) were dissolved in 9 mL diphenyl ether. The mixture was heated to 185 °C under argon atmosphere. The reaction lasted for 12 h and diluted with CH₂Cl₂ after being cooled to r.t.. The organic phase was washed with brine (30 mL), extracted with CH₂Cl₂ and dried with MgSO₄. After evaporation of solvent under reduced pressure, the product was purified by column chromatography with gradient eluent (petroleum ether → petroleum ether/CH₂Cl₂ 8/1 → petroleum ether/CH₂Cl₂ 5/1). 2.54 g compound **2-51** were collected as white solid in a yield of 40%.

FD-MS (8 kV): $m/z = 1245.8$ (100%, M⁺), (calcd. for C₃₅H₁₁₇BrSi = 1246.87 g mol⁻¹)

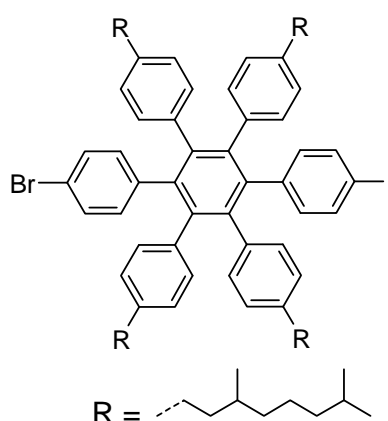
¹H-NMR (250 MHz, CD₂Cl₂): δ = 7.01 (d, ³J = 7.8 Hz, 2H, aryl-*H*), 6.98 (d, ³J = 8.2 Hz, 2H, aryl-*H*), 6.72-6.63 (m, 18H, aryl-*H*), 2.40-2.33 (m, 8H, α-CH₂), 1.27-1.14 (m, 41H, alkyl-*H*), 0.88-0.80 (m, 35H, -CH₃), 0.10 (s, 9H, -CH₃) ppm.

¹³C-NMR (125 MHz, CD₂Cl₂): δ = 141.81, 141.22, 140.80, 140.73, 140.59, 140.51, 140.41, 139.51, 138.27, 138.19, 136.94, 133.61, 131.71, 131.61, 131.13, 129.87, 127.05,

126.83, 119.38, 39.77, 39.74, 39.25, 38.96, 37.48, 33.32, 33.18, 32.73, 32.42, 28.37, 25.06, 25.04, 22.84, 22.77, 19.78, 19.75, 1.15, -1.13 ppm.

Elemental Analysis: C 81.83%, H 9.45% (calcd. for C₈₅H₁₁₇BrSi, C 81.88%, H 9.46%, Br 6.41%, Si 2.25%).

1-(4'-iodophenyl)-4-(4'-bromophenyl)-2,3,5,6-tetrakis[4'-(3'',7'')-dimethyloctyl)phenyl] benzene (2-52):



Compound **2-51** (860 mg, 0.69 mmol) was dissolved in 30 mL chloroform. The solution was bubbled with argon for 20 min at 0 °C. ICl in CH₂Cl₂ solution (0.72 mL, 1 M) was then added dropwise. After being stirred for 10 min at 0 °C, the mixture was allowed to warm to ambient temperature. 40 min. later, large amount of 10 % Na₂SO₃ aqueous solution (50 mL) was added to quench the excess ICl. The crude compound was further washed with brine (50 mL) and extracted with CH₂Cl₂ (100 mL × 3). The combined organic layer was dried over MgSO₄ and filtered. The solvent was evaporated under reduced pressure and the residue was further purified by column chromatography with petroleum ether (PE) /CH₂Cl₂ 15/1 as eluent affording 854 mg **2-52** as white solid in a yield of 95.2%.

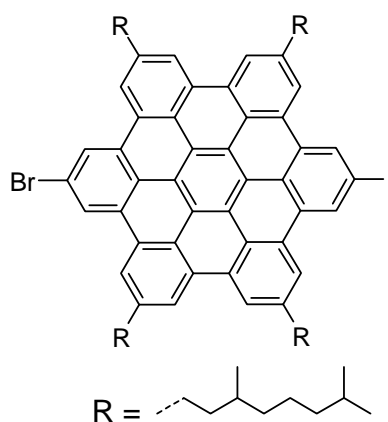
FD-MS (8 kV): $m/z = 1301.6$ (100%, M⁺), $m/z = 650.5$ (8%, M²⁺), (calcd. for C₈₂H₁₀₈BrI = 1300.6 g mol⁻¹).

$^1\text{H-NMR}$ (250 MHz, CD_2Cl_2): $\delta = 7.17$ (d, $^3J = 7.9\text{Hz}$, 2H, aryl-*H*), 6.97 (d, $^3J = 8.1\text{Hz}$, 2H, aryl-*H*), 6.69 (s, 18H, aryl-*H*), 6.58 (d, $^3J = 8.0\text{Hz}$, 2H, aryl-*H*), 2.43-2.35 (m, 8H, $\alpha\text{-CH}_2$), 1.26-1.14 (m, 38H, alkyl-*H*), 0.88-0.81 (m, 36H, -CH_3) ppm.

$^{13}\text{C-NMR}$ (175 MHz, CD_2Cl_2): $\delta = 141.20, 140.78, 140.73, 140.66, 139.96, 139.89, 138.02, 135.96, 133.85, 133.58, 131.59, 129.94, 127.12, 119.50, 90.98, 39.80, 39.01, 37.52, 33.23, 32.49, 30.11, 28.41, 25.11, 22.88, 22.82, 19.82, 19.78$ ppm.

Elemental Analysis: C 74.98%, H 8.31% (calcd. for $\text{C}_{82}\text{H}_{108}\text{BrI}$, C 75.73%, H 8.37%, Br 6.14%, I 9.76%).

2-Iodo-11-bromo-5,8,14,17-tetra(3',7'-dimethyloctyl)-hexa-*peri*-hexabenzocoronene (2-47):



Compound **2-51** (89 mg, 0.07 mmol) was dissolved in CH_2Cl_2 (83 mL). The solution was bubbled with argon for 15 min at r.t.. FeCl_3 (255.6 mg, 1.57 mmol) in nitromethane (0.84 mL) solution was then added dropwise. The mixture was stirred for 40 min at r.t. and the reaction was quenched with methanol (300 mL). The solvent was removed in vacuo and the residue was filtered through a silica gel pad with hot toluene. After removing toluene, the residue was dissolved in THF (2mL) and precipitated in methanol (100 mL). 84 mg **2-47** was collected as yellow powder in a yield of 93%.

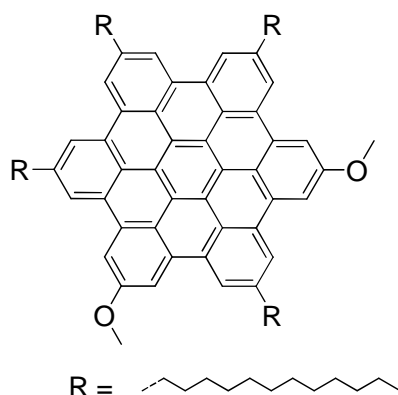
MALDI-TOF MS (TCNQ): $m/z = 1288$ (100%, M^+), (calcd. for $\text{C}_{82}\text{H}_{96}\text{BrI} = 1288.49$ g mol^{-1}).

$^1\text{H-NMR}$ (250 MHz, CD_2Cl_2): $\delta = 6.95\text{-}6.41$ (m, 12H, aryl-*H*), 2.11-2.03 (m, 8H, $\alpha\text{-CH}_2$), 1.43-0.84 (m, 76H, alkyl-*H*) ppm.

$^{13}\text{C-NMR}$ (125 MHz, CD_2Cl_2): $\delta = 138.18, 138.01, 133.66, 131.13, 129.84, 128.88, 127.93, 127.69, 127.31, 126.62, 126.08, 125.79, 125.62, 125.51, 121.82, 121.73, 119.95, 119.48, 118.99, 116.20, 115.74, 115.48, 115.34, 91.49, 40.24, 39.92, 37.74, 34.49, 33.91, 30.07, 28.51, 25.46, 23.09, 22.95, 20.01$ ppm.

Elemental Analysis: C 76.05%, H 7.47% (calcd. for $\text{C}_{82}\text{H}_{96}\text{BrI}$, C 76.44%, H 7.51%, Br 6.20%, I 9.85%).

2,8-Dimethoxy-5,11,14,17-tetradodecyl-hexa-*peri*-hexabenzocoronene (2-40):



2-36 (200 mg, 0.16 mmol) was dissolved in CH_2Cl_2 (200 mL) and the solution was bubbled with argon for 20 min. $\text{FeCl}_3/\text{CH}_3\text{NO}_2$ solution (1.7 mL, 1.89 M, 3.2 mmol) was then added dropwise. The reaction was quenched by adding methanol (300 mL) after 20 min. The solvent was removed under reduced pressure and the crude product was filtered through a short silica-pad with hot toluene. **2-40** (40 mg, 20%) was obtained as a yellow powder after purification by recrystallization from toluene.

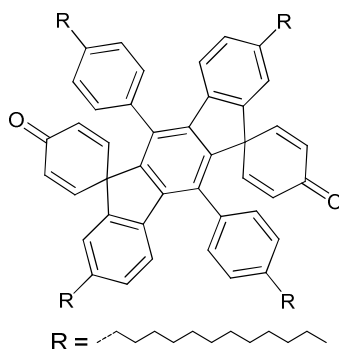
MALDI-TOF MS (TCNQ): $m/z = 1256$ (100%, M^+), (calcd. for $\text{C}_{92}\text{H}_{118}\text{O}_2 = 1255.97$ g mol^{-1}).

¹H-NMR (500 MHz, CDCl₃): δ = 7.91 (s, 2H, aryl-*H*), 7.87 (s, 2H, aryl-*H*), 7.67 (s, 2H, aryl-*H*), 7.40 (s, 2H, aryl-*H*), 7.36 (s, 2H, aryl-*H*), 7.21 (s, 2H, aryl-*H*), 3.75 (s, 6H, -OCH₃), 2.78 (t, ³J = 7.7 Hz, 2H, α -CH₂), 2.65 (t, ³J = 7.7 Hz, 4H, α -CH₂), 2.36 (t, ³J = 7.7 Hz, 2H, α -CH₂), 1.85 (m, 2H, β -CH₂), 1.77 (m, 6H, β -CH₂), 1.52-1.23 (m, 86H, alkyl-*H*), 0.88 (m, 12H, -CH₃) ppm.

¹³C-NMR (125 MHz, CDCl₃): δ = 148.0, 130.3, 130.1, 130.0, 121.9, 121.8, 120.4, 120.3, 119.8, 119.6, 113.9, 113.7, 111.9, 111.8, 111.7, 110.5, 110.4, 110.2, 110.1, 109.9, 108.8, 108.5, 97.1, 97.0, 46.2, 28.4, 28.2, 27.9, 23.4, 23.3, 23.1, 22.9, 21.3, 21.3, 21.2, 21.1, 21.0, 20.9, 20.8, 20.5, 13.8, 5.1 ppm.

Elemental Analysis: C 87.25%, H 9.88%, (calcd. for C₉₂H₁₁₈O₂, C 87.98%, H 9.47%).

5,11-Bis[4'-dodecylphenyl]-2,8-didodecyl-6,12-bis[spiro(6'-oxo-cyclohexa-1',4'-diene)-3']indeno[1,2-b]fluorene (2-41):



The mother liquor, which was used for the recrystallization of **2-40**, was concentrated. Column chromatography was used for the purification with an eluent of petroleum ether (PE) /CH₂Cl₂ (2/3). The resulting product was further recrystallized from a CH₂Cl₂/acetone (1/1) mixture to afford **2-41** (138 mg, 70% yield) as brown crystals.

FD-MS (8 kV): m/z (%) = 1236.8 (100%, M⁺), 618.2 (21%, M²⁺), (calcd. for C₉₀H₁₂₂O₂ = 1235.97 g mol⁻¹).

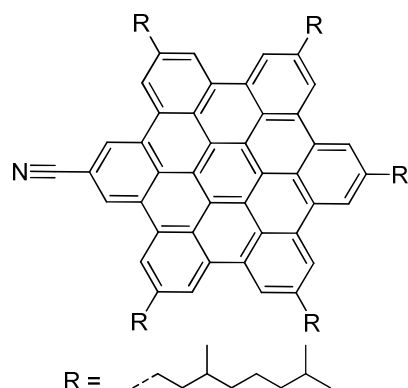
¹H-NMR (250 MHz, CD₂Cl₂): δ = 7.19 (s, 8H, aryl-*H*), 6.82 (s, 2H, aryl-*H*), 6.81 (d, ³J = 8.6 Hz, 2H, aryl-*H*), 6.54 (d, ³J = 9.8 Hz, 4H, ethenyl-*H*), 6.19 (d, ³J = 7.9 Hz, 2H, aryl-

H), 6.05 (d, $^3J = 9.8$ Hz, 4H, ethenyl-*H*), 2.69 (t, $^3J = 7.2$ Hz, 4H, α - CH_2), 2.46 (t, $^3J = 7.7$ Hz, 4H, α - CH_2), 1.67 (m, 4H, β - CH_2), 1.39-1.21 (m, 76H, alkyl-*H*), 0.91-0.84 (m, 12H, - CH_3) ppm.

^{13}C -NMR (62.5 MHz, CD_2Cl_2): $\delta = 185.7, 149.9, 144.0, 143.4, 143.3, 142.8, 139.7, 139.2, 136.2, 133.9, 130.0, 129.3, 128.9, 128.4, 124.5, 123.7, 56.9, 36.1, 32.3, 32.3, 31.9, 31.9, 30.1, 30.1, 29.99, 29.97, 29.91, 29.8, 29.7, 29.6, 23.1, 14.3, 14.2$ ppm.

Elemental Analysis: C 87.35%, H 9.98%, (calcd. for $C_{90}H_{122}O_2$, C 87.46%, H 9.95%).

2-Cyano-5,8,11,14,17-penta(3,7-dimethyloctanyl)-hexa-*peri*-hexabenzocoronene (4-1):



113 mg (0.09 mmol) 2-Bromo-5,8,11,14,17-penta(3,7-dimethyloctanyl)-hexa-*peri*-hexabenzocoronene (**4-2**) and 15.5 mg (0.18 mmol) cuprous cyanate were mixed with 5 mg (4.4×10^{-3} mmol) $Pd(PPh_3)_4$ in 3 mL NMP in a 5 mL septum-sealed microwave tube. The solution was irradiated in a monomode microwave cavity (170 °C, 300 W, 6 h). After cooling, the mixture was washed with 3×15 mL saturated ammonium chloride solution and extracted with dichloromethane. The organic phase was dried over $MgSO_4$ and the solvent was removed under reduced pressure. The residue was purified by column chromatography using petroleum ether (PE) / CH_2Cl_2 (3/1) as eluent. The product was further precipitated in 80 mL methanol and collected as yellow powder in a yield of 80 % (87mg).

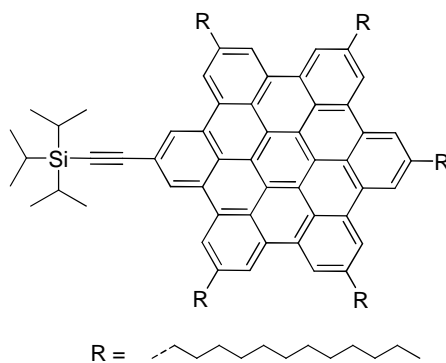
MALDI-TOF MS (TCNQ): $m/z = 1249$ (100%, M^+) (calcd. for $C_{93}H_{117}N = 1248.98$ g mol^{-1}).

1H -NMR (250 MHz, THF- d_8): $\delta = 7.92$ (s, 2H, aryl- H), 7.79 (s, 2H, aryl- H), 7.46 (s, 2H, aryl- H), 7.39 (s, 2H, aryl- H), 7.31 (s, 2H, aryl- H), 7.11 (s, 2H, aryl- H), 2.94 (bs, 2H, α - CH_2), 2.72 (bs, 4H, α - CH_2), 2.36 (bs, 4H, α - CH_2), 1.37 - 0.98 ppm (m, 95H, alkyl- H).

^{13}C -NMR (125 MHz, THF- d_8): $\delta = 141.02, 140.52, 140.42, 130.20, 129.68, 129.36, 129.18, 127.71, 125.73, 123.13, 122.73, 122.53, 122.26, 122.00, 121.64, 121.42, 121.07, 120.29, 120.00, 119.29, 118.81, 117.00, 109.31, 41.30, 41.09, 40.66, 40.60, 40.58, 38.56, 35.86, 35.73, 35.33, 34.63, 34.57, 34.50, 30.57, 29.08, 26.05, 23.29, 23.18, 20.47, 20.39$ ppm.

Elemental Analysis: C 88.20%, H 9.62%, N 0.86%, (calcd. for $C_{93}H_{117}N$, C 89.44%, H 9.44%, N 1.12%).

2-[2'-Tris(1'''-methylethyl)silylethynyl]-5,8,11,14,17-penta(dodecyl)-hexa-*peri*-hexabenzocoronene (4-5):



2-Bromo-5,8,11,14,17-penta(dodecyl)-hexa-*peri*-hexabenzocoronene (200 mg, 0.14 mmol), triisopropylsilyl acetylene (38.3 mg, 0.21 mmol), $Pd(PPh_3)_4$ (8 mg, 7×10^{-3} mmol) and CuI (2.7 mg, 0.01 mmol) were dissolved in THF/ Et_3N 1/1 co-solvent (6 mL). The mixture was carefully degassed three times by the freeze-and-thaw method and stirred at 50 °C for 20 h. After cooling to r.t., the reaction was quenched with water (30 mL). The

organic phase was extracted with CH_2Cl_2 (3×50 mL) and dried over MgSO_4 . The solvent was removed in vacuo and the product was purified by column chromatography by using petroleum ether (PE) / CH_2Cl_2 (10/1) as the eluent to afford product as a yellow powder (121 mg, 56 %).

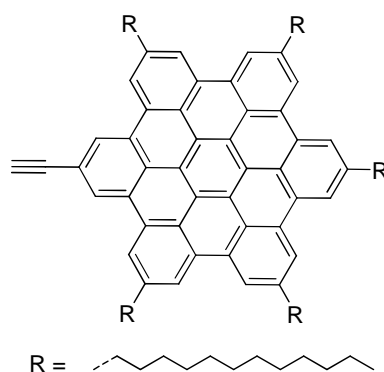
MALDI-TOF MS (TCNQ): $m/z = 1544$ (100%, M^+) (calc. for $\text{C}_{113}\text{H}_{158}\text{Si} = 1544.60$ g mol^{-1}).

$^1\text{H-NMR}$ (250 MHz, THF- d_8): $\delta = 8.72$ (s, 2H, aryl- H), 7.95 (s, 2H, aryl- H), 7.82 (s, 2H, aryl- H), 7.78 (s, 2H, aryl- H), 7.73 (s, 2H, aryl- H), 7.71 (s, 2H, aryl- H), 3.01-2.95 (m, 4H, $\alpha\text{-CH}_2$), 2.84 - 2.79 (m, 6H, $\alpha\text{-CH}_2$), 1.99 - 1.96 (m, 10H, $\beta\text{-CH}_2$), 1.36 - 1.11 (m, 105H, alkyl- H), 0.92 - 0.90 ppm (m, 21H, alkyl- H).

$^{13}\text{C-NMR}$ (75 MHz, THF- d_8): $\delta = 140.00, 139.92, 139.88, 129.80, 129.61, 129.04, 124.81, 123.08, 122.82, 122.07, 121.48, 121.44, 120.46, 119.68, 119.46, 119.11, 118.44, 110.81, 91.20, 90.22, 82.14, 66.33, 38.10, 33.32, 33.16, 32.77, 31.19, 31.15, 31.10, 30.91, 30.80, 30.70, 30.60, 30.22, 23.39, 19.63, 18.76, 14.21, 12.84, 12.18$ ppm.

Elemental Analysis: C 87.61%, H 10.14%, (calcd. for $\text{C}_{113}\text{H}_{158}\text{Si}$, C 87.87%, H 10.31%, Si 1.82%).

2-Ethynyl-5,8,11,14,17-penta(dodecyl)-hexa-*peri*-hexabenzocoronene (4-3):



Mono-triisopropylsilylethynyl HBC **4-5** (100 mg, 0.06 mmol) and tetra *n*-butyl ammonium fluoride (34 mg, 0.11 mmol) were dissolved in dry THF (20 mL). The

mixture was stirred at ambient temperature for 20 min. The mixture was poured into methanol (60 mL). The organic phase was washed with brine, extracted with dichloromethane (3×150 mL) and dried over MgSO_4 . The product was precipitated in 100 ml methanol after the solvents were removed *in vacuo*. 75 mg product was collected as brown solid in a yield of 95 %.

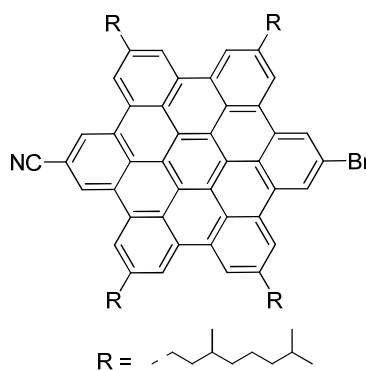
MALDI-TOF MS (TCNQ): $m/z = 1388$ (100%, M^+) (calc. for $\text{C}_{104}\text{H}_{138} = 1388.26$ g mol^{-1}).

$^1\text{H-NMR}$ (250 MHz, THF- d_8): $\delta = 7.92$ (s, 2H, aryl-*H*), 7.58 (s, 2H, aryl-*H*), 7.49 (s, 2H, aryl-*H*), 7.41 (s, 2H, aryl-*H*), 7.37 (s, 2H, aryl-*H*), 7.12 (s, 2H, aryl-*H*), 3.69 (s, 1H, $\text{CH}\equiv$), 2.59 - 2.44 (m, 10H, $\alpha\text{-CH}_2$), 1.37 - 1.28 (m, 95H, alkyl-*H*), 0.94 - 0.93 ppm (m, 20H, alkyl-*H*).

$^{13}\text{C-NMR}$ (62.5 Hz, THF- d_8): $\delta = 139.71, 139.49, 130.92, 129.43, 129.27, 129.15, 129.04, 128.87, 128.82, 128.46, 124.27, 124.19, 122.51, 122.38, 121.34, 121.05, 120.98, 120.90, 119.02, 118.69, 118.50, 86.22, 33.01, 31.28, 31.10, 31.01, 30.94, 30.89, 30.84, 30.49, 23.65, 14.54$ ppm.

Elemental Analysis: C 89.97%, H 10.01%, (calcd. for $\text{C}_{104}\text{H}_{138}$, C 89.98%, H 10.02%).

2-Cyano-11-bromo-5,8,14,17-tetra(3',7'-dimethyloctyl)-hexa-*peri*-hexabenzocoronene (5-4):



para-Iodo bromo HBC **2-47** (130 mg, 0.10 mmol), CuCN (10.8 mg, 0.12 mmol) and Pd(PPh₃)₄ (5.8 mg, 0.01 mmol) were mixed with THF (6 mL) in a 25 mL Schlenk tube with a cooling condenser. The system was degassed with two “freeze-pump-thaw” cycles. After warming to r.t., the mixture was heated to 65 °C and stirred for 15 h under argon atmosphere. Methanol (15 mL) was then added to quench the reaction when the mixture was cooled down. The organic phase was washed with brine (3 × 100 mL) and extracted with DCM. After being dried over MgSO₄, the solvents were removed *in vacuo*. The residue was absorbed on minimum silica gel and purified by column chromatography (eluent: petroleum ether (PE) / CH₂Cl₂ (7/4)). The product was further precipitated in methanol (100 mL) affording 97 mg compound **5-4** as yellow powder in a yield of 81%.

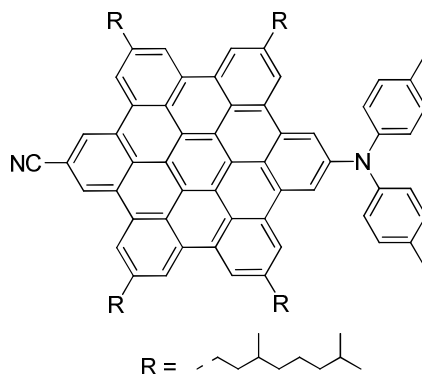
MALDI-TOF MS (TCNQ): $m/z = 1188$ (100%, M⁺) (calc. for C₈₃H₉₆BrN = 1187.56 g mol⁻¹).

¹H-NMR (500 MHz, CDCl₂-CDCl₂, 140 °C): $\delta = 8.17$ (s, 2H, aryl-*H*), 8.13 (s, 2H, aryl-*H*), 7.94 (s, 4H, aryl-*H*), 7.84 (s, 2H, aryl-*H*), 7.78 (s, 2H, aryl-*H*), 3.01 – 2.99 (m, 8H, α -CH₂), 2.05 – 1.29 (m, 40H, alkyl-*H*), 1.04 – 0.87 ppm (m, 36H, -CH₃).

¹³C-NMR (125 Hz, CDCl₂-CDCl₂, 140 °C): $\delta = 157.50, 141.36, 140.41, 128.52, 127.91, 126.69, 123.16, 122.81, 122.46, 121.36, 120.66, 108.75, 39.81, 39.30, 38.03, 37.64, 34.43, 33.64, 29.73, 28.24, 25.15, 25.12, 22.85, 22.79, 20.49, 19.98$ ppm.

Elemental Analysis: C 82.54%, H 7.98%, N 1.01%, (calcd. for C₈₃H₉₆BrN, C 83.94%, H 8.15%, N 1.18%).

2-Cyano-11-(ditolyamino)-5,8,14,17-tetra(3',7'-dimethyloctyl)-hexa-*peri*-hexabenzocoronene (5-1):



5-4 (120 mg, 0.11 mmol), ditolyl amine (99.7 mg, 0.51 mmol), Pd₂(dba)₃ (4.6 mg, 0.01 mmol), *t*-Bu₃P (2.0 mg, 0.01 mmol) and sodium *tert*-butoxide (48.5 mg, 0.51 mmol) were mixed in a pre-dried 25 mL Schlenk tube with dry toluene (12 mL). The system was degassed with three “freeze-pump-thaw” cycles. After warming to r.t., the mixture was heated to 80 °C and stirred for 16 h under argon atmosphere. Methanol (10 mL) was then added to quench the reaction after the mixture was cooled down. The organic phase was then washed with brine (3 × 100 mL) and extracted with DCM. After being dried over MgSO₄, the solvents were removed *in vacuo*. The residue was absorbed on minimum silica gel and purified by column chromatography (eluent: petroleum ether (PE) / CH₂Cl₂ (3/1)). The product was further precipitated in methanol (100 mL) affording 104 mg compound **5-1** as yellow powder in a yield of 79%.

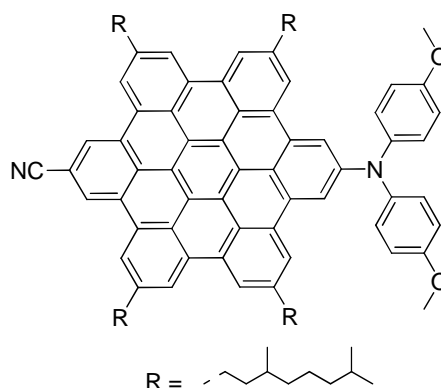
MALDI-TOF MS (TCNQ): $m/z = 1303$ (100%, M⁺) (calc. for C₉₇H₁₁₀N₂ = 1302.87 g mol⁻¹).

¹H-NMR (500 MHz, CDCl₂-CDCl₂, 90 °C): δ = 8.56 (s, 2H, aryl-*H*), 8.28 (s, 2H, aryl-*H*), 8.20 (s, 2H, aryl-*H*), 8.09 (s, 2H, aryl-*H*), 7.89 (s, 2H, aryl-*H*), 7.66 (s, 2H, aryl-*H*), 7.49 (d, ³J = 8.05 Hz, 4H, aryl-*H*), 7.36 (d, ³J = 8.00 Hz, 4H, aryl-*H*), 3.13 – 3.07 (m, 4H, α-CH₂), 2.88 – 2.80 (m, 4H, α-CH₂), 2.50 (s, 6H, aryl-CH₃), 2.00 – 1.17 (m, 40H, alkyl-*H*), 0.96 - 0.92 ppm (m, 36H, -CH₃).

^{13}C -NMR (125 Hz, $\text{CDCl}_2\text{-CDCl}_2$, 110 °C): δ = 147.38, 147.35, 145.89, 141.03, 140.95, 133.60, 131.70, 130.57, 129.73, 129.60, 129.47, 127.81, 125.61, 123.09, 123.02, 122.61, 122.22, 121.93, 121.84, 121.13, 120.18, 120.01, 119.93, 119.89, 118.91, 115.73, 108.92, 39.80, 39.59, 39.47, 37.77, 37.74, 34.80, 34.74, 33.50, 33.40, 29.82, 28.21, 25.13, 25.07, 22.88, 22.80, 21.12, 20.04, 20.02 ppm.

Elemental Analysis: C 86.88%, H 8.40%, N 2.05%, (calcd. for $\text{C}_{97}\text{H}_{110}\text{N}_2$, C 88.35%, H 8.50%, N 2.15%).

2-Cyano-11-[bis-(4'-methoxyphenyl)-amino]-5,8,14,17-tetra(3',7'-dimethyloctyl)-hexa-*peri*-hexabenzocoronene (5-2):



5-4 (120 mg, 0.11 mmol), di-(4-methoxyphenyl) amine (125 mg, 0.55 mmol), $\text{Pd}_2(\text{dba})_3$ (5.0 mg, 0.01 mmol), *t*- Bu_3P (2.2 mg, 0.01 mmol) and sodium *tert*-butoxide (52.5 mg, 0.55 mmol) were mixed in a pre-dried 25 mL Schlenk tube with dry toluene (12 mL). The system was degassed with two “freeze-pump-thaw” cycles. After warming to r.t., the mixture was heated to 80 °C and stirred for 16 h under argon atmosphere. Methanol (10 mL) was then added to quench the reaction after the mixture was cooled down. The organic phase was then washed with brine (3×100 mL) and extracted with DCM. After being dried over MgSO_4 , the solvents were removed *in vacuo*. The residue was absorbed on minimum silica gel and purified by column chromatography (eluent: petroleum ether (PE) / CH_2Cl_2 (2/3)). The product was further precipitated in methanol (100 mL) affording 108 mg compound **5-2** as yellow powder in a yield of 74%.

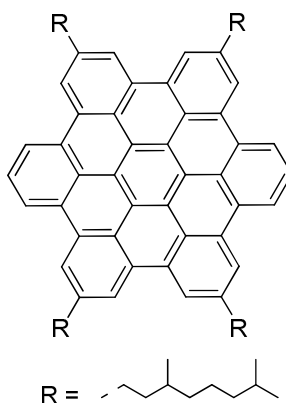
MALDI-TOF MS (TCNQ): $m/z = 1336$ (100%, M^+) (calc. for $C_{97}H_{110}N_2O_2 = 1335.92$ g mol^{-1}).

1H -NMR (700 MHz, $CDCl_2-CDCl_2$, 90 °C): $\delta = 8.57$ (s, 2H, aryl-*H*), 8.43 (s, 2H, aryl-*H*), 8.31 (s, 2H, aryl-*H*), 8.27 (s, 2H, aryl-*H*), 8.16 (s, 2H, aryl-*H*), 7.90 (s, 2H, aryl-*H*), 7.54 (d, $^3J = 7.56$ Hz, 4H, aryl-*H*), 7.14 (d, $^3J = 7.57$ Hz, 4H, aryl-*H*), 3.96 (s, 6H, $-OCH_3$), 3.16 – 3.12 (m, 4H, $\alpha-CH_2$), 2.96 – 2.89 (m, 4H, $\alpha-CH_2$), 2.02 – 1.16 (m, 40H, alkyl-*H*), 0.96 - 0.92 ppm (m, 36H, $-CH_3$).

^{13}C -NMR (75 Hz, $CDCl_2-CDCl_2$, 120 °C): $\delta = 195.00, 191.14, 190.59, 157.23, 141.56, 141.34, 131.80, 130.03, 129.90, 129.87, 128.24, 127.41, 123.37, 123.10, 122.54, 122.13, 121.45, 120.38, 119.19, 115.89, 109.22, 91.86, 56.08, 39.76, 39.48, 37.72, 34.77, 34.73, 33.41, 33.28, 29.78, 28.17, 25.05, 25.01, 22.81, 22.74, 20.03, 19.98$ ppm.

Elemental Analysis: C 87.24%, H 8.33%, N 2.02%, (calcd. for $C_{97}H_{110}N_2O_2$, C 87.21%, H 8.30%, N 2.40%).

2,5,11,14-Tetra(3',7'-dimethyloctyl)-hexa-*peri*-hexabenzocoronene (5-3):



Dibromo HBC **2-1** (200 mg, 0.16 mmol) and *n*-butyl lithium (0.61 mL 1.6 M hexane solution, 0.97 mmol) were mixed with THF (6 mL) in a flame-dried 25 mL Schlenk tube at -78 °C. The mixture was stirred at -78 °C for 30 min followed by quenching with methanol (2 mL). The solution was washed with brine (3×100 mL) and extracted with DCM. After being dried over $MgSO_4$, the solvents were removed under

reduced pressure. The residue was dissolved in minimum amount of THF and precipitated in MeOH (100 mL). 157 mg **5-3** were collected as brown solid in 90% yield.

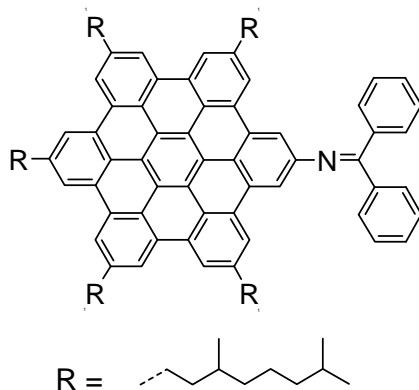
MALDI-TOF MS (TCNQ): $m/z = 1083$ (100%, M^+) (calc. for $C_{82}H_{98} = 1083.65$ g mol⁻¹).

¹H-NMR (500 MHz, CDCl₂-CDCl₂, 140 °C): $\delta = 8.70$ (d, $^3J = 7.21$ Hz, 4H, aryl-*H*), 8.51 (s, 8H, aryl-*H*), 7.82 (t, $^3J = 7.42$ Hz, 2H, aryl-*H*), 3.11 (m, 8H, α -CH₂), 2.04 – 1.18 (m, 40H, alkyl-*H*), 0.97 - 0.95 ppm (m, 36H, -CH₃).

¹³C-NMR (75 Hz, CDCl₂-CDCl₂, 120 °C): $\delta = 140.85, 130.14, 130.08, 130.01, 125.16, 123.32, 121.60, 121.52, 120.00, 119.86, 39.83, 39.53, 37.74, 34.81, 33.39, 29.79, 28.21, 25.06, 22.84, 22.78, 20.11$ ppm.

Elemental Analysis: C 89.96%, H 9.39%, (calcd. for $C_{82}H_{98}$, C 90.88%, H 9.12%).

2-Benzophenonimino-5,8,11,14,17-penta(3,7-dimethyloctyl)-hexa-*peri*-hexabenzocoronene (6-4):



In a 25 ml Schlenk flask, 2-bromo-5,8,11,14,17-penta(3,7-dimethyloctanyl)-hexa-*peri*-hexabenzocoronene (**4-2**) (261.3 mg, 201.0 μ mol), Pd₂(dba)₃ (4.9 mg, 5.0 μ mol), BINAP (10.0 mg, 16.0 μ mol), and sodium *tert*-butoxide (461.0 mg, 4.8 μ mol) were dissolved in 10 ml of dry toluene and heated to 80 °C under argon. benzophenonimene (870.0 mg, 4.8 μ mol) were added dropwise. The mixture was stirred at 80 °C for 16 h. After cooling, the mixture was poured into methanol (100 mL). The precipitated yellow

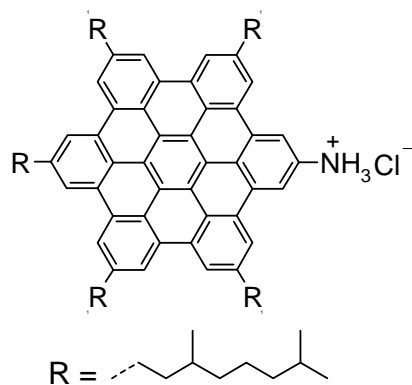
solid was filtrated, redissolved in a minimum amount of THF and precipitated in methanol twice. **6-4** (265 mg) was obtained as yellow solid in 95% yield.

MALDI-TOF MS (TCNQ): $m/z = 1404$ (100%, M^+), (calcd. for $C_{105}H_{127}N = 1403.2$ g mol^{-1}).

1H -NMR (250 MHz, $CDCl_3$): $\delta = 8.26 - 8.30$ (m, 6H, aryl-*H*), 8.12 – 8.16(m, 6H, aryl-*H*), 7.59 – 7.60 (m, 4H, aryl-*H*), 7.37 – 7.40 (m, 2H, aryl-*H*), 7.11 – 7.20 (m, 4H, aryl-*H*), 2.90 – 3.04 (m, 10H, α - CH_2), 1.14 – 1.98 (m, 65H, alkyl-*H*), 0.90 – 0.92 (m, 30H, $-CH_3$) ppm.

^{13}C -NMR (62.5 MHz, $THF-d_8$): $\delta = 168.1, 148.9, 141.2, 140.8, 140.7, 140.6, 138.0, 131.6, 130.9, 130.6, 130.5, 130.4, 130.3, 129.4, 129.1, 129.0, 123.8, 123.7, 123.6, 122.3, 121.9, 121.7, 120.0, 119.9, 119.8, 116.2, 41.1, 41.0, 40.5, 38.6, 38.5, 35.8, 34.4, 29.1, 23.3, 23.2, 20.4$ ppm.

2-Amino-5,8,11,14,17-penta(3',7'-dimethyloctyl)-hexa-*peri*-hexabenzocoronene hydrochloride (6-5):



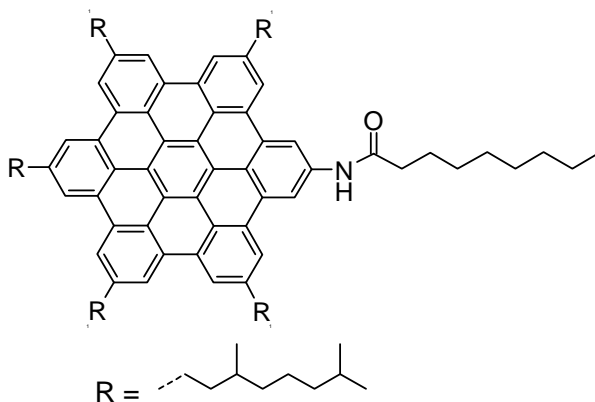
Compound **6-4** (297.3 mg, 0.2 mmol) was dissolved in THF (10 mL) and 2.5 M HCl (70 ml) was added under an argon atmosphere. The solution immediately but temporarily turned black, followed by a yellow powder-like solid suspended in the aqueous solution. The mixture was stirred vigorously for 5 h and filtered out. The solid washed with water until the pH value of the filtrate was close to 7, then washed by

acetone to remove the excess diphenylketone as monitored by TLC. The ammonium salt **6-5** (236 mg) was collected as a yellow powder in 87% yield after being dried under high vacuum.

MALDI-TOF MS (TCNQ): $m/z = 1239$ (100%, M^+), (calcd. for $[C_{92}H_{121}N]^+ = 1240.0$ g mol^{-1}).

This compound was directly used for the next step, due to the instability of 2-amino-5,8,11,14,17-penta(3,7-dimethyloctanyl)-hexa-*peri*-hexabenzocoronene. The NMR spectroscopy was not used for the structural characterization, but rather that of derivatives was measured.

2-Nonylamido-5,8,11,14,17-penta(3',7'-dimethyloctyl)-hexa-*peri*-hexabenzocoronene (6-1a):



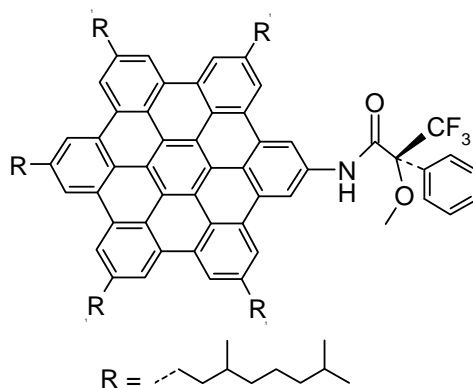
Compound **6-5** (0.06 mmol, 74.3 mg), triethyl amine (0.5 mL) and LiBr (110.0 mg) were mixed in toluene/THF (1:1) mixture (5 mL) and heated to 80 °C under argon atmosphere. The nonanoyl chloride (10.6 mg, 0.6 mmol) was added dropwise. The mixture was stirred at 80 °C overnight. After cooling to r.t., the mixture was poured into methanol (100 mL). The precipitate were collected and further purified by column chromatography with petroleum ether (PE) / CH_2Cl_2 (2/1) as eluent affording **6-1a** (79 mg) as yellow powder in 88% yield.

MALDI-TOF MS (TCNQ): $m/z = 1379$ (100%, M^+), (calcd. for $C_{101}H_{135}NO = 1379.2$ g mol^{-1}).

1H -NMR (250 MHz, THF- d_8 /LiBr, 50 °C): $\delta = 10.91$ (s, 1H, -NH), 9.32 (s, 2H, aryl-H), 8.47 (s, 2H, aryl-H), 8.36 (s, 2H, aryl-H), 8.19 – 8.27 (m, 6H, aryl-H), 3.00 (b, 12H, α - CH_2), 2.01 (b, 12H, β - CH_2), 1.15 – 1.57 (m, 65H, alkyl-H), 0.88 – 0.96 (m, 33H, - CH_3) ppm.

^{13}C -NMR (62.5 MHz, THF- d_8 /LiBr, 50 °C): $\delta = 173.3, 146.3, 140.8, 140.3, 140.2, 138.9, 135.7, 130.8, 130.6, 130.4, 130.2, 130.0, 129.9, 125.9, 123.7, 123.5, 122.4, 121.7, 121.6, 121.4, 119.9, 119.6, 119.5, 119.4, 114.6, 41.0, 40.9, 40.5, 38.5, 34.4, 34.3, 32.8, 31.8, 31.0, 30.9, 30.5, 29.0, 23.2, 23.1, 20.3, 14.4$ ppm.

2-(R)-(-)- α -methoxy- α -(trifluoromethyl)phenylethylamido-5,8,11,14,17-penta(3',7'-dimethyloctyl)-hexa-*peri*-hexabenzocoronene (6-1b):



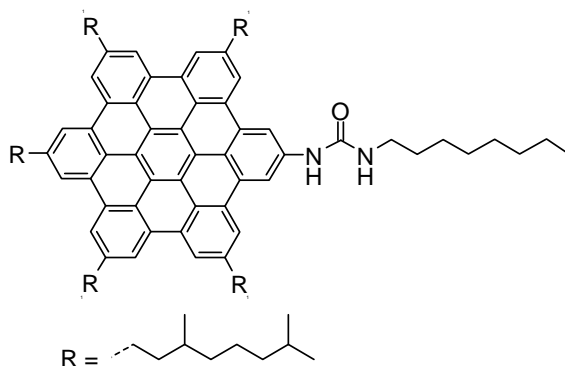
Compound **6-5** (0.06 mmol, 74.3 mg), triethyl amine (0.5 mL) and LiBr (110.0 mg) were mixed in toluene/THF (1:1) mixture (5 mL) and heated to 80 °C under argon atmosphere. The (R)-(-)- α -methoxy- α -(trifluoromethyl)phenylacetyl chloride (152 mg, 0.6 mmol) was added dropwise. The mixture was stirred at 80 °C overnight. After cooling to r.t., the mixture was poured into methanol (100 mL). The precipitate were collected and further purified by column chromatography with petroleum ether (PE) / THF (10/1) as eluent affording **2-1b** (72 mg) as a yellow powder in 81% yield.

MALDI-TOF MS (TCNQ): $m/z = 1455$ (100%, M^+), (calcd. for $C_{102}H_{126}F_3NO_2 = 1455.1 \text{ g mol}^{-1}$).

$^1\text{H-NMR}$ (250 MHz, THF- d_8): $\delta = 10.01$ (s, 1H, -NH), 9.57 (s, 2H, aryl-H), 8.77 (b, 4H, aryl-H), 8.69 (s, 2H aryl-H), 8.61 – 8.63 (m, 4H, aryl-H), 7.96 (d, $^3J = 7.2 \text{ Hz}$, 2H, aryl-H), 7.53 – 7.57 (m, 3H, aryl-H), 3.90 (s, 3H, -OCH₃), 3.3 (m, 10H, α -CH₂), 1.21 – 2.01 (m, 68H, alkyl-H), 0.91 – 0.93 (m, 33H, -CH₃) ppm.

$^{13}\text{C-NMR}$ (175 MHz, THF- d_8): $\delta = 168.8, 144.5, 144.3, 144.2, 140.4, 137.8, 134.7, 133.9, 133.7, 133.6, 127.2, 126.9, 126.1, 123.3, 123.1, 116.9, 44.1, 43.9, 43.5, 41.5, 38.8, 38.7, 37.3, 37.2, 33.6, 32.0, 26.2, 26.1, 23.3$ ppm.

2-(N'-Octanyl-ureido)-5,8,11,14,17-penta(3',7'-dimethyloctyl)-hexa-*peri*-hexabenzocoronene (6-2a):



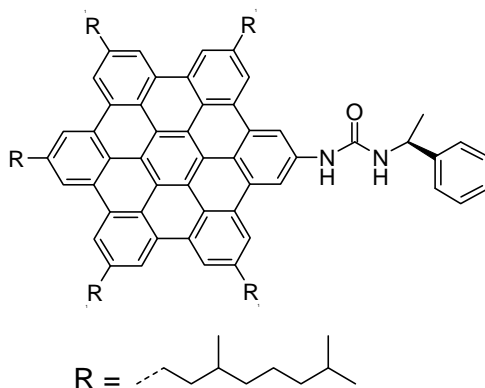
Compound **6-5** (123.9 mg, 0.1 mmol), LiBr (55 mg) and triethyl amine (0.5 mL) were mixed in toluene/THF (1:1) mixture (5 mL) and heated to 80 °C under argon. Octyl isocyanate (202 mg, 1.3 mmol) was added dropwise, and the reaction stirred at 80 °C for 45 h. After the mixture was cooled down, the crude product was precipitated in methanol (250 mL) and dried under vacuum after filtration. The crude product was further purified by column chromatography petroleum ether (PE) /CH₂Cl₂ (3/1) as eluent affording **6-2a** (75 mg) as brown solid in 60% yield.

MALDI-TOF MS (TCNQ): $m/z = 1394$ (100%, M^+), (calcd. for $C_{101}H_{136}N_2O = 1394.2 \text{ g mol}^{-1}$).

¹H-NMR (250 MHz, THF-*d*₈/LiBr, 50 °C): δ = 9.81 (s, 1H, -NH), 8.97 (b, 2H, aryl-*H*), 8.64 (s, 2H, aryl-*H*), 8.17 – 8.41 (m, 8H, aryl-*H*), 7.59 (s, 1H, -NH), 3.41 (b, 2H, α-CH₂), 3.13 (b, 10H, α-CH₂), 1.83 – 2.17 (m 12H, β-CH₂), 1.14 – 1.65 (m, 65H, alkyl-*H*), 0.82 – 0.95 (m, 33H; -CH₃) ppm.

¹³C-NMR (175MHz, THF-*d*₈/LiBr, 50°C): δ = 160.8, 144.5, 144.6, 144.3, 144.2, 135.8, 133.6, 126.9, 126.6, 125.7, 125.3, 125.1, 123.6, 123.3, 122.6, 44.7, 44.3, 44.2, 43.8, 43.6, 41.6, 38.8, 38.6, 37.5, 37.4, 37.2, 36.1, 35.9, 33.9, 33.8, 33.7, 33.5, 33.4, 33.3 32.1, 31.2, 23.4, 17.5 ppm.

2-(N'-(S)-(-)-1'-phenylethyl-ureido)-5,8,11,14,17-penta(3',7'-dimethyloctanyl)-hexa-*peri*-hexabenzocoronene (6-2b):



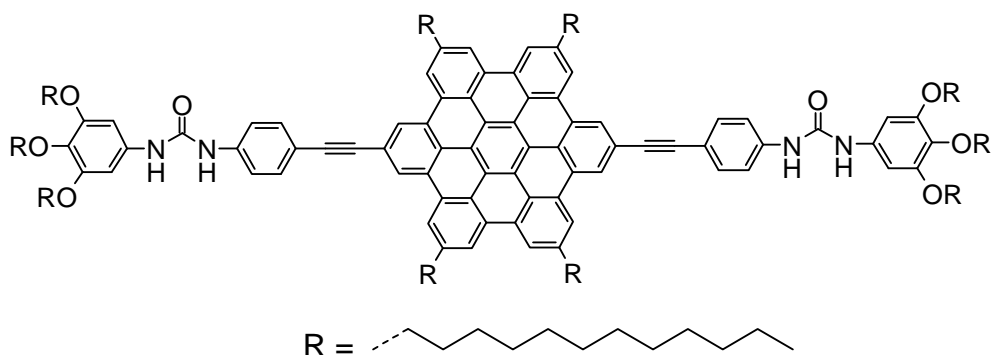
Compound **6-5** (123.9 mg, 0.1 mmol), LiBr (55 mg) and triethyl amine (0.5 mL) were mixed in toluene/THF (1:1) mixture (5 mL) and heated to 80 °C under argon. (S)-(-)-α-methylbenzyl isocyanate (191.3 mg, 1.3 mmol) was added dropwise, and the reaction stirred at 80 °C for 45 h. After the mixture was cooled down, the crude product was precipitated in methanol (250 mL) and dried under vacuum after filtration. The crude product was further purified by column chromatography petroleum ether (PE) /CH₂Cl₂ (3/2) with LiBr and then LiBr/THF as eluent as eluent affording **6-2b** (81 mg) as brown solid in 54% yield.

MALDI-TOF MS (TCNQ): $m/z = 1386$ (100%, M^+), (calcd. for $C_{101}H_{128}N_2O = 1386.1$ g mol⁻¹).

¹H-NMR (250 MHz, THF-*d*₈/LiBr; 50 °C): $\delta = 10.12$ (s, 1H, -NH), 9.01 (s, 2H, aryl-*H*), 8.51 (b, 4H, aryl-*H*), 8.42 (b, 2H, aryl-*H*), 8.33 (b, 4H, aryl-*H*), 8.03 (b, 1H, -NH), 7.78 (d, ³J = 7.2 Hz, 2H, aryl-*H*), 7.41 (t, ³J = 7.9 Hz, 2H, aryl-*H*), 7.24 (t, ³J = 7.5 Hz, 1H, aryl-*H*), 5.50 (s, 1H, *t*-CH), 3.14 (m, 10H, α -CH₂), 1.23 – 2.05 (m, 65H, alkyl-*H*), 0.93 – 0.97 (m, 33H, -CH₃) ppm.

¹³C-NMR (125 MHz, THF-*d*₈/LiBr, 50 °C): $\delta = 157.1, 147.2, 140.6, 140.1, 139.9, 139.7, 130.9, 130.4, 130.3, 130.2, 129.9, 129.1, 127.3, 127.1, 123.7, 123.6, 123.5, 122.5, 121.6, 121.5, 121.3, 120.9, 119.9, 119.5, 119.2, 119.1, 113.8, 50.5, 41.1, 40.9, 40.8, 40.5, 38.5, 35.9, 35.7, 35.6, 34.4, 34.34, 30.5, 29.0, 23.2, 23.1, 20.4$ ppm.

2,11-Bis-[N'-(3'',4'',5''-tris-(dodecyloxyphenyl)-ureido)-4'-phenyl-1'-ethynyl]-5,8,14,17-tetra-dodecanyl-hexa-*peri*-hexabenzocoronene (6-3):



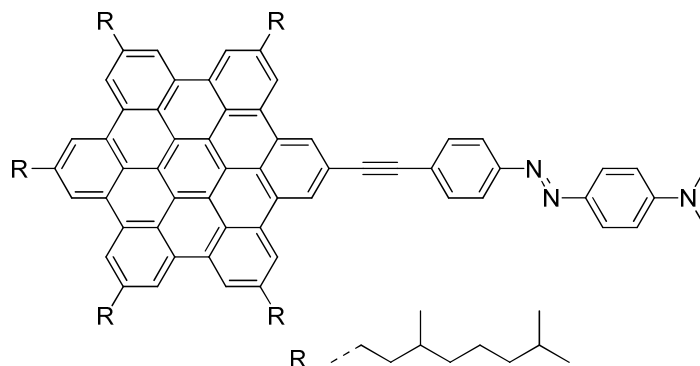
Compound **6-6** (109 mg, 0,08 mmol), compound **6-7** (152 mg, 0,19 mmol), Pd(PPh₃)₄ (18 mg, 0,02 mmol), CuI (6 mg, 0,03 mmol) and LiBr (100 mg) were dissolved in Et₃N/THF (2:1) mixture (15 mL). The mixture was carefully degassed twice by “freeze-pump-thaw” method and the reaction lasted for 4 days at 50 °C under argon atmosphere. After it was cooled to r.t., the reaction was quenched with water. The organic phase was extracted with CH₂Cl₂ (50 mL × 3) and dried over MgSO₄. After evaporation of solvent in vacuo, the residue was purified by column chromatography using THF/CH₂Cl₂ (3/1) with LiBr as eluent affording **6-3** (81 mg) as yellow powder in 13% yield.

MALDI-TOF MS (TCNQ): $m/z = 2770$ (100%, M^+), (calcd. for $C_{192}H_{278}N_4O_8 = 2770.4$ g mol⁻¹).

¹H-NMR (500 MHz, THF-*d*₈/LiBr, 50 °C): $\delta = 8.53$ (s, 4H, aryl-*H*), 8.01 – 8.22 (m, 12H, aryl-*H*), 7.72 (d, 4H, ³J = 7 Hz, 4H, aryl-*H*), 7.51 (d, 4H, ³J = 7 Hz, 4H, aryl-*H*), 6.82 (s, 4H, aryl-*H*), 3.91 (t, ²J = 6 Hz, 12H, -OCH₂), 2.89 (b, 8H, α -CH₂), 1.30 – 1.56 (m, 180H, -CH₂), 0.87 – 0.92 (m, 50H, alkyl-*H*) ppm.

¹³C-NMR (125 MHz, THF-*d*₈/LiBr, 50 °C): $\delta = 166.0, 159.5, 151.7, 140.8, 138.6, 135.8, 133.9, 133.7, 133.1, 123.2, 118.3, 116.5, 116.5, 114.6, 114.5, 114.2, 113.8, 113.0, 112.8, 112.6, 109.3, 107.3, 106.2, 60.1, 33.0, 32.7, 30.6, 27.9, 26.4, 25.0, 22.7, 21.2, 18.1, 18.0, 15.3, 15.2, 12.5$ ppm.

2-[2'-(4''-Dimethylazobenzene-4''')-ethyn-1-yl]-5,8,14,17-penta-(3',7'-dimethyloctyl)hexa-*peri*-hexabenzocoronene (7-1):



7-6 (64 mg, 0.05mmol), Pd(PPh₃)₄ (15 mg, 0.01mmol), CuI (5mg, 0.02 mmol) and 4-iodo-4'-dimethylamino azobenzene (90mg, 0.26mmol) were mixed in 5 mL THF and 5 mL Et₃N. The mixture was degassed with two “freeze-pump-thaw” cycles and heated to 50 °C. The mixture was then stirred overnight. The reaction was quenched with methanol after being cooled to r.t.. After being washed with brine, further extracted with DCM and dried over MgSO₄, the solvents were evaporated under reduced pressure. The catalysts were removed by a short silicon pad with DCM as eluent. The concentrated product was then dissolved in minimum amount of THF and precipitated in MeOH. 35mg **7-1** was collected as reddish solid in a yield of 46%.

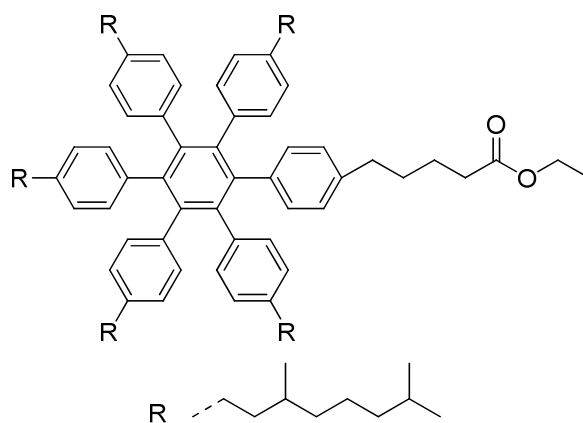
MALDI-TOF MS (TCNQ): $m/z = 1472$, (100%, M^+), (calcd. for $C_{108}H_{131}N_3 = 1472.2$ g mol^{-1}).

1H -NMR (250 MHz, r.t. THF- d_8): $\delta = 8.61$ -7.92 (m, 18H, aryl- H), 6.88 (d, $^3J = 7.5$ Hz, 2H, aryl- H), 3.14 (s, 6H, $-NCH_3$), 3.01 (m, 10H, α - CH_2), 1.47-0.95 (m, 95H, alkyl- H) ppm.

^{13}C -NMR (62.5 MHz, r.t. THF- d_8): $\delta = 153.9$, 153.7, 144.9, 140.7, 140.5, 133.4, 130.3, 130.1, 129.9, 129.3, 126.0, 125.7, 124.8, 124.4, 123.5, 123.3, 123.2, 122.0, 121.7, 121.6, 120.6, 120.1, 119.8, 118.8, 112.4, 94.2, 90.4, 74.3, 41.3, 41.2, 41.1, 40.5, 40.3, 38.5, 35.9, 35.8, 35.7, 35.1, 34.5, 30.6, 30.5, 29.1, 26.2, 26.0, 23.3, 23.2, 20.4, 14.4 ppm.

Elemental Analysis: C 87.58%, H 8.44%, N 1.99% (calcd. for $C_{108}H_{131}N_3$, C 88.17%, H 8.97%, N 2.86%).

1-[4'-(Ethoxycarbonylbutyl)phenyl]-2,3,4,5,6,-pentakis-[4'-(3'',7'')-dimethyloctyl)phenyl]-benzene (7-8):



Zink (0.82 g, 12.52 mmol) and iodine (79.40 mg, 0.31 mmol) were mixed in 30 mL anhydrous DMA in a flame-baked Schlenk flask. After the color of iodine disappeared, ethyl 5-bromovalerate (1.30 g, 6.26 mmol) was added to the solution. The mixture was then stirred at 80 °C for 16 h. The obtained zink reagent was transferred to another flame-baked two-neck flask, which was charged with mono-bromo HPB (7-7) (823 mg, 0.63

mmol), Pd(dppf)Cl₂ (816.60 mg, 0.03 mmol) and 30 mL dry THF. The mixture was stirred at 50 °C under argon overnight. After being cooled to r.t., the reaction was quenched with water (50 mL). The organic phase was extracted with DCM and washed with brine. The solvents were removed *in vacuo* after being dried over MgSO₄. The product was then purified by column chromatography using petroleum ether (PE) / CH₂Cl₂ (4/1) as eluent. 778 mg compound **7-8** was collected as yellow oil.

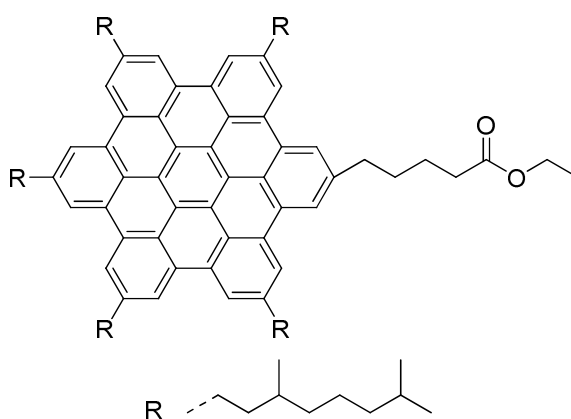
FD-MS (8 kV): $m/z = 1365.9$ (100%, M⁺), (calcd. for C₉₉H₁₄₂O₂ = 1364.41 g mol⁻¹).

¹H-NMR (250 MHz, CD₂Cl₂): $\delta = 6.66$ (m, 24H, aryl-*H*), 4.09 (tetra, 2H, ³J = 7.5Hz, –OCH₂–), 2.40-2.28 (m, 12H, α -CH₂), 2.21 (t, ³J = 7.5Hz, 2H, –CO-CH₂–), 1.44-1.13 (m, 54H, alkyl-*H*), 0.88-0.85 (m, 48H, –CH₃) ppm.

¹³C-NMR (62.5 MHz, CD₂Cl₂): $\delta = 172.5, 139.6, 139.5, 138.9, 138.0, 137.8, 137.5, 130.6, 130.5, 125.6, 59.2, 38.6, 38.0, 36.3, 34.1, 33.2, 32.1, 31.4, 29.8, 28.9, 27.2, 23.9, 23.4, 21.7, 21.6, 18.6, 13.3$ ppm.

Elemental Analysis: C 86.96%, H 9.91% (calcd. for C₉₉H₁₄₂O₂, C 87.16%, H 10.49%, O 2.35%).

2-(Ethoxycarbonylbutyl)-5,8,14,17-penta-(3',7'-dimethyloctyl)hexa-*peri*-hexabenzocoronene (7-9):



Compound **7-8** (200 mg, 0.15 mmol) was dissolved in 200 mL dry DCM. The solution was bubbled with argon for 15 min. FeCl₃ (573.60 mg, 3.53 mmol) in

nitromethane (1.86 mL) was added dropwise. After being stirred at r.t. for 35 min with argon bubbling, the reaction was quenched by adding large amount methanol (300 mL). The solvents were evaporated under reduced pressure and the residue was filtered over a silica-gel pad with hot toluene. The concentrated residue was then dissolved in minimum amount THF and precipitated in methanol affording 174 mg product as yellow powder in a yield of 88%.

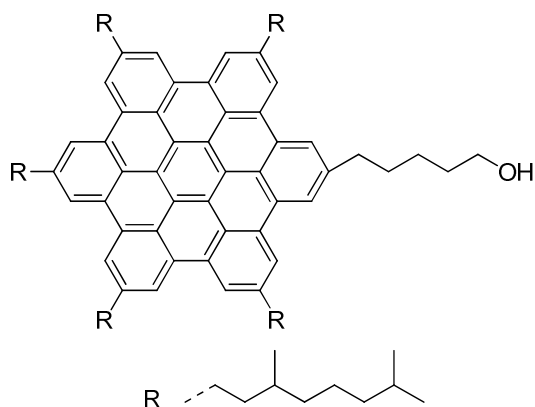
MALDI-TOF MS (TCNQ): $m/z = 1352$ (100%, M^+), (calcd. for $C_{99}H_{130}O_2 = 1352.41$ g mol^{-1}).

1H -NMR (250 MHz, THF- d_8): $\delta = 8.53$ (s, 12H, Ar-H), 4.09 (tetra, 2H, $^3J = 7.04$ Hz, –OCH₂–), 3.08 (m, 12H, α -CH₂), 2.44 (m, 2H, –CO-CH₂–), 2.05-1.21 (m, 54H, alkyl-H), 0.97-0.94 (m, 35H, –CH₃) ppm.

^{13}C -NMR (175 MHz, THF- d_8): $\delta = 173.2, 141.2, 141.20, 141.18, 141.2, 130.7, 124.1, 122.1, 122.0, 120.4, 120.3, 67.8, 67.6, 60.4, 40.8, 40.4, 38.4, 37.6, 35.6, 34.7, 34.2, 34.1, 32.5, 30.4, 28.9, 26.0, 25.79, 25.78, 25.6, 25.5, 24.9, 24.8, 23.0, 22.9, 20.2, 14.6$ ppm.

Elemental Analysis: C 86.25%, H 9.20% (calcd. for $C_{99}H_{130}O_2$, C 87.94%, H 9.69%, O 2.37%).

2-(5'-Hydroxypentyl)-5,8,14,17-penta-(3',7'-dimethyloctyl)hexa-*peri*-hexabenzocoronene (7-10):



Compound **7-9** (150 mg, 0.11 mmol) and $LiAlH_4$ (42 mg, 1.10 mmol) were mixed in a 250 mL two-neck pre-dried flask with 60 mL dry THF at 0 °C. The mixture was

slowly warmed to r.t. and stirred overnight under argon atmosphere. The reaction was then quenched with MeOH. After being washed with brine and extracted with DCM, the organic phase was dried over MgSO₄. The solvents were removed under reduced pressure and the product was precipitated in 100 mL MeOH resulting in 133 mg compound **7-10** as yellow powder in a yield of 92%.

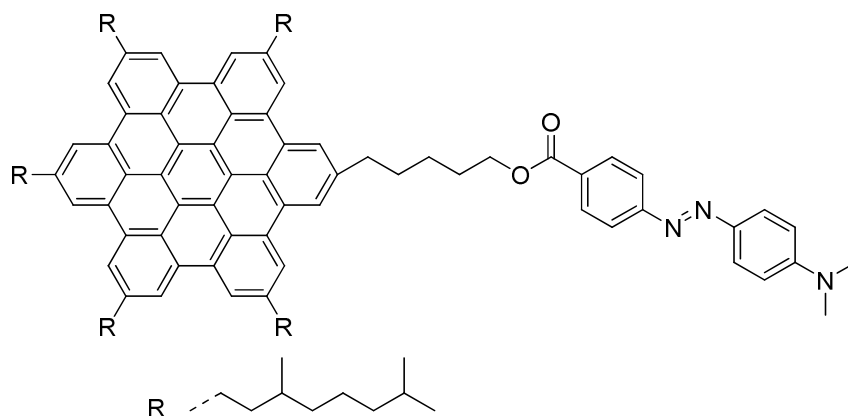
MALDI-TOF MS (TCNQ): $m/z = 1311$ (100%, M⁺), (calcd. for C₉₇H₁₂₈O = 1310.41 g mol⁻¹).

¹H-NMR (250 MHz, r.t., THF-*d*₈): $\delta = 8.49-8.45$ (m, 12H, aryl-*H*), 3.07-3:05 (m, 12H, α -CH₂), 2.48 (s, 2H, -CH₂-OH), 2.02-2.00 (m, 8H, alkyl-*H*), 1.34-1.21 (m, 55H, alkyl-*H*), 0.98-0.95 (m, 45H, alkyl-*H*) ppm.

¹³C-NMR (75 MHz, r.t., THF-*d*₈): $\delta = 140.1, 139.3, 129.6, 123.1, 121.2, 119.4, 63.0, 40.2, 39.8, 37.8, 35.1, 33.6, 33.4, 28.4, 25.3, 23.2, 20.1$ ppm.

Elemental Analysis: C 88.98%, H 9.33% (calcd. for C₉₇H₁₂₈O, C 88.93%, H 9.85%, O 1.22%).

2-[5-(4''-Dimethylazobenzene-4'''-carboxyl)-pentanoate]-5,8,14,17-penta-(3',7'-dimethyloctyl)hexa-*peri*-hexabenzocoronene (7-2):



4-dimethylamino-azobenzene-4'-carboxylic acid (221.9 mg, 0.82 mmol), EDC (157.9 mg, 0.82 mmol) and DMAP (20.1 mg, 0.17 mmol) were dissolved in 5 mL dry DCM in a 50 mL Schlenk tube. The mixture was stirred for 20 min at r.t. and cooled to 0

°C. A DCM solution (5 mL) of Compound **7-10** (135 mg, 0.10 mmol) was then added dropwise. The solution was kept being stirred for 30 min at 0 °C and then slowly warmed to r.t. The reaction lasted for 3 d and was quenched by methanol. After being washed with brine and extracted with DCM, the organic phase was dried over MgSO₄. The solvents were removed *in vacuo*. The residue was purified by column chromatography using petroleum ether (PE) / CH₂Cl₂ 1:3 as eluent. 66 mg product was collected as reddish solid in a yield of 41%.

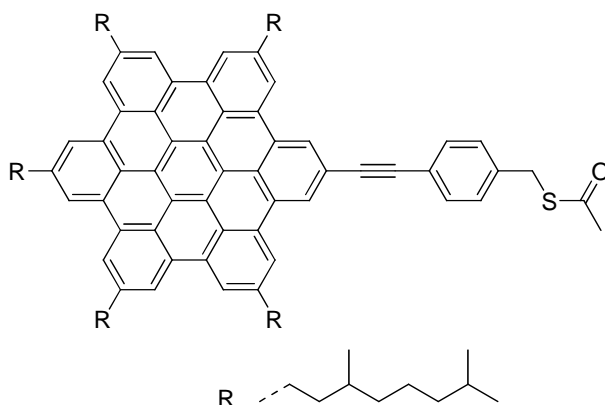
MALDI-TOF MS (TCNQ): $m/z = 1561$ (100%, M⁺), (calcd. for C₁₁₂H₁₄₁N₃O₂ = 1561.39 g mol⁻¹).

¹H-NMR (250 MHz, r.t., THF-*d*₈): $\delta = 8.40$ (s, 12H, aryl-*H*), 8.14 (d, ³J = 8.6 Hz, 2H, aryl-*H*), 7.79 (d, ³J = 9.3 Hz, 2H, aryl-*H*), 7.74 (d, ³J = 9.4 Hz, 2H, aryl-*H*), 6.73 (d, ³J = 9.1 Hz, 2H, aryl-*H*), 4.45 (t, ³J = 6.8 Hz, 2H, -CO-CH₂), 3.06 (s, 6H, -N-CH₃), 2.98 (bs, 12H, α -CH₂), 2.08 - 1.99 (m, 12H, β -CH₂), 1.54 – 0.93 (m, 80H, alkyl-*H*) ppm.

¹³C-NMR (62.5 MHz, r.t., THF-*d*₈): $\delta = 166.2, 156.7, 153.9, 141.1, 141.07, 141.01, 131.5, 131.1, 130.6, 126.0, 123.9, 122.6, 121.9, 120.24, 120.21, 112.1, 66.5, 41.1, 40.5, 40.1, 38.5, 35.78, 35.75, 34.3, 30.6, 29.0, 23.3, 23.2, 23.1, 20.3$ ppm.

Elemental Analysis: C 86.19%, H 9.04% N 2.02% (calcd. for C₁₁₂H₁₄₁N₃O₂, C 86.16%, H 9.10%, N 2.69%, O 2.05%).

2-[2'-[4''-(*S*-Acetylthiomethyl)phenyl]ethyn-1-yl]-5,8,14,17-penta-(3',7'-dimethyloctyl)hexa-*peri*-hexabenzocoronene (7-3):



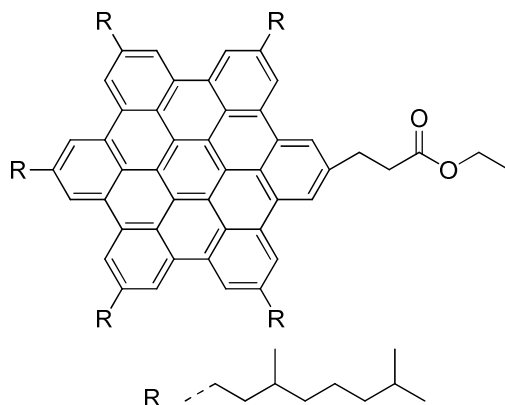
Mono-ethynyl HBC **7-6** (100 mg, 0.08 mmol), 4-iodo-benzylthioacetate **7-11** (233.6 mg, 0.8 mmol), Pd₂(dba)₃ (3.67 mg, 4×10⁻³ mmol), CuI (1.5 mg, 0.01 mmol) and P(*o*-tol)₃ (4.87 mg, 0.02 mmol) were mixed in a flame-baked Schlenk tube with DIEA (1 mL). THF (4 mL) was then added. The mixture was carefully degassed by two “freeze-pump-thaw” cycles. The mixture was heated to 50°C and stirred for 3 d. After being cooled to r.t., the mixture was washed with brine and extracted with DCM. The organic phase was dried over MgSO₄ and the solvents were removed *in vacuo*. The crude product was further purified by column chromatography with petroleum ether (PE) / CH₂Cl₂ (15/1) as eluent. 46 mg product was collected as yellow powder in a yield of 41%.

MALDI-TOF MS (TCNQ): $m/z = 1412$ (100%, M⁺), (calcd. for C₁₀₃H₁₂₆OS = 1412.17 g mol⁻¹); fragmentation was found with high incident laser power.

¹H-NMR (250 MHz, r.t. THF-*d*₈): δ = 8.64 (s, 2H, aryl-*H*), 8.35 (m, 10H, aryl-*H*), 7.81 (d, ³J = 8 Hz, 2H, aryl-*H*), 7.52 (d, ³J = 8 Hz, 2H, aryl-*H*), 4.31 (s, 2H, -S-CH₂), 3.06 (bs, 10H, α-CH₂), 2.44 (s, 3H, -CO-CH₃), 1.99-2.05 (m, 6H, alkyl-*H*), 1.29-1.46 (m, 50H, alkyl-*H*), 1.29-1.46 (m, 50H, alkyl-*H*), 0.94-0.98 (m, 45H, -CH₃) ppm.

¹³C-NMR (125 MHz, THF-*d*₈): δ = 225.5, 141.5, 141.3, 139.9, 132.9, 130.9, 130.7, 130.6, 130.1, 129.90, 129.86, 124.9, 123.9, 122.6, 122.3, 120.5, 120.2, 41.1, 41.0, 40.6, 38.6, 35.83, 35.78, 34.4, 30.7, 29.1, 23.2, 23.1, 20.4 ppm.

2-(Ethoxycarbonyl)ethyl-5,8,14,17-penta-(3',7'-dimethyloctyl)hexa-*peri*-hexabenzocoronene (7-12):



Zinc (1 g, 15.40 mmol) and iodine (97.7 mg, 0.38 mmol) were mixed with 10 mL dry DMA in a flash-baked 25 mL Schlenk tube. After the color of iodide disappeared, ethoxy-carbonyl ethyl bromide (1.4 g, 7.70 mmol) was added. The mixture was heated to 80 °C and stirred overnight. The resulted zinc reagent was then transferred to another flame-baked 50 mL Schlenk tube, which was charged with mono-bromo HBC **2-40** (200 mg, 0.15 mmol), Pd(dppf)Cl₂ (6.28 mg, 0.01 mmol) and 10 mL dry THF. The mixture was further stirred at 50 °C for 2 d. After being cooled down, the mixture was washed with brine and extracted with DCM. The combined organic layer was dried over MgSO₄ and the solvents were evaporated under reduced pressure. The crude compound was purified by column chromatography using Hexane / THF 10:1 as eluent affording 84 mg **7-12** as yellow powder in a yield of 42%.

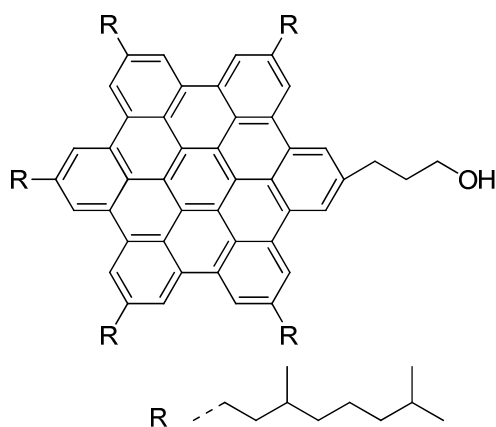
MALDI-TOF MS (TCNQ): $m/z = 1323$ (100%, M⁺), (calcd. for C₉₇H₁₂₆O₂ = 1323,21 g mol⁻¹).

¹H NMR (250 MHz, r.t. THF-d₈): $\delta = 8.54$ (m, 12H, aryl-*H*), 4.21 (s, 4H, -COCH₂, -OCH₂), 3.12-2.94 (m, 12H, α -CH₂), 2.45 (s, 3H, -CO-CH₂-CH₃), 2.04-1.99 (m, 8H, alkyl-*H*), 1.32-1.22(m, 50H, alkyl-*H*), 1.21-0.93 (m, 45H, -CH₃) ppm.

$^{13}\text{C-NMR}$ (125 MHz, 50 °C, THF- d_6): δ = 172.6, 141.1, 141.0, 130.6, 130.5, 130.4, 123.8, 123.7, 121.8, 121.6, 120.1, 120.0, 67.6, 60.4, 40.6, 40.2, 40.1, 40.0, 38.1, 38.0, 36.7, 35.4, 35.3, 34.0, 33.9, 33.8, 32.6, 30.2, 28.7, 22.8, 22.7, 20.0, 14.5 ppm.

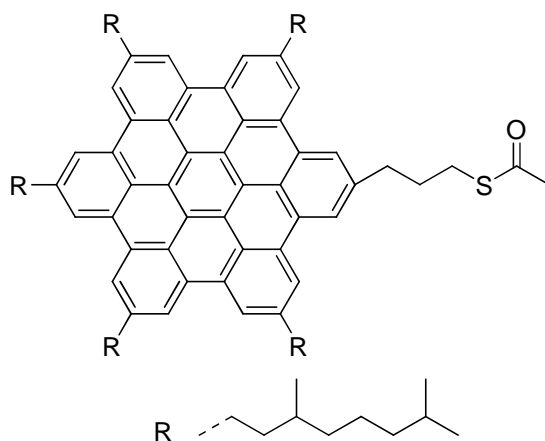
Elemental Analysis: C 86.71%, H 9.91% (calcd. for $\text{C}_{97}\text{H}_{126}\text{O}_2$, C 87.99%, H 9.59%, O 2.42%).

2-(3'-Hydroxypropyl)-5,8,14,17-penta-(3',7'-dimethyloctyl)hexa-*peri*-hexabenzocoronene (7-13):



Compound **7-12** (84 mg, 0.16 mmol) and LiAlH_4 (1 mL, 1M THF solution) were mixed in a 100 mL two-neck pre-dried flask with 40 mL dry THF at 0 °C. The mixture was slowly warmed to r.t. and stirred overnight under argon atmosphere. The reaction was then quenched with MeOH. After being washed with brine and extracted with DCM, the organic phase was dried over MgSO_4 . The solvents were removed under reduced pressure and the product was precipitated in MeOH (100 mL) resulting in 76 mg compound **7-13** as yellow powder. This compound was directly used in the next step without further purification.

2-(3'-S-Acetylthiopropyl)-5,8,14,17-penta-(3',7'-dimethyloctyl)hexa-*peri*-hexabenzocoronene (7-4):



Compound **7-13** (76 mg, 0.06 mmol) was dissolved in THF (1 mL). The solution was cooled to 0 °C followed by adding Et₃N (0.2 mL) and methanesulfonyl chloride (0.1 mL). After being stirred at 0 °C for 1 h, the mixture was warmed to r.t. and stirred overnight. H₂O (5 mL) was used to dilute the mixture and the organic phase was extracted with DCM. The solvents were then removed under reduced pressure and the residue was further dried under high vacuum. The residue was mixed with potassium acetate (277 mg, 2.1 mmol) in dry DMF (1 mL). The resulting solution was stirred at 45 °C for 6 d. After being cooled down, the reaction was quenched with water and the organic phase was extracted with DCM. The combined organic layer was dried over MgSO₄ and then the solvents were removed *in vacuo*. The crude product was purified by column chromatography with hexane / chloroform 10:1 as eluent. 45 mg **7-4** was collected as yellow powder in a yield of 56%.

MALDI-TOF MS (TCNQ): $m/z = 1340$ (100%, M⁺), (calcd. for C₉₇H₁₂₆OS = 1340.10 g mol⁻¹); fragmentation was observed with high incident laser beam power.

¹H NMR (250 MHz, r.t. CD₂Cl₂): $\delta = 8.25$ -8.12 (m, 12H, aryl-*H*), 3.14 (t, ³J = 7.25 Hz, 2H, α -CH₂), 3.01 (m, 10H, α -CH₂), 2.44 (s, 3H, -CO-CH₃), 2.21 (t, ³J = 7.5 Hz, 2H, -S-CH₂), 2.00-1.26 (m, 52H, alkyl-*H*), 0.97-0.83 (m, 45H, -CH₃) ppm

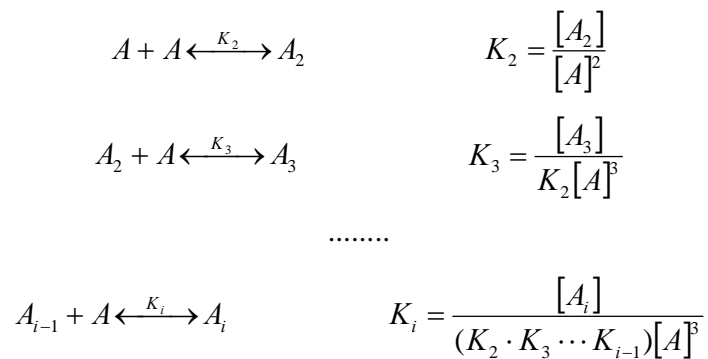
¹³C-NMR (125 MHz, CD₂Cl₂): 147.1, 145.1, 141.44, 141.42, 141.3, 133.5, 131.3, 130.9, 130.85, 130.79, 130.7, 130.3, 128.4, 124.1, 123.2, 122.3, 122.13, 122.10, 120.9, 120.5, 120.4, 120.3, 114.87, 114.84, 113.6, 40.7, 40.3, 38.3, 35.5, 34.1, 30.4, 29.5, 28.8, 23.0, 22.9, 20.1 ppm.

Appendix I

Set-up of Attenuated Model (AK) for Molecular Aggregation in solution

The attenuated model for molecular aggregation in solution was set up according to “Comparisons of Indefinite Self-Association Models”, Martin, R. B., *Chem. Rev.* **1996**, *96*, 3034-3064.

In a solution, the formation of molecular dimer, trimer, tetramer.... can be described by the following reactions:



where K_2 is the equilibrium constant of the formation of dimer, K_3 is the equilibrium constant of the formation of trimer, The concentration of the sample C_T can thus be written as equation 1.

$$C_T = [A] + 2[A_2] + 3[A_3] + \dots + i[A_i] = [A] \cdot (1 + 2K_2[A] + 3K_2K_3[A]^2 + \dots) \quad (1)$$

Two dimensionless variables, L and x , which are related with the solution conce C_T and the monomer concentration $[A]$, are defined as follow

$$L = K_A \cdot C_T \quad (2)$$

$$x = K_A \cdot [A] \quad (3)$$

In the Attenuated model (AK) model, it considers the fact that the probability for a monomer to attach to an $(i-1)$ -mer leading to an i -mer gradually decreases due to the entropic reason, i.e. $K_2 > K_3 > K_4 > \dots > K_i$. The relation between K_i and the ensemble association constant, K_A , is assumed as $K_2 \propto \frac{K_A}{2}, K_3 \propto \frac{K_A}{3}, \dots, K_i \propto \frac{K_A}{i}$. Since the dimer forms much easier than the subsequent additions, it is reasonable to introduce a new parameter τ to individually describe the K_2 . For a simplification reason, this kind of parameters is assumed as 1 for the equilibrium constant (K_i) of forming larger aggregates, which leads to

$$K_2 = \tau \cdot \frac{K_A}{2}, K_3 = \frac{K_A}{3}, \dots, K_i = \frac{K_A}{i} \quad (4)$$

A value of $\tau > 2/3$ indicates the favor of dimer formation.

The substitution of eq.4 into eq.1 eq.2 and eq.3 gives the following equation 5.

$$L = x(1 + \tau(x + \frac{x^2}{2!} + \frac{x^3}{3!} + \dots + \frac{x^i}{i!})) = x(1 + \tau(e^x - 1)) \quad (5)$$

In the AK model, only the property of the monomer, the molecule within a stack and the molecules at the two ends of a stack are considered to contribute the overall property of the system. The mole fractions of the monomer, the end molecules and those molecules within a stack are respectively defined as α , λ and ξ , which are quantized as

$$\alpha = \frac{[A]}{C_T} \quad (6), \quad \lambda = \frac{2[A_2] + 2[A_3] + 2[A_4] + \dots + 2[A_i]}{C_T} \quad (7)$$

$$\xi = \frac{[A_3] + 2[A_4] + 3[A_5] + \dots + (i-2)[A_i]}{C_T} \quad (8)$$

where it holds $\alpha + \lambda + \xi = 1$. From eq.2, eq.3, eq.5, eq.6 and eq.7 it can be derived that

$$\alpha = \frac{[A]}{C_T} = \frac{x}{L} = \frac{1}{1 + \tau(e^x - 1)} \quad (9), \quad \lambda = 2\tau(e^x - 1 - x) \quad (10) \quad \xi = 1 - \alpha - \lambda \quad (11)$$

As mentioned before, the overall property (P) of a system can be expressed as the linear summation of those of the monomer (P_α), the end molecules (P_λ) and the molecules within a stack (P_ξ):

$$P = \alpha \cdot P_\alpha + \lambda \cdot P_\lambda + \xi \cdot P_\xi \quad (12)$$

In order to simplify the later mathematic simulation, it is necessary to reduce the number of parameters. The property of these ending molecules (P_λ), therefore, is assumed as a linear combination of these of monomer (P_α) and molecules within a molecular stack (P_ξ). A new parameter, f , is then introduced, which describes the relationship between the properties of P_λ , P_α and P_ξ .

$$P_\lambda = (1 - f) \cdot P_\alpha + f \cdot P_\xi \quad (13)$$

With eq.5, eq.9, eq.10, eq.11 and eq.13, the eq.12 can be re-written as

$$P = \frac{1}{1 + \tau(e^x - 1)} \cdot P_\alpha + ((1 - f) \cdot P_\alpha + f \cdot P_\xi) \cdot \frac{2\tau(e^x - 1 - x)}{K_A C_T} + \left(1 - \frac{1}{1 + \tau(e^x - 1)} - \frac{2\tau(e^x - 1 - x)}{K_A C_T}\right) \cdot P_\xi \quad (14)$$

where x and K_A hold the relationship:

$$L = K_A \cdot C_T = x(1 + \tau(e^x - 1)) \quad (15)$$

In the $^1\text{H-NMR}$ experiments, the overall property (P) corresponds the measured chemical shift of a specific proton in a solution with the concentration of C_T . By applying a series mathematic curve fitting operations, the five parameter K_A , τ , f , P_α and P_ξ can then be deduced.

Program used for curve fitting

A mathematic program was composed based on non-linear least square analytical method with MATLAB[®] 7.4.0.287 (R2007a) software by Lei Xie from Prof. R. Nordmann's group at TU-Darmstadt.

With this program, the association constant of HBC-C₁₂ **3-31** was first derived with the NMR data from Dr. A. Fechtenkötter to verify the accuracy of this new program. Table App-1 show the results obtained from the new program and the one used by Fechtenkötter (see Fechtenkötter's PhD thesis, Uni-Mainz, 2001).

Table App-1.

calculated from the program used by Fechtenkötter	calculated with new program	Difference in percent
$K_A = 457.32$ L/mol	$K_A = 462.16(6)$ L/mol	1.049 %
$\tau = 3.834$	$\tau = 3.832(6)$	0.026 %
$f = 0.3773$	$f = 0.379(0)$	0.500 %
$P\alpha = 8.978$ ppm	$P\alpha = 8.979(0)$ ppm	0.011 %
$P\xi = 7.239$ ppm	$P\xi = 7.245(5)$ ppm	0.097 %

The maximum 1.05% difference between the values calculated from the two different programs provides the liability of the data calculated with the new program.

Original Program Codes

```

clc
clear all
close all

load data_dou253           % load experimental data
xCT = data_dou253(:,1);   % concentration / CT
yppm = data_dou253(:,2); % Chemical shift ppm
figure(1)
semilogx(xCT,yppm,'*-')
xlabel('Concentration / CT')
ylabel('Chemical Shift [ppm]')
title(' Experimental data and AK model')

%%%%%%%%%%%%%%%%%%%%%%%%%%%%%%%%%%%%%%%%%%%%%%%%%%%%%%%%%%%%%%%%%%%%%%%%
% Set the starting parameters

```

```

%
% Ka = starting(1);
% Pal = starting(2);
% Pxi = starting(3);
% f = starting(4);
% tao = starting(5);
%%%%%%%%%%%%%%%%%%%%%%%%%%%%%%%%%%%%%%%%%%%%%%%%%%%%%%%%%%%%%%%%%%%%%%%%
starting = [457.32;8.978;7.239;0.3773;3.834];
options = optimset('Display','iter');
estimation = fminsearch(@modelfit,starting,options, xCT, yppm);

CT = [1e-7:1e-2:1e-1]';
CT = [xCT(end):1e-2:xCT(1)]';
fit_yppm = model(estimation,CT);
hold on
semilogx(CT,fit_yppm,'r-')

```

2 model.m

```

function output = model(params,input)

%%%%%%%%%%%%%%%%%%%%%%%%%%%%%%%%%%%%%%%%%%%%%%%%%%%%%%%%%%%%%%%%%%%%%%%%
% Constant parameters for the simplest AK model
%%%%%%%%%%%%%%%%%%%%%%%%%%%%%%%%%%%%%%%%%%%%%%%%%%%%%%%%%%%%%%%%%%%%%%%%
% 1. Ka KA: association constant;
% 2. Pal P $\alpha$ : NMR shift of monomer;
% 3. Pxi P $\zeta$ : NMR shift of the interior molecule.
% 4. f f: factor relating shift of end molecule to that of the
monomer
% and the interior molecule (  $P\lambda=(1-f)P\alpha+fP\zeta$  ),  $0<f<1$ 
% 5. tao  $\tau$ : factor by which dimer formation differs from other polymer
% formation in AK models ( $K_2=\tau KA/2$ );
%%%%%%%%%%%%%%%%%%%%%%%%%%%%%%%%%%%%%%%%%%%%%%%%%%%%%%%%%%%%%%%%%%%%%%%%
% Variabls for the simplest AK model
%%%%%%%%%%%%%%%%%%%%%%%%%%%%%%%%%%%%%%%%%%%%%%%%%%%%%%%%%%%%%%%%%%%%%%%%
% xCT : input concentration / CT
% yppm : output Chemical shift ppm
% x : Intermediate variables
% %%%%%%%%%%%%%%%%%%%%%%%%%%%%%%%%%%%%%%%%%%%%%%%%%%%%%%%%%%%%%%%%%%%%%%%%%
% Reference
%%%%%%%%%%%%%%%%%%%%%%%%%%%%%%%%%%%%%%%%%%%%%%%%%%%%%%%%%%%%%%%%%%%%%%%%
% R. Bruce Martin, "Comparisons of Indefinite Self-Association Models",
% Chemical Review. 1996 Dec 19;96(8):3043-3064
% %%%%%%%%%%%%%%%%%%%%%%%%%%%%%%%%%%%%%%%%%%%%%%%%%%%%%%%%%%%%%%%%%%%%%%%%%
% Xie lei, Dou xi 18,06,2008
%%%%%%%%%%%%%%%%%%%%%%%%%%%%%%%%%%%%%%%%%%%%%%%%%%%%%%%%%%%%%%%%%%%%%%%%

Ka = params(1);
Pal = params(2);
Pxi = params(3);
f = params(4);
tao = params(5);
xCT = input;
x = fncxCT(params,xCT);

```



```

output = 1./(1+tao.*(exp(x)-1))*Pal + ...
        [(1-f)*Pal+f*Pxi]*2*tao.*(exp(x)-1-x)./(Ka.*xCT)+...
        [1- 1./(1+tao.*(exp(x)-1)) - 2*tao.*(exp(x)-1-x)./(Ka.*xCT)].*Pxi;

```

3 modelfit.m

```

function sse = modelfit(params , input , actual_output)

```

```

fit_curve = model(params,input);
error_vector = fit_curve - actual_output;
% when curve fitting , a typical quantity to
% minimize is the sum of squares error
sse = sum(error_vector.^2);

```

4.fncxCT.m

```

function x = fncxCT(params,xCT);

```

```

Ka = params(1);
Pal = params(2);
Pxi = params(3);
f = params(4);
tao = params(5);

```

```

L = Ka * xCT;
x_list = [0:1e-4:100];
L_list = x_list.*(1+tao.*(exp(x_list)-1));

```

```

if(max(L)>max(L_list) || min(L)< min(L_list))
    disp('the L = Ka* xCT is out of the L list setting,please reset')
    keyboard
end

```

```

for i = 1:length(xCT)
    [y,index] = min(abs(L_list-L(i)));
    x(i,1) = x_list(index);

```

```

end

```

Appendix II

Single crystal structure data of 5,11-Bis[4'-dodecylphenyl]-2,8-didodecyl-6,12-bis[spiro(6'-oxo-cyclohexa-1',4'-diene)-3']indeno[1,2-b]fluorene (2-41):

Atom Label	Xfrac	Yfrac	Zfrac
O1	0.0494	0.0465	0.2938
C1	0.0245	0.6460	0.5416
C2	0.0544	0.5783	0.4974
C3	0.0306	0.4417	0.4570
C4	0.0738	0.3911	0.4144
C5	0.0503	0.4272	0.3545
C6	0.0447	0.2931	0.3153
C7	0.0609	0.0857	0.3283
C8	0.0898	0.0487	0.3857
C9	0.0955	0.1867	0.4254
C10	0.1231	0.5344	0.4351
C11	0.1741	0.5635	0.4106
C12	0.2152	0.6956	0.4335
C13	0.2063	0.7964	0.4836
C14	0.1550	0.7684	0.5085
C15	0.1134	0.6388	0.4838
C16	0.2716	0.7336	0.4089
C17	0.2719	0.9371	0.3802
C18	0.2321	0.9603	0.3248
C19	0.2303	11.725	0.3035
C20	0.1880	12.183	0.2512
C21	0.1791	14.369	0.2413
C22	0.1291	14.931	0.1946
C23	0.1181	17.155	0.1907
C24	0.0646	17.737	0.1502
C25	0.0545	19.919	0.1462
C26	0.0000	20.517	0.1058
C27	0.0100	22.738	0.1048
C28	0.0509	0.7877	0.5843
C29	0.0455	0.9914	0.5758
C30	0.0707	11.208	0.6162
C31	0.1005	10.599	0.6671
C32	0.1059	0.8580	0.6754
C33	0.0812	0.7268	0.6350
C34	0.1254	11.989	0.7139
C35	0.0846	12.297	0.7590
C36	0.1160	13.273	0.8125

C37	0.1372	15.354	0.8068
C38	0.1773	16.091	0.8575
C39	0.1929	18.223	0.8568
C40	0.2439	18.839	0.9012
C41	0.2561	21.033	0.9052
C42	0.3069	21.639	0.9478
C43	0.3184	23.824	0.9515
C44	0.3691	24.474	0.9941
C45	0.3796	26.664	0.9972
H51	0.0399	0.5587	0.3445
H61	0.0299	0.3305	0.2777
H81	0.1066	-0.0775	0.3933
H91	0.1138	0.1532	0.4622
H111	0.1807	0.4939	0.3776
H131	0.2356	0.8855	0.4998
H141	0.1490	0.8291	0.5431
H161	0.3044	0.7240	0.4376
H162	0.2745	0.6359	0.3811
H171	0.2596	10.305	0.4057
H172	0.3109	0.9659	0.3740
H181	0.1935	0.9202	0.3293
H182	0.2465	0.8797	0.2973
H191	0.2192	12.528	0.3328
H192	0.2685	12.079	0.2965
H201	0.1512	11.589	0.2542
H202	0.2032	11.663	0.2193
H211	0.1697	14.898	0.2757
H212	0.2146	14.934	0.2330
H221	0.0944	14.267	0.2009
H222	0.1401	14.529	0.1594
H231	0.1109	17.567	0.2271
H232	0.1517	17.812	0.1811
H241	0.0307	17.089	0.1596
H242	0.0716	17.340	0.1136
H251	0.0484	20.318	0.1830
H252	0.0880	20.568	0.1359
H261	-0.0334	19.887	0.1169
H262	0.0060	20.066	0.0694
H271	-0.0435	23.054	0.0784
H272	-0.0158	23.181	0.1413
H273	0.0235	23.360	0.0938
H291	0.0250	10.373	0.5411
H301	0.0680	12.586	0.6103
H321	0.1257	0.8122	0.7104
H331	0.0856	0.5895	0.6409
H341	0.1613	11.454	0.7315
H342	0.1323	13.231	0.6981
H351	0.0691	11.057	0.7676
H352	0.0534	13.143	0.7442
H361	0.0901	13.275	0.8402

H362	0.1496	12.501	0.8255
H371	0.1040	16.189	0.8001
H372	0.1583	15.405	0.7753
H381	0.1572	15.894	0.8892
H382	0.2121	15.326	0.8617
H391	0.1600	19.012	0.8617
H392	0.2047	18.493	0.8209
H401	0.2339	18.439	0.9367
H402	0.2783	18.169	0.8940
H411	0.2221	21.692	0.9139
H412	0.2643	21.434	0.8690
H421	0.2994	21.178	0.9836
H422	0.3412	21.024	0.9381
H431	0.2842	24.430	0.9615
H432	0.3253	24.281	0.9155
H441	0.3622	24.027	10.303
H442	0.4034	23.865	0.9842
H451	0.4123	26.962	10.246
H452	0.3456	27.284	10.073
H453	0.3868	27.123	0.9613
O1	-0.0494	10.464	0.7062
C1	-0.0245	0.3541	0.4584
C2	-0.0544	0.4216	0.5026
C3	-0.0306	0.5584	0.5430
C4	-0.0738	0.6088	0.5856
C5	-0.0503	0.5729	0.6455
C6	-0.0447	0.7069	0.6847
C7	-0.0609	0.9142	0.6717
C8	-0.0898	0.9512	0.6143
C9	-0.0955	0.8134	0.5746
C10	-0.1231	0.4655	0.5649
C11	-0.1741	0.4364	0.5894
C12	-0.2152	0.3045	0.5665
C13	-0.2063	0.2037	0.5164
C14	-0.1550	0.2317	0.4915
C15	-0.1134	0.3613	0.5162
C16	-0.2716	0.2663	0.5911
C17	-0.2719	0.0628	0.6198
C18	-0.2321	0.0398	0.6752
C19	-0.2303	-0.1726	0.6965
C20	-0.1879	-0.2182	0.7488
C21	-0.1791	-0.4369	0.7587
C22	-0.1291	-0.4932	0.8054
C23	-0.1181	-0.7155	0.8093
C24	-0.0646	-0.7736	0.8498
C25	-0.0545	-0.9920	0.8538
C26	0.0000	-10.517	0.8942
C27	0.0100	-12.739	0.8952
C28	-0.0509	0.2123	0.4157
C29	-0.0455	0.0085	0.4242

C30	-0.0707	-0.1209	0.3838
C31	-0.1005	-0.0600	0.3329
C32	-0.1059	0.1419	0.3246
C33	-0.0812	0.2731	0.3650
C34	-0.1253	-0.1990	0.2861
C35	-0.0846	-0.2298	0.2410
C36	-0.1160	-0.3272	0.1875
C37	-0.1372	-0.5353	0.1932
C38	-0.1773	-0.6091	0.1425
C39	-0.1929	-0.8224	0.1432
C40	-0.2439	-0.8839	0.0988
C41	-0.2561	-11.034	0.0948
C42	-0.3069	-11.638	0.0522
C43	-0.3184	-13.823	0.0485
C44	-0.3691	-14.475	0.0059
C45	-0.3796	-16.663	0.0028
H51	-0.0399	0.4413	0.6555
H61	-0.0299	0.6696	0.7223
H81	-0.1066	10.776	0.6067
H91	-0.1138	0.8469	0.5378
H111	-0.1807	0.5060	0.6224
H131	-0.2356	0.1146	0.5002
H141	-0.1490	0.1710	0.4569
H161	-0.3044	0.2760	0.5624
H162	-0.2745	0.3642	0.6189
H171	-0.2596	-0.0305	0.5943
H172	-0.3109	0.0340	0.6260
H181	-0.1935	0.0797	0.6707
H182	-0.2465	0.1203	0.7027
H191	-0.2192	-0.2528	0.6672
H192	-0.2685	-0.2078	0.7035
H201	-0.1512	-0.1588	0.7458
H202	-0.2032	-0.1664	0.7807
H211	-0.1697	-0.4898	0.7243
H212	-0.2146	-0.4934	0.7670
H221	-0.0944	-0.4266	0.7991
H222	-0.1401	-0.4530	0.8406
H231	-0.1109	-0.7568	0.7729
H232	-0.1517	-0.7811	0.8189
H241	-0.0307	-0.7088	0.8404
H242	-0.0716	-0.7340	0.8864
H251	-0.0484	-10.319	0.8170
H252	-0.0880	-10.569	0.8641
H261	0.0334	-0.9886	0.8831
H262	-0.0060	-10.065	0.9306
H271	0.0435	-13.055	0.9216
H272	0.0158	-13.182	0.8587
H273	-0.0235	-13.360	0.9062
H291	-0.0250	-0.0373	0.4589
H301	-0.0680	-0.2586	0.3897

H321	-0.1257	0.1877	0.2896
H331	-0.0856	0.4104	0.3591
H341	-0.1613	-0.1454	0.2685
H342	-0.1323	-0.3231	0.3019
H351	-0.0691	-0.1058	0.2324
H352	-0.0534	-0.3143	0.2558
H361	-0.0901	-0.3274	0.1598
H362	-0.1496	-0.2502	0.1745
H371	-0.1040	-0.6188	0.1999
H372	-0.1583	-0.5405	0.2247
H381	-0.1572	-0.5893	0.1108
H382	-0.2121	-0.5325	0.1383
H391	-0.1600	-0.9012	0.1383
H392	-0.2047	-0.8494	0.1791
H401	-0.2339	-0.8438	0.0633
H402	-0.2783	-0.8169	0.1060
H411	-0.2221	-11.693	0.0861
H412	-0.2643	-11.434	0.1310
H421	-0.2994	-11.178	0.0164
H422	-0.3412	-11.024	0.0619
H431	-0.2842	-14.430	0.0385
H432	-0.3253	-14.280	0.0845
H441	-0.3622	-14.026	-0.0303
H442	-0.4034	-13.865	0.0158
H451	-0.4123	-16.962	-0.0246
H452	-0.3456	-17.284	-0.0073
H453	-0.3868	-17.122	0.0387
O1	10.494	-0.0465	0.2938
C1	10.245	0.6460	0.5416
C2	10.544	0.5783	0.4974
C3	10.305	0.4417	0.4570
C4	10.738	0.3911	0.4144
C5	10.503	0.4272	0.3545
C6	10.447	0.2931	0.3153
C7	10.609	0.0857	0.3283
C8	10.898	0.0487	0.3857
C9	10.955	0.1867	0.4254
C10	11.231	0.5344	0.4351
C11	11.741	0.5635	0.4106
C12	12.152	0.6956	0.4335
C13	12.063	0.7964	0.4836
C14	11.550	0.7684	0.5085
C15	11.134	0.6388	0.4838
C16	12.716	0.7336	0.4089
C17	12.719	0.9371	0.3802
C18	12.321	0.9603	0.3248
C19	12.303	11.725	0.3035
C20	11.880	12.183	0.2512
C21	11.791	14.369	0.2413
C22	11.291	14.931	0.1946

C23	11.181	17.155	0.1907
C24	10.646	17.737	0.1502
C25	10.545	19.919	0.1462
C26	10.000	20.517	0.1058
C27	0.9900	22.738	0.1048
C28	10.509	0.7877	0.5843
C29	10.455	0.9914	0.5758
C30	10.707	11.208	0.6162
C31	11.005	10.599	0.6671
C32	11.059	0.8580	0.6754
C33	10.812	0.7268	0.6350
C34	11.253	11.989	0.7139
C35	10.846	12.297	0.7590
C36	11.160	13.273	0.8125
C37	11.372	15.354	0.8068
C38	11.773	16.091	0.8575
C39	11.929	18.223	0.8568
C40	12.439	18.839	0.9012
C41	12.561	21.033	0.9052
C42	13.069	21.639	0.9478
C43	13.184	23.824	0.9515
C44	13.691	24.474	0.9941
C45	13.796	26.664	0.9972
H51	10.399	0.5587	0.3445
H61	10.299	0.3305	0.2777
H81	11.066	-0.0775	0.3933
H91	11.138	0.1532	0.4622
H111	11.807	0.4939	0.3776
H131	12.356	0.8855	0.4998
H141	11.490	0.8291	0.5431
H161	13.044	0.7240	0.4376
H162	12.745	0.6359	0.3811
H171	12.596	10.305	0.4057
H172	13.109	0.9659	0.3740
H181	11.935	0.9202	0.3293
H182	12.465	0.8797	0.2973
H191	12.192	12.528	0.3328
H192	12.685	12.079	0.2965
H201	11.512	11.589	0.2542
H202	12.032	11.663	0.2193
H211	11.697	14.898	0.2757
H212	12.146	14.934	0.2330
H221	10.944	14.267	0.2009
H222	11.401	14.529	0.1594
H231	11.109	17.567	0.2271
H232	11.517	17.812	0.1811
H241	10.307	17.089	0.1596
H242	10.716	17.340	0.1136
H251	10.484	20.318	0.1830
H252	10.880	20.568	0.1359

H261	0.9666	19.887	0.1169
H262	10.060	20.066	0.0694
H271	0.9565	23.054	0.0784
H272	0.9842	23.181	0.1413
H273	10.235	23.360	0.0938
H291	10.250	10.373	0.5411
H301	10.680	12.586	0.6103
H321	11.257	0.8122	0.7104
H331	10.856	0.5895	0.6409
H341	11.613	11.454	0.7315
H342	11.323	13.231	0.6981
H351	10.691	11.057	0.7676
H352	10.534	13.143	0.7442
H361	10.901	13.275	0.8402
H362	11.496	12.501	0.8255
H371	11.040	16.189	0.8001
H372	11.583	15.405	0.7753
H381	11.572	15.894	0.8892
H382	12.121	15.326	0.8617
H391	11.600	19.012	0.8617
H392	12.047	18.493	0.8209
H401	12.339	18.439	0.9367
H402	12.783	18.169	0.8940
H411	12.221	21.692	0.9139
H412	12.643	21.434	0.8690
H421	12.994	21.178	0.9836
H422	13.412	21.024	0.9381
H431	12.842	24.430	0.9615
H432	13.253	24.281	0.9155
H441	13.622	24.027	10.303
H442	14.034	23.865	0.9842
H451	14.123	26.962	10.246
H452	13.456	27.284	10.073
H453	13.868	27.123	0.9613
O1	0.9506	10.464	0.7062
C1	0.9755	0.3541	0.4584
C2	0.9456	0.4216	0.5026
C3	0.9694	0.5584	0.5430
C4	0.9262	0.6088	0.5856
C5	0.9497	0.5729	0.6455
C6	0.9553	0.7069	0.6847
C7	0.9391	0.9142	0.6717
C8	0.9102	0.9512	0.6143
C9	0.9045	0.8134	0.5746
C10	0.8768	0.4655	0.5649
C11	0.8258	0.4364	0.5894
C12	0.7848	0.3045	0.5665
C13	0.7937	0.2037	0.5164
C14	0.8450	0.2317	0.4915
C15	0.8866	0.3613	0.5162

C16	0.7284	0.2663	0.5911
C17	0.7281	0.0628	0.6198
C18	0.7679	0.0398	0.6752
C19	0.7697	-0.1726	0.6965
C20	0.8121	-0.2182	0.7488
C21	0.8209	-0.4369	0.7587
C22	0.8709	-0.4932	0.8054
C23	0.8819	-0.7155	0.8093
C24	0.9354	-0.7736	0.8498
C25	0.9455	-0.9920	0.8538
C26	10.000	-10.517	0.8942
C27	10.100	-12.739	0.8952
C28	0.9491	0.2123	0.4157
C29	0.9545	0.0085	0.4242
C30	0.9293	-0.1209	0.3838
C31	0.8995	-0.0600	0.3329
C32	0.8941	0.1419	0.3246
C33	0.9188	0.2731	0.3650
C34	0.8746	-0.1990	0.2861
C35	0.9154	-0.2298	0.2410
C36	0.8839	-0.3272	0.1875
C37	0.8628	-0.5353	0.1932
C38	0.8227	-0.6091	0.1425
C39	0.8071	-0.8224	0.1432
C40	0.7561	-0.8839	0.0988
C41	0.7439	-11.034	0.0948
C42	0.6931	-11.638	0.0522
C43	0.6816	-13.823	0.0485
C44	0.6309	-14.475	0.0059
C45	0.6203	-16.663	0.0028
H51	0.9601	0.4413	0.6555
H61	0.9701	0.6696	0.7223
H81	0.8934	10.776	0.6067
H91	0.8862	0.8469	0.5378
H111	0.8193	0.5060	0.6224
H131	0.7644	0.1146	0.5002
H141	0.8510	0.1710	0.4569
H161	0.6956	0.2760	0.5624
H162	0.7255	0.3642	0.6189
H171	0.7404	-0.0305	0.5943
H172	0.6891	0.0340	0.6260
H181	0.8065	0.0797	0.6707
H182	0.7535	0.1203	0.7027
H191	0.7808	-0.2528	0.6672
H192	0.7315	-0.2078	0.7035
H201	0.8488	-0.1588	0.7458
H202	0.7968	-0.1664	0.7807
H211	0.8303	-0.4898	0.7243
H212	0.7854	-0.4934	0.7670
H221	0.9056	-0.4266	0.7991

H222	0.8599	-0.4530	0.8406
H231	0.8891	-0.7568	0.7729
H232	0.8483	-0.7811	0.8189
H241	0.9693	-0.7088	0.8404
H242	0.9284	-0.7340	0.8864
H251	0.9516	-10.319	0.8170
H252	0.9120	-10.569	0.8641
H261	10.334	-0.9886	0.8831
H262	0.9940	-10.065	0.9306
H271	10.435	-13.055	0.9216
H272	10.158	-13.182	0.8587
H273	0.9765	-13.360	0.9062
H291	0.9750	-0.0373	0.4589
H301	0.9320	-0.2586	0.3897
H321	0.8743	0.1877	0.2896
H331	0.9144	0.4104	0.3591
H341	0.8387	-0.1454	0.2685
H342	0.8677	-0.3231	0.3019
H351	0.9309	-0.1058	0.2324
H352	0.9466	-0.3143	0.2558
H361	0.9099	-0.3274	0.1598
H362	0.8504	-0.2502	0.1745
H371	0.8960	-0.6188	0.1999
H372	0.8417	-0.5405	0.2247
H381	0.8428	-0.5893	0.1108
H382	0.7879	-0.5325	0.1383
H391	0.8400	-0.9012	0.1383
H392	0.7953	-0.8494	0.1791
H401	0.7661	-0.8438	0.0633
H402	0.7217	-0.8169	0.1060
H411	0.7779	-11.693	0.0861
H412	0.7357	-11.434	0.1310
H421	0.7006	-11.178	0.0164
H422	0.6588	-11.024	0.0619
H431	0.7158	-14.430	0.0385
H432	0.6747	-14.280	0.0845
H441	0.6378	-14.026	-0.0303
H442	0.5966	-13.865	0.0158
H451	0.5877	-16.962	-0.0246
H452	0.6544	-17.284	-0.0073
H453	0.6132	-17.122	0.0387
O1	0.4506	-0.5465	0.7062
C1	0.4755	0.1460	0.4584
C2	0.4456	0.0784	0.5026
C3	0.4694	-0.0583	0.5430
C4	0.4262	-0.1089	0.5856
C5	0.4497	-0.0728	0.6455
C6	0.4553	-0.2069	0.6847
C7	0.4391	-0.4143	0.6717
C8	0.4101	-0.4512	0.6143

C9	0.4045	-0.3134	0.5746
C10	0.3769	0.0345	0.5649
C11	0.3258	0.0635	0.5894
C12	0.2848	0.1956	0.5665
C13	0.2937	0.2964	0.5164
C14	0.3450	0.2683	0.4915
C15	0.3866	0.1388	0.5162
C16	0.2283	0.2336	0.5911
C17	0.2281	0.4372	0.6198
C18	0.2679	0.4602	0.6752
C19	0.2697	0.6725	0.6965
C20	0.3120	0.7182	0.7488
C21	0.3209	0.9370	0.7587
C22	0.3708	0.9932	0.8054
C23	0.3819	12.155	0.8093
C24	0.4354	12.738	0.8498
C25	0.4455	14.920	0.8538
C26	0.5000	15.517	0.8942
C27	0.5101	17.739	0.8952
C28	0.4491	0.2878	0.4157
C29	0.4546	0.4915	0.4242
C30	0.4292	0.6209	0.3838
C31	0.3995	0.5600	0.3329
C32	0.3941	0.3581	0.3246
C33	0.4188	0.2269	0.3650
C34	0.3747	0.6990	0.2861
C35	0.4154	0.7298	0.2410
C36	0.3839	0.8274	0.1875
C37	0.3627	10.354	0.1932
C38	0.3227	11.091	0.1425
C39	0.3071	13.223	0.1432
C40	0.2561	13.840	0.0988
C41	0.2438	16.033	0.0948
C42	0.1931	16.640	0.0522
C43	0.1815	18.825	0.0485
C44	0.1309	19.475	0.0059
C45	0.1204	21.663	0.0028
H51	0.4601	0.0587	0.6555
H61	0.4701	-0.1696	0.7223
H81	0.3934	-0.5774	0.6067
H91	0.3862	-0.3468	0.5378
H111	0.3193	-0.0060	0.6224
H131	0.2644	0.3854	0.5002
H141	0.3510	0.3292	0.4569
H161	0.1956	0.2239	0.5624
H162	0.2255	0.1357	0.6189
H171	0.2404	0.5305	0.5943
H172	0.1891	0.4659	0.6260
H181	0.3065	0.4203	0.6707
H182	0.2535	0.3796	0.7027

H191	0.2808	0.7528	0.6672
H192	0.2315	0.7078	0.7035
H201	0.3488	0.6587	0.7458
H202	0.2968	0.6664	0.7807
H211	0.3303	0.9898	0.7243
H212	0.2854	0.9935	0.7670
H221	0.4056	0.9266	0.7991
H222	0.3599	0.9530	0.8406
H231	0.3891	12.567	0.7729
H232	0.3483	12.812	0.8189
H241	0.4693	12.087	0.8404
H242	0.4284	12.340	0.8864
H251	0.4516	15.319	0.8170
H252	0.4120	15.568	0.8641
H261	0.5334	14.887	0.8831
H262	0.4940	15.066	0.9306
H271	0.5435	18.054	0.9216
H272	0.5158	18.182	0.8587
H273	0.4765	18.359	0.9062
H291	0.4750	0.5372	0.4589
H301	0.4320	0.7585	0.3897
H321	0.3743	0.3123	0.2896
H331	0.4144	0.0895	0.3591
H341	0.3387	0.6454	0.2685
H342	0.3677	0.8231	0.3019
H351	0.4309	0.6058	0.2324
H352	0.4466	0.8143	0.2558
H361	0.4099	0.8274	0.1598
H362	0.3504	0.7502	0.1745
H371	0.3960	11.189	0.1999
H372	0.3417	10.404	0.2247
H381	0.3428	10.894	0.1108
H382	0.2879	10.327	0.1383
H391	0.3400	14.011	0.1383
H392	0.2953	13.493	0.1791
H401	0.2661	13.438	0.0633
H402	0.2217	13.169	0.1060
H411	0.2779	16.692	0.0861
H412	0.2357	16.434	0.1310
H421	0.2006	16.177	0.0164
H422	0.1588	16.025	0.0619
H431	0.2158	19.431	0.0385
H432	0.1747	19.279	0.0845
H441	0.1378	19.026	-0.0303
H442	0.0966	18.866	0.0158
H451	0.0877	21.962	-0.0246
H452	0.1544	22.283	-0.0073
H453	0.1132	22.123	0.0387
O1	0.5494	0.5465	0.2938
C1	0.5245	-0.1460	0.5416

C2	0.5544	-0.0784	0.4974
C3	0.5306	0.0583	0.4570
C4	0.5738	0.1089	0.4144
C5	0.5503	0.0728	0.3545
C6	0.5447	0.2069	0.3153
C7	0.5609	0.4143	0.3283
C8	0.5899	0.4512	0.3857
C9	0.5955	0.3134	0.4254
C10	0.6231	-0.0345	0.4351
C11	0.6742	-0.0635	0.4106
C12	0.7152	-0.1956	0.4335
C13	0.7063	-0.2964	0.4836
C14	0.6550	-0.2683	0.5085
C15	0.6134	-0.1388	0.4838
C16	0.7717	-0.2336	0.4089
C17	0.7719	-0.4372	0.3802
C18	0.7321	-0.4602	0.3248
C19	0.7303	-0.6725	0.3035
C20	0.6879	-0.7182	0.2512
C21	0.6791	-0.9370	0.2413
C22	0.6291	-0.9932	0.1946
C23	0.6181	-12.155	0.1907
C24	0.5646	-12.738	0.1502
C25	0.5545	-14.920	0.1462
C26	0.5000	-15.517	0.1058
C27	0.4899	-17.739	0.1048
C28	0.5508	-0.2878	0.5843
C29	0.5454	-0.4915	0.5758
C30	0.5707	-0.6209	0.6162
C31	0.6005	-0.5600	0.6671
C32	0.6059	-0.3581	0.6754
C33	0.5812	-0.2269	0.6350
C34	0.6253	-0.6990	0.7139
C35	0.5846	-0.7298	0.7590
C36	0.6161	-0.8274	0.8125
C37	0.6373	-10.354	0.8068
C38	0.6773	-11.091	0.8575
C39	0.6929	-13.223	0.8568
C40	0.7439	-13.840	0.9012
C41	0.7562	-16.033	0.9052
C42	0.8069	-16.640	0.9478
C43	0.8185	-18.825	0.9515
C44	0.8691	-19.475	0.9941
C45	0.8796	-21.663	0.9972
H51	0.5399	-0.0587	0.3445
H61	0.5299	0.1696	0.2777
H81	0.6066	0.5774	0.3933
H91	0.6138	0.3468	0.4622
H111	0.6807	0.0060	0.3776
H131	0.7356	-0.3854	0.4998

H141	0.6490	-0.3292	0.5431
H161	0.8044	-0.2239	0.4376
H162	0.7745	-0.1357	0.3811
H171	0.7596	-0.5305	0.4057
H172	0.8109	-0.4659	0.3740
H181	0.6935	-0.4203	0.3293
H182	0.7465	-0.3796	0.2973
H191	0.7192	-0.7528	0.3328
H192	0.7685	-0.7078	0.2965
H201	0.6512	-0.6587	0.2542
H202	0.7032	-0.6664	0.2193
H211	0.6697	-0.9898	0.2757
H212	0.7146	-0.9935	0.2330
H221	0.5944	-0.9266	0.2009
H222	0.6401	-0.9530	0.1594
H231	0.6109	-12.567	0.2271
H232	0.6517	-12.812	0.1811
H241	0.5307	-12.087	0.1596
H242	0.5716	-12.340	0.1136
H251	0.5484	-15.319	0.1830
H252	0.5880	-15.568	0.1359
H261	0.4666	-14.887	0.1169
H262	0.5060	-15.066	0.0694
H271	0.4565	-18.054	0.0784
H272	0.4842	-18.182	0.1413
H273	0.5235	-18.359	0.0938
H291	0.5250	-0.5372	0.5411
H301	0.5680	-0.7585	0.6103
H321	0.6257	-0.3123	0.7104
H331	0.5856	-0.0895	0.6409
H341	0.6613	-0.6454	0.7315
H342	0.6323	-0.8231	0.6981
H351	0.5691	-0.6058	0.7676
H352	0.5534	-0.8143	0.7442
H361	0.5901	-0.8274	0.8402
H362	0.6496	-0.7502	0.8255
H371	0.6040	-11.189	0.8001
H372	0.6583	-10.404	0.7753
H381	0.6572	-10.894	0.8892
H382	0.7121	-10.327	0.8617
H391	0.6600	-14.011	0.8617
H392	0.7047	-13.493	0.8209
H401	0.7339	-13.438	0.9367
H402	0.7783	-13.169	0.8940
H411	0.7221	-16.692	0.9139
H412	0.7643	-16.434	0.8690
H421	0.7994	-16.177	0.9836
H422	0.8412	-16.025	0.9381
H431	0.7842	-19.431	0.9615
H432	0.8253	-19.279	0.9155

H441	0.8622	-19.026	10.303
H442	0.9034	-18.866	0.9842
H451	0.9123	-21.962	10.246
H452	0.8456	-22.283	10.073
H453	0.8868	-22.123	0.9613
O1	0.4506	0.4536	0.7062
C1	0.4755	11.459	0.4584
C2	0.4456	10.783	0.5026
C3	0.4694	0.9417	0.5430
C4	0.4262	0.8910	0.5856
C5	0.4497	0.9271	0.6455
C6	0.4553	0.7932	0.6847
C7	0.4391	0.5858	0.6717
C8	0.4101	0.5488	0.6143
C9	0.4045	0.6866	0.5746
C10	0.3769	10.346	0.5649
C11	0.3258	10.636	0.5894
C12	0.2848	11.955	0.5665
C13	0.2937	12.964	0.5164
C14	0.3450	12.683	0.4915
C15	0.3866	11.387	0.5162
C16	0.2283	12.335	0.5911
C17	0.2281	14.371	0.6198
C18	0.2679	14.603	0.6752
C19	0.2697	16.726	0.6965
C20	0.3120	17.182	0.7488
C21	0.3209	19.369	0.7587
C22	0.3708	19.931	0.8054
C23	0.3819	22.156	0.8093
C24	0.4354	22.737	0.8498
C25	0.4455	24.920	0.8538
C26	0.5000	25.518	0.8942
C27	0.5101	27.739	0.8952
C28	0.4491	12.877	0.4157
C29	0.4546	14.914	0.4242
C30	0.4292	16.208	0.3838
C31	0.3995	15.599	0.3329
C32	0.3941	13.580	0.3246
C33	0.4188	12.269	0.3650
C34	0.3747	16.989	0.2861
C35	0.4154	17.298	0.2410
C36	0.3839	18.273	0.1875
C37	0.3627	20.354	0.1932
C38	0.3227	21.092	0.1425
C39	0.3071	23.223	0.1432
C40	0.2561	23.839	0.0988
C41	0.2438	26.033	0.0948
C42	0.1931	26.639	0.0522
C43	0.1815	28.824	0.0485
C44	0.1309	29.475	0.0059

C45	0.1204	31.663	0.0028
H51	0.4601	10.588	0.6555
H61	0.4701	0.8304	0.7223
H81	0.3934	0.4225	0.6067
H91	0.3862	0.6532	0.5378
H111	0.3193	0.9941	0.6224
H131	0.2644	13.854	0.5002
H141	0.3510	13.291	0.4569
H161	0.1956	12.240	0.5624
H162	0.2255	11.358	0.6189
H171	0.2404	15.306	0.5943
H172	0.1891	14.658	0.6260
H181	0.3065	14.204	0.6707
H182	0.2535	13.797	0.7027
H191	0.2808	17.527	0.6672
H192	0.2315	17.078	0.7035
H201	0.3488	16.588	0.7458
H202	0.2968	16.664	0.7807
H211	0.3303	19.897	0.7243
H212	0.2854	19.934	0.7670
H221	0.4056	19.266	0.7991
H222	0.3599	19.530	0.8406
H231	0.3891	22.567	0.7729
H232	0.3483	22.812	0.8189
H241	0.4693	22.088	0.8404
H242	0.4284	22.341	0.8864
H251	0.4516	25.320	0.8170
H252	0.4120	25.568	0.8641
H261	0.5334	24.887	0.8831
H262	0.4940	25.066	0.9306
H271	0.5435	28.053	0.9216
H272	0.5158	28.183	0.8587
H273	0.4765	28.360	0.9062
H291	0.4750	15.373	0.4589
H301	0.4320	17.586	0.3897
H321	0.3743	13.123	0.2896
H331	0.4144	10.894	0.3591
H341	0.3387	16.455	0.2685
H342	0.3677	18.232	0.3019
H351	0.4309	16.058	0.2324
H352	0.4466	18.144	0.2558
H361	0.4099	18.274	0.1598
H362	0.3504	17.502	0.1745
H371	0.3960	21.189	0.1999
H372	0.3417	20.405	0.2247
H381	0.3428	20.894	0.1108
H382	0.2879	20.326	0.1383
H391	0.3400	24.012	0.1383
H392	0.2953	23.493	0.1791
H401	0.2661	23.438	0.0633

H402	0.2217	23.170	0.1060
H411	0.2779	26.692	0.0861
H412	0.2357	26.433	0.1310
H421	0.2006	26.178	0.0164
H422	0.1588	26.024	0.0619
H431	0.2158	29.430	0.0385
H432	0.1747	29.280	0.0845
H441	0.1378	29.026	-0.0303
H442	0.0966	28.865	0.0158
H451	0.0877	31.963	-0.0246
H452	0.1544	32.284	-0.0073
H453	0.1132	32.123	0.0387
O1	0.5494	15.464	0.2938
C1	0.5245	0.8541	0.5416
C2	0.5544	0.9217	0.4974
C3	0.5306	10.583	0.4570
C4	0.5738	11.090	0.4144
C5	0.5503	10.729	0.3545
C6	0.5447	12.068	0.3153
C7	0.5609	14.142	0.3283
C8	0.5899	14.512	0.3857
C9	0.5955	13.134	0.4254
C10	0.6231	0.9654	0.4351
C11	0.6742	0.9364	0.4106
C12	0.7152	0.8045	0.4335
C13	0.7063	0.7036	0.4836
C14	0.6550	0.7317	0.5085
C15	0.6134	0.8613	0.4838
C16	0.7717	0.7665	0.4089
C17	0.7719	0.5629	0.3802
C18	0.7321	0.5397	0.3248
C19	0.7303	0.3274	0.3035
C20	0.6879	0.2818	0.2512
C21	0.6791	0.0631	0.2413
C22	0.6291	0.0069	0.1946
C23	0.6181	-0.2156	0.1907
C24	0.5646	-0.2737	0.1502
C25	0.5545	-0.4920	0.1462
C26	0.5000	-0.5518	0.1058
C27	0.4899	-0.7739	0.1048
C28	0.5508	0.7123	0.5843
C29	0.5454	0.5086	0.5758
C30	0.5707	0.3792	0.6162
C31	0.6005	0.4401	0.6671
C32	0.6059	0.6420	0.6754
C33	0.5812	0.7731	0.6350
C34	0.6253	0.3011	0.7139
C35	0.5846	0.2702	0.7590
C36	0.6161	0.1727	0.8125
C37	0.6373	-0.0354	0.8068

C38	0.6773	-0.1092	0.8575
C39	0.6929	-0.3223	0.8568
C40	0.7439	-0.3839	0.9012
C41	0.7562	-0.6033	0.9052
C42	0.8069	-0.6639	0.9478
C43	0.8185	-0.8824	0.9515
C44	0.8691	-0.9475	0.9941
C45	0.8796	-11.663	0.9972
H51	0.5399	0.9412	0.3445
H61	0.5299	11.696	0.2777
H81	0.6066	15.775	0.3933
H91	0.6138	13.468	0.4622
H111	0.6807	10.059	0.3776
H131	0.7356	0.6146	0.4998
H141	0.6490	0.6709	0.5431
H161	0.8044	0.7760	0.4376
H162	0.7745	0.8642	0.3811
H171	0.7596	0.4694	0.4057
H172	0.8109	0.5342	0.3740
H181	0.6935	0.5796	0.3293
H182	0.7465	0.6203	0.2973
H191	0.7192	0.2473	0.3328
H192	0.7685	0.2922	0.2965
H201	0.6512	0.3412	0.2542
H202	0.7032	0.3336	0.2193
H211	0.6697	0.0103	0.2757
H212	0.7146	0.0066	0.2330
H221	0.5944	0.0734	0.2009
H222	0.6401	0.0470	0.1594
H231	0.6109	-0.2567	0.2271
H232	0.6517	-0.2812	0.1811
H241	0.5307	-0.2088	0.1596
H242	0.5716	-0.2341	0.1136
H251	0.5484	-0.5320	0.1830
H252	0.5880	-0.5568	0.1359
H261	0.4666	-0.4887	0.1169
H262	0.5060	-0.5066	0.0694
H271	0.4565	-0.8053	0.0784
H272	0.4842	-0.8183	0.1413
H273	0.5235	-0.8360	0.0938
H291	0.5250	0.4627	0.5411
H301	0.5680	0.2414	0.6103
H321	0.6257	0.6877	0.7104
H331	0.5856	0.9106	0.6409
H341	0.6613	0.3545	0.7315
H342	0.6323	0.1768	0.6981
H351	0.5691	0.3942	0.7676
H352	0.5534	0.1856	0.7442
H361	0.5901	0.1726	0.8402
H362	0.6496	0.2498	0.8255

H371	0.6040	-0.1189	0.8001
H372	0.6583	-0.0405	0.7753
H381	0.6572	-0.0894	0.8892
H382	0.7121	-0.0326	0.8617
H391	0.6600	-0.4012	0.8617
H392	0.7047	-0.3493	0.8209
H401	0.7339	-0.3438	0.9367
H402	0.7783	-0.3170	0.8940
H411	0.7221	-0.6692	0.9139
H412	0.7643	-0.6433	0.8690
H421	0.7994	-0.6178	0.9836
H422	0.8412	-0.6024	0.9381
H431	0.7842	-0.9430	0.9615
H432	0.8253	-0.9280	0.9155
H441	0.8622	-0.9026	10.303
H442	0.9034	-0.8865	0.9842
H451	0.9123	-11.963	10.246
H452	0.8456	-12.284	10.073
H453	0.8868	-12.123	0.9613

Atom1	Atom2	Bond length / Å	Atom1	Atom2	Bond length / Å
C1	C2	1.415	C23	C24	1.513
C2	C3	1.399	C24	C25	1.506
C3	C4	1.557	C25	C26	1.531
C4	C5	1.480	C26	C27	1.531
C5	C6	1.303	C1	C28	1.475
O1	C7	1.226	C28	C29	1.406
C6	C7	1.484	C29	C30	1.377
C7	C8	1.463	C30	C31	1.376
C4	C9	1.491	C31	C32	1.393
C8	C9	1.329	C28	C33	1.377
C4	C10	1.530	C32	C33	1.380
C10	C11	1.397	C31	C34	1.518
C11	C12	1.366	C34	C35	1.536
C12	C13	1.419	C35	C36	1.534
C13	C14	1.407	C36	C37	1.512
C2	C15	1.498	C37	C38	1.506
C10	C15	1.409	C38	C39	1.498
C14	C15	1.375	C39	C40	1.532
C12	C16	1.520	C40	C41	1.522
C16	C17	1.548	C41	C42	1.500
C17	C18	1.512	C42	C43	1.513
C18	C19	1.532	C43	C44	1.508
C19	C20	1.510	C44	C45	1.512
C20	C21	1.518	C5	H51	0.949
C21	C22	1.539	C6	H61	0.950
C22	C23	1.537	C8	H81	0.950

C9	H91	0.951	C42	H422	0.951
C11	H111	0.949	C43	H431	0.949
C13	H131	0.950	C43	H432	0.949
C14	H141	0.951	C44	H441	0.950
C16	H161	0.950	C44	H442	0.950
C16	H162	0.950	C45	H451	0.949
C17	H171	0.951	C45	H452	0.951
C17	H172	0.950	C45	H453	0.949
C18	H181	0.951	C3	C1	1.406
C18	H182	0.950	C1	C2	1.415
C19	H191	0.950	C1	C3	1.406
C19	H192	0.949	C2	C3	1.400
C20	H201	0.951	C3	C4	1.557
C20	H202	0.950	C4	C5	1.480
C21	H211	0.950	C5	C6	1.302
C21	H212	0.949	O1	C7	1.226
C22	H221	0.950	C6	C7	1.484
C22	H222	0.951	C7	C8	1.463
C23	H231	0.949	C4	C9	1.492
C23	H232	0.950	C8	C9	1.329
C24	H241	0.951	C4	C10	1.530
C24	H242	0.951	C10	C11	1.397
C25	H251	0.950	C11	C12	1.365
C25	H252	0.950	C12	C13	1.419
C26	H261	0.950	C13	C14	1.407
C26	H262	0.950	C2	C15	1.498
C27	H271	0.951	C10	C15	1.408
C27	H272	0.950	C14	C15	1.375
C27	H273	0.949	C12	C16	1.520
C29	H291	0.951	C16	C17	1.548
C30	H301	0.950	C17	C18	1.512
C32	H321	0.950	C18	C19	1.532
C33	H331	0.950	C19	C20	1.510
C34	H341	0.949	C20	C21	1.518
C34	H342	0.949	C21	C22	1.540
C35	H351	0.951	C22	C23	1.537
C35	H352	0.951	C23	C24	1.513
C36	H361	0.950	C24	C25	1.507
C36	H362	0.951	C25	C26	1.531
C37	H371	0.950	C26	C27	1.531
C37	H372	0.950	C1	C28	1.475
C38	H381	0.949	C28	C29	1.407
C38	H382	0.951	C29	C30	1.377
C39	H391	0.950	C30	C31	1.376
C39	H392	0.952	C31	C32	1.393
C40	H401	0.949	C28	C33	1.377
C40	H402	0.951	C32	C33	1.380
C41	H411	0.951	C31	C34	1.518
C41	H412	0.950	C34	C35	1.536
C42	H421	0.949	C35	C36	1.534

C36	C37	1.512	C36	H362	0.951
C37	C38	1.507	C37	H371	0.950
C38	C39	1.498	C37	H372	0.950
C39	C40	1.531	C38	H381	0.949
C40	C41	1.523	C38	H382	0.951
C41	C42	1.500	C39	H391	0.949
C42	C43	1.513	C39	H392	0.952
C43	C44	1.508	C40	H401	0.949
C44	C45	1.511	C40	H402	0.950
C5	H51	0.950	C41	H411	0.951
C6	H61	0.950	C41	H412	0.950
C8	H81	0.951	C42	H421	0.949
C9	H91	0.951	C42	H422	0.951
C11	H111	0.949	C43	H431	0.949
C13	H131	0.950	C43	H432	0.949
C14	H141	0.951	C44	H441	0.951
C16	H161	0.950	C44	H442	0.951
C16	H162	0.951	C45	H451	0.949
C17	H171	0.951	C45	H452	0.951
C17	H172	0.950	C45	H453	0.949
C18	H181	0.951	C1	C2	1.415
C18	H182	0.950	C2	C3	1.399
C19	H191	0.950	C3	C4	1.557
C19	H192	0.949	C4	C5	1.480
C20	H201	0.950	C5	C6	1.303
C20	H202	0.949	O1	C7	1.226
C21	H211	0.950	C6	C7	1.484
C21	H212	0.949	C7	C8	1.463
C22	H221	0.950	C4	C9	1.491
C22	H222	0.951	C8	C9	1.329
C23	H231	0.949	C4	C10	1.530
C23	H232	0.949	C10	C11	1.397
C24	H241	0.951	C11	C12	1.366
C24	H242	0.951	C12	C13	1.419
C25	H251	0.950	C13	C14	1.407
C25	H252	0.950	C2	C15	1.498
C26	H261	0.951	C10	C15	1.409
C26	H262	0.950	C14	C15	1.375
C27	H271	0.951	C12	C16	1.520
C27	H272	0.950	C16	C17	1.548
C27	H273	0.948	C17	C18	1.512
C29	H291	0.951	C18	C19	1.532
C30	H301	0.949	C19	C20	1.510
C32	H321	0.950	C20	C21	1.518
C33	H331	0.950	C21	C22	1.539
C34	H341	0.949	C22	C23	1.537
C34	H342	0.949	C23	C24	1.513
C35	H351	0.951	C24	C25	1.506
C35	H352	0.951	C25	C26	1.531
C36	H361	0.950	C26	C27	1.531

C1	C28	1.475	C27	H273	0.949
C28	C29	1.406	C29	H291	0.951
C29	C30	1.377	C30	H301	0.950
C30	C31	1.376	C32	H321	0.950
C31	C32	1.393	C33	H331	0.950
C28	C33	1.377	C34	H341	0.949
C32	C33	1.380	C34	H342	0.949
C31	C34	1.518	C35	H351	0.951
C34	C35	1.536	C35	H352	0.951
C35	C36	1.534	C36	H361	0.950
C36	C37	1.512	C36	H362	0.951
C37	C38	1.506	C37	H371	0.950
C38	C39	1.498	C37	H372	0.950
C39	C40	1.532	C38	H381	0.949
C40	C41	1.522	C38	H382	0.951
C41	C42	1.500	C39	H391	0.950
C42	C43	1.513	C39	H392	0.952
C43	C44	1.508	C40	H401	0.949
C44	C45	1.512	C40	H402	0.951
C5	H51	0.949	C41	H411	0.951
C6	H61	0.950	C41	H412	0.950
C8	H81	0.950	C42	H421	0.949
C9	H91	0.951	C42	H422	0.951
C11	H111	0.949	C43	H431	0.949
C13	H131	0.950	C43	H432	0.949
C14	H141	0.951	C44	H441	0.950
C16	H161	0.950	C44	H442	0.950
C16	H162	0.950	C45	H451	0.949
C17	H171	0.951	C45	H452	0.951
C17	H172	0.950	C45	H453	0.949
C18	H181	0.951	C3	C1	1.406
C18	H182	0.950	C1	C2	1.415
C19	H191	0.950	C1	C3	1.406
C19	H192	0.949	C2	C3	1.400
C20	H201	0.951	C3	C4	1.557
C20	H202	0.950	C4	C5	1.480
C21	H211	0.950	C5	C6	1.302
C21	H212	0.949	O1	C7	1.226
C22	H221	0.950	C6	C7	1.484
C22	H222	0.951	C7	C8	1.463
C23	H231	0.949	C4	C9	1.492
C23	H232	0.950	C8	C9	1.329
C24	H241	0.951	C4	C10	1.530
C24	H242	0.951	C10	C11	1.397
C25	H251	0.950	C11	C12	1.365
C25	H252	0.950	C12	C13	1.419
C26	H261	0.950	C13	C14	1.407
C26	H262	0.950	C2	C15	1.498
C27	H271	0.951	C10	C15	1.408
C27	H272	0.950	C14	C15	1.375

C12	C16	1.520	C22	H221	0.950
C16	C17	1.548	C22	H222	0.951
C17	C18	1.512	C23	H231	0.949
C18	C19	1.532	C23	H232	0.949
C19	C20	1.510	C24	H241	0.951
C20	C21	1.518	C24	H242	0.951
C21	C22	1.540	C25	H251	0.950
C22	C23	1.537	C25	H252	0.950
C23	C24	1.513	C26	H261	0.951
C24	C25	1.507	C26	H262	0.950
C25	C26	1.531	C27	H271	0.951
C26	C27	1.531	C27	H272	0.950
C1	C28	1.475	C27	H273	0.948
C28	C29	1.407	C29	H291	0.951
C29	C30	1.377	C30	H301	0.949
C30	C31	1.376	C32	H321	0.950
C31	C32	1.393	C33	H331	0.950
C28	C33	1.377	C34	H341	0.949
C32	C33	1.380	C34	H342	0.949
C31	C34	1.518	C35	H351	0.951
C34	C35	1.536	C35	H352	0.951
C35	C36	1.534	C36	H361	0.950
C36	C37	1.512	C36	H362	0.951
C37	C38	1.507	C37	H371	0.950
C38	C39	1.498	C37	H372	0.950
C39	C40	1.531	C38	H381	0.949
C40	C41	1.523	C38	H382	0.951
C41	C42	1.500	C39	H391	0.949
C42	C43	1.513	C39	H392	0.952
C43	C44	1.508	C40	H401	0.949
C44	C45	1.511	C40	H402	0.950
C5	H51	0.950	C41	H411	0.951
C6	H61	0.950	C41	H412	0.950
C8	H81	0.951	C42	H421	0.949
C9	H91	0.951	C42	H422	0.951
C11	H111	0.949	C43	H431	0.949
C13	H131	0.950	C43	H432	0.949
C14	H141	0.951	C44	H441	0.951
C16	H161	0.950	C44	H442	0.951
C16	H162	0.951	C45	H451	0.949
C17	H171	0.951	C45	H452	0.951
C17	H172	0.950	C45	H453	0.949
C18	H181	0.951	C1	C2	1.415
C18	H182	0.950	C2	C3	1.399
C19	H191	0.950	C3	C4	1.557
C19	H192	0.949	C4	C5	1.481
C20	H201	0.950	C5	C6	1.303
C20	H202	0.949	O1	C7	1.226
C21	H211	0.950	C6	C7	1.484
C21	H212	0.949	C7	C8	1.463

C4	C9	1.492	C17	H171	0.951
C8	C9	1.329	C17	H172	0.950
C4	C10	1.529	C18	H181	0.950
C10	C11	1.398	C18	H182	0.950
C11	C12	1.365	C19	H191	0.950
C12	C13	1.419	C19	H192	0.950
C13	C14	1.407	C20	H201	0.951
C2	C15	1.498	C20	H202	0.949
C10	C15	1.409	C21	H211	0.950
C14	C15	1.375	C21	H212	0.948
C12	C16	1.521	C22	H221	0.950
C16	C17	1.548	C22	H222	0.951
C17	C18	1.513	C23	H231	0.949
C18	C19	1.532	C23	H232	0.949
C19	C20	1.510	C24	H241	0.951
C20	C21	1.519	C24	H242	0.951
C21	C22	1.539	C25	H251	0.950
C22	C23	1.537	C25	H252	0.950
C23	C24	1.513	C26	H261	0.950
C24	C25	1.506	C26	H262	0.949
C25	C26	1.531	C27	H271	0.951
C26	C27	1.531	C27	H272	0.950
C1	C28	1.475	C27	H273	0.949
C28	C29	1.406	C29	H291	0.950
C29	C30	1.377	C30	H301	0.949
C30	C31	1.376	C32	H321	0.950
C31	C32	1.393	C33	H331	0.950
C28	C33	1.377	C34	H341	0.950
C32	C33	1.380	C34	H342	0.949
C31	C34	1.518	C35	H351	0.950
C34	C35	1.536	C35	H352	0.950
C35	C36	1.535	C36	H361	0.950
C36	C37	1.512	C36	H362	0.951
C37	C38	1.506	C37	H371	0.951
C38	C39	1.498	C37	H372	0.949
C39	C40	1.532	C38	H381	0.950
C40	C41	1.522	C38	H382	0.950
C41	C42	1.500	C39	H391	0.950
C42	C43	1.513	C39	H392	0.951
C43	C44	1.507	C40	H401	0.950
C44	C45	1.511	C40	H402	0.951
C5	H51	0.949	C41	H411	0.951
C6	H61	0.950	C41	H412	0.950
C8	H81	0.950	C42	H421	0.950
C9	H91	0.951	C42	H422	0.951
C11	H111	0.949	C43	H431	0.950
C13	H131	0.950	C43	H432	0.948
C14	H141	0.952	C44	H441	0.950
C16	H161	0.949	C44	H442	0.950
C16	H162	0.951	C45	H451	0.950

C45	H452	0.951	C42	C43	1.513
C45	H453	0.949	C43	C44	1.507
C3	C1	1.408	C44	C45	1.511
C1	C2	1.415	C5	H51	0.949
C1	C3	1.407	C6	H61	0.950
C2	C3	1.399	C8	H81	0.950
C3	C4	1.557	C9	H91	0.951
C4	C5	1.481	C11	H111	0.949
C5	C6	1.303	C13	H131	0.950
O1	C7	1.226	C14	H141	0.952
C6	C7	1.484	C16	H161	0.949
C7	C8	1.463	C16	H162	0.951
C4	C9	1.492	C17	H171	0.951
C8	C9	1.329	C17	H172	0.950
C4	C10	1.529	C18	H181	0.950
C10	C11	1.398	C18	H182	0.950
C11	C12	1.365	C19	H191	0.950
C12	C13	1.419	C19	H192	0.950
C13	C14	1.407	C20	H201	0.951
C2	C15	1.498	C20	H202	0.950
C10	C15	1.409	C21	H211	0.950
C14	C15	1.375	C21	H212	0.948
C12	C16	1.521	C22	H221	0.950
C16	C17	1.548	C22	H222	0.951
C17	C18	1.513	C23	H231	0.949
C18	C19	1.532	C23	H232	0.949
C19	C20	1.510	C24	H241	0.951
C20	C21	1.519	C24	H242	0.951
C21	C22	1.539	C25	H251	0.950
C22	C23	1.537	C25	H252	0.951
C23	C24	1.513	C26	H261	0.950
C24	C25	1.506	C26	H262	0.949
C25	C26	1.531	C27	H271	0.951
C26	C27	1.531	C27	H272	0.950
C1	C28	1.475	C27	H273	0.949
C28	C29	1.406	C29	H291	0.950
C29	C30	1.377	C30	H301	0.949
C30	C31	1.376	C32	H321	0.950
C31	C32	1.393	C33	H331	0.950
C28	C33	1.377	C34	H341	0.950
C32	C33	1.380	C34	H342	0.949
C31	C34	1.518	C35	H351	0.950
C34	C35	1.536	C35	H352	0.950
C35	C36	1.535	C36	H361	0.950
C36	C37	1.512	C36	H362	0.951
C37	C38	1.506	C37	H371	0.951
C38	C39	1.498	C37	H372	0.949
C39	C40	1.532	C38	H381	0.949
C40	C41	1.522	C38	H382	0.950
C41	C42	1.500	C39	H391	0.950

C39	H392	0.951	C32	C33	1.380
C40	H401	0.949	C31	C34	1.518
C40	H402	0.951	C34	C35	1.536
C41	H411	0.951	C35	C36	1.534
C41	H412	0.950	C36	C37	1.512
C42	H421	0.950	C37	C38	1.507
C42	H422	0.951	C38	C39	1.497
C43	H431	0.950	C39	C40	1.532
C43	H432	0.948	C40	C41	1.522
C44	H441	0.950	C41	C42	1.500
C44	H442	0.950	C42	C43	1.513
C45	H451	0.950	C43	C44	1.507
C45	H452	0.951	C44	C45	1.511
C45	H453	0.949	C5	H51	0.950
C1	C2	1.415	C6	H61	0.950
C2	C3	1.399	C8	H81	0.951
C3	C4	1.557	C9	H91	0.951
C4	C5	1.481	C11	H111	0.949
C5	C6	1.302	C13	H131	0.951
O1	C7	1.226	C14	H141	0.951
C6	C7	1.484	C16	H161	0.949
C7	C8	1.463	C16	H162	0.950
C4	C9	1.491	C17	H171	0.951
C8	C9	1.329	C17	H172	0.950
C4	C10	1.530	C18	H181	0.950
C10	C11	1.398	C18	H182	0.950
C11	C12	1.364	C19	H191	0.949
C12	C13	1.419	C19	H192	0.950
C13	C14	1.407	C20	H201	0.951
C2	C15	1.498	C20	H202	0.949
C10	C15	1.408	C21	H211	0.950
C14	C15	1.375	C21	H212	0.948
C12	C16	1.521	C22	H221	0.950
C16	C17	1.548	C22	H222	0.950
C17	C18	1.513	C23	H231	0.949
C18	C19	1.532	C23	H232	0.949
C19	C20	1.510	C24	H241	0.951
C20	C21	1.518	C24	H242	0.950
C21	C22	1.539	C25	H251	0.950
C22	C23	1.538	C25	H252	0.949
C23	C24	1.513	C26	H261	0.951
C24	C25	1.507	C26	H262	0.950
C25	C26	1.531	C27	H271	0.951
C26	C27	1.531	C27	H272	0.950
C1	C28	1.475	C27	H273	0.949
C28	C29	1.406	C29	H291	0.951
C29	C30	1.377	C30	H301	0.950
C30	C31	1.376	C32	H321	0.949
C31	C32	1.393	C33	H331	0.951
C28	C33	1.377	C34	H341	0.949

C34	H342	0.950	C21	C22	1.539
C35	H351	0.950	C22	C23	1.538
C35	H352	0.950	C23	C24	1.513
C36	H361	0.950	C24	C25	1.507
C36	H362	0.951	C25	C26	1.531
C37	H371	0.951	C26	C27	1.531
C37	H372	0.949	C1	C28	1.475
C38	H381	0.950	C28	C29	1.406
C38	H382	0.950	C29	C30	1.377
C39	H391	0.951	C30	C31	1.376
C39	H392	0.951	C31	C32	1.393
C40	H401	0.949	C28	C33	1.377
C40	H402	0.950	C32	C33	1.380
C41	H411	0.951	C31	C34	1.518
C41	H412	0.950	C34	C35	1.536
C42	H421	0.949	C35	C36	1.534
C42	H422	0.951	C36	C37	1.512
C43	H431	0.950	C37	C38	1.507
C43	H432	0.949	C38	C39	1.497
C44	H441	0.950	C39	C40	1.532
C44	H442	0.951	C40	C41	1.522
C45	H451	0.950	C41	C42	1.500
C45	H452	0.951	C42	C43	1.513
C45	H453	0.949	C43	C44	1.507
C3	C1	1.407	C44	C45	1.511
C1	C2	1.415	C5	H51	0.950
C1	C3	1.406	C6	H61	0.950
C2	C3	1.399	C8	H81	0.951
C3	C4	1.557	C9	H91	0.951
C4	C5	1.481	C11	H111	0.949
C5	C6	1.302	C13	H131	0.951
O1	C7	1.226	C14	H141	0.951
C6	C7	1.484	C16	H161	0.949
C7	C8	1.463	C16	H162	0.950
C4	C9	1.491	C17	H171	0.951
C8	C9	1.329	C17	H172	0.950
C4	C10	1.530	C18	H181	0.950
C10	C11	1.398	C18	H182	0.950
C11	C12	1.364	C19	H191	0.949
C12	C13	1.419	C19	H192	0.950
C13	C14	1.407	C20	H201	0.951
C2	C15	1.498	C20	H202	0.950
C10	C15	1.408	C21	H211	0.950
C14	C15	1.375	C21	H212	0.948
C12	C16	1.521	C22	H221	0.950
C16	C17	1.548	C22	H222	0.950
C17	C18	1.513	C23	H231	0.949
C18	C19	1.532	C23	H232	0.949
C19	C20	1.510	C24	H241	0.951
C20	C21	1.518	C24	H242	0.950

C25	H251	0.950	C38	H382	0.950
C25	H252	0.950	C39	H391	0.951
C26	H261	0.951	C39	H392	0.951
C26	H262	0.950	C40	H401	0.949
C27	H271	0.951	C40	H402	0.950
C27	H272	0.950	C41	H411	0.951
C27	H273	0.949	C41	H412	0.950
C29	H291	0.951	C42	H421	0.949
C30	H301	0.950	C42	H422	0.951
C32	H321	0.949	C43	H431	0.950
C33	H331	0.951	C43	H432	0.949
C34	H341	0.949	C44	H441	0.950
C34	H342	0.950	C44	H442	0.951
C35	H351	0.950	C45	H451	0.950
C35	H352	0.950	C45	H452	0.951
C36	H361	0.950	C45	H453	0.949
C36	H362	0.951			
C37	H371	0.951			
C37	H372	0.949			
C38	H381	0.949			
